UNIVERSITÉ PARIS DIDEROT - PARIS 7

THÈSE
Spécialité: Champs, particules, matières

Présentée par

PEREZ PEREZ Luis Alejandro

Pour obtenir le grade de Docteur de L'Université Paris VII

Time-Dependent Amplitude Analysis of $B^0 \to K^0_S\pi^+\pi^-$ decays with the *BABAR* Experiment and constraints on the CKM matrix using the $B \to K^*\pi$ and $B \to \rho K$ modes

Soutenue le Mardi 9 Décembre 2008

Jury :

Rapporteurs: Adrian Bevan
Tatsuya Nakada

Examinateurs: Pascal Debu
François Le Diberder
Luis Oliver

Directeur de thèse: José Ocariz

Acknowledgements

I gratefully acknowledge Adrian Bevan and Tatsuya Nakada for accepting to be the referee of this thesis. I thanks Pascal Debu, François Le Diberder and Luis Oliver for accepting to be part of the jury for this thesis.

I am specially grateful with Pascal Debu for hosting me at the LPNHE-Paris during these three years of thesis.

I would like to acknowledge to the LPNHE *BABAR* group: Jacques, José, Eli, Simon and Jennifer. You gave me many scientific and technical knowledge, many advice and your friendship. These three year that I spend with you has been really enriching. I want to give special thanks to my advisor José Ocariz and Jacques Chauveau for their support and for all that they could teach me in these three years.

I want to thanks my working team in the experimental analysis performed in this thesis, Eli Ben Haïm and Mathew Graham, Pablo Del Amo Sanchez, Timothy Gershon, Jelena Ilic, Thomas Latham, Gagan Mohanty, Nitesh Soni and Pierini, Maurizio.

I want to give special to Jerome Charles for his guide and Robert Cahn for his help in the interpretation part of this thesis. I thanks Reina Camacho for her dedicated work, without which this thesis would have not been completed.

I appreciated very much the long period when I worked as *commissioner* on the *BABAR* Cherenkov detector. I thanks Nicolas Arnaud, Joe Schwiening, Emmanuele Salvati and José Benites for having hosted me in their team.

I would like to thanks to the *BABAR* PhD. students: Francesco, Elisa, Neus, Diego, Viola, Enrico, Jordi, Jesko, Emmanuele, Carlos, José Benitez and Dana. Whom gave me their friendship and with whom I had many special moments. I want to thanks to all my friends in the LPNHE: Rui, Pietro, Stefania, Florant, Jerome, Silvant and Simon. And also to my Venezuelan friends: Henso, Arturo, Hebert, Joany, Reina and Victor. Thank you for you sincere friendship and support.

I would like to thank the rest of the *BABAR* comunity national and international: Italian, Spanish, German, USA, Canadian, British, with whom I shared my daily life in California.

I would like to thanks to the administrative and informatic services teams of the LPNHE for their help.

I would like to thank to the ALBAN program for its financial support during my three years of PhD studies. I want also thank to the HELEN program for giving me the opportunity to share my knowledge about high energy physics with my origin institution in Venezuela (Universidad de Los andes, ULA).

I want to give special thanks to my mother, whom helped me very much in this adventure. Yuly, I thank you for give me all your love, and for being with me in one of the most difficult and enriching moments of my life.

Résumé en français

Le Modèle Standard et la physique des saveurs

Le Modèle Standard des interactions fortes et électrofaibles (MS) résume l'essentiel des connaissances actuelles sur la physique subatomique et des interactions fondamentales (hormis la gravitation). A la date d'aujourd'hui, même si de nombreuses questions restent sans réponse, aucun résultat expérimental ne contredit les prédictions du MS.

Le MS peut se diviser en plusieurs secteurs, faisant reférence aux processus et aux particules auxquelles on s'interesse. Bien qu'il y ait un grand nombre de paramètres libres dans la théorie, l'ajustement électrofaible global révèle un excellent accord avec les données. De ces paramètres, environ la moitié proviennent du secteur de mélange des quarks. Il y a à peine une décennie, ce secteur était un des moins bien testés du modèle (avec les neutrinos), alors même qu'il est le seul où ait été mis en évidence un phénomène de grande importance, à savoir la *violation de CP*.

La violation de CP a éte découverte en 1964, dans les désintégrations des kaons neutres. Peu après, Sakharov montra que celle-ci est un élément nécéssaire pour expliquer l'asymétrie matière/antimatière de l'univers. La matrice de Cabbibo-Kobayashi-Maskawa (CKM), dont les paramètres représentent les amplitudes de mélange des quarks, permet d'accomoder la violation de CP dans le cadre du MS. On sait cependant que ce *mécanisme CKM* est insuffisant pour expliquer l'asymétrie matière/antimatière observée ; on tend à considèrer que la matrice CKM (ainsi que l'ensemble du MS) est une représentation à basse énergie d'une théorie plus fondamentale.

L'étude du secteur des saveurs, en particulier à travers des effets liés à la violation de CP, pourrait révéler une Nouvelle Physique (NP) au-delà du MS. Du fait du succès incontestable du MS, il convient de placer la violation de CP dans un cadre théorique bien établi, pour s'assurer que les possibles déviations par rapport au MS puissent être interprétées comme dues à des effets de NP.

La matrice CKM décrit les transitions entre quarks en termes de quatre paramètres seulement : trois angles de rotation et une phase irréductible. Cette phase contient toute l'information sur la violation de CP. Ce nombre réduit de paramètres fondamentaux fait que le secteur des saveurs est hautement prédictif. L'ambition du programme de physique des saveurs est d'obtenir des mesures redondantes d'observables liées à la matrice CKM.

Dans ce cadre, le but principal des *usines à B*, dont les expériences *BABAR* et Belle sont les représentants en activité depuis une décennie, est de produire une étude systématique des asymétries de CP dans les désintégrations des mésons B. Au-delà de la métrologie de la matrice CKM, qui en est le premier objectif, le programme des usines à B s'est continuellement élargi vers une recherche d'effets de NP ; non seulement en améliorant constamment la précision des mesures, mais aussi en étendant le nombre de processus étudiés, grâce à l'augmentation des échantillons des données disponibles.

Des équipes d'analyse de phénoménologie, où le groupe CKMfitter est un acteur de premier rôle, produisent des études combinées de l'ensemble des mesures disponibles, afin de produire un ajustement global de la matrice CKM. La conséquence est une confirmation éclatante du mécanisme CKM.

Au vu de ce grand succès du MS, un scénario de *Violation Minimale de la Saveur* (VMS) est considéré de nos jours comme une alternative vraisemblable : les possibles contributions de NP se manifesteraient sous la forme de petites perturbations au mécanisme CKM. L'objectif de physique des usines à B s'oriente ainsi de plus en plus vers la recherche d'effets en provenance de cette VMS.

Une approche prometteuse est celle des *analyses en amplitudes*. Egalement appelées analyses de Dalitz, elles permettent d'accèder directement aux amplitudes de désintégration, et de séparer les phases faibles et fortes qui y contribuent, par la résolution des profils d'interférence entre états intermédiaires résonants. Dans le cas des désintégrations des mésons B en trois hadrons légers, les canaux $B \to K\pi\pi$ ont la particularité d'être dominés par des contributions aux ordres supérieurs (boucles), tout en ayant des taux de désintégration relativement importants. De ce fait, les analyses de Dalitz de ces modes peuvent avoir une meilleure sensibilité aux contributions provenant de la NP. Cette approche sous-tend le travail expérimental et phénoménologique présenté dans cette thèse.

Le cadre de travail : l'expérience *BABAR*

Le travail de recherche exposé dans cette thèse s'est réalisé dans le cadre de l'expérience *BABAR*, qui est une collaboration internationale regroupant des institutions de dix pays. Le détecteur *BABAR* est placé auprès du collisionneur PEP-II du Stanford Linear Accelerator Center SLAC, en Californie (Etats-Unis). PEP-II est une usine à B, constitué d'un double anneau de stockage d'électrons et positrons. Les paramètres de collision des faisceaux sont ajustés à la résonance $\Upsilon(4S)$, dont la masse est très légèrement supérieure au seuil de production de paires $B-\bar{B}$; des mésons B sont ainsi produits à un taux très élevé. Le détecteur *BABAR* a été conçu pour enregistrer les produits des désintégrations des mésons B avec d'excellentes performances en termes d'efficacité et de résolution. La période de prise de données de l'expérience *BABAR* a commencé en 1999, et s'est prolongée jusqu'en 2008. La richesse et qualité de la production scientifique de la collaboration *BABAR* contribuent grandement au succès actuel de la physique des saveurs.

Cette thèse comprend deux travaux complémentaires. En premier lieu, la thèse décrit un travail d'analyse de données expérimentales, sous la forme d'une *analyse en amplitudes dépendantes du temps du mode de désintégration* $B^0 \to K^0_S\pi^+\pi^-$. Cette analyse se traduit par plusieurs résultats, du fait de la variété de processus contribuant à la dynamique de ce mode de désintégration. Ensuite vient une analyse de phénoménologie, qui exploite un sous-échantillon des résultats expérimentaux obtenus précédemment, ainsi que les résultats disponibles provenant des autres modes $B \to K\pi\pi$, dans le but d'extraire des contraintes sur la matrice CKM. Cette dernière étude se base sur des travaux théoriques récents, qui sont ici étendus et modifiés avec des contributions originales.

Analyses de physique et résultats

Analyses en ampitudes $B \to K\pi\pi$: Motivation physique

Une prédiction du mécanisme CKM est que les asymétries de CP dépendantes du temps dans les transitions du type $b \to q\bar{q}s$ ("modes dominés par les pingouins"), doivent être, avec une très bonne approximation, les mêmes que dans les transitions du type $b \to c\bar{c}s$ ("modes en or"). Pour ces derniers, les paramètres S et C des asymétries dépendantes du temps (correspondant respectivement à la violation de CP induite par le mélange et à la violation directe de CP) ont pour valeur $S = \sin 2\beta$ et $C = 0$, où β est un des angles du *triangle d'unitarité* de la matrice CKM. Les modes en or sont insensibles à d'éventuelles contributions de NP ; par contre, les termes en boucles sont dominants dans les amplitudes des modes $b \to q\bar{q}s$, et de ce fait leurs amplitudes peuvent être modifiées substantiellement par des contributions au-delà du MS. La mesure de S et C dans les modes dominés par les pingouins représente un test important du MS : un écart significatif par rapport aux valeurs dans les modes en or serait une indication de NP.

Dans l'amplitude de désintégration $B^0 \to K^0_S\pi^+\pi^-$, deux résonances intermédiaires correspondent à des modes dominés par les pingouins : le $\rho^0(770)K^0_S$ et le $f_0(980)K^0_S$. Un avantage additionel d'étudier ces modes avec une analyse de Dalitz dépendante du temps provient du fait que l'interférence entre ces modes permet de mesurer directement la phase β_{eff} de l'asymétrie de CP dépendante du temps, alors que les analyses basées sur des taux de comptage ne peuvent accèder qu'au paramètre $S = \sin 2\beta_{\text{eff}}$.

L'analyse en amplitudes des modes $B \to K\pi\pi$ permet en outre de mesurer les phases relatives entre les modes résonants intermédiaires en pseudoscalaire-vecteur dans l'état final. Pour le canal $B^0 \to K^0_S\pi^+\pi^-$, en plus du mode $\rho^0(770)K^0_S$ déjà évoqué, l'état final a aussi une contribution du mode $K^{*+}(892)\pi^-$. Bien que ce soit un mode spécifique de saveur, l'analyse de Dalitz permet de mesurer la phase relative $\Delta\phi(K^{*-}(892)\pi^+, K^{*+}(892)\pi^-)$ entre l'amplitude de désintégration et son amplitude conjuguée de CP, par le biais du profil d'interférence du $K^{*+}(892)$ avec les résonances accessibles à la fois aux B^0 et aux $\bar{B}^0$. Des travaux théoriques récents ont évoqué la possibilité d'utiliser la valeur de cette observable pour contraindre l'angle γ de la matrice CKM.

Analyse des données expérimentales du mode $B^0 \to K^0_S\pi^+\pi^-$

Ce travail commence par établir un algorithme de sélection des données enregistrées par BABAR, en vue d'analyser un échantillon riche en événements $B^0 \to K^0_S\pi^+\pi^-$. Cet algorithme est basé sur des critères d'optimisation de l'identification du signal, et sur la caractérisation et la réjection des bruits de fond.

La deuxième étape consiste à établir un modèle statistique, basé sur une fonction de vraisemblance étendue, définie de sorte à ce qu'elle décrive les données de l'échantillon, et qu'elle permette d'en extraire les mesures expérimentales des observables physiques définissant le processus $B^0 \to K^0_S\pi^+\pi^-$. Le défi le plus important de cette étape est le développement d'un modèle physique décrivant la dynamique de la désintégration $B^0 \to K^0_S\pi^+\pi^-$ sous la forme d'un *modèle isobare,* une approximation où l'amplitude totale de désintégration est considérée comme une somme cohérente d'amplitudes, correspondant à des états résonants intermédiaires. De nombreux critères de validation ont été appliqués sur ce modèle, pour s'assurer de sa robustesse et de sa fiabilité.

Finalement, l'échantillon des données a été soumis à un ajustement de vraisemblance maximale étendue. Les mesures expérimentales sont extraites du résultat de cet ajustement, et se présentent principalement sous la forme d'*observables quasi-deux-corps,* qui sont des fonctions des paramètres de l'amplitude isobare. Les observables mesurées incluent principalement : les taux de désintégration et les asymétries de CP de toutes les composantes intermédiaires, ainsi qu'un taux de désintégration inclusif et une asymétrie de CP globale ; les paramètres des asymétries dépendantes du temps pour les composantes accessibles aussi bien aux B^0 qu'aux $\bar{B}^0$; les phases isobares relatives entre composantes dans un même plan de Dalitz; enfin, pour les composantes spécifiques de saveur, la phase relative entre l'amplitude isobare et son amplitude conjuguée de CP.

L'ajustement a identifié huit composantes significatives dans l'amplitude totale ; de ce fait, le nombre d'observables mesurées est considérable. Parmi les résultats obtenus, les principaux sont les suivants :

- L'ajustement trouve deux solutions, avec des figures de mérite équivalentes sur la qualité de l'ajustement. Les valeurs des fractions isobare et des asymétries directes sont très proches dans les deux solutions ; cependant, certaines des phases isobare ont des valeurs nettement différentes. Ainsi, ce résultat provient d'une ambiguité double dans la résolution des profils d'interférence dans le plan de Dalitz. Les résultats sur les observables physiques sont obtenus à partir de ces deux maximums de la fonction de vraisemblance complète, et aucune approximation n'est faite dans l'extraction des intervalles de confiance sur les paramètres mesurés.

- La mesure des paramètres (β_{eff}, C) dans le mode $f_0(980)K^0_S$, tout en étant en bon accord avec les modes en or, exclut la conservation de CP avec une signification de $3,5$ écarts standard, en incluant les intertitudes systématiques. L'erreur totale est dominée par la statistique, et la contribution principale à la systématique provient des incertitudes sur le modèle isobare utilisé.

- Pour le $\rho^0(770)K^0_S$, les résultats sont aussi en accord avec les modes en or. Par ailleurs, la valeur $(\beta_{\text{eff}} = 180°, C = 0)$ de conservation de CP est exclue à $3,9$ écarts standard, et le résultat est compatible avec la valeur $(\beta_{\text{eff}} = 0°, C = 0)$ à mieux que 1 écart standard. Comme pour le $f_0(980)K^0_S$, l'erreur totale est dominée par la statistique, et la contribution principale à la systématique provient des incertitudes sur le modèle isobare utilisé.

- Pour le mode $K^{*+}(892)\pi^-$, la mesure du paramètre de violation directe de CP donne $A_{\text{CP}} = -0.20 \pm 0.10 \pm 0.02 \pm 0.01$; la valeur non nulle a une signification de 2.0 écarts standard. La phase relative $\Delta\phi(K^{*-}(892)\pi^+, K^{*+}(892)\pi^-)$ entre l'amplitude et son amplitude conjuguée est mesurée pour la première fois. Ce dernier résultat est limité par la faible sensibilité due à la taille limitée des zones d'interference avec d'autres résonances, et ne permet que d'exclure l'intervalle $[-132^\circ : +25^\circ]$ à 95% niveau de confiance. Si bien la mesure de $\Delta\phi(K^{*-}(892)\pi^+, K^{*+}(892)\pi^-)$ est dominée par la statistique, l'écart entre les deux maximums de la vraisemblance dilue sensiblement la contrainte obtenue.

- La présence d'une contribution significative au spectre $\pi^+\pi^-$, dans la région autour de $m_{\pi^+\pi^-} \sim 1.5~\mathrm{GeV}/c^2$, est établie avec une signification de $4,8$ écarts standard. Ce signal est paramétré comme une somme cohérente de deux contributions, le tenseur $f_2(1270)$ et une autre résonance $f_X(1300)$ non repertoriée, et qui a été identifée pour la première fois dans les modes $B^+ \to K^+\pi^-\pi^+$. Comme dans ces autres analyses de Dalitz, le meilleur ajustement s'obtient en utilisant un scalaire pour le $f_X(1300)$.

Une version préliminaire de ce travail a été présentée au nom de la collaboration *BABAR*, à la conférence Lepton-Photon en 2007, et est disponible dans `arXiv:0708.2097`. La version finale est actuellement en cours de validation interne dans la collaboration (étapes finales de révision éditoriale), et doit à être publiée dans *Physical Review D*.

Interprétation phénoménologique des modes $B \to K^*\pi$ et $B \to K\rho$

Le but de ce travail phénoménologique est d'extraire des contraintes sur la matrice CKM à partir des mesures d'observables sur les modes en pseudoscalaire-vecteur dans les désintégrations $B \to K\pi\pi$. Ces mesures incluent des résultats de l'analyse des données décrite ci-dessus. La stratégie est basée essentiellement sur la symétrie d'isospin, reliant les quatre amplitudes de désintégration $B \to K^*\pi$ d'une part, et les quatre amplitudes de désintégration $B \to K\rho$ de l'autre. Au-delà de l'isospin, le nombre d'hypothèses dynamiques extérieures est réduit au minimum, le but recherché étant d'obtenir des résultats aussi indépendants du modèle que possible.

La méthode dite "CPS/GPSZ" a été utilisée comme base de référence ; les auteurs suggèrent que la mesure de $\Delta\phi(K^{*-}(892)\pi^+, K^{*+}(892)\pi^-)$, combinée avec les phases relatives entre le $K^{*+}(892)\pi^-$ et le $K^{*0}(892)\pi^0$, accessibles par l'analyse de Dalitz (indépendante du temps) du mode $B^0 \to K^+\pi^-\pi^0$, permettent de poser une contrainte non triviale sur les paramètres de la matrice CKM. Qui plus est, les auteurs affirment que, sous l'hypothèse de négliger les contributions dites en *pingouins électrofaibles* (P_{EW}), cette contrainte donnerait accès direct à l'angle γ de la matrice CKM.

Cette thèse s'est d'abord fixée comme objectif de produire une extension de la métode CPS/GPSZ, visant à maximiser l'utilisation de l'information expérimentale disponible. Cependant, cette démarche a aussi permis de démontrer que certaines des conditions invoquées par la méthode CPS/GPSZ ne sont pas correctes. Pour CPZ/GPSZ, l'accès à l'angle γ repose sur l'hypothèse que la mesure de la phase relative $\Delta\phi(K^{*-}(892)\pi^+, K^{*+}(892)\pi^-)$ peut se faire avec une analyse de Dalitz *intégrée en temps* du mode $B^0 \to K^0_S\pi^+\pi^-$, afin que cette mesure soit indépendante du mélange $B^0 - \bar{B}^0$. Or cette affirmation est doublement incorrecte : non seulement cette phase n'est accessible qu'avec une analyse dépendante du temps, mais de plus, l'observable physique correspondante contient nécéssairement l'information sur la phase du paramètre q/p du mélange $B^0 - \bar{B}^0$. De ce fait, la méthode CPS/GPSZ repose sur une contrainte qui n'est pas une fonction d'observables physiques.

Une méthode correcte est dévéloppée et utilisée dans cette thèse ; on démontre que la contrainte basée sur des observables physiques donnerait lieu, dans l'hypothèse où on néglige les P_{EW}, à une contrainte sur l'angle α de la matrice CKM (et non pas γ). Les conditions de validité de cette hypothèse extérieure sont testées, à la fois en termes de la structure des relations d'isospin, et en utilisant les contraintes provenant des mesures expérimentales disponibles. On montre que pour les système $B \to K^*\pi$, les mesures ne favorisent pas le scénario de P_{EW} négligleables ; qui plus est, les mesures actuelles sur $K^*\pi$ n'ont qu'une faible compatibilité avec les estimations théoriques disponibles sur les P_{EW}.

De ce fait, les contraintes obtenues sur la matrice CKM sont dominées par des incertitudes d'origine théorique.

Finalement, une méthode qui exploite conjointement l'ensemble des mesures sur $K^*\pi$ et $K\rho$ est développée. Le potentiel de cette analyse combinée $K^*\pi + K\rho$ est estimé à l'aide d'une analyse prospective, basée sur une extrapolation des incertitudes expérimentales. Les résultats permettent d'illustrer le potentiel de physique de ces analyses dans le cadre de l'expérience LHCb, ainsi que des projets SuperB ou Belle-upgrade.

Cette étude se fait dans le cadre du groupe CKMfitter, notamment en collaboration avec Jérôme Charles. Une version préliminaire de ce travail de phénoménologie est présentée dans cette thèse. La version finale contiendra probablement quelques extensions de la méthode dans un cadre plus élargi que la seule symétrie d'isospin. L'objectif final est de soumettre ce travail à publication dans *Journal of High Energy Physics*.

Contents

List of Figures

List of Tables

Introduction

The Standard Model (SM) of strong and electroweak interactions summarizes the current knowledge on subatomic physics and the fundamental interactions (excluding gravitation). Although several questions remain without answer, no experimental result contradicts the SM predictions to date.

The SM can be divided into several sectors making reference to the processes considered. Although the SM has a large number of parameters that have to be extracted from experiment, the global electroweak fit reveals a very good agreement with data. Among the SM parameters, about half of them come from the quark flavor sector. Until a decade ago, this sector (and that of the neutrinos) was the least tested, but it is the only one where a phenomenon of great importance, CP violation, has been observed.

CP violation was discovered in 1964 in decays of neutral kaons. Later, Sakharov remarked that CP violation is one key requirement to explain the matter/antimatter asymmetry in the Universe. The Cabbibo-Kobayashi-Maskawa (CKM) quark mixing matrix enables to incorporate CP violation into the SM framework. However, it has been shown that the *CKM mechanism* is insufficient to explain the observed matter/antimatter asymmetry; it is widely believed that the CKM matrix (and the entire SM) is a low-energy representation of a more fundamental theory.

Measurements of CP violation related effects, could reveal New Physics (NP) beyond the SM if they cannot be accounted within the SM framework.

The CKM matrix describes the transitions between quarks with only four parameters: three real rotation angles and one irreducible phase. This phase contains all the information about CP violation. This reduced number of fundamental parameters makes the flavor sector highly predictive. The ambition of the flavor physics program is to obtain redundant observables linked to the CKM matrix.

In this context, the main goal of the B factories, where the *BABAR* and Belle experiments are the representatives in activity in the past decade, is to produce a systematic study of CP asymmetries in B meson decays. Beyond CKM metrology, the B factories program has continuously broadened the search of NP effects, not only by improving the precision of the measurements, but also by extending the number of processes studied, thanks to the increase of available data samples.

Several phenomenology groups, where CKMfitter plays an active role, combine the available experimental measurements to produce a global fit of the CKM matrix. The result is a striking confirmation of the CKM mechanism.

Given the great success of the SM, a scenario of *Minimal Flavor Violation* (MFV) is the favored hypothesis to date: possible contributions of NP would appear as small perturbations of the CKM mechanism. B factories today are increasingly oriented to study processes sensitive to MFV.

A promising approach is that of *amplitudes analyses*, or Dalitz analyses for three-body decays. They provide direct access to decay amplitudes, and thereby disentangle weak and strong phases by resolving the interference patterns between intermediate resonant states.

Among three-body decays of B mesons to light hadrons, the rather abundant $B \to K\pi\pi$ channels are dominated by high order diagrams (loops). Dalitz analysis may therefore offer high sensitivity to NP contributions. This approach subtends the experimental and phenomenological analyses presented in this thesis.

This thesis is divided into four parts. In Part I an introduction of the theoretical concepts used in this thesis are given. In Chapter 1, CP violation within the SM is described. Then, the B meson system is reviewed emphasizing the experimental advantages of studying such a system, and summarizing the current constraints on the CKM parameters. Chapter 2 discusses kinematics and dynamics of the three body decays, which are essential tools for the time-dependent amplitude analysis of the $B^0 \to K^0_S\pi^+\pi^-$ mode. Chapter 3 provides a theoretical introduction to the different methods that can be used to constraint the CKM parameters from the measurements of $B \to K^*\pi$ and $B \to \rho K$ modes, using mainly the $SU(2)$ isospin symmetry.

Part II is devoted to the description of the PEP-II accelerator and the BABAR detector. This is where the characteristics of the detector which are important for reconstruction and selection of $B^0 \to K^0_S\pi^+\pi^-$ decays are introduced.

The statistical analysis of $B^0 \to K^0_S\pi^+\pi^-$ decays is presented in Part III. Chapter 5 describes the data samples used for the present analysis, and the reconstruction and selection algorithms applied to them. The relevant backgrounds from other B decays are presented. In Chapter 6 the construction of the likelihood function used to fit the $B^0 \to K_S\pi^+\pi^-$ final data sample is described. The validation of the likelihood function, based on Monte Carlo (MC) simulations, is presented there as well. Finally, Chapter 7 presents the fit results and the estimation of the systematic uncertainties.

Part IV, the last of this thesis, is dedicated to the interpretation of the experimental results on the $B \to K^*\pi$ and $B \to \rho K$ system, using a phenomenological analysis based mainly on isospin $SU(2)$ symmetry. The derived constraints on hadronic and CKM parameters are explored.

Part I

Theoretical Introduction

Chapter 1

Weak interactions, quark mixing and CP violation

CP violation in weak interactions was first observed in 1964 [1] in decays of neutral K mesons. Later on, Sakharov remarked that CP violation is one key requirement to explain the matter/antimatter asymmetry in the Universe [2]. While the Standard Model of particle physics incorporates a mechanism to accommodate CP violation [3, 4], it has been shown that it is insufficient to explain the matter/antimatter asymmetry [5].

The Standard Model (SM) is the theory that describes all the known phenomena at the subatomic scale. Although the SM has a large number of parameters that have to be extracted from experiment, the global electroweak fit reveals a very good agreement with data [6]. However, many theoretical arguments motivate the search for New Physics. Today most of the experimental effort is directed to falsify the SM, which is considered a low-energy representation of a more fundamental theory.

Studying the flavor sector of the SM, in particular through CP violation related effects, could reveal New Physics. Due to the impressive success of the SM, it is convenient to place the CP violation within its theoretical framework in order to constrain the SM parameters or to throw some light on possible deviations due to New Physics.

This chapter describes the mechanism of CP violation in weak interactions in the SM framework. Then, the B meson system is described emphasizing the experimental advantages of studying such a system. Finally, a short summary of the achievements of B factories in the measurement of CP violation and constraints on SM parameters is given.

1.1 CP Violation in the Standard Model

The SM is a renormalizable quantum field theory constructed under the principle of local gauge invariance with the $SU(3)_C \otimes SU(2)_L \otimes U(1)_Y$ symmetry group. This group includes the strong interaction symmetry group of color rotations, $SU(3)_C$, and the electroweak interaction group $SU(2)_L \otimes U(1)_Y$. The SM predicts that the latter is spontaneously broken to $SU(2)_L \otimes U(1)_Y \to U(1)_{em}$, where $U(1)_{em}$ is the group of the electromagnetic interaction. Noether's theorem associates conserved quantities (charges) with gauge symmetries of strong and electromagnetic interactions. The weak interaction does not have an associated conserved quantity as its gauge symmetry is broken.

1.1.1 Elementary constituents

The SM is based on a limited number of particles: the fermions, which are the elementary constituents of matter; the bosons, which are the mediators of the interactions between the fermions; and the Higgs boson, which is the responsable of the particles masses, and of CP violation through the Yukawa couplings (cf. Sec. 1.1.2).

Gauge bosons

There are twelve gauge mediators in the SM: the gluons, the mediators of the strong interaction, and the γ, $W^{\pm}$ and Z^0, which mediate the electromagnetic and weak interactions, respectively.

The gluons are massless, electrically neutral and carry color charge. There are eight gluons, corresponding to the number of $SU(3)$ generators.

The electromagnetic interaction is mediated by the photon, a massless particle that carries no electric charge and generates an interaction of infinite range. The weak interaction bosons, $W^{\pm}$ and Z^0, acquire mass through spontaneous symmetry breaking. They can interact with each other through weak interaction couplings, and the $W^{\pm}$, due to its electric charge, couples with the photon.

Fermions

The fermions can be separated in two categories: quarks, susceptible to all three interactions, and leptons, only capable of interacting weak and electrically. All fermions can be organized in three families with identical properties except for their masses. The fermionic fields have left chirality components transforming as $SU(2)_L$ doublets and right chirality components transforming as singlets. The weak interaction only acts on left chirality components.

$$\begin{array}{lcccc}
\text{1st family} & \begin{pmatrix} \nu_e \\ e^- \end{pmatrix}_L, & e^-_R, & \begin{pmatrix} u \\ d \end{pmatrix}_L, & u_R,\ \ d_R \\
\text{2nd family} & \begin{pmatrix} \nu_\mu \\ \mu^- \end{pmatrix}_L, & \mu^-_R, & \begin{pmatrix} c \\ s \end{pmatrix}_L, & c_R,\ \ s_R \\
\text{3rd family} & \begin{pmatrix} \nu_\tau \\ \tau^- \end{pmatrix}_L, & \tau^-_R, & \begin{pmatrix} t \\ b \end{pmatrix}_L, & t_R,\ \ b_R
\end{array} \tag{1.1}$$

This configuration assumes that neutrinos are massless. The Super-Kamiokande, SNO and KamLAND experiments observed that neutrinos from one family can be transformed, by oscillation, to neutrinos of another family [7] with frequencies proportional to their mass square differences. It is possible to extend the SM to take ν masses into account. However, this has no effect in the following discussion which mainly deals with the weak interactions of the quark sector.

The Higgs boson

The $SU(3)_C \otimes SU(2)_L \otimes U(1)_Y$ symmetry group prevents the bare masses of leptons and quarks to appear in the Lagrangian density. To evercome to this problem, the SM is completed with a last particle: the Higgs boson, which is a Lorentz scalar, electrically neutral and is a weak isospin doublet with four degrees of freedom, $\phi = \begin{pmatrix} \phi^+ \\ \phi^0 \end{pmatrix}$. Spontaneous breakdown of electroweak symmetry (the Higgs mechanism [8]) dynamically generates masses for the fermions due to the Yukawa couplings of fermion fields and the Higgs doublet (cf. Sec. 1.1.2). The Higgs particle has not been experimentally observed. Direct searches by LEP II set a lower limit ($m_H > 114.4 \text{ GeV at } 95\%$) [9] and the electroweak precision fit sets an upper limit [6]. Searches made at Tevetron by the CDF and $D\varnothing$ collaborations extended the explored phase space, but still no observation has been made. *ATLAS* and *CMS* experiments, constructed on the Large Hadron Collider (*LHC*) at *CERN*, are ready to take data, and will look for direct evidence of the Higgs boson.

1.1.2 CP violation and the *CKM* Matrix

In a first stage the electroweak Lagrangian is analyzed to detect possible sources of CP violation. The electroweak Lagrangian can be written as the sum of three contributions,

$$\mathcal{L}_{EW} = \mathcal{L}_{kinetic} + \mathcal{L}_{Higgs} + \mathcal{L}_{Yukawa} \, . \tag{1.2}$$

There is also a term that couples the Higgs field to the gauge bosons, that has no consequence on CP violation. The first term on the right side is the kinetic lagrangian of quarks and leptons, the second and third ones are the Higgs field and the Yukawa Lagrangians, respectively. The last term describes the coupling of the Higgs boson with the fermionic fields.

After spontaneous symmetry breaking, the Higgs field [8] confers a mass to each fermion through the Yukawa couplings. The Yukawa Lagrangian for the couplings between Higgs and fermion fields, is given, after symmetry breaking, by (the mass term for neutrinos is ignored)

$$\mathcal{L}_{Yukawa} = -(\bar{\mathbf{u}}'_L M^u \mathbf{u}'_R + \bar{\mathbf{d}}'_L M^d \mathbf{d}'_R + \bar{\mathbf{e}}'_L M^e \mathbf{e}'_R + \text{h.c.})(1 + \frac{\phi_0}{v}) \, , \tag{1.3}$$

where:

- ϕ_0 and v are the Higgs scalar field and the Higgs field mean value in vacuum, respectively;
- $\mathbf{u}'_{R,L}$, $\mathbf{d}'_{R,L}$ and $\mathbf{e}'_{R,L}$ are the up and down quark and charged leptons (e^-, μ^- and τ^-) vectors in the 3D flavor space:

$$\mathbf{u}'_{R,L} = \left(\tfrac{1\mp\gamma_5}{2}\right) \begin{pmatrix} u' \\ c' \\ t' \end{pmatrix} \quad , \quad \mathbf{d}'_{R,L} = \left(\tfrac{1\mp\gamma_5}{2}\right) \begin{pmatrix} d' \\ s' \\ b' \end{pmatrix} \quad \text{and} \quad \mathbf{e}'_{R,L} = \left(\tfrac{1\mp\gamma_5}{2}\right) \begin{pmatrix} e' \\ \mu' \\ \tau' \end{pmatrix} \; ; \tag{1.4}$$

- M^u,M^d and M^e are complex mass matrices 3×3 for the up and down quarks and charged leptons, respectively.

The quark mass spectrum is obtained by diagonalizing the mass matrices. The $M^{u,d,e}$ arbitrary complex matrices can be diagonalized by using two unitary matrices, $U_L^{u,d,e}$ and $U_R^{u,d,e}$, as follows,

$$U_R^\chi M^\chi U_L^\chi = M_{diag}^\chi \quad \chi = u, d, e \; , \tag{1.5}$$

where M_{diag}^χ is a diagonal real matrix ($(M_{diag}^\chi)_{ij} = m_i^\chi \delta_{ij}$). This is where the fermion masses m_i are input by hand into the SM. The quark and lepton fields expressed in the mass eigenstates base (without primes) are given by,

$$\begin{aligned}(\mathbf{u}_{(R,L)})_i &= (U_{(R,L)}^u)_{ij}(\mathbf{u}'_{(R,L)})_j \; , \\ (\mathbf{d}_{(R,L)})_i &= (U_{(R,L)}^d)_{ij}(\mathbf{d}'_{(R,L)})_j \; , \\ (\mathbf{e}_{(R,L)})_i &= (U_{(R,L)}^e)_{ij}(\mathbf{e}'_{(R,L)})_j \; .\end{aligned} \tag{1.6}$$

In the new basis the Yukawa Lagrangian can be written as

$$\mathcal{L}_{Yukawa} = -(\bar{\mathbf{u}}_L M_{diag}^u \mathbf{u}_R + \bar{\mathbf{d}}_L M_{diag}^d \mathbf{d}_R + \bar{\mathbf{e}}_L M_{diag}^e \mathbf{e}_R + h.c.)(1 + \frac{\phi_0}{v}) \; . \tag{1.7}$$

The $U_{(R,L)}^\chi$ matrices being absent, the interactions of the Higgs field and fermions fields are C, P and CP conserving. The kinetic term remains invariant in the new basis. What is interesting is to see the weak interaction Lagrangian (the couplings of the fermion fields to the $W^\pm$ and Z^0 bosons). This can be separated into charged and neutral current pieces, $\mathcal{L}_{int} = \mathcal{L}_{NC} + \mathcal{L}_{CC}$. In the mass eigenstates basis, the $\mathcal{L}_{NC}$ remains invariant because its terms are of the form $\bar{\phi}'_{(L,R)}\gamma_\mu\phi'_{(L,R)}$ ($\phi = \mathbf{u}, \mathbf{d}, \mathbf{e}, \nu$). As an example,

$$\bar{\mathbf{u}}'_L \gamma_\mu \mathbf{u}'_L = \bar{\mathbf{u}}_L U_L^u \gamma_\mu U_L^{u\dagger} \mathbf{u}_L = \bar{\mathbf{u}}_L \gamma_\mu \mathbf{u}_L \; . \tag{1.8}$$

However, the quark charged-current term is modified by the basis transformation. In effect, after the spontaneous symmetry breaking, the Lagrangian term describing the $W^\pm$ boson and quark field coupling is given by

$$\mathcal{L}_{CC} = \frac{g}{\sqrt{2}} \, [\bar{\mathbf{u}}'_L \gamma^\mu \mathbf{d}'_R] \, W_\mu^+ + h.c. \; , \tag{1.9}$$

where g is the $SU(2)_L$ coupling constant and W_μ^+ is the $SU(2)_L$ gauge field. There is a similar term for the coupling of $W^\pm$ and lepton fields, that corresponds to replacing $\mathbf{u} \rightarrow \mathbf{e}$ and $\mathbf{d} \rightarrow \nu$. In the mass eigenstate basis, Eq.(1.9) can be written as

$$\mathcal{L}_{CC} = \frac{g}{\sqrt{2}} \, [\bar{\mathbf{u}}_L \gamma^\mu V_{CKM} \mathbf{d}_R] \, W_\mu^+ + \text{h.c.} \; , \tag{1.10}$$

where the matrix V_{CKM}, given by

$$V_{CKM} = U_L^u U_R^{d\dagger} = \begin{pmatrix} V_{ud} & V_{us} & V_{ub} \\ V_{cd} & V_{cs} & V_{cb} \\ V_{td} & V_{ts} & V_{tb}, \end{pmatrix} \tag{1.11}$$

is the Cabibbo-Kobayashi-Maskawa (CKM) Matrix. This matrix was introducted by Kobayashi and Maskawa [3] for three quark families, as an extension of Cabibbo's model [4] of two quark families. This matrix is complex and unitary, and, as will be discussed later, is the source of CP violation in the SM.

In the approximation of zero neutrino masses, the rotation matrix for the neutrino fields can be chosen to be the same as that for the charged leptons (U_L^e). This leaves lepton charged-current term invariant. In the case of non-zero neutrino masses there exists an analogous matrix to V_{CKM} known as PMNS matrix [10].

1.1.3 *CKM* matrix properties

Number of independent parameters

The fact that V_{CKM} has a complex phase does not necessarily mean that there is CP violation in the SM. In the case of N quark families, V_{CKM} will be a complex $N \times N$ matrix, and being the product of two unitary matrices, it is itself unitary. Not all its parameters are physically meaningful, as $2N-1$ of its phases can be absorbed in the quark fields by phase redefinitions ($\mathbf{u}_{Lk} \rightarrow e^{i\phi_k^u}\mathbf{u}_{Lk}$, and the same for the down quarks). Furthermore, the fact that V_{CKM} is unitary implies that it can be parameterized with $N(N-1)/2$ rotation angles (Euler angles). All this leaves $(N-1)(N-2)/2$ independent phases. For the case of $N = 2$ families, V_{CKM} is real and there is no CP violation. It is then necessary that the number of families be $N \geq 3$ to have CP violation in the SM. This is the "KM ansatz" to explain CP violation. In the case of $N = 3$, four parameters are needed to describe V_{CKM}: 3 (real) rotation angles and one phase. All the information on CP violation is contained in this phase, thus making the quark flavor sector of the SM highly predictive.

Conditions for CP violation

CP is not necessarily violated in the 3 families SM. If two quarks of the same charge had equal masses, one rotation angle and one phase could be removed from V_{CKM}. Likewise, if the value of any of the three rotation angles were 0 or $\pi/2$, then the phase could be removed. Finally, CP would not be violated if the value of the phase was 0 or π. All these conditions can be merged into one, parameterization independent, condition [11], which can be stated as,

$$det[M^u, M^d] = -2iF_uF_dJ \neq 0 \Longleftrightarrow CP \text{ violation}\ , \tag{1.12}$$

where $F_{u(d)} = (m_{t(b)} - m_{c(s)})(m_{t(b)} - m_{u(d)})(m_{c(s)} - m_{u(d)})/m_{t(b)}^3$, and J is a measure of CP violation independent of any phase convention, known as the Jarlskog invariant. In case there is no degeneracy for the quark masses of the up and down quarks,

$$J \neq 0 \Longleftrightarrow CP \text{ violation}\ . \tag{1.13}$$

The are several parameterizations for V_{CKM}. The two most used are the Standard and Wolfestein parameterizations, which are now described.

Standard parameterization

The Standard parameterization was proposed by Chau and Keung [12]. It is obtained as the product of three (complex) rotation matrices and a overall phase,

$$V_{CKM} = \begin{pmatrix} c_{12}c_{13} & s_{12}c_{13} & s_{13}e^{-i\delta} \\ -s_{12}c_{23} - c_{12}s_{23}s_{13}e^{i\delta} & c_{12}c_{23} - s_{12}s_{23}s_{13}e^{i\delta} & s_{23}c_{13} \\ s_{12}s_{23} - c_{12}c_{23}s_{13}e^{i\delta} & -c_{12}s_{23} - s_{12}c_{23}s_{13}e^{i\delta} & c_{23}c_{13} \end{pmatrix} , \qquad (1.14)$$

where $c_{ij} = \cos\theta_{ij}$, $s_{ij} = \sin\theta_{ij}$ for $i < j = 1, 2, 3$, and the θ_{ij} are the rotation angles between families.

Wolfenstein parameterization

Following the experimental observation of a the hierarchy on the V_{CKM} elements, Wolfenstein [13] proposed an expansion of the CKM matrix in terms of four parameters λ, A, ρ and η ($\lambda \simeq |V_{us}| \sim 0.22$ being the expansion parameter),

$$V_{CKM} = \begin{pmatrix} 1 - \frac{\lambda^2}{2} & \lambda & A\lambda^3(\rho - i\eta) \\ -\lambda & 1 - \frac{\lambda^2}{2} & A\lambda^2 \\ A\lambda^3(1 - \rho - i\eta) & -A\lambda^2 & 1 \end{pmatrix} + \mathcal{O}(\lambda^4) \, . \qquad (1.15)$$

In this parameterization η contains the CP violation information, *i.e.* CP violation when $\eta \neq 0$. To all orders in λ, the exact Wolfenstein parameterization can be defined as,

$$\begin{aligned} s_{12} &\equiv \lambda \, , \\ s_{23} &\equiv A\lambda^2 \, , \\ s_{13}e^{-i\delta} &\equiv A\lambda^3(\rho - i\eta) \, , \end{aligned} \qquad (1.16)$$

inserted in the standard parameterization (cf. Eq.(1.14)), so that unitarity is achieved to all orders[1] This exact parameterization is used in the phenomenology studies performed with the CKMfitter group [14, 15] described in Chapter 8.

The Unitarity Triangle

The *CKM* matrix is unitary under the hypothesis of universal weak couplings, *i.e.* $g^l = g^\nu = g^u = g^d$, which explains the presence of a unique gauge group, $SU(2)_L$, for all families.

---

[1] The Taylor expansion of Eq.(1.14), in terms of Eq.(1.16), up to $\mathcal{O}(\lambda^9)$ reads,

$$\begin{aligned}
&V_{ud} = 1 - \tfrac{1}{2}\lambda^2 - \tfrac{1}{8}\lambda^4 - \tfrac{1}{16}\lambda^6(1 + 8A^2(\rho^2 + \eta^2)) - \tfrac{1}{128}\lambda^8(5 - 32A^2(\rho^2 + \eta^2)) \, , \\
&V_{us} = \lambda - \tfrac{1}{2}A^2\lambda^7(\rho^2 + \eta^2) \, , \\
&V_{ub} = A\lambda^3(\rho - i\eta) \, , \\
&V_{cd} = -\lambda + \tfrac{1}{2}A^2\lambda^5(1 - 2(\rho + i\eta)) + \tfrac{1}{2}A^2\lambda^7(\rho + i\eta) \, , \\
&V_{cs} = 1 - \tfrac{1}{2}\lambda^2 - \tfrac{1}{8}\lambda^4(1 + 4A^2) - \tfrac{1}{16}\lambda^6(1 - 4A^2 + 16A^2(\rho + i\eta)) - \tfrac{1}{128}\lambda^8(5 - 8A^2 + 16A^4) \, , \\
&V_{cb} = A\lambda^2 - \tfrac{1}{2}A^3\lambda^8(\rho^2 + \eta^2) \, , \\
&V_{td} = A\lambda^3(1 - \rho - i\eta) + \tfrac{1}{2}A\lambda^5(\rho + i\eta) + \tfrac{1}{8}A\lambda^7(1 + 4A^2)(\rho + i\eta) \, , \\
&V_{ts} = -A\lambda^2 - A\lambda^4(1 - 2(\rho + i\eta)) + \tfrac{1}{8}A\lambda^6 + \tfrac{1}{16}A\lambda^8(1 + 8A^2(\rho + i\eta)) \, , \\
&V_{tb} = 1 - \tfrac{1}{2}A^2\lambda^4 - \tfrac{1}{2}A^2\lambda^6(\rho^2 + \eta^2) - \tfrac{1}{8}A^4\lambda^8 \, .
\end{aligned}$$

This unitarity implies various relations among the V_{CKM} elements. Three of them are useful for probing the SM prediction of CP violation as they involve the non-trivial *CKM* phase:

$$V_{ud}V_{us}^* + V_{cd}V_{cs}^* + V_{td}V_{ts}^* = 0\ , \tag{1.17}$$

$$V_{us}V_{ub}^* + V_{cs}V_{cb}^* + V_{ts}V_{tb}^* = 0\ , \tag{1.18}$$

$$V_{ud}V_{ub}^* + V_{cd}V_{cb}^* + V_{td}V_{tb}^* = 0\ . \tag{1.19}$$

Each of these three relations requires the sum of three complex quantities to vanish and so can be geometrically represented in the complex plane as triangles of same area $J/2$. The phase transformations of the quark fields modify the triangle orientations in the complex plane, but their shapes remain invariant, *i.e.* the internal angles and sides of these triangles are independent of phase convention and are directly related to CP violation observables. These are the "unitarity triangles", represented with a common scale in the left hand side of Fig. 1.1.

The first two triangles are related to the *CKM* matrix elements that governs the $K^0 - \bar{K}^0$ and $B_s^0 - \bar{B}_s^0$ systems, respectively. For each of those triangles one side is much shorter than the others, and it almost collapses into a line. This offers an intuitive understanding of why CP violation is expected to be small on those systems. Decays related to the small sides (*e.g.* $K \longrightarrow \pi\nu\bar{\nu}$) are rare but can exhibit significant CP violation.

The most exciting physics lies in B_d decays. It is related to the third triangle, which has wide angles and therefore implies large CP violation effects. Eq.(1.19) is thus known as the "Unitarity Triangle" (UT) drawn on the right hand side plot of Fig. 1.1. Note that in this representation a phase convention has been chosen in which $V_{cd}V_{cb}^*$ is real and all sides have been divided by $|V_{cd}V_{cb}^*|$.

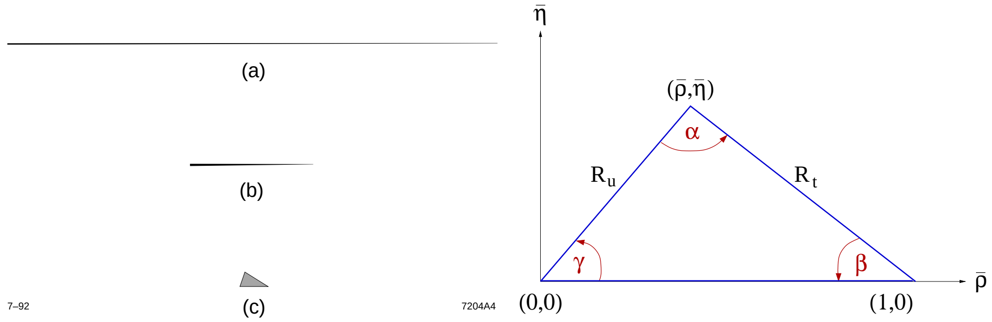

Figure 1.1: *On the Left: geometrical representation of relations (1.17-1.19), drawn with a common scale. On the Right: geometrical representation of the Unitarity Triangle choosing a phase convention in which $V_{cd}V_{cb}^*$ is real, and dividing all sides by $|V_{cd}V_{cb}^*|$. This fixes one of the sides along the real axis and gives it unit length.*

Depicting the rescaled Unitarity Triangle in the $\bar{\rho}-\bar{\eta}$ complex plane, defined by $\bar{\rho}+i\bar{\eta} \equiv -V_{ud}V_{ub}^*/V_{cd}V_{cb}^*$, the lengths of the two complex sides are

$$R_u = \left|\frac{V_{ud}V_{ub}^*}{V_{cd}V_{cb}^*}\right| = \sqrt{\bar{\rho}^2 + \bar{\eta}^2}\ , \tag{1.20}$$

$$R_t = \left| \frac{V_{td}V_{tb}^*}{V_{cd}V_{cb}^*} \right| = \sqrt{(1-\bar{\rho})^2 + \bar{\eta}^2} \, . \tag{1.21}$$

The three angles of the UT are denoted by α, β and γ:

$$\alpha \equiv arg \left(-\frac{V_{td}V_{tb}^*}{V_{ud}V_{ub}^*} \right) \;,\quad \beta \equiv arg \left(-\frac{V_{cd}V_{cb}^*}{V_{td}V_{tb}^*} \right) \;,\quad \gamma \equiv arg \left(-\frac{V_{ud}V_{ub}^*}{V_{cd}V_{cb}^*} \right) \;, \tag{1.22}$$

with $\alpha + \beta + \gamma = \pi$. The unitarity triangle relations allow to test the V_{CKM} matrix unitarity. To test unitarity is to explore violations of the consequences of the 3 families SM. Any deviations would mean new physics effects. This sets the case for measuring the angles and sides of the UT. Several of these parameters are directly related with CP violation observables from the B meson system. Overconstraining the UT parameters with such observables allows us to test the SM.

1.2 The B Meson System

This section describes the quantum mechanical properties of the B meson system. The emphasis is set on introducing convention-free physical quantities related to CP violation. Three different kinds of CP violation are distinguished. The term B meson refers to mesons made of a $\bar{b}$ antiquark, plus another quark from to the first or second family. Only the B_d^0 and B_u^+ (denoted in the following B^0 and B^+) are produced by PEP-II.

1.2.1 The quantum mechanics of neutral B mesons

In presence of strong and electromagnetic interactions only, a neutral meson state and its CP conjugated would be stable and form a particle-antiparticle pair with common mass. Due to weak interactions, those states can decay. To describe the neutral meson system, different neutral states are relevant: two flavor eigenstates, which have definite quark content and are useful for understanding particle production and particle decay processes; and two Hamiltonian eigenstates (mass eigenstates) with definite mass and lifetime, which propagate in spacetime in a definite fashion. If the CP symmetry were conserved ($[CP, \mathcal{H}] = 0$) then the mass eigenstates would also be CP eigenstates. In any case, mass eigenstates are not flavor eigenstates, and so flavor eigenstates get mixed as they propagate. This phenomenon which is well known for neutral kaons [16], has been observed for neutral B_d [17] and B_s [18], and more recently for neutral D [19] mesons. In the following only the neutral B_d meson system, $B^0 = d\bar{b}$ and $\bar{B}^0 = b\bar{d}$, is considered.

An arbitrary linear combination of the flavor eigenstates,

$$a(t)|B^0\rangle + b(t)|\bar{B}^0\rangle \;, \tag{1.23}$$

is governed by the time-dependent Schrödinger equation

$$i\frac{d}{dt}\begin{pmatrix} a(t) \\ b(t) \end{pmatrix} = \mathcal{H}\begin{pmatrix} a(t) \\ b(t) \end{pmatrix} = (M - \frac{i}{2}\Gamma)\begin{pmatrix} a(t) \\ b(t) \end{pmatrix} \;, \tag{1.24}$$

where M and Γ are two 2×2 hermitic matrices known as mass and decay matrices, respectively. CPT invariance ($[CPT, \mathcal{H}] = 0$) imposes $M_{11} = M_{22} = M$ and $\Gamma_{11} = \Gamma_{22} = \Gamma$, and CP conservation would imply $arg(M_{12}/\Gamma_{12}) = 0$. The diagonal terms in M are dominated by the flavor eigenstates masses, and the off-diagonal ones represent the $B^0 \rightleftharpoons \bar{B}^0$ transition *via* virtual intermediate states (dispersive part). The diagonal terms of Γ describe the decays $B^0 \to f$ and $\bar{B}^0 \to \bar{f}$, and the off-diagonal ones represent transitions *via* real intermediate states (absorptive part), $B^0 \to f \to \bar{B}^0$ and $\bar{B}^0 \to f \to B^0$ where f is a final state common to B^0 and $\bar{B}^0$.

After diagonalizing the Hamiltonian, $\mathcal{H}$, the physical states can be written as,

$$|B_L\rangle = p|B^0\rangle + q|\bar{B}^0\rangle, \quad |B_H\rangle = p|B^0\rangle - q|\bar{B}^0\rangle \ , \tag{1.25}$$

where the subindex L (H) refers to the lighter (heavier) Hamiltonian eigenstate with eigenvalue $\lambda_L = M_L - i\Gamma_L/2$ ($\lambda_H = M_H - i\Gamma_H/2$), and p and q satisfy $|p|^2 + |q|^2 = 1$. The mass and width difference are defined as follows,

$$\Delta m_d = M_H - M_L, \quad \Delta\Gamma = \Gamma_H - \Gamma_L \ , \tag{1.26}$$

so that Δm is positive by definition. Finding the eigenstates of Eq.(1.24) the following relations are derived

$$(\Delta m_d)^2 - \frac{1}{4}(\Delta\Gamma)^2 = 4(|M_{12}|^2 - \frac{1}{4}|\Gamma_{12}|^2) \ , \tag{1.27}$$

$$\Delta m_d \Delta\Gamma = 4\mathcal{R}e(M_{12}\Gamma_{12}^*) \ . \tag{1.28}$$

Finally, the ratio q/p is given by

$$\frac{q}{p} = -\frac{\Delta m_d - \frac{i}{2}\Delta\Gamma}{2(M_{12} - \frac{i}{2}\Gamma_{12})} \ . \tag{1.29}$$

The Schrödinger equation is solved immediately. Any B state can be written as an admixture of B_L and B_H

$$|B(t)\rangle = a_H(t)|B_H\rangle + a_L(t)|B_L\rangle \ . \tag{1.30}$$

The amplitudes of this admixture evolve in time as

$$a_H(t) = a_H(0)e^{-iM_H t}e^{-\frac{1}{2}\Gamma_H t} \ , \quad a_L(t) = a_L(0)e^{-iM_L t}e^{-\frac{1}{2}\Gamma_L t} \ . \tag{1.31}$$

In the case of the B_d mesons, they are expected to have negligible difference in lifetime (width). This difference is produced by decay amplitudes of channels common to B^0 and $\bar{B}^0$. The branching ratios for such channels are at or below the level of 10^{-3}. As many channels contribute with different signs, then it is expected that the sum does not exceed the individual level, hence $\Delta\Gamma_{B_d}/\Gamma_{B_d} \sim \mathcal{O}(10^{-2})$. The measured value of $\Delta m_d/\Gamma_{B_d} \sim 0.73$ implies then $\Delta\Gamma_{B_d} \ll \Delta m_d$ model-independently. It follows that (using Eqs. 1.27-1.29) $|\Gamma_{12}| \ll |M_{12}|$ and $|q/p| \sim 1$.

A state which is created at time $t = 0$ as an initially pure B^0 ($\bar{B}^0$), denoted by $|B^0_{phys}\rangle$ ($|\bar{B}^0{}_{phys}\rangle$), has (cf. Eq. 1.25) $a_L(0) = a_H(0) = 1/(2p)$ ($a_L(0) = -a_H(0) = 1/(2p)$). The time evolution of these states are, neglecting $\Delta\Gamma_{B_d}$ in front of Δm_d, given by

$$|B^0_{phys}(t)\rangle = e^{-i(M_H+M_L)t/2}e^{-\Gamma_d t/2}\left[\cos\left(\frac{\Delta m_d t}{2}\right)|B^0\rangle + i\frac{q}{p}\sin\left(\frac{\Delta m_d t}{2}\right)|\bar{B}^0\rangle\right], \quad (1.32)$$

$$|\bar{B}^0{}_{phys}(t)\rangle = e^{-i(M_H+M_L)t/2}e^{-\Gamma_d t/2}\left[\cos\left(\frac{\Delta m_d t}{2}\right)|\bar{B}^0\rangle + i\frac{p}{q}\sin\left(\frac{\Delta m_d t}{2}\right)|B^0\rangle\right]. \quad (1.33)$$

This oscillation phenomenon is governed by the Feynman diagrams shown in Fig. 1.2. In these diagrams are included three different up-quarks (u, c, t) loops , since all of them couple with the W boson *via* a λ^6 CKM factor. However, integrating over the internal degrees of freedom (up-quark and W boson momenta) yields an expansion that weights the contribution of each amplitude by the ratio of the corresponding quark mass to that of the W boson [20]. The top quark contribution is the dominant one, the corresponding CKM factor gives $(V_{td}V^*_{tb})^2 \sim e^{-2i\beta}$. Then, the B^0 states that oscillate into $\bar{B}^0$ pick up an extra phase -2β, known as the *mixing phase*, with respect to the B^0 states that do not oscillate. This phase is measurable whenever both B^0 and $\bar{B}^0$ decay to a common final state.

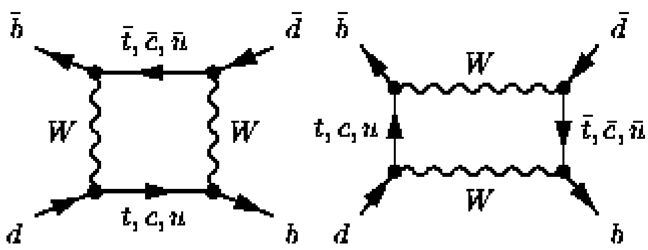

Figure 1.2: *Box Feynman diagrams for neutral B_d mixing.*

In the neutral B mesons, the amplitude for the mixing process is rather large due to the relative proximity of the values for their lifetime $\tau_{B^0} = (1.530 \pm 0.009)\mathrm{ps}$ and the oscillation frequency $\Delta m_d = (0.507 \pm 0.005)\mathrm{ps}^{-1}$ [21]. They give a large oscillation probability before decay

$$\chi_d = \frac{(\tau_{B^0}\Delta m_d)^2}{2[1 + (\tau_{B^0}\Delta m_d)^2]} = 0.1878 \pm 0.0024\,, \quad (1.34)$$

hence the prominent role of the mixing process. An immediate consequence is the large time-dependent CP asymmetries that mixing produces, which are described in Sec. 1.2.3 (CP violation in mixing and decay).

1.2.2 Tagging and Δt measurement from coherent $B^0\bar{B}^0$ production at *BABAR*

At an e^+e^- collider operating at the $\Upsilon(4S)$ resonance, neutral $B^0 - \bar{B}^0$ mesons are produced from the $\Upsilon(4S)$ decay in a coherent P-wave state. The $\Upsilon(4S)$ resonance is a spin 1

$b\bar{b}$ bound state with mass just above $B\bar{B}$ production threshold, and the B meson has spin zero. According to Bose-Einstein statistics, the total wave function has to be symmetric with respect to $B^0 - \bar{B}^0$ exchange. Conservation of angular momentum implies that the $B^0 - \bar{B}^0$ system is in a $l = 1$ relative orbital angular momentum state, so the spatial wave function is antisymmetric. Hence, the flavor wave function also has to be antisymmetric. Then, as long as both B mesons have not decayed, the system evolves in such a way that at any time there is only one B^0 and one $\bar{B}^0$ meson. If one of the B mesons, referred as $B_{\rm tag}$, decays to a state of known flavor (B^0 or $\bar{B}^0$) at a given time $t_{\rm tag}$, the other B, referred as B_{CP}, *at that time* must be of the opposite flavor (this is one case of the Einstein-Podolsky-Rosen paradox [22]). However once one of the particles decays, the other continues to evolve according to Eqs.(1.32) or (1.33), and events with two B^0 or two $\bar{B}^0$ are possible. This is the rationale for the flavor tagging technique of neutral B mesons used at BABAR when studying the $B^0/\bar{B}^0 \to f/\bar{f}$ decays. In this technique one of the B's is fully reconstructed, at the time t_{CP}, to the f final state (B_{CP}). The other B is partially reconstructed, at the time $t_{\rm tag}$, and its flavor is deduced from its decay products ($B_{\rm tag}$) (*e.g.* in semileptonic decays the charge of the lepton gives directly the B flavor, cf. Sec. 5.3). Knowing the B_{tag} flavor gives directly the B_{CP} flavor at $t_{\rm tag}$. Δt is defined as the time difference between B_{CP} and $B_{\rm tag}$ decays $\Delta t \equiv t_{CP} - t_{\rm tag}$ (cf. Fig. 1.3). The technique to measure Δt will be described with more details in Chapter 5.

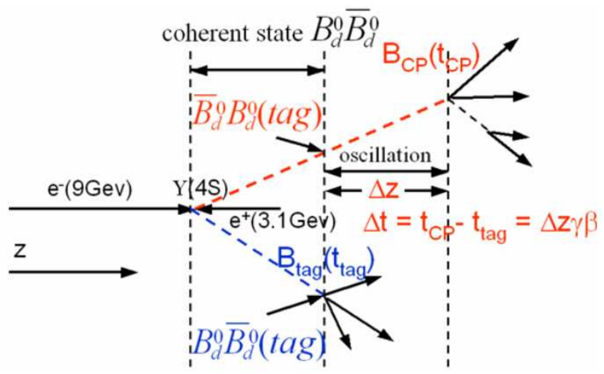

Figure 1.3: *Principle of the B flavor tagging and $\Delta t \equiv t_{CP} - t_{tag}$ measurement based on the coherent production of $B_d^0\bar{B}_d^0$ mesons pairs via the $\Upsilon(4S)$ resonance. If the $B_{\rm tag}$ meson is in the B_d^0 ($\bar{B}_d^0$) state at time $t = t_{\rm tag}$, then the B_{CP} is in the $\bar{B}_d^0$ (B_d^0) state at the same time.*

1.2.3 Three types of CP violation

The B ($\bar{B}$) meson decay amplitude to a final state f ($\bar{f}$), denoted by A_f ($\bar{A}_{\bar{f}}$), is written as

$$A_f = \langle f|\mathcal{H}|B\rangle \,, \tag{1.35}$$

$$\bar{A}_{\bar{f}} = \langle \bar{f}|\mathcal{H}|\bar{B}\rangle \,, \tag{1.36}$$

where $\mathcal{H}$ is the Hamiltonian governing the decay. A given process is made of different contributions, and the total amplitude is the sum of all of them

$$A_f = \sum_j a_j e^{i\delta_j} e^{i\phi_j} \ , \tag{1.37}$$

$$\bar{A}_{\bar{f}} = \sum_j a_j e^{i\delta_j} e^{-i\phi_j} \ , \tag{1.38}$$

where a_j is the modulus of the contributing amplitude, and δ_j and ϕ_j are the strong (CP-even) and weak (CP-odd) phases of that amplitude. In the SM the weak phases come from the *CKM* matrix elements, and the strong phases from the quark "dressing" (cf. Chapter 3).

The possible manifestations of CP violation can be classified in a model-independent way (cf. Fig. 1.4): 1) CP violation in decay; 2) CP violation in mixing; and 3) CP violation in the interference between decays with and without mixing. In each case it is useful to define the corresponding convention free CP-violating quantity.

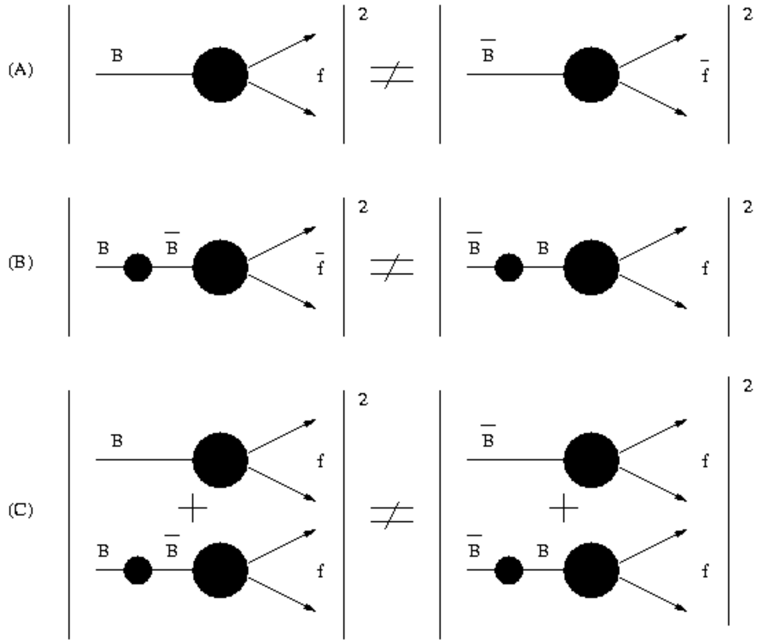

Figure 1.4: *Scheme representing the three types of CP violation: (A) direct CP violation, (B) CP violation in mixing, (C) CP violation in the interference between decays with and without mixing.*

1) Direct CP violation

There is direct CP violation if the transition probability $B^0 \to f$ is different from that of $\bar{B}^0 \to \bar{f}$,

$$\Gamma[B \to f] \neq \Gamma[\bar{B} \to \bar{f}] \iff \text{direct } CP \text{ violation} \ , \tag{1.39}$$

where Γ is the process rate. The CP asymmetry is defined as

$$\mathcal{A}_{CP} = \frac{\Gamma(\bar{B} \to \bar{f}) - \Gamma(B \to f)}{\Gamma(\bar{B} \to \bar{f}) + \Gamma(B \to f)} \; . \tag{1.40}$$

As the process rate is proportional to the total amplitude square, then Eq.(1.40) can be written as

$$\mathcal{A}_{CP} = \frac{1 - |A_f/\bar{A}_{\bar{f}}|^2}{1 + |A_f/\bar{A}_{\bar{f}}|^2} \; . \tag{1.41}$$

Hence, the direct CP violation condition can be written in terms of the convention free quantity

$$\left|\frac{\bar{A}_{\bar{f}}}{A_f}\right| \neq 1 \quad \Longrightarrow \quad \text{direct } CP \text{ violation} \tag{1.42}$$

This CP violation results from the interference among various terms in the decay amplitude. From Eqs.(1.37), (1.38) and (1.41), it can be seen that this type of CP violation will not occur unless at least two terms that have different weak and strong phases interfere,

$$|A_f|^2 - |\bar{A}_{\bar{f}}|^2 = -2 \sum_{i,j} a_i a_j \sin(\phi_i - \phi_j) \sin(\delta_i - \delta_j) \; . \tag{1.43}$$

Direct CP violation is the only kind of CP violation possible for the charged modes.

Direct CP violation in the interference pattern. Another observable related with this kind of CP violation can be obtained from Dalitz plot analyses (cf. Chapter 2). Due to interference between different components over the Dalitz plot, relative isobar phases (cf. Sec. 2.4.3) are directly accessible. If these phases between two interferring components are different for B and $\bar{B}$ decays, then there is CP violation. Let ϕ_{ij} and $\bar{\phi}_{ij}$ be the phase differences between components i and j for B and $\bar{B}$ decays, respectively. Then, the quantity $\Delta\phi_{ij} = \phi_{ij} - \bar{\phi}_{ij}$ is a CP violation observable

$$\Delta\phi_{ij} \neq 0 \quad \Longrightarrow \quad \text{direct } CP \text{ violation} \; . \tag{1.44}$$

This CP violation will be realized as a difference in the interference pattern in the B and $\bar{B}$ Dalitz plots. This can occur even if each component has $\mathcal{A}_{CP} = 0$ (cf. Eq.(1.40)).

Dalitz plot analyses of the $B^+ \to K^+\pi^-\pi^+$ [23, 24] decay channel have recently shown evidence for this manifestation of direct CP violation. If the result is confirmed, would be the first observation of direct CP violation in the decay of a charged particle.

2) CP violation in mixing

The fact that B^0 can turn into its CP conjugate gives rise to a different type of CP violation. It manifests itself as a difference in the transition probabilities $B^0 \to \bar{B}^0$ and $\bar{B}^0 \to B^0$:

$$\Gamma[B^0 \to \bar{B}^0] \neq \Gamma[\bar{B}^0 \to B^0] \quad \Longleftrightarrow \quad CP \text{ violation in mixing} \; . \tag{1.45}$$

This CP violation is related to the fact that mass eigenstates are not CP eigenstates. This difference can be expressed in terms of the convention free quantity $|q/p|$ (cf. Eq. 1.29) as

$$\left|\frac{q}{p}\right|^2 = \left|\frac{M_{12}^* - \frac{i}{2}\Gamma_{12}^*}{M_{12} - \frac{i}{2}\Gamma_{12}}\right| \; , \tag{1.46}$$

because the $B^0 \to \bar{B}^0$ and $\bar{B}^0 \to B^0$ transitions are described by the matrix elements $M_{12} - \frac{i}{2}\Gamma_{12}$ and $M_{12}^* - \frac{i}{2}\Gamma_{12}^*$, respectively. Then

$$|q/p| \neq 1 \implies CP \text{ violation in mixing} \, . \tag{1.47}$$

This type of CP violation was observed in the neutral K system in 1964 [1]. This phenomenon is expected to be negligible in the neutral B mesons (cf. section 1.2.1), so in the following the approximation $|q/p| \sim 1$ will be used.

3) CP violation in the interference of mixing and decay

CP violation in the interference between decays with and without mixing (or shortly CP violation in mixing and decay) occurs whenever

$$\Gamma[B^0 \to f] \neq \Gamma[\bar{B}^0 \to f] \; , \tag{1.48}$$

where f is a final state accessible to both B^0 and $\bar{B}^0$. This type of CP violation comes from the interference of amplitudes $A(B^0 \to f)$ and $A(B^0 \to \bar{B}^0 \to f)$ (and conversely for $\bar{B}^0$). In the following only the case of B^0 and $\bar{B}^0$ decaying to a common CP eigenstate f_{CP} with eigenvalue η_{CP} will be considered. The case in which f is not a CP eigenstate is more complicated, for an account see chapter 6 of [25].

The amplitudes for the processes $B^0_{phys}(t) \to f_{CP}$ and $\bar{B}^0{}_{phys}(t) \to f_{CP}$ are given by (cf. Eq.(1.32) and (1.33))

$$\begin{aligned} \langle f_{CP}|\mathcal{H}|B^0_{phys}(t)\rangle &= \eta_{CP} A_{f_{CP}} (g_+(t) + \lambda_{f_{CP}} g_-(t)) \; , & (1.49)\\ \langle \bar{f}_{CP}|\mathcal{H}|\bar{B}^0{}_{phys}(t)\rangle &= \eta_{CP} \langle f_{CP}|\mathcal{H}|\bar{B}^0{}_{phys}(t)\rangle = \eta_{CP} \frac{p}{q} A_{f_{CP}} (g_-(t) + \lambda_{f_{CP}} g_+(t)) \; , & (1.50) \end{aligned}$$

where $g_\pm(t)$ are written as

$$\begin{aligned} g_+(t) &= e^{-i(M_H+M_L)t/2} e^{-\Gamma_d t/2} \cos\left(\Delta m_d t/2\right) \; , & (1.51)\\ g_-(t) &= e^{-i(M_H+M_L)t/2} e^{-\Gamma_d t/2} i \sin\left(\Delta m_d t/2\right) \; , & (1.52) \end{aligned}$$

and where

$$\lambda_{f_{CP}} = \eta_{CP} \frac{q}{p} \frac{\bar{A}_f}{A_f} \; , \tag{1.53}$$

is the convention free quantity carrying the CP violation information. Consequently, the time-dependent CP asymmetry is given by (using Eq.(1.40), (1.49) and (1.50)),

$$\mathcal{A}_{CP}(t) = \frac{1 - |\lambda_{CP}|^2}{1 + |\lambda_{CP}|^2} \cos(\Delta m_d t) - \frac{2\mathcal{I}m(\lambda_{CP})}{1 + |\lambda_{CP}|^2} \sin(\Delta m_d t) \, . \tag{1.54}$$

Then, there will be CP violation if,

$$\lambda_{CP} \neq \pm 1 \quad \Longrightarrow \quad CP \text{ violation in mixing decay interference} \, . \tag{1.55}$$

It has to be noted that both direct ($|\bar{A}_f/A_f| \neq 1$) and mixing-induced CP violation ($|q/p| \neq 1$) verify Eq.(1.55). However, there are circumstances in which both $|\bar{A}_f/A_f| = |q/p| = 1$ and there is still CP violation through

$$|\lambda_{CP}| = 1, \quad \mathcal{I}m(\lambda_{CP}) \neq 0 \, . \tag{1.56}$$

In this case Eq.(1.54) is simplified to

$$\mathcal{A}_{CP}(t) = -\mathcal{I}m(\lambda_{CP}) \sin(\Delta m_d t) \, . \tag{1.57}$$

1.2.4 B factories achievements

First observation of CP violation in the B meson system and the measurement of $\sin(2\beta)$

The first major achievement of B factories is the precision measurement of the $\sin 2\beta$ parameter. A non-zero value was first measured in 2001 by the BABAR and Belle collaborations [26, 27] by studying CP violation in decays governed by $b \to c\bar{c}s$ transitions, known as *golden* modes (*e.g.* $B^0 \to J/\Psi K^0_S$). In these modes, the observed CP violation is from decay-mixing interference. The advantages in studying these modes are two-fold:

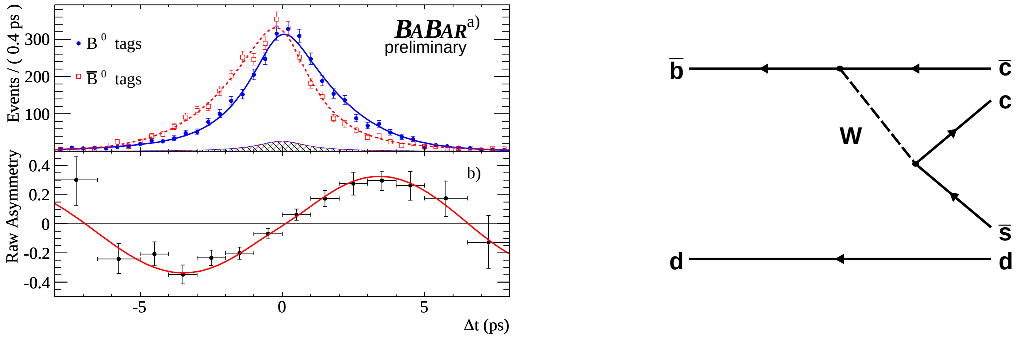

Figure 1.5: *On the left: The top histograms represent the time Δt distributions for $B_{\text{tag}} = B^0$ (red) and $B_{\text{tag}} = \bar{B}^0$ (blue) events in $B^0/\bar{B}^0 \to J/\Psi K^0_S$ decays. On the bottom the derived time-dependent asymmetry. On these plots the fitted probability density function is superimposed. On the right: dominant tree diagram for the $B^0 \to J/\Psi K^0_S$.*

- These modes have a very distinctive experimental signature, and so very clean event samples are available. This is illustrated on the left plot of Fig. 1.5, displaying the time distributions for $B_{\text{tag}} = B^0$ and $B_{\text{tag}} = \bar{B}^0$ events. At the bottom of the same plot the derived time-dependent CP-asymmetry is shown. It can be seen that the time evolution of B^0 and $\bar{B}^0$ mesons is different, which establishes the CP violation.

- Theoretically the *golden* modes are a clean way to have access to the β angle of the CKM matrix. For decays governed by $b \to c\bar{c}s$ transitions (cf. right plot of Fig. 1.5) such as $B^0 \to J/\Psi K^0_S$, and explicit representation of λ_{CP} (cf. Eq.(1.53)) can be found from the ratio of the amplitude for $\bar{B}^0 \to (c\bar{c})\bar{K}^0$ to the interfering process $\bar{B}^0 \to B^0 \to (c\bar{c})K^0 \to (c\bar{c})\bar{K}^0$. The decay $B^0 \to (c\bar{c})K^0$ involves a $\bar{b} \to \bar{c}c\bar{s}$ transition with an amplitude proportional to $[V^*_{cb}V_{cs}]$, while $\bar{B}^0 \to (c\bar{c})\bar{K}^0$ provides analogously a factor $\eta_{CP}[V_{cb}V^*_{cs}]$. Because $B^0 \to \bar{B}^0$ mixing is dominated by a loop diagram with a t quark, it introduces a factor $[V^*_{td}V_{tb}/V_{td}V^*_{tb}]$, while $K^0 \to \bar{K}^0$ mixing, dominated by the c quark loop, adds a factor of $[V^*_{cd}V_{cs}/V_{cd}V^*_{cs}]$. Altogether, for transitions of the type $b \to c\bar{c}s$,

$$\begin{aligned}\lambda_{CP} &= \eta_{CP}\left(\frac{V_{td}V^*_{tb}}{V^*_{td}V_{tb}}\right)\left(\frac{V_{cb}V^*_{cs}}{V^*_{cb}V_{cs}}\right)\left(\frac{V^*_{cd}V_{cs}}{V_{cd}V^*_{cs}}\right) \\ &= \eta_{CP}e^{-2i\beta} \ . \end{aligned} \tag{1.58}$$

  Then, for these modes $\mathcal{I}m(\lambda_{CP}) = sin(2\beta)$. The current HFAG average of $\sin(2\beta)$ for all the *charmonium* modes is [28]

$$\sin(2\beta) = 0.691 \pm 0.029 \pm 0.014 \ , \tag{1.59}$$

  where the first and second errors are statistical and systematical, respectively.

First observation of direct CP violation in the B mesons system

The first observation of direct CP violation was made in 2004 by *BABAR* and Belle [29, 30]. The *BABAR* measurement is represented in Fig. 1.6, where it is shown an sPlot[2] [31] of the energy difference (ΔE) for $B^0 \to K^+\pi^-$ (solid blue line) and $\bar{B}^0 \to K^-\pi^+$ (dotted red line) events. This variable is defined as the difference of $\sqrt{s}/2 - E^*_B$, where E^*_B is the reconstructed B meson energy in the collision e^+e^- CM frame (cf. Sec. 5.6.1). The $B^0/\bar{B}^0$ rate asymmetry is evidently non-zero. The current World Average value is $A_{K^+\pi^-} = -0.098^{+0.012}_{-0.011}$ [28].

1.3 Constraints on the *CKM* Matrix and B factories

The main purpose of flavor physics is to obtain redundant measurements of CKM related observables that can reveal physics beyond the SM. The CKMfitter group [14, 15] produces a global fit to the CKM matrix, known as the "standard CKM fit", based on a list of experimental constraints on the *CKM* matrix elements where theoretical errors are under control. The current list of "standard" inputs is given below:

- B factories allow to measure observables by studying the B_d and B_u mesons. *BABAR* and Belle have contributed with precision measurements of Δm_d and $\sin 2\beta$. Other parameters are also accessible given the high statistics accumulated by these two experiments: $|V_{ub}|$, $|V_{cb}|$, and the UT angles α and γ.

---

[2] An sPlot is technique to contruct background-subtracted event weights distributions.

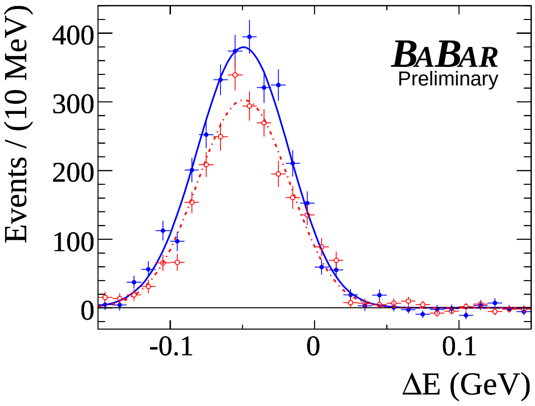

Figure 1.6: *sPlot of the distribution of ΔE for signal $B^0/\bar{B}^0 \to K^{\pm}\pi^{\mp}$ events, comparing (solid) B^0 and (dashed) $\bar{B}^0$ decays. The distribution is not centered at zero as the energy of the B meson candidate is calculated with a pion hypothesis for the kaon.*

  - $\Delta m_d = (0.507 \pm 0.005)\ \mathrm{ps}^{-1}$, extracted from oscillations in the neutral B_d system;
  - $\sin 2\beta$, measured from decays governed by $b \to c\bar{c}s$ transitions (cf. Sec. 1.2.4 for a description of this measurement);
  - $|V_{cb}| = (42.0 \pm 1.0) \times 10^{-3}$, most accurately obtained from exclusive $B \to D^{(*)}\ell\bar{\nu}_\ell$ and inclusive semileptonic $b \to c$ decays;
  - $|V_{ub}| = (3.90 \pm 0.68) \times 10^{-3}$, which can be extracted from either from inclusive $\mathcal{B}(B \to X_u\ell\overline{\nu_\ell})$ decays, or from exclusive decays such as $B \to \{\pi, \rho, \omega, \eta\}\ell\nu_\ell$;
  - α, measured from the isospin analysis of the $b \to u\bar{u}d$ charmless channels: $B \to \pi\pi$, $B \to \rho\pi$ and $B \to \rho\rho$;
  - γ, extracted from decays governed by $b \to c\bar{u}s$ quark level transitions (*e.g.* $B^+ \to \overline{D}^{(*)0}K^{(*)+}$).

- Studies in the neutral K and B_s systems, and β decays allow access to:

  - $|\epsilon_K| = (2.229 \pm 0.010) \times 10^{-3}$, from CP violation studies of neutral kaons;
  - $\Delta m_s = (17.77 \pm 0.12)\mathrm{ps}^{-1}$, the mass difference between B_H and B_L eigenstates in the neutral B_s meson system, is measured from oscillations of neutral B_s mesons. CDF [32] gives the strongest constraint;
  - $|V_{ud}| = 0.97418 \pm 0.00026$, from β decays of nuclei, neutrons and pions;
  - $|V_{us}| = 0.2246 \pm 0.0012$, from Kaon and hyperon semi-leptonic decays;

The most up to date result on the $(\bar{\rho}, \bar{\eta})$ plane, obtained with the latest measurements for the ICHEP08 conference, is presented in Fig. 1.7. The elliptical region shows the allowed region by the SM for the apex of the UT.

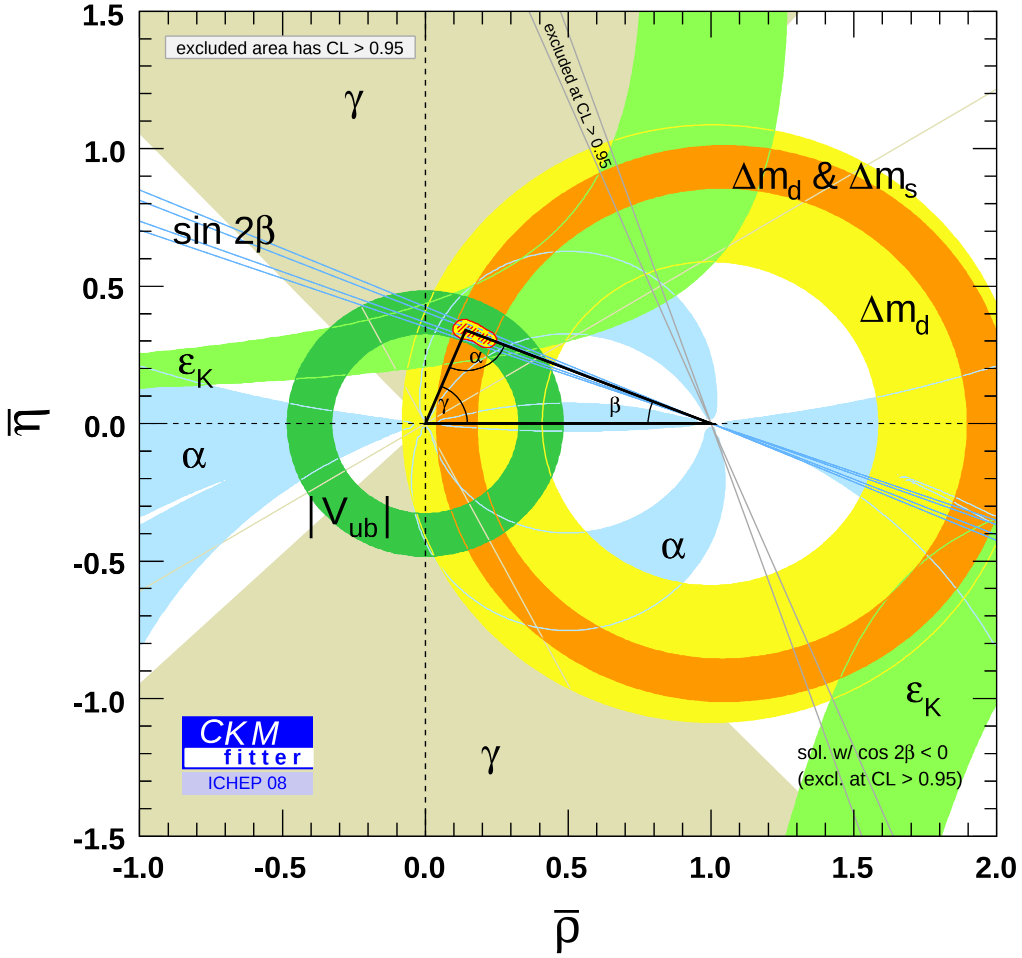

Figure 1.7: *Individual constraints on the* $(\bar{\rho}, \bar{\eta})$ *plane from the* $|\varepsilon_K|$, $|V_{ud}|$, $|V_{us}|$, $|V_{cd}|$, $|V_{ud}|$, $|V_{cs}|$, Δm_d, Δm_s, $|V_{ts}|$, *and the direct measurements of the UT angles* α, β *and* γ. *The regions containing the points with a CL higher than* 5% *are drawn in color. The global* CKM *fit gives an almost "elliptical" constraint in the center of the plot.*

All the measurements of the CKM parameters are compatible among themselves and with the SM. The compatibility delimits a much reduced area in the parameter space. This result combines measurements of processes of different nature: processes that violate/conserve CP, processes dominated by tree amplitudes or dominated by loops, and processes that come from very diverse sectors (nuclei, neutrons, pions, kaons, B and B_s mesons). The constrained region in Fig. 1.7 indicates that the CKM mechanism gives a solid description of the experimental data, which reduces strongly the parameter space for possible flavor mixing scenarios beyond the SM.

The contribution of B factories to the knowledge of the CKM parameters is not limited to metrological purposes (*i.e.* to measure the *CKM* matrix elements in the hypothesis that the SM is correct). Precision measurements in search for new physics are also performed. New physics searches have been broadened not only by improving the precision of the measurements, but also by increasing the number of processes used to obtain the desired parameters. One example is the study of $B \to K^*\pi$ and $B \to \rho K$ modes presented in Chapter 3.

Given the great success of the SM, a scenario of *Minimal Flavor Violation* is the hypothesis favored up to date: non-standard physics contributions would appear as small perturbations of the CKM mechanism. B factories today are increasingly oriented to study processes sensitive to effects of this non-standard physics.

A possible candidate to achieve such a goal, are amplitudes analyses (cf. Chapter 2) where weak and strong phases can be directly disentangled by resolving the interference patterns, and so could have a better sensitivity to contributions from physics beyond the SM. This approach subtends the statistical and phenomenological analyses presented in Part III and Chapter 8.

Chapter 2

$B^0 \to K^0_S\pi^+\pi^-$ and Charmless 3-body B decays

2.1 Introduction

Decays of B mesons to three-body charmless hadronic final states have attracted considerable attention in recent years. Amplitude (Dalitz Plot) analyses for a number of three-body final states have been performed ($K^+\pi^-\pi^+$, $K^+\pi^-\pi^0$, $K^0_S\pi^+\pi^-$, $K^+K^-K^+$, $K^+K^-K^0_S$), where branching fractions for many quasi-two body (Q2B) (the two bodies being a stable particle and a resonance, hence the term "quasi") resonant states have been measured for the first time or with a significantly improved accuracy. The three-body charmless final states provide a rich laboratory for studying different aspects of strong interactions, but more importantly they provide new possibilities for searches of CP-violation, and many new tests of the CKM framework for charged current weak interactions. In decays to three-body final states that are often dominated by Q2B channels, the strong phase motion along the lineshape of interfering resonances are measured and can be used to constrain the CKM phases. While in decays to two-body final states ($B \to K\pi, \pi\pi$) direct CP-violation can be observed as a difference in the B and $\bar{B}$ decay rates, in the three-body channels CP-violation can furthermore manifest itself as a difference in interference pattern of two Q2B interfering amplitudes contributing to B and $\bar{B}$.

This chapter discusses the kinematics and dynamics of the three body decays, which are essential tools for the time-dependent amplitude analysis of the $B^0 \to K^0_S\pi^+\pi^-$ mode. First, the experimental and theoretical status of Dalitz plot analyses is summarized. Then a word is said about searches for New Physics with the measurement of $\sin(2\beta_{eff})$ with the Penguin-dominated modes $B^0 \to f_0(980)K^0_S$ and $B^0 \to \rho^0(770)K^0_S$ that contribute to the decay channel studied in this thesis. The rest of the chapter is dedicated to the theoretical description of time-dependent Dalitz Plot analyses. The kinematics of three body decays are presented with the definition of the Dalitz Plot (DP). The isobar model is presented, which is used to describe the decay dynamics, giving the Dalitz Plot dependence of the decay amplitudes. The time and DP dependence of the probability density function (PDF) used in the Maximum Likelihood Fit is given. Finally, the definitions of physical parameters in terms of fit parameters are presented.

2.2 Experimental and theoretical status

The study of charmless Q2B and three-body B decays is one of the main topics in the physics program of B factories. Since branching fractions for most hadronic channels are of the order of 10^{-5} to 10^{-6} [33], the higher accumulated statistics allows for Dalitz Plot analyses for the most prominent modes or those with high reconstruction efficiencies, such as $B^+ \to \pi^+\pi^-\pi^+$ [34], $B^0 \to (\rho\pi)^0$ [35, 36], $B^+ \to K^+K^-K^+$ [37], $B^0 \to K^+K^-K^0$ [38], $B^0 \to K^+\pi^-\pi^0$ [39, 40], $B^+ \to K^+\pi^-\pi^+$ [23, 24]. In this latter mode, BABAR and Belle find the first evidence for direct CP-violation in a charged mode, with the $B^+ \to \rho^0K^+$ submode, both experiments yielding a similar level of significance.

The $B^0 \to (\rho\pi)^0$ result was the first amplitude analysis including flavor tagging and time-dependence, and later on the $B^0 \to K^+K^-K^0$ analysis followed. For the mode $B^0 \to K^0_S\pi^+\pi^-$, only Q2B [41] and tag- and time-integrated Dalitz plot [42] analyses had been performed before the analysis presented in this thesis. The Q2B approach isolates different components on the Dalitz plot and measures the corresponding yields. The disadvantage of this approach is that interference between components is ignored. This introduces substantial systematic uncertainties. Specifically, there is no access to the phase differences between interfering components, and only the corresponding branching ratios and CP-asymmetries (provided the tagging information is not ignored) can be extracted. CP-averaged interference patterns can be extracted from tag- and time-integrated Dalitz plot analyses, which enables one to measure average phase differences and relative magnitudes between the amplitudes of the different components. The fact that the time and tagging information are ignored means that no CP-asymmetries are accessible. The analysis treated in this thesis includes simultaneously the tag, time and Dalitz plot information, determining with improved accuracy phase differences, CP-asymmetries and branching fractions. Also, as explained in chapter 3, the observables accessible from this analysis are ingredients for the phenomenological analyses of the $K^*\pi$ and $K\rho$ systems.

From previous Q2B [41, 43, 44, 45] and time-integrated amplitude analyses [42], an inclusive branching fraction of $\mathcal{B}(B^0 \to K^0\pi^+\pi^-) = (44.8 \pm 2.5) \times 10^{-6}$ was measured, and significant yields for the $K^*(892)$, $K^*_0(1430)$, $f_0(980)$ and $\rho^0(770)$ resonant states were found. In their time-integrated amplitude analysis, Belle finds an excess in the $\pi^+\pi^-$ invariant mass spectrum around $\sim 1.3\mathrm{GeV}/c^2$, which they model as the coherent sum of a $f_2(1270)$ and a scalar, somewhat arbitrarily. Branching fractions and Dalitz plot structure are in agreement with the ones found in $B^+ \to K^+\pi^-\pi^+$ and $B^0 \to K^+\pi^-\pi^0$ modes, as expected. Tables 2.1 and 2.2 summarize the experimental findings.

On the theoretical side, there exist predictions for the branching fractions and CP-asymmetries for the $B^0 \to K^{*+}(892)\pi^-$, $B^0 \to \rho^0(770)K^0_S$ and $B^0 \to f_0(980)K^0_S$ resonant modes, which contribute to the $B^0 \to K^0_S\pi^+\pi^-$ final state. For the $f_0(980)$ there is no strong consensus about its quark structure. Some claim it to be a two-quark state, where $s\bar{s}$, $(u\bar{u} + d\bar{d})/\sqrt{2}$ states are mixed, due to the fact that this resonance can decay to KK and $\pi\pi$. Other claim that is a four-quark state. So the theoretical calculations are difficult to interpret. Those predictions are based on QCD factorization [46], $SU(3)$ flavor symmetry [47] and QCD factorization including final state interactions [48]. The direct CP-asymmetries are predicted to be large for the $K^{*\pm}(892)\pi^\mp$ and $\rho^0(770)K$ components. The predicted

Parameter	BABAR	Belle
$\mathcal{B}(B^0 \to \rho^0(770)K^0_S)$	$4.9 \pm 0.8 \pm 0.9$ [45]	$6.1 \pm 1.0^{+1.1}_{-1.2}$ [42]
$\mathcal{B}(B^0 \to f_0(980)(\to \pi^+\pi^-)K^0_S)$	$5.5 \pm 0.7 \pm 0.6$ [41]	$7.6 \pm 1.7^{+0.9}_{-1.3}$ [42]
$\mathcal{B}(B^0 \to K^{*+}(892)\pi^-)$	$12.6^{+2.7}_{-1.6} \pm 0.9$ [40]	$8.4 \pm 1.1^{+1.0}_{-0.9}$ [42]
$\mathcal{A}_{CP}(B^0 \to K^{*+}(892)\pi^-)$	$-0.19^{+0.20}_{-0.15} \pm 0.04$ [40]	—
$\mathcal{B}(B^0 \to (K\pi)^*_0)$	$9.4^{+1.1+1.4}_{-1.3-1.1} \pm 1.8$ [40]	$49.7 \pm 3.8^{+6.8}_{-8.2}$ [42]
$\mathcal{B}(B^0 \to K^0_S\pi^+\pi^-)_{NR}$	—	$19.9 \pm 2.5^{+1.7}_{-2.0}$ [42]
$\mathcal{B}(B^0 \to K^0_S\pi^+\pi^-)_{tot}$	$43.0 \pm 2.3 \pm 2.3$ [41]	$47.5 \pm 2.4 \pm 3.7$ [42]

Table 2.1: *Summary of the total and partial Branching fractions (in units of 10^{-6}), and direct CP-asymmetry (only for the $B^0 \to K^+(892)\pi^-$) measurements made by BABAR and Belle before the present analysis. The $(K\pi)^*_0$ notation refers to the S-wave $K\pi$.*

time-dependent CP-asymmetries are usually large.

2.3 $b \to s\bar{q}q$ Penguin Dominated Modes and New Physics

It is possible to detect physics beyond the SM (or New Physics (NP)) by measuring the β angle in $b \to q\bar{q}s$ ($q = u, d, s$) Penguin dominated decays. Such loops are dominated by virtual t-quarks, which involve a single CKM factor $V^*_{tb}V_{ts}$. Thus, in the context of the SM, if the CP-asymmetry in the $B_d \to f_{CP}$ is measured, where f_{CP} is an CP eigenstate with eigenvalue $\eta_{CP} = \pm 1$, and the decay is dominated by a $b \to q\bar{q}s$ hadronic Penguin, a probe to NP is made. In effect, the CKM phase involved in the $b \to q\bar{q}s$ Penguin dominated decays is the same as that probed in $b \to c\bar{c}s$ (golden modes, *e.g.* $B^0_d \to J/\psi K^0_S$), so it is expected to have $\sin 2\beta_{q\bar{q}s} = -\eta_{CP} \sin 2\beta_{c\bar{c}s}$ for the mixing induced CP-asymmetry and also $\mathcal{A}_{CP} \sim 0$ for the direct CP-asymmetry. Therefore, a discrepancy would clearly point to NP, which would indicate that there are new amplitudes contributing to the hadronic $b \to q\bar{q}s$ Penguin decays, corresponding to new particles circulating in the loop.

A number of $b \to q\bar{q}s$ Penguin dominated decay channels have been identified; among them are $K^+K^-K^0_S$, ϕK^0_S, $\eta' K^0_S$, $K^0_S K^0_S K^0_S$, $\pi^0 K^0_S$, ωK^0_S, $\pi^0\pi^0 K^0_S$, $f_0(980)K^0_S$ and $\rho^0(770)K^0_S$. The last two modes contribute to the $B^0 \to K^0_S\pi^+\pi^-$ signal (the decay channel studied in the thesis). Depending on the mode, the decay amplitudes can get contributions from the quark-level $b \to u\bar{u}s$ Tree diagram, so that the level of Penguin-dominance is mode-dependent (for instance, ϕK^0_S, $K^0_S K^0_S K^0_S$ and $\eta' K^0_S$ are considered very clean). What is measured with these modes is not directly β but rather β_{eff}, which includes the Tree contamination. Currently, the discrepancies between charmonium and charmless time-dependent asymmetries are not statistically significant, but compilations [28] (cf. Fig. 2.1) show that most central values of $\sin 2\beta_{eff}$ are below $\sin 2\beta$ from the golden modes. As a general rule, theoretical estimations [48] would push $\sin(2\beta_{eff})$ above $\sin(2\beta_{c\bar{c}s})$.

In this analysis it is possible to measure $\sin 2\beta_{eff}$ for the $B^0 \to f_0(980)K^0_S$ and $B^0 \to \rho^0(770)K^0_S$ Penguin dominated decays. Such measurements have been performed previously on smaller data samples with the Q2B approaches [43, 44, 45]. A Dalitz plot analysis of

Parameter	BABAR	Belle
$S(B^0 \to \rho^0(770)K^0_S)$	$0.20 \pm 0.52 \pm 0.24$ [45]	—
$C(B^0 \to \rho^0(770)K^0_S)$	$0.64 \pm 0.41 \pm 0.20$ [45]	—
$S(B^0 \to f_0(980)(\to \pi^+\pi^-)K^0_S)$	$-1.62^{+0.56}_{-0.51} \pm 0.09$ [43]	$0.18 \pm 0.23 \pm 0.11$ [44]
$C(B^0 \to f_0(980)(\to \pi^+\pi^-)K^0_S)$	$0.27 \pm 0.36 \pm 0.12$ [43]	$0.15 \pm 0.15 \pm 0.07$ [44]

Table 2.2: *Summary of the direct and mixing induced CP-asymmetry measurements for the $B^0 \to f_0(980)(\to \pi^+\pi^-)K^0_S$ and $B^0 \to \rho^0(770)K^0_S$ modes made by BABAR and Belle before the present analysis.*

the larger data sample is justified, since it can improve the Q2B measurements shown on table 2.2, by properly accounting for the interference between resonances. Also, whereas the Q2B analyses are sensitive only to $\sin 2\beta_{eff}$, an amplitude analysis can use the interferences with the other resonances to extract directly the β_{eff} phase.

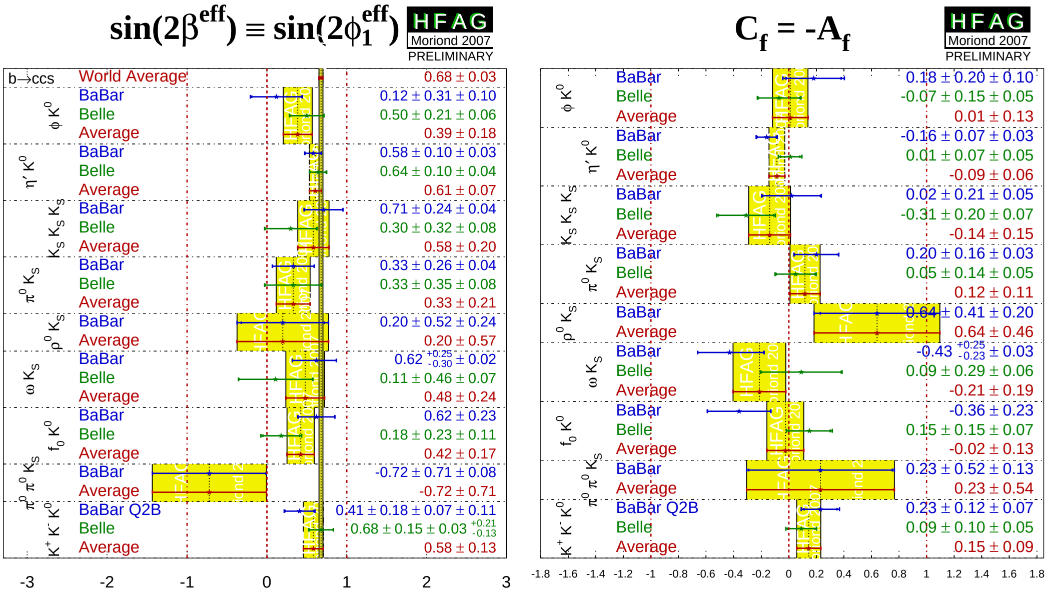

Figure 2.1: *Summary of the $\sin 2\beta_{eff}$ (left) and A_{CP} (right) measurements from the Penguin dominated modes compared with the golden modes ($b \to c\bar{c}s$) measurements, according to the Heavy Flavor Averaging Group* [28] *after the 2007 Winter conferences (updated summary figures will be shown in Chapter 8, including results from this thesis). The central values of the Penguin modes tend to be below the values of the golden modes ($b \to c\bar{c}s$), but the discrepancies are not statistically significant. For the direct CP-asymmetries all measurements are consistent with zero, as expected in the SM.*

2.4 Three-Body Decays and the $B^0 \rightarrow K^0_S\pi^+\pi^-$ Channel

This section recalls the basic properties of three-body decay kinematics and the dynamical model, as far as they are needed to motivate the various choices and conventions that are used in the analysis. It is important to describe in detail the latter, as a single sign or a different helicity convention will change the numerical value for the parameters that will be extracted. This section is based on [21, 35, 49].

The main challenge of Dalitz Plot analyses is the construction of a realistic signal probability density function (PDF), where both the kinetic and dynamical properties as well as their time dependence are modeled to good accuracy.

2.4.1 Particle Decays

The partial decay rate of a mother particle of mass M into n daughters in its rest frame is given in terms of the Lorentz-invariant matrix element $\mathcal{A}$ by

$$d\Gamma = \frac{(2\pi)^4}{2M}|\mathcal{A}|^2 d\Phi_n(P;p_1,...,p_n)\ , \tag{2.1}$$

where $d\Phi_n$ is an element of n-body phase space given by

$$d\Phi_n(P;p1,...,p_n) = \delta^4(P - \sum_{i=1}^{n} p_i)\prod_{i=1}^{n}\frac{d^3\mathbf{p}_i}{(2\pi)^3}2E_i\ , \tag{2.2}$$

where P and p_i are the four-momentum of the mother and i-th daughter particles, respectively, and $\mathbf{p_i}$ and E_i are the three-momentum and energy, respectively, of the i-th daughter in the mother particle rest frame. This phase space can be generated recursively,

$$\begin{array}{rcl} d\Phi_n(P;p_1,...,p_n) & = & d\Phi_j(q;p_1,...,p_j) \\ & \times & d\Phi_{n-j+1}(P;p_{j+1},...,p_n)(2\pi)^3 dq^2\ , \end{array} \tag{2.3}$$

where $q = \sum_{i=1}^{j} p_i$. This form is particularly useful in the case where a particle decays into another particle that subsequently decays.

2.4.2 The Dalitz Plot

Consider the decay of a spin-zero B^0 meson with four-momentum p_B into three daughters $\pi^+(p_+)$, $\pi^-(p_-)$ and $K^0_S(p_0)$, with corresponding four-momenta. The original number of 12 unknowns in the B^0 rest frame is reduced to 2, taking advantage of the known masses of the four particles involved (4 constraints), energy and momentum conservation (4) and the fact that two spatial angles are irrelevant (no direction is preferred) (2). As independent variables, the two-body invariant masses squared (Mandelstam variables) are used

$$s_+ = (p_+ + p_0)^2,\quad s_- = (p_- + p_0)^2\ . \tag{2.4}$$

The invariant mass of the positive and negative pion, $s_0 = (p_+ + p_-)^2$, is obtained from energy and momentum conservation:

$$s_0 = m^2_{B^0} + 2m^2_{\pi^+} + m^2_{K^0_S} - s_- - s_+ \; . \tag{2.5}$$

Using the Mandelstam variables to describe the B^0 decay process, the differential width reads

$$d\Gamma(B^0 \to K^0_S\pi^+\pi^-) = \frac{1}{(2\pi)^3}\frac{|\mathcal{A}|^2}{32m^3_{B^0}}ds_+ds_- \; , \tag{2.6}$$

where $\mathcal{A}$ is the Lorentz-invariant amplitude for the $B^0 \to K^0_S\pi^+\pi^-$ transition. In the following, $\bar{\mathcal{A}}$ will represent the amplitude for the $\bar{B}^0 \to K^0_S\pi^+\pi^-$ transition. Note that a trivial integration over the spatial angles has been performed prior to Eq. 2.6. The scatter plot in s_+ and s_- plane is called the *Dalitz Plot*. In the following, the notation $\{DP\}$ for the Dalitz plot coordinates $\{s_+, s_-\}$ will be used, and, correspondingly, $\{dDP\}$ for the Dalitz plot element $\{ds_+ds_-\}$. Similarly, $\{\overline{DP}\}$ will refer to the pair $\{s_-, s_+\}$. The symmetric boundaries of the DP are obtained when, *e.g.* for a $K^{*+} \to K^0_S\pi^+$ resonance, $\mathbf{p}_+$ and $\mathbf{p}_0$ are parallel (minimum mass-squared) or anti-parallel (maximum mass-squared). As a function of s_+, the kinematic boundaries $s_-[max]$ and $s_-[min]$ are given by

$$s_-[max/min](s_+) = (E^*_- + E^*_0)^2 - \left(\sqrt{E^{*2}_- - m^2_{\pi^+}} \mp \sqrt{E^{*2}_0 - m^2_{K^0_S}}\right)^2 \; , \tag{2.7}$$

where

$$E^*_+ = \frac{s_+ - m^2_{K^0_S} + m^2_{\pi^+}}{2\sqrt{s_+}} \; , \tag{2.8}$$

$$E^*_0 = \frac{s_+ - m^2_{\pi^+} + m^2_{K^0_S}}{2\sqrt{s_+}} \; , \tag{2.9}$$

$$E^*_- = \frac{m^2_{B^0} - s_+ - m^2_{\pi^+}}{2\sqrt{s_+}} \; , \tag{2.10}$$

are the energies in the $(K^0_S\pi^+)$ rest frame. For events close to the edges of the DP one of the s_i ($i = +, 0, -$) takes a small value while the others are rather large, whereas in the center of the DP the invariant masses of the three pairs of particles take approximately the same values. This implies that in the latter case, the directions of the three particles are distributed quite isotropically, and they carry similar energies, whereas in the former case, one particle in the final state is back-to-back to the other two, which move in parallel, giving the event a strong directionality. Finally, for an event lying near the corners of the DP, one of the particles is slow.

If $|\mathcal{A}|^2$ is constant, the allowed region on the DP will be uniformly populated with events. A nonuniformity in the DP gives immediate information on $|\mathcal{A}|^2$. As an example with the $B^0 \to K^0_S\pi^+\pi^-$ decay mode, bands appear when $s_+ = m^2_{K^{*+}(892)}$, reflecting the decay chain $B^0 \to K^{*+}(892)(\to K^0_S\pi^+)\pi^-$.

Due to angular momentum conservation, the distribution of events decaying through a scalar resonance will uniformly populate the band of mass associated to the intermediate state, since the lack of spin means there is no preferred direction for the daughters of the resonance. For a vector intermediate state, however, a privileged direction exists due to the fact that in this case the resonance is polarized in a helicity-zero state. Therefore, one needs to compute three helicity angles (one for each $(K_S^0\pi^+)$, $(K_S^0\pi^-)$ and $(\pi^+\pi^-)$ pair of particles), *e.g.* the $cos\theta_+$ is defined as the cosine of the angle between the negative B^0 momentum in the $(K_S^0\pi^+)$ rest frame (which is the flight direction of the $(K_S^0\pi^+)$ pair in the B^0 rest frame, and the negative flight direction of the π^- in the B^0 rest frame) and the momentum $\mathbf{p}_+^*$ of the π^+ in the $(K_S^0\pi^+)$ rest frame. It is given by

$$cos\theta_+ = -\frac{2E_+^*E_-^* + 2m_{\pi^+}^2 - s_0}{2|\mathbf{p}*_+||\mathbf{p}*_-|} \ , \tag{2.11}$$

and the expansion as a function of the Dalitz variables s_+, s_-, leads to

$$\begin{aligned} cos\theta_+ \quad = \quad & -\left[s_+(s_- - s_0) - \left(m_{B^0}^2 - m_{\pi^+}^2\right)\left(m_{K_S^0}^2 - m_{\pi^+}^2\right)\right] \\ & \times \left[m_{\pi^+}^4 + \left(s_+ - m_{K_S^0}^2\right)^2 - 2m_{\pi^+}^2\left(s_+ + m_{K_S^0}^2\right)\right]^{-1/2} \\ & \times \left[m_{\pi^+}^4 + \left(s_+ - m_{\pi^+}^2\right)^2 - 2m_{\pi^+}^2\left(s_+ + m_{\pi^+}^2\right)\right]^{-1/2} \quad , \end{aligned} \tag{2.12}$$

where s_0 is obtained from Eq. 2.5. Exchanging $s_+ \leftrightarrow s_-$ in Eq. 2.12 yields the cosine of the helicity angle of the $(K_S^0\pi^-)$ pair, $cos\theta_-$, and replacing $s_+ \longrightarrow s_0$ together with $m_{K_S^0} \leftrightarrow m_{\pi^+}$ gives $-cos\theta_0$ for the $(\pi^+\pi^-)$ pair. Fig. 2.2 illustrates the conventions that are adopted for the helicity angles:

- $\mathbf{cos}\theta_+(\mathbf{K_S^0}\pi^+)$ is defined as the angle between the π^+ in the $(K_S^0\pi^+)$ rest frame and the $(K_S^0\pi^+)$ flight direction in the B^0 rest frame.
- $\mathbf{cos}\theta_-(\mathbf{K_S^0}\pi^-)$ is defined as the angle between the π^- in the $(K_S^0\pi^-)$ rest frame and the $(K_S^0\pi^-)$ flight direction in the B^0 rest frame.
- $\mathbf{cos}\theta_\mathbf{0}(\pi^+\pi^-)$ is defined as the angle between the π^+ in the $(\pi^+\pi^-)$ rest frame and the $(\pi^+\pi^-)$ flight direction in the B^0 rest frame.

For vanishing relative strong phases, each resonance overlap comes with a relative minus sign so that maximal destructive interference is observed at all points with equal masses squared.

2.4.3 The isobar model

The amplitude $\mathcal{A}$ contains all the underlying dynamics of the $B^0 \to K_S^0\pi^+\pi^-$ decay. In the isobar model approximation [50, 51] the amplitude is modeled as the coherent sum of terms with individual couplings, propagators and spins J, each representing a resonant state in one pair of particles,

$$\mathcal{A}(DP) = \sum_{i=j}^{N} c_j F_j^J(DP) \ , \tag{2.13}$$

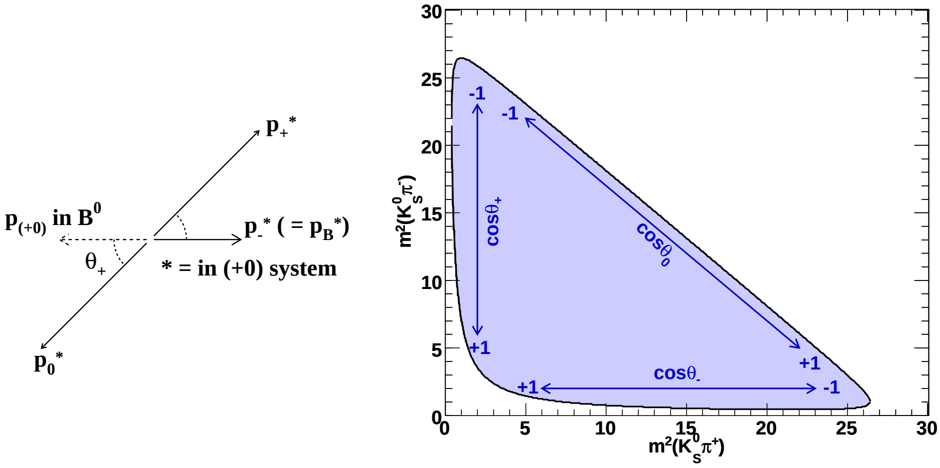

Figure 2.2: *Convention adopted for the helicity angles. Left: Example for the θ_+ helicity angle definition. Right: graphical representation of the helicity conventions on the Dalitz plot. For vanishing relative strong phases it leads to destructive interference in all points of the Dalitz plot where at least two of the three mass combinations are equal. See text for the geometrical definition.*

$$\overline{\mathcal{A}}(DP) = \sum_{j=1}^{N} \overline{c}_j \overline{F}_j(DP) \,, \tag{2.14}$$

where N is the number of intermediate states considered, c_j ($\overline{c}_j$) are complex amplitudes describing the couplings of the B^0 ($\bar{B}^0$) meson to the particular resonant final state, and $F_j^J(DP)$ ($\overline{F}_j^J(DP)$) are the DP-dependent dynamical amplitudes for each spin J resonant state. All the weak phase dependence is contained in c_j (it also contains strong phases), while $F_j^J(DP)$ contains the strong dynamics only, therefore

$$F_j^J(DP) = \overline{F}_j^J(\overline{DP}) \,. \tag{2.15}$$

The F_j^J term is represented by the product of the invariant mass factor and angular distributions, *i.e.*

$$F_j^J(DP) = R_j^J(m) \times X_J(|\mathbf{p}^*|r_j) \times X_J(|\mathbf{q}|r_j) \times T_j(J, \mathbf{p}, \mathbf{q}) \,, \tag{2.16}$$

where:

- m is the invariant mass of the two decay products of the resonance,
- $R_j^J(m)$ is the resonance mass term or “lineshape” (*e.g.* Breit-Wigner),
- $T_j(J, \mathbf{p}, \mathbf{q})$ is the angular distribution,
- X_J are the Blatt-Weisskopf penetration factors (barrier factors) with parameter r_j,

- $\mathbf{p}^*$ is the momentum of the bachelor particle (*i.e.* the accompanying particle b in the decay $B \to R\, b$, where R is the resonant state) evaluated in the B^0 rest frame,

- $\mathbf{p}$ and $\mathbf{q}$ are the momenta of the bachelor particle and one of the resonance daughters, respectively, both evaluated in the resonance rest frame. The modulus of $\mathbf{q}$ is a function of m and the resonance daughter masses, m_a and m_b, given by

$$|\mathbf{q}| = \frac{m}{2}\left(1 - \frac{(m_a + m_b)^2}{m^2}\right)^{1/2}\left(1 - \frac{(m_a - m_b)^2}{m^2}\right)^{1/2} , \tag{2.17}$$

The conventions adopted for these terms are described in detail in the following.

A Dalitz plot or amplitude analysis extracts the complex couplings c_j and $\overline{c}_j$ from data, out of a specific model for the resonant structure. As will be seen later, the time and DP-dependent probability density function (PDF) depends on $|\mathcal{A}|^2$, $|\overline{\mathcal{A}}|^2$ and $\overline{\mathcal{A}}\mathcal{A}^*$ (cf. Eq. 2.43), which means that bilinear terms on the dynamical amplitudes will appear in the model of the distribution over the DP. These terms, which are proportional to $F_jF_k^*$, $F_j\overline{F}_k^*$ or $\overline{F}_j\overline{F}_k^*$, respectively, are sensitive to the interference between two resonances j and k, thus allowing for the relative phase between c_j and c_k, c_j and $\overline{c}_k$ or $\overline{c}_j$ and $\overline{c}_k$ to be determined. For the c_j and $\overline{c}_k$ complex amplitudes, a polar parameterization in terms of moduli and phases can be adopted, $c_j = |c_j|e^{i\phi_j}$ and $\overline{c}_k = |\overline{c}_k|e^{i\overline{\phi}_k}$.

Finally, it is important to mention that the Isobar Model (Eqs. 2.13, 2.14) neglects rescattering of the final state particles and is known to lead to unitarity violation whenever the overlapping of two resonances is significant. Alternatives, such as the K-matrix [52, 53, 54] model, exist but their complexity outweights their merits for the present analysis given the current statistics.

2.4.4 Mass term description

For the resonance mass terms, several different forms are used. A summary of the parameters, as masses and widths, used in the lineshapes of the different resonances is given on Tables 2.3 and 2.4.

Relativistic Breit-Wigner lineshape

The relativistic Breit-Wigner (RBW) [21, 55, 56] lineshape is used to describe the $K^*(892)$ and $f_X(1300)$ resonant states, and also *minor* resonances that are added to the nominal signal model for systematics studies (cf. Sec. 7.3). For this parameterization:

$$R_j^J(m) = \frac{1}{[(m_j^0)^2 - m^2)] - i m_j^0 \Gamma_j^J(m)} , \tag{2.18}$$

where m is the invariant mass of the two-daughter combination, m_j^0 is the resonance pole mass and $\Gamma_j^J(m)$ is the width dependent on the invariant mass m, defined by

$$\Gamma_j^J(m) = \Gamma_j^0 \left(\frac{|\mathbf{q}|}{|\mathbf{q}|_0}\right)^{2J+1}\left(\frac{m_j^0}{m}\right) X_J^2(|\mathbf{q}|r_j) , \tag{2.19}$$

Resonance	Parameters	Form Factor	Ref. for Parameters
$f_0(980)$	mass $= 965 \pm 10$	Flatte	[59]
	$g_\pi = 165 \pm 18$		
	$g_K = 695 \pm 93$		
$\rho^0(770)$	mass $= 775.5 \pm 0.4$	GS	[21]
	width $= 146.4 \pm 1.1$		
	radius $= 5.3^{+0.9}_{-0.7}$		
$K^{*+}(892)$	mass $= 891.66 \pm 0.26$	RBW	[21]
	width $= 50.8 \pm 0.9$		
	radius $= 3.6 \pm 0.6$		
$K^{*+}(1430)$	mass $= 1415 \pm 3$	LASS	[60]
	width $= 300 \pm 6$		
	Effective Range term cutoff$= 1800$		
	$a = 2.07 \pm 0.1(\mathrm{GeV}/c)^{-1}$		
	$r = 3.32 \pm 0.34(\mathrm{GeV}/c)^{-1}$		
$f_X(1300)$	mass $= 1471 \pm 7$	RBW	[23, 42]
	width $= 97 \pm 15$		
$f_2(1270)$	mass $= 1275.4 \pm 1.1$	RBW	[21]
	width $= 185.2^{+3.1}_{-2.5}$		
	radius $= 3.0$		[60]
$\chi_{c0}(1P)$	mass $= 3414.75 \pm 0.35$	RBW	[21]
	width $= 10.4 \pm 0.7$		
NR		flat phase space	

Table 2.3: *Parameters of lineshapes for resonances that will be used in the nominal Dalitz plot model. Masses and widths are in* MeV/c^2*, and resonance radii in* $(\mathrm{GeV}/c)^{-1}$*, unless mentioned otherwise.*

where $\Gamma_j^0 = \Gamma_j^J(m_j^0)$ is the resonance decay width, and the $|\mathbf{q}|_0$ symbol denotes the value of $|\mathbf{q}|$ when $m = m_j^0$.

Gounaris-Sakurai lineshape

An alternative form for describing the $\rho^0(770)$ lineshape (and also minor resonances) is the Gounaris-Sakurai parameterization [57] of the P-wave scattering amplitude for a broad resonance, decaying to two pions:

$$R_j^J(m) = \frac{1 + d \cdot \Gamma_j^0 m_j^0}{[(m_j^0)^2 - m^2] + f(m) - i m_j^0 \Gamma_j^J(m)} \,, \tag{2.20}$$

where $\Gamma_j^J(m)$ is the same as in Eq. 2.19, the function $f(m)$ is fiven by

$$f(m) = \Gamma_j^0 \frac{(m_j^0)^2}{|\mathbf{q}|_0^3} \left\{ |\mathbf{q}|^2 [h(m) - h(m_j^0)] + [(m_j^0)^2 - m^2] |\mathbf{q}|_0^2 \left. \frac{dh}{dm} \right|_{m_j^0} \right\} \,, \tag{2.21}$$

and the function $h(m)$ is defined as

$$h(m) = \frac{2}{\pi} \frac{|\mathbf{q}|}{m} \ln \left(\frac{m + 2|\mathbf{q}|}{2m_{\pi^+}} \right) \,, \tag{2.22}$$

Resonance	Parameters	Form Factor	Ref. for Parameters
$K^{*+}(1410)$	mass $= 1414 \pm 15$ width $= 232 \pm 21$	RBW	[21]
$K^{*+}(1680)$	mass $= 1717 \pm 27$ width $= 322 \pm 110$	RBW	[21]
$K_2^{*+}(1410)$	mass $= 1425.6 \pm 1.5$ width $= 98.5 \pm 2.7$	RBW	[21]
$f_0(1710)$	mass $= 1724 \pm 7$ width $= 137 \pm 8$	RBW	[21]
$\rho^0(1450)$	mass $= 1465 \pm 25$ width $= 400 \pm 60$ radius $= 3.0$	RBW	[21]
$\rho^0(1450)$	mass $= 1465 \pm 25$ width $= 400 \pm 60$ radius $= 3.0$	GS	[21]
$\rho^0(1700)$	mass $= 1720 \pm 20$ width $= 250 \pm 100$ radius $= 3.0$	GS	[21]
$\chi_{c2}(1P)$	mass $= 3556.20 \pm 0.09$ width $= 2.03 \pm 0.12$ radius $= 3.0$	RBW	[21]

Table 2.4: *Parameters of lineshapes for minor resonances that will be considered for systematics studies. Masses and widths are in* MeV/c^2*, and resonance radii in* $(\mathrm{GeV}/c)^{-1}$.

with

$$\left.\frac{dh}{dm}\right|_{m_j^0} = h(m_j^0)\left[(8|\mathbf{q}|_0^2)^{-1} - (2(m_j^0)^2)^{-1}\right] + [2\pi(m_j^0)^2]. \tag{2.23}$$

The normalization condition at $R_j^J(0)$ fixes the parameter $d = f(0)/\Gamma_j^0 m_j^0$. It is found to be [57]

$$d = \frac{3}{\pi}\frac{m_{\pi^+}^2}{|\mathbf{q}|_0^2}\ln\left(\frac{m_j^0 + 2|\mathbf{q}|_0}{2m_{\pi^+}}\right) + \frac{m_j^0}{2\pi|\mathbf{q}|_0} - \frac{m_{\pi^+}^2 m_j^0}{\pi|\mathbf{q}|_0^3}\ . \tag{2.24}$$

Flatté lineshape

The conditions under which a Breit-Wigner lineshape is a good representation are rather restrictive. A particular phenomenon not accounted for, and that is relevant to the present analysis, is the change in the lineshape resulting from the opening of a threshold. An example is the $f_0(980)$ state, whose main decay modes are $f_0(980) \to \pi\overline{\pi}$ and $f_0(980) \to K\overline{K}$. The mass of the $K\overline{K}$ at rest is $\sim 990 MeV/c^2$, within a fraction of the width of the resonance mass. This means that events decaying through the $f_0(980)$ state with masses below that threshold can proceed essentially only to the $\pi\pi$ final state, whereas events with masses above the threshold also have the possibility of producing the $K\overline{K}$ final state. The final effect is an asymmetry in the lineshape.

The Flatté [58], or coupled channel Breit-Wigner lineshape, is used to describe the $f_0(980)$ resonance. It is given by

$$R^J_j(m) = \frac{1}{[(m^0_j)^2 - m^2] - im^0_j(\Gamma_{\pi\pi}(m) + \Gamma_{KK}(m))} , \tag{2.25}$$

where the symbols previously defined are used. The decay widths of the resonance in the $\pi\pi$ and KK final states are given by:

$$\Gamma_{\pi\pi}(m) = g_\pi \left(\frac{1}{3}\sqrt{1 - 4m^2_{\pi^0}/m^2} + \frac{2}{3}\sqrt{1 - 4m^2_{\pi^+}/m^2} \right) , \tag{2.26}$$

$$\Gamma_{KK}(m) = g_K \left(\frac{1}{2}\sqrt{1 - 4m^2_{K^+}/m^2} + \frac{1}{2}\sqrt{1 - 4m^2_{K^0}/m^2} \right) , \tag{2.27}$$

where g_π and g_K are coupling constants (measured in previous experiments) for which the following values are used

$$\begin{aligned} g_\pi &= (0.165 \pm 0.010 \pm 0.015) GeV/c^2 , \\ g_K/g_\pi &= (4.21 \pm 0.25 \pm 0.25) . \end{aligned} \tag{2.28}$$

These are taken from results by the BES experiment [59]. When m is below the K^+K^- threshold, Γ_{KK} becomes imaginary and so contributes to the real part of the denominator. Above the K^+K^- threshold but below the $K^0\overline{K}^0$ threshold, the K^+K^- part of $\Gamma_{K^+K^-}$ contributes to the imaginary part of the denominator, making the total width bigger due to the K^+K^- coupling, while the $K^0\overline{K}^0$ part contributes to the real part. Above $K^0\overline{K}^0$ threshold the whole Γ_{KK} is real and so contributes to the imaginary part of the denominator.

LASS lineshape

It is known that the $I = 1/2$ S-wave $K\pi$ resonance, while dominated by the $K^*_0(1430)$ below 2 GeV/c^2, is not a simple Relativistic Breit-Wigner [40, 23, 60, 61]. Up to the $K\eta'$ threshold, the wave is rather elastic. Adding an effective-range term to the RBW term, was suggested [62] to describe the slowly increasing phase as a function of $K\pi$ mass. This parameterization is denoted here as LASS, in reference to the Large Aperture Superconducting Solenoid spectrometer (LASS) experiment, that introduced it for the first time in $K\pi$ scattering studies [63]. As commented in [24], while this approach is reasonably well motivated from the experimental point of view (as it stems from measurements to scattering data), the use of the LASS parameterization is limited to the elastic region of $M(K\pi) \leq 2.0$ GeV/c^2, which is the kinematical range probed by the LASS experiment. The values obtained by LASS have to be scaled by a $m_{K\pi}/|\mathbf{q}|$ factor for B decays [60]. The lineshape is given by

$$R^J_j(m) = \frac{m}{|\mathbf{q}| \cot \delta_B - i|\mathbf{q}|} + e^{2i\delta_B} \frac{m^0_j \Gamma^0_j \frac{m^0_j}{|\mathbf{q}|_0}}{[(m^0_j)^2 - m^2] - im^0_j \Gamma^0_j \frac{|\mathbf{q}|}{m} \frac{m^0_j}{|\mathbf{q}|_0}} , \tag{2.29}$$

where the first and second terms in the right hand side are the effective range and resonant terms of the lineshape, respectively. The m^0_j and Γ^0_j parameters are the mass and width of the $K^*_0(1430)$ resonance and $\cot\delta_B$ is given by

$$\cot\delta_B = \frac{1}{a|\mathbf{q}|} + \frac{1}{2}r|\mathbf{q}| \; . \tag{2.30}$$

The parameters a and r are the scattering length and the effective range, respectively, and are taken from a 37-point fit to the LASS data [60]

$$\begin{aligned} a &= (2.07 \pm 0.10)(\mathrm{GeV}/c)^{-1} \; , \\ r &= (3.32 \pm 0.34)(\mathrm{GeV}/c)^{-1} \; . \end{aligned} \tag{2.31}$$

In this thesis, the non-resonant term of the amplitude is cut off at $1.8\ \mathrm{GeV}/c^2$, which is the same configuration adopted the in *BABAR* analysis of the charged $B^+ \to K^+\pi^-\pi^+$ mode [34].

Non-resonant lineshape

Signal in the center of the DP is described with a flat distribution, constant over the whole DP.

The parameters in the lineshapes could in principle be obtained from a fit to data, but this approach has a technical disadvantage. When normalizing the PDF (cf. Sec. 2.4.8, Eq.(2.43)), integrals of the terms $F_j(DP)F^*_k(DP)$ over the whole DP have to be calculated each time one of the parameters of the resonance lineshape varies. This would make the fitting process unacceptably heavy in CPU-time. For this reason these parameters are kept fixed, and the integrals of the $F_j(DP)F^*_k(DP)$ terms over the DP are only calculated once.

2.4.5 Blatt-Weisskopf Factors

The functions X_J are the nuclear *Blatt-Weisskopf penetration factors* [64]. They are semi-classical and motivated by the potential $\hbar J(J+1)/(2m\rho^2)$ occurring in the Schrödinger equation, expressed in the spherical coordinates, for the scattering of a particle with orbital angular momentum $J > 0$ in a central field. The repulsive potential is equivalent to a rotation energy, and can thus be denoted as *centrifugal barrier*. For growing J or decreasing radial distance ρ, the centrifugal barrier increases, which entails a decreasing transition probability. One can empirically determine a radial distance, called *interaction radius*, r, of the resonance, which separates an outside region (with respect to the centrifugal barrier), with little interaction, from an inside region where the interaction between the particles is strong [65]. The transition coefficients of the centrifugal barrier are the Blatt-Weisskopf factors. They are derived using spherical Bessel and Hankel functions and read from the lowest orbital momenta (spins):

$$\begin{aligned}
X_{J=0}(z) &= 1\,, \\
X_{J=1}(z) &= \sqrt{\frac{1+z_0^2}{1+z^2}}\,, \\
X_{J=2}(z) &= \sqrt{\frac{z_0^4+3z_0^2+9}{z^4+3z^2+9}}\,,
\end{aligned} \tag{2.32}$$

where z_0 represents the value of z (which is equal to $|\mathbf{q}|r$ or $|\mathbf{p}^*|r$) when the invariant mass is equal to the pole mass of the resonce. This factor only has an effect for $J > 0$. The values of the interaction radius for the different resonant states used in this thesis are listed in tables 2.3 and 2.4.

2.4.6 Angular Distribution

The angular distribution depends on the spin of the resonance. For a B decay into a scalar resonance $\{\kappa\sigma\}$ (with $\{\kappa\sigma\} = \{0+\}, \{0-\}, \{+-\}$) it is simply given by

$$T_j(J=0,\mathbf{p},\mathbf{q}) = 1\ . \tag{2.33}$$

In the case of a B decay into a vector resonance $\{\kappa\sigma\}$ and a bachelor $\{\tau\}$, it can be written as

$$\begin{aligned}
T_j(J=1,\mathbf{p},\mathbf{q}) &= (p_{B^0}+p_\tau)_\mu \textstyle\sum_i \epsilon_i^\mu(p_{\kappa\sigma})\epsilon_i^{\nu *}(p_{\kappa\sigma})(p_\kappa - p_\sigma)_\nu \\
&= s_{\kappa+\sigma} - s_{\sigma+\tau} + (1/s_{\kappa+\sigma})\left(m_{B^0}^2 - m_\tau^2\right)\left(m_\sigma^2 - m_\kappa^2\right) \\
&= -4\mathbf{p}_\kappa \cdot \mathbf{p}_\tau \\
&= -4|\mathbf{p}_\kappa||\mathbf{p}_\tau|\cos\theta_{\kappa+\tau}\ ,
\end{aligned} \tag{2.34}$$

where all four-momenta p_i are given in the resonance rest frame, $\theta_{\kappa+\tau}$ is the helicity angle, and the relation

$$\sum_i \epsilon_i^\mu(p)\epsilon_i^{\nu *}(p) = -\eta^{\mu\nu} + \frac{p^\mu p^\nu}{p^2}, \tag{2.35}$$

for the sum over the polarizations four-vectors has been used. The last two lines of Eq. 2.34 reproduce the convention for the cosines of the helicity angles defined in Eq. 2.11 and Fig. 2.2. Note that the occurrence of the $\cos\theta_{\kappa+\tau}$ in the propagator substantially enhances the interference of different vector resonances in the corners of the DP. For tensor resonances the angular distribution is

$$\begin{aligned}
T_j(J=2,\mathbf{p},\mathbf{q}) &= (8/3)\,(3(\mathbf{p}_\kappa\cdot\mathbf{p}_\tau)^2 - (|\mathbf{p}_\kappa||\mathbf{p}_\tau|)^2) \\
&= (8/3)|\mathbf{p}_\kappa|^2|\mathbf{p}_\tau|^2\,(3\cos^2\theta_{\kappa+\tau} - 1)\ .
\end{aligned} \tag{2.36}$$

One has to decide which daughter of the resonance to choose for the calculation of the helicity angle. For the $B^0 \to K^0_S\pi^+\pi^-$ mode this issue is slightly complicated. For resonances in $m_{K^0_S\pi^+}$ or $m_{K^0_S\pi^-}$ one can always choose the K^0_S, as one only gets B^0 ($\bar{B}^0$) decaying to resonances in $m_{K^0_S\pi^+}$ ($m_{K^0_S\pi^-}$). This means one choses K^0_S and π^- (π^+) for $\mathbf{p}_\tau$ and $\mathbf{p}_\kappa$ in the case of a B^0 ($\bar{B}^0$) decay. For resonances in $m_{\pi^+\pi^-}$ one would like to choose the pion such that the same choice is maintained. However, since the flavor of the B at its decay to the CP eigenstate is not known, this cannot be done. Therefore, the convention adopted here is to always choose the π^+ daughter; keeping in mind that this must be taken into account in the likelihood function (cf. Chapter 6) by introducing a $(-1)^J$ factor for CP eigenstate decays of the $\bar{B}^0$.

2.4.7 The Square Dalitz Plot

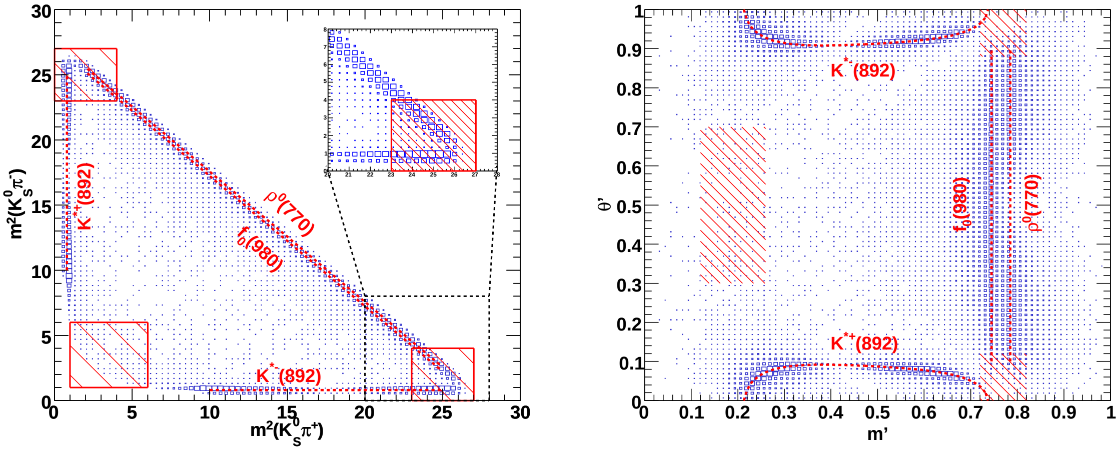

Figure 2.3: *Nominal (left) and square (right)* $B^0 \to K^0_S\pi^+\pi^-$ *Dalitz plots obtained from highly simplified Monte Carlo without detector simulation, generated with an arbitrary model including* $f_0(980)K^0_S$, $\rho^0(770)K^0_S$ *and* $K^{*\pm}(892)\pi^\mp$ *resonances. The hatched areas indicate the main overlap regions between the* $\pi^+\pi^-$ *resonant states* $f_0(980)K^0_S$ *and* $\rho^0(770)K^0_S$ *and the* $K^{*\pm}(892)\pi^\mp$ *bands, which are removed in the Q2B analyses. The contour lines correspond to* $m_{K^0_S\pi^\pm} = 0.892\ \mathrm{GeV}/c^2$, $m_{\pi^+\pi^-} = 0.770\ \mathrm{GeV}/c^2$ *and* $m_{\pi^+\pi^-} = 0.980\ \mathrm{GeV}/c^2$.

Due to the low final state masses, $m_j^0 \ll m_{B^0}$, signal events tend to populate the kinematic boundaries of the Dalitz plot. It turns out that due to combinatorics, the dominant $e^+e^- \to q\bar{q}$ ($q = u, d, s, c$) continuum background (cf. Sec. 5.5) also accumulates at the boundaries, so the classical DP representation (Eq. 2.6) turns out to be inadequate when one intends to use empirical reference shapes in a likelihood fit (cf. Chapter 6). Therefore the concept of a square Dalitz plot (denoted *square* DP or $\{SDP\}$ in the following) is introduced, by defining the transformation

$$d_+, ds_- \longrightarrow |detJ|, dm', d\theta', \tag{2.37}$$

where

$$m' \equiv \frac{1}{\pi}\arccos\left(2\frac{m_{\pi^+\pi^-} - m_{\pi^+\pi^-}[min]}{m_{\pi^+\pi^-}[max] - m_{\pi^+\pi^-}[min]} - 1\right) , \tag{2.38}$$

$$\theta' \equiv \frac{1}{\pi}\theta_{\pi^+\pi^-} , \tag{2.39}$$

where $m_{\pi^+\pi^-}[max] = m_{B^0} - m_{K^0_S}$ and $m_{\pi^+\pi^-}[min] = 2m_{\pi^+}$ are the boundaries of $m_{\pi^+\pi^-}$ invariant mass, $\theta_{\pi^+\pi^-}$ is the $\pi^+\pi^-$ helicity angle, and $|detJ|$ is the Jacobian of the transformation. The new variables have validity ranges in $(0, 1)$. The determinant of the Jacobian is given by

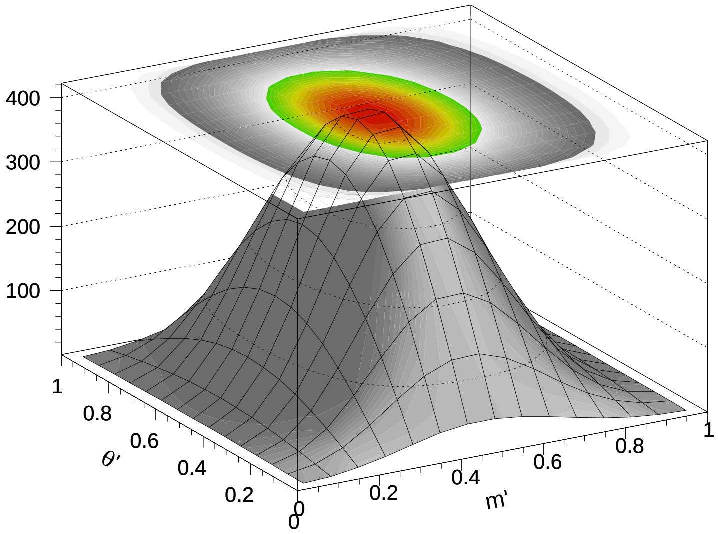

Figure 2.4: *Jacobian determinant (Eq. 2.40) of the transformation (Eq. 2.37). The plot shows the distribution that would be obtained in the square Dalitz plot for a uniform (non-resonant) in the nominal Dalitz plot.*

$$|detJ| = 4\,|\mathbf{p}^*_+||\mathbf{p}^*_0|m_{\pi^+\pi^-} \cdot \frac{\partial m_{\pi^+\pi^-}}{\partial m'} \cdot \frac{\partial \cos\theta_0}{\partial\theta'} , \tag{2.40}$$

where $|\mathbf{p}^*_+| = \sqrt{E^*_+ - m^2_{\pi^+}}$ and $|\mathbf{p}^*_0| = \sqrt{E^*_0 - m^2_{\pi^0}}$, and the energies E^*_+ and E^*_0 are evaluated in the $\pi^+\pi^-$ rest frame. The partial derivatives in Eq. (2.40) read

$$\frac{\partial m_{\pi^+\pi^-}}{\partial m'} = -\frac{\pi}{2}\sin(\pi m')\left(m_{\pi^+\pi^-}[max] - m_{\pi^+\pi^-}[min]\right) , \tag{2.41}$$

$$\frac{\partial\cos\theta_0}{\partial\theta'} = -\pi\sin(\theta'\pi) . \tag{2.42}$$

Figure 2.3 shows the original (left hand plot) and the transformed (right hand plot) Dalitz plots from highly simplified Monte Carlo $B^0 \to K^0_S\pi^+\pi^-$ events, generated with an arbitrary model including $f_0(980)K^0_S$, $\rho^0(770)K^0_S$ and $K^{*\pm}(892)\pi^{\mp}$ resonances. The hatched areas indicate the main overlap regions between the different $f_0(980)K^0_S$ and $\rho^0(770)K^0_S$ and the $K^{*\pm}(892)\pi^\mp$ bands, which are removed in the Q2B analyses. The plots illustrate the homogenization of the Dalitz plot obtained after the transformation (2.37). The determinant of the Jacobian (Eq. 2.40) is shown in Fig. 2.4. It is the distribution that would be obtained in the square Dalitz plot for a uniform (non-resonant) prior in the nominal DP.

2.4.8 Time and DP-Dependent PDF

With $\Delta t = t_{CP} - t_{tag}$ defined as the proper time interval between the decay of the fully reconstructed $B^0 \to K^0_S\pi^+\pi^-$ (B^0_{CP}) and that of the other meson (B^0_{tag}) from the $\Upsilon(4S)$, the tagging, time and DP-dependent decay rate is given by [25]

$$\begin{aligned}
|\mathcal{A}_{CP}(\Delta t, DP, q_{tag})|^2 = & \frac{e^{|\Delta t|/\tau_{B^0}}}{4\tau_{B^0}} \bigg[|\mathcal{A}(DP)|^2 + |\overline{\mathcal{A}}(DP)|^2 \\
& - q_{tag}\left(|\mathcal{A}(DP)|^2 - |\overline{\mathcal{A}}(DP)|^2\right)\cos\left(\Delta m_d \Delta t\right) \\
& + q_{tag}\mathcal{I}m\left[\exp(-2i\phi_{\rm mix})\overline{\mathcal{A}}(DP)\mathcal{A}^*(DP)\right]\sin\left(\Delta m_d \Delta t\right)\bigg] ,
\end{aligned} \tag{2.43}$$

where q_{tag} is $+1$ (-1) when the B^0_{tag} is B^0 ($\bar{B}^0$), τ_{B^0} is the neutral B meson lifetime, Δm_d is the $B^0\bar{B}^0$ mass difference (the mixing frequency) and $\exp(-2i\phi_{\rm mix})$ is the q/p phase (the mixing phase, which is the CKM angle β in the SM). The DP dependence is contained in the $\mathcal{A}$ and $\overline{\mathcal{A}}$. Here it is assumed that there is no CP violation in mixing ($|q/p| \sim 1$). In the following a phase convention whereby the phase from the $B^0\bar{B}^0$ mixing is absorbed into the $\bar{B}^0$ decay amplitude (*i.e.* in $\bar{\mathcal{A}}$, and therefore in all the $\overline{c}_j$) is used. Lifetime differences between B_L and B_H eigenstates is negligible (cf. Sec. 1.2.1, Eq.(1.25)). Eq. 2.43 does not include the non-zero probability of mistagging nor the resolution in the Δt measurement, effects that will be described in Secs. 5.3 and 5.4.3, respectively.

2.4.9 Physical observables

A fit to data allows us to measure directly the relative magnitudes and phases of the isobar amplitudes, for all components in the signal DP model. These measured isobar amplitudes c_j ($\overline{c}_j$), where the index represents the j-th component, are used to extract the Q2B parameters, for which the definitions are below.

For a resonant decay mode j which is a CP eigenstate, *e.g.* $B^0 \to \rho^0(770)K^0_S$, the following Q2B parameters are extracted: the ϕ angle, defined as,

$$\phi(j) = 2\beta_{eff}(j) = arg(c_j\overline{c_j^*}) , \tag{2.44}$$

It is worth recalling that in the convention used here, the $\bar{B}^0$ decay amplitudes absorbs the q/p term from $B^0\bar{B}^0$ mixing. In this way, for Penguin dominated decays such as $f_0(980)K^0_S$ and $\rho^0(770)K^0_S$, this ϕ angle corresponds to the $2\beta_{eff}(j)$ parameter.

The parameters of direct and mixing-induced CP-asymmetries are defined as:

$$C(j) = \frac{|c_j|^2 - |\overline{c}_j|^2}{|c_j|^2 + |\overline{c}_j|^2} \;, \tag{2.45}$$

$$S(j) = \eta_{CP} \frac{2\mathcal{I}m(\overline{c}_j c_j^*)}{|c_j|^2 + |\overline{c}_j|^2} = -\eta_{CP}\sqrt{1 - C^2(j)}\sin\phi(j) \;, \tag{2.46}$$

where η_{CP} is the CP eigenvalue of the final state. As this last parameter is a function of $\phi(j)$ and $C(j)$, and Dalitz Plot analyses are sensitive directly to phases, the results are mostly presented in terms of the ϕ_j and C_j parameters, out of which constraints on $S(j)$ can be derived.

For a self-tagging resonant decay mode j, *e.g.* $B^0 \to K^{*+}(892)\pi^-$, it is customary to define the CP-asymmetry as:

$$A_{CP}(j) = \frac{|\overline{c}_{\overline{j}}|^2 - |c_j|^2}{|\overline{c}_{\overline{j}}|^2 + |c_j|^2} \;. \tag{2.47}$$

The relative isobar phase difference between any two resonances j and k is defined by:

$$\Delta\phi(j,k) = arg(c_j c_k^*) \;. \tag{2.48}$$

A similar quantity can be defined for a self-tagging resonant decay mode j and its CP conjugated $\overline{j}$:

$$\Delta\phi(j,\overline{j}) = arg(c_j \overline{c}_{\overline{j}}^*) \;, \tag{2.49}$$

here again, this phase difference $\Delta\phi(j,\overline{j})$ has implicitly absorbed the phase from $B^0\bar{B}^0$ mixing.

The relative isobar fraction $FF(j)$ (or fit fraction) of a resonance j is defined as follows:

$$FF(j) = \frac{(|c_j|^2 + |\overline{c}_j|^2)\langle F_j F_j^*\rangle}{\sum_{\mu\nu}(c_\mu c_\nu^* + \overline{c}_\mu \overline{c}_\nu^*)\langle F_\mu F_\nu^*\rangle} \;, \tag{2.50}$$

where

$$\langle F_\mu F_\nu^*\rangle = \int_{DP} F_\mu F_\nu^* d(DP) \;. \tag{2.51}$$

Finally, the inclusive direct CP-asymmetry and branching fraction [1],

$$A_{CP}^{incl} = \frac{\int_{DP}[|\mathcal{A}(DP)|^2 - |\overline{\mathcal{A}}(DP)|^2]d(DP)}{\int_{DP}[|\mathcal{A}(DP)|^2 + |\overline{\mathcal{A}}(DP)|^2]d(DP)} \;, \tag{2.52}$$

$$\mathcal{B}^{incl} = \mathcal{B}(B^0 \to K^0\pi^+\pi^-) = \frac{N_{sig}}{\mathcal{B}(K^0 \to K^0_S)\langle\varepsilon\rangle N_{B\overline{B}}} \;, \tag{2.53}$$

---

[1] Results are stated in terms of the K^0 final state, taking into account the probability for $\mathcal{B}(K^0 \to K^0_S) = 0.5$ and for $\mathcal{B}(K^0_S \to \pi^+\pi^-) = (69.20\pm0.05)\%$ [21]. The latter is already taken into account in the reconstruction efficiency, $\langle\varepsilon\rangle$.

where N_{sig} is the fitted signal yield (cf. Sec. 6.1), $N_{B\overline{B}}$ is the number of $B^0\bar{B}^0$ pairs produced in the period between 1999 and September 2006 (cf. Sec. 5.1.1), and $\langle\varepsilon\rangle$ is the model-dependent average signal reconstruction efficiency over the Dalitz plot. With the inclusive branching fraction and the isobar fractions the partial branching fraction for component j can be calculated as follows,

$$\mathcal{B}(j) = FF_j\mathcal{B}^{incl}. \tag{2.54}$$

The methods to extract confidence intervals for these observables will be presented on Sec. 6.7.

Chapter 3

Theory Elements for the $B \to K^*\pi$ and $B \to \rho K$ Modes

3.1 Introduction

Within the Standard Model, hadronic B decays proceed at the quark level *via* both Tree and loop (Penguin) diagrams [66]. In the $b \to c\bar{c}s$ processes (*e.g.* $B^0 \to J/\psi K_S^0$) the CKM phase in the dominant Tree amplitude is the same as that of the Cabibbo suppressed Penguin diagrams, which in the Wolfenstein parameterization is real and so the only weak phase to consider is the $B^0\bar{B}^0$ mixing phase 2β. In this case, the CKM angle β can be extracted without hadronic uncertainties from the time-dependent CP-asymmetry, which is proportional to $\sin(2\beta)$. In the case of charmless B decays, different weak phases have to be considered, hence the extraction of CKM couplings is more difficult. In $b \to du\bar{u}$ processes (*e.g.* $B \to \pi\pi^1$) the two leading amplitudes carry different CKM phases, so that extracting $\sin(2\alpha)$ from the time dependent CP-asymmetry suffers from hadronic uncertainties. Methods to determine α where the two body $B \to \pi\pi$ decay amplitudes are related by $SU(2)$ isospin symmetry have been proposed [67], and are of standard usage. With such an "isospin analysis", the CKM phase for the Tree level diagram can be separated from the Penguin contamination. The information from branching fractions and CP-asymmetries makes possible to constrain α up to discrete ambiguities.

For the $b \to u\bar{u}s$ processes (*e.g.* $B \to K\pi$) the situation is partly different: not only do the Tree and Penguin amplitudes carry different CKM phases, but also they are comparable in magnitude (although the Tree process is strongly CKM suppressed). Isospin methods using the $B \to K\pi$ modes have also been suggested, which disentangle the Penguin contribution of the decay amplitude to set constraints on the CKM parameters given that an hadronic scenario has been set. In some cases, such analyses claim to provide access to the UT angle γ [68], although the cleanliness of such methods is subject of debate. Finally, methods using both $B \to \pi\pi$ and $B \to K\pi$ systems using $SU(3)$ flavor symmetry to relate all the decay amplitudes have been proposed to provide more stringent constraints in the $(\bar{\rho}, \bar{\eta})$ plane [14, 69]. The $SU(3)$ symmetry is not exact, and breakdown effects have

---

[1] When charges are not shown, reference is made to all charge combinations.

to be carefully taken into account. The drawback of these approaches stems from the difficulty to disentangle the constraints on CKM parameters from unwanted consequences of the different hypotheses.

This chapter provides a theoretical introduction to the different methods that can be used to constraint the CKM parameters from the measurements of $B \to K^*\pi$ (where K^* refers to any $K\pi$ resonant state like $K^*(892)$ or $K^*(1430)$) and $B \to \rho K$ modes. These modes have been already discussed in the literature [112]. Three approaches are proposed: an isospin analysis of $B \to K^*\pi$ modes (here, a word is said about a method known as CPS/GPSZ that uses observables from the $B^0 \to K^{*+}\pi^-$ and $B^0 \to K^{*0}\pi^0$ subsystem to constrain the $(\bar{\rho}, \bar{\eta})$ plane); a similar isospin analysis of $B \to K\rho$ modes; finally, a method based on $SU(2)$ symmetry which combines all accessible information from both $B \to K^*\pi$ and $B \to K\rho$ system, is mentioned.

Throughout this chapter, the approximation of no CP-violation in mixing, *i.e.* $|q/p| = 1$, is assumed. This hypothesis has no visible impact on the constraints and significantly simplifies the calculations.

3.2 Isospin Analysis for the $B \to K^*\pi$ modes

3.2.1 Decay Amplitudes

The extraction of CKM parameters out of CP-violation observables is complicated in some cases by the presence of hadronic matrix elements relating the quark field operators used in writing down the theory with the hadrons detected by experiment. For the purposes of the present analysis, a phenomenological parameterization of the amplitude will be adopted, where the hadronic matrix elements are unknowns. In the SM, the general form of the $B^0 \to K^{*+}\pi^-$ decay amplitude is:

$$A^{+-} \equiv A(B^0 \to K^{*+}\pi^-) = V_{ub}^* V_{us} M_u + V_{cb}^* V_{cs} M_c + V_{tb}^* V_{ts} M_t \ . \tag{3.1}$$

The dominant diagrams are represented in Fig. 3.1, where are shown the Tree (left) and gluonic Penguins (right) contributions, the latter having three contributions for the quarks circulating in the W^+ loop (u, c, t). There are also contributions of Penguin amplitudes in which the gluon emitted in the loop is replaced by a γ or Z^0 gauge boson. Such diagrams are called electroweak Penguins, and are suppressed with respect to gluonic Penguins by the ratio of electroweak to strong coupling constants, α_{em}/α_S, but this suppression is compensated by a large quark top mass dependence, which make then not negligible [145]. There is a similar equation for the CP conjugated amplitude $\bar{A}^{+-}$, the CKM factors appearing as complex conjugated. The unitarity relation Eq. 1.19 can be used to write this expression in term of only two CKM factors. There exist three equivalent ways of re-writing Eq. 3.1, that will be referred to as $\mathbb{U}$, $\mathbb{C}$ and $\mathbb{T}$ conventions:

$$A^{+-} = \left\{ \begin{array}{ccccl} & & V_{cb}^* V_{cs}(M_c - M_u) & + & V_{tb}^* V_{ts}(M_t - M_u) \quad (\mathbb{U}) \\ V_{ub}^* V_{us}(M_u - M_c) & + & & & V_{tb}^* V_{ts}(M_t - M_c) \quad (\mathbb{C}) \\ V_{ub}^* V_{us}(M_u - M_t) & + & V_{cb}^* V_{cs}(M_c - M_t) & & \quad (\mathbb{T}) \end{array} \right. \tag{3.2}$$

where the amplitude coefficients M_u $(\mathbb{U})$, M_c $(\mathbb{C})$ and M_t $(\mathbb{T})$, respectively, have been replaced. Adopting the $\mathbb{C}$ convention, the A^{+-} is written as,

$$A^{+-} = V_{ub}^* V_{us} T^{+-} + V_{tb}^* V_{ts} P^{+-} \ , \tag{3.3}$$

where T^{+-} and P^{+-} are defined as

$$T^{+-} \equiv M_u - M_c \quad \text{and} \quad P^{+-} \equiv M_t - M_c \ , \tag{3.4}$$

and similar expressions for the remaining three $A^{ij} \equiv A(B^{i+j} \to K^i \pi^j)$ $((i,j) = (0,+)$, $(+,0)$, $(0,0))$ amplitudes

$$A^{+0} \equiv A(B^+ \to K^{*+}\pi^0) = V_{ub}^* V_{us} T^{+0} + V_{tb}^* V_{ts} P^{+0} \ , \tag{3.5}$$

$$A^{0+} \equiv A(B^+ \to K^{*0}\pi^+) = V_{ub}^* V_{us} T^{0+} + V_{tb}^* V_{ts} P^{0+} \ , \tag{3.6}$$

$$A^{00} \equiv A(B^0 \to K^{*0}\pi^0) = V_{ub}^* V_{us} T^{00} + V_{tb}^* V_{ts} P^{00} \ . \tag{3.7}$$

The T^{ij} and P^{ij} complex numbers include implicitly the strong phases, while the weak phases are contained explicitly in the CKM factors, and are usually referred as Tree and Penguin amplitudes. The adopted $\mathbb{C}$ convention in writing the A^{ij} decay amplitude is totally arbitrary and has no physical implication. Any of the other conventions can be used, however each choice changes the content of the T^{ij} and P^{ij} phenomenological amplitudes, which contain different topological contributions, *e.g.* Tree, Penguin, annihilation, etc. (see later).

The CKM ratio $|V_{ts}V_{tb}^*/V_{us}V_{ub}^*| \sim 50$ increases significantly the Penguin contribution with respect to the Tree diagram: this may provide a better sensitivity to unknown virtual particles, and then to NP effects, but this implies also a more complicated hadronic dynamics.

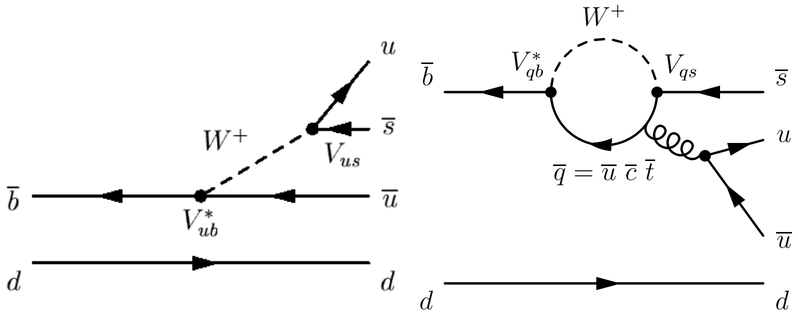

Figure 3.1: *Tree (left) and Penguin (right) diagrams for the $B^0 \to K^{*+}\pi^-$ decay.*

3.2.2 Physical observables

In Chapter 8, the measured branching fractions, CP-asymmetries and phase differences for the $B \to K^*\pi$ modes are used in a phenomenological analysis. While a $K\pi$ pair can resonate via several intermediate states, and all of them can in principle be used, the phenomenological analysis performed in this thesis only observables from $K^*(892)$-mediated modes are used, so in the following K^* exclusively refers to $K^*(892)$ vector resonant state. The four CP averaged branching fractions are defined as

$$\mathcal{B}^{ij} = \Phi \frac{\tau_{B^{i+j}}}{2} \left(|A^{ij}|^2 + |\bar{A}^{ij}|^2 \right) \ , \tag{3.8}$$

where $\tau_{B^{i+j}}$ is the relevant B meson lifetime and Φ is the decay phase space constant given by

$$\Phi = \frac{1}{8\pi\hbar} \left(\frac{G_F}{\sqrt{2}} \right)^2 \frac{1}{2m_B} \sqrt{ \left[1 - \left(\frac{m_{K^*} + m_\pi}{m_B} \right)^2 \right] \left[1 - \left(\frac{m_{K^*} - m_\pi}{m_B} \right)^2 \right] } \ , \tag{3.9}$$

where $\hbar$ is the Planck constant, G_F is the Fermi constant, and m_B, m_π and m_{K^*} are the B meson, π pion and K^* resonance masses, respectively. The four CP-asymmetries are defined as

$$\mathcal{A}^{ij}_{CP} = \frac{|\bar{A}^{ij}|^2 - |A^{ij}|^2}{|\bar{A}^{ij}|^2 + |A^{ij}|^2} \ . \tag{3.10}$$

These observables can be extracted from Q2B and Dalitz Plot analyses (cf. Chapter 2). Also five phase differences are accessible from Dalitz Plot analyses (the definitions here deviate slightly from the ones introduced in Chapter 2):

- The $\Delta\phi$ phase difference is defined as

  $$\Delta\phi = arg\left(\frac{q}{p} \frac{\bar{A}^{+-}}{A^{+-}} \right) , \tag{3.11}$$

  which is extracted from the decay mode studied in this thesis, $B^0 \to K^0_S\pi^+\pi^-$. The $B^0 \to K^{*+}(892)(\to K^0\pi^+)\pi^-$ ($\bar{B}^0 \to K^{*-}(892)(\to \bar{K}^0\pi^-)\pi^+$) resonant decay contribute to the B^0 ($\bar{B}^0$) DalitzPlot (DP). This phase difference can be measured in two ways: 1) the resonant contributions interfere through mixing (thus the q/p factor) due to the fact that the final state $K^0_S\pi^+\pi^-$ is accessible both to B^0 and $\bar{B}^0$. But as discussed in Chapter 2, they interferere in a too small region of the DP to provide significant sensitivity; 2) the resonant contributions can significantly interfere with other components, *e.g.* $B^0 \to K^0\rho^0(\to \pi^+\pi^-)$ ($\bar{B}^0 \to \bar{K}^0\rho^0(\to \pi^+\pi^-)$), that are present in the same B^0 ($\bar{B}^0$) DP and that interfere with each other through mixing in a significant DP region. The DP amplitude technique exploits simultaneously both informations.

- The $\phi^{(00,+-)}$ and $\bar{\phi}^{(00,+-)}$ phase differences are defined as

  $$\phi^{(00,+-)} = arg(A^{00}/A^{+-}) \quad \text{and} \quad \bar{\phi}^{(00,+-)} = arg(\bar{A}^{00}/\bar{A}^{+-}), \tag{3.12}$$

  which can be extracted from the $B^0 \to K^+\pi^-\pi^0$ Dalitz Plot analysis [40], due to the interference of the $B^0 \to K^{*+}(892)(\to K^+\pi^0)\pi^-$ and $B^0 \to K^{*0}(892)(\to K^+\pi^-)\pi^0$ ($\bar{B}^0 \to K^{*-}(892)(\to K^-\pi^0)\pi^+$ and $\bar{B}^0 \to \bar{K}^{*0}(892)(\to K^+\pi^-)\pi^0$) resonant components on the B^0 ($\bar{B}^0$) DP planes.

- Finally, two other phase differences can be defined,
$$\phi^{(0+,+0)} = arg(A^{0+}/A^{+0}) \quad \text{and} \quad \bar{\phi}^{(0+,+0)} = arg(\bar{A}^{0+}/\bar{A}^{+0}), \tag{3.13}$$
which are accessible in a $B^+ \to K^0_S\pi^+\pi^0$ Dalitz Plot analysis, due to the interference of the $B^+ \to K^{*0}(892)(\to K^0\pi^0)\pi^+$ and $B^+ \to K^{*+}(892)(\to K^0\pi^+)\pi^0$ ($B^- \to \bar{K}^{*0}(892)(\to \bar{K}^0\pi^0)\pi^-$ and $B^- \to K^{*-}(892)(\to \bar{K}^0\pi^-)\pi^0$) resonant components on the B^+ (B^-) DP planes. As no experimental results are available yet, these observables will only be considered in prospective studies, assuming expected uncertainties on these modes.

In summary, the $B \to K^*\pi$ observables are: four branching fractions, four CP-asymmetries and five phase differences, which gives a total of thirteen observables. Experimental results are currently available on eleven out of these thirteen observables.

3.2.3 Isospin Relations

The π^+, π^0 and π^- mesons form an isospin triplet and have $I_3 = +1, 0, -1$ as third isospin component, respectively. The K^{*0} and K^{*+} mesons have isospin number $I = 1/2$, as do B mesons, with third isospin component $I_3 = 1/2, -1/2$. The $K^*\pi$ states have a total isospin number $I = 3/2$ or $I = 1/2$. Assuming that isospin symmetry holds, the $B^0 \to K^{*+}\pi^-$, $B^+ \to K^{*+}\pi^0$, $B^+ \to K^{*0}\pi^+$ and $B^0 \to K^{*0}\pi^0$ amplitudes can be decomposed in terms of $I = 3/2$ and $I = 1/2$ isospin amplitudes, which will be referred to as $A_{1,3/2}$, $A_{1,1/2}$ and $A_{0,1/2}$, where the first index is the difference of the final and initial isospin number ΔI, and the second the final isospin I_f. The decomposition will be made explicit in the following, and is based on [67].

In order to simplify the discussion, the $B \to K^*\pi$ decays can be described in two steps:

- The weak decay (W): the B decays into $\bar{u}u\bar{s}d$ quarks for the neutral Bs and into $\bar{u}u\bar{s}u$ for the charged Bs *via* weak interactions,which do not conserve isospin.
- The hadronization and rescattering effects (S): the quarks hadronize into pions and kaons via strong interactions, conserving both total isospin and its third component.

The total Hamiltonian can be factorized in two components $\mathcal{H} = \mathcal{H}_S\mathcal{H}_W$. The $\mathcal{H}_W$ operator is the weak interaction Hamiltonian responsable for the weak decay $\bar{b} \to \bar{u}u\bar{s}$, in which the d (in the case of B^0 decays) or u (in the case of B^+ decays) quarks are treated as spectators. More explicitly, the action of $\mathcal{H}_W$ over a B^0 or B^+ state can expressed as follows
$$\begin{aligned} \mathcal{H}_W|B^0\rangle = \mathcal{H}_W(|d\rangle|\bar{b}\rangle) = |d\rangle(\mathcal{H}_W|\bar{b}\rangle)\ , \\ \mathcal{H}_W|B^+\rangle = \mathcal{H}_W(|u\rangle|\bar{b}\rangle) = |u\rangle(\mathcal{H}_W|\bar{b}\rangle)\ . \end{aligned} \tag{3.14}$$

The $\bar{u}u\bar{s}$ state has isospin number $I = 1$ or $I = 0$, and $|d\rangle = |I = \frac{1}{2}, I_3 = -\frac{1}{2}\rangle$ ($|u\rangle = |I = \frac{1}{2}, I_3 = \frac{1}{2}\rangle$), so the action of $\mathcal{H}_W$ on the B^0 or B^+ states can be decomposed into isospin eigenstates with the help of the Clebsch-Gordan coefficients as follows
$$\begin{aligned} \mathcal{H}_W|B^0\rangle &= |d\rangle(a_0|0,0\rangle + a_1|1,0\rangle) \\ &= a_0|\tfrac{1}{2},-\tfrac{1}{2}\rangle + a_1(\sqrt{\tfrac{2}{3}}|\tfrac{3}{2},-\tfrac{1}{2}\rangle + \sqrt{\tfrac{1}{3}}|\tfrac{1}{2},-\tfrac{1}{2}\rangle)\ , \end{aligned} \tag{3.15}$$

for the neutral B decays, and

$$\begin{aligned}\mathcal{H}_W|B^+\rangle &= |u\rangle(a_0|0,0\rangle + a_1|1,0\rangle) \\ &= a_0|\tfrac{1}{2},\tfrac{1}{2}\rangle + a_1(\sqrt{\tfrac{2}{3}}|\tfrac{3}{2},\tfrac{1}{2}\rangle - \sqrt{\tfrac{1}{3}}|\tfrac{1}{2},\tfrac{1}{2}\rangle)\ ,\end{aligned} \tag{3.16}$$

for the charged B decays. The a_0 and a_1 are complex numbers containing the weak phases from the decay process. The $\mathcal{H}_S$ operator is the strong interaction Hamiltonian responsable for the hadronization. Summarizing all these, the four amplitudes can be written as follows:

$$A(B \to K^{*+}\pi^-) = \langle K^{*+}\pi^-|\mathcal{H}_S\mathcal{H}_W|B^0\rangle\ , \tag{3.17}$$

$$A(B \to K^{*0}\pi^0) = \langle K^{*0}\pi^0|\mathcal{H}_S\mathcal{H}_W|B^0\rangle\ , \tag{3.18}$$

$$A(B \to K^{*+}\pi^0) = \langle K^{*+}\pi^0|\mathcal{H}_S\mathcal{H}_W|B^+\rangle\ , \tag{3.19}$$

$$A(B \to K^{*0}\pi^+) = \langle K^{*0}\pi^+|\mathcal{H}_S\mathcal{H}_W|B^+\rangle\ . \tag{3.20}$$

The $K^*\pi$ final states can be decomposed into isospin eigenstates with the help of the Clebsch-Gordan coefficients

$$\begin{aligned}|K^{*+}\pi^-\rangle &= \left|\tfrac{1}{2},\tfrac{1}{2}\right\rangle|1,-1\rangle &&= \sqrt{\tfrac{1}{3}}\left|\tfrac{3}{2},-\tfrac{1}{2}\right\rangle + \sqrt{\tfrac{2}{3}}\left|\tfrac{1}{2},-\tfrac{1}{2}\right\rangle\ , \\ |K^{*+}\pi^0\rangle &= \left|\tfrac{1}{2},\tfrac{1}{2}\right\rangle|1,0\rangle &&= \sqrt{\tfrac{2}{3}}\left|\tfrac{3}{2},\tfrac{1}{2}\right\rangle + \sqrt{\tfrac{1}{3}}\left|\tfrac{1}{2},\tfrac{1}{2}\right\rangle\ , \\ |K^{*0}\pi^+\rangle &= \left|\tfrac{1}{2},-\tfrac{1}{2}\right\rangle|1,+1\rangle &&= \sqrt{\tfrac{1}{3}}\left|\tfrac{3}{2},\tfrac{1}{2}\right\rangle - \sqrt{\tfrac{2}{3}}\left|\tfrac{1}{2},\tfrac{1}{2}\right\rangle\ , \\ |K^{*0}\pi^0\rangle &= \left|\tfrac{1}{2},-\tfrac{1}{2}\right\rangle|1,0\rangle &&= \sqrt{\tfrac{2}{3}}\left|\tfrac{3}{2},-\tfrac{1}{2}\right\rangle + \sqrt{\tfrac{1}{3}}\left|\tfrac{1}{2},-\tfrac{1}{2}\right\rangle\ .\end{aligned} \tag{3.21}$$

Using Eqs. 3.15, 3.17 and the first equation from 3.21 the decomposition of the $A(B^0 \to K^{*+}\pi^-)$ amplitude in terms of isospin amplitudes can be made

$$\begin{aligned}A(B^0 \to K^{*+}\pi^-) &= \sqrt{\tfrac{2}{3}}a_0\left\langle\tfrac{1}{2},-\tfrac{1}{2}|\mathcal{H}_S|\tfrac{1}{2},-\tfrac{1}{2}\right\rangle \\ &+ \tfrac{\sqrt{2}}{3}a_1\left\langle\tfrac{3}{2},-\tfrac{1}{2}|\mathcal{H}_S|\tfrac{3}{2},-\tfrac{1}{2}\right\rangle \\ &- \tfrac{\sqrt{2}}{3}a_1\left\langle\tfrac{1}{2},-\tfrac{1}{2}|\mathcal{H}_S|\tfrac{1}{2},-\tfrac{1}{2}\right\rangle\ .\end{aligned} \tag{3.22}$$

As $\mathcal{H}_S$ respects isospin symmetry, it has to satisfy $\langle I, I_3|\mathcal{H}_S|I, I_3\rangle = h_I$, *i.e.* the matrix element only depends on the isospin number and not on its third component. Using this, the $A(B^0 \to K^{*+}\pi^-)$ amplitude can be finally written as

$$\frac{1}{\sqrt{2}}A(B^0 \to K^{*+}\pi^-) = \frac{1}{3}A_{1,3/2} - \frac{1}{3}A_{1,1/2} + \sqrt{\frac{1}{3}}A_{0,1/2}\ , \tag{3.23}$$

where $A_{1,3/2} = a_1h_{3/2}$, $A_{1,3/2} = a_1h_{1/2}$ and $A_{0,1/2} = a_0h_{1/2}$ incorporate the change in magnitude as well as the strong-phase-shift corrections to a_0 and a_1 due to hadronization and rescattering effects for the final $I = 1/2$ and $I = 3/2$ states, respectively. Similarly, the decomposition of the remaining $B \to K^*\pi$ amplitudes is summarized on table 3.1. The same relations are valid for the CP conjugated amplitudes, where the $A_{\Delta I,I_f}$ amplitudes have opposite weak phases. Examining the amplitudes on table 3.1, summing the second

Modes	Decay Amplitudes
$K^*\pi$	$A(B^+ \to K^{*+}\pi^0) = \frac{2}{3}A_{1,3/2} - \frac{1}{3}A_{1,1/2} + \sqrt{\frac{1}{3}}A_{0,1/2}$
	$A(B^0 \to K^{*0}\pi^0) = \frac{2}{3}A_{1,3/2} + \frac{1}{3}A_{1,1/2} - \sqrt{\frac{1}{3}}A_{0,1/2}$
	$\frac{1}{\sqrt{2}}A(B^+ \to K^{*0}\pi^+) = \frac{1}{3}A_{1,3/2} + \frac{1}{3}A_{1,1/2} - \sqrt{\frac{1}{3}}A_{0,1/2}$
	$\frac{1}{\sqrt{2}}A(B^0 \to K^{*+}\pi^-) = \frac{1}{3}A_{1,3/2} - \frac{1}{3}A_{1,1/2} + \sqrt{\frac{1}{3}}A_{0,1/2}$

Table 3.1: *$B \to K^*\pi$ decay amplitudes decomposition in terms of isospin amplitudes $A_{\Delta I}, I_f$, where ΔI and I_f are the transition isospin difference and final state isospin, respectively.*

and the fourth row, and the first and third one, a quadrilateral relation is fulfilled between the four $K^*\pi$ amplitudes, and the same holds true for the CP conjugated,

$$A^{0+} + \sqrt{2}A^{+0} = A^{+-} + \sqrt{2}A^{00}, \tag{3.24}$$

$$\bar{A}^{0+} + \sqrt{2}\bar{A}^{+0} = \bar{A}^{+-} + \sqrt{2}\bar{A}^{00}. \tag{3.25}$$

3.2.4 Reparameterization Invariance

The two complex isospin relations Eqs.(3.24) and (3.25) eliminate four real parameters, which brings their number to thirteen. This number matches the total number of physical observables (cf. Sec. 3.2.2). In the general parameterization there are 16 real hadronic parameters, there is a non-physical global phase, and the 2 real CKM parameters ρ and η (the A and λ parameters being very well known, are kept fixed, cf. Sec. 1.3). Isospin symmetry provides two new independent complex relations, which eliminate 4 real parameters, there are then $16 - 1 + 2 - 4 = 13$ parameters left. It could be thought that in this situation (13 observables for 13 unknowns) there is no need for any other external hypothesis, other than $SU(2)$ symmetry, to fit for the unknowns in terms of measurements. But this statement is incorrect, due to *reparameterization invariance*.

The developments in this section are based on [71]. In a general fashion (not only in the context of the SM) the decay amplitude of a B meson (neutral or charged) into a final state f can be written in the following way,

$$\begin{array}{rcl} A_f & = & M_1 e^{i\phi_{A1}} e^{i\delta_1} + M_2 e^{i\phi_{A2}} e^{i\delta_2} \ , \\ \bar{A}_{\bar{f}} & = & M_1 e^{-i\phi_{A1}} e^{i\delta_1} + M_2 e^{-i\phi_{A2}} e^{i\delta_2} \ , \end{array} \tag{3.26}$$

where ϕ_{Aj} ($j = 1, 2$) are CP-odd weak phases, δ_j are CP-even strong phases and M_j are the magnitudes of the corresponding terms. In the case of a neutral B decaying into a CP eigenstate with eigenvalue $\eta_f = \pm 1$, the right hand side of the $\bar{A}_{\bar{f}}$ expression is multiplied by η_f.

Any additional term $M_3 e^{i\phi_{A3}} e^{i\delta_3}$ contributing to the amplitude, bringing an additional weak phase, can be expressed in terms of $e^{i\phi_{A1}}$ and $e^{i\phi_{A2}}$ as long as there exist a and b

parameters such as

$$\begin{aligned} e^{i\phi_{A3}} &= a e^{i\phi_{A1}} + b e^{i\phi_{A2}} \,, \\ e^{-i\phi_{A3}} &= a e^{-i\phi_{A1}} + b e^{-i\phi_{A2}} \,. \end{aligned} \tag{3.27}$$

In effect,

$$\begin{aligned} A'_f &= A_f + M_3 e^{i\phi_{A3}} e^{i\delta_3} &&= M'_1 e^{i\phi_{A1}} e^{i\delta'_1} + M'_2 e^{i\phi_{A2}} e^{i\delta'_2} \,, \\ \bar{A}'_{\bar{f}} &= \bar{A}_{\bar{f}} + M_3 e^{-i\phi_{A3}} e^{i\delta_3} &&= M'_1 e^{-i\phi_{A1}} e^{i\delta'_1} + M'_2 e^{-i\phi_{A2}} e^{i\delta'_2} \,, \end{aligned} \tag{3.28}$$

with

$$\begin{aligned} M'_1 e^{i\delta'_1} &= M_1 e^{i\delta_1} + M_3 e^{i\delta_3} a \,, \\ M'_2 e^{i\delta'_1} &= M_2 e^{i\delta_2} + M_3 e^{i\delta_3} b \,, \end{aligned} \tag{3.29}$$

and where the solutions for the CP-even parameters a and b are given by,

$$\begin{aligned} a &= \frac{\sin(\phi_{A3} - \phi_{A2})}{\sin(\phi_{A2} - \phi_{A1})} \,, \\ b &= \frac{\sin(\phi_{A3} - \phi_{A1})}{\sin(\phi_{A2} - \phi_{A1})} \,. \end{aligned} \tag{3.30}$$

The solutions are only valid in the case where $\phi_{A1} - \phi_{A2} \neq n\pi$ (n integer), *i.e.* when there is more than one weak phase. These results can be easily extended to the case where the amplitude has an arbitrary number N of distinct contributions, each one with different weak phases.

Usually, within some particular model, the weak phases that appear in Eqs.(3.26) are inspired from the Lagrangian. In the SM those are directly the phases of the CKM elements involved in the calculation of the decay amplitude (cf. Sec. 3.2.1). On general grounds, and without any hypothesis about the CP-even terms M_j and δ_j, the decay amplitudes can be expressed in terms of any pair of weak phases $\{\varphi_{A1}, \varphi_{A2}\}$, as long as $\varphi_{A1} - \varphi_{A2} \neq n\pi$. Specifically,

$$\begin{aligned} A_f &= \mathcal{M}_1 e^{i\varphi_{A1}} e^{i\Delta_1} + \mathcal{M}_2 e^{i\varphi_{A2}} e^{i\Delta_2} \,, \\ \bar{A}_{\bar{f}} &= \mathcal{M}_1 e^{-i\varphi_{A1}} e^{i\Delta_1} + \mathcal{M}_2 e^{-i\varphi_{A2}} e^{i\Delta_2} \,, \end{aligned} \tag{3.31}$$

where the CP-even part of the amplitude transforms as

$$\begin{aligned} \mathcal{M}_1 e^{i\Delta_1} &= M_1 e^{i\delta_1} \frac{\sin(\phi_{A1} - \varphi_{A2})}{\sin(\varphi_{A2} - \varphi_{A1})} + M_2 e^{i\delta_2} \frac{\sin(\phi_{A2} - \varphi_{A2})}{\sin(\varphi_{A2} - \varphi_{A1})} \,, \\ \mathcal{M}_2 e^{i\Delta_2} &= M_1 e^{i\delta_1} \frac{\sin(\phi_{A1} - \varphi_{A1})}{\sin(\varphi_{A2} - \varphi_{A1})} + M_2 e^{i\delta_2} \frac{\sin(\phi_{A2} - \varphi_{A1})}{\sin(\varphi_{A2} - \varphi_{A1})} \,. \end{aligned} \tag{3.32}$$

This change in the set of weak basis does not have any physical implications, hence the name *reparameterization invariance* (RpI).

It has to be stressed that this invariance has nothing to do with the unitarity relation of the CKM matrix (cf. Eq.(1.19)); nor is unitarity needed in order to justify any of the $\mathbb{U}$, $\mathbb{C}$ or $\mathbb{T}$ choices (cf. Sec. 3.2.1). The weak phases in $V_{us}V_{ub}^*$ and $V_{ts}V_{tb}^*$ can be used as basis, regardless of whether the CKM matrix is unitary or not, and regardless of whether the quark-level diagrams contributing to the decay amplitudes carry these precise CKM couplings.

Now consider two sets of weak phases $\{\phi_{A1}, \phi_{A2}\}$ and $\{\phi_{A1}, \varphi_{A2}\}$ with $\phi_{A2} \neq \varphi_{A2}$. If an algorithm allows to write ϕ_{A2} as a function of physical observables then, owing to the similarity of Eqs.(3.26) and (3.31), φ_{A2} would be extracted with exactly the same function, leading to $\phi_{A2} = \varphi_{A2}$, in contradiction with the assumptions. Then, the weak phases in the parameterization of the decay amplitudes have no physical meaning and cannot be extracted without additional hadronic hypothesis.

In the discussion above it was assumed that the two weak phases that are used to describe the decay amplitudes are different (modulo π). In the case in which only one weak phase can be used to describe the decay amplitude, then weak phases can be extracted from experiment. An example is the decay of neutral B to CP eigenstates. In the case of no direct CP-asymmetry, $\mathcal{A}_{CP} = 0$, the decay amplitudes can be expressed in terms of a single weak phase, which can be extracted with the measurement of the phase of $\lambda_{CP} = (q/p)\bar{A}_{\bar{f}}/A_f$ (cf. Sec. 1.2.3). Reciprocally, when the amplitude can be described with only one weak phase, there is no direct CP-violation. Explicitly, λ_{CP} can be written as (cf. Eq.(1.53))

$$\lambda_{CP} = \eta_f \frac{q}{p}\frac{\bar{A}_f}{A_f} = \eta_f \frac{q}{p} e^{-2i\phi_{A1}} \frac{1 + re^{i(\phi_{A1}-\phi_{A2})}e^{i\delta}}{1 + re^{-i(\phi_{A1}-\phi_{A2})}e^{i\delta}} \ , \tag{3.33}$$

where $\delta = \delta_2 - \delta_1$ and $r = M_2/M_1$. The CP-asymmetry $\mathcal{A}_{CP}$ is given by

$$\mathcal{A}_{CP} = -\frac{1 - |\lambda_{CP}|^2}{1 + |\lambda_{CP}|^2} = -\frac{2r\sin(\phi_{A1} - \phi_{A2})\sin\delta}{1 + 2r\cos(\phi_{A1} - \phi_{A2})cos\delta + r^2} \ . \tag{3.34}$$

Assuming $\mathcal{A}_{CP} = 0$ implies that: i) $r = 0$ (there is only one amplitude); or ii) $\phi_{A1} = \phi_{A2}$ (there is only one weak phase); or that iii) $\delta_1 = \delta_2$. In the last case, it is always possible to find a magnitude M_3 and a weak phase $e^{i\phi_{A3}}$ such that

$$\begin{array}{rclcl} A_f & = & (M_1 e^{i\phi_{A1}} + M_2 e^{i\phi_{A2}})e^{i\delta_1} & = & M_3 e^{i\phi_{A3}} e^{i\delta_1} \ , \\ \bar{A}_{\bar{f}} & = & \eta_f (M_1 e^{i\phi_{A1}} + M_2 e^{-i\phi_{A2}})e^{i\delta_1} & = & \eta_f M_3 e^{-i\phi_{A3}} e^{i\delta_1} \ , \end{array} \tag{3.35}$$

with M_3 and $e^{i\phi_{A3}}$ given by

$$\begin{array}{rcl} M_3 & = & M_1^2 + M_2^2 + 2M_1M_2\cos(\phi_{A1} - \phi_{A1}) \ , \\ e^{-2i\phi_{A3}} & = & \dfrac{M_1 e^{-i\phi_{A1}} + M_2 e^{-i\phi_{A2}}}{M_1 e^{i\phi_{A1}} + M_2 e^{i\phi_{A2}}} = \dfrac{1 + re^{i(\phi_{A1}-\phi_{A2})}}{1 + re^{-i(\phi_{A1}-\phi_{A2})}} e^{-2i\phi_{A1}} \ . \end{array} \tag{3.36}$$

In cases i) and ii) $\lambda_{CP} = \eta_f(q/p)e^{-2i\phi_{A1}}$; in case iii) $\lambda_{CP} = \eta_f(q/p)e^{-2i\phi_{A3}}$. The classical example of ii) is the $B^0 \to J/\psi K^0_S$ decay, where the dominant Tree and Penguin amplitudes have (to a very good approximation) the same weak phases and are real, and this fact ensures that the mixing phase $arg(q/p)$ can be safely extracted from the measurement of the time-dependent CP-asymmetry. In case iii) ϕ_{A3} depends on CKM phases and on the penguin to tree ratio, which makes difficult to set a clean constraint on CKM phases without additional theoretical input.

3.2.5 Parameterizations

Classical parameterization

Eq. 3.24 and 3.25 can be used to eliminate two complex quantities. For the decay amplitudes parameterization the hadronic amplitudes T^{+-}, P^{+-}, $N^{0+} = T^{0+}$, T_C^{00}, P^{EW} and P_C^{EW} can be used

$$\begin{array}{rcll} A^{+-} & = & V_{us}V_{ub}^{*}T^{+-} & + \; V_{ts}V_{tb}^{*}P^{+-} \, , \\ A^{0+} & = & V_{us}V_{ub}^{*}N^{0+} & + \; V_{ts}V_{tb}^{*}(-P^{+-} + P_C^{EW}) \, , \\ \sqrt{2}A^{+0} & = & V_{us}V_{ub}^{*}(T^{+-} + T_C^{00} - N^{0+}) & + \; V_{ts}V_{tb}^{*}(P^{+-} - P_C^{EW} + P^{EW}) \, , \\ \sqrt{2}A^{00} & = & V_{us}V_{ub}^{*}T_C^{00} & + \; V_{ts}V_{tb}^{*}(-P^{+-} + P^{EW}) \, . \end{array} \tag{3.37}$$

This parameterization is frequently used in the literature, and will be referred to as the "classical" parameterization. The notation N^{0+} makes reference to the fact that the contribution to the $K^{*0}\pi^+$ proportional to $V_{us}V_{ub}^*$ has a annihilation or exchange topology, which are equivalent from the phenomenological point of view (in these amplitudes there are also mixed u and c Penguins contributions). The corresponding diagrams are shown in Fig. 3.2. The $B^0 \to K^{*0}\pi^0$ Tree amplitude being color suppressed is denoted as T_C^{00} (cf. Fig. 3.3). The EW notation in the P^{EW} and P_C^{EW} amplitudes refers to "Electro-weak", and makes reference to the Penguin amplitudes contributing to the $B^+ \to K^{*+}\pi^0$ and $B^+ \to K^{*0}\pi^+$ decays, P_C^{EW} being color suppressed with respect to P^{EW}. The gluonic emission on the loop (shown in the right diagram of Fig. 3.1) has to give a $\Delta I = 0$ due to isospin conservation in strong interactions. As the $\bar{b}$ and $\bar{s}$ quarks have isospin zero, the total isospin difference only can be $\Delta I = 0$. As a consequence, the $\Delta I = 1$ components for the $B \to K^{*+}\pi^0$ and $B \to K^{*0}\pi^+$ modes do not have any gluonic Penguin contribution. Then, the "EW" notation actually makes reference to the $\Delta I = 1$ electroweak Penguin, the other ($\Delta I = 0$) being absorbed in the gluonic Penguins P^{+-}.

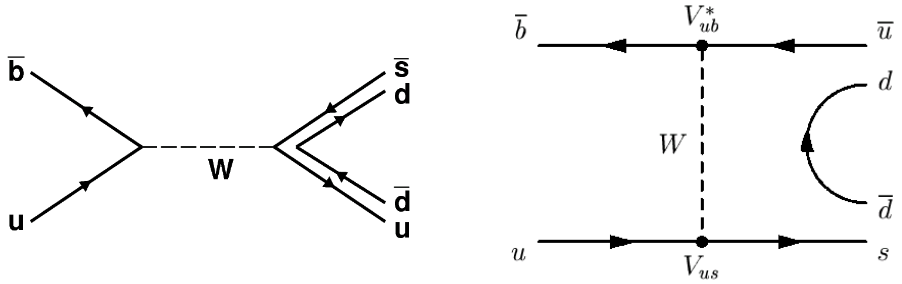

Figure 3.2: *Annihilation (left) and Exchange (right) diagrams contribution to the N^{0+} amplitude for the $B^+ \to K^{*0}\pi^+$ decay. The two contributions are equivalent from the phenomenological point of view.*

Parameterization *à la* Pivk-Le Diberder

There is another parameterization which has a simpler form with respect to the hadronic amplitudes and where the CKM factors are expressed in terms $\bar{\rho}$ and $\bar{\eta}$ only [72]. It is inspired

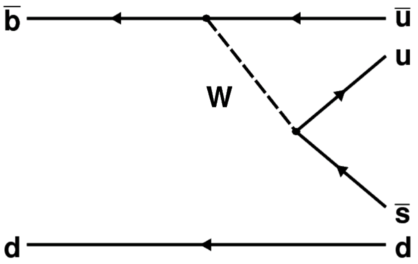

Figure 3.3: *Color suppressed diagram for the* $B^{+} \to K^{*0}\pi^{+}$ *decay.*

on a parameterization used in [73] for a study of CKM constraints using the $B \to \pi\pi$ system. It will be referred in the following as the “Pivk-Le Diberder” (PLD) parameterization. Using the following identities (cf. Eqs.(1.16) and recalling $q/p = V_{td}V_{tb}^{*}/V_{td}^{*}V_{tb}$),

$$\begin{aligned}
V_{us}V_{ub}^{*} &= \frac{\lambda}{\sqrt{1-\lambda^{2}}}V_{td}V_{tb}^{*}\left[\frac{1}{1-\bar{\rho}-i\bar{\eta}}-1\right] , \\
\frac{q}{p}V_{us}^{*}V_{ub} &= \frac{\lambda}{\sqrt{1-\lambda^{2}}}V_{td}V_{tb}^{*}\left[\frac{1}{1-\bar{\rho}+i\bar{\eta}}-1\right] , \\
\frac{V_{ts}V_{tb}^{*}}{V_{us}V_{ub}^{*}} &= -\frac{1-\lambda^{2}}{\lambda}\frac{1}{\bar{\rho}+i\bar{\eta}}-1+A^{2}\lambda^{2} = \left(-\frac{1}{\lambda^{2}}+1\right)\frac{\bar{\rho}-i\bar{\eta}}{\bar{\rho}^{2}+\bar{\eta}^{2}}-1 , \qquad (3.38)
\end{aligned}$$

the decay amplitudes can be written as

$$\begin{aligned}
A^{+-} &= \lambda_{u}\tilde{T}^{+-}\left[1+\frac{V_{ts}V_{tb}^{*}}{V_{us}V_{ub}^{*}}\frac{P^{+-}}{T^{+-}}\right] , \\
A^{0+} &= \lambda_{u}\tilde{T}^{+-}\left[\frac{N^{0+}}{T^{+-}}+\frac{V_{ts}V_{tb}^{*}}{V_{us}V_{ub}^{*}}\left(-\frac{P^{+-}}{T^{+-}}+\frac{P_{C}^{EW}}{T^{+-}}\right)\right] , \\
\sqrt{2}A^{+0} &= -A^{0+}+\lambda_{u}\tilde{T}^{+-}\left[1+\frac{T^{00}}{T^{+-}}\right]\left[1+\frac{V_{ts}V_{tb}^{*}}{V_{us}V_{ub}^{*}}\frac{P^{EW}}{T_{3/2}}\right] , \\
\sqrt{2}A^{00} &= -A^{+-}+\lambda_{u}\tilde{T}^{+-}\left[1+\frac{T^{00}}{T^{+-}}\right]\left[1+\frac{V_{ts}V_{tb}^{*}}{V_{us}V_{ub}^{*}}\frac{P^{EW}}{T_{3/2}}\right] , \qquad (3.39)
\end{aligned}$$

where $T_{3/2} = T^{+-} + T_{C}^{00}$ is the Tree contribution to the $I = 3/2$ final state, and $\tilde{T}^{+-}$ and λ_{u} are given by

$$\tilde{T}^{+-} = \frac{\lambda}{\sqrt{1-\lambda^{2}}}V_{td}V_{tb}^{*}\frac{T^{+-}}{(1-\bar{\rho})^{2}+\bar{\eta}^{2}} . \qquad (3.40)$$

$$\lambda_{u} \equiv \left[\bar{\rho}(1-\bar{\rho})-\bar{\eta}^{2}-i\bar{\eta}\right] \qquad (3.41)$$

This parameterization is well adapted to extract ratios of pure hadronic amplitudes, and to apply the constraints on hadronic hypothesis that will be described in Sec. 3.2.7, which relate the electro-weak Penguins to the Tree hadronic amplitudes.

3.2.6 The $B^0 \to K^{*+}\pi^-$ and $B^0 \to K^{*0}\pi^0$ subsystem and the $CPS/GPSZ$ technique

Using the observables from the $B^0 \to K^{*+}\pi^-$ and $B^0 \to K^{*0}\pi^0$ decays, a constraint on the CKM angle α can be set in the hypothesis of negligible EWPs, as suggested by [74, 75] (this assumption on the EWPs ensures the reparameterization invariance breaking). This method, which will be called CPS/GPSZ in this thesis, is illustrated here as follows: taking the Eq.(3.37) parameterization, and considering the two combinations of amplitudes

$$A^0 = A(B^0 \to K^{*+}\pi^-) + \sqrt{2}A(B^0 \to K^{*0}\pi^0) = V_{us}V_{ub}^*(T^{+-} + T_C^{00})\,, \tag{3.42}$$

$$\bar{A}^0 = A(\bar{B}^0 \to K^{*-}\pi^+) + \sqrt{2}A(\bar{B}^0 \to \bar{K}^{*0}\pi^0) = V_{us}^*V_{ub}(T^{+-} + T_C^{00})\,, \tag{3.43}$$

one defines the convention-independent ratio

$$R^0 = \frac{q}{p}\frac{\bar{A}^0}{A^0} = e^{-2i\beta}e^{-2i\gamma} = e^{-2i\alpha} \tag{3.44}$$

that provides a clean determination of the α weak phase. The A^0 amplitude can be extracted using the decay chains $B^0 \to K^{*+}(\to K^+\pi^0)\pi^-$ and $B^0 \to K^{*0}(\to K^+\pi^-)\pi^0$ contributing to the $B^0 \to K^+\pi^-\pi^0$ DP. Similarly, $\bar{A}^0$ can be extracted from the $\bar{B}^0 \to K^-\pi^+\pi^0$ DP using the same procedure. The $B^0 \to K^+\pi^-\pi^0$ decay channel being self-tagging (see Sec. 5.3) no mixing is possible, and the $A(K^{*+}\pi^-)$ and $A(K^{*-}\pi^+)$ ($A(K^{*0}\pi^0)$ and $A(\bar{K}^{*0}\pi^0)$) amplitudes can not interfere.

The phase difference between $A(K^{*+}\pi^-)$ and $A(K^{*-}\pi^+)$ (cf. Sec. 3.2.2) is extracted from the $B^0 \to K_S^0\pi^+\pi^-$ DP, considering the decay chain $B^0 \to K^{*+}(\to K^0\pi^+)\pi^-$ and the CP conjugated $\bar{B}^0 \to K^{*-}(\to \bar{K}^0\pi^-)\pi^+$. These channels do interfere through mixing but in a small DP region, and they both interfere with the decays $B^0\bar{B}^0 \to \rho^0(\to \pi^+\pi^-)K_S^0$ and with other resonances (which also interfere between them through mixing) contributing to the same DP. In this way the phase difference between $A(K^{*+}\pi^-)$ and $(q/p)A(K^{*-}\pi^+)$ can be extracted.

A similar ratio can be constructed, again in the hypothesis of negligible EWPs, using the charged B decays, using the following two combinations of amplitudes

$$A^+ = A(B^+ \to K^{*0}\pi^+) + \sqrt{2}A(B^+ \to K^{*0}\pi^+) = V_{us}V_{ub}^*(T^{+-} + T_C^{00}), \tag{3.45}$$

$$A^- = A(B^- \to \bar{K}^{*0}\pi^-) + \sqrt{2}A(B^- \to K^{*-}\pi^0) = V_{us}^*V_{ub}(T^{+-} + T_C^{00})\,. \tag{3.46}$$

Then, the free of phase convention ratio

$$R^{\mp} = \frac{q}{p}\frac{\bar{A}^-}{A^+} = e^{-2i\beta}e^{-2i\gamma} = e^{-2i\alpha} \tag{3.47}$$

can be in principle used for the extraction of α. As before, $A^\pm$ can be extracted from the decay chains $B^\pm \to K^{*\pm}(\to K^0\pi^\pm)\pi^0$ and $B^\pm \to K^{*0}(\to K^0\pi^0)\pi^\pm$ entering in the $B^\pm \to K_S^0\pi^\pm\pi^0$ DP. Electric charge forbids the extraction of the relative phase of the two DP's along the way discussed above, so that further theoretical arguments have to be adopted in order to fix the relative phases between opposite-sign amplitudes [74]. Alternatively, the full information coming from the charged and neutral B decays can be combined to improve the accuracy of the α determination.

The inclusion of the EWPs completely changes Eqs.(3.44) and (3.47). In fact, even though EWPs yield a subdominant contribution to branching fractions (because of the α_{em} suppression with respect to the strong Penguin contribution), they provide an $\mathcal{O}(1)$ contribution to R^0 and $R^{\mp}$ (more generally, they provide an $\mathcal{O}(1)$ correction to CP-violating effects in charmless $b \to s$ decays). Furthermore, the CKM couplings amplify the contribution of EWPs to the amplitudes. The net effect of the EWPs is that the CKM dependence of R^0 and $R^{\mp}$ does not factorise into a single α dependence, so that the CPS/GPSZ technique provides a more complicated constraint on the $(\bar{\rho}, \bar{\eta})$ parameters. The argument of the ratio R^0,

$$\phi_{3/2} = arg(R^0) \ , \tag{3.48}$$

is a physical observable as it is a function of physical observables. Given a theoretical hypothesis it can be expressed as a function of the $\bar{\rho}$ and $\bar{\eta}$ parameters, and can then be used to set a constraint in the $(\bar{\rho}, \bar{\eta})$ plane. As an example, in the hypothesis of $P^{EW} = 0$ we have the relation $\phi_{3/2} = \alpha$.

Dalitz plot analyses combined with isospin have already shown their effectiveness in the extraction of α from $B \to \pi\pi\pi$ [76]. A proposal relying on isospin for extracting the UT angle γ using a global analysis of $B \to K^0_S(\pi\pi)_{I=0,2}$, including time-dependent CP-asymmetries at fixed values of the DP variables (cf. Sec. 2.4) can be found in ref. [77].

It has to be said that the methods described originally in [74, 75] do not include the q/p term in Eqs.(3.44) and (3.47). The authors then claim instead to have direct access to the UT angle γ in the hypothesis of negligible electro-weak Penguin contributions. The issue is that the ratios Eqs.(3.44) and (3.47) without the inclusion of the q/p mixing factors are not physical observables as they are not invariant under phase redefinitions of the $B/\bar{B}$ fields [25]. In effect, without the inclusion of the q/p factor, the $\tilde{R}^0$ ratio is written as

$$\tilde{R}^0 = \frac{\langle K^{*-}\pi^+|\mathcal{H}|\bar{B}^0\rangle + \sqrt{2}\langle \bar{K}^{*0}\pi^0|\mathcal{H}|\bar{B}^0\rangle}{\langle K^{*+}\pi^-|\mathcal{H}|B^0\rangle + \sqrt{2}\langle K^{*0}\pi^0|\mathcal{H}|B^0\rangle} \ . \tag{3.49}$$

By performing the phase transformation $|B^0_\zeta\rangle \to e^{-i\zeta}|B^0\rangle$, $|\bar{B}^0_\zeta\rangle \to e^{i\zeta}|\bar{B}^0\rangle$, the amplitude ratio transforms as $\tilde{R}^0_\zeta \to e^{2i\zeta}\tilde{R}^0$, proving that its phase is not a physical observable. Note in contrast that as a consequence of the phase transformation, $(q/p)_\zeta \to e^{-2i\zeta}(q/p)$, so that the real physical observable is $R^0 = (q/p)\tilde{R}^0$.

Another claim of [74] is that the phase difference between the $A(K^{*+}\pi^-)$ and $A(K^{*-}\pi^+)$ can be measured with a time-integrated Dalitz plot analysis of $B^0 \to K^0_S\pi^+\pi^-$. As shown in Chapter 2, the only term sensitive to phase differences between B^0 and $\bar{B}^0$ decay amplitudes in the time-dependent Dalitz plot PDF, Eq.(2.43), is the sinus term with the cross factor $\mathcal{I}m\left[\overline{\mathcal{A}}\mathcal{A}^*\right]$. When a time integration is performed, the PDF then is written as

$$|\mathcal{A}_{CP}(DP, q_{tag})|^2 \propto |\mathcal{A}(DP)|^2 + |\overline{\mathcal{A}}(DP)|^2 - q_{tag}\Delta\left(|\mathcal{A}(DP)|^2 - |\overline{\mathcal{A}}(DP)|^2\right) \ , \tag{3.50}$$

where Δ is a constant that depends on the B^0 lifetime. It can be seen that after the time-integration there is no cross term, and thus there is no sensitivity to phase differences between B^0 and $\bar{B}^0$ decay amplitudes.

3.2.7 Hadronic hypothesis

The effective Hamiltonian governing the decays $B \to K(K^*)\pi$ has the form [78]

$$\mathcal{H} = \frac{G_F}{\sqrt{2}} \left\{ \sum_{i=1,2} c_i \left(\Omega_u Q_i^u + \Omega_c Q_i^c \right) - \Omega_t \sum_{i=3}^{10} c_i Q_i \right\} + \mathtt{h.c.} \; , \tag{3.51}$$

where $\Omega_q = V_{qs} V_{qb}^*$ are products of CKM matrix elements, c_i are Wilson coefficients, and Q_i are local four-quark operators. There is a hierarchy in the values of the Wilson coefficients for electro-weak operators: $|c_{9,10}| \gg |c_{7,8}|$ [79]. In this approximation the electro-weak Hamiltonian can be written as follows,

$$\mathcal{H}_{EWP} \simeq c_9 Q_9 + c_{10} Q_{10} \; , \tag{3.52}$$

which is useful since there are general relations between $Q_{9,10}$ and the current-current operators $Q_{1,2}$. The operators $Q_{9,10}$ have a $(V-A) \times (V-A)$ Dirac structure, and can then be written as linear combination of the operators Q_{1-4} [79],

$$\begin{aligned} Q_9 &= \frac{3}{2} Q_1^u + \frac{3}{2} Q_1^c - \frac{1}{2} Q_3 \; , \\ Q_{10} &= \frac{3}{2} Q_2^u + \frac{3}{2} Q_2^c - \frac{1}{2} Q_4 \; , \end{aligned} \tag{3.53}$$

which holds in the convention where Q_2 is the dominant operator ($c_2 \sim 1$). $Q_{1,2}^c$ and $Q_{3,4}$ operators are $\Delta I = 0$, thus from Eq.(3.53) the $\Delta I = 1$ electro-weak Penguin (EWP) Hamiltonian writes

$$\begin{aligned} [\mathcal{H}_{EWP}]_{\Delta I=1} &= \frac{3}{2} \left[c_9 Q_1^u + c_{10} Q_2^u \right]_{\Delta I=1} \\ &= \frac{3}{2} \frac{c_9 + c_{10}}{2} \left[Q_1^u + Q_2^u \right]_{\Delta I=1} + \frac{3}{2} \frac{c_9 - c_{10}}{2} \left[Q_1^u - Q_2^u \right]_{\Delta I=1} \; , \end{aligned} \tag{3.54}$$

while the $\Delta I = 1$ current-current Hamiltonian is given by

$$[\mathcal{H}_{CC}]_{\Delta I=1} = \frac{c_1 + c_2}{2} \left[Q_1^u + Q_2^u \right]_{\Delta I=1} + \frac{c_1 - c_2}{2} \left[Q_1^u - Q_2^u \right]_{\Delta I=1} \; . \tag{3.55}$$

Numerically, the ratios $(c_9 + c_{10})/(c_1 + c_2)$ and $(c_9 - c_{10})/(c_1 - c_2)$ satisfy (see Table XXII of [80])

$$\left(\frac{c_9 + c_{10}}{c_1 + c_2} \simeq -0.0084 \right) \simeq \left(\frac{c_9 - c_{10}}{c_1 - c_2} \simeq +0.0084 \right) \; , \tag{3.56}$$

which are calculated at the next to leading order (NLO) in the framework of QCD factorization. Denoting $R = (3/2)(c_9 + c_{10})/(c_1 + c_2)$, $[\mathcal{H}_{EWP}]_{\Delta I=1}$ can be casted into

$$[\mathcal{H}_{EWP}]_{\Delta I=1} = R \frac{c_1 + c_2}{2} \left[Q_1^u + Q_2^u \right]_{\Delta I=1} - R \frac{c_1 - c_2}{2} \left[Q_1^u - Q_2^u \right]_{\Delta I=1} \tag{3.57}$$

which is not proportional to $[\mathcal{H}_{CC}]_{\Delta I=1}$ in Eq.(3.55), because of the sign flip in the second term of the right hand side. Then, $[\mathcal{H}_{EWP}]_{\Delta I=1}$ is not simply proportional to $[\mathcal{H}_{CC}]_{\Delta I=1}$.

In order to exploit Eq.(3.57), one has to look for a combination of amplitudes that receive contributions of only one of the terms in Eq.(3.57). In the $SU(3)$ limit [74, 75], it is found that in the $\Delta I = 1$ combination $A(B^0 \to K^{*+}\pi^-) + \sqrt{2}A(B^0 \to K^{*0}\pi^0)$ (the same combination described in the CPS/GPSZ methods) the EWP contributions are proportional to the CC ones. Then, the following relation can be set

$$P^{EW} = RT_{3/2}\ , \tag{3.58}$$

with $R = (1.35 \pm 0.12) \times 10^{-2}$, where the error comes from neglecting the $Q_{7,8}$ operators, and from a residual scale dependence of the Wilson coefficients, as they are calculated on a specific energy scale. Now, in the $SU(3)$ limit the two mesons in the final state, K^* and π, are not identical. Then, instead of Eq.(3.58) a modified relation is set

$$P^{EW} = R_{\text{eff}}T_{3/2}\ , \tag{3.59}$$

where $R_{\text{eff}} = R(1{+}r_{VP})/(1{-}r_{VP})$, and where the r_{VP} (VP standing for vector-pseudoscalar) parameter is given by

$$r_{VP} = \frac{\langle K^*\pi(I=3/2)|Q_-|B\rangle}{\langle K^*\pi(I=3/2)|Q_+|B\rangle}\ , \tag{3.60}$$

with $Q_\pm = (Q_1 \pm Q_2)/2$. While for $B \to K\pi$ decays the $SU(3)$ flavor symmetry guarantees that $\langle K\pi(I=3/2)|Q_-|B\rangle$ vanishes [74, 75], the same argument does not apply to $K^*\pi$ final states. To leading order in QCD factorization [81] the final state dependent r_{VP} coefficient is given by

$$r_{VP} = \left|\frac{f_{K^*}F_0^{B\to\pi} - f_\pi A_0^{B\to K^*}}{f_{K^*}F_0^{B\to\pi} + f_\pi A_0^{B\to K^*}}\right| \lesssim 0.05\ , \tag{3.61}$$

where $F_0^{B\to\pi}$ and $A_0^{B\to K^*}$ denote pseudoscalar and vector form factors, and f_π and f_{K^*} denote decay constants. Corrections to QCD factorization are expected to be of the order to $\sim 20\%$, enhancing the value of r_{VP}, which makes the estimate in Eq.(3.61) too optimistic. For the phenomenological analysis discussed in this thesis, two scenarios can be tested:

- "Aggressive" scenario: $|r_{VP}| \leq 0.05$ (GPSZ estimation);
- Nominal scenario: $|r_{VP}| \leq 0.2$;

In the $SU(3)$ limit, a similar relation can be found for the $\mathcal{P}_C^{EW}$, but it depends on subleading terms that contribute in $\rho\pi$ and $K^*\bar{K}$ modes. While an analysis including information stemming from those modes appeals to be very interesting, is lies certainly beyond the time scale for the present work.

3.2.8 Conclusion

The $B \to K^*\pi$ system can offer more information on the CKM parameters than the $B \to K\pi$ system due to the fact that additional observables are available, namely the five phase differences accessible from Dalitz Plot analyses. Even though the number of observables and parameters are the same, the system is not closed due to reparameterization invariance. To break RpI, and extract information on CKM phases, additional external hypothesis have to be made; in this analysis we limit the possible choices to a single hypothesis, based on $SU(3)$ symmetry and QCD factorization, relating the color-allowed EWP to the Tree amplitudes.

3.3 Isospin Analysis for the $B \to \rho K$ modes

3.3.1 Introduction

This section describes the isospin analysis of $B \to \rho K$ modes. This system having the same isospin relations as $B \to K^*\pi$, the decay amplitudes can be parameterized similarly in terms of hadronic amplitudes and CKM factors. The fundamental difference between the $B \to \rho K$ system with respect to the $B \to K^*\pi$ system is the fewer number of observables experimentally accessible. In particular only one phase difference can be extracted from Dalitz Plot analyses.

3.3.2 Decay Amplitudes

The decay amplitudes for the $B \to \rho K$ system have exactly the same isospin structure as the ones for the $B \to K^*\pi$ system, so the same isospin relations hold. Adopting the $\mathbb{C}$ convention, the amplitudes can be written using the classical parameterization

$$\begin{array}{lclll}
a^{+-} & \equiv & A(B^0 \to K^+\rho^-) = & V_{us}V_{ub}^* t^{+-} & + \ V_{ts}V_{tb}^* p^{+-}, \\
a^{0+} & \equiv & A(B^+ \to K^0\rho^+) = & V_{us}V_{ub}^* n^{0+} & + \ V_{ts}V_{tb}^*(-p^{+-} + p_C^{EW}), \\
a^{+0} & \equiv & A(B^+ \to K^+\rho^0) = & V_{us}V_{ub}^*(t^{+-} + t_C^{00} - n^{0+}) & + \ V_{ts}V_{tb}^*(p^{+-} - p_C^{EW} + p^{EW}), \\
a^{00} & \equiv & A(B^0 \to K^0\rho^0) = & V_{us}V_{ub}^* t_C^{00} & + \ V_{ts}V_{tb}^*(-p^{+-} + p^{EW}).
\end{array} \tag{3.62}$$

where the t^{+-}, p^{+-}, t_C^{00}, n^{0+}, p^{EW} and p_C^{EW} hadronic amplitudes are different from the ones of the $B \to K^*\pi$ modes, but have the same topological interpretation. The $B \to \rho K$ system alone has the same number of hadronic parameters as the $B \to K^*\pi$ system, which adding the two CKM parameters $(\bar{\rho}, \bar{\eta})$ gives a total of thirteen parameters.

3.3.3 The physical observables

As with the $B \to K^*\pi$ system, four CP averaged branching fractions and four CP-asymmetries are observables from Q2B and Dalitz Plot analyses. Those are similarly defined as in Eqs.(3.8) and (3.10), but the $\mathcal{A}^{ij}$ amplitudes are replaced by the a^{ij} amplitudes, and in the corresponding phase space constant for the branching fractions the m_{K^*} and m_π masses are replaced by the m_K and m_ρ masses, respectively.

For the $B \to \rho K$ system there are less observable phase differences than in the $B \to K^*\pi$ system, because only one ρK resonant decay can contribute to a given DP, so the only way of observing interference between two $B \to \rho K$ amplitudes is through $B^0\bar{B}^0$ mixing in $\rho^0(770)K_S^0$. The only phase difference measurable is

$$2\beta_{eff} = arg\left(\frac{q}{p}\frac{\bar{a}^{00}}{a^{00}}\right), \tag{3.63}$$

which is extracted from the mode studied in this thesis, $B^0 \to K_S^0\pi^+\pi^-$. As was mentioned in Sec. 3.2.2, the $B^0 \to K^0\rho^0(\to \pi^+\pi^-)$ and $\bar{B}^0 \to \bar{K}^0\rho^0(\to \pi^+\pi^-)$ decays interfere through mixing, thus the presence of the q/p factor in Eq. 3.63.

In summary, the $B \to \rho K$ observables are: four branching fractions, four CP-asymmetries and one phase difference, which gives a total of nine observables.

3.3.4 Hadronic hypothesis

When considering the ρK system alone the same hadronic hypothesis made for the $K^*\pi$ system can be applied. In this case this is written as

$$p^{EW} = R\frac{1+r_{VP}}{1-r_{VP}}t_{3/2} \ , \tag{3.64}$$

where again $t_{3/2} = t^{+-} + t^{00}_C$. As for the $K^*\pi$ system, two scenarios can be explored:

- "Aggressive" scenario: $|r_{VP}| \leq 0.05$.
- Nominal scenario: $|r_{VP}| \leq 0.2$.

3.3.5 Conclusion

Despite that the $B \to \rho K$ system obeys the same isospin relations as $B \to K^*\pi$, a reduced number of observables is accessible: nine observables out of 13 parameters. Even with the theoretical assumption described in Sec. 3.3.4 (which eliminates other two parameters) the system remains under-constrained. The only advantage of $B \to \rho K$ is the cleaner access to the mixing phase $2\beta_{\text{eff}}$ in $B^0 \to \rho^0 K_S$ (if compared to the two-body system $B \to K\pi$, where only the time-dependent CP-asymmetry S is accessible in $B^0 \to \pi^0 K_S$); this single advantage does not compensate for the drawback of having and under-constrained system.

3.4 Combining the $B \to K^*\pi$ and $B \to \rho K$ modes

3.4.1 Introduction

$K^*\pi$ and ρK resonant states can contribute to the same DP and interfere, so more phase differences are accessible. In a combined study of observables from both systems, more observables are added, while the total number of CKM plus hadronic parameters staying almost unchanged. When studding the $K^*\pi$ or ρK systems alone, there is always an unphysical global phase. But when studding both systems together, there is only one global unphysical phase, due to the fact that a phase difference between both subsystems is now observable. In this section the new observables are listed, and a description of how the two systems can be combined is presented.

Most of the published phenomenological analyses combining $B \to K(K^*)\pi$ and $B \to K\pi(\rho)$ systems rely on $SU(3)$ flavor symmetry in order to relate hadronic amplitudes from both systems, reducing the number of unknowns [14, 69]. In the analysis here presented, the experimental access to observables linking the $B \to K^*\pi$ and $B \to \rho K$ amplitudes, give a natural relation between both systems. Therefore a phenomenological analysis can be based primarily on $SU(2)$ isospin only.

3.4.2 The physical observables

Several $K^*\pi$ and ρK resonant decays contribute to the same DP. The following additional phase differences are accessible:

- $\phi(K^{*+}\pi^-, K^0\rho^0) = arg(A(B^0 \to K^{*+}\pi^-)A^*(B^0 \to K^0\rho^0))$ due to interference of the decay chains $B^0 \to K^{*+}(\to K^0_S\pi^+)\pi^-$ and $B^0 \to K^0\rho^0(\to \pi^+\pi^-)$ both contributing to the $B^0 \to K^0_S\pi^+\pi^-$ decay mode.

- $\phi(K^{*+}\pi^-, K^+\rho^-) = arg(A(B^0 \to K^{*+}\pi^-)A^*(B^0 \to K^+\rho^-))$ due to interference of the decay chains $B^0 \to K^{*+}(\to K^+\pi^0)\pi^-$ and $B^0 \to K^+\rho^-(\to \pi^-\pi^0)$ both contributing to the $B^0 \to K^+\pi^-\pi^0$ decay mode. Also accessible is the CP conjugated phase $\bar{\phi}(K^{*-}\pi^+, K^-\rho^+) = arg(A(\bar{B}^0 \to K^{*-}\pi^+)A^*(\bar{B}^0 \to K^-\rho^+))$.

- $\phi(K^{*0}\pi^+, K^+\rho^0) = arg(A(B^+ \to K^{*0}\pi^+)A^*(B^+ \to K^+\rho^0))$ due to interference of the decay chains $B^+ \to K^{*0}(\to K^+\pi^-)\pi^+$ and $B^+ \to K^+\rho^0(\to \pi^+\pi^-)$ both contributing to the $B^+ \to K^+\pi^-\pi^+$ decay mode. Also accessible is the CP conjugated phase $\bar{\phi}(\bar{K}^{*0}\pi^-, K^-\rho^0) = arg(A(B^- \to \bar{K}^{*0}\pi^-)A^*(B^- \to K^-\rho^0))$.

- $\phi(K^{*+}\pi^0, K^0\rho^+) = arg(A(B^+ \to K^{*+}\pi^0)A^*(B^+ \to K^0\rho^+))$ due to interference of the decay chains $B^+ \to K^{*+}(\to K^0\pi^+)\pi^0$ and $B^+ \to K^0\rho^+(\to \pi^+\pi^0)$ both contributing to the $B^+ \to K^0_S\pi^+\pi^0$ decay mode. Also accessible is the CP conjugated phase $\bar{\phi}(K^{*-}\pi^0\bar{K}^0\rho^-) = arg(A(B^- \to K^{*-}\pi^0)A^*(B^- \to \bar{K}^0\rho^-))$.

In total, there are seven additional phase differences experimentally accessible from the combination of both systems, which considering the previous thirteen observables from the $B \to K^*\pi$ system alone, and the nine observables from the $B \to \rho K$, make a total of $13 + 9 + 7 = 29$ observables. Because both $K^*\pi$ and ρK systems are considered simultaneously, there is only one single irrelevant global phase, which makes fourteen parameters for each system minus a global phase, giving a total of $14 + 14 - 1 = 27$.

It could be now thought that the system is overconstrained, but in fact not all the observables are theoretically independent, as all experimental observables are functions of the decay amplitudes only. For each system, there are eight complex decay amplitudes (four for the B decays and four the $\bar{B}$ decays), which gives thirty-two real parameters; then there are two isospin relations for each system, which eliminates eight other parameters; finally, taking into account the single unphysical global phase gives a total of $2(16) - 8 - 1 = 23$ theoretically independent observables that can be constructed. This means that the 29 observables listed above are not all theoretically independent. But as their experimental extraction comes from independent analyses, these measurements provide redundant information, that act as an effective enhancement of sensitivity, and thus further constrain the phenomenological analysis.

3.4.3 Hadronic hypothesis

Here again, external information needs to be added to break RpI. When considering both $K^*\pi$ and ρK systems together, instead of applying again the relations in 3.59 and 3.64, a more relaxed hadronic hypothesis can be tested. In the $SU(3)$ limit the r_{VP} parameters for both systems satisfy the following relation

$$r_{K^*\pi} = -r_{\rho K} \ . \tag{3.65}$$

The following parameterization is then adopted

$$\begin{aligned} r_{K^*\pi} &= +r_f + \frac{1}{2} r_{SU3} \ , \\ r_{\rho K} &= -r_f + \frac{1}{2} r_{SU3} \ , \end{aligned} \tag{3.66}$$

where r_f is the $SU(3)$ symmetric correction to QCD factorization, and r_{SU3} parameterizes $SU(3)$ breaking. In this case, the following scenarios are considered:

- "Aggressive" scenario: $|r_f| \leq 0.05$, $|r_{SU3}| \leq 0.05$.
- Nominal scenario: $|r_f| \leq 0.05$, $|r_{SU3}| \leq 0.30$.

3.4.4 Conclusion

A combined study of both $B \to K^*\pi$ and $B \to \rho K$ systems together adds seven new experimental observables. These are phase differences, accessible when both resonant decays contribute to the same DP and interfere. In the combined isospin analysis, there is only one spurious phase in the decay amplitudes, which gives a total of 23 parameters, to be extracted out of 29 experimental observables. Combining both systems promises an access to tighter constraints on these parameters, in light of the higher number of experimentally independent observables. As a single hadronic hypothesis suffices to break RpI, a safer, more relaxed relation between hadronic parameters can be tested, to extract information on the $(\bar{\rho}, \bar{\eta})$ parameters of the CKM matrix.

3.5 Strategies for a phenomenological analysis

For the phenomenological analysis (see Chapter 8) two different scenarios can be considered:

1. **Scenario 1:** using external information (the global CKM fit) on the CKM parameters, constraints can be made on the ratio of the hadronic amplitudes. This approach has the advantage that the theoretical hypothesis made are relatively safe, *i.e.* it is only assumed the unitarity of the CKM matrix. The inputs used in this scenario are the results on $\bar{\rho}$ and $\bar{\eta}$ from the global CKM fit and the experimental measurements for the system considered (*i.e.* $B \to K^*\pi$ or $B \to \rho K$). Two kind of outputs can be obtained from this approach:
    - Constraints on unavailable observables (*e.g.* $\phi^{(0+,+0)}$ and $\bar{\phi}^{(0+,+0)}$, cf. Eq.(3.13)), which gives the predicted value of the observables under the safe hypothesis of the unitarity of the CKM matrix.

  - Constraints on the ratio of hadronic parameters, which can be used to test theoretical hypothesis, including the ones described in this chapter (cf. Sec. 3.2.7).

2. **Scenario 2:** using an hadronic hypothesis (*e.g.* Sec. 3.2.7), constraints are made on CKM parameters (*i.e.* on the $(\bar{\rho}, \bar{\eta})$ plane). In this case the stability of the hadronic hypothesis can be evaluated by measuring how sensitive are the constraints on the CKM parameters on the theoretical uncertainties. One of the main goals of this phenomenological analysis is to test the CPS/GPSZ method.

In a fist step, the two scenarios described above are studied using the observables from $B \to K^{*}\pi$ modes. A similar study using $B \to \rho K$ modes has a more limited impact, due to the reduced number of observables, but still bounds on ratios of hadronic parameters can be set. Finally, a combined study using observables from both systems will be discussed. The results on these two approaches will be shown in Secs. 8.3, 8.4 and 8.5, respectively.

Prospective studies will be presented in Sec. 8.5.3, where the potential of the methods described in this chapter are extrapoled, based on numbers stemming from the future integrated luminosities, and expected performances of the Belle-upgrade, Super-B, and/or LHCb projects.

Part II

PEP-II and the *BABAR* Experiment

Chapter 4

An Introduction to the *BABAR* experiment

The primary goal of the *BABAR* experiment is the systematic study of CP asymmetries in the decays of the neutral B mesons to CP eigenstates. Other priority goals are the precision measurements of decays of bottom and charm mesons and of τ leptons, and searches for rare process that become accessible with the high luminosity of the PEP-II B factory (cf. Sec. 4.1). As discussed in Sec. 1.3, the measurement of the β angle of the CKM matrix, which was the key design objective of *BABAR*, relies on the measurement of time-dependent CP asymmetries in the neutral modes induced by $b \to c\bar{c}s$ transitions. In a similar spirit, time-dependent measurements with $B^0 \to \pi^+\pi^-$ and $B^0 \to \rho^+\rho^-$ are important for constraining the α angle of the CKM matrix. In order to observe the time-dependent CP asymmetries, the detector has to be capable to:

- reconstruct completely exclusive final states;
- determine the flavor of the decaying neutral B mesons;
- measure the time difference between the two B mesons in the event. (cf. Sec. 1.2.2).

The principal channels considered with priority at the time of *BABAR* conception include:

- For $\sin 2\beta$: $B^0 \to J/\psi K^0_S$, $B^0 \to J/\psi K^0_L$, $B^0 \to J/\psi K^{*0}$, $B^0 \to D^+D^-$, $B^0 \to D^{*+}D^{*-}$.
- For $\sin 2\alpha$: $B^0 \to \pi^+\pi^-$, $B^0 \to \pi^+\pi^-\pi^0$, $B^0 \to a_1\pi$.

Due to the smallness of the branching fractions of these final states ($< 10^{-5}$), $B\bar{B}$ mesons pairs have to be produced copiously. The *BABAR* detector was designed and optimized to achieve the physics goals described above. The asymmetric e^+e^- collider B factory PEP-II B, was designed to deliver the B mesons to the experiment.

This chapter describes the experimental facility used for collecting the data used in the analyses presented in this thesis. The beam particles production and accelerator system, the storage rings and the PEP-II collider [82] are described in the first section (Sec. 4.1). Then (Sec. 4.2) the *BABAR* detector [83], which surrounds the PEP-II interaction point (IP), is described. This detector is composed of several subsystems. Each of them provides part of information for a complete event reconstruction: the tracking system, composed of the silicon vertex tracker (SVT) and the drift chamber (DCH); the particle identification system (PID), which is composed mainly of the detector of Cherenkov radiation (DIRC); the electromagnetic calorimeter (EMC); and the muon and hadron detector (IFR), instrumented within the magnetic flux return steel. The way in which this information is used for the reconstruction of the particles forming the B decay final states will be presented in Chapter 5.

4.1 e^+e^- B factories and *PEP-II*

In the late 1980s, studies [84] indicated that the best source of B mesons for a B physics program was an e^+e^- collider running in asymmetric mode, *i.e.* with beams of unequal energy, operating at the $\Upsilon(4S)$ resonance mass ($10.58\ \mathrm{GeV}/c^2$). The B mesons are produced in pairs from the process $e^+e^- \to \Upsilon(4S) \to B\bar{B}$. The $\Upsilon(4S)$ resonance,a $b\bar{b}$ bound state, decays exclusively to $B^0\bar{B}^0$ and B^+B^- pairs ($\mathcal{B}(\Upsilon(4S) \to B\bar{B}) > 96\%$ [21], with $\mathcal{B}(\Upsilon(4S) \to B^0\bar{B}^0)/\mathcal{B}(\Upsilon(4S) \to B^+B^-) \sim 1$), and thus provides an ideal laboratory for the study of B mesons. PEP-II is such a collider housed in the former PEP (Positron-Electron Project) tunnel, on the SLAC (Stanford Linear Accelerator Center) laboratory, located in California. Two of the main design criteria are:

- Produce high luminosities ($3.0 \times 10^{33}\mathrm{cm}^2\mathrm{s}^{-1}$ was the project goal).
- Operate in an asymmetric mode, resulting in B^0 mesons with high enough momenta in the laboratory frame to infer their decay times from their decay lengths, which are measured from the location of decay vertex (cf. Sec. 5.4).

There are several advantages to the e^+e^- environment over an hadronic environment, namely:

- a high signal-to-background ratio, (characterized by the cross section ratio $\sigma_{b\bar{b}}/\sigma_{TOT} \simeq 0.2$);
- clean events, with a mean charged multiplicity of ~ 11 for B decays and smaller for other reactions;
- low interaction rates $\sim 10\mathrm{Hz}$ (physics rate);
- the possibility to reconstruct final states containing π^0s and photons, thereby allowing exclusive measurements in many channels.

Also the PEP-II configuration provides several kinematical advantages: knowledge of the exact 4-momentum of the two-B meson system; the knowledge of the momentum magnitudes of the two B mesons individually in the center-of-mass (CM) system. These informations can be used as constraints, which considerably help in suppressing backgrounds (cf. Sec. 5.6.1).

4.1.1 The *LINAC* and the storage rings

PEP-II is made of two storage rings of $2.2\ \mathrm{Km}$ of circumference in which the collision takes place. Fig. 4.1 shows an schematic view of the PEP-II collider and the LINAC accelerator. The LINAC (LINear ACcelerator) constitutes the PEP-II injection system. It is $3\ \mathrm{Km}$ long and accelerates the particles up to their nominal energies. The LINAC is a facility also used for other purposes, being able to produce beams with energies up to $50\ \mathrm{GeV}$. The electrons and positrons used by PEP-II only use part of the accelerator capabilities. These electrons and positrons produced in the LINAC are accelerated until their nominal energies, and then injected to PEP-II storage rings placed at the end of the linear accelerator. Once there, the electrons and positrons, which circulate in bunches in separate rings, are made to collide at the IP, around which the *BABAR* detector is located.

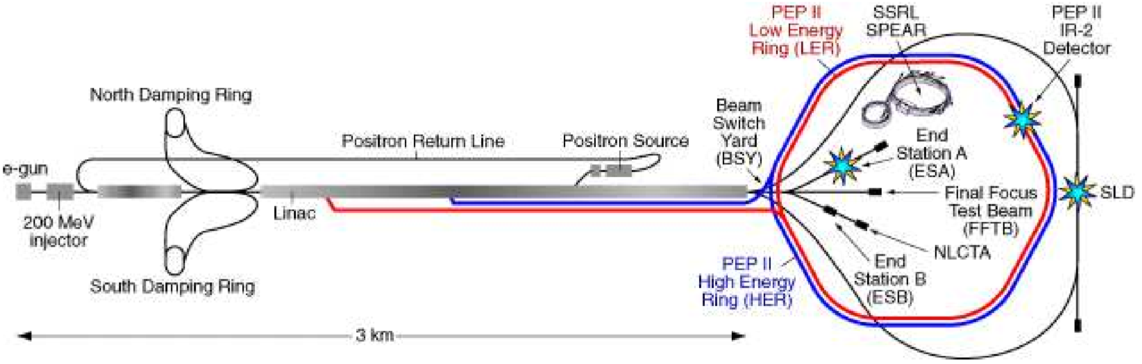

Figure 4.1: *The linear accelerator at SLAC and the PEP-II collider.*

The High Energy Ring (HER) produces electron beams with $9.0\ \mathrm{GeV}$ of energy, while the Low Energy Ring (LER), delivers positrons with an energy of $3.1\ \mathrm{GeV}$, which upon collision, result in a boost of $\langle\beta\gamma\rangle \sim 0.56$ along the e^- beam direction in the laboratory frame. This boost allows the measurement of the B_{CP}/B_{tag} mesons time difference (cf. Sec. 1.2.2). The parameters for these storage rings are summarized on table 4.1.

4.1.2 The interaction region

The interaction region is instrumented with magnets that focus the beams before collision, direct them so that there is no crossing angle at the IP, and finally separate them before the exiting bunch of particles collides with a bunch from the other beam (cf. Fig. 4.2). The next quadrupole magnets, labelled by QD and QF, are located outside the *BABAR* detector. They focus the high and low energy beams. The bunches are brought together, collide head-on, and are separated magnetically in the horizontal plane by a pair of dipole magnets ($B1$), followed by a series of quadrupole magnets ($Q1$). The $B1$ dipoles, located at $\pm 21\ \mathrm{cm}$ on either side of the IP, and the $Q1$ quadrupoles are permanent magnets placed inside the *BABAR* solenoid (cf. Sec. 4.2.6). This close distance from the IP was designed to obtain a small spacing of bunches in the beams ($1.26\ \mathrm{m}$), so the beams have to be separated very quickly in

Parameters	Design	Typical
Energy HER/LER (GeV)	$9.0/3.1$	$9.0/3.1$
Current HER/LER(A)	$0.75/2.15$	$1.9/2.9$
# of bunches	1658	1722
Bunches spacing (ns)	4.2	8.4
σ_{Lx} (μm)	110	120
σ_{Ly} (μm)	3.3	5.6
σ_{Lz} (mm)	9	9
Luminosity ($10^{33} cm^{-2} s^{-1}$)	3.0	9.0
Luminosity (pb^{-1}/day)	130	700

Table 4.1: *PEP-II beams parameters. Values are given for both design and typical colliding beam operation in April 2008.* σ_{Lx}, σ_{Lz} *and* σ_{Lz} *refer to horizontal, vertical and longitudinal RMS size of the luminous region.*

order to avoid parasitic collisions. The first unwanted crossing point is located $63\ \mathrm{cm}$ away from the IP.

The collision axis is offset from the z-axis of the *BABAR* detector by about $20\ \mathrm{mrad}$ in the horizontal plane to minimize the perturbation on the beams by the solenoidal field. In order to have the highest possible solid angle, the $B1$ and $Q1$ components have to be very compact, and in order not to compromise the vertexing resolution, the vertex detector (cf. Sec. 4.2.1) has to be as close to the water-cooled beryllium beam pipe as practical. The beam pipe has an internal radius of $2.6\ \mathrm{cm}$ and its inner surface is coated with a $4\ \mu\mathrm{m}$ thin layer of gold to attenuate synchrotron radiation. The SVT and the $B1$ and $Q1$ magnets are placed inside a support tube of $4.5\ \mathrm{m}$ long and $27.7\ \mathrm{cm}$ inner diameter inside the beamline supports. The quasi-vertical dotted lines of Fig. 4.2 represent the acceptance of *BABAR*.

4.1.3 Monitoring of the beam parameters

The most critical beam parameters for *BABAR* performance are: luminosity; energies of the two beams; and positions, angles, and size of the luminous region. While PEP-II measures radiative Bhabha scattering events to provide a fast monitoring of the relative luminosity, *BABAR* derives the absolute luminosity offline from other QED processes, primarily e^+e^- and $\mu^+\mu^-$ pairs. The measured rates are consistent and stable as a function of time. During operation, the mean energies of the two beams are calculated from the total magnetic bending strength and the average deviations of the accelerating frequencies from their central values. The RMS energy spreads of the LER and HER beams are $2.3\ \mathrm{MeV}$ and $5.5\ \mathrm{MeV}$, respectively. To ensure that the data is recorded close to the peak $\Upsilon(4S)$ resonance, the observed ratio of the $B\bar{B}$ enriched events to lepton pair production is monitored online. Near the peak of the resonance, a 2.5% change in the ratio corresponds to a $2\ \mathrm{MeV}$ change in the C.M. energy, but this drop does not distinguish between energy settings below or above the $\Upsilon(4S)$ peak. The best monitor and absolute calibration of the C.M. energy is derived from the measured C.M. momentum of fully reconstructed B mesons combined with the known

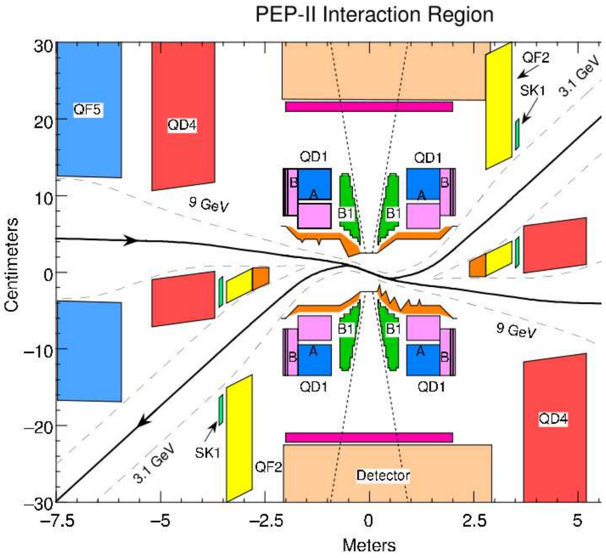

Figure 4.2: *The PEP-II optics around the interaction point seen in the horizontal plane. The scale is contracted in the vertical axis. The electrons go into the detector from the left. The roles of the different magnets is described are the text.*

B-meson mass. The beam energies are necessary input for the calculation of two kinematic variables commonly used to separate signal from background in the analysis of exclusive B-meson decays (cf. Sec 5.6.1). The direction of the beams relative to BABAR is measured iteratively run-by-run[1] using $e^+e^- \to e^+e^-$ and $e^+e^- \to \mu^+\mu^-$ events. The size and position of the luminous region (see design values in Table 4.1) are critical parameters for the time-dependent analyses. They are determined from the closest approach to the z-axis of two-charged particles events as a function of the azimuth angle, and from the position of the two tracks.

4.1.4 Machine backgrounds

The primary source of accelerator backgrounds are, in order of increasing importance: synchrotron radiation around the IP; interaction of beam particles with residual gas in the storage rings; electromagnetic showers generated in beam-beam collisions. These backgrounds should be avoided as they can lead to degradation of the performance of the detector, due to sustained radiation damage, and large dead times in which the readout of the detector subsystems are idle.

Synchrotron radiation in the nearby dipoles, the $Q1$ quadrupoles and $B1$ dipoles generates a severe background. The beam orbits, vacuum-pipe apertures and synchrotron radiations masks have been designed such that most of these photons are channeled to a distant dump; the remainder are subject to multiple scatters before they can enter the BABAR acceptance.

---

[1] A "run" is a small period of data taking (~ 50 min) in which the beam quality is stable.

Beam-gas bremsstrahlung and Coulomb scattering of residual gas molecules cause in some cases beam particles to escape the acceptance of the ring and hit the beam pipe producing electromagnetic showers that spread over the detector. Vacuum pumps maintain the residual pressure to a minimum, and collimators cut the beam tails generated by betatron oscillations and beam-gas interactions. Beam-gas scattering is the primary source of radiation damage in the SVT and the dominant source of background in all detectors systems, except for the DIRC.

Radiative Bhabha scattering results in low energy electrons or positrons that hit aperture limitations within a few meters of the IP and spray BABAR with electromagnetic showers. This background is proportional to the instantaneous luminosity. This is the dominant background in the DIRC.

4.1.5 The continuous injection system

At the beginning of BABAR in 1999, the electrons and positrons were injected in the storage rings in bunches of 10^9 particles with a frequency between $(1-30)\mathrm{Hz}$, with a mean time spacing of $4\mathrm{ns}$. In normal operation the injection was made every $(40-50)$ min. These periods of injection (of ~ 5 min) generated intense backgrounds in BABAR. Also, the injection induced dead time, because it was necessary to ramp down the high voltages of detector systems for protection purposes. Data taking was interrupted regularly. Additionally, beam currents decreased continuously, and the recorded luminosity was not optimal.

A system of continuous injection known as trickle injection was established since 2004. A new injection is only arranged when the instantaneous luminosity falls below a pre-established threshold, and can be made continuously at a low rate. This was first achieved for the LER, resulting in a gain in luminosity of 35%. Later on it was implemented in the HER, giving a additional gain of 12% (cf. Fig. 4.3). The inconvenient of this new method is in the difficulty to limit the backgrounds created by the injection. In successive tests it was shown that these backgrounds could be kept to a manageable level, and the default operation has been this trickle injection since 2004.

4.1.6 Types of data delivered

The nominal operation of PEP-II, with the beam C.M. energies tuned to be at the $\Upsilon(4S)$ resonance peak ($\sqrt{s} = 10.58$ GeV), is known as *On-peak* operation mode. Due to their high mass ($m_B = 5.279$ GeV$/c^2$), the B-mesons have a momentum in the C.M. frame of $p^*_B = \sqrt{s/4 - m^2_B} \simeq 341$ MeV$/c$. In this frame $\gamma^*_B = E^*_B/p^*_B = 1.002$ and $\beta^*_B = p^*_B/E^*_B = 0.064$, and so the B-mesons are non-relativistic. PEP-II also delivers *Off-peak* data taken 40 MeV below the nominal C.M. energy, where the B-meson production is null. These data, which represent 10% of the total integrated luminosity, are used for detailed studies of non-resonant backgrounds.

The $b\bar{b}$ production is not the only process that takes place at the $\Upsilon(4S)$ peak. There are also events of the type $e^+e^- \rightarrow q\bar{q}$ (where $q = c, s, u, d$), $e^+e^- \rightarrow \ell^+\ell^-$ ($\ell^- = e^-, \mu^-, \tau^-$) and $e^+e^- \rightarrow \gamma\gamma$. Table 4.2 shows the production cross sections for these other processes.

The $e^+e^- \to q\bar{q}$ events are particularly important in the analysis presented in this thesis because they are the dominant background component.

$e^+e^- \to$	Cross-Section (nb)
$b\bar{b}$	1.10
$c\bar{c}$	1.30
$s\bar{s}$	0.35
$u\bar{u}$	1.39
$d\bar{d}$	0.35
$\tau^+\tau^-$	0.94
$\mu^+\mu^-$	1.16
e^+e^-	~ 40

Table 4.2: *Cross Sections at* $\sqrt{s} = 10.58\ \mathrm{GeV}$ *taken from [25].*

4.1.7 Performance

The design luminosity and accelerator parameter goals were met by PEP-II within the first year of running. After that, the design performances have been surpassed repeatedly in terms of instantaneous and integrated luminosity per day and per month. Table 4.3 shows the luminosity records achieved by PEP-II. A value of $1.2 \times 10^{34}\mathrm{cm}^{-2}\mathrm{s}^{-1}$ instantaneous luminosity was eventually reached. The machine stopped running at the $\Upsilon(4S)$ peak in September 2007, having recorded a total of $432.9\mathrm{fb}^{-1}$ integrated luminosity. After that, the data taking was performed at the $\Upsilon(2S)$ and $\Upsilon(3S)$ resonances (which are located at 10.023 GeV and 10.355 GeV [21], respectively), finishing with integrated luminosities of $20.3\mathrm{fb}^{-1}$ and $14.5\mathrm{fb}^{-1}$, respectively. This last operation mode was decided mainly for two reasons: a) to study bottomonium physics, and what let to the discovery of the bottomonium ground state $\eta_b(1S)$ in the transition $\Upsilon(3S) \to \gamma\eta_b$ [85]; and b) to search for a light CP-odd Higgs boson, which is predicted in Next-to-Minimal Supersymmetric extensions of the Standard Model [86], in the channel $\Upsilon(3S) \to \gamma A^0(\to \mathrm{invisible})$. No evidence was found [87]. A summary of the time integrated luminosity delivered by PEP-II and recorded by *BABAR* is presented in Fig. 4.3, from the beginning of the data taking at 1999 until the end in 2008.

4.2 The *BABAR* Detector

The requirements to study CP-violation mentioned at the beginning of the chapter place stringent constraints on the detector, which must have:

- a large and uniform acceptance, down to small polar angles relative to the boost direction;
- good reconstruction efficiencies for charged tracks and for photons, down to $60\ \mathrm{MeV}/c$ and 20 MeV/c, respectively;

	PEP-II Records	
Quantity	Date	Record
Peak Luminosity	16 Aug 2006	$1.2 \times 10^{34}\mathrm{cm}^{-2}\mathrm{s}^{-1}$
Best shift (8hrs)	16 Aug 2006	$339.0\mathrm{pb}^{-1}$
Best best day	19 Aug 2007	$858.4\mathrm{pb}^{-1}$
Best weak	12-18 Aug 2007	$5.137\mathrm{fb}^{-1}$
Best month	Aug 2007	$19.732\mathrm{fb}^{-1}$
Peak HER current	29 Feb 2008	2069mA
Peak LER current	7 Apr 2008	3213mA

Table 4.3: *PEP-II delivered instantaneous, integrated per day, per weak and per month luminosity, and LER and HER currents records for the whole data taking period 1999-2008.*

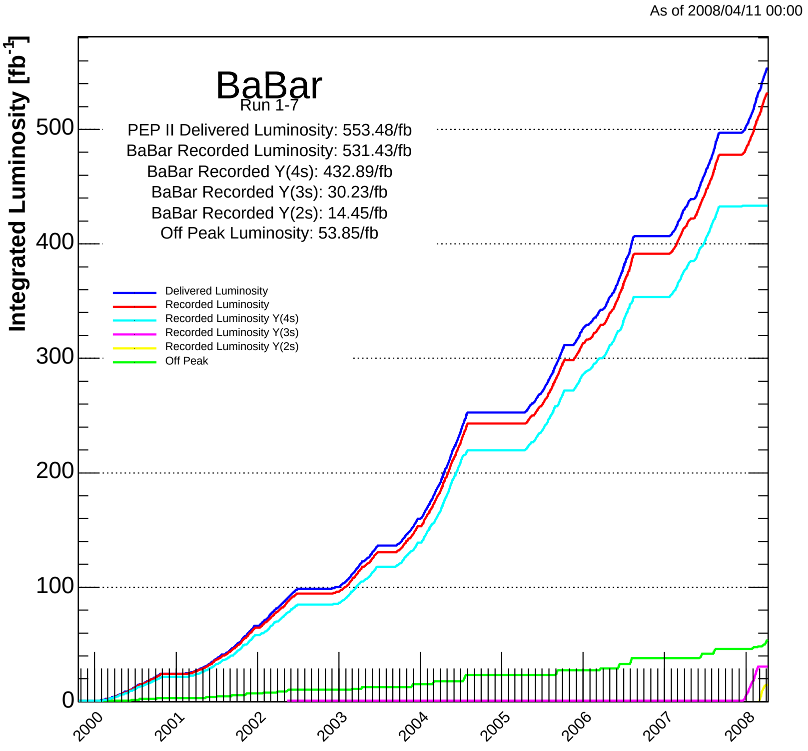

Figure 4.3: *Integrated luminosity delivered by PEP-II and integrated by BABAR for the whole data taking period 1999-2008. The curves show the delivered luminosity by PEP-II (dark blue), the total luminosity recorded by BABAR (red), and the fractions recorded on the $\Upsilon(4S)$ (light blue), $\Upsilon(3S)$ (magenta) and $\Upsilon(2S)$ (yellow) resonances. Also is shown the recorded off-peak luminosity (green). The improvement in the integrated luminosity after 2004 due to the trickle injection can be seen in the figure.*

- very good momentum resolution for signal-background separation;
- excellent energy and angular resolution for the photons which come from π^0 and η and for radiative decays;
- sufficient vertex resolution to measure the time difference between B_{CP} and $B_{\rm tag}$ decays (cf. Sec, 5.4);
- efficient hadron and lepton identification, as these are crucial to the tagging algorithm (cf. Sec. 5.3);
- a selective and redundant trigger system;
- dead times as short as possible, so that higher luminosities can be handled;
- components resisting to radiation, and capable of operate reliably under high background conditions.

The *BABAR* detector, installed around the IP of the PEP-II collider, was built to achieve these goals. It is a classic almost 4π acceptance detector. To maximize the geometrical acceptance for the boosted $\Upsilon(4S)$ decays, the detector is shifted relative to the IP by $0.37\ \mathrm{m}$ in the direction of the LER. Fig. 4.4 shows a longitudinal section through the detector center, and Fig. 4.5 shows an end view.

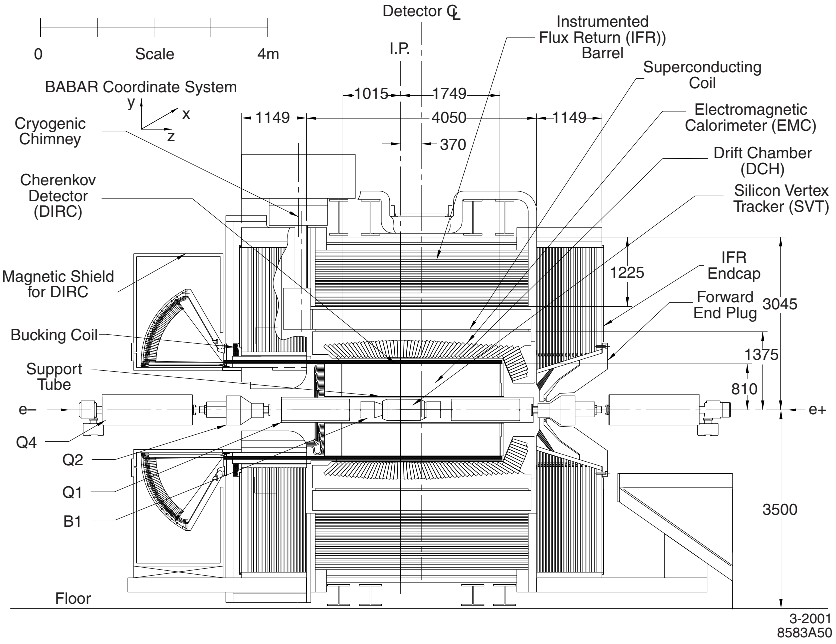

Figure 4.4: *BABAR detector longitudinal section.*

The detector consists of five subsystems: a silicon vertex tracker (SVT) used to measure angles and positions of charged particles just outside the beam pipe; a drift chamber (DCH),

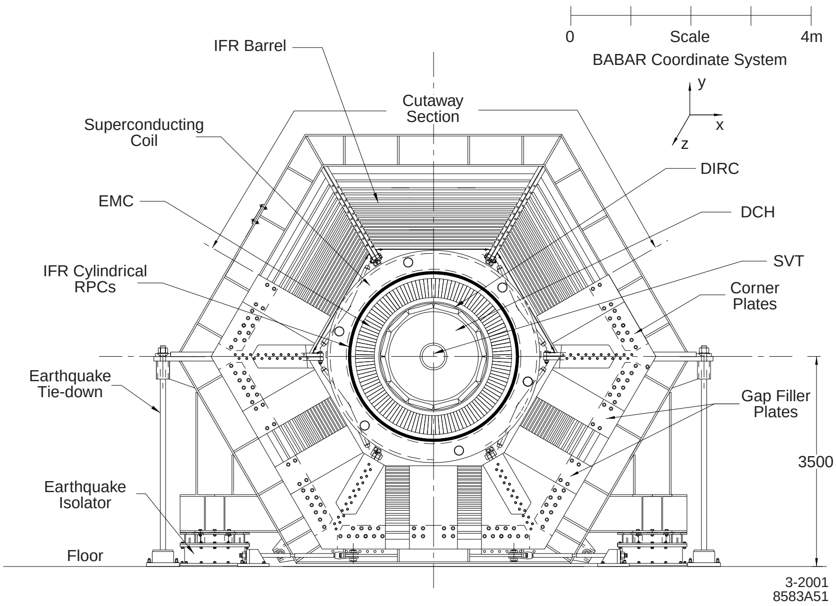

Figure 4.5: *BABAR detector end view.*

whose purpose is the measurement of momentum of charged particles; together they compose the *BABAR* tracking system; a ring-imaging Cherenkov detector (DIRC), which provides information to identify charged particles (in particular K/π separation); a CsI crystal electromagnetic calorimeter (EMC), designed to measure the energies of photons and electrons, and used for electron identification. These subsystems are surrounded by a superconducting solenoid. Finally, the steel flux return is instrumented (IFR) for muon and neutral hadron detection. The polar angle coverage extends to $350\ \mathrm{mrad}$ and $400\ \mathrm{mrad}$ in the forward and backward directions, respectively, defined with respect to the HER. As indicated in Figs. 4.4 and 4.5, the *BABAR* right-handed coordinate system is fixed on the main tracking system (DCH), with the z-axis coinciding with its principal axis offset by $20\ \mathrm{mrad}$ with respect to the electron beam direction. The positive y-axis points upward and the positive x-axis points away from the center of the PEP-II storing rings.

In the following sections, each detector subsystem is described with some detail.

4.2.1 The Silicon Vertex Tracker (*SVT*)

Physical requirements

The SVT [88] has been designed to provide a precise reconstruction of the decay vertices near the IP. This is critical for the measurement of the time-difference between B and $\bar{B}$ decays, and that of the flight distances of D mesons and τ leptons. The mean separation between the two B-mesons is of the order of $260\ \mu m$. To avoid a significant impact on the Δt resolution, the mean vertex resolution along the z-axis for fully reconstructed B decays must be better than $80\ \mu m$. The required resolution in the $x-y$ plane of $\sim 100\ \mu m$ arises for the need to reconstruct secondary vertices in τ and D decays.

The detector also provides precise reconstruction of trajectories of charged particles. It provides a standalone tracking for particles with low transverse momentum $p_t < 120\,\mathrm{MeV}/c$, the minimum that can be measured reliably in the DCH alone. This capability is fundamental for the identification of slow pions from D^* decays. The SVT is also used in association with the DCH for the reconstruction of charged particles with high transverse momentum (p_t).

The SVT is used for particle identification through its own measurement of ionization energy loss dE/dx. This also gives the best determination of the track angles, which is relevant to achieve design resolution for the Cherenkov angle (cf. Sec. 4.2.4) for high momentum tracks.

Design

In order to minimize the impact of multiple Coulomb scattering, the SVT is located as close as possible to the IP. It consists of 5 concentric layers ($300\ \mu m$ thickness each) of double-sided silicon strip sensors. These sensors are assembled into modules with readout at each end, so that the passive material in the acceptance volume is reduced (cf. Fig. 4.6). The strips on opposite sides of each sensor are mutually orthogonal: the strips in the ϕ (z) direction are parallel (transverse) to the beam axis, giving the two coordinates at the impact location. In order to avoid dead zones in ϕ, the layers 4 and 5 are divided in two sub-layers (4a,4b,5a and 5b) and located at slightly different radii. The three inner layers give the position and angle information for the measurement of the decay vertex position. The outer two layers are at a much larger radii, and provide the coordinate and angle measurements needed to match SVT and DCH tracks. The layers are organized in 6, 6, 6, 16 and 18 modules, respectively. Each module contains from 4 to 8 silicon detectors and has its own readout electronics. In total, the SVT has 340 silicon detectors covering a area of $0.96\ \mathrm{m}^2$, with a total of 150,000 readout channels. The geometrical acceptance of the detector is constrained by the components of PEP-II. The angular coverage goes from 17^o to 150^o in the polar angle.

Once a day, and each time the SVT configuration changes, calibrations are performed in absence of circulating beams. All electronic channels are tested for different values of the injected charge. Gains, thresholds, and electronic noise are measured, and defective channels are identified. The calibration results have proven very stable and repeatable.

The SVT, located very close to the beams, is significantly affected by radiation. The most significant problem is the integrated radiation dose. This can affect the detector by changing its crystalline structure, or by increasing the front-end electronic noise. The detector was designed to resist to a maximum of $5\ \mathrm{Mrad}$ of integrated radiation dose. Protection from high backgrounds is made with a customized online protection system, called SVTRAD. This system permits BABAR to stop automatically the beams when the instantaneous or integrated radiation doses go above predefined thresholds.

Performance

The average efficiency in track reconstruction of the SVT as measured in $e^+e^- \to \mu^+\mu^-$ data is 97%. The high efficiency achieved by the SVT for low p_t particles enables to perform demanding physics analyses, such as the BABAR recent evidence of $D^0 - \bar{D}^0$ mixing [19]. In

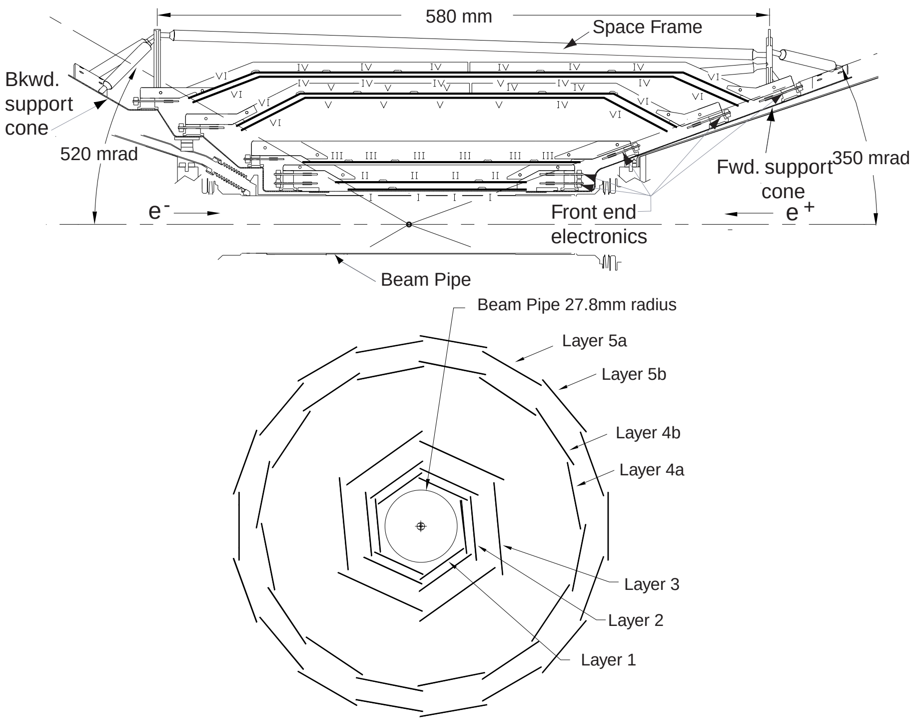

Figure 4.6: *Schematic view of SVT: (top) longitudinal section, (bottom) transverse section.*

this analysis the flavor of the D-mesons, coming from the decay $D^{*+} \to D^0\pi^+$, are tagged with the slow charged pion.

The strip sensors provide up to ten ionization energy loss dE/dx measurements per charged track. The resolution on this energy loss measurement is approximately 14%. A 2σ separation between kaons and pions can be achieved up to a momentum of $500\ \mathrm{MeV}/c$, and between kaons and protons below $1\ \mathrm{GeV}/c$.

4.2.2 The Drift Chamber (*DCH*)

Physical requirements

The principal purpose of the drift chamber [89] is the efficient detection of charged particles and the measurement of their momenta and angles with high precision. This allows for reconstruction of exclusive B and D meson decays with low background. As multiple scattering can be significant in track resolution, the material in front and inside the chamber volume was kept to a minimum. The DCH complements the measurements of impact parameter and directions of tracks provided by the SVT near the IP. It also plays a critical role in the extrapolation of charged tracks to the DIRC, EMC and IFR. Finally, it provides one of the main inputs to the L1 trigger (cf. Sec. 4.2.8).

The reconstruction of decay and interaction vertices of long-lived particles outside the SVT volume, like the K_S^0 (present in the final state of the decay channel studied in this thesis, and in many other channels studied in time-dependent analyses), relies solely on the DCH. For this purpose, the chamber should be able to measure longitudinal positions with a resolution of $\sim 1\ \mathrm{mm}$.

The DCH is used for the identification of low momentum particles with the measurement of the ionization energy loss dE/dx. The achieved design resolution of about 7% allows to separate kaons from pions up to momentum of $700\ \mathrm{MeV}/c$. This capability complements the DIRC in the barrel regions. In the forward and backward directions the DCH is the only device which provides some discrimination between charged particles of different mass.

Design

The DCH is cylindrical and $3\ \mathrm{m}$ long. It is bounded in the radial direction by the support tube (the DIRC) at its inner (outer) radius. It is composed of 7104 small hexagonal drift cells, arranged in 40 cylindrical layers. In this way it is possible to make up to 40 spatial and ionization loss measurements for charged particles with momentum larger than $180\ \mathrm{MeV}/c$. The multiple scattering inside the chamber is held to a minimum by choosing aluminium field wires with low mass, and a mixture of helium isobutane gas ($80\% : 20\%$). This represents less than $0.2\% X_0$ radiations lengths. To facilitate matching of the SVT and DCH tracks, and in order not to deteriorate DIRC and EMC performances, the material in the inner and outer walls and in the forward direction is thin and minimum. The middle of the chamber in z is located asymmetrically with respect the IP to maximize the acceptance given the boost of the e^+e^- collision, being offset by $\sim 370\ \mathrm{mm}$ in the HER direction. This asymmetry is such that particles at polar angles of 17.2^o or 152.6^o traverse half of the layers of the chamber. Fig. 4.7 shows a longitudinal section of the DCH.

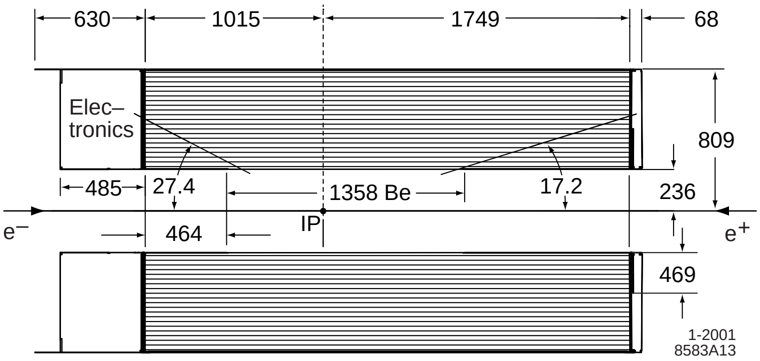

Figure 4.7: *Longitudinal section of the DCH. The chamber is offset from the IP by* $370\ \mathrm{mm}$ *in the HER direction.*

The layers are grouped by four into ten superlayers, with different stereo angles. The stereo angle is defined as the angle between the cells wires and the z-axis, in a revolution plane around the z-axis. The stereo angles of the superlayers alternate between axial (null stereo angle: A) and stereo (non-null stereo angle: U,V) pairs, in the order AUVAUVAUVA.

This layout is shown in the left hand plot of Fig. 4.8. 24 of the 40 layers form a small stereo angle with the z-axis. The stereo layers give the longitudinal position information of the tracks with a resolution of $1\ \mathrm{mm}$. In this way the three-dimensional measurement is obtained. The axial layers are used to measure the curvature angle of the tracks, which allows for the measurement of the tracks momentum. The drift cells have a hexagonal shape, with typical dimensions of $11.9\ mm \times 19.0\ mm$. Each cell consists of gold-coated sense wires made of tungsten-rhenium ($20\ \mu m$ in diameter). This sense wires are surrounded by six field aluminium wires coated with gold ($80\ \mu m$ and $120\ \mu m$ in diameter). The cell layout is shown in the right hand side plot of Fig. 4.8. The fields that separate the superlayers have a potential of $340\ \mathrm{V}$, and the other field wires are at ground potential. A positive high voltage $1960\ \mathrm{V}$ is applied to the sense wires. The voltages have been chosen to optimize the gas gain.

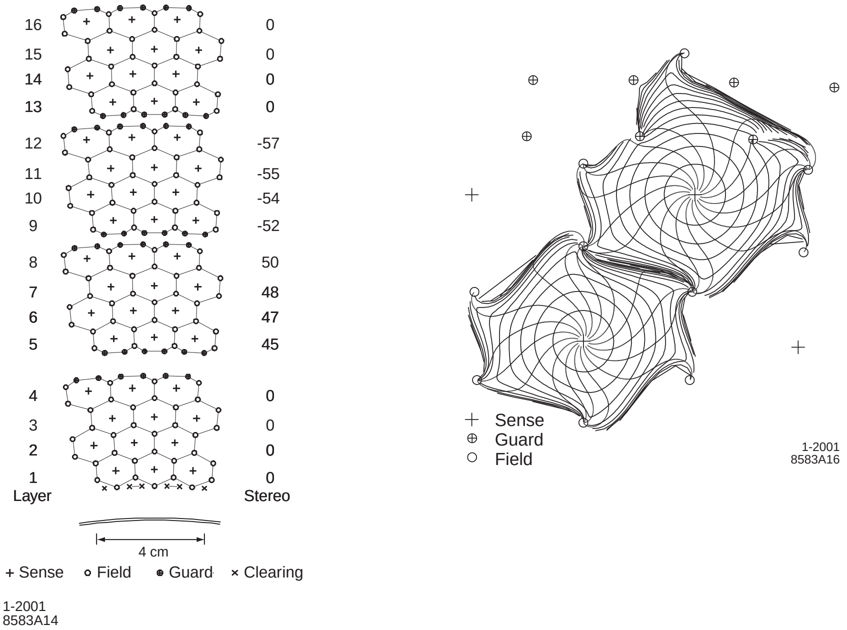

Figure 4.8: *(left) Schematic layout of the DCH cells for the four innermost superlayers. Lines have been added between field wires for visualization purposes. The numbers on the right side give the stereo angles (*mrad*) of the sense wires in each layer. (right) Drift cells isochrones, i.e. contours of equal drift times of ions in cells of layers 3 and 4 of an axial superlayer. The isochrones are spaced by* $100\ \mathrm{ns}$.

The front-end electronics are calibrated daily to determine the channel-by-channel correction constants and thresholds. The entire online calibration takes less than two minutes.

Performance

The energy loss dE/dx for charged particles traversing the DCH is derived from the total charge deposited in each drift cell [83]. The left plot in Fig. 4.9 shows the distribution of dE/dx measurements as a function of the track momenta. The superimposed Bethe-Bloch prediction for particles of different masses have been determined from selected control samples. The measured dE/dx resolution for Bhabha events is shown in the right plot of Fig. 4.9. The RMS resolution is typically 7.5%.

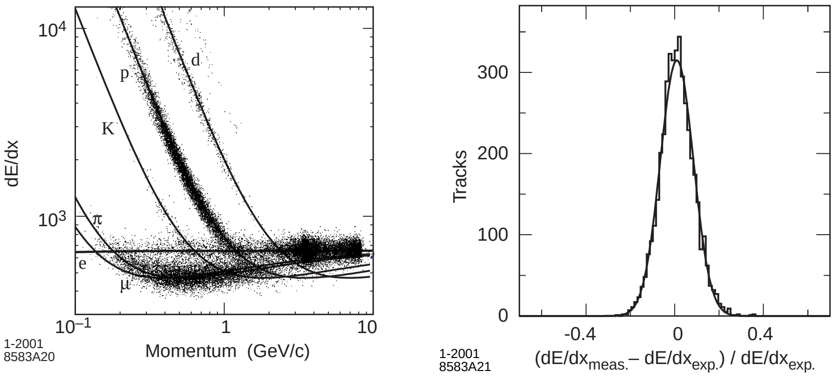

Figure 4.9: *Performance of the BABAR drift chamber for particle identification using ionization energy loss measurements. (left) Measurement of* dE/dx *as a function of track momentum. The curves show the Bethe-Bloch predictions fitted on selected control samples of particles of different masses. (right) Difference between the measured and expected energy loss* dE/dx *for* $e^{\pm}$ *from Bhabha scattering, measured in the DCH at a operating voltage of* $1960\ \mathrm{V}$. *The curve represents a Gaussian fit to data with a resolution of* 7.5%.

The performace of the tracking system, SVT and DCH, will be described in the next section.

4.2.3 Performance of the charged particle tracking system

The main purpose of the BABAR charged particle tracking system, SVT and DCH, is the efficient detection of charged particles and the measurement of their momenta and angles with high precision. These measurements allow for the reconstruction of exclusive B and D mesons decays. Reconstruction of multiple decay vertices of weakly decaying B and D mesons is of primary importance.

The reconstruction of charged tracks relies on data from both tracking systems, the SVT and the DCH. Charged tracks are defined by five parameters (d_0, ϕ_0, ω, z_0, $\tan\lambda$) and their associated error matrix. These parameters are measured at the point of closest approach to the z-axis. d_0 and z_0 are the distances to this point from the origin of the coordinate system in the $x-y$ plane and along the z-axis, respectively. The angle ϕ_0 is the azimuth of the track, λ is the dip angle relative to the transverse plane. Finally, $\omega = 1/p_t$ is the curvature. d_0 and ω are signed variables. Their sign depends on the charge of the track. The procedures for track finding and fitting use the Kalman filter algorithm [90], which takes into account the distribution of material in the detector and the map of the magnetic field.

The efficiency for reconstructing tracks in the DCH, with samples of multi-hadrons events, has been measured as a function of transverse momentum, polar and azimuthal angles in events with multiple tracks. The absolute DCH tracking efficiency is the ratio of

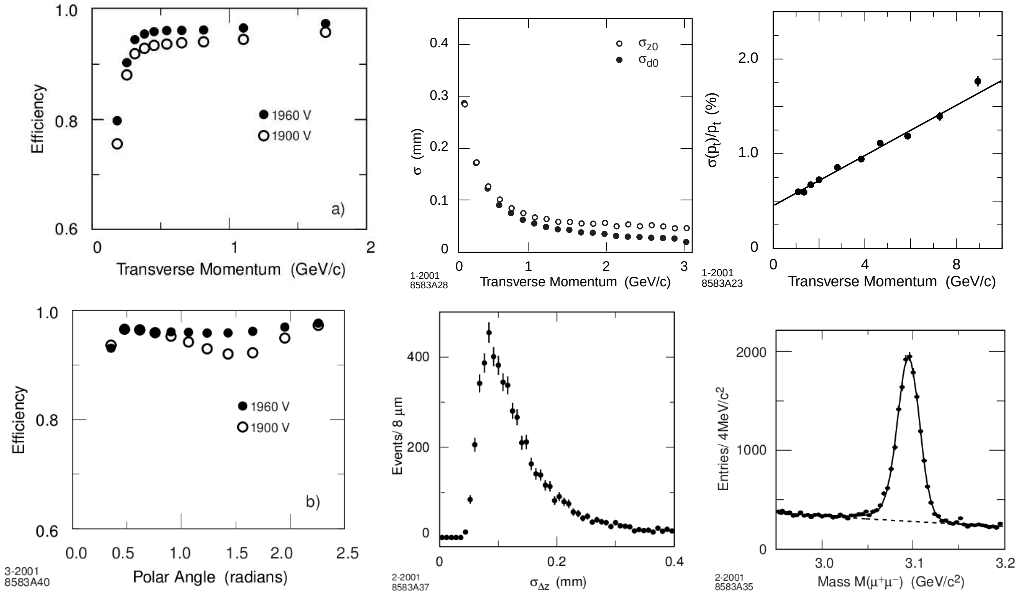

Figure 4.10: *Top and bottom left: The track reconstruction efficiency in the DCH at operating voltages of* 1900 V *and* 1960 V*, as a function of transverse momentum (top) and polar angle (bottom). Top middle: Resolution in the parameters* d_0 *and* z_0 *for tracks in multi-hadrons events as a function of the transverse momentum. Bottom middle: Distribution of the error on the difference* Δz *between* B *meson vertices for a sample of events in which one* B^0 *is fully reconstructed. Top Right: Resolution in the transverse momentum* p_t *determined from cosmics ray muons traversing the DCH and SVT. Bottom Right: Reconstruction of the decay* $J/\psi \rightarrow \mu^+\mu^-$ *in selected* $B\bar{B}$ *events.*

reconstructed DCH tracks to tracks detected in the SVT. The top and bottom plots on the left in Fig. 4.10 show the results for two voltage settings of the DCH. At the design voltage of 1960 V, the average efficiency is $(98 \pm 1)\%$ for tracks above $200\ \mathrm{MeV}/c$ and with polar angle $\theta > 500\ \mathrm{mrad}$.

The resolution in the five track parameters is monitored using e^+e^- and $\mu^+\mu^-$ pair events. It is also estimated off-line for tracks in events with multiple hadrons and with cosmic rays muons. The dependence of the resolution in d_0 and z_0 on the transverse momentum p_t is presented in the top middle plot of Fig. 4.10. The d_0 and z_0 resolutions are about $25\ \mu m$ and $40\ \mu m$, respectively, at $p_t = 3\ \mathrm{GeV}/c$.

The average vertex resolution of a decaying B-meson is $60\ \mu m$ when it is reconstructed exclusively (B_{CP}, cf. Sec 1.2.2). The bottom middle plot of Fig. 4.10 shows the estimated error in the measurement of the difference along the z-axis between the vertices of two neutral B mesons (B_{CP} and B_{tag}), where one of them is fully reconstructed, and the other serves as a flavor tag. The average resolution for the two B_{CP} and B_{tag} vertex separation is $190\ \mu m$, which is dominated by the B_{tag} vertex reconstruction. This resolution is only ~ 0.73 times the mean separation of between the two B-mesons. Studies on Monte-Carlo simulations have shown that this gives a degradation of only 10% in the measurement of time-dependent CP asymmetries.

The DCH contributes primarily to the p_t measurement. The top right plot of Fig. 4.10 shows the resolution in the transverse momentum as a function of the transverse momentum, derived from cosmic ray muons. The data are well represented by a linear function $\sigma_{p_t}/p_t = (0.13 \pm 0.01)\% \cdot p_t + (0.45 \pm 0.03)\%$, where p_t is in GeV/c.

Finally, the bottom right hand plot in Fig. 4.10 shows the mass resolution for J/ψ mesons reconstructed in the $\mu^+\mu^-$ final state using different data samples.

4.2.4 The Detector of Internally Reflected Cerenkov Light (*DIRC*)

Physical requirements

CP violation studies in neutral B-mesons decays rely on determining the flavor of the B_{tag} meson decay (cf. Sec 5.3). This flavor tagging is done using the correlation of charges of certain particles, mostly leptons and kaons, with the flavor of the parent meson (cf. Sec. 5.3). The identification of these charged particles is needed as the charge-flavor correlation depends on the particle species used. The leptons are identified mainly with the EMC (for the electrons), and the IFR (for the muons). As mentioned before, the tracking system can be used to identify reliably charged hadrons (kaons, pions, protons) with a momentum up to $700\ \mathrm{MeV}/c$. The kaons used for flavor tagging have a momentum spectrum that extends up to $2\ \mathrm{GeV}/c$, with most of them below $1\ \mathrm{GeV}/c$. On the other hand, pions and kaons from rare two body decays as $B^0 \rightarrow K^+\pi^-$ and $B^0 \rightarrow \pi^+\pi^-$ have momenta between 1.7 and $4.2\ \mathrm{GeV}/c$. It is then crucial to avoid contamination in the isolation of such final states as they have different CP asymmetries.

The DIRC separates kaons from pions with a significance of 4σ or greater, for all tracks from B-meson decays from the pion Cherenkov threshold up to $3.0\ \mathrm{GeV}/c$. The particle identification (PID) below $700\ \mathrm{MeV}/c$ relies primarily on the dE/dx measurements made by the DCH and the SVT.

Design

The main component of the PID system used in BABAR is the ring-imaging Cherenkov detector, called DIRC [91]. The detector is based on the fact that a charged particle traversing a medium of refractive index n produces, when its velocity is above the threshold $v/c = \beta > 1/n$, a Cherenkov radiation cone with angle $cos\theta_C = 1/n\beta$. Knowing the medium refractive index and the particle momentum obtained by the tracking system one has $\beta = p/\sqrt{p^2 + M^2_{\mathrm{particle}}}$. The particle can be then identified by calculating its mass: $M_{\mathrm{particle}} = p\sqrt{n^2 cos\theta_C - 1}$.

The DIRC radiator material is synthetic fused silica in the form of long ($4.9\ m$) thin bars, with rectangular cross-section ($3.5 \times 1.7\ m^2$). The bars serve both as radiators and as a light guide for the portion of the light that get trapped in the radiator by total internal reflection. The measurement principle is presented in Fig. 4.11, where the DIRC geometry is shown, and where the principle of light production, transport and imaging is illustrated. The fused silica is chosen because of its properties: resistance to ionization radiation, long

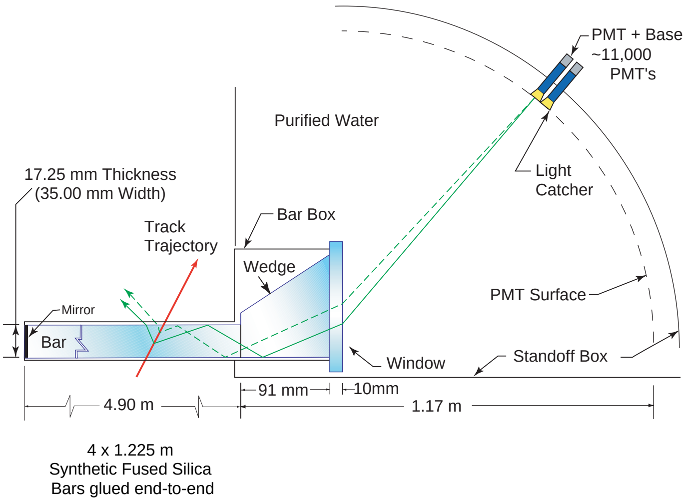

Figure 4.11: *Schematics of the DIRC fused silica radiator bar and imaging region. Not shown is a* $6\ \mathrm{mrad}$ *angle on the bottom of the surface of the wedge (see text).*

attenuation length, large index of refraction ($n = 1.473$) and low chromatic dispersion within the wavelength acceptance of the DIRC. The bars are placed in 12 containers hermetically sealed called *bar boxes* (cf. left hand plot of Fig. 4.12). They form a 12-sided polygonal barrel (cf. right hand plot of Fig. 4.12) with a radius of $810\ \mathrm{mm}$, located between the DCH and the EMC. Each bar box contains 12 bars, for a total 144 bars. Within a bar box the 12 bars are optically isolated by a $\sim 150\ \mu m$ air gap between the neighboring bars. They are also placed in a flux of Nitrogen gas, with a index of refraction sufficiently different from the fused silica to make the surface very reflecting. The gas flow maintains the bar boxes free from condensation. Because of the C.M. boost, particles are produced mostly in the forward direction. To minimize interference with other detector systems in the forward region, the DIRC photon detector is placed at the backward end.

For relativistic particles, $\beta \simeq 1$, some photons always lie within the total internal reflection limit of the fused silica bars, and are transported on either one of both ends of the bar, depending on the angle of the incident particle. The emission angle of the photon with respect to the particle track is conserved by multiple reflections in the bar walls (between 50 and 300). A mirror is placed at the forward end, perpendicular to the bar axis, to reflect the photons to the backward part which is instrumented. Once the photons arrive at the instrumented end, most of them emerge into a expansion region filled with water, *called standoff box* (SOB), which is a toroidal tank containing $6000\ \ell$ of pure water with a refractive index of $n = 1.33$. This refractive index is reasonably close to that of the fused silica, minimizing in this way the total internal reflection at interface of the two media.

The photons are detected by an array of 10752 phomultipliers tubes (PMTs) at the rear of the SOB, arranged in 12 sectors. The expected Cherenkov light pattern at this surface is essentially a conic section, where the opening angle of the cone is the Cherenkov production angle. A fused silica wedge of $91\ \mathrm{mm}$ long and trapezoidal profile is located at the bar exit. It increases the angular coverage of the detection surface. The wedge reflects the photons

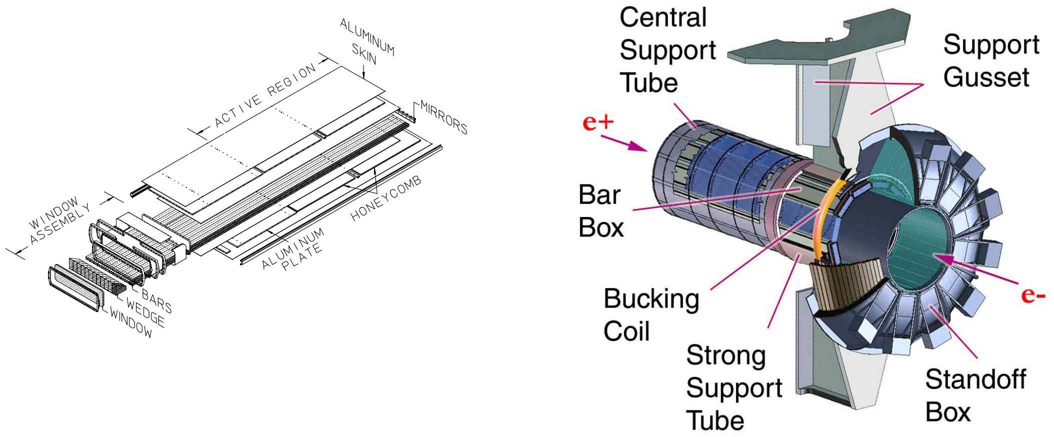

Figure 4.12: *Left: Schematics of the DIRC bar box assembly. Right: Exploited view of the DIRC mechanical support structure. The steel magnetic shield is not shown.*

with large angles with respect to the bar axis direction. This reduces the number of PMTs needed, and recovers photons that would have been lost by internal reflection at the fused silica/water interface. The bottom of the wedge has a slight upward slope (~ 6 mrad) in order to improve the focalization of photons on the PMTs. This is presented in Fig. 4.11, where are shown the paths of the Cherenkov photons produced by the same particle. The path of the photon having (not having) a reflection in the wedge is shown by the plain (dotted) line. If the bottom wedge surface had not a slope, the two photons would have parallel paths, and would not hit the same PMT.

The DIRC occupies 80 mm of radial space in the central volume including supports, with a total of $17\%X_0$ radiation lengths at normal incidence. The coverage of the radiator bars is of 94% in azimuth and a polar angle between 25.5^o and 147^o. The distance from the end of the bar to the PMTs is ~ 1.2 m, which together with the size of the bars and PMTs, gives a geometric contribution to the single photon Cherenkov angle resolution of ~ 7 mrad. This value is slightly larger than the RMS spread of the photon production (dominated by a ~ 5.4 mrad chromatic term) and transmission dispersions. The overall single photon resolution is about $\sigma_{C,\gamma} = 10$ mrad.

Performance

The image obtained in the detection surface represents a fraction of the Cherenkov cone, with, sometimes, several branches. The ambiguities stem from the odd/even, top/bottom, left/right number of reflections on the sides of the bars; and also because direct and end mirror reflected photons contribute.

The left hand plot in Fig. 4.13 shows an $e^+e^- \rightarrow \mu^+\mu^-$ event in the transverse $x - y$ plane. For each PMT hit the expected arrival time of the photon produced by a given charged particle can be calculated. Due to the unknown number of reflections in the bars, the mirrors and the wedge, there is a 16-fold ambiguity in the association of a PMT hit with a given

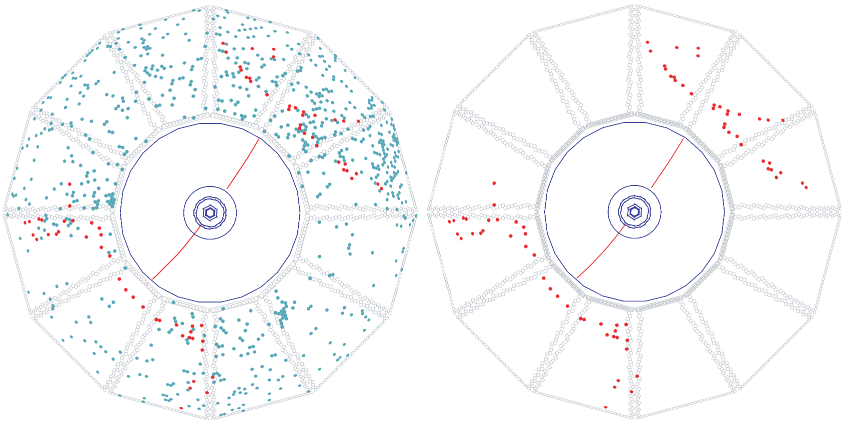

Figure 4.13: *Display of an* $e^+e^- \rightarrow \mu^+\mu^-$ *event in the* $x-y$ *plane. The tracks are reconstructed by the tracking system. The points corresponds to PMTs hits in a time window of* ± 300 ns. *On the left: all the PMTs with hits are shown. On the right: selection of PMTs hits with an arrival time at* ± 8 ns *from the expected time. The reflection of the photons in the bars surfaces, the mirrors andthe wedge produce symmetric images.*

track. A selection according to the Δt_γ, the difference between the measured and expected photon arrival time, allows not only to reduce the number of ambiguities (around 3 cutting at $\Delta t_\gamma < 8$ ns), but also suppress beam-induced backgrounds. More importantly, it excludes other tracks in the same event as the source of the photon (cf. right hand plot in Fig. 4.13). The calibration for unknown PMT time response uses two independent approaches. The first is a conventional pulser control system. It is performed online using a light pulser system with blue LEDs, one per sector. About 65,000 light pulses are used to determine the mean time response of the PMTs. The second approach uses reconstructed tracks from collision data. It uses approximately 100,000 collected track to construct the distribution of single channel Δt_γ, which is fitted to extract the global time offset.

The reconstruction of the Cherenkov angle is made with a maximum likelihood method that uses the spatial (polar and azimuth angles of the produced photons by the charged track) and temporal (Δt_γ) measured informations. The reconstruction routine currently provides a likelihood value for each of the five stable particle types (e,μ,π,K,p) if the track passes through the active volume of the DIRC. These likelihoods are calculated by maximizing the likelihood value of the entire event while testing different hypothesis for each track.

In the left plot of Fig. 4.14 the number of detected photons (N_{pe}) produced in $e^+e^- \rightarrow \mu^+\mu^-$ events is shown. It goes from 20, at normal incidence, to 65 at large polar angles. This variation is reproduced by Monte-Carlo simulations (represented by the red curve in the figure). The number of Cherenkov photons varies with the pathlength of the track in the silica bars. It is smallest at perpendicular incidence at the center, and increases towards the ends of the bars. The peak at perpendicular incidence is explained as photons produced in both $z > 0$ and $z < 0$ directions are detected.

The resolution on the Cherenkov angle is given by: $\sigma_{C,track} = (\sigma_{C,\gamma}/\sqrt{N_{pe}}) \oplus \sigma_{trace}$, where $\sigma_{C,\gamma}$ is the single photon Cherenkov angle resolution, and the constant term σ_{trace} is

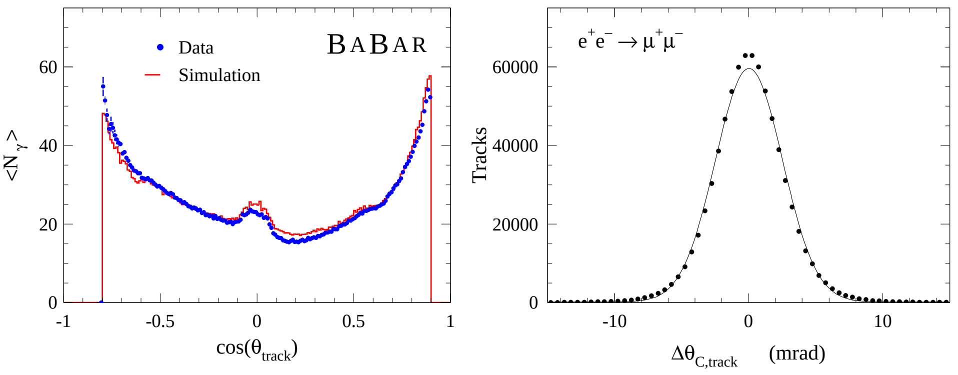

Figure 4.14: *Left: Number of detected photons in the DIRC versus track polar angle for reconstructed tracks in di-muon events compared to Monte-Carlo simulation. Right: Difference between the measured and expected Cherenkov angle,* $\Delta\theta_{track}$*, for single muons in* $\mu^+\mu^-$ *events.*

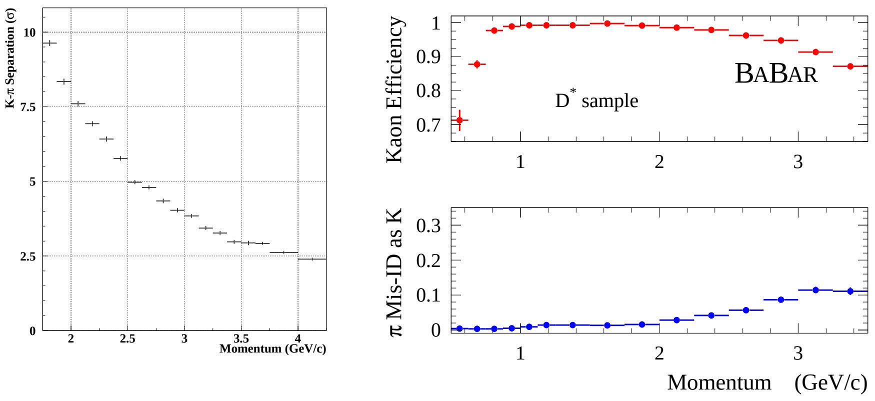

Figure 4.15: *In the left:* $K-\pi$ *separation (in* σ *units) of the DIRC as a function of the track momentum; and in the right: efficiency and misidentification probability of the selection of charged kaons as a function of track momentum, both obtained from a data sample of* $D^{*+} \to D^0(\to K^-\pi^+)\pi^+$ *decays.*

the uncertainty in the track parameters. The track Cherenkov resolution for $\mu^+\mu^-$ events is shown in right hand plot of Fig. 4.14. The width of the fitted Gaussian distribution is $2.5\ \mathrm{mrad}$ compared with the design goal $2.2\ \mathrm{mrad}$. The K/π separation can be inferred from the measured single track resolution *vs.* momentum in $\mu^+\mu^-$ events, and the difference between expected and measured Cherenkov angles of charged pions and kaons. The left hand plot of Fig. 4.15 show the $K-\pi$ separation as a function of momentum obtained from a data sample of $D^{*+} \to D^0(\to K^-\pi^+)\pi^+$ decays. The expected separation between kaons and pions at $3\ \mathrm{GeV}/c$ is about 4.2σ. The efficiency for correctly identifying a charged kaon that traverses the radiator bar, and the probability to wrongly identify a pion as a kaon as a function of momentum is obtained from a data sample of $D^{*+} \to D^0(\to K^-\pi^+)\pi^+$ decays (cf. right plot of Fig. 4.15). The average kaon efficiency and pion misidentification are 96.2 ± 0.2 and 2.1 ± 0.1, respectively.

Contribution to the subdetector maintenance as DIRC commissioner

During the period between January and July 2007, I was member of the DIRC maintenance crew, working as commissioner. My responsabilities were to monitor the correct behavior of the detector components, *i.e.* PMTs array, Front-End and data transmission electronics, the cooling system, the SOB water system and the gas system. During this 6-month period no major problems occurred, only routine repairs were performed, replacing malfunctioning electric components and unplugging noisy PMTs.

4.2.5 The Electromagnetic Calorimeter (*EMC*)

Physical requirements

The EMC [92] detects electromagnetic showers of particles that pass through it, measuring their energy and angular position. This allows the detection of photons from π^0 and η decays as well as from electromagnetic processes. It is used to identify electrons and to differentiate e from π (e/π separation) through the measurement of E/p (where E is the energy deposited on the calorimeter and p is the momentum measured by the tracking system). Electron identification is important for neutral B-meson flavor tagging *via* leptonic decays, for the reconstruction of vector mesons like J/ψ, and to study semi-leptonic and rare decays of B and D mesons, and τ leptons.

The EMC detects particles with an excellent efficiency in a energy range between $20\ \mathrm{MeV}$ and $9\ \mathrm{GeV}$. The upper bound is set by the need to measure QED processes like $e^+e^- \to e^+e^-(\gamma)$ and $e^+e^- \to \gamma\gamma$, which are used for calibration and luminosity measurements. The lower bound is set by the need for highly efficient reconstruction of B-meson decays containing π^0 and η.

Design

The EMC consists of a cylindrical barrel and a conical forward endcap. It has full coverage in azimuth and from 15.8^o to 141.8^o in polar angle (cf. Fig. 4.16). The barrel (endcap) contains 5760 (820) crystals arranged in 48 (8) rings with 120 identical crystals each, adding up a total of 6580 crystals. In each crystal, a high energy electron initiates a shower by first emitting bremsstrahlung photons which in turn convert into a e^+e^- pair, the new e^+ (e^-) thenselves emit photons and sort of chain reaction develop as a shower. This process gives an exponential increase in the shower particles. The shower stops when the photon energy goes below the pair production threshold. The crystals act not only as a total-absorption scintillating medium, but also as a light guide funneling light to the photodiodes that are mounted in the rear surface of the crystals, from which the energy of the particle is estimated. The thallium-doped CsI crystals properties meet the BABAR needs: the high light yield ($\sim$

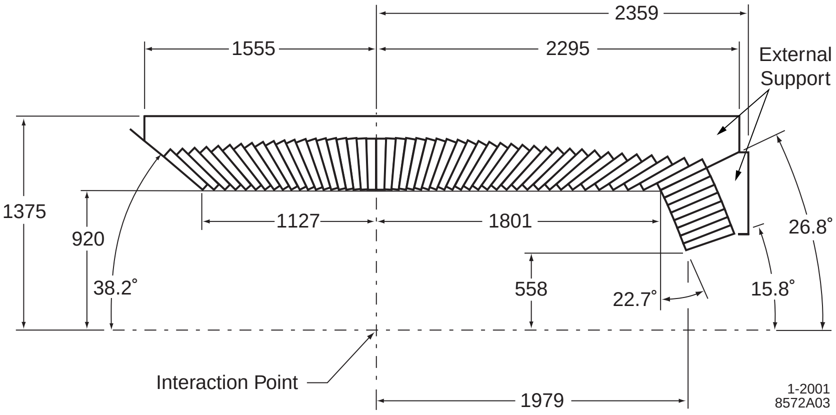

Figure 4.16: *A longitudinal cross-section of the EMC (dimensions are in mm). Only half of the detector is shown, which is symmetric around the z-axis. The figure show the arrangement of the 56 crystals rings.*

$50000\gamma/$ MeV) and small Molière radius (3.8 cm) allow for excellent energy and angular resolution; the short radiation length (1.85 cm) allows for shower containment. The crystals have a trapezoidal shape, their length increases from $29.6\ cm$ (16.1 radiation lengths) in the backward to $32.4\ cm$ (17.6 radiation lengths) in the forward direction. This limits the effect of shower leakage from increasingly high energy particles. All these characteristics permit an efficient single crystal detection (close to 100% at low energy) with relatively compact dimensions.

The EMC energy calibration is made in two steps. First, the collected light in single crystals is translated to the actual energy deposited. This is performed at low energies with two devices, a radioactive photon source and a light pulser, while at at higher energies the relation between polar angle and energy of $e^{\pm}$ from Bhabha events is exploited. In the second step, the energy deposited in a shower spreading over several adjacent crystals is related to the energy of incident photons or electrons. This correction is made as a function of cluster energy and angle. At low energies it is derived from $\pi^0 \rightarrow \gamma\gamma$ decays, and at higher energies the correction is estimated from single photon Monte-Carlo simulations.

Performance

The energy resolution of a homogeneous crystal calorimeter can be described empirically in terms of the sum of two terms added in quadrature: $\sigma_E/E = (a/[E(GeV)]^{1/4}) \oplus b$ [83]. The energy dependent term, a, which is dominant at low energies, arises primarily from the fluctuation in photon statistics, but is also depends on electronic noise and beam-generated background. The constant term, b, which is dominant at high energies, arises from non-uniformity in the light collection, leakage or absorption in the material between and in front the crystals, and uncertainties in the calibration. At low energy it is directly measured with the radioactive source, yielding $\sigma_E/E = 5.0 \pm 0.8\%$ at 6.13 MeV. At higher energies the energy resolution is derived from Bhabha scattering, yielding $\sigma_E/E = 1.9 \pm 0.07\%$

at $7.5\ \mathrm{GeV}$. The left plot of Fig 4.17 shows the energy resolution extracted from several processes as a function of energy. A fit to the energy dependence results in

$$\frac{\sigma_E}{E} = \frac{(2.32 \pm 0.30)\%}{\sqrt[4]{E(\mathrm{GeV})}} \oplus (1.85 \pm 0.12)\% \,. \tag{4.1}$$

Angular resolution is determined by the transverse crystal size and the distance from the IP. It can, as in the case of the energy resolution, be parameterized empirically as a sum of an energy dependent and a constant term: $\sigma_\theta = \sigma_\phi = (c/\sqrt{E(\mathrm{GeV})}) + d$. The measurement of the angular resolution is based on the analysis of π^0 and η decays to two photons of approximately equal energy. The result is presented in the right hand plot of Fig 4.17. A fit to the data points results in

$$\sigma_\theta = \sigma_\phi = \left(\frac{3.87 \pm 0.07}{\sqrt{E(\mathrm{GeV})}} + (0.00 \pm 0.04)\% \right) \mathrm{mrad} \,. \tag{4.2}$$

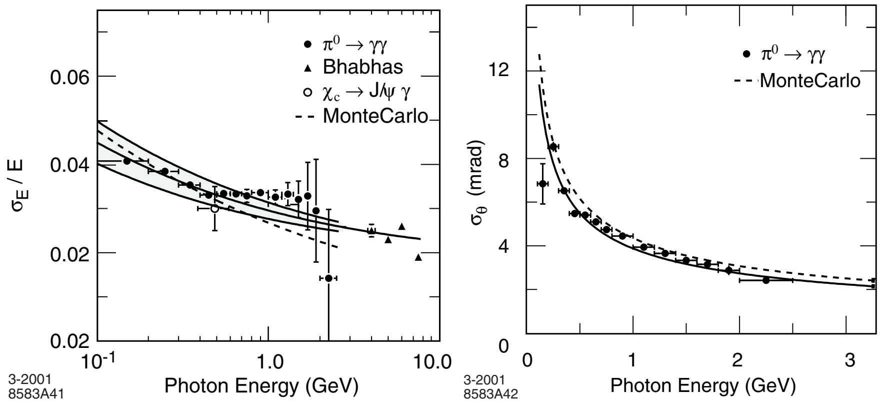

Figure 4.17: *On the left: the energy resolution for the EMC measured for photons and electrons from various processes. The solid curve is a fit using an empirical formula (cf. Eq. 4.1) and the shaded area denotes the RMS error of the fit. On the right: the angular resolution on the EMC for photons from π^0 decays. The solid curve is also an empirical formula (cf. Eq. 4.2).*

In Fig. 4.18 is shown the two-photon invariant mass in $B\bar{B}$ events, the solid blue curve being a fit to data. The reconstructed π^0 mass is measured to be $135.1\ \mathrm{MeV}/c^2$, and the width of $6.9\ \mathrm{MeV}/c^2$ agrees with Monte-Carlo simulation. It has to be noted that the π^0 mass resolution function is asymmetric, due to leakage in the energy measurement.

Electrons are separated from charged hadrons primarily on the basis of the shower energy, lateral shower moments (which describe the shape of the associated cluster), and track momentum. In addition, the dE/dx energy loss measured by the tracking system and the DIRC Cherenkov angle are required to be consistent with an electron. The most discriminant electron/hadron variable is the E/p ratio. Fig. 4.19 shows the efficiency for electron identification and pion misidentification as a function of the particle momentum

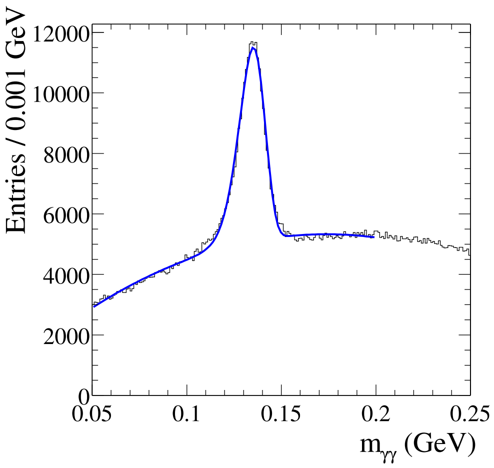

Figure 4.18: *Invariant mass of two photons in* $B\bar{B}$ *events. The energies of the photons and the* π^0 *are required to exceed* $30\ \mathrm{MeV}$ *and* $300\ \mathrm{MeV}$, *respectively. The solid line is a fit to data.*

(left) and polar angle (right). The electron efficiency is measured using radiative Bhabhas $e^+e^- \rightarrow e^+e^-e^+e^-$ events. The pion misidentification is measured from selected charged pions from $K^0_S \rightarrow \pi^+\pi^-$ decays. The electron identification efficiency is 94.8% and the probability of pion misidentification is 0.3%.

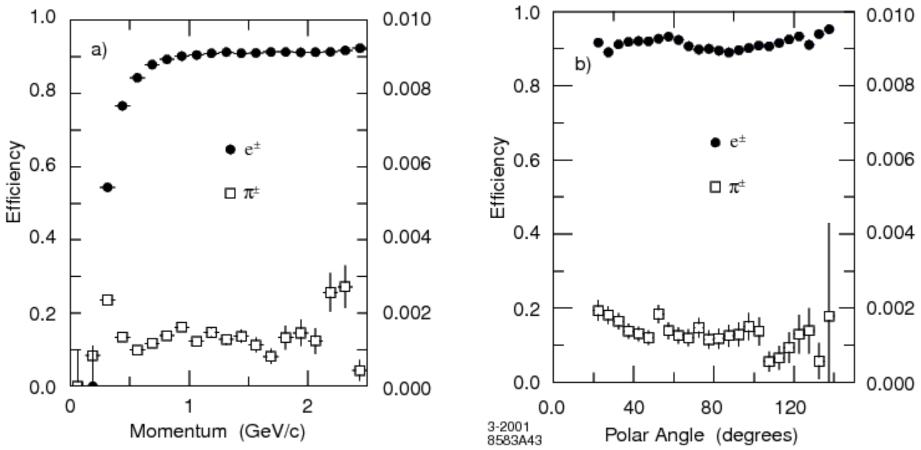

Figure 4.19: *The electron identification efficiency and pion misidentification probability as a function of the particle momentum (left) and the polar angle (left) in the laboratory system.*

4.2.6 The Superconducting Solenoid Magnet

For the measurement of charge and momentum of charged particles, the *BABAR* tracking system is immersed in a magnetic field of $1.5\ \mathrm{T}$ ($\pm 0.2\ \mathrm{mT}$), which is principally on the

z-axis. This magnetic field is produced by a superconducting solenoid located around the EMC. Its superconducting material is a $10\ \mathrm{Km}$ cable composed of niobium-titanium (NbTi) filaments incrusted in aluminium. The solenoid current is $4600\ \mathrm{A}$. It is cooled to an operating temperature of $4.5\ \mathrm{K}$ using liquid helium. It does not occupy a big radial space in order to not deteriorate the neutral hadrons and muons detection by the IFR. The most important design constraint was to minimize the disturbance of operation of the PEP-II beam elements. In particular, its radial component must be under $0.25\ \mathrm{T}$ in order to not impact the $B1$ and $Q1$ magnets. The steel magnet segmented flux return is also used to protect the PEP-II quadrupoles, to support the detector components on the inside, and to give them protection against magnetic forces and from potential earthquakes. This structure is also used to host the outer BABAR subdetector, the IFR.

4.2.7 The Instrumented Flux Return (*IFR*)

Physical requirements

The IFR [93] is designed to identify muons with high efficiency and good purity. Muons are important for B-meson flavor tagging *via* semi-leptonic decays and for the reconstruction of vector mesons like J/ψ. This is also important for the study of semi-leptonic and rare decays involving leptons from B and D mesons and τ leptons. The detector is also designed to detect neutral hadrons (primarily K_L^0 and neutrons), allowing the study of B-mesons exclusive decays, in particular CP eigenstates.

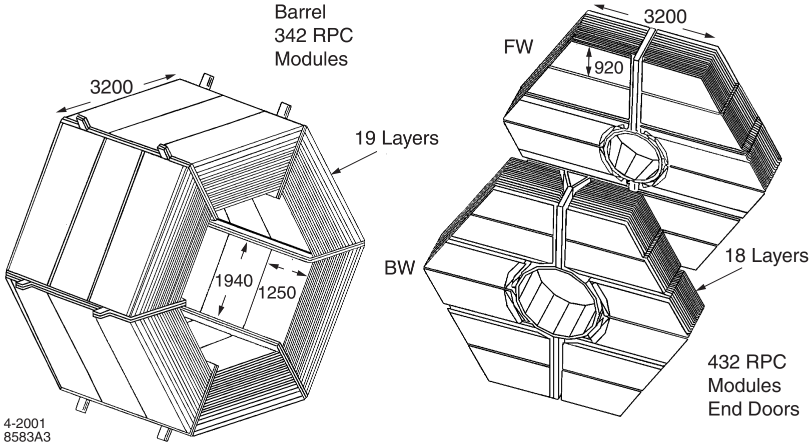

Figure 4.20: *Schematic view of the IFR sections: Barrel, forward (FW) and backward (BW) end doors. The shape of the RPC modules and their dimensions are indicated.*

Design

The IFR uses the steel flux return of the magnet, as a muon filter and hadron absorber. Single gap resistive plate chambers (RPCs) and limited streamer tubes (LSTs) detectors with two-coordinate readout are installed in the gaps of the segmented steel of the barrel and end doors flux return (cf. Fig. 4.20). The steel is segmented into 18 plates, increasing in thickness from $2\ \mathrm{cm}$ to $10\ \mathrm{cm}$ with radius. There are 19 LST layers in the barrel and 18 RPCs in the endcaps. In addition, two layers of cylindrical RPCs are installed between the EMC and the solenoid coil to detect particles exiting the EMC.

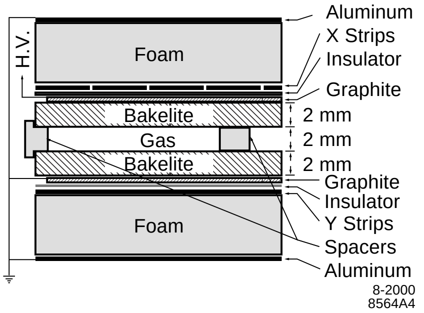

Figure 4.21: *Cross section of a planar RPC used in the IFR.*

The RPC (cf. Fig. 4.21) consists of two bakelite sheets, $2\ mm$-thick separated by a gap of $2\ mm$, connected to high voltage ($\sim 8\ \mathrm{kV}$) and ground. The gap between the two sheets is filled with a non-flammable gas mixture of argon, freon and isobutane ($56.7\% : 38.8\% : 4.5\%$). This gas mixture has been chosen for their absorption properties in the UV, avoiding the photons propagation.

The LST has similar but more performant behavior than the RPCs. It consists of a silver wire coated with plate of $100\ \mu\mathrm{m}$ in diameter, which is located at the center of a cell of $9 \times 9\mathrm{mm}^2$ section. A plastic structure (profile) contains 8 such cells, which is coated with a resistive layer of graphite. The profiles are inserted in plastic tubes filled with a non-flammable CO_2 based gas.

The IFR covers a total active area of about $2000\ \mathrm{m}^2$, with a total of 806 RPC/LST modules, 57 in each of the 6 barrel sectors, 108 in each of the four half end doors, and 32 in the two cylindrical layers. The size and the shape of the modules are matched to the steel dimensions. The RPC/LST detect showers from ionizing particles via capacitive readout strips made of aluminium and located at the end of the detectors. The strips are arranged to make a bi-dimensional array in the (z, ϕ) coordinates for the barrel and in the (x, y) for the end doors. When a ionizing charged particle passes through the gas, produces a spark, the hit strips are used to measure the impact position. The muons being heavier than electrons, the bremsstrahlung is less effective as a mechanism of energy loss. Since they have relatively long lifetimes and do not participate in nuclear interactions, they are very penetrating particles. The steel flux return is then used as a muon filter. For neutral hadrons the IFR is used as a primitive calorimeter. The steel is used as an absorber where the hadrons interact producing shower with charged particles that are then detected by the RPCs/LSTs. The informations obtained by the IFR are combined with those obtained by the other subdetectors.

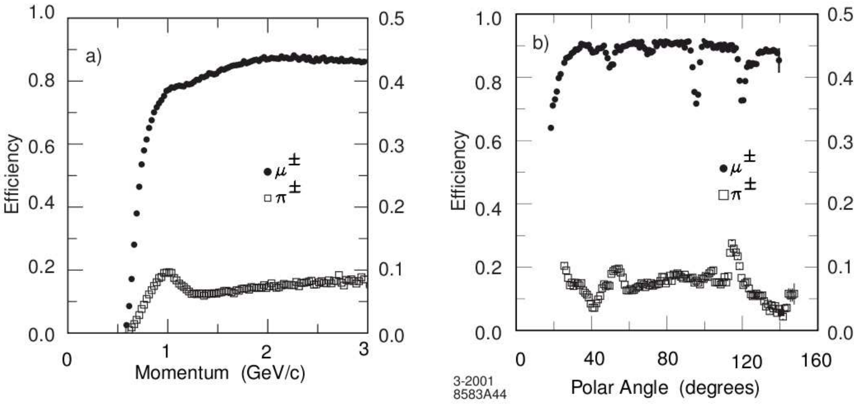

Figure 4.22: *muon efficiency (left scale) and pion misidentification probability (right scale) as a function of laboratory track momentum (left plot) and polar angle (left plot) measured mostly in the IFR.*

Performance

The muon identification relies almost entirely on the IFR, the other subdetectors provide complementary information. The charged particles, reconstructed by the tracking system, are muon candidates if they meet the minimum ionization particles criteria in the EMC. The charged tracks reconstructed in the SVT and DCH are extrapolated to the IFR taking into account non-uniformities in the magnetic field, multiple scattering and average energy loss. The extrapolated tracks are associated with clusters in the IFR if the impact parameter is consistent with the cluster position. The performance, illustrated in the plots of Fig. 4.22 has been obtained from samples of muons from $e^+e^- \to \mu^+\mu^-e^+e^-$ and pions from three-prong τ decays and $K^0_S \to \pi^+\pi^-$ decays. A muon detection efficiency close to 90% is achieved in the momentum range of $1.5 < p < 2.0\ \mathrm{GeV}/c$, with a fake rate of pions about $6-8\%$.

The K^0_L and other neutral hadrons interact in the steel of the IFR and can be identified as clusters that are not associated with a charged track. Monte-Carlo simulations predict that about 65% of K^0_L above $p > 1\ \mathrm{GeV}/c$ produce clusters in the cylindrical RPC, or a cluster with hits in two or more planar RPC layers. The detection efficiency and angular resolution of the clusters for K^0_L have been studied with $e^+e^- \to \phi(\to K^0_S K^0_L)\gamma$ events. The results are a detection efficiency between $20-40\%$, and angular resolutions around $60\ \mathrm{mrad}$ for K^0_L not interacting with the EMC. When EMC information is also provided, the angular resolution improves by a factor of 2.

4.2.8 The Trigger

The high BABAR luminosity implies that an important number of particles are present in the detector at each instant. The aim of the trigger is to record physics events with high efficiency and to reject a maximum number of background events. A random trigger records control event samples that are used for efficiency calculation and validation studies. In BABAR two trigger levels are used: $L1$ and $L3$.

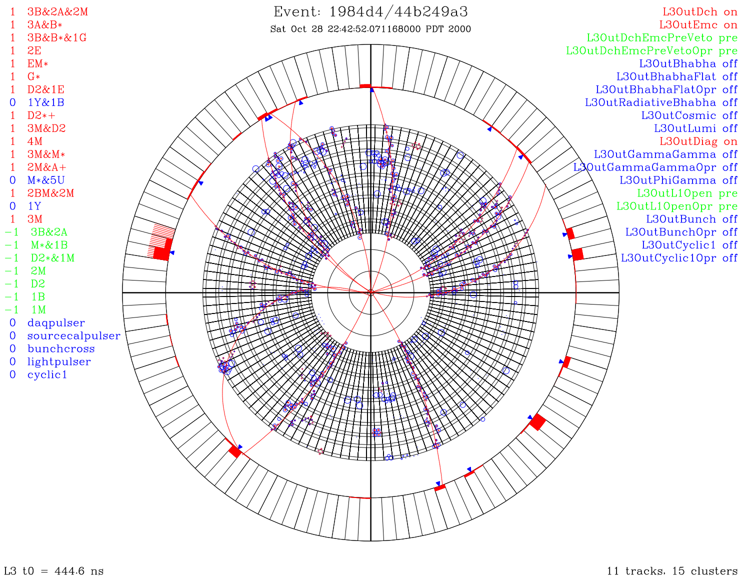

Figure 4.23: *Schematic representation of an event from the L_3 trigger in the detector in transversal cut. The circles are hits in the DCH, the red curves the reconstructed tracks, the EMC crystals are colored according the deposited energy and the squares represents the centroid location of the EMC clusters.*

The $L1$ trigger is implemented in hardware. This system consists of a global trigger (GLT) that combines the input from several individual triggers linked to the DCH (DCT), the EMC (EMT) and the IFR (IFT). These are continuously passing data describing the objects found by the subdetectors, which is then passed to the GLT. The GLT tries to match them to any of the 24 *trigger lines* which represent events of interest. If the timing of the trigger signal coincides with a bunch crossing, the fast control and timing system (FCTS) issues an accept signal. It is at this point that some classes of physics events, such as QED processes that are used only for calibration, are scaled down, making their acceptance less likely. The trigger frequency of $L1$ is required to be less than 4.5 kHz for a luminosity of $\sim 10^{34}\mathrm{cm}^{-2}\mathrm{s}^{-1}$.

The $L3$ trigger is implemented in software running in computing farms, and uses the information from all subdetectors. This trigger must reduce by ~ 10 the number of events accepted by the $L1$. Examples of rejected events are tracks not originating from the IP or inconsistent with a bunch crossing (machine background). The trigger system have a total efficiency of 99.7% for $B\bar{B}$ events, and of the order of 90% for $\tau^+\tau^-$ and $\mu^+\mu^-$ events. An event display of the $L3$ trigger system is shown in Fig. 4.23.

4.2.9 The Data Acquisition System (DAQ)

The *BABAR* data acquisition system refers to the overall architecture by which the detector, the triggers and the computing structure operate. This is schematically illustrated in Fig. 4.24.

The Front-End electronics processes and digitizes the signals coming from the detector and passes the output to the $L1$ trigger. If an accept signal is issued by the FCTS, the event is passed to the $L3$ trigger. Finally, the event passes through the fast reconstruction and is recorded to disk, where it is written to the event store. Once there, the events will be totally reconstructed in a matter of days. The DAQ system also records the detector conditions during data taking that will be used for the final reconstruction of events and for Monte-Carlo event production (to reproduce the running conditions, cf. Sec. 5).

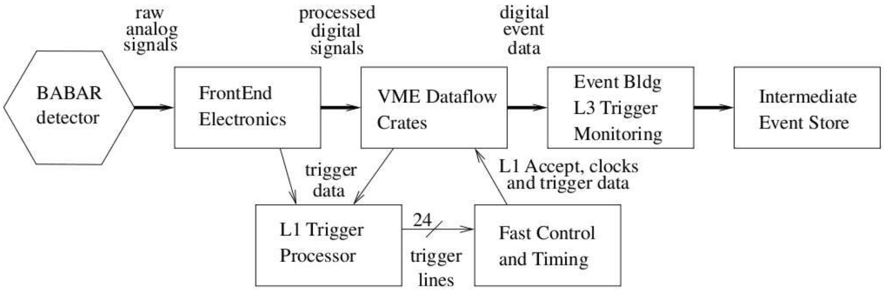

Figure 4.24: *Schematic diagram of the BABAR data acquisition system.*

4.2.10 Online Prompt Reconstruction (OPR)

The Online Prompt Reconstruction (OPR) is the bridge between the online and the offline systems. This system reads raw data recorded in disk. Operating in a computing farm it selects physical events, performs complete reconstruction, obtains *rolling calibrations*, collects extensive monitoring data for quality assurance and writes the result to an event store. The rolling calibration is the generation of reconstruction calibration constants during normal events processing. For the event selection and reconstruction two level filters are used: Digifilter and BGFilter. The first one uses only the information obtained from $L1$ and $L3$. Its principal purpose is to eliminate calibration events, like Bhabha scattering. The events passing this first level pass to a first reconstruction stage, where pattern algorithms try to find tracks in the DCH, clusters in the EMC and particle identification is calculated. These events are then classified, using the fast reconstruction information, in subfilters mutually exclusive. An event, at this level, is essentially a collection of tracks and clusters in the EMC and IFR. Those are then accessed by the reconstruction code of the analyst to form candidates for a given decay channel.

Part III

Analysis of the $B^0 \rightarrow K_S^0\pi^+\pi^-$ mode

Chapter 5

Data Sample, Reconstruction and Selection

As discussed in the previous chapter, data is collected by the DAQ system and processed by OPR, then recorded to disk in mutually exclusive subfilters. Data is available for the analyst for full reconstruction and selections. This chapter describes the data samples used for the present analysis, the reconstruction algorithms and the selection applied to them. The techniques for flavor tagging and time-dependent CP asymmetries measurements are also described. The different event species: signal and various backgrounds, present in the data samples are described. A classification of background components is presented, and the discriminant variables used to distinguish background from signal are introduced.

5.1 The Data Sample

5.1.1 The *On-peak* and *Off-peak* data samples

The analysis is based on data taken by BABAR in the running period 1999-2006. The Run1-5 data sample is made of 382.9×10^6 $B\bar{B}$ meson pairs, equivalent to an integrated luminosity of 347.3 fb^{-1} at the $\Upsilon(4S)$ peak. In addition, the available 36.6 fb^{-1} of data, taken 40 MeV below the $\Upsilon(4S)$ resonance, are also used. The dataset is summarized in Table 5.1.

Sample	$\mathcal{L}_{\mathrm{on}}(\mathrm{fb}^{-1})$	$N_{B\bar{B}}(10^6)$	$\mathcal{L}_{\mathrm{off}}(\mathrm{fb}^{-1})$
Run 1	20.72	22.43	2.65
Run 2	60.92	67.32	6.90
Run 3	32.28	35.70	2.47
Run 4	100.31	110.48	10.12
Run 5	133.02	146.93	14.47
Total	347.25	382.86	36.61

Table 5.1: *Summary of the integrated on-resonance and off-resonance data. A "Run" is a period of continuous data taking, lasting typically some ten months.*

5.1.2 Monte Carlo Samples

Simulated data, or Monte-Carlo (MC), is essential for understanding detection effects (*e.g.* misreconstructed signal, reconstruction efficiencies, etc.), backgrounds and systematics that affect the analysis procedure. In a first stage, physics events are generated with the `EvtGen` package [94], which provides an accurate representation of phenomena as mixing and interference (crucial for a faithful modeling of CP violation), and angular distributions of decay products (*e.g.* pseudoscalar-to-vector-vector). Although the vast majority of B decays are generated with `EvtGen`, generic B decays to hadronic final states and continuum events are simulated with an interface to `JETSET` [95]. `EvtGen` generates charmless 3-body decays using the isobar model with the same lineshapes and angular distributions as presented in Secs. 2.4.3-2.4.6. The output of this first stage is a list of particles with the corresponding 4-vectors and vertices for decay products.

In a second stage, the interaction of decay products with the detector as they propagate (and possibly decay, *e.g* $K^0_S \to \pi^+\pi^-$) is simulated using a *BABAR* customized software based on the `GEANT4` package [96]. Processes like rescattering and photon production, and a detailed account of energy loss and deposition by particles in different parts of the detector (*e.g.* silicon strips in SVT, gas and wires in DCH and crystal in EMC) are simulated, which requires a detailed modeling of detector geometry and matter distribution. Each of these interactions (or *hits*) are used to simulate the data read out by the electronics, trigger and DAQ system. At this stage, *hits* from electronic noise and machine backgrounds characterizing a period of running are also taken into account. For this, real events recorded with a random trigger are aggregated to simulated events. In a last stage, the simulated electronic output is processed with the same version of *BABAR* reconstruction software used for real data.

The MC samples used to characterize signal and background, and to optimize the selection are the following:

- 6219k non-resonant (NR) $B^0 \to K^0_S\pi^+\pi^-$events.
- 1321k $B^0 \to K^0_S\pi^+\pi^-$ (custom Dalitz plot Model[1]) events.
- 155k $B^0 \to \rho^0(\to \pi^+\pi^-)K^0_S$ events.
- 155k $B^0 \to f_0(980)(\to \pi^+\pi^-)K^0_S$ events.
- 138k $B^0 \to K^{*+}(\to K^0_S\pi^+)\pi^-$ events.
- 3745k $B^0 \to a_1^+(\to K^0_S\pi^+)\pi^-$ events.
- 1641k $B^0 \to D^+\rho^-$ events.
- 1754k $B^0 \to D^+\pi^-$ events.
- 1664k $B^0 \to D^-(K^0_S\pi^-)\pi^+$ events.
- 1551k $B \to \Psi(2S)X$ events.

---

[1] For details see Sec. 6.6.1.

- $155\mathrm{k}\; B^+ \to K^{*+}(K^0_S\pi^+)K^{*0}(K^+\pi^-)$ events.
- $170\mathrm{k}\; B^0 \to D^-(K^+\pi^-\pi^-)\pi^+$ events.
- $677\mathrm{k}\; B^0 \to \chi_{c1}(J/\Psi\gamma)K^0_S$ events.
- $644\mathrm{k}\; B^0 \to D^{*+}(D^0(K^0_S\pi^0)\pi^+)\pi^-$ events.
- $1478\mathrm{k}\; B^0 \to D^{*+}(D^+(K^0_S\pi^+)\pi^0)\pi^-$ events.
- $212\mathrm{k}\; B^0 \to D^+(K^0_SK^+)\pi^-$ events.
- $21\mathrm{k}\; B^0 \to K^*_0(1430)^+(K^0_S\pi^+)\pi^-$ events.
- $21\mathrm{k}\; B^0 \to \Psi(2S)K^0_S$ events with $\Psi(2S) \to ll$, $\Psi(2S) \to J/\Psi\pi\pi$, or $\Psi(2S) \to \chi\gamma$.
- $777\mathrm{k}\; B^0 \to \eta'(\rho\gamma)K^0_S$ events.
- 66.2×10^6 continuum $u\bar{u}, d\bar{d}, s\bar{s}$ events.
- 57.6×10^6 continuum $c\bar{c}$ events.
- 471.6×10^6 generic $B^0\bar{B}^0$ events.
- 469.2×10^6 generic B^+B^- events.

The neutral (charged) generic B MC is a cocktail of several final states from $e^+e^- \to B^0\bar{B}^0$ (the relative abundances of different decay channels being tuned to the experimental branching fractions [21, 28]). These MC samples are used for B-background studies (see Sec. 5.8), and corresponds to approximately 2.7 times the size of the data sample.

5.2 Reconstruction

Event reconstruction proceeds in two stages. First, the Offline Prompt Reconstruction software finds tracks and calorimeter clusters from hits in the DCH and SVT, and crystals with energy deposits in the EMC, respectively. Cherenkov photons and energy loss dE/dx informations are used to form particle identification selectors. In the second step, objects that are not directly detected but that can be inferred from properties and correlations of their decay products, are reconstructed. Such objects are known as *composites*, the D- and B-mesons being good examples. Combinations of tracks and neutral objects are used to form composite "candidates", allowing the vertexing of the B-mesons, and so the Δt measurement. In this section, the algorithms for tracking, calorimeter reconstruction, particle identification and vertexing are briefly described. The definitions used for the event selection are introduced.

5.2.1 Tracking algorithms

The charged tracks, following helicoidal trajectories in the solenoid field, are described by five parameters d_0, z_0, ϕ_0, λ and ω (which were introduced in Sec. 4.2.3), that are fitted using a Kalman filter algorithm [90]. The algorithm starts from the DCH hits found by the $L3$ trigger to form a track, further hits are added if they are consistent with the primary track. Then a search is made for tracks that may not have originated from the IP (*e.g.* K_S^0 that lived enough to decay outside the SVT), or may not be energetic enough to traverse the whole chamber. Finally, SVT hits are added to the DCH ones if consistent, otherwise the SVT hits are examined for low momentum SVT-only tracks. Reconstructed tracks are stored in standard lists with different quality requirements.

In the present analysis, pion candidates are taken from the standard `GoodTrackLoose` list, which consist of tracks with: $p_t > 0.1\ \mathrm{GeV}/c$; $p < 10.0\ \mathrm{GeV}/c$; a minimum of 12 hits in the DCH; $d_0 < 1.5\ cm$ and $z_0 < 10\ cm$.

5.2.2 Calorimeter algorithms

A typical electromagnetic shower spreads over several adjacent crystals, forming a cluster of energy deposits. This cluster may be due to more than one particle, and hence present energy distributions with more than one maximum, each of them being referred as a *bump*. The calorimeter reconstruction routines are intended to locate such bumps, extract their shapes and estimate the energy of the passing particle. The algorithm starts by finding "seed" crystals with an energy above $10\ \mathrm{MeV}$. Clusters are build by adding surrounding crystals with energies above $1\ \mathrm{MeV}$, or from neighboring seeds with at least $3\ \mathrm{MeV}$. Local bumps are located by standard methods [92]. Given a bump, each crystal is given a weight w_j that depends on its distance to the bump location, its deposited energy (E_j) and Molière radius. This weight is then used to estimate the bump energy as $E_{\mathrm{bump}} = \sum_j w_j E_j$, the sum running over all the crystals in the cluster. Finally, a bump is associated with a charged particle if the projected track to the inner face of the EMC is consistent with the bump location. Otherwise, it is assumed to originate from a neutral particle.

5.2.3 Particle identification (*PID*)

The long-lived charged particles tracked in *BABAR* are: electrons, muons, pions, kaons and protons. Their correct identification is crucial for the physics goals, and it is achieved by exploiting the different interactions that those particles have with each subdetector. Information from all subdetectors (SVT, DCH, DIRC, EMC and IFR) is used to construct a PDF that represents the likelihood of a particle to belong to a given species. In the case of electrons and muons, this PDF is made from informations collected in the EMC and IFR, respectively. The proton production is limited in *BABAR* and is of no interest for the present analysis. The likelihood for kaon and pion hypothesis is constructed as the product of PDFs from the SVT, DCH and DIRC for the corresponding particle hypothesis. The first two contribute with dE/dx measurements, which are compared with the Bethe-Bloch expectation. The DIRC PDF is a binned likelihood obtained from MC, and uses the number of Cherenkov photons and the angle of those photons with the track (Cherenkov angle). For a given hypothesis, cuts on the likelihood are applied to generate mutually exclusive categories: `VeryLoose`, `Loose`, `Tight` and `VeryTight` for pions, and `NotPion`, `VeryLoose`, `Loose`, `Tight` and `VeryTight` for kaons. In the present analysis, pions in the `Loose` category are selected, with an efficiency and kaon misidentification rate around 95% and $5 - 15\%$, respectively [97].

5.2.4 Vertexing

Candidates for composite particles are first formed from all possible combinations of charged and neutral particles matching the decay daughters. In the present analysis, K_S^0 candidates are formed from all possible oppositely charged tracks in the event assumed to be pions, with a invariant mass, after vertexing, within $25\ \mathrm{MeV}/c^2$ of the K_S^0 mass [21]. This selection of K_S^0 candidates is referred as `KsDefault` list. B candidates are formed from all K_S^0 candidates and two oppositely charged tracks. For each K_S^0 or B candidate, its decay vertex is calculated with a geometrical fit in which the daughters are required to emerge from a common vertex. This task is performed by the `TreeFitter` package [98], which fits the whole decay chain applying a Kalman filter. For the B vertexing, constraints are applied to reduce resolution effects, which have a high impact in Dalitz plot analyses, as resolution may cause events to go outside the kinematical boundaries. For this, a vertexing fit is performed constraining the composite B candidate to have the nominal B mass, from which the DP coordinates and the related event shape variables are calculated. A second vertexing fit is made with no mass-constraint to calculate the discriminant kinematical variables (cf. Sec. 5.6.1).

5.3 The flavor tagging

A key ingredient in the measurement of time-dependent CP asymmetries is to determine the flavor of one of the two B mesons, referred as B_{tag} (cf. Sec. 1.2.2). This is achieved with the analysis of the B_{tag} decay products when it decays into a flavor-specific state. For example, in the semileptonic decay $B^0 \to D^{*-}\ell^+\nu_\ell$ ($\bar{B}^0 \to D^{*+}\ell^-\bar{\nu}_\ell$), the charge of the lepton unambiguously identifies the decaying neutral B-meson as a B^0 or a $\bar{B}^0$. Also, the subsequent decay $D^{*-} \to D^0(\to K^-X^+)\pi^-$ gives a soft pion and kaon in the final state whose charges uniquely identify the B_{tag} flavor. The purpose of the tagging algorithm is to determine the flavor of the B_{tag} with the highest possible efficiency $\varepsilon_{\mathrm{tag}}$ and the lowest possible probability ω of assigning a wrong flavor to B_{tag}. These goals are crucial for time-dependent analyses, where the statistical error on time-dependent parameters (like $\sin 2\beta$ and Δm_d) is inversely proportional to the square-root of the "effective tagging efficiency",

$$\sigma \propto 1/\sqrt{(}Q), \quad \text{with} \quad Q = \varepsilon_{tag}(1-2\omega)^2. \tag{5.1}$$

The $\varepsilon_{\mathrm{tag}}$ is calculated with respect to the sample of events that satisfy the requirements of the tag-side vertexing and that have at least one fully reconstructed candidate. Various mutually exclusive tagging categories can be defined with their own $\varepsilon^c_{\mathrm{tag}}$ and ω_c (see Sec. 5.3.1). The

Q factor in this case is $Q = \sum_c \varepsilon^c_{tag}(1-2\omega_c)^2$. The effective tagging efficiency of *BABAR*, for the tagging protocol used in this analysis, is $Q = 30.5 \pm 0.3\%$.

Other quantities, which are more convenient from the experimental point of view (see Sec. 6.3.2, Eq. 6.15), can be defined as a function of ω_c ($\bar{\omega}_c$), which are the probabilities of incorrectly identifying a $B_{\rm tag} = B^0$ as $\bar{B}^0$ (or $B_{\rm tag} = \bar{B}^0$ as B^0), for events in the tagging category c. These quantities are defined as,

$$\begin{array}{lcl} \langle\omega_c\rangle = \frac{1}{2}(\omega_c + \bar{\omega}_c) & , & \Delta\omega_c = \omega_c - \bar{\omega}_c \\ \mathcal{D}_c = 1 - 2\omega_c & , & \bar{\mathcal{D}}_c = 1 - 2\bar{\omega}_c \\ \langle\mathcal{D}_c\rangle = \frac{1}{2}(\mathcal{D}_c + \bar{\mathcal{D}}_c) = 1 - (\omega_c + \bar{\omega}_c) & , & \Delta\mathcal{D}_c = \mathcal{D}_c - \bar{\mathcal{D}}_c = -2(\omega_c - \bar{\omega}_c), \end{array} \tag{5.2}$$

where $\Delta\mathcal{D}_c$ parameterizes a possible difference in performance of the tagging procedure for the two tags, B^0 and $\bar{B}^0$.

5.3.1 The *BABAR* flavor tagging algorithm

The tagging algorithm [99] is based on multivariate techniques that combine several different signatures to achieve optimal separation between B^0 and $\bar{B}^0$ events. It starts by removing all reconstructed charged tracks that belong to the fully reconstructed B_{CP} candidate, the rest being assigned to $B_{\rm tag}$. A set of loose criteria are applied to these in order to reject ghost tracks. To improve the vertex resolution, K^0_S or Λ^0 candidates are used in place of their daughters. The remaining candidates are used for a geometrical fit to a common vertex, taking into account the beam energies, the beam spot position and the flight direction of the other, fully reconstructed, B candidate.

The B_{tag} flavor is determined from a combination of nine different tag signatures, such as the properties of charged leptons, kaons and pions. For each of these signatures, properties such as charge, momentum and decay angles are used as input to a Neural Network (NN), or "*sub-tagger*": `Lepton, Kaon, slow pion, Kaon-slow pion, maximum momentum, fast-slow particles correlation` and `Lambda`. To illustrate the procedure, two of the more important sub-taggers are now described: `Lepton` and `Kaon`.

Lepton sub-tagger

Electrons and muons produced in direct semileptonic decays (with a $\mathcal{B} = 10.4\%$ [21]), or *primary leptons*, provide excellent tag information. The charge of an electron (or muon) from a $b \to c\ell^-\bar{\nu}$ transition is directly associated to the flavor of the B^0 meson: a positively (negatively) charged lepton indicates B^0 ($\bar{B}^0$). Leptons from cascade decays, or *secondary leptons*, occurring *via* the $b \to W^-c(\to s\ell^+\nu)$ transition, carry tagging information as well: their charge is opposite to that of the primary lepton. To isolate primary from secondary leptons, several discriminant variables are used: the CM momentum of the track, p^*, as secondary leptons are characterized by a softer momentum spectrum; the cosine of the angle between the missing momentum (which approximates that of the neutrino) and the lepton's momentum, $\cos\theta_{\rm miss}$, since the directions of the primary $\ell\nu$ pair are expected to be anti-correlated in the CM frame; finally, the energy contained in the hemisphere defined by the direction of the virtual $W^{\pm}$. For primary leptons, the W recoils against a c quark and leads to a virtually empty hemisphere. In contrast, for secondary leptons the c quark that emits the W has recoiled from the decay of the b with an appreciable boost, and all its decay products will be boosted in the same direction.

The flavor tagging algorithm uses three different sub-taggers exploiting the presence of a lepton in the final state:

- The electron sub-tagger, with tracks that satisfy the `VeryTight` electron ID criteria.
- The muon sub-tagger, with tracks that satisfy the `Tight` muon ID criteria.
- Kinematical lepton sub-tagger, designed to recover the primary leptons that did not pass the selection criteria for electrons and muons, this tagger achieve the tagging based solely on kinematics.

Kaon sub-tagger

The kaon sub-tagger exploits the presence of charged kaons in the decay of the B_{tag} meson. The dominant source of charged kaons is from $b \rightarrow c \rightarrow s$ transition giving the cascade decays $B^0 \rightarrow \bar{D}(\rightarrow K^+X)X$ or $\bar{B}^0 \rightarrow D(\rightarrow K^-X)X$, where the charge of the kaon tags the flavor of the B_{tag}. The high probability of producing a charged kaon in the decay of a B-meson ($78 \pm 8\%$ [21]) coupled with the much higher fraction of *right sign* (coming from the $b \rightarrow W^-c(\rightarrow s \rightarrow K^-)$ transition) vs. *wrong sign* (decay products of the W^-, *e.g.* $b \rightarrow XW^-(\rightarrow \bar{c}s/d)$, $\bar{c} \rightarrow \bar{s} \rightarrow K^+$) kaons ($0.58 \pm 0.08$ vs. 0.13 ± 0.06 [100]) and the good signal to background ratio, makes the kaon tagger the most powerful source of tagging information. The NN uses as inputs the charges and likelihood of up to three kaon candidates, the number of K^0_S, and the transverse momentum squared of the charged tracks on the tag side, $p_t^2(tot) = \sum p_t^2$. A high $p_t^2(tot)$ increases the likelihood that a charged kaon was produced from a W rather from a c quark, and a non-zero number of K^0_S, likely created in a $b \rightarrow c \rightarrow s$ transition, makes it less likely that a charged kaon is a true kaon that tags the B_{tag} flavor.

The NN outputs of the nine sub-taggers are combined in a single NN called `Tag04`, trained to assign the correct flavor to B_{tag}. The output of `Tag04` is a signed probability, where the magnitude represents the confidence of the estimation and the sign the flavor of the B_{tag} meson ($NN > 0 \Rightarrow B_{\text{tag}} = B^0$, and $NN < 0 \Rightarrow B_{\text{tag}} = \bar{B}^0$). The algorithm classifies the event in seven disjoint categories according to the NN output value, which are now listed in increasing order of mistag probability: `Lepton`, `KaonI`, `KaonII`, `Kaon-Pion`, `Pion`, `Other` and `Notag`, where the last one is a category where no reliable tagging information is provided ($\mathcal{D}_{\texttt{NoTag}} = 0$). The name given to each category indicates the dominant physics contributing to the flavor identification.

The algorithm is trained and checked using MC, and is validated on data using a large-"B_{flav}" sample of fully reconstructed flavor-specific decays, $B^0 \rightarrow D^{(*)-}\pi^+$, $B^0 \rightarrow D^{(*)-}\rho^+$ and $B^0 \rightarrow D^{(*)-}a_1^+$. These decays are self-tagging, since a $D^{(*)-}h^+$ ($D^{(*)+}h^-$) is only accessible from a B^0 ($\bar{B}^0$). A fit to the Δt distribution (see Sec. 6.3.2, Eq. 6.15) allows the extraction mistag probabilities (see Table 5.2).

Category	$\varepsilon_{tag}(\%)$	$\Delta\varepsilon_{tag}(\%)$	$\omega(\%)$	$\Delta\omega(\%)$	$Q(\%)$	$\Delta Q(\%)$
Lepton	8.69 ± 0.07	-0.0 ± 0.2	3.1 ± 0.3	-0.1 ± 0.6	7.66 ± 0.12	0.04 ± 0.41
KaonI	10.96 ± 0.08	0.2 ± 0.2	5.2 ± 0.4	-0.1 ± 0.7	8.78 ± 0.16	0.21 ± 0.50
KaonII	17.23 ± 0.10	0.1 ± 0.3	15.4 ± 0.4	-0.5 ± 0.6	8.26 ± 0.18	0.29 ± 0.54
Kaon-Pion	13.78 ± 0.09	-0.3 ± 0.3	23.5 ± 0.5	-1.8 ± 0.7	3.88 ± 0.14	0.43 ± 0.38
Pion	14.37 ± 0.09	-0.7 ± 0.3	32.9 ± 0.5	5.1 ± 0.7	1.67 ± 0.10	-1.08 ± 0.26
Other	9.57 ± 0.08	0.3 ± 0.2	41.8 ± 0.6	4.6 ± 0.9	0.26 ± 0.04	-0.28 ± 0.10
Total	74.61 ± 0.12	-0.4 ± 0.6			30.50 ± 0.30	-0.4 ± 1.0

Table 5.2: *Performance of the tagging algorithm on data. The results are a fit to a data sample of over* 80000 *fully reconstructed* B_{flav} *decays. Here* $\Delta\varepsilon = \varepsilon_{B^0} - \varepsilon_{\bar{B}^0}$, $\Delta\omega = \omega_{B^0} - \omega_{\bar{B}^0}$ *and* $\Delta Q = Q_{B^0} - Q_{\bar{B}^0}$ *refer to differences between* B^0 *and* $\bar{B}^0$ *tags in tagging efficiency, mistag fraction and effective tagging efficiency, respectively.*

5.4 Δt measurement

The difference between B decay times, $\Delta t = t_{CP} - t_{tag}$, is determined from the measured separation Δz between the vertices of the reconstructed B_{CP} meson and the flavor-tagging B_{tag} meson along the z axis. The resolution on Δz is dominated by the uncertainty on the z position for the B_{tag} vertex.

5.4.1 Δz Measurement

In the reconstruction of the B_{CP} vertex, all daughter tracks are used. Daughter tracks from K^0_S and D candidates are first fit to a separate vertex and the resulting parent momentum and position are used in the fit to the B_{CP} vertex. The RMS resolution in z for the B_{CP} vertex in MC simulation is about $65\ \mu m$ for more than 99% of the B candidates. The resolution is about 5% worse in data than in MC simulation.

The vertex of the B_{tag} decay is constructed from all tracks in the event except the daughters of B_{CP}. For fully reconstructed modes, as the one studied in this thesis, an additional constraint is provided by the calculated B_{tag} production point and three-momentum. This is determined from the knowledge of the three-momentum of the fully reconstructed B_{CP} candidate, its decay vertex and error matrix, and from the knowledge of the average position of the interaction point and the $\Upsilon(4S)$ average boost (cf. Fig. 5.1). The average beam spot position and the angle of the beam in the detector are updated once per run, while the beam energies are recorded more frequently for any change above $0.05\ \text{MeV}$. These B_{tag} parameters are used as input to a geometrical fit to one single vertex, including all the other tracks in the event except those used to reconstruct B_{CP}. In order to reduce bias and tails due to long-lived particles, K^0_S and Λ^0 candidates are used as input to the fit in place of their daughters. In addition, tracks consistent with photon conversions ($\gamma \to e^+e^-$) are excluded. To reduce contributions from charm products, which tend to bias the determination of the vertex position, the track with the largest vertex χ^2 contribution ($\chi^2 > 6$) is removed, the fit is redone until no track fails the χ^2 requirement. In MC simulation the RMS of the core and tail Gaussian components of the residual Δz distribution (measured minus true Δz) is $190\ \mu m$. This residual distribution is fitted with the sum of three Gaussian distributions and it is found that the RMS of the narrowest Gaussian, which contains 70% of the area, is about $100\ \mu m$. Only 1% of the area is in the widest Gaussian.

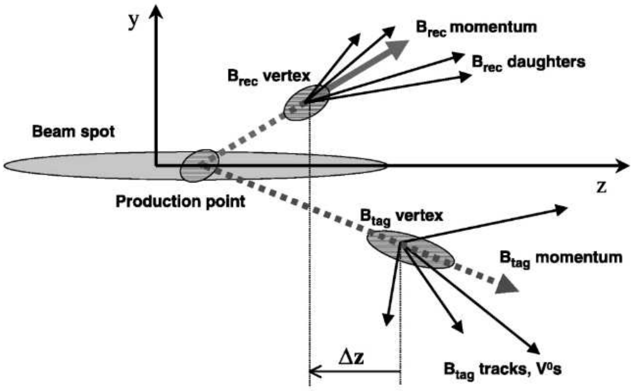

Figure 5.1: *Schematic view of the geometry in the yz plane for a $\Upsilon(4S) \rightarrow B\bar{B}$ decay. For fully reconstructed decay modes, the line of flight of the B_{tag} can be estimated from the (reverse) momentum vector and the vertex position of the B_{CP}, and from the beam spot position in the xy plane and the $\Upsilon(4S)$ average boost. Note that the scale in the y direction is substantially magnified compared to that of the z direction.*

5.4.2 Δt Calculation

By far the dominant limitation on the accuracy with which Δt is determined from the measured decay length difference, Δz, is the experimental resolution on the Δz measurement. The second limitation in the Δt measurement comes from the B meson momentum of about $340\ \mathrm{MeV}/c$ in the $\Upsilon(4S)$ CM frame. A correction is applied for this effect, and is described below. The impact on the Δt measurement of the spread in the two beam energies, which results in a momentum spread with a Gaussian width of about $6\ \mathrm{MeV}/c$, is negligible. Finally, a correction is applied for the $20\ \mathrm{mrad}$ angle between the $\Upsilon(4S)$ boost direction (the z axis in the following discution) and the axis of the symmetry of the detector, along which the separation between the vertices is measured.

Neglecting the B momentum in the $\Upsilon(4S)$ frame, the relation between Δz and Δt can be written as

$$\Delta z = \beta\gamma c \Delta t, \tag{5.3}$$

where $\beta\gamma$ is the $\Upsilon(4S)$ boost factor, with average value of $\langle\beta\gamma\rangle = 0.56$. The boost factor is calculated directly from the beam energies, which are monitored every $5\ \mathrm{sec}$, with an accuracy of 0.1%.

In the case of a fully reconstructed B_{CP}, its momentum direction is measured with good precision, and is used to correct for B momentum in the $\Upsilon(4S)$ frame. However, the correction depends on the sum of the $t_{CP} + t_{tag}$, which can only be determined with very poor resolution. The estimate $t_{CP} + t_{tag} = \tau_B + |\Delta t|$ is used to correct for the measured B_{CP}

momentum direction and extract Δt from the following expression:

$$\Delta z = \beta\gamma\gamma^*_{CP} c\Delta t + \gamma\beta^*_{CP}\gamma^*_{CP}\cos\theta^*_{CP} c(\tau_B + |\Delta t|), \tag{5.4}$$

where θ^*_{CP}, β^*_{CP} and γ^*_{CP} are the polar angle with respect to the beam direction, the velocity and the boost factor of the B_{CP} in the $\Upsilon(4S)$ rest frame. The difference between Δt calculated with Eq.(5.3) and Eq.(5.4) is very because $\gamma^*_{CP} = 1.002$ and $\beta^*_{CP} = 0.064$. The events-by-event difference in Δt calculated with the two methods has an RMS of 0.20 ps. Eq.(5.4) improves the Δt resolution by about 5%. In addition, it removes a correlation between the resolution on Δt and the true value of Δt. This correlation is due to the fact that the RMS in the second term in Eq.(5.4) depends on the expectation value of $(t_{CP} + t_{tag})^2$, which in turn depends on $|\Delta t|$. Eq.(5.4) is used for all B decays to hadronic final states, as in the present thesis, while Eq.(5.3) is used for semileptonic modes since the B direction cannot be measured for these decays.

5.4.3 Δt resolution Model

The Δt resolution function is represented in terms of $\delta_t = \Delta t - \Delta t_{\text{true}}$ by a sum of three Gaussian distributions (called the core, tail and outlier components) with different means and widths,

$$\begin{aligned}\mathcal{R}(\delta_t;\hat{a}) &= (1 - f_{\text{tail}} - f_{\text{out}})G\left(\delta_t, s^b_{\text{core}}\sigma_{\Delta t}, s^\sigma_{\text{core}}\sigma_{\Delta t}\right) \\ &\quad + f_{\text{tail}}G\left(\delta_t, s^b_{\text{tail}}\sigma_{\Delta t}, s^\sigma_{\text{tail}}\sigma_{\Delta t}\right) + f_{\text{out}}G\left(\delta_t, s^b_{\text{out}}, s^\sigma_{\text{out}}\right)\ ,\end{aligned} \tag{5.5}$$

where $G(x, x_0, \sigma)$ is a Gaussian with bias x_0 and standard deviation σ. For the core and tail Gaussian, the measured error $\sigma_{\Delta t}$ derived from the vertex fit for each event is used, allowing us to separate scale factors s^σ_{core} and s^σ_{tail} to accommodate an overall underestimate ($s^\sigma_k > 1$) or overestimate ($s^\sigma_k < 1$) of the errors for all events. The core and tail Gaussian distributions are allowed to have a nonzero mean to account for residual charm decay products included in the B_{tag} vertex. In the resolution function, these mean offsets are scaled by $\sigma_{\Delta t}$ to account for an observed correlation between the mean of the δ_t distribution and $\sigma_{\Delta t}$ in MC simulation. This correlation is due to the fact that, in B decays, the vertex error ellipse for the D decay products is oriented with its major axis along the D flight direction, leading to a correlation between the D flight direction and the calculated uncertainty on the vertex position in z for the B_{tag} candidate. In addition, the flight length of the D in the z direction is correlated with its flight direction. Therefore, the bias in the measured B_{tag} position due to inclusion of D decay products is correlated with the D flight direction.

MC simulations confirm the expectation that the resolution function is less biased for events with a primary lepton tag than those with a kaon tag. Therefore, the mean of the core Gaussian is allowed to be different for each tagging category. One common mean is used for the tail component. The third Gaussian has a fixed width of 8 ps and no offset (*i.e.* $s^b_{\text{out}} = 0$ and $s^\sigma_{\text{out}} = 8$ ps in Eq.(5.5)); it accounts for the fewer than 1% of events with incorrectly reconstructed vertices.

Since the B_{tag} vertex position dominates the Δt resolution, no significant difference is expected between the Δt resolution function of different B decays to hadronic final states without a D-meson. Hence, identical resolution functions are used when applicable for all modes. This assumption is supported by MC simulation.

5.5 Event Kinematics and Shape

Three event species are distinguished in the data:

- Signal events $B^0 \to K^0_S\pi^+\pi^-$.
- Continuum background events, of the type $e^+e^- \to q\bar{q}$ ($q = u, d, s, c$); this species represents the dominant background.
- Background events coming from B decays different from the signal.

This section describes the properties of the species mentioned above. The goal is to use all available information for discriminating signal with respect to backgrounds. The discriminant variables used to exploit these properties are described in Sec. 5.6.

5.5.1 Kinematics

One of the fundamental differences between signal and combinatorial background is the kinematics of the underlying production. The $\Upsilon(4S)$ decays in two particles of the same mass, B and $\bar{B}$, imposing two constraints in the CM frame. If the B-meson is correctly reconstructed, the energy of its decay products has to be equal to half the beam energy in the $\Upsilon(4S)$ rest frame, and its reconstructed mass has to be equal to that of the B-meson:

$$\begin{aligned} E^*_{\rm rec} &= E_{\rm beam}/2 = \sqrt{s}/2, \\ m_{\rm rec} &= m_B. \end{aligned} \tag{5.6}$$

These constraints allow us to discriminate signal against background events. For continuum, a flat distribution for $E^*_{\rm rec}$ and $m_{\rm rec}$ is expected in the whole dynamical range, excluding acceptance effects. Most of the B-background components are characterized by higher or lower multiplicity than signal, or by misidentification of a particle (the $B^0 \to D^-(\to K^0_S\pi^+)\pi^+$ B-background component being an exception, see Sec. 5.8 for more details). In both cases the reconstructed mass and energy are calculated with an incorrect number of decay products or with an incorrect mass hypothesis, with the effect that the distributions are shifted with respect to that of the signal, and their shapes distorted. These differences are used to construct the two main kinematical variables for the analysis (cf. Sec. 5.6.1).

5.5.2 Event topology

The e^+e^- collisions do not produce only $\Upsilon(4S)$ events, but also hadronic background $e^+e^- \to q\bar{q}$ (where $q = u, d, s, c$), and leptonic background $e^+e^- \to \ell^+\ell^-(\gamma)$ (where $\ell = e, \mu, \tau$). Table 4.2 summarizes properties and production rates for these events. Each of these backgrounds has its own characteristics, different from the signal, which are used to discriminate them from the signal. These differences are called event shapes in the e^+e^- CM frame (cf. table 5.3).

In an $e^+e^- \to q\bar{q}$ event, where q = u, d, s, c, a small amount of the initial energy is invested in rest masses of the quarks. Most of the available energy is carried as kinematic

Background component	Shape
$e^+e^- \to q\bar{q}$ (where $q = u, d, s, c$)	Several hadrons decay in two back-to-back jets
$e^+e^- \to \Upsilon(4S) \to BB$	Several hadrons isotropic decay in the CM
$e^+e^- \to \ell^+\ell^-$ (where $\ell = e, \mu, \tau$)	Two back-to-back high momentum tracks
$e^+e^- \to \gamma\gamma$	Two back-to-back high momentum photons

Table 5.3: *Shape of the different kinds of events. The third row denotes how important the background component is for the present analysis.*

energy, and both quarks fragment in two back-to-back jets (cf. left hand plot of Fig. 5.2). This implies that the event will roughly follow a $(1 + \cos^2\theta)$ distribution, where θ is the CM angle of one of the jet with respect to the z-axis, as predicted by lowest order Feynman QED diagram for an $e^+e^- \to f\bar{f}$, where f is a spin-$1/2$ fermion. In contrast, in an $e^+e^- \to \Upsilon(4S) \to B\bar{B}$ event, the spin-1 $\Upsilon(4S)$ decaying into two spin-0 B mesons gives, by conservation of angular momentum, a $\sin^2(\theta)$ angular distribution of the B decays (in the $\Upsilon(4S)$ rest frame), where θ is the angle between the B direction and the z-axis. Furthermore, the $\Upsilon(4S) \to B\bar{B}$ reaction is barely allowed kinematically, and the B-mesons have low momentum in the CM frame ($\sim 340\ \mathrm{MeV}/c$), compared with that of their daughters ($\sim 1-2\ \mathrm{GeV}/c$). This means that the decay products of the B-meson will not follow its flight direction due to the small boost. Finally, the B-meson being a pseudoscalar, no direction is preferred in its decay, and so the distribution of their daughters will be approximately spherical in the $\Upsilon(4S)$ CM frame (cf. right hand plot of Fig. 5.2).

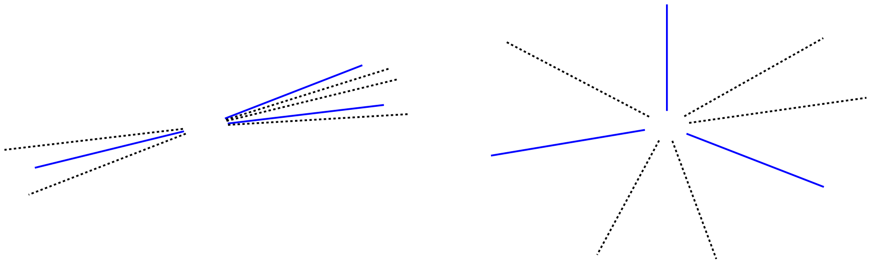

Figure 5.2: *Shape of $e^+e^- \to q\bar{q}$ (left) and $e^+e^- \to \Upsilon(4S) \to B\bar{B}$ (right) events in the e^+e^- CM frame. The solid blue lines represent the directions of reconstructed particles forming the B candidate, the dashed black lines represent the other particles in the event, denoted as "rest of the event" (ROE).*

Among the events produced by PEP-II (cf. table 5.3), the continuum background is the most difficult to reduce. A large amount can be reduced with simple cuts, but it remains the dominant background component in the final sample, and its discrimination in a maxi- mum likelihood fit (see chapter 6) is a crucial challenge of the analysis. The variables defined to exploit these event shape properties are generally referred to as "shape variables", and are described in Sec. 5.6.2.

The rare leptonic events that contribute to the sample have characteristics very similar to those of continuum background, and are then treated as continuum events in this analysis. The B-background events, having very similar shapes as the signal, are only discriminated using the kinematical and DP variables.

5.6 Main discriminant Variables

In this section the general properties of the different event species contributing to the data sample are exploited to define the discriminant variables. These variables will be used in two ways:

- Cuts will be applied on these variables in order to enhance the signal in the data sample,
- Some of these variables will be used in the maximum likelihood fit.

5.6.1 Kinematic Variables

In order to exploit the specifics of B decay kinematics, two variables are defined, ΔE and m_{ES}, which are used in the maximum likelihood fit (cf. Chapter 6). Two criteria illustrate their discriminant power: they exploit in an optimal way the information contained in Eqs. (5.6); also, possible correlations among them and with the other variables used in the likelihood fit (a Neural Network, Δt and the DP variables) are small.

The energy difference ΔE

The energy difference, ΔE, can be expressed in a Lorentz-invariant form as

$$\Delta E = (2q_B q_0 - s)/2\sqrt{s}, \tag{5.7}$$

where $\sqrt{s} = 2E^*_{\text{beam}}$ is the total energy of the e^+e^- system in the CM frame, and q_B and $q_0 = (E_0, \mathbf{p}_0)$ are the Lorentz vectors representing the momentum of the B candidate and of the e^+e^- system, $q_0 = q_{e^+} + q_{e^-}$. In the CM frame, ΔE takes the more familiar form

$$\Delta E = E^*_B - E^*_{\text{beam}}, \tag{5.8}$$

here E^*_B is the reconstructed energy of the B-meson. The ΔE distribution receives a sizeable contribution from the beam energy spread, but is generally dominated by detector energy resolution (this being clearly the dominant term for modes involving neutral particles).

The energy-substituted mass m_{ES}

The second kinematical variable is the energy-substituted mass, m_{ES}. In the laboratory frame, m_{ES} can be determined from the measured three-momentum $\mathbf{p}_B$ of the B candidate without explicit knowledge of the masses of the decay products:

$$m_{ES} = \sqrt{\left(s/2 + \mathbf{p}_B \cdot \mathbf{p}_0\right)^2 / E_0^2 - p_B^2}. \tag{5.9}$$

In the CM frame ($\mathbf{p}_0 = 0$), this variable takes the familiar form

$$m_{ES} = \sqrt{E_{\text{beam}}^{*2} - p_B^{*2}}, \tag{5.10}$$

where p_B^{*2} is the CM momentum of the B-meson, derived from the momenta of their decay products, and the B-meson energy is substituted by E_{beam}^{*}. As the B-mesons are almost at rest in the CM frame, the resolution on m_{ES} is dominated by the spread in the beam energy.

For signal events, m_{ES} yields the mass of the B-meson and shows a clean peak. For continuum events, composed of light quarks, the only way of reaching the B rest mass is by artificially associating random tracks. As a consequence, their distribution displays a slowly varying shape, as expected from their combinatoric nature.

The idea behind ΔE is different and complementary to that of m_{ES}. Whereas the latter is by construction independent of the mass hypothesis for each of the tracks, ΔE depends strongly on them. If, for example, a kaon is misidentified as a pion, its energy, and consequently that of the B candidate, will be smaller than its true energy. The event then will be shifted towards negative values of ΔE. In contrast, the distribution for signal events peaks at zero as expected, making ΔE especially helpful for discriminating from B-background events.

In modes with no neutral particles in the final state, the resolution for the ΔE and m_{ES} variables are $\sim 15\ \mathrm{MeV}$ and $\sim 3\ \mathrm{MeV}/c^2$, respectively. The parameterization used for their distributions are described in Sec. 6.3.1. Plots of both variables for signal and background can be seen in Fig. 5.5.

5.6.2 Shape Variables and the neural network

In order to exploit the topological differences between $B\bar{B}$ and continuum events several variables can be defined. All of them use the same starting information (particle flight direction in the $\Upsilon(4S)$ rest frame) and are therefore strongly correlated. A Multivariate Analyzer technique is adopted to define a single variable to be used for selection and discrimination in the maximum likelihood fit. A non-linear Neural Net (NN) [101] is used, that combines the variables defined below.

$\cos(\theta_B)$

The cosine of the angle between the CM B candidate direction and the z axis. In the case of perfect reconstruction, this variable follows a $\sin^2\theta_B = 1 - \cos^2\theta_B$ distribution for the signal. In contrast, for continuum background events, the B candidate is formed by random combination of tracks, which mean that $\cos\theta_B$ will have random values, and hence a flat distribution (out of acceptance effects).

$\cos(\theta_T)$

The cosine of the angle between the B candidate thrust axis and the z axis. The thrust of a collection of particles is defined as the direction, $\hat{t}$ (with $|\hat{t}| = 1$), in which the sum, T, of the projections of the momenta of the particles is maximized:

$$T \equiv \mathrm{Max}_{\hat{t}} \left\{ \frac{\sum_i |\hat{t} \cdot \mathbf{p}_i|}{\sum_i p_i} \right\}, \tag{5.11}$$

where the i index runs over all the particles in the collection. Given the spherical nature of B decays, the thrust axis of the true B candidate is essentially random. For continuum events in contrast, which are strongly collimated, the above definition ensures that the thrust axis approximates the direction of the hadronic jets, even when the tracks are selected artificially to form a B candidate. In the case of perfect reconstruction, the distribution of this variable is expected to be uniform ($1 + \cos^2\theta_T$) for signal (continuum background) events.

The monomials L_n

Other variables can be defined to exploit the difference in the angular distributions of the B candidate decay products for signal and continuum events. Since the present analysis explores the whole allowed phase space of the three-body decay, the signal-side angular information cannot be used without biasing the data sample, but the fact that the other B behaves statistically, but independently, in the same way can be exploited. The variables described in the following are calculated excluding the signal B candidate particles; the remaining collection of particles is referred to as the rest-of-the-event (ROE). Using tracks from the ROE has the advantage of eliminating possible correlations with the kinematical variables, as the construction of these last ones uses only the B candidate particles, and so there is very little common information: to first order, these correlations are assumed to be negligible (cf. see Sec. 6.2). It should be noted that the intrinsic symmetry of continuum events, due to their jet-like structure, leads to correlations between the values of their ROE and signal-side quantities. Since the signal-side is used to calculate the DP coordinates, it is then expected a correlation between these and some discriminant variables. This correlation is taken into account in the construction of the continuum PDF (cf. see appendix A, Sec. A.2).

In order to exploit the angular correlations, a set of monomials momentum-weighted sums over the angles of the tracks in the ROE with respect to the beam axis are defined:

$$L_n = \sum_{i=roe} p_i \times |\cos(\theta_{B,i})|^n \,. \tag{5.12}$$

A calculation of the separation power of the monomials for signal and background enables to identify those with the largest separation power. As it is customary in charmless analyses in BABAR, the present analysis uses the zeroth and the second order ones, L_0 and L_2, as in [102].

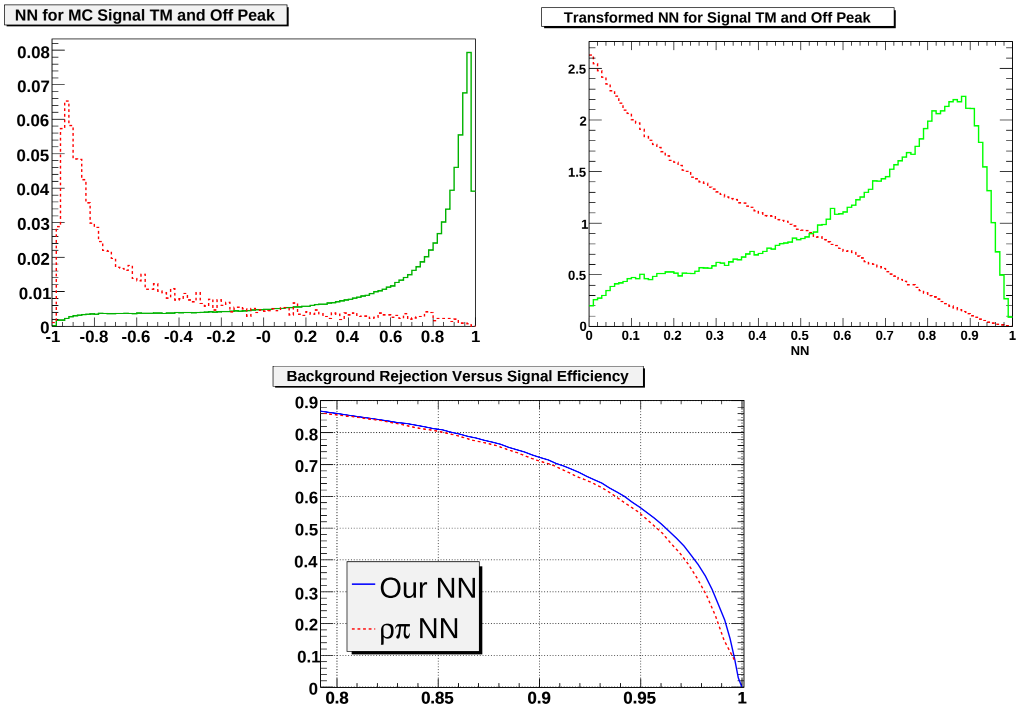

Figure 5.3: *Top left: Distribution of the NN variable for truth-matched signal (solid line), and off-resonance data (dashed line). Top Right: Distribution of the transformed NN variable for truth-matched signal (solid line), and off-resonance data (dashed line), which will be used in the final maximum likelihood fit. Bottom: background rejection versus signal efficiency, obtained by different cuts on the* NN *outputs (solid line). For comparison, the same curve is shown for the* NN *trained for the* BABAR $B^0 \rightarrow (\rho\pi)^0$ *analysis [35], and applied to the present data.*

The variables just defined are used as inputs to a Neural Network, which has the following structure:

- number of input variables: $N_{\rm var} = 4$;
- number of output classes: 2 (signal and background);
- number of layers: 4 (input, output & 2 hidden layers);
- number of neurons per layer: $N_{\rm var}$, $N_{\rm var} - 1$, $N_{\rm var} - 2$, 2;
- number of training cycles: ca. 20000;
- size of the training samples: 27K signal truth-matched [2] non resonant MC events and 27K off-resonance data events.

---

[2] A definition of truth-matched will be given in Sec. 5.7.2

The optimal signal/continuum discriminating power of the NN is chosen with a training procedure, using independent subsets of signal MC and off-resonance data as training and validation samples.

The NN distributions for truth-matched signal, and off-resonance data are shown in the top left hand side plot of Fig. 5.3. The right hand plot of the same figure show the distribution, for signal and background, of a transformed NN that will be used in the maximum likelihood fit, which will be described later on (cf. see Eq.(5.13)). The discriminating power is shown on Fig. 5.3, where the background rejection is plotted against signal efficiency for different values of the cuts on the NN output. For comparison, the rejection-efficiency curve is also shown for the NN trained for the BABAR $B^0 \rightarrow (\rho\pi)^0$ analysis [35], and applied to the present data.

5.7 Event Selection

After reconstruction, the data is subject to different stages of selection criteria. In a first stage, B candidates are formed by requiring a K^0_S candidate from the `KsDefault` list (cf. Sec. 5.2.4), and two oppositely charged tracks taken from `GoodTracksLoose` (cf. Sec. 5.2.1). All this is done before applying the following requirements,

- $m_{ES} > 5.2\ \mathrm{GeV/c^2}$,
- $4.99 < E^*_B < 5.59$ GeV (cf. Sec. 5.6.1),
- total energy of the event (in the CM frame) $E_{\mathrm{Total}} < 20.0\ \mathrm{GeV}$.

As a second step, some additional cuts are applied,

- The cosine of the angle between the momentum of the K^0_S candidate and the line that connects its decay vertex with that of the B candidate must satisfy $\cos\alpha_{K^0_S} > 0.999$.
- The K^0_S lifetime significance is required to satisfy $\tau_{K^0_S}/\sigma_{\tau_{K^0_S}} > 5.0$, rejecting in this way combinatorial background.
- The K^0_S candidate mass is constrained to be in the range $|m_{\pi^+\pi^-} - m_{K^0_S}| < 15\ \mathrm{MeV/c^2}$, where $m_{K^0_S}$ is the PDG [21] value of the K^0_S mass.
- Charged tracks are required to satisfy the `PiLoose` requirements (cf. Sec. 5.2.3).
- Loose cuts are applied on Δt and its error, $|\Delta t| < 20\ \mathrm{ps}$ and $\sigma_{\Delta t} < 2.5\ \mathrm{ps}$, as is standard in BABAR time-dependent analyses.
- To further discriminate signal from continuum background it is required $NN > -0.4$. This cut is not designed to suppress a maximum amount of background; rather, as the NN is one of the variables used in the maximum likelihood fit, the purpose of this cut is to have a signal efficiency of approximately 90%, while removing roughly 70% of continuum background. The motivation is to reduce the size of the dataset to

a value that is compatible with the available CPU constraints, both for the maximum likelihood fit and MC simulations.

As the NN distributions show sharp peaks both for signal and continuum background, the empirical description of the NN output shape is made simpler by means of a transformation, defined so that it is confined within $[0, 1]$ after selection,

$$NN \rightarrow 1 - \frac{arccos(NN + A) + B}{B + C}, \tag{5.13}$$

where $A = 0.001$, $B = 0.98$ and $C = 0.92$. This transformed NN, with its distribution shown in the top right hand plot of Fig. 5.3, is used in the maximum likelihood fit.

- Cuts on the kinematic variables m_{ES} and ΔE are applied to select three regions of interest in the $(m_{ES}, \Delta E)$ plane (cf. Fig. 5.4):

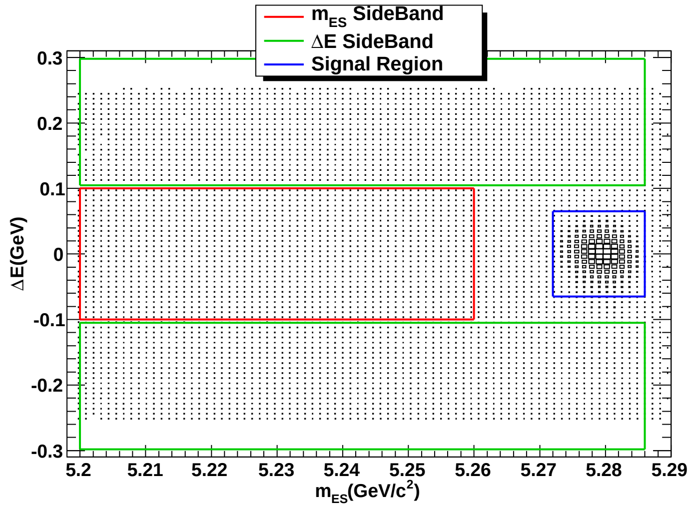

Figure 5.4: $(m_{ES}, \Delta E)$ *plane, showing signal region (blue box),* m_{ES} *(red box) and* ΔE *(green boxes) sidebands. The box histogram is non-resonant MC. The signal concentrates predominantly in the signal box.*

1. the signal region, where the signal events $B^0 \rightarrow K^0_S\pi^+\pi^-$ are expected to be, is defined as: $5.272 < m_{ES} < 5.286\ \mathrm{GeV/c^2}$ and $65 < \Delta E < 65\ \mathrm{MeV}$,
2. the m_{ES} *sideband*, $5.2 < m_{ES} < 5.26\ \mathrm{GeV/c^2}$ and $-0.1 < \Delta E < 0.1\ \mathrm{GeV}$,
3. the ΔE *sideband*, $|\Delta E| > 0.1\ \mathrm{GeV}$.

The last two regions are used to characterize the continuum distributions (see Sec. 6.3.4).

- Additional vetoes are applied to reduce misidentification of the charged particles: both tracks are required to fail the `Tight` electron, kaon and proton PID requirement, and at least one track must fail the `Tight` muon PID requirement. Muon and protons vetoes have a negligible effect is this analysis, and have only been kept because they are standard cuts in charmless analyses in *BABAR*.

The distributions of m_{ES}, ΔE, $m_{K^0_S}$, and K^0_S lifetime significance for truth-matched and misreconstructed Self Cross Feed (see definition later) signal events, and onpeak sideband events are shown in Figs. 5.5 and 5.6.

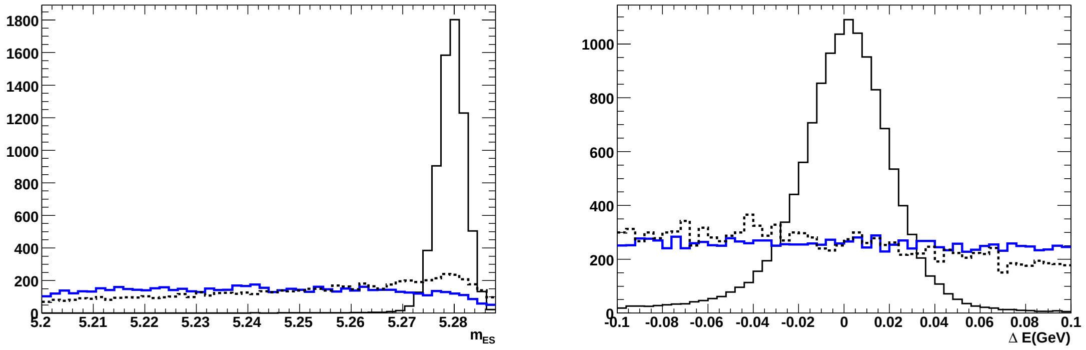

Figure 5.5: *Distributions of m_{ES} (left) and ΔE (right) for truth matched signal events (black solid histogram), SCF events (black dashed) and onpeak sideband events (blue histogram).*

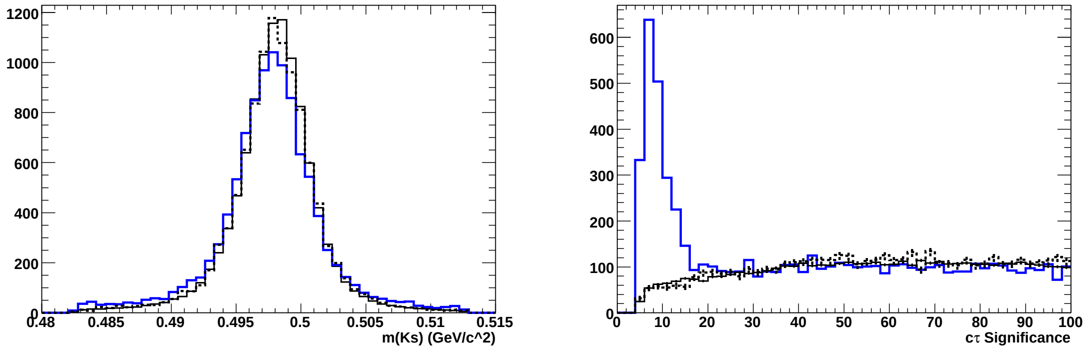

Figure 5.6: *Distributions of $m_{K^0_S}$ (left) and K^0_S lifetime significance (right) for truth matched signal events (black solid histogram), SCF events (black dashed) and onpeak sideband events (blue histogram).*

The summary of selection efficiencies for each cut is given in Table 5.4, together with the total selection efficiency. Values are given for non-resonant MC and for several resonant modes entering the Dalitz model (cf. Sec. 6.8). Differences between efficiencies for the different modes are significant. They are mainly due to the dependence of efficiency over the Dalitz Plot, and also to different rates of misreconstructed events (see Fig. 6.7). It has been checked that efficiency in a given DP point is independent of the MC used.

Cut	NR	$B^0 \to K^0_S f_0$	$B^0 \to K^0_S \rho^0$	$B^0 \to K^{*+}\pi^-$	Offpeak
Reconstruction	0.400	0.417	0.423	0.411	—
5.272 GeV$< m_{ES} <$ 5.286 GeV	0.904	0.903	0.857	0.822	0.183
-65 MeV$< \Delta E <$ 65 MeV	0.922	0.910	0.872	0.874	0.221
$\lvert m_{K^0_S} - m^{PDG}_{K^0_S}\rvert <$ 15 MeV	0.983	0.986	0.984	0.975	0.680
$\tau_{K^0_S}/\sigma_{\tau_{K^0_S}} > 20$	0.936	0.955	0.950	0.922	0.376
$\cos\alpha_{K^0_S} > 0.999$	0.991	0.996	0.996	0.986	0.955
$\lvert\Delta t\rvert <$ 20ps and $\sigma_{\Delta t} <$ 2.5ps	0.955	0.950	0.945	0.953	0.898
Kaon PID veto	0.956	0.963	0.964	0.953	0.614
Electron PID veto	0.964	0.955	0.953	0.961	0.913
Muon PID veto	1.000	0.999	1.000	0.999	1.000
Proton PID veto	1.000	1.000	1.000	1.000	1.000
$NN > -0.4$ and $NN < 0.999$	0.899	0.898	0.895	0.896	0.293
Total	0.2412 $\pm$0.0002	0.252 $\pm$0.001	0.229 $\pm$0.001	0.205 $\pm$0.001	—

Table 5.4: Summary of selection efficiency for TM+SCF events in different signal MC samples. The efficiencies quoted are relative efficiencies. The Total efficiency is the product of the relative ones.

5.7.1 Multiple candidates

When an event has several (n) candidates that pass the selection criteria, one of them is chosen arbitrarily. The index of the selected event is the remainder of the Time Stamp of the events divided by n. This approach avoids any bias, while being fully reproducible. In the signal MC samples, the multiplicity varies between 1.1% in the center of the DP, up to several percent in the $\rho^0(770)K^0_S$ and $K^*(892)^+\pi^-$ bands. Depending on the mode, $3-5\%$ of the multiple candidate events have more than two candidates. Fig. 5.7 shows the event multiplicities for different MC samples and off-peak data.

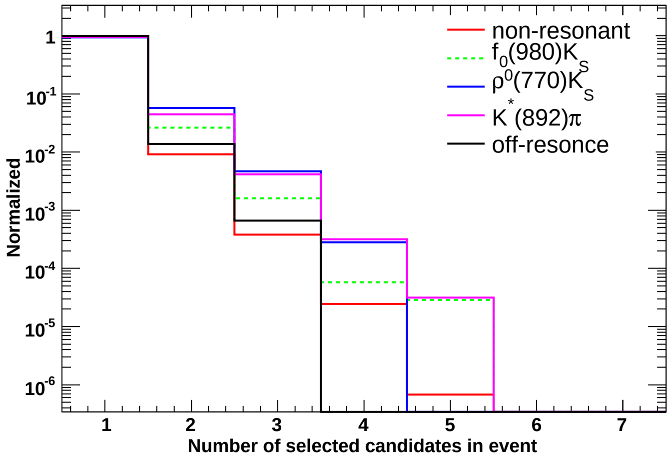

Figure 5.7: *Number of candidates per event passing the full selection. Shown are* $B^0 \to f_0(980)K^0_S$, $B^0 \to \rho 0(770)K^0_S$, $B^0 \to K^{*\pm}(892)\pi^{\mp}$, *non-resonant MC and the continuum-background components, represented in different colors and line-styles.*

5.7.2 Misreconstructed signal and migration over the DP

Misreconstructed signal events, also called Self Cross Feed (SCF), also present in the selected the data sample. A simulated signal event is classified as truth matched (TM) if the two pions and the K_S^0 are matched with the right particles at the generator level. In addition to this, it is required that the mothers of the matched generator level particles be the expected ones, according to each specific signal MC mode. All signal events that fail the truth matching criterion are classified as SCF. Fig. 5.8 shows a comparison between TM and SCF events in the non-resonant MC for m_{ES} and ΔE. Fig. 5.9 shows the migration over the square DP for TM and SCF events. On the horizontal (vertical) axis of these plots is shown the difference between true and reconstructed value of the m' (θ') variable, $m'_{\rm true} - m'_{\rm rec.}$ ($\theta'_{\rm true} - \theta'_{\rm rec.}$). The fraction of misreconstructed events per tagging category and MC mode is detailed in Table 5.5. The average fractions have been calculated using the branching fractions measured in [41].

Details about the parameterization of SCF events in the maximum likelihood fit are described in Sec. 6.3.2.

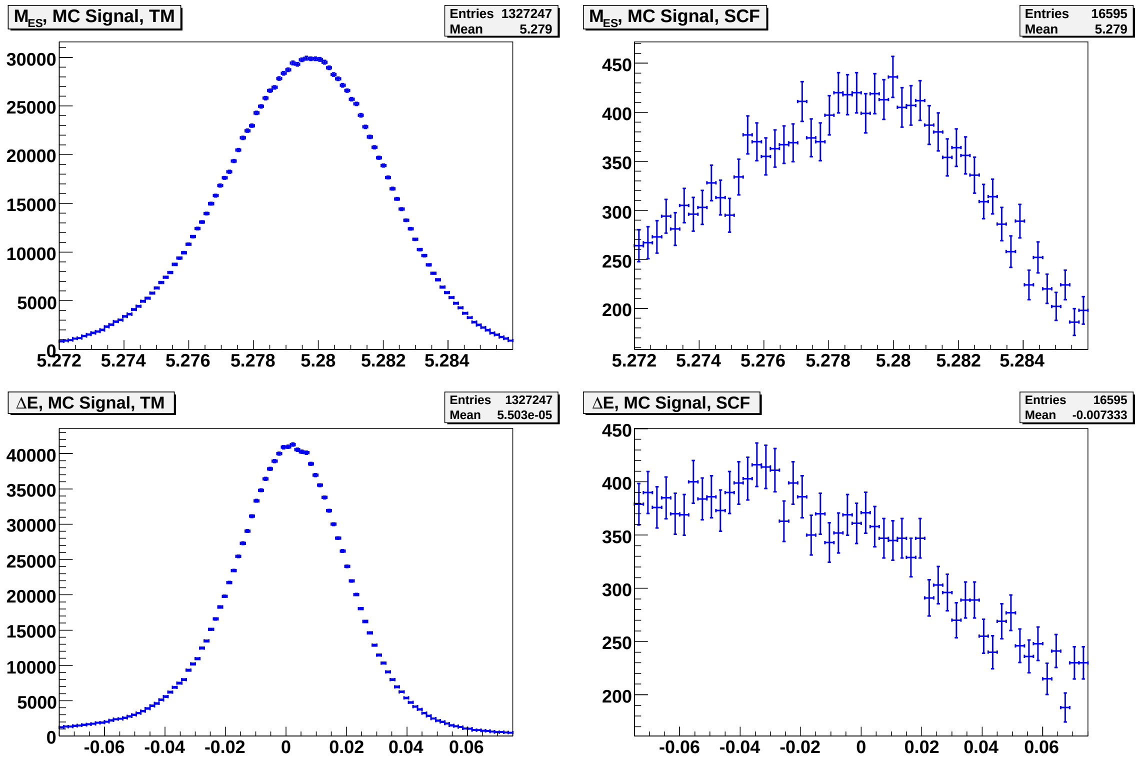

Figure 5.8: m_{ES} *(top) and* ΔE *(bottom) distributions for TM (left) and SCF (right) events in NR MC.*

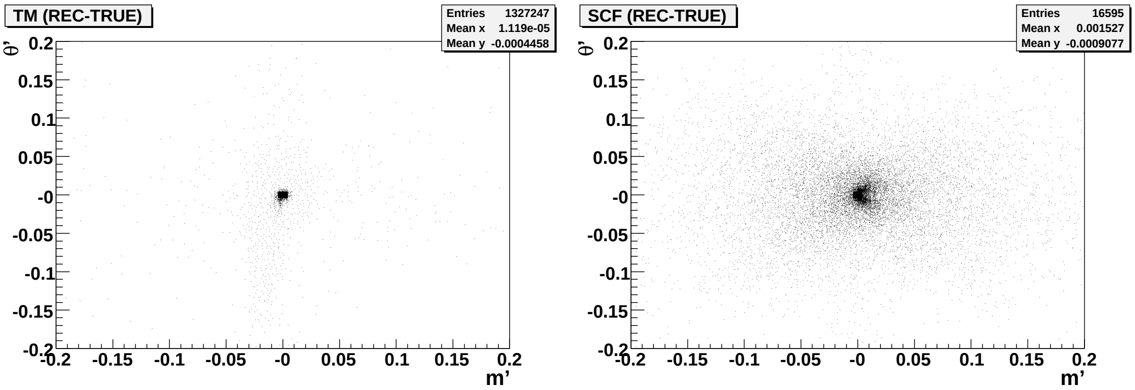

Figure 5.9: *Migration over the square DP for TM (left) and SCF (right) events in NR MC.*

Tag. Cat.	NR	$f_0 K^0_S$	$\rho^0 K^0_S$	$K^* \pi$	$K^{**} \pi$	average
Lepton	0.0072	0.0216	0.0462	0.0458	0.0137	0.0249
Kaon1	0.0095	0.0305	0.0618	0.0514	0.0206	0.0323
Kaon2	0.0111	0.0371	0.0799	0.0642	0.0245	0.0398
KaonPion	0.0110	0.0372	0.0827	0.0694	0.0213	0.0395
Pion	0.0111	0.0356	0.0800	0.0598	0.0223	0.0374
Other	0.0118	0.0425	0.0934	0.0692	0.0281	0.0447
NoTag	0.0124	0.0425	0.0835	0.0660	0.0317	0.0450
Total	0.0110	0.0368	0.0778	0.0623	0.0245	0.0391

Table 5.5: *Fraction of misreconstructed events per tagging category and MC mode. The average fractions have been calculated using the branching fractions measured in [41].*

5.8 B-background

An additional sources of background come from other B decays that can be misidentified as signal events. Several kinds of B background can be distinguished:

- B decays having the same multiplicity as signal events. Belong to this category the $B^0 \to D^-(\to K^0_S \pi^-)\pi^+$, $B^0 \to J/\Psi(\to l^+ l^-)K^0_S)$, and $B^0 \to \Psi(2S)(\to l^+ l^-)K^0_S)$ modes. The long-living mode $B^0 \to D^-(\to K^0_S \pi^-)\pi^+$ has exactly the same final state as the studied decay mode. It is treated as part of the B-background since it does not interfere with strongly decaying charmless resonances. For the charmonium resonances (J/Ψ and $\Psi(2S)$), the two leptons (typically muons) in the final state have been misidentified as pions. These backgrounds could in principle be simply eliminated from the sample, by applying narrow vetoes on the Dalitz plane. On the other hand, these events are useful to determine some parameters of signal likelihood variables (such as m_{ES}, ΔE) directly from the fit, and so are kept in the sample.
- B decays having lower multiplicity than signal. In this case, one or more particles of

the (ROE) are wrongly considered as coming from the B candidate. In general, these background events do not peak simultaneously both in m_{ES} and ΔE.

- B decays having higher multiplicity than signal. In this case, one or more particles of the final state are wrongly considered as coming from the rest of the event (ROE). As in the previous case, these events are not distributed as a peaking component both in m_{ES} and ΔE.

In order to characterize the list of channels generating B backgrounds in the present analysis, the reconstruction and selection algorithms have been applied to the neutral and charged generic MC samples, $B^0\bar{B}^0$ and B^+B^-. The procedure followed is described below.

5.8.1 Neutral B background

In a first stage, the signal modes are vetoed from the neutral generic sample, and the largest contributions of background are identified, which show peaking structures over the DP. These modes are:

- $B^0 \to D^-\pi^+$ $(D^- \to K^0_S\pi^-)$,
- $B^0 \to J/\Psi K^0_S$ $(J/\Psi \to l^+l^-)$,
- $B^0 \to \eta^{'} K^0_S$ $(\eta^{'} \to \rho^0\gamma)$,
- $B^0 \to \Psi(2S)K^0_S$ $(\Psi(2S) \to \mu^+\mu^-$ and $\Psi(2S) \to X)$.

Each of these contributions is treated individually in the fit. In a second step, the ≈ 970 remaining reconstructed events in the neutral generic sample are examined, after a second veto on the modes above. The resulting breakdown of the surviving events according to the B daughters is given in Table 5.6. Both sides of each event, B and $\bar{B}$ decays, have been taken into account. These remaining events still show several peaking structures on the DP, mainly in the D band. The left hand plot of Fig. 5.10 shows $m_{\pi^+K^0_S}$ around the D mass for the neutral generic B background component. In this plot, the two most prominent peaking structures ($B^0 \to D^+\pi^-$ and $B^0 \to D^{*+}\pi^-$) have been isolated.

The most frequent modes from Table 5.6 have been examined to check which exact decays have been reconstructed. It has been found that a few of the modes, in particular the semileptonic modes with D^* were, to a negligible number of exceptions, reconstructed only when in the other side of the same event there was another known source of B background. The frequent presence of these modes in Table 5.6 is explained rather by their large cross section than by the sensitivity to the present analysis. Therefore these modes are treated exclusively.

Modes with similar properties (similar peaking structure over the DP, and similar m_{ES} and ΔE shapes) are treated in a semi-inclusive way, grouping them into categories. These modes are detailed in Table 5.7, with the expected number of each one of them in the data sample. The categories are detailed in the rightmost column in the same table, where modes with the same category number are grouped together. Modes that have been used in the study

Frequency	Decay Mode (+ C.C)
212	$D^{+}\pi^{-}$
47	$D^{*+}\pi^{-}$
36	$D^{+}K^{-}$
30	$D^{+}\rho^{-}$
24	$D^{*+}\mu^{-}\overline{\nu_{\mu}}$
18	$D^{*+}e^{-}\overline{\nu_{e}}$
17	$D^{+}\mu^{-}\overline{\nu_{\mu}}$
13	$D^{*+}D_{s}^{-}$
12	$K_{S}^{0}\overline{K_{0}^{*0}}$
10	$D^{*+}D^{*-}K_{S}^{0}$
10	$K_{S}^{0}\mu^{-}\mu^{+}$
8	$D^{+}a_{1}^{-}$
7	$K_{0}^{*+}K^{-}$
7	$D_{s}^{*+}D^{*-}$
7	$D^{+}e^{-}\overline{\nu_{e}}$
6	$D^{*+}\rho^{-}$
6	$D^{*+}K^{-}\overline{D^{*0}}$
6	$D^{+}\pi^{-}\nu_{\mu}\mu^{+}D^{*-}$
5	$a_{1}^{+}\pi^{-}$

Table 5.6: *Most frequent modes reconstructed in the vetoed neutral generic MC sample. The* $B^0 \to D^-\pi^+$ *events do not include the decay* $D^- \to K_S^0\pi^-$ *that has been added exclusively to the DP model.*

of B background, and have not been included in the semi-exclusive PDFs are detailed in the bottom of Table 5.7 without mention of the category.

To avoid uncontrolled overlap between the channels, the numbers in the Table 5.7 and are based on a sample where only one side of an event is a known source of B background. The right hand plot of Fig. 5.10 illustrates the rationale behind this strategy, by showing the pollution from other modes in the Dalitz Plot of $B^0 \to X, \overline{B^0} \to D^{*+}\pi^-, D^{*+} \to D^0\pi^+, D^0 \to X + C.C.$ mode without "other side filtering". Contributions of decay modes from the other B in the event, like $J/\Psi K_S^0$ and $B^0 \to D^-(K_S^0\pi^-)\pi^+$ are seen, which have been already treated exclusively.

The remaining events from modes that have not been treated exclusively or semi-exclusively (< 300), do not show any peaking structures on the Dalitz plot, as shown in left hand plot of Fig. 5.11. These events are taken as a neutral generic component in the fit.

5.8.2 Charged B background

A similar study has been applied to the charged generic sample (except for the step of vetoing the signal model). The most frequently reconstructed modes are detailed in Table 5.8. In this sample, no obvious peaking structures are present, as shown in right hand plot of Fig. 5.11 and therefore the whole sample is used as a charged generic component in the fit.

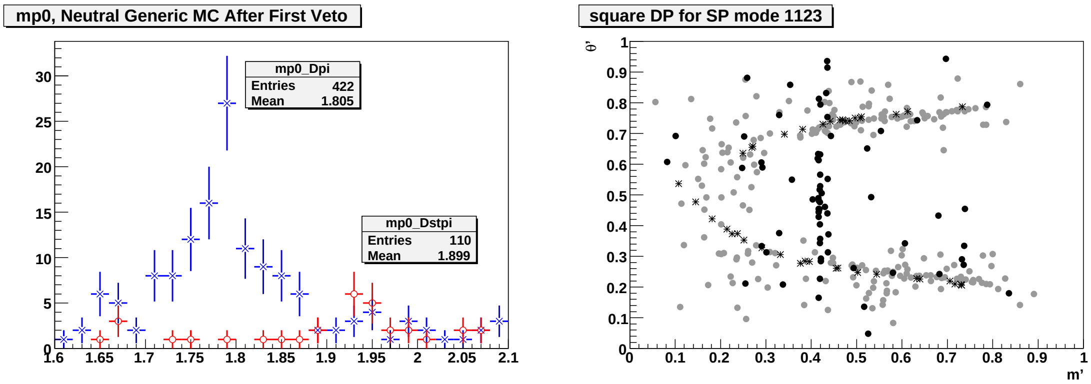

Figure 5.10: *Left:* $m_{\pi^+ K_S^0}$ *around the* D *mass for the neutral generic B background component. The two most dominant peaking structures have been isolated. The marked peak around* 1.95 GeV *(red O) represents* $B^0 \to D^{*+}\pi^-$*. The wider peak around* 1.8 GeV *(blue X) represents* $B^0 \to D^+\pi^-$*. Right: Square DP of* $B^0 \to X, \overline{B^0} \to D^{*+}(\to D^0(\to X + C.C.)\pi^+)\pi^-$ *mode. The black/gray entries represent events with/without known* B *background contribution in the other side. Events where the other side decay channel is* $B^0 \to D^-(K_S^0\pi^-)\pi^+$ *are marked by *. Contribution from* $J/\Psi K_S^0$ *is also clearly seen (vertical cluster of events for* $m' \simeq 0.42$*, marked by black dots). This illustrates the pollution from other modes when no "other side filtering" is applied.*

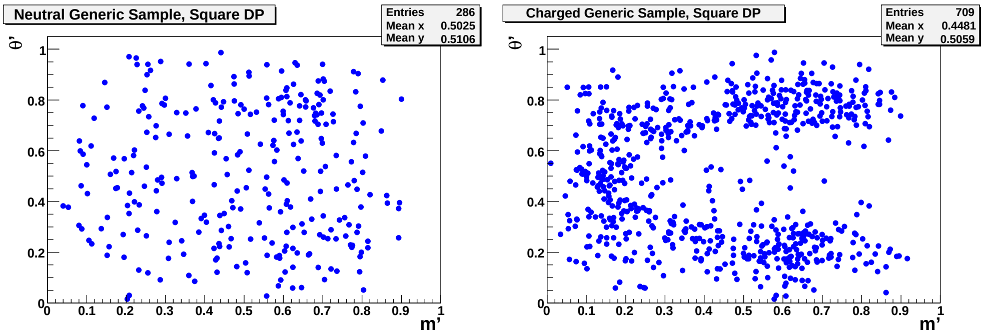

Figure 5.11: *Left: Square DP of the neutral generic sample vetoed from signal events and from all the modes treated exclusively. Right: Square DP of the charged generic sample.*

5.8.3 Summary on B background

In summary, the B-background is separated into 10 categories. There are five exclusive modes that include: $B^0 \to D^-(\to K_S^0\pi^-)\pi^+$, $B^0 \to J/\Psi(\to \ell^+\ell^-)K_S^0$, $B^0 \to \Psi(2S)K_S^0$ (with $\Psi(2S) \to \ell^+\ell^-$, $J/\Psi\pi\pi$ or $\chi\gamma$), $B^0 \to \eta'(\to \rho\gamma)K_S^0$ and $B^0 \to a_1^+(\to K_S^0\pi^+)\pi^-$ modes. There are three semi-inclusive categories, whose definition is summarized in table 5.7. Finally, there are two inclusive categories referred as neutral and charged generic. The fractions of events per tagging category for some B backgrounds are detailed in table 5.9.

Mode	Eff.	BF	Expected Yield in data sample	Cat.
$B^0 \to X, \overline{B^0} \to D^{*+}(\to D^0(\to X)\pi^+)\pi^- + C.C.$	4.20E-05	1.77E-03	27.80	1
$B^0 \to X, \overline{B^0} \to D^{*+}(\to D^+(\to X)\pi^0)\pi^- + C.C.$	5.33E-05	8.01E-04	15.98	1
$B^0 \to X, \overline{B^0} \to D^+\pi^-, D^+ \to X + C.C.$	3.17E-03	2.76E-03	3271.78	2
$B^0 \to D^-(\to K^0_S\pi^-)K^+$	5.18E-02	2.08E-06	40.28	2
$\overline{B^0} \to D^+(\to K^0_s K)\pi^- + C.C.$	1.23E-02	8.17E-06	37.74	2
$B^0 \to D^-(\to K^+\pi^-\pi^-)\pi^+$	7.67E-05	2.62E-04	7.54	2
$B^0 \to D^-(\to K^0_s\pi^-)\mu^+\nu, \overline{B^0} \to X + C.C.$	8.93E-05	2.16E-04	7.21	2
$B^0 \to X, \overline{B^0} \to D^+(\to X)\rho^- + C.C.$	9.71E-06	7.50E-03	27.25	3
$B^0 \to X, \overline{B^0} \to D^+(\to K^0_S\pi^+)\rho^- + C.C.$	3.31E-04	1.10E-04	13.66	3
$B^0 \to X, \overline{B^0} \to D^+(\to K^0_S K^+)\rho^- + C.C.$	1.11E-04	2.22E-05	0.92	3
$B^0 \to X, \overline{B^0} \to D^{*+}(\to D(\to X)\rho^-)\pi^0 + C.C.$	1.16E-06	2.09E-03	0.91	3
$B^0 \to X, \overline{B^0} \to D^{*+}(\to D^0(\to X)\pi)\rho^- + C.C.$	1.94E-07	4.60E-03	0.33	3
$a_1^+\pi^-$	4.88E-04	3.97E-05	7.25	4
$B^0 \to X, \overline{B^0} \to D^{*+}(\to D^0(D^0 \to K^-\pi^+)\pi^+)\pi^- + C.C.$	7.06E-04	6.71E-05	17.74	
$B^0 \to D^{*+}\pi^-, D^{*+} \to D^0(\to K^0_S\pi^0)\pi^- + C.C.$	7.92E-04	2.01E-05	5.98	
$B^0 \to D^{*+}\pi^-, D^{*+} \to D^+(\to K^0_S\pi^+)\pi^0 + C.C.$	1.35E-03	1.18E-05	5.96	
$B^0 \to D^{*+}\rho^-, D^{*+} \to D^0(\to K^0_S\pi^0)\pi^+ + C.C.$	2.25E-05	5.25E-05	0.44	
$B^0 \to X, \overline{B^0} \to D^{*+}(\to D^0(\to K^-\pi^+)\pi)\rho^- + C.C.$	4.95E-06	1.75E-04	0.32	
$B^0 \to D^{*+}\rho^-, D^{*+} \to D^+(\to K^0_s\pi^+)\pi^0 + C.C.$	2.33E-05	3.07E-05	0.27	
$\chi_{c1}K^0_S$	1.69E-05	2.90E-06	0.02	
$B^0 \to D^-K^+(D^- \to \pi^-\pi^0)\overline{B^0} \to X + C.C.$	4.25E-05	2.61E-07	0.00	
$\overline{B^0} \to D^{*+}(\to D^+(\to K^0_S\pi^+)\pi^0)\mu^-\overline{\nu_\mu} + C.C.$			< 1	
$\overline{B^0} \to D^{*+}(\to D^0(\to K^0_S\pi^0)\pi^+)\mu^-\overline{\nu_\mu} + C.C.$			< 1	
$\overline{B^0} \to D^{*+}(\to D^+(\to K^0_S\pi^0)\pi^0)e\overline{\nu_e} + C.C.$			< 1	
$\overline{B^0} \to D^{*+}(\to D^0(\to K^0_S\pi^0)\pi)e\overline{\nu_e} + C.C.$			< 1	

Table 5.7: *Exclusive neutral B background modes. Modes from each category are taken as a single PDF, as a weighted sum of the individual contributions. Modes without a category number are grouped in a neutral generic category. Branching fractions are taken from the PDG [21] and, when available, from HFAG [28].*

Frequency	Decay Mode (+ C.C)
164	$\pi^+\overline{D^0}$
63	$\pi^+\overline{D^{*0}}$
30	$K_0^{*0}\pi^+$
29	$\rho^+\overline{D^0}$
21	$\nu_\mu\mu^+\overline{D^{*0}}$
11	$\nu_e e^+\overline{D^{*0}}$
9	$a_1^0\pi^+$
8	$\rho^+\overline{D^{*0}}$
8	$\nu_\mu\mu^+\overline{D^0}$
6	$D_s^{*+}\overline{D^{*0}}$
6	$D_s^+\overline{D^0}$
6	$D_s^+\overline{D^*0}$
6	$\pi^+\pi^+\pi^0D^{*-}$
6	$\pi^+\overline{D^0}D^0D_s^-$
6	$\pi^+\overline{D^0}D^0D_s^{*-}$
6	$\nu_\mu\mu^+\overline{D^{*0}}D^0\pi^-$
6	$\nu_\mu\mu^+\overline{D_1'^0}$
5	$a_1^+\overline{D^{*0}}$

Table 5.8: *Most frequent modes reconstructed in the generic* $B^\pm$ *MC sample.*

Tag. Cat.	$D^-\pi^+$	$J/\Psi K_S^0$	$\eta' K_S^0$	neu. gen	ch. gen	$\Psi(2S)K_S^0$
Lepton	0.0889	0.0914	0.0831	0.0622	0.0349	0.0912
Kaon1	0.1031	0.1030	0.0954	0.0895	0.0699	0.0965
Kaon2	0.1671	0.1680	0.1636	0.1662	0.1755	0.1830
KaonPion	0.1386	0.1403	0.1390	0.1399	0.1525	0.1433
Pion	0.1484	0.1459	0.1533	0.1584	0.1541	0.1485
Other	0.1025	0.0990	0.1090	0.1178	0.1183	0.0924
NoTag	0.2513	0.2524	0.2565	0.2659	0.2947	0.2450

Table 5.9: *Fraction of events per tagging category for some B backgrounds.*

Chapter 6

The Maximum Likelihood Fit

This chapter describes the likelihood function used to fit the $B^0 \rightarrow K_S\pi^+\pi^-$ final data sample. First, the treatment of the discriminant (m_{ES}, ΔE and NN) and dynamical (Δt and Dalitz plot) variables are described. Then a validation of the likelihood function, based on MC studies, is presented. These studies will set the statistical approach for extracting confidence intervals on the physical parameters. Finally, the nominal signal Dalitz plot model is introduced.

6.1 The likelihood function

The selected on-resonance data sample consists of signal, continuum-background and B-background components, separated by the flavor and category of the tag side. The variables m_{ES}, ΔE, NN output, and DP discriminate signal from background. The Δt measurement allows to determine mixing-induced CP-violation, and provides additional continuum-background rejection. The amplitude analysis allows us access to the relative phases among different intermediate resonances. The signal likelihood is the sum of a correctly reconstructed (TM) component and a misreconstructed (SCF) component. The fit strategy is to determine as many continuum shape and asymmetry parameters as possible simultaneously with the signal parameters. This strategy reduces systematic effects from the description of the dominant background piece. The probability density $\mathcal{P}_i^c$ for a single event i in tagging category c is the sum of the probability densities (PDF) of all components:

$$\begin{aligned}
\mathcal{P}_i^c \equiv\; & f^c_{\mathrm{sig}}\left[(1-\bar{f}^c_{\mathrm{SCF}})\mathcal{P}^c_{\mathrm{sig-TM},i} + \bar{f}^c_{\mathrm{SCF}}\mathcal{P}^c_{\mathrm{sig-SCF},i}\right] \\
& + f^c_{q\bar{q}}\frac{1}{2}\left(1+q_{\mathrm{tag},i}A_{q\bar{q},\mathrm{tag}}\right)\mathcal{P}^c_{q\bar{q},i} \\
& + \sum_{j=1}^{N^{B^+}_{\mathrm{class}}} f^c_{B^+j}\frac{1}{2}\left(1+q_{\mathrm{tag},i}A_{B^+,\mathrm{tag},j}\right)\mathcal{P}^c_{B^+,ij} + \sum_{j=1}^{N^{B^0}_{\mathrm{class}}} f^c_{B^0j}\mathcal{P}^c_{B^0,ij}\;, \qquad (6.1)
\end{aligned}$$

where,

- $f^c_{\rm sig}$ is the fraction of signal events that are tagged in category c;
- $\bar{f}^c_{SCF}$ is the fraction of misreconstructed signal events (SCF) in tagging category c, averaged over the DP;
- $\mathcal{P}^c_{{\rm sig-TM},i}$ and $\mathcal{P}^c_{{\rm sig-SCF},i}$ are the products of PDFs of the discriminating variables used in tagging category c, for TM and SCF events, respectively;
- $f^c_{q\bar{q}}$ is the faction of continuum events tagged in category c;
- $q_{{\rm tag},i}$ is the tag flavor of the event; namely $q_{{\rm tag},i} = 1$ for B^0-tag (in other words, a $\bar{B}^0$ in the signal side when the tagging $B_{\rm tag}$ decays) and $q_{{\rm tag},i} = -1$ for $\bar{B}^0$-tag;
- $A_{q\bar{q},{\rm tag}}$ is a tag asymmetry, parameterizing a possible charge asymmetry in continuum events;
- $\mathcal{P}^c_{q\bar{q},i}$ is the continuum PDF for tagging category c;
- N_{B^+j} (N_{B^0j}) is the number of expected events in the charged (neutral) B-related background class j;
- $f^c_{B^+j}$ ($f^c_{B^0j}$) is the fraction of charged (neutral) B-related background events of class j that are tagged in category c;
- $A_{B^+,{\rm tag},j}$ describes the tag asymmetry in charged B background of class j; this parametrizes an eventual charge asymmetry. Note that the tag-charge correlation is absorbed in the tag flavor-dependent PDF of the DP (see later);
- $\mathcal{P}^c_{B^+,ij}$ is the B^+-background PDF for tagging category c and class j;
- $\mathcal{P}^c_{B^0,ij}$ is the B^0-background PDF for tagging category c and class j; the time-dependent PDF is non-trivial as neutral B-background can exhibit direct and mixing-induced CPV (see later);

The PDFs $\mathcal{P}^c_X$ are the product of the PDFs of the five discriminating variables (m_{ES}, ΔE, NN, DP and Δt) x_k, $k = 1, \ldots, 5$ (except for the continuum NN and DP variables, for which a non-negligible correlation is taken into account in the likelihood function, see appendix A):

$$\mathcal{P}^c_{X,i(j)} \equiv \prod_k \mathcal{P}^c_{X,i(j)}(x_k) \; . \tag{6.2}$$

Finally, the extended likelihood over all tagging categories is given by

$$\mathcal{L} \equiv \prod_{c=1}^{5} e^{-\overline{N}^c} \prod_i^{N^c} \mathcal{P}^c_i \; , \tag{6.3}$$

where is the number of events expected in category c

$$\overline{N}^c = N^c_{\rm sig} + N^c_{q\bar{q}} + \sum_{j=1}^{N^{B^+}_{\rm class}} N_{B^+j} + \sum_{j=1}^{N^{B^0}_{\rm class}} N_{B^0j} \tag{6.4}$$

where $N_{\rm sig}$ is the total number of $B^0 \to K^0_S\pi^+\pi^-$ signal events in the data sample; $N^c_{q\bar{q}}$ is the number of continuum events that are tagged in category c; $N^{B^+}_{\rm class}$ ($N^{B^0}_{\rm class}$) is the number of charged (neutral) B-related background classes considered. Including this term allows for the direct fitting of event yields rather than fractions.

The expression in Eq. 6.1 implies that all correlations among likelihood variables have been neglected. This statement was tested for ΔE, m_{ES}, Δt, and NN on non-resonant signal MC and on m_{ES} sideband in data. The results for signal and background are shown in Tab. 6.1 and 6.2 respectively. All correlations are small except that for the signal m_{ES} and ΔE. The $\sim 10\%$ negative correlation a known feature and previous analyses have shown that the effect of neglecting it is small for yield estimations and CP-violation asymmetries measurements. This induces a systematic uncertainty which is evaluated using fully-simulated signal events (cf. Sec. 6.6). Additional care is required for the Dalitz model (see Sec. 6.2).

	m_{ES}	ΔE	NN	Δt
m_{ES}	100	-9.6	-0.1	-0.0
ΔE	-	100	0.3	0.0
NN	-	-	100	0.3
Δt	-	-	-	100

Table 6.1: *Correlation matrix among m_{ES}, ΔE, NN, and Δt in a sample of signal MC $B^0 \to K^0_S\pi^+\pi^-$ non-resonant decays. Values are quoted in percentage.*

	m_{ES}	ΔE	NN	Δt
m_{ES}	100	-0.01	-1.06	-0.79
ΔE	-	100	-0.04	-4.06
NN	-	-	100	-0.37
Δt	-	-	-	100

Table 6.2: *Correlation matrix among m_{ES}, ΔE, NN, and Δt in a sample of background events from m_{ES} sideband. Values are quoted in percentage.*

6.2 Correlation of fit variables with Dalitz Plot, tag and tagging category

Since the Dalitz plot itself is used in the maximum likelihood fit as a two-dimensional PDF, it is important to take care of the dependence of the preceding variables all over the Dalitz plane. In order to do that, the mean and RMS of the distribution of each variable in different bins of the DP are compared. Figures 6.1–6.5 show the corresponding plots for non-resonant signal (TM and SCF, cf. Sec. 5.7.2) of m_{ES}, ΔE, Δt, $\sigma_{\Delta t}$ and the NN. As mentioned before, the SCF events are clustered mostly at the corners of the DP.

For the m_{ES} variable (cf. Fig. 6.1), the TM and SCF events show a reasonably uniform distribution of their mean and RMS values over the DP, with a small peak-to-peak spread compared with the mean RMS value. For the ΔE variable (cf. Fig. 6.2), the TM shows a complicated correlation with the DP, but the peak-to-peak spread is small compared with the mean RMS value. The same can be concluded for the SCF component. The Δt variable (cf. Fig. 6.3) for the TM events also shows a rather uniform distribution. For SCF events, the peak-to-peak spread is of the same order as the RMS value, this correlation of Δt with the DP is neglected as SCF represents only a small fraction of the total signal. The $\sigma_{\Delta t}$ (cf. Fig. 6.4) also shows a complicated correlation with the DP, but here the peak-to-peak spread is small compared with the mean RMS value. Finally, the NN variable (cf. Fig. 6.5) show a flat distribution over the DP both for TM and SCF events. In summary, the correlations of these variables with the DP for signal is assumed to be small enough, and are neglected in the likelihood; a systematic uncertainty will be assigned to this assumption, and it will be evaluated using fully-simulated signal events (cf. Sec. 6.6).

For continuum background, the same test is performed on offpeak data, where the only variable that shows a visible dependence on the Dalitz plot is the NN, as is illustrated in Fig. 6.6. This figure also shows the profile of the Δ_{Dalitz} in the Square Dalitz plane; this variable is defined as the smallest of the three invariant masses, rescaled in the $(0, 1)$ range, where 1 (0) represents the center (edges) of the Dalitz plot. The average value of NN for offpeak events as function of Δ_{Dalitz} variable is also shown. It is clearly seen that there is a non-negligible correlation between NN and the Dalitz plot.

6.3 Parameterization of distributions

The probability density functions of signal and B-backgrounds are obtained from fully simulated MC samples. Whenever possible, these PDFs are described using parametric functions. For $q\bar{q}$ the overall strategy is to determine as many continuum background related distributions as possible, simultaneously with signal from the fit to the final data sample. In contrast, it remains impractical to determine the continuum DP distribution in the same fashion. In light of this, the continuum DP PDF is determined from the onpeak data sidebands (cf. Sec 5.7) and off-peak data.

6.3.1 ΔE, m_{ES} and NN parameterizations

The parameterizations used for the kinematical variables and the NN output for the components sin the likelihood function are briefly described here. Specific details of the parameterizations can be found in Appendix A.

The m_{ES} distribution of TM signal events is described with a bifurcated Crystal Ball function, which is a combination of bifurcated Gaussian function with a power law tail (cf. Eq.(A.1)). The mean and two widths of this function are determined by the fit. A non-parametric function is used to describe the SCF signal component. The ΔE distribution of TM events is described with a double Gaussian function. Misreconstructed events are described by a non-parametric function. Both m_{ES} and ΔE PDFs are described by non-

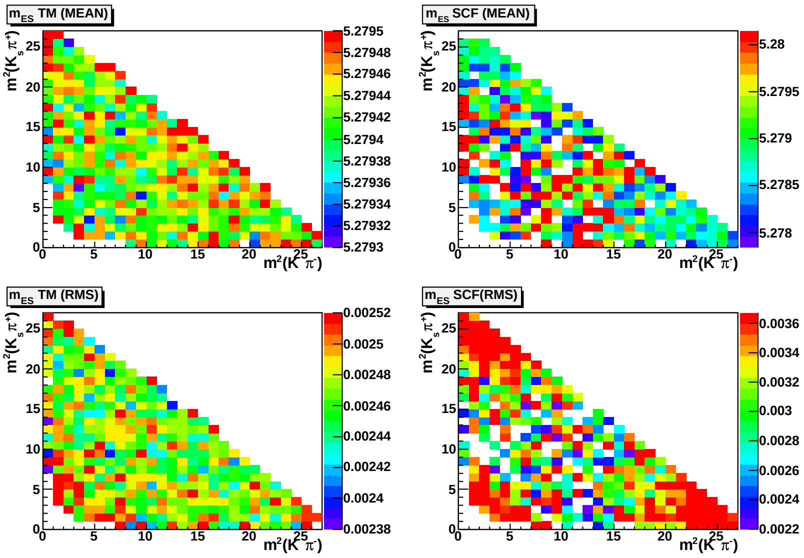

Figure 6.1: *Dependence of mean (top) and RMS (bottom) value of* m_{ES} *distributions in different bins of the DP, for TM (left) and SCF (right) NR signal events. The SCF events are mostly clustered at the corners of the DP. The peak-to-peak spread are small compared to the mean RMS value of the distributions. TM:* $\Delta Mean \sim 0.2\ \mathrm{MeV}/c^2$, $\Delta RMS \sim 0.14\ \mathrm{MeV}/c^2$, *compared to* $\mathrm{RMS} = 2.5\ \mathrm{MeV}/c^2$. *SCF:* $\Delta Mean \sim 2.0\ \mathrm{MeV}/c^2$, $\Delta RMS \sim 1.4\ \mathrm{MeV}/c^2$, *compared to* $\mathrm{RMS} = 3.7\ \mathrm{MeV}/c^2$.

parametric functions for all B background classes. Exceptions to this are the m_{ES} PDFs for $B^0 \to D^-\pi^+$ and $B^0 \to J/\psi K^0_S$ components, and the ΔE PDF for $B^0 \to D^-\pi^+$, which are the same as the corresponding distributions of TM signal events. The m_{ES} and ΔE PDFs for continuum events are parameterized with an ARGUS shape function [103] and a first-order polynomial, respectively, with parameters determined by the fit.

Non-parametric functions are used to empirically describe the distributions of the NN output found in the MC simulation for TM and SCF signal events, and for B background events. For TM signal events, different PDFs are used per tagging category to account for differences observed in the shapes. The continuum NN distribution is parameterized by a third-order polynomial that is constrained to take positive values in the range populated by the data. The coefficients of the polynomial are determined by the fit. Continuum events exhibit a correlation between the DP coordinate and the shape of the event that is exploited in the NN. To correct for residual effects, a linear dependence of the polynomial coefficients on the distance of the DP coordinate from the kinematic boundaries of the DP is introduced. The parameters describing this dependence are determined by the fit.

Other issues concerning the individual PDFs in Eq. (6.1) are discussed in the following sections. The most important modeling for this analysis is that of the DP from which the module and phase of complex amplitudes of resonances are determined. The detailed parameterization is described separately below.

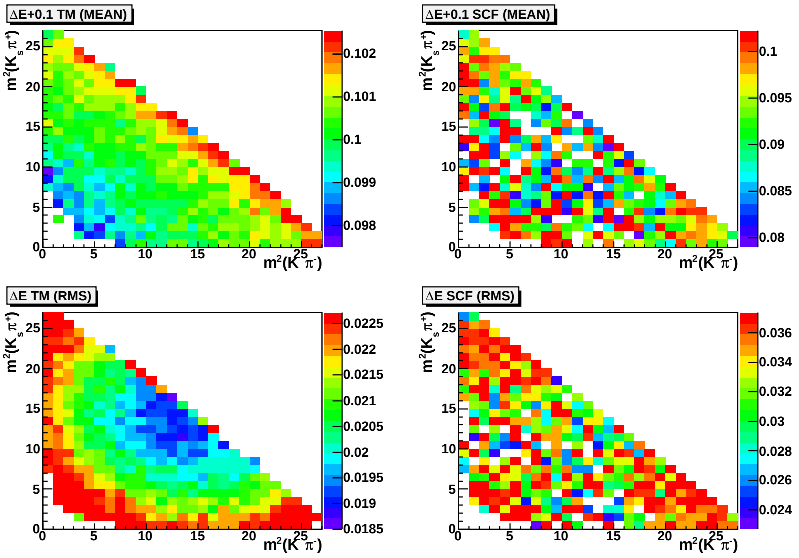

Figure 6.2: *Dependence of mean (top) and RMS (bottom) value of* ΔE *distributions in different bins of the DP, for TM (left) and SCF (right) NR signal events. The SCF events are mostly clustered at the corners of the DP. The peak-to-peak spread are small compared to the mean RMS value of the distributions. TM:* $\Delta Mean \sim 4.0\ \mathrm{MeV}$, $\Delta RMS \sim 4.0\ \mathrm{MeV}$, *compared to* $\mathrm{RMS} = 21\ \mathrm{MeV}$. *SCF:* $\Delta Mean \sim 20.0\ \mathrm{MeV}$, $\Delta RMS \sim 12.0\ \mathrm{MeV}$, *compared to* $\mathrm{RMS} = 36\ \mathrm{MeV}$.

6.3.2 Time and Dalitz Plot PDFs

The connection of time and DP dependence leads to rather involved PDFs, both conceptually and technically. It has been implemented in a dedicated multi-dimensional `RooFit` package [104], inserted into a customized class called `PiPiKsTools`. The DP and Δt connection is discussed below for the signal and background components. The different lineshapes used for describing the components entering the signal DP model are discussed in Sec. 2.4.3. The description of the signal DP model is given in Sec. 6.8.

DP-dependent selection efficiency and SCF fraction

Dalitz plot PDFs and DP-averaged quantities, like normalization or SCF fractions, require the knowledge of the DP-dependent relative selection efficiency $\varepsilon = \varepsilon(m', \theta')$. This quantity which is independent of decay dynamics, is obtained from high statistics MC simulation, as shown in Fig. 6.7. Note that the selection efficiency is not charge asymmetric, *i.e.* the selection efficiency map has to be symmetric with respect to $\theta' = 0.5$. The Square Dalitz plane is then folded at $\theta' = 0.5$ in order to increase the available statistics in the selection efficiency calculation. One observes a rather flat efficiency over the main DP. The efficiency drops close to the extreme corners of the DP, which is where two particles are back-to-back, while the third is (almost) at rest, and acceptance is necessarily low due to the minimum p_T requirements for the charged particles.

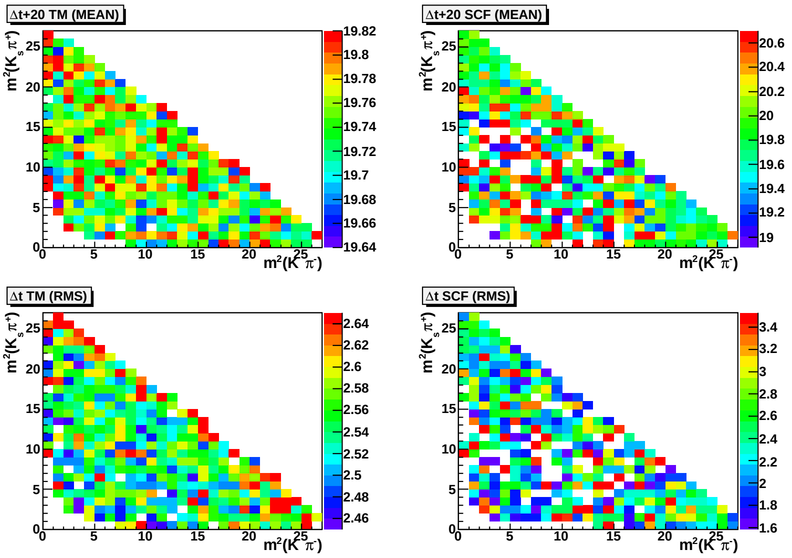

Figure 6.3: *Dependence of mean (top) and RMS (bottom) value of* Δt *distributions in different bins of the DP, for TM (left) and SCF (right) NR signal events. The SCF events are mostly clustered at the corners of the DP. For the TM the peak-to-peak spread are small compared to the mean RMS value of the distributions:* $\Delta Mean \sim 0.2$ ps, $\Delta RMS \sim 0.4$ ps, *compared to* $\mathrm{RMS} = 2.6$ ps*. This is not the case for the SCF:* $\Delta Mean \sim 1.6$ ps, $\Delta RMS \sim 1.8$ ps, *compared to* $\mathrm{RMS} = 2.6$ ps*, but this component represents only a small fraction of the signal events.*

Moreover, the DP term in the likelihood component for TM and SCF signal (cf. Eq. 6.1) must be expanded to account for a DP-dependent SCF fraction $f_{\rm SCF} = f_{\rm SCF}(m', \theta')$. Again, the DP-dependent SCF fraction does not depend on the decay dynamics. For an event i, with Square DP coordinates (m'_i, θ'_i), the TM and SCF PDFs are written as

$$P_{{\rm sig-TM},i} = \varepsilon_i \, (1 - f_{\rm SCF,i}) \, |{\rm det} J_i| \, \frac{|\mathcal{A}^{\pm}(\Delta t)|^2}{\langle |N_{\rm TM}|^2 \rangle} \, , \tag{6.5}$$

$$P_{{\rm sig-SCF},\, i} = \varepsilon_i \, f_{\rm SCF,i} \, |{\rm det} J_i| \, \frac{|\mathcal{A}^{\pm}(\Delta t)|^2}{\langle |N_{\rm SCF}|^2 \rangle} \, , \tag{6.6}$$

where $\varepsilon_i = \varepsilon(m'_i, \theta'_i)$ and $f_{\rm SCF,i} = f_{\rm SCF}(m'_i, \theta'_i)$. The normalization constants $\langle |N_{\rm TM}|^2 \rangle$ and $\langle |N_{\rm SCF}|^2 \rangle$ is the phase space integration, that has to take into account the DP-dependent efficiencies and SCF fractions

$$|N_{\rm TM}|^2 = \sum_{\kappa,\sigma} A^{\kappa} A^{\sigma *} \langle \varepsilon \, (1 - f_{\rm SCF}) \, |{\rm det} J| \, F_{\kappa} F^{*}_{\sigma} \rangle \, , \tag{6.7}$$

$$|N_{\rm SCF}|^2 = \sum_{\kappa,\sigma} A^{\kappa} A^{\sigma *} \langle \varepsilon \, f_{\rm SCF} \, |{\rm det} J| \, F_{\kappa} F^{*}_{\sigma} \rangle \, , \tag{6.8}$$

and similarly for $|\overline{N}_{\rm TM}|^2$ and $|\overline{N}_{\rm SCF}|^2$. The indices κ, σ run over all resonances of the signal model. The expectation values occurring in Eqs. (6.7, 6.8) are model-dependent and are

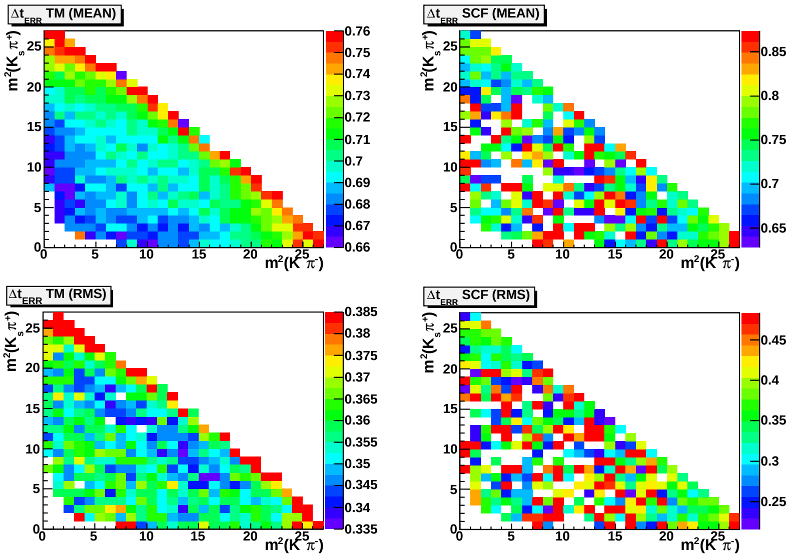

Figure 6.4: *Dependence of mean (top) and RMS (bottom) value of* $\sigma_{\Delta t}$ *distributions in different bins of the DP, for TM (left) and SCF (right) NR signal events. The SCF events are mostly clustered at the corners of the DP. The peak-to-peak spread are small compared to the mean RMS value of the distributions. TM:* $\Delta Mean \sim 0.12$ ps, $\Delta RMS \sim 0.05$ ps, *compared to* $\mathrm{RMS} = 0.8$ ps. *SCF:* $\Delta Mean \sim 0.2$ ps, $\Delta RMS \sim 0.2$ ps, *compared to* $\mathrm{RMS} = 0.9$ ps.

computed with high statistics MC integration over the square DP:

$$\langle \varepsilon\,(1 - f_{\rm SCF})\,|{\rm det}J|\,F_\kappa F_\sigma^*\rangle \;=\; \frac{\int_0^1\int_0^1 \varepsilon\,(1-f_{\rm SCF})\,|{\rm det}J|\,F_\kappa F_\sigma^*\,dm'd\theta'}{\int_0^1\int_0^1 \varepsilon\,|{\rm det}J|\,F_\kappa F_\sigma^*\,dm'd\theta'}\,, \qquad (6.9)$$

and similarly for $\langle \varepsilon\;|{\rm det}J|\;F_\kappa F_\sigma^*\rangle$, where all quantities in the integrands are DP-dependent. Note that the integral (6.9) depends on the lineshapes assumed for the components in the signal model. If parameters on those lineshapes are determined from a fit to data, the determination of Eq. (6.9) would have to be iterative.

DP-averaged SCF fraction

Equation (6.1) invokes the phase space-averaged SCF fraction $\overline{f}_{\rm SCF}$. As for the PDF normalization, this is a decay dynamics-dependent quantity, since it is obtained from an integral of the decay amplitude-squared over the Dalitz plot

$$\overline{f}_{\rm SCF} \;=\; \frac{\int_0^1\int_0^1 \varepsilon\,f_{\rm SCF}\,|{\rm det}J_i|\,|\mathcal{A}^{\pm}(\Delta t)|^2\,dm'd\theta'}{\int_0^1\int_0^1 \varepsilon\,|{\rm det}J_i\,|\mathcal{A}^{\pm}(\Delta t)|^2\,dm'd\theta'}\,. \qquad (6.10)$$

It is computed iteratively, though the remaining systematic uncertainty after one iteration step is usually sufficiently small. The SCF fractions are determined separately for each tagging category from (interfering) MC simulation, weighted by the branching fractions of the contributing signal modes (cf. Table 5.5).

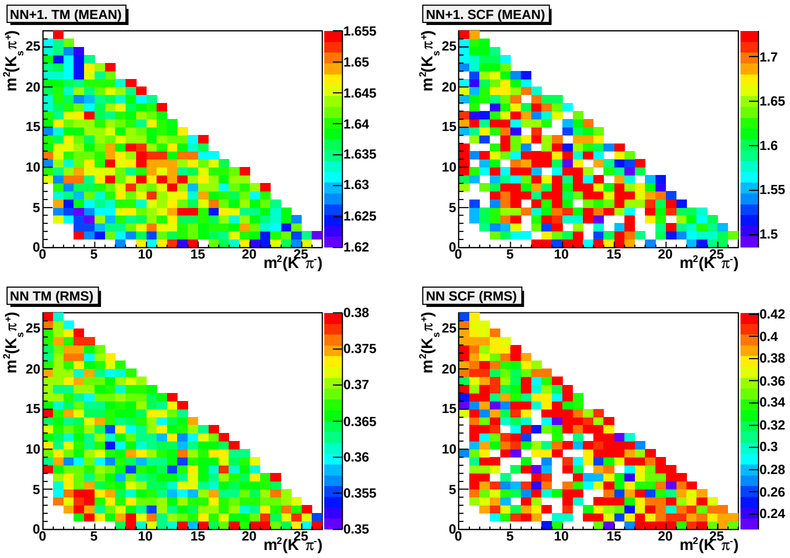

Figure 6.5: *Dependence of mean (top) and RMS (bottom) value of NN distributions in different bins of the DP, for TM (left) and SCF (right) NR signal events. The SCF events are mostly clustered at the corners of the DP. For the TM peak-to-peak spread are small compared to the mean RMS value of the distributions:* $\Delta Mean \sim 0.13$, $\Delta RMS \sim 0.03$, *compared to* $\mathrm{RMS} = 0.36$. *This is not the case for the SCF:* $\Delta Mean \sim 0.2$, $\Delta RMS \sim 0.18$, *compared to* $\mathrm{RMS} = 0.39$, *but this component is only* $\sim 2\%$ *of the signal events.*

TM resolution

The most narrow resonance that is known to contribute the $B^0 \to K^0_S\pi^+\pi^-$ Dalitz plot is $f_0(980)$[1]. The intrinsic width of the dominant $f_0(980)$ resonance expressed in standard deviations of a double Gaussian fit function gives approximately

$$\sigma_{\rm core}(F_{f_0(980)}) \approx 0.5\,\Gamma_{f_0(980)} \approx 20\ \mathrm{MeV}/c^2\ , \tag{6.11}$$

$$\sigma_{\rm tail}(F_{f_0(980)}) \approx 2.0\,\Gamma_{f_0(980)} \approx 80\ \mathrm{MeV}/c^2\ . \tag{6.12}$$

This value can be compared to the mass resolution for TM events ($\sim 8\ \mathrm{MeV}/c^2$ in RMS). Even the worst tail-Gaussian resolution is narrower than the core width of the double Gaussian fit to the $f_0(980)$ lineshape. Therefore, resolution effects in the TM model are not accounted for. A systematical uncertainty stemming from neglecting resolutions, and other reconstruction-related effects, is evaluated using fully-reconstructed samples of simulated signal events (cf. Sec. 6.6).

---

[1] Actually the most narrow resonance in the signal DP model (cf. Sec. 6.8) is the χ_{c0} with a width of $10\ \mathrm{MeV}/c^2$, ~ 5 times smaller than that of $f_0(980)$. This resonance almost does not overlap with the others because it is too narrow and isolated in the DP. As a consequence, the effect in neglecting TM DP migration for this component is expected to yield a negligible effect; in any case a systematic uncertainty is assigned to this effect.

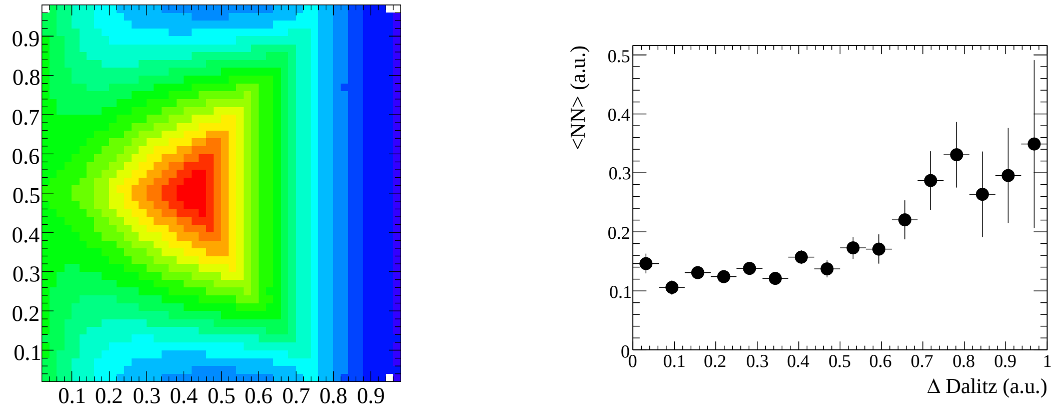

Figure 6.6: *Left: Profile of the* Δ_{Dalitz} *variable in the (square) DP; this variable is defined as the smallest of the three invariant masses, rescaled in the* $(0, 1)$ *range. Right: Average value of Neural Network, for offpeak continuum events, as a function of the* Δ_{Dalitz} *variable. A significant correlation between* NN *and the DP is seen.*

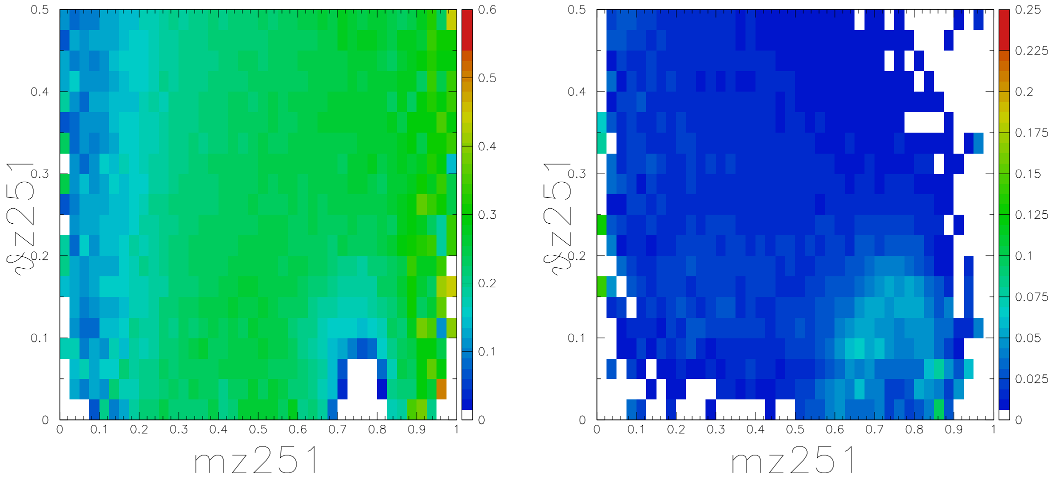

Figure 6.7: *Selection efficiency for TM (left) and SCF (right) events. Note that the selection efficiency is not charge asymmetric, i.e. the selection efficiency map has to be symmetric with respect to* $\theta' = 0.5$*. The Square Dalitz plane is then folded at* $\theta' = 0.5$ *in order to increase the available statistics in the selection efficiency calculation.*

SCF resolution

Misreconstructed events are concentrated in the corners of the Dalitz plot and have a mass resolution that dramatically varies across the DP. In contrast to TM, resolution effects cannot be ignored for SCF events (cf. Figs. 5.9). In order to account for these resolution effects, a

2×2-dimensional convolution function $R_{\rm SCF}(m'_r, \theta'_r, m'_t, \theta'_t)$ is introduced,

$$R_{\rm SCF}(m'_r, \theta'_r, m'_t, \theta'_t) \; , \tag{6.13}$$

which represents the probability to reconstruct at the coordinate (m'_r, θ'_r) an event that has the true coordinate (m'_t, θ'_t). It obeys the unitarity condition

$$\int\limits_0^1 \int\limits_0^1 R_{\rm SCF}(m'_r, \theta'_r, m'_t, \theta'_t)\, dm'_r d\theta'_r \;=\; 1 \; , \qquad \forall \; (m'_t, \theta'_t) \in {\rm SDP} \; . \tag{6.14}$$

The $R_{\rm SCF}$ function is obtained from MC simulation and implemented as a four-dimensional smoothed histogram, computed once and cached during construction of the PDF. Fig. 6.8 shows the resolution function of TM (left) and SCF (right) for two arbitrary generated values of the Square DP coordinates $(m'_t = 0.10, \theta'_t = 0.25)$ and $(m'_t = 0.72, \theta'_t = 0.04)$.

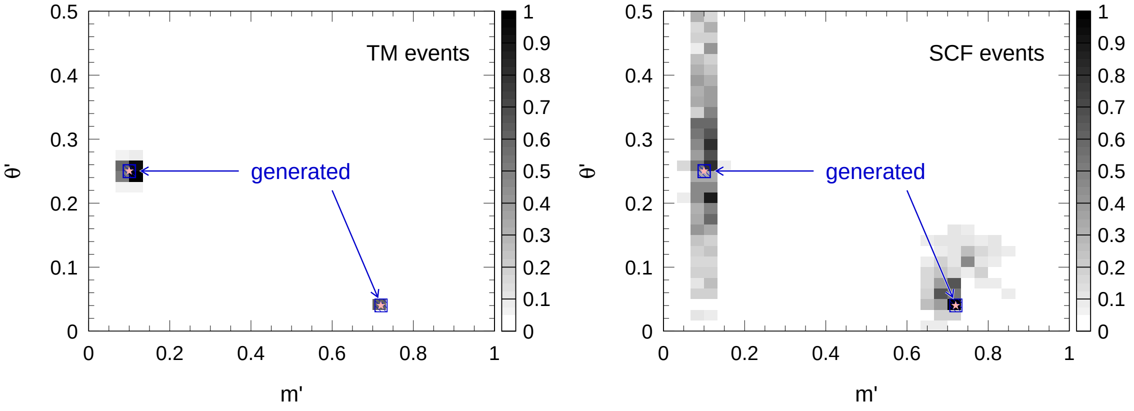

Figure 6.8: *Resolution for TM (left) and SCF (right) events for two chosen generated values in the Square DP, indicated by the open stars (see text for the numerical values).*

Signal parameterization of Δt and Dalitz Plot

The reference distribution for the physical Dalitz plot (efficiency and resolution corrections have been discussed in the previous sections) is obtained from the signal model described in Sec. 2.4.2. It depends on the underlying resonance structure and is connected with Δt via the matrix element (6.5,6.6), which serves as PDF.

Since the PDF deals with measured quantities, the physical time-dependent matrix element is extended to include mistag probabilities and convolved with the Δt resolution $\mathcal{R}_{\rm sig}$.

For an event with tag-flavor $q_{\rm tag}$, true $\Delta t'$ and measured Δt, this leads to:

$$\begin{aligned}
|\mathcal{A}(\Delta t, \sigma_{\Delta t})|^2 &= \frac{e^{-|\Delta t'|/\tau_{B^0}}}{4\tau_{B^0}} \Bigg[1 + q_{\rm tag}\frac{\Delta D^c}{2} - q_{\rm tag}\langle D\rangle^c \frac{|\mathcal{A}|^2 - |\overline{\mathcal{A}}|^2}{|\mathcal{A}|^2 + |\overline{\mathcal{A}}|^2}\cos(\Delta m_d \Delta t') \\
&\qquad + q_{\rm tag}\langle D\rangle^c \frac{2{\rm Im}\left[\overline{\mathcal{A}}\mathcal{A}^*\right]}{|\mathcal{A}|^2 + |\overline{\mathcal{A}}|^2}\sin(\Delta m_d \Delta t') \\
&\qquad \Bigg] \otimes \mathcal{R}_{\rm sig}(\Delta t' - \Delta t, \sigma_{\Delta t}) \, , \qquad (6.15)
\end{aligned}$$

where $\langle D\rangle^c$ and ΔD^c are the tagging-category-specific average and difference of the tagging dilutions defined in Eq.(5.2) with the (tagging category dependent) mistag rates ω^c and $\overline{\omega}^c$ for B^0 and $\bar{B}^0$ tags, respectively. In the last formula, and in the following, the DP dependence of amplitudes is implicit: $\mathcal{A} = \mathcal{A}(\rm DP)$. As mentioned previously, it has been assumed that CP violation in mixing can be neglected ($|q/p| \approx 1$), and the amplitude parameterization uses a convention where the phase from the $B^0\bar{B}^0$ mixing is absorbed into the $\bar{B}^0$ decay amplitude, $e^{-2i\beta}\bar{\mathcal{A}} \rightarrow \bar{\mathcal{A}}$.

The resolution model that incorporates the finite vertex resolution has been described in Sec. 5.4.3. The biases and relevant scale factors were measured in a so-called `BReco` sample [105], which is a set of fully reconstructed B decay events with a high signal/background ratio. They are given together with values obtained for comparison purposes from MC simulation. The core biases depend on the tagging category c (not indicated in Eq. (5.5)). These parameters are fixed in the fit. A list of their values is given in Appendix C.

6.3.3 B background parameterization

The DP- and Δt-dependent PDFs factorize for the charged B-background modes, but not for the neutral B-background due to $B^0\bar{B}^0$ mixing.

Charged B-background

The charged B-background contribution to the likelihood (6.1) invokes the parameter $A_{B^+,{\rm tag}}$, multiplied by the tag flavor $q_{\rm tag}$ of the event. In the presence of significant tag-“charge” correlation (denoting an effective tag-versus-Dalitz coordinate correlation), it parameterizes possible direct CPV in these events. To parameterizes the tag-“charge” correlation, a distinct square DP PDF for each reconstructed B flavor tag is used, while a tag-averaged PDF is used for untagged events. The DP-dependent PDF (from which the time dependence factorizes) reads

$$\begin{aligned}
P^c_{B^+,ij}({\rm DP}_i) &= (1 + q_{{\rm tag},i}A_{B^+,{\rm tag},j})\,(1-\omega^c)P^c_{B^+j}({\rm DP}_i, q_{\rm tag,i}) \\
&\quad + (1 - q_{{\rm tag},i}A_{B^+,{\rm tag},j})\,\omega^c P^c_{B^+j}({\rm DP}_i, -q_{\rm tag,i}) \qquad (6.16)
\end{aligned}$$

where ω^c are the tagging-category-specific mistag probabilities defined in Eqs. (5.2). The `BReco` values [106] for charged B decays are used, while tagging efficiencies are obtained from MC. The PDFs $P^c_{B^+,j}(\mathrm{DP}, \pm q_{\mathrm{tag}})$ are obtained from MC simulation requiring the true B flavor. Smoothed Keys histograms are used as parameterization (cf. Appendix A, Sec. A.3).

Since the tag-“charge” correlation is implemented in the DP PDF, the Δt PDF for B^+ background class j is simply given by the exponential decay rate

$$P_{B^+,ij}(\Delta t) \;=\; e^{-|\Delta t|/\tau_j} \otimes \mathcal{R}_{\mathrm{sig}}(\Delta t' - \Delta t, \sigma_{\Delta t}) \;, \tag{6.17}$$

where τ_j is an effective lifetime, with a value very close to τ_{B^+}. The resolution function $\mathcal{R}$ is similar to the one used for the signal (see (Eq. 5.5)). In cases where secondary vertices occur, *e.g.*, in D decays, the effective lifetime and/or resolution can be significantly altered.

Neutral B-background

The Neutral B background in Eq. (6.1) is parameterized using tag-dependent PDFs. Neutral B backgrounds are classified in three categories. Concerning CP-eigenstates, correlation between the tag and the Dalitz coordinate are of detector/reconstruction origin and expected to be small. Non-CP eigenstates may exhibit tag-“charge” correlation. Moreover, both types of decays can have direct and mixing-induced CPV. The third class of neutral B decays involves charged kaons and hence does not exhibit mixing-induced CPV, but instead exhibits a strong tag-“charge” correlation, because it consists of B-flavor eigenstates.

Since neutral B mesons oscillate, a treatment as for charged B background, using effective lifetimes as part of the resolution model, is not possible. Therefore, mode-specific resolution parameters are applied. The following combined Δt and DP PDF for an event with tag q_{tag} is built:

$$\begin{aligned}
P^c_{B^0,ij}(\Delta t_i, \sigma_{\Delta t,i}, \mathrm{DP}_i) \;=\;& (1 + a_{cp,j}\, q_{\mathrm{tag}}) \cdot \left(|A_{B^0,j}|^2 + |\overline{A}_{B^0,j}|^2\right) \cdot \frac{e^{-|\Delta t'|/\tau_j}}{4\tau_j} \\
& \times \Bigg[1 + q_{\mathrm{tag}} \frac{\Delta D^c_j}{2} + q_{\mathrm{tag}} \langle D^c_j \rangle \,(S_j + \Delta S_j) \sin(\Delta m_d \Delta t'_i) \\
& - q_{\mathrm{tag}} \langle D^c_j \rangle \left(C_j + \frac{|A_{B^0,j}|^2 - |\overline{A}_{B^0,j}|^2}{|A_{B^0,j}|^2 + |\overline{A}_{B^0,j}|^2} \Delta C_j \right) \cos(\Delta m_d \Delta t'_i) \\
& \Bigg] \otimes \mathcal{R}_{\mathrm{sig}}(\Delta t'_i - \Delta t_i, \sigma_{\Delta t,i}) \;,
\end{aligned} \tag{6.18}$$

where the $\langle D^c_j \rangle$ and ΔD^c_j are the tag dilutions in category c and B-background class j (cf. Eq. (5.2)). They are obtained from MC simulation. $a_{cp,j}$ is the overall tag asymmetry for B-background class j. Usually “charge” asymmetry and “charge”-dependent mixing-induced CPV are introduced into the PDF model. The parameters C_j, S_j and ΔS_j in class j are unknown in general. When this is the case they are set to zero in the nominal model. They are varied in an allowed range for systematic studies. The situation is different for the tag-”charge” correlation parameter ΔC_j. For most of the modes, tag-charge correlation in the

Dalitz plot can be reliably taken from MC simulation, via the coefficient in front of the ΔC_j, where the amplitude moduli-squared are simply the normalized DP distributions in B^0 and $\bar{B}^0$ decays. The values of a_{cp}, C, ΔC, S and ΔS, used for each class of neutral B background in the nominal fit are summarized in Table 6.3. Errors quoted in the table refer to shifts in the parameter used to evaluate the systematic effect. The DP PDFs are obtained from smoothed histograms of MC-simulated events.

Note that the physical parameters in the time-dependent PDF are diluted by the (mostly) incomplete reconstruction of B-background events.

	a_{cp}	C	ΔC	S	ΔS
$D^-\pi^+$	0 ± 0.04	0	$1.$	0	0
$J/\psi K^0_S$	0 ± 0.03	0	0	0.697 ± 0.041	0
$\eta^{\prime} K^0_S$	0 ± 0.13	0	0	0.43 ± 0.17	0
Neutral Generic	0 ± 0.6	$0 \pm 1.$	0 ± 0.6	0 ± 0.6	0 ± 0.6
$\psi(2S) K^0_S$	0 ± 0.07	0	0	0.8893 ± 0.119	0
$a_1^+\pi^-$	-0.07 ± 0.07	-0.10 ± 0.17	0.26 ± 0.17	0.37 ± 0.22	-0.14 ± 0.22
B-Bkg. Cat. 1	0 ± 0.1	0	1	0	0
B-Bkg. Cat. 2	0 ± 0.04	0	1	0	0
B-Bkg. Cat. 3	0 ± 0.12	0	1	0	0

Table 6.3: *Values of a_{cp}, C, ΔC, S and ΔS, used for each class of neutral B background in the nominal fit. Quoted errors refer to the shift of the parameter used to evaluate the systematic effect.*

Figures in Appendix A.3 show all bi-dimensional DP PDFs used for the charged and neutral B-background components.

6.3.4 Continuum parameterization

The Dalitz Plot

The Dalitz plot treatment continuum events is similar to the one used for charged B background (6.16), with mistag probabilities set to zero. In particular, DP and Δt PDFs factorize. The continuum contribution to the likelihood (6.1) invokes the parameter $A_{q\bar{q},\mathrm{tag}}$, multiplied by the tag flavor q_{tag} of the event. It parameterizes a possible direct CPV in these events and is determined by the fit. A tag-averaged PDF for all tagging categories is used. This PDF is symmetrized with respect to θ' (as in the case of the selection signal efficiency, see Fig. 6.7) so that the CPV information is only contained in the $A_{q\bar{q},\mathrm{tag}}$ parameter.

The square DP PDF for continuum events is obtained from off-resonance data using signal region (SR) and grand m_{ES} and ΔE sidebands (cf. Sec. 5.7). To increase the available statistics, sideband on-resonance events are also included. Since this empirical shape is non-parametric, its precise shape can not be determined from the fit to the final data sample, and so the validity of the sideband extrapolation has to be tested. This introduces systematic uncertainties, which will be accounted for in Sec. 7.3. The square DP is broken into regions and smoothed using different smoothing parameters for each region, as there are peaking structures of different widths (i.e. peaks in the ρ^0, K^* bands due to real ρ^0s and K^*s). Fig. 6.9 shows the DP PDF used for the continuum.

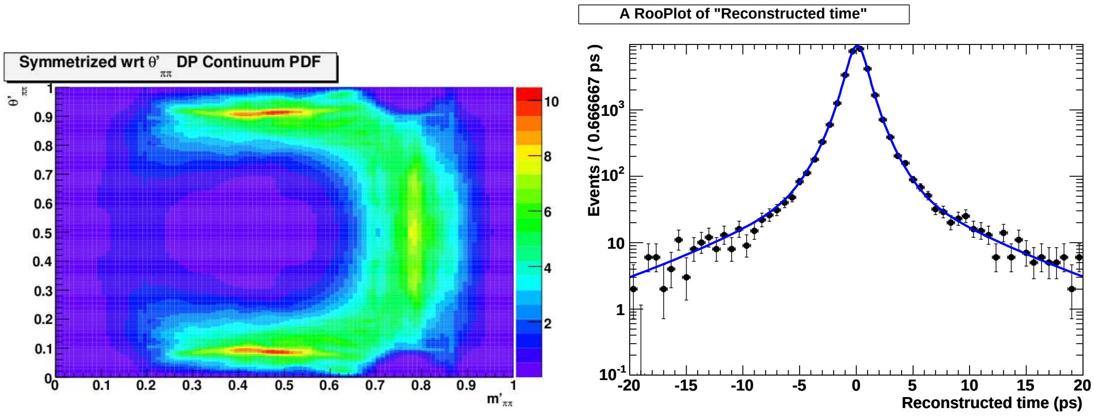

Figure 6.9: *Left: Continuum DP PDF, symmetrized with respect to* $\theta' = 0.5$. *Right: Fit to the continuum* Δt *to the off-resonance data.*

The Δt PDF

The continuum Δt PDF is parameterized as the sum of three Gaussian distributions with common mean (which has the unit of time), two relative fractions, and three distinct widths (without units) that scale the Δt event-by-event error, $\sigma_{\Delta t}$, yielding six free parameters:

$$\begin{aligned} P_{q\bar{q},i}(\Delta t, \sigma_{\Delta t}) &= (1 - f_{\text{tail}} - f_{\text{out}}) \cdot G\left(\Delta t, \mu, s_{\text{core}}\sigma_{\Delta t}\right) \\ &\quad + f_{\text{tail}} \cdot G\left(\Delta t, \mu, s_{\text{tail}}\sigma_{\Delta t}\right) \\ &\quad + f_{\text{out}} \cdot G\left(\Delta t, \mu, s_{\text{out}}\sigma_{\Delta t}\right) \ . \end{aligned} \tag{6.19}$$

The model is motivated by the observation [107] that the Δt average is independent of $\sigma_{\Delta t}$, and that the Δt RMS depends linearly on $\sigma_{\Delta t}$. The fit of Δt to the off-resonance data is given in the right hand plot of Fig. 6.9.

6.4 Validation of fit performance with toy studies

The extraction of physical parameters is tested in simulation by means of toy pseudo-experiments. A "toy" experiment is a data sample produced with a simplified Monte Carlo generation, whose output are random data samples with the likelihood variables, following the PDF defined in Eq. 6.1. A validation study of the likelihood function can be performed, either as a function of the fitted isobar parameters, or in terms of the direct CP asymmetries, phase differences and branching fractions. Two different sets of tests have been undertaken:

- High-statistics, signal-only toy experiments, which allow one to disentangle intrinsic features of the model from statistical effects.

- More realistic toys, with Continuum and B-background components, and a signal DP model including the components from which uncontroversial signal were observed in Q2B analyses ($f_0(980)K^0_S$, $\rho^0(770)K^0_S$, $K^{*\pm}(892)\pi^{\mp}$ and $(K\pi)^{*\pm}_0\pi^{\mp}$ [2]).

The randomization method

For all these toy experiments, toy datasets are generated and fitted with various models. Initial values of the amplitude parameters are randomized before the fit in the following way:

- For moduli, the randomization uses a flat distribution within 0.1 - 2.0 times the generated module.
- For phases, the randomization uses a flat distribution in the interval $(-\pi, \pi)$.

6.4.1 Signal-only high statistics toys

As a first study, a simple model, made only of one resonance, is considered. Other components are then added one by one. Toy data sets are generated using the values of physical parameters described in Table 6.4. Fig. 2.3 shows the distribution over the DP for a signal model with the components enumerated in Table 6.4, illustrating their location and interference. After translating the Q2B quantities into moduli and phases of the isobar amplitudes, the generation of the dataset is performed. As the normalized likelihood function depends only on ratios of isobar amplitudes, one c_i or $\bar{c}_i$ has to be fixed in the fit. The choice of a particular fixed component is a convention that has no physical consequence. This property has been checked with toys : values of fitted Q2B parameters are independent of convention. In the following the $c(B^0 \to f_0(980)K^0_S)$ isobar amplitude is fixed to be real, with modulus 4.

One resonance model

Several independent toy data samples of $f_0(980)K^0_S$ decays, with 4K signal events each, are generated. For each sample, the $2\beta_{eff}(f_0(980)K^0_S)$ parameter is fitted. In the absence of other resonances to interfere with, mirror solutions can not be disentangled from the true solution. This is shown in Fig. 6.10, where the output value of $2\beta_{eff}(f_0(980)K^0_S)$ is given as a function of the generation value. For each generated value, the fit can converge on two distinct points, with approximately the same probability; this happens because the likelihood function has two equivalent minima in these values. This can be seen in Fig. 6.11, which shows the distribution of fitted values for the $2\beta_{eff}(f_0(980)K^0_S)$ parameter, for a single toy data sample fitted several times with random initial values of the isobar amplitudes. There are two equivalents peaks located at the generated value (blue) and at the mirror solution (red), the distribution of $-log(L)$ at minimum showing only one peak, indicating that the likelihood function has two equivalent minima. There is a complete degeneracy in this case.

---

[2] The notation of the $B^{\pm} \to K^{\pm}\pi^{\mp}\pi^{\pm}$ [34] and $B^0 \to K^{\pm}\pi^{\mp}\pi^0$ [40] papers is followed here.

Nominal Values	
$C(f_0(980)K_S^0)$	-0.05
$S(f_0(980)K_S^0)$	-0.75
$2\beta_{eff}(f_0(980)K_S^0)$	49.0
$BF(f_0(980)K_S^0)$	0.16
$C(\rho^0(770)K_S^0)$	+0.05
$S(\rho^0(770)K_S^0)$	+0.65
$2\beta_{eff}(\rho^{(}770)K_S^0)$	41.0
$BF(\rho^0(770)K_S^0)$	0.10
$A_{CP}(K^{*\pm}(892)\pi^{\mp})$	-0.10
$\Delta\phi(K^{*+}(892)\pi^-, K^{*-}(892)\pi^+)$	0.0
$BF(K^{*\pm}(892)\pi^{\mp})$	0.27
$A_{CP}(K^{*\pm}(1430)\pi^{\mp})$	0.0
$\Delta\phi(K^{*+}(1430)\pi^-, K^{*-}(1430)\pi^+)$	0.0
$BF(K^{*\pm}(1430)\pi^{\mp})$	0.48
$\Delta\phi(\rho^0(770)K_S^0, f_0(980)K_S^0)$	40.0

Table 6.4: *Nominal values of physical parameters for the generation of the data sets for the toy studies. Phases are in degrees.*

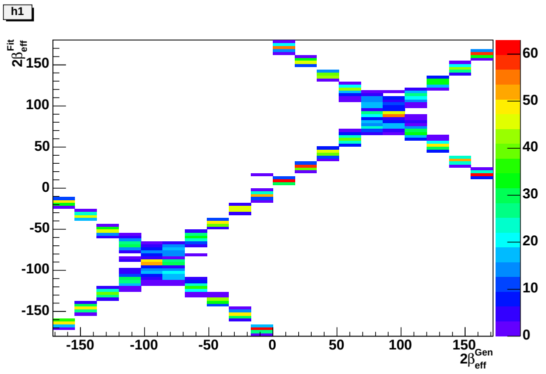

Figure 6.10: *Scan in the parameter $2\beta_{eff}(f_0(980)K_S^0)$ for the one resonance model ($f_0(980)K_S^0$). This is a scan with 20 values within (-180, 180) degrees. The horizontal and vertical axis show the generated and fitted values, respectively.*

Two resonance model

The $\rho^0(770)K_S^0$ intermediate state is added to the Dalitz model used in the previous section. There are then two resonances in the model. A similar toy MC study is performed, on several independent samples containing 6.5K events each. In these fits, three additional parameters can be determined: $2\beta_{eff}(\rho^0(770)K_S^0)$, $\Delta\phi(f_0(980), \rho^0(770))$, and $C(\rho^0(770)K_S^0)$. Fig. 6.12 shows three different scans of $2\beta_{eff}(f_0(980)K_S^0)$, for three different, arbitrary values of $\Delta\phi(f_0(980), \rho^0(770))$. In this case, the mirror solution is disfavored, as the fit does converge more often on the true solution. This feature is further illustrated by performing randomized fits to a single dataset, whose results are shown in Fig. 6.13. The left hand

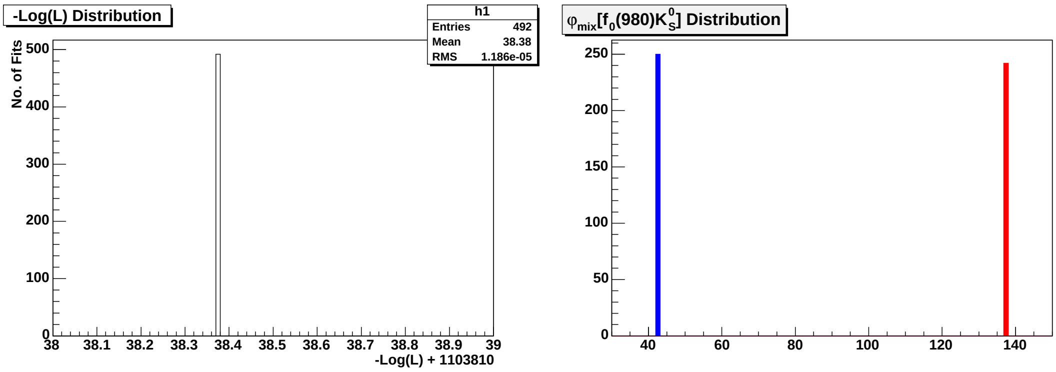

Figure 6.11: *Distributions of NLL (negative log likelihood, $-log(L)$) (left) and $2\beta_{eff}(f_0(980)K^0_S)$ (right) at minima for randomized fits to one data set for the one resonance model with the $f_0(980)K^0_S$ intermediate state. In the right hand plot the peak in blue is the angle corresponding to the generated value (42 degrees) and in red peak corresponds to the degenerated mirror solution (138 degrees).*

plot shows the distribution of $-log(\mathcal{L})$ at minimum. In this case there are two peaks very well separated by 4100 units of likelihood (this big difference stems from the high statistics, and absence of backgrounds, in the toy sample used). 78% of the fits converge to the global minimum of $-log(\mathcal{L})$ (in blue), at a value corresponding to the generated value of $2\beta_{eff}(f_0(980)K^0_S)$. The remaining 22% of the fits converge to the local minimum (in red), at a value corresponding to the now non-degenerated mirror solution. The interference pattern between different intermediate states helps in raising the degeneracy of the solution.

Scans in $\Delta\phi(f_0(980), \rho^0(770))$ and $C_{f_0(980)K^0_S}$ are shown in Fig. 6.14. For these parameters, a single solution for the fitted value is found for all the scan values. In the case of the $C_{f_0(980)K^0_S}$ scan, the distribution tends to be narrower in the regions close to the limits of this parameters, as $C_{f_0(980)K^0_S}$ is bound to lie in the $(-1, 1)$ interval.

Four resonance model

As a further step with respect to the previous section, the $K^{*\pm}(892)\pi^{\mp}$ intermediate state to the Dalitz model is now added. This time, 10K events are generated for each toy data sample are generated. In this case, there are eight parameters to fit for, the additional ones being $\Delta\phi(K^{*\pm}(892)\pi^{\mp})$ and $A_{CP}(K^{*+}(892)\pi^-, K^{*-}(892)\pi^+)$. Fig. 6.15 shows the scans for several of the unknown parameters. For $\Delta\phi(f_0(980), \rho^0(770))$, no mirror solution is found. On the other hand, $2\beta_{eff}(f_0(980)K^0_S)$, $\Delta\phi(f_0(980), K^{*+}(892))$ and $\Delta\phi(f_0(980), K^{*-}(892))$ parameters are affected by mirror solutions, identified as local maxima of the likelihood function. Comparing the output of this test to the result of the previous section, one concludes that the additional intermediate state in the Dalitz model helps in reducing the degeneracy of the mirror solutions. As an additional test on the impact of including the $K^{*\pm}(892)\pi^{\mp}$, randomized fits to the same data set are performed, as shown in Fig. 6.16. The left plot shows the distribution of $-log(\mathcal{L})$ at minimum. Two well defined peaks, separated by 2800 units

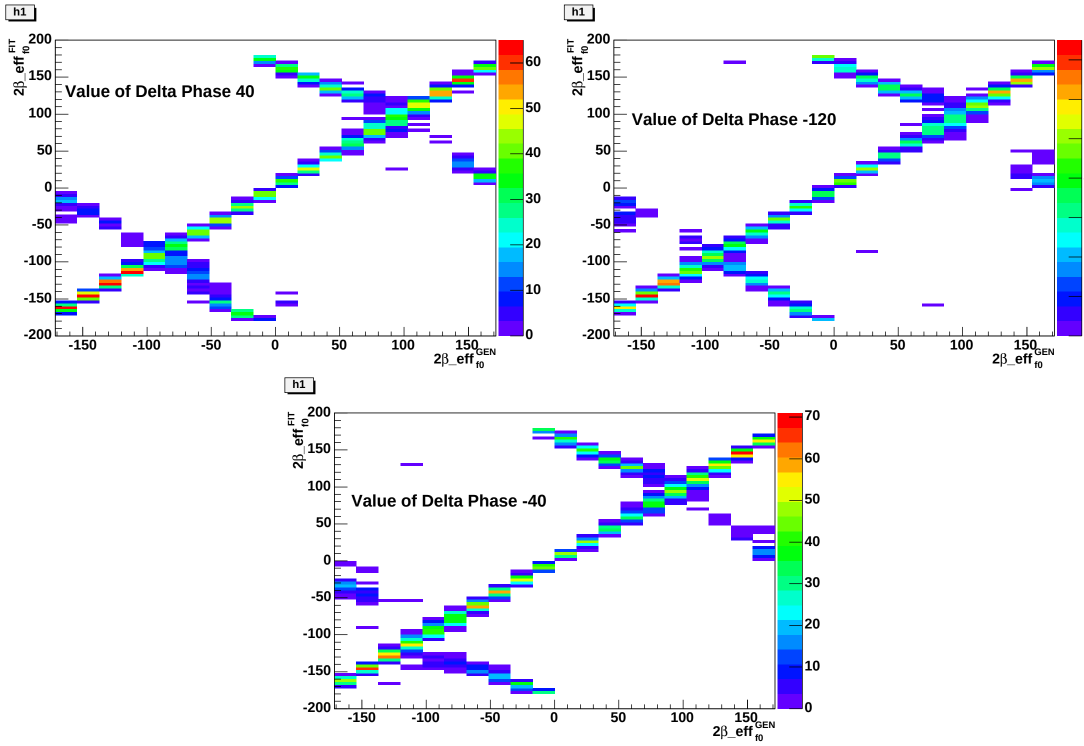

Figure 6.12: *Scan for 20 values in the range* $(-180, 180)$ *in the parameter* $2\beta_{eff}(f_0(980)K_S^0)$ *for the two intermediate state model (*$f_0(980)$ *and* $\rho^0(770)$*). The horizontal and vertical axis show the generated and fitted values, respectively. The (upper left), (upper right) and (lower left) plots are the scans for values of* $\Delta\phi(f_0(980), \rho^0(770))$ *of 40, -120 and -40 degrees, respectively.*

of likelihood, are observed. The fit converges to the global minimum $-log(\mathcal{L})$ in 82% of the cases (shown in blue in the plot). This minimum corresponds to the generated value of $2\beta_{eff}(f_0(980)K_S^0)$. The remaining 18% of the fits converged to the local minimum (in red).

The conclusion that stems from this last study is that the inclusion of the $K^{*\pm}(892)\pi^{\mp}$ intermediate state helps, but not as significantly as the $\rho^0(770)K_S^0$, in raising the degeneracy on the $2\beta_{\rm eff}$ parameter for $f_0(980)K_S^0$. This is not unexpected, as the interference region of the $f_0(980)K_S^0$ with the $\rho^0(770)K_S^0$ is larger compared with that of the $K^{*\pm}(892)\pi^{\mp}$, which occurs only at the corners of the Dalitz Plot (cf. Fig. 2.3).

In principle, a further test could have been performed, adding the $(K\pi)_0^{*\pm}\pi^{\mp}$ S-wave to the Dalitz model in order to check for further degeneracies. Since the interference pattern of this component is similar to that of $K^{*\pm}(892)\pi^{\mp}$, it is expected that its addition provides further improvement, by decreasing the percentage of fits converging to the mirror solution.

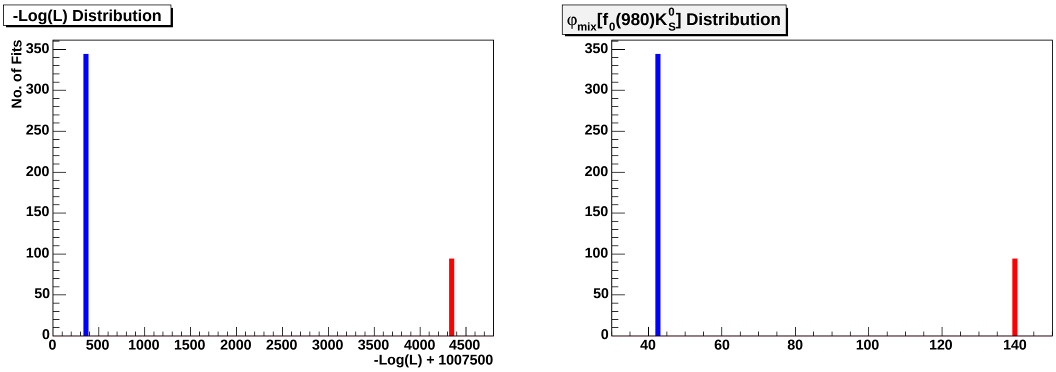

Figure 6.13: *Distributions of* $-log(\mathcal{L})$ *(shifted to zero) (left) and* $2\beta_{eff}(f_0(980)K_S^0)$ *(right) at minimum for randomized fits to one data set for the model of* $f_0(980)K_S^0$ *and* $\rho^0(770)K_S^0$ *intermediate states. In these plots peaks of the same color correspond mutually. In the right hand plot in blue peak corresponds to the generated value (42 degrees) and the red peak corresponds to the now non-degenerated mirror solution (138 degrees).*

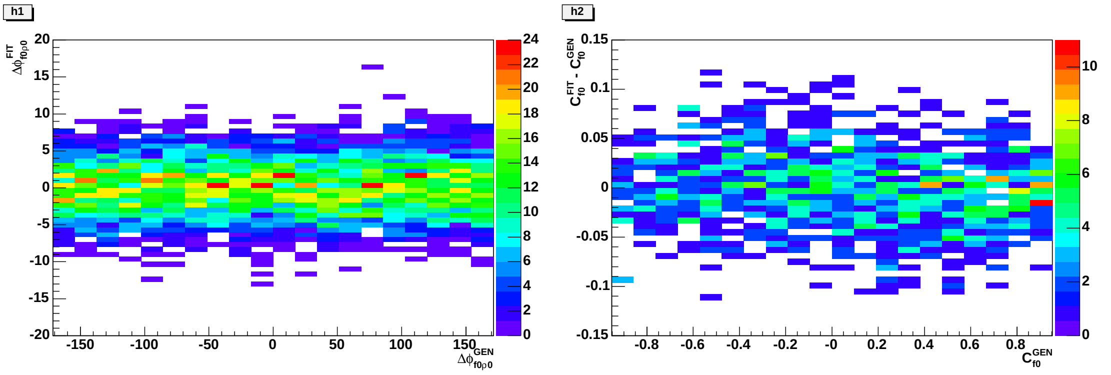

Figure 6.14: *Scan for 20 values in the range (-180, 180) for* $\Delta\phi(f_0(980), \rho^0(770))$ *(left) and in the range (-1,1) for* C_{f_0} *(right) for the two resonances model (*$f_0(980)K_S^0$ *and* $\rho^0(770)K_S^0$*). The horizontal and vertical axis show the generated value and the difference between the fitted and generated values, respectively.*

6.4.2 Realistic toys with signal, continuum and B background components

As a second step, more realistic toys are generated, including continuum and B-background components. Each toy was generated using the expected yield on the data sample: 2200 signal events, 14200 continuum background, 5470 neutral B-background events, split into 5 classes ($J/\psi K_S^0$, $\psi(2S)K_S^0$, $D\pi$, $\eta' K_S^0$ and Neutral Generic) and 280 charged events treated as a single class (charged generic). The number of events per species are generated at random, following a Poisson distribution, and event distributions with respect to the fit variables are generated with the PDFs of the corresponding component.

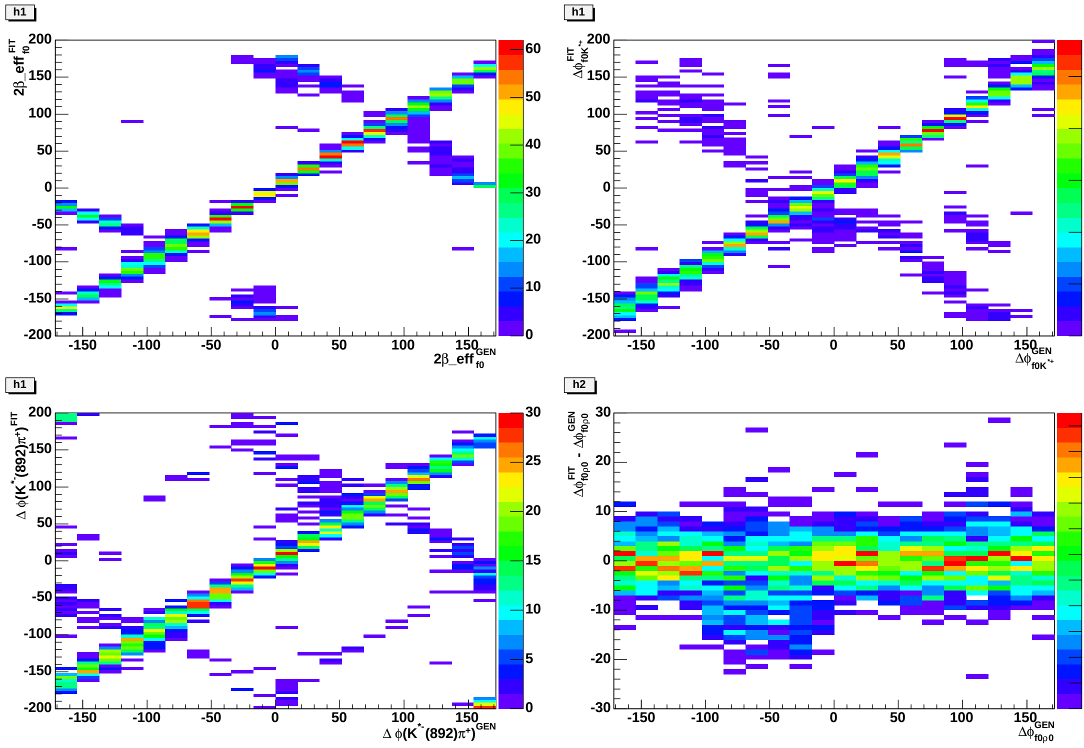

Figure 6.15: *Scan for 20 values in the range (-180, 180) for* $2\beta_{eff}(f_0(980)K^0_S)$ *(upper left),* $\Delta\phi(f_0(980), K^{*+}(892))$ *(upper right),* $\Delta\phi(f_0(980), K^{*-}(892))$ *(lower left) and* $\Delta\phi(f_0(980), \rho^0(770))$ *(lower right) for the four intermediate states model (*$f_0(980)K^0_S$*,* $\rho^0(770)K^0_S$ *and* $K^{*\pm}(892)\pi^{\mp}$*). For the* $2\beta_{eff}(f_0(980)K^0_S)$*,* $\Delta\phi(f_0(980), K^{*+}(892))$ *and* $\Delta\phi(f_0(980), K^{*-}(892))$ *the horizontal and vertical axes represent the generated and fitted values, respectively. For the scan in* $\Delta\phi(f_0(980), \rho^0(770))$*, the horizontal and vertical axes represent the generated and fitted minus generated values, respectively.*

For the signal, the model contains six intermediate states : $f_0(980)K^0_S$, $\rho^0(770)K^0_S$, $K^{*\mp}(892)\pi^{\pm}$ and $(K\pi)^{*\mp}_0\pi^{\pm}$ S-wave. The signal fit parameters are : a global signal yield and all relative modules and phases of isobar amplitudes. The generation values for the isobar amplitudes are obtained from the values of physical parameters on Tab. 6.4. Continuum background yield is fitted simultaneously with the signal yield. Charmless and charmed B-background yields are fixed at expectation values (which are evaluated using world averages for the branching fractions, and efficiencies from MC). The complete list of fit parameters used in this fit configuration is detailed in Table 6.5.

Local minima solutions have been observed in several previous Dalitz analysis. This feature can be illustrated in $B^0 \rightarrow K_S\pi^+\pi^-$ analysis, by means of fits to a full toy dataset, generated with a signal model as described in the last paragraph. When Maximum Likelihood fits with randomized starting values are performed, a fraction of the fits end up converging to solutions (local minima) with larger values of $-log(\mathcal{L})$, as shown in the likelihood distributions shown in Fig. 6.17.

Parameter	Description	Value
$N_{K^0_S\pi^+\pi^-}$	Number of $B \to K^0_S\pi^+\pi^-$ events	2200
$N_{q\bar{q}}(tagKaon1)$	Continuum events in tagging Kaon1	801
$N_{q\bar{q}}(tagKaon2)$	Continuum events in tagging Kaon2	2133
$N_{q\bar{q}}(tagKaonPion)$	Continuum events in tagging KaonPion	1780
$N_{q\bar{q}}(tagLepton)$	Continuum events in tagging Lepton	47
$N_{q\bar{q}}(tagOther)$	Continuum events in tagging Other	1620
$N_{q\bar{q}}(tagPion)$	Continuum events in tagging Pion	2032
$N_{q\bar{q}}(Notag)$	Continuum events in Notag	5787
$N_{Continuum}$	Total Number of continuum events	14200
$N_{B\overline{B}}$	Number B Background events	5750
$A_{B^0\to f_0(980)K^0_S}$	Magnitude of the amplitude of $B^0 \to f_0(980)K^0_S$	1.0 (fixed)
$\phi_{B^0\to f_0(980)K^0_S}$	phase of the amplitude of $B^0 \to f_0(980)K^0_S$	0.0 (fixed)
$A_{\overline{B}^0\to f_0(980)K^0_S}$	Magnitude of the amplitude of $\overline{B}^0 \to f_0(980)K^0_S$	1.051
$\phi_{\overline{B}^0\to f_0(980)K^0_S}$	phase of the amplitude of $\overline{B}^0 \to f_0(980)K^0_S$	-49
$A_{B^0\to\rho^0(770)K^0_S}$	Magnitude of the amplitude of $B^0 \to \rho 0(770)K^0_S$	0.092
$\phi_{B^0\to\rho 0(770)K^0_S}$	phase of the amplitude of $B^0 \to \rho 0(770)K^0_S$	-40
$A_{\overline{B}^0\to\rho 0(770)K^0_S}$	Magnitude of the amplitude of $\overline{B}^0 \to \rho 0(770)K^0_S$	0.087
$\phi_{\overline{B}^0\to\rho 0(770)K^0_S}$	phase of the amplitude of $\overline{B}^0 \to \rho 0(770)K^0_S$	-81
$A_{B^0\to K^*(892)^+\pi^-}$	Magnitude of the amplitude of $B^0 \to K^*(892)^+\pi^-$	0.158
$\phi_{B^0\to K^*(892)^+\pi^-}$	phase of the amplitude of $B^0 \to K^*(892)^+\pi^-$	-40
$A_{\overline{B}^0\to K^*(892)^-\pi^+}$	Magnitude of the amplitude of $\overline{B}^0 \to K^*(892)^-\pi^+$	0.175
$\phi_{\overline{B}^0\to K^*(892)^-\pi^+}$	phase of the amplitude of $\overline{B}^0 \to K^*(892)^+\pi^-$	-40
$A_{B^0\to K^{0*}(1430)^+\pi^-}$	Magnitude of the amplitude of $B^0 \to K^{0*}(1430)^+\pi^-$	5.964
$\phi_{B^0\to K^{0*}(1430)^+\pi^-}$	phase of the amplitude of $B^0 \to K^{0*}(1430)^+\pi^-$	-57
$A_{\overline{B}^0\to K^{0*}(1430)^-\pi^+}$	Magnitude of the amplitude of $\overline{B}^0 \to K^{0*}(1430)^-\pi^+$	5.964
$\phi_{\overline{B}^0\to K^{0*}(1430)^-\pi^+}$	phase of the amplitude of $\overline{B}^0 \to K^{0*}(1430)^+\pi^-$	-68

Table 6.5: *Parameters and their input values that are used in the toy experiments. Parameters are free to vary in the fit unless stated* fixed*. In total, there are 26 floating parameters in the fit.*

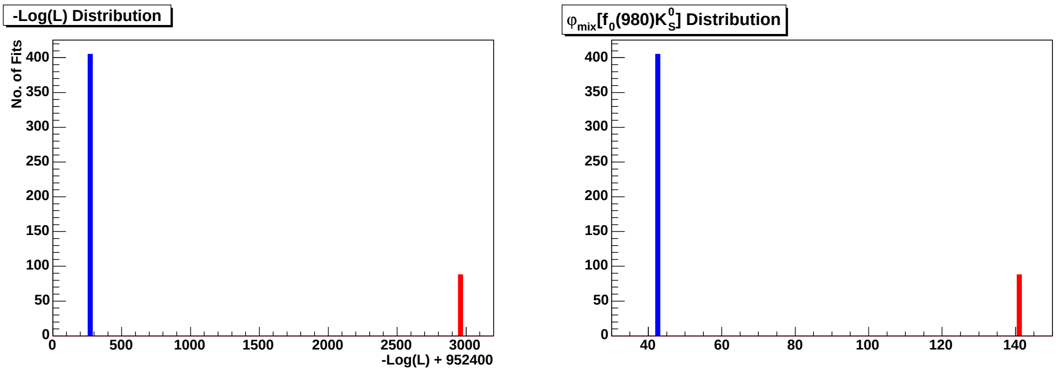

Figure 6.16: *Distributions of $-log(\mathcal{L})$ (left) and $2\beta_{eff}(f_0(980)K^0_S)$ (right) at minimum for randomized fits to one data set for the model of $f_0(980)K^0_S$, $\rho^0(770)K^0_S$ and $K^{*\pm}(892)\pi^\mp$ intermediate states. In these plots peaks of the same color correspond mutually. In the right hand plot the peak in blue corresponds to the generated value (42 degrees) and the red peak corresponds to the now non-degenerate mirror solution (138 degrees).*

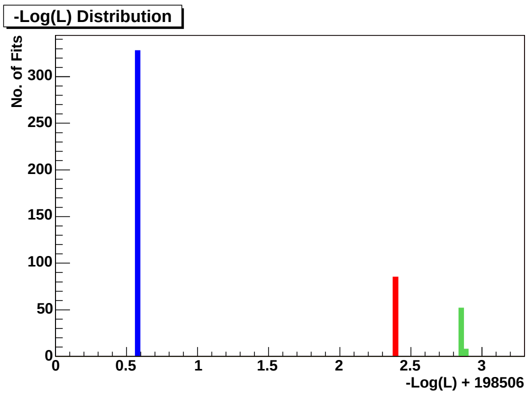

Figure 6.17: *Distributions of $-log(\mathcal{L})$ at minimum for randomized fits to one data set generated with the signal model described in the text, and Continuum and B-background components.*

Three minima of the likelihood function can be observed. 71% of the fits converged to the global minimum (in blue), but 18% (in red) and 11% (in green) of the fits converged to other local minima. The global minimum is separated from the others two by 2.0 units of likelihood, and the local minima are separated from each other by a half of unit. Thus, several randomized fits to data need to be performed, to make sure the global minimum is properly identified. The distributions for several parameters are shown in the Fig. 6.18 and Fig. 6.19. A color code indicates the different solutions, *e.g.* entries in blue correspond to fits that converged in the global minimum. The entries below each narrow likelihood peak yield identical results. Fitted parameters usually yield very similar values in all three solutions, the differences are much smaller than the statistical errors; the exceptions are the values of phases, for which the mirror solutions can lie far away from each other. In other words, while event rates (*i.e.* fit fractions) and direct CP asymmetries, are well constrained by the likelihood fit, the sensitivity to interference patterns is less, *i.e.* several different isobar configurations can provide an equivalent description of data.

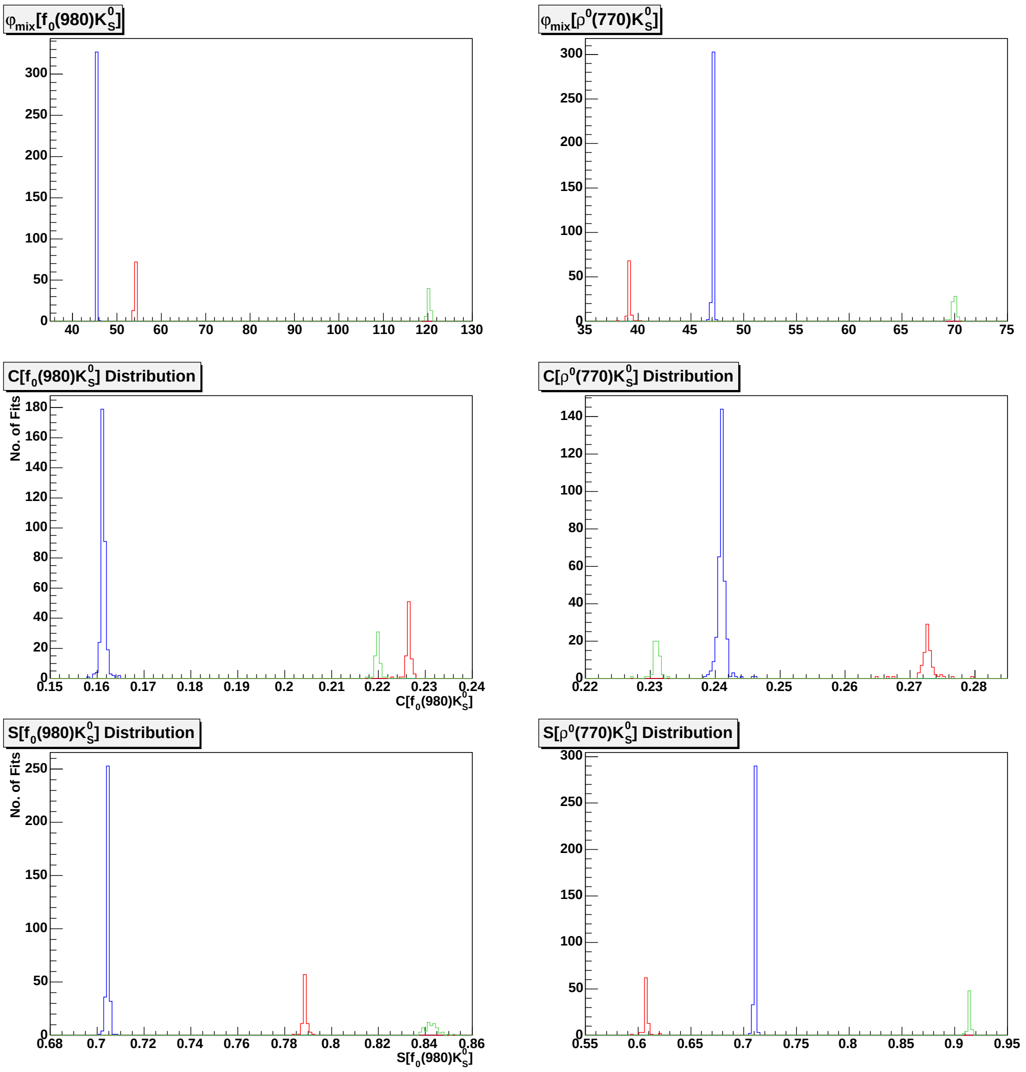

Figure 6.18: *Distributions of* $2\beta_{eff}(f_0(980)K^0_S)$ *(upper left),* $2\beta_{eff}(\rho^0(770)K^0_S)$ *(upper right),* $C(f_0(980)K^0_S)$ *(middle left),* $C(\rho^0(770)K^0_S)$ *(middle right),* $S(f_0(980)K^0_S)$ *(lower left) and* $S(\rho^0(770)K^0_S)$ *(lower right) at minimum for randomized fits to one data set generated with the signal model described in the text, and Continuum and B background components.*

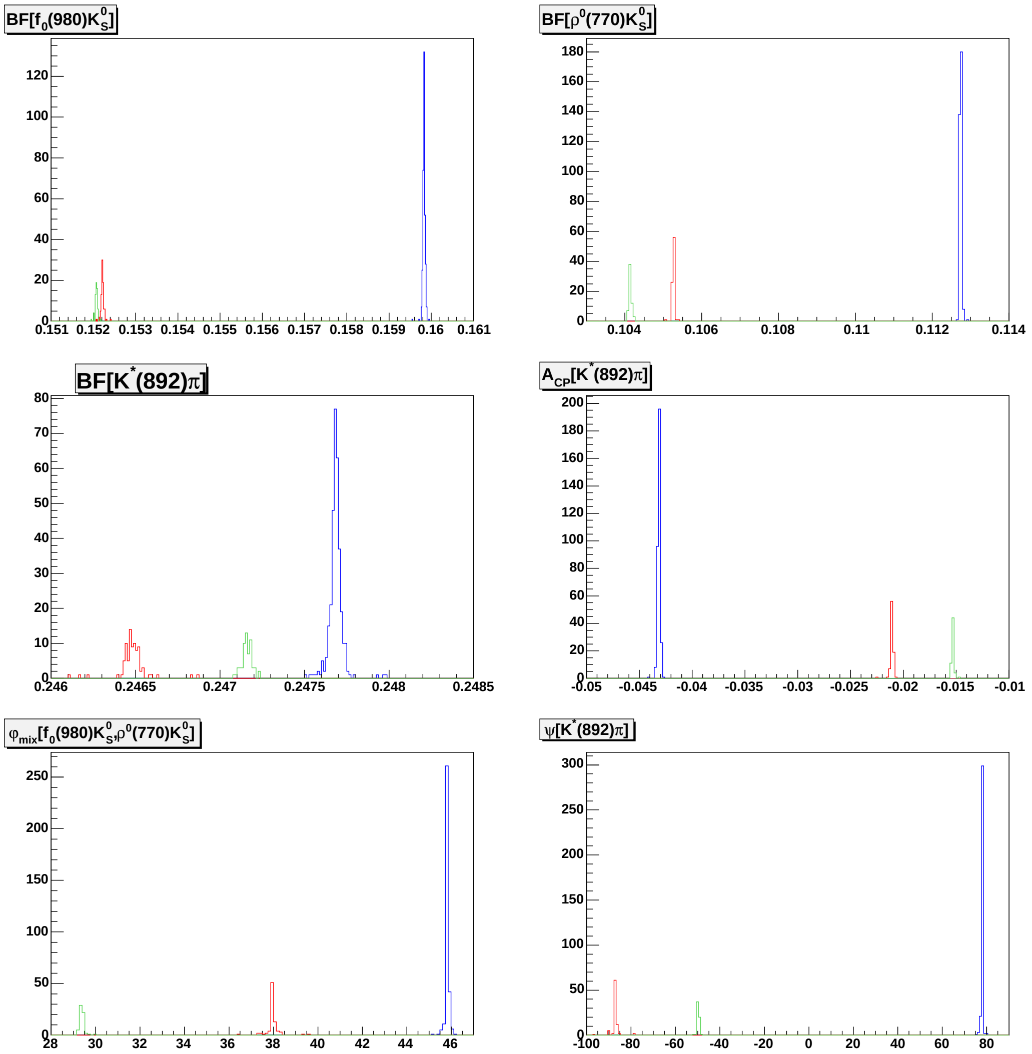

Figure 6.19: *Distributions of* $FF(f_0(980)K^0_S)$ *(upper left),* $FF(\rho^0(770)K^0_S)$ *(upper right),* $FF(K^{*\pm}(892)\pi^{\mp})$ *(middle left),* $A_{CP}(K^{*\pm}(892)\pi^{\mp})$ *(middle right),* $\Delta\phi(f_0(980), \rho^0(770))$ *(lower left) and* $\Delta\phi(K^{*+}(892)\pi^-, K^{*-}(892)\pi^+)$ *(lower right) at minimum for randomized fits to one data set generated with the signal model described in the text, and Continuum and B background components.*

6.5 Likelihood vs. $2\beta_{eff}(f_0(980)K^0_S)$ Scans

A total degeneracy on phase differences occurs when the signal model contains only one intermediate state, *i.e.* in the complete absence of interference. Information stemming from interference patterns helps resolve the degeneracies the degeneracies, as illustrated by scanning the $2\beta_{eff}(f_0(980)K^0_S)$ parameter on toy datasets. For this study, datasets with different values of the weak mixing phase for the $f_0(980)K^0_S$ are generated; the relative phases of the $f_0(980)K^0_S$ amplitude with respect to the amplitudes of the other resonances are also generated at different values. For each independent dataset, the likelihood as a function of some isobar parameter p_1 (or set of isobar parameters $\vec{p_1}$) is scanned the following way: 1) the parameter p_1 is set to a fixed value; 2) the toy dataset is fitted several times with the fitting algorithm starting from random initial values of the isobar parameters; 3) the lowest likelihood value obtained in these fits is selected; 4) the process is reiterated for different sequential values of the p_1 parameter. The output of this sequence is $\mathcal{L}$ *vs.* p_1, on "likelihood scan" curve.

As always, one amplitude (both module and phase) has to be fixed in the fit. If the c_σ isobar amplitude is taken as the reference, with its phase chosen to be zero, then the $\phi(\sigma)$ observable is just obtained as (minus) the phase of its CP-conjugated isobar amplitude $\overline{c}_\sigma$. The likelihood scan as a function of the $\phi(\sigma)$ phase is obtained by re-fitting the same dataset using different fixed values of the $\overline{c}_\sigma$ phase. The same procedure can be used to scan the direct CP-violation parameter C. Choosing c_σ as reference, and fixing its modulus to a, the $C(\sigma)$ observable is a function of $|\overline{c}_\sigma|$ only (cf. Eq. 2.45). Then, in order to set C to a specific value C_{val}, the $|\overline{c}_\sigma|$ parameter has to be fixed to the value

$$|\overline{c}_\sigma| = a\left(\frac{1-C_{\text{val}}}{1+C_{\text{val}}}\right)^{1/2} . \tag{6.20}$$

Using these same relations, a two-dimensional scan of the likelihood as a function of $\phi(\sigma)$ and $C(\sigma)$ can be performed, by simultaneously fixing the module and phase of the $|\overline{c}_\sigma|$ parameter at several consecutive values.

6.5.1 High statistics, signal-only likelihood scans

In the case of two minima, the likelihood should look like the envelope of two multi-Gaussian likelihoods centered at the corresponding minima. The central shape will depend on, both the difference in likelihood values at each minimum, and the width of each Gaussian. For example, if the difference in likelihoods in both minima is very large, and the Gaussians are very wide, the secondary minimum may not be visible on the scan; in contrast, if the two minima have similar likelihood values, and the Gaussians are narrow, it should be easy to resolve them.

In presence of backgrounds, the errors of the physical parameters are larger, the Gaussian around each minimum appears wider. Therefore, backgrounds can potentially alter the potential to resolve local minima. A study using high statistics signal only toy datasets is used to illustrate this feature. For these toys, generated with 10k events each, the signal model is made of only two components, the $f_0(980)K^0_S$ and the $\rho^0(770)K^0_S$, as previous studies have shown that the interference pattern of these two components provides the dominant information on the $2\beta_{eff}(f_0(980)K^0_S)$ scan. In the case of two components, the discrimination power between the correct and the mirror solutions depends on the values of two parameters: the value of the mixing phase itself, and the relative phase with respect to the other resonance as well. On the one hand, it depends on the mixing angle: if the correct solution is 2β, the distance to its mirror solution gets smaller as $2\beta \to \pi/2$. On the other hand, it depends also on the phase difference $\Delta\phi(f_0(980), \rho^0(770))$, because the value of this phase determines the interference pattern of these two components over the Dalitz plot.

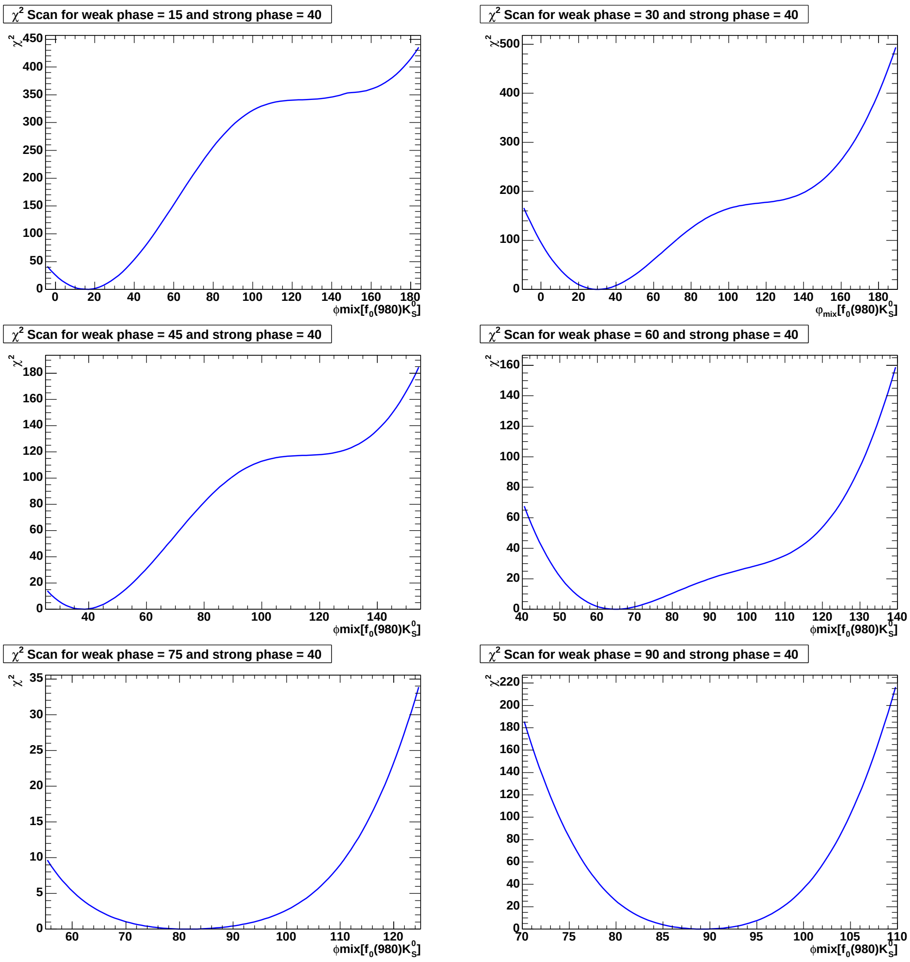

Figure 6.20: *Likelihood Scans in* $2\beta_{eff}(f_0(980)K^0_S)$. *Each plot is made with a single toy dataset, generated with* $\Delta\phi(f_0(980), \rho^0(770)) = 40^o$ *and different values of* $2\beta_{eff}(f_0(980)K^0_S)$, *namely* 15^o, 30^o, 45^o, 60^o, 75^o *and* 90^o, *counting from left to right and from top to bottom.*

In Fig. 6.20, scans for one fixed value of the phase difference $\Delta\phi(f_0(980), \rho^0(770))$ and different generation values of the mixing angle $2\beta_{eff}(f_0(980)K^0_S)$ are shown. It can be seen that the position of the two minima depends on the generation value of $2\beta_{eff}(f_0(980)K^0_S)$: they get closer as $2\beta_{eff}(f_0(980)K^0_S)$ approaches 90^o, in which case they coincide. In similar spirit, Fig. 6.21 shows scans for one generation value of $2\beta_{eff}(f_0(980)K^0_S)$ and different generation values of $\Delta\phi(f_0(980), \rho^0(770))$. These plots show that the positions of the two minima are fixed, but the difference in likelihood units of the two minima depends on $\Delta\phi(f_0(980), \rho^0(770))$. The conclusion of this study is that the ability of resolving the two minima is a multivariate function of the values for the isobar phases.

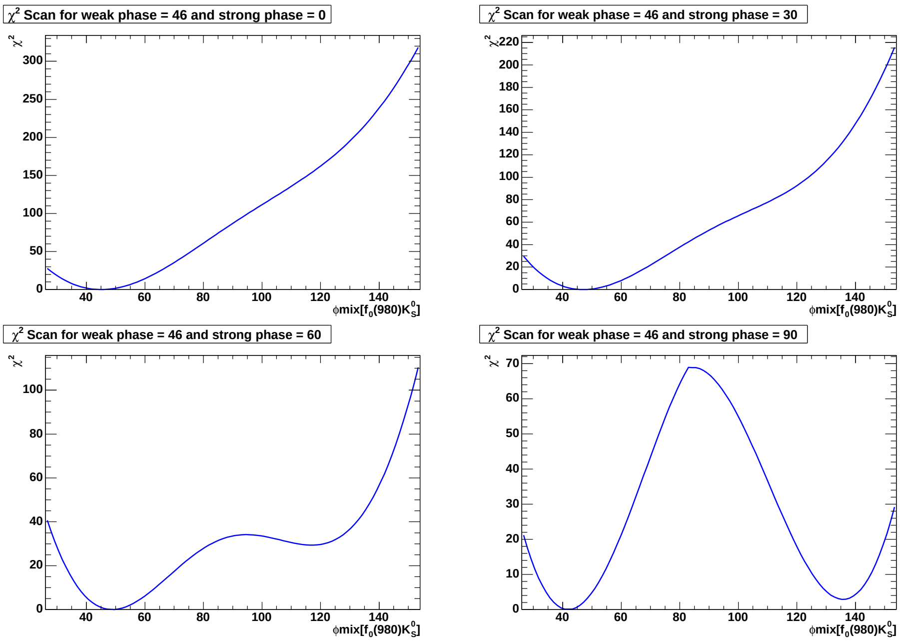

Figure 6.21: *Likelihood Scans in* $2\beta_{eff}(f_0(980)K_S^0)$. *Each plot is made with a single toy dataset, generated with* $2\beta_{eff}(f_0(980)K_S^0) = 46^o$ *and different values of* $\Delta\phi(f_0(980)\rho^0(770)$, *namely* 0^o, 30^o, 60^o, *and* 90^o, *counting from left to right and from top to bottom.*

6.6 Studies using fully simulated MC samples

A useful validation consists in generating datasets with components of signal, continuum and B-background from different independent sources, merging them together and fitting them to check if the results obtained by the analysis tool are compatible with the generated values. Such studies are called "embedded fits". This study is particularly relevant when fully simulated MC events are used as signal, because effects like reconstruction and misreconstructed events are under control.

6.6.1 Dalitz plot model for embedded fits

The signal component in the embedded fits is a DP model MC sample generated using `EvtGen`. The sample has $1321K$ generated events, with the following resonances and lineshapes (C.C. means charge conjugated):

- $B^0 \rightarrow f_0(980)K_S^0$ and C.C (Flatté lineshape)
- $B^0 \rightarrow \rho^0(770)K_S^0$ and C.C (RBW lineshape)
- $B^0 \rightarrow K^{*-}(892)\pi^+$ and C.C. (RBW lineshape)

Generated values for phases and physical parameters are summarized in Table 6.6. The generated phases for the different resonances are also represented graphically on Figure 6.22

(note that the moduli of amplitudes in the figure do not correspond to the values in the actual sample).

Parameter	Generated Value
Phases	
$A(f_0(980)K^0_S)$	0.0
$\overline{A}(f_0(980)K^0_S)$	-37.2
$A(\rho^0(770)K^0_S)$	134.7
$\overline{A}(\rho^0(770)K^0_S)$	78.0
$A(K^{*-}(892)\pi^+)$	-36.1
$\overline{A}(K^{*+}(892)\pi^-)$	-80.9
Physical parameters	
$C(f_0(980)K^0_S)$	0.0
$S(f_0(980)K^0_S)$	-0.61
$2\beta_{eff}(f_0(980)K^0_S)$	37.2
$BF(f_0(980)K^0_S)$	38.2%
$C(\rho^0(770)K^0_S)$	0.0
$S(\rho^0(770)K^0_S)$	0.84
$2\beta_{eff}(\rho^(770)K^0_S)$	56.7
$BF(\rho^0(770)K^0_S)$	26.4%
$A_{CP}(K^{*\pm}(892)\pi^\mp)$	0.0
$\Delta\phi(K^{*+}(892)\pi^-, K^{*-}(892)\pi^+)$	44.7
$BF(K^{*\pm}(892)\pi^\mp)$	33.3%
$\Delta\phi(\rho^0(770)K^0_S)$	-134.7
$\Delta\phi(K^{*+}(892)\pi^-)$	36.1

Table 6.6: *Generated values for phases and physical parameters in the DP model. Phases are given in degrees.*

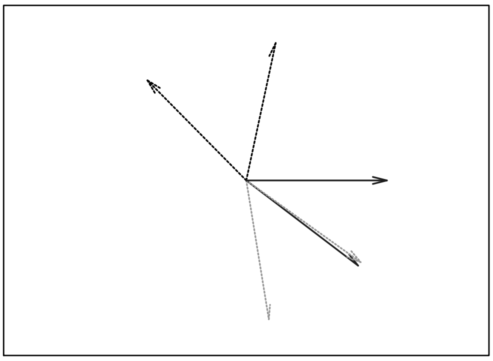

Figure 6.22: *Phases of different amplitudes in the DP MC. The $\overline{A}$ amplitudes are represented with a half arrow-head. Dark solid arrows stand for $f_0(980)K^0_S$, dark dotted arrows for $\rho^0(770)K^0_S$ and gray dotted arrows for $K^*(892)\pi$. Moduli of amplitudes in the figure do not correspond to the values in the sample.*

6.6.2 Embedded fits

The event sample of signal MC described above has been split into 200 datasets. The average number of events in each sample is 2200. Those signal subsamples were embedded into datasets made of continuum, neutral generic and charged generic events that were generated with the simplified toy simulation. The average number of events is 14200, 114 and 280 for continuum, neutral generic and charged generic events, respectively. These numbers roughly correspond to the expectation yields in the data sample. Each merged dataset has been fitted 20 times with random initial values; the numbers reported below correspond to the best fit result to each data set.

Distributions of the Q2B parameters are shown in Figs. 6.23 and 6.24. All the distributions show a Gaussian-like shape, and they are centered at the generated value, except for the $f_0(980)K^0_S$ and $K^*(892)\pi$ fit fractions. For these last two distributions, the mean value deviates by 1.2% from the generated one. This difference will be assigned as a systematic uncertainty on the fit fractions (cf. Sec. 7.3.1).

Pulls for yields are shown in the Figs. 6.25 and 6.26. The mean value of the signal yield pull (bottom right hand plot in Fig. 6.26) shows a bias of $\sim 0.28\sigma$, corresponding to ~ 14 events. Also, the width of the pull is slightly narrow (0.9). Both effects are addressed as systematical errors (cf. Sec. 7.3.1). For the other parameters no significant bias is observed. It can be concluded from this study on embedded samples that the fitting tool is reasonably unbiased.

6.7 Extraction of confidence intervals on the physical parameters

6.7.1 The statistical likelihood scans

In the extended maximum likelihood fit, the total yield of $B^0 \to K^0_S\pi^+\pi^-$ events, and the magnitude and phase for each intermediate state, are directly extracted from the fit. A further step is needed to translate the complex isobar amplitudes into information on physics quantities. The relevant physical parameters are phase differences, inclusive and exclusive direct CP asymmetries, fit fractions and branching ratios (cf. Sec. 2.4.9). These parameters are functions of the fit parameters; their functional dependence can be highly non trivial. Two approaches will be used to estimate the mean values and errors out of the fit results: the Parabolic Likelihood approach, which assumes a parabolic behavior around a minimum of the (negative logarithmic) likelihood function; and the more accurate method of likelihood scans, which does not make any assumptions at all.

- **The Parabolic Likelihood (PL) Method:** in this method, it is assumed that the (negative log) likelihood function can be approximated to a hyperparaboloid near a given minimum. Let X_i $(i = 1, ..., N_{\rm fit})$ be the $N_{\rm fit}$ parameters allowed to vary in the fit. Then, the likelihood function can be approximated by,

$$-2\log(\mathcal{L}) \simeq \sum_{ij} \left(X_i - X_i^{fit}\right) \mathcal{C}^{-1}_{ij} \left(X_j - X_j^{fit}\right) \tag{6.21}$$

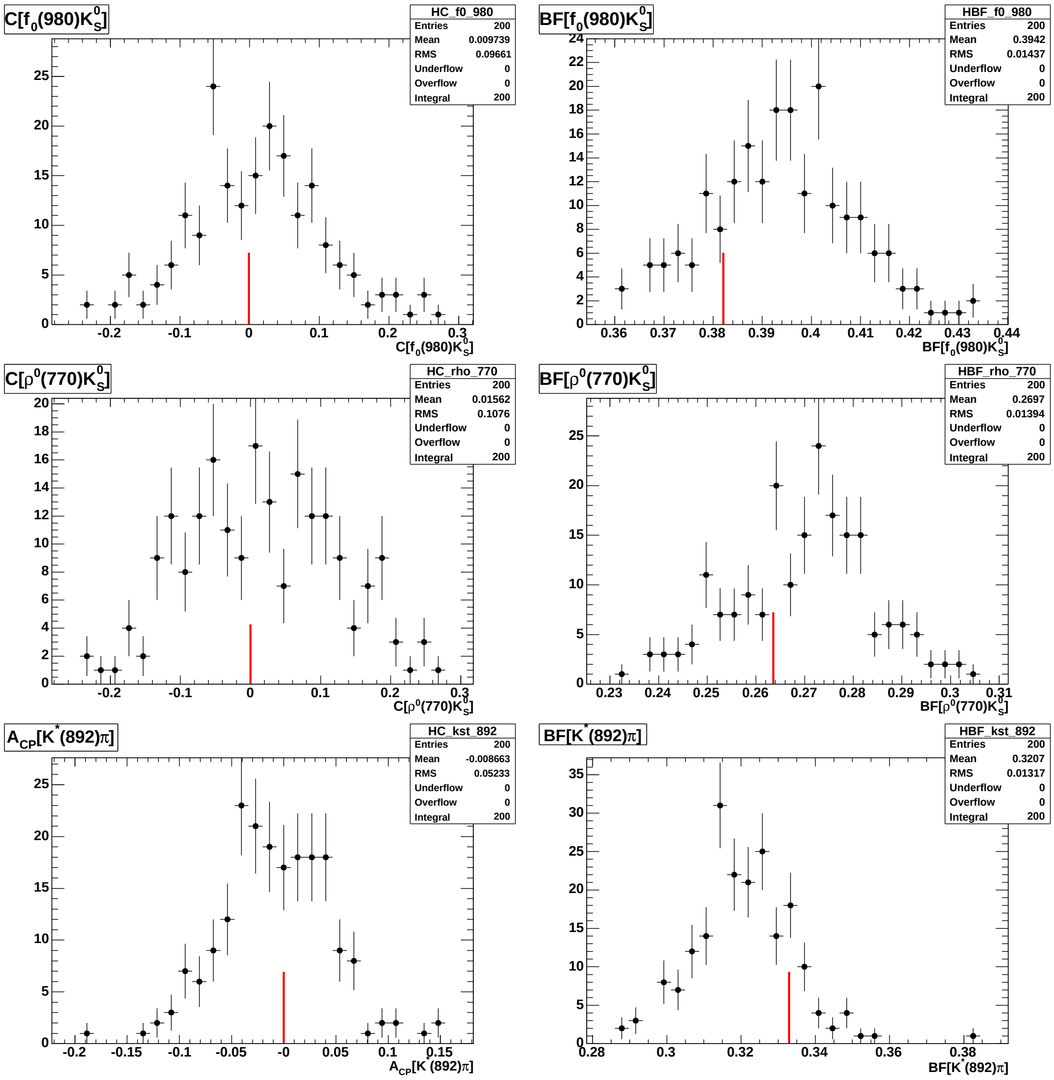

Figure 6.23: *Distributions of fitted Q2B parameters on embedded samples.* $C(f_0(980)K^0_S)$ *(top left),* $BF(f_0(980)K^0_S)$ *(top right),* $C(\rho^0(770)K^0_S)$ *(middle left),* $BF(\rho^0(770)K^0_S)$ *(middle right),* $A_{CP}(K^*(892)\pi)$ *(bottom left),* $BF(K^*(892)\pi)$ *(bottom right). The red marks indicate the generated values.*

where X_i^{fit} are the fitted values and $\mathcal{C}$ is the fit covariance matrix. Writing this approximation, in order to obtain the likelihood scan ($-2\log\mathcal{L}(F)$) of a given observable which is a function of the fit parameters $F(X_i)$ (*e.g.* a direct CP asymmetry), this hyperparaboloid is just projected in the direction of $F(X_i)$. By construction, the PL method takes into account the linear correlations among fit parameters, and propagates them into the physical quantity one is interested in.

As discussed in Sec. 6.4, the likelihood function is expected to have several local minima. In general, the empirical observation shows that values of CP asymmetries

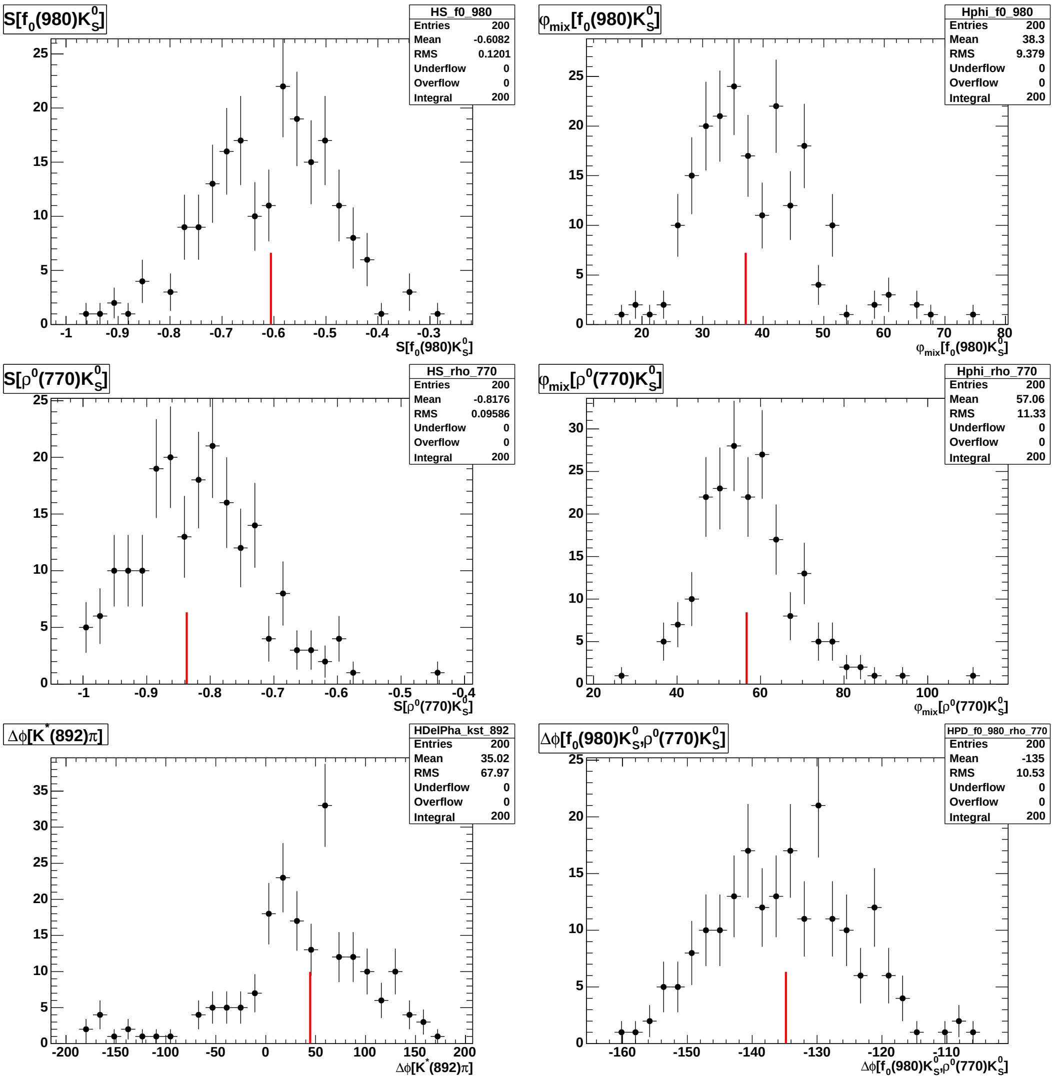

Figure 6.24: *Distributions of fitted Q2B parameters on embedded samples.* $S(f_0(980)K_S^0)$ *(top left),* $2\beta_{eff}(f_0(980)K_S^0)$ *(top right),* $S(\rho^0(770)K_S^0)$ *(middle left),* $2\beta_{eff}(\rho^0(770)K_S^0)$ *(middle right),* $\Delta\phi(K^*(892)\pi)$ *(bottom left),* $\Delta\phi(f_0(980)K_S^0, \rho^0(770)K_S^0)$ *(bottom right). The red marks indicate the generation values.*

and fit fractions tend to be very similar among local minima, in contrast to isobar phase differences, that can show larger differences. For the former parameters, it is thus safer to apply an approximate method, which is referred as the PL-envelope method. The procedure goes as follows:

1. Having identified the n local minima (solutions) of the likelihood function, obtained from randomized fits to data, a $-2\log\mathcal{L}_i(F)$ is built for each minimum.
2. Using the $NNL_{\rm min}$ value, the NLL value of the global minimum, the $\Delta\chi^2_{i,\rm min} = 2(NLL_i - NLL_{\rm min})$ is added to each $-2\log\mathcal{L}_i(F)$.

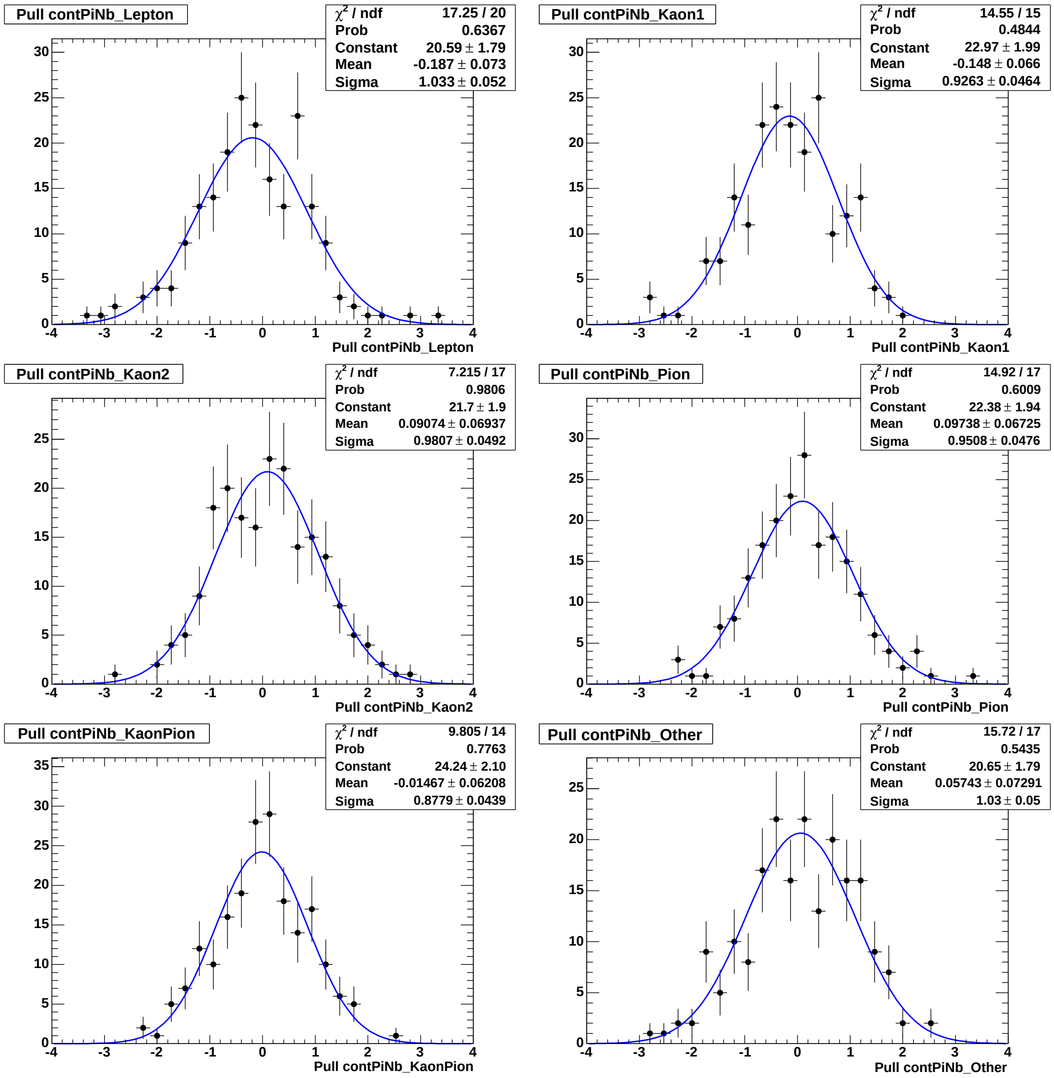

Figure 6.25: *Pull on Yields for embedded fits. Continuum yields for categories* `Lepton` *(top left),* `Kaon1` *(top right),* `Kaon2` *(middle left),* `Pion` *(middle right),* `KaonPion` *(bottom left) and* `Other` *(bottom right). The blue line is a Gaussian fit.*

3. Then, the function

$$-2\Delta log(\mathcal{L})(F) = Min\left\{-2\log\mathcal{L}_i(F) + \Delta\chi^2_{i,\min}\right\}, \tag{6.22}$$

which can be seen as the envelope of all $-2\log\mathcal{L}_i(F)$ curves, is taken as the total statistical scan. The confidence level (CL) is defined as

$$\mathrm{CL}(F) = \mathtt{Prob}(-2\Delta log(\mathcal{L})(F), 1) ;$$

the $1-\sigma$ ($2-\sigma$) intervals are inferred from the F values for which $CL = 32\%$ (5%).

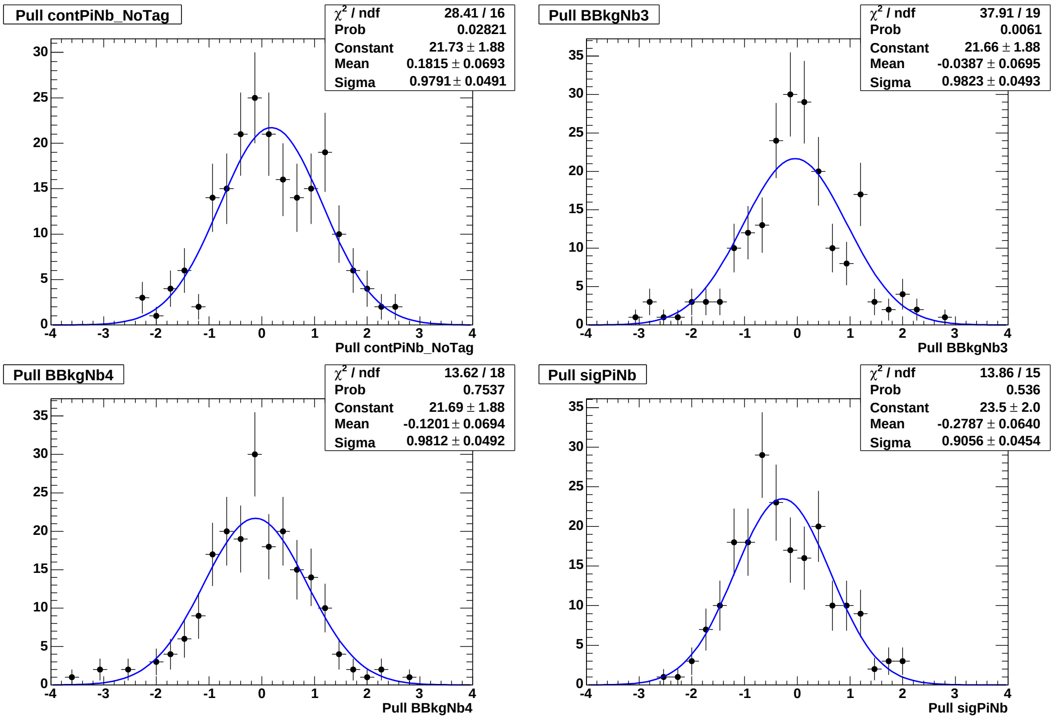

Figure 6.26: *Yields distributions for Embedded fits. Yields for continuum* `NoTag` *category (top left), Neutral Generic (top right), Charged Generic (bottom left) and signal (bottom right). The blue line is a Gaussian fit.*

While this approach does not take into account the non-parabolic behavior of the likelihood function, and so the nonlinear correlations between the fit parameters, the PL-envelope method provides an acceptable technique for setting $1-\sigma$ and $2-\sigma$ intervals. Tests have shown that the PL-envelope method reproduces the complete likelihood scan (see later) when the relevant component is uncontroversial. The PL-envelope will be used for setting confidence intervals on direct CP asymmetries, fit fractions and some of the phase differences (*e.g.* $\phi(\chi_C(0)K^0_S)$).

As an illustration, an example is produced using a realistic toy dataset, generated and fitted with a 6-resonance model: $f_0(980)$, $\rho^0(770)$, $K^{*\pm}(892)$ and $(K\pi)^{*\pm}_0$. Initial generation values, and fitted results on this particular toy experiment are shown on Table 6.7, and Fig. 6.27 shows the correlation matrix obtained from the fit. Note that the strongest correlations occur between the phases.

Figs. 6.28 and 6.29 show the $\mathcal{L}(F)$ (and the CL) likelihood scans using the PL method for some physical parameters (S, C, FF, A_{CP} and phase differences) using only one minimum ($n=1$) of the likelihood function.

- **Complete likelihood scans:** when the parabolic approximation can not be used safely, a more correct, CPU-consuming, method will be used. This concerns in particular the phase differences and some bi-dimensional likelihood scans (see Sec. 6.8 for an

Parameter Name	Generation Value	Initial Value in Fit	Fit Result
`A-k0st-1430-p`	5.964	2.416	(5.4949 ± 0.553)
`A-kst-892-p`	0.158	0.110	(0.14844 ± 0.0158)
`A-rho-770-z`	0.092	0.030	(0.095087 ± 0.0148)
`Ab-f0-980-z`	1.051	1.131	(0.84986 ± 0.162)
`Ab-k0st-1430-m`	5.964	8.585	(5.4481 ± 0.538)
`Ab-kst-892-m`	0.175	0.049	(0.14215 ± 0.0148)
`Ab-rho-770-z`	0.087	0.102	(0.074304 ± 0.0132)
`DESlope`	-0.141	-0.141	(-0.200 ± 0.342)
`DESq`	0.000	0.000	(0.099998 ± 0.104)
`contPiNb-Kaon1`	1562	1562	(1585.6 ± 41.7)
`contPiNb-Kaon2`	3921	3921	(3825.5 ± 64.2)
`contPiNb-KaonPion`	3525	3525	(3671.6 ± 62.6)
`contPiNb-Lepton`	64	64	(57.111 ± 9.68)
`contPiNb-NoTag`	11165	11165	(11385 ± 109)
`contPiNb-Other`	3113	3113	(3077.5 ± 57.2)
`contPiNb-Pion`	3942	3942	(3901.7 ± 64.6)
`phA-k0st-1430-p`	-57	80	(-84.085 ± 21.3)
`phA-kst-892-p`	-40	48	(-56.187 ± 20.8)
`phA-rho-770-z`	-40	147	(-46.08 ± 18.7)
`phAb-f0-980-z`	-49	-90	(-45.657 ± 16.8)
`phAb-k0st-1430-m`	-68	95	(7.77 ± 33.1)
`phAb-kst-892-m`	-40	28	(45.075 ± 32.4)
`phAb-rho-770-z`	-81	-166	$(-93.295 \pm 23.6e)$
`sigPiNb`	2200	2200	(2232.1 ± 65.8)

Table 6.7: *Initial generation values, and fit results for a specific Toy MC experiment.*

account of the nominal DP signal model), namely:

- **One-dimensional likelihood scans,**

$$
\begin{aligned}
&-2\beta_{eff}(f_0(980)K^0_S) = arg\left[c(B^0 \to f_0(980)K^0_S)c^*(\bar{B}^0 \to f_0(980)K^0_S)\right]\\
&-2\beta_{eff}(\rho^0(770)K^0_S) = arg\left[c(B^0 \to \rho^0(770)K^0_S)c^*(\bar{B}^0 \to \rho^0(770)K^0_S)\right]\\
&-\Delta\phi(K^*(892)\pi) = arg\left[c(B^0 \to K^{*+}(892)\pi^-)c^*(\bar{B}^0 \to K^{*-}(892)\pi^+)\right]\\
&-\Delta\phi((K\pi)^*_0\pi) = arg\left[c(B^0 \to (K\pi)^{*+}_0\pi^-)c^*(\bar{B}^0 \to (K\pi)^{*-}_0\pi^+)\right]\\
&-\Delta\phi(f^0(980)K^0_S, \rho(770)K^0_S) = arg\left[c(B^0 \to f_0(980)K^0_S)c^*(B^0 \to \rho^0(770)K^0_S)\right]\\
&-\Delta\phi(\rho(770)K^0_S, K^*(892)\pi) = arg\left[c(B^0 \to \rho^0(770)K^0_S)c^*(B^0 \to K^{*+}(892)\pi^-)\right]\\
&-\Delta\phi(\rho(770)K^0_S, (K\pi)^*_0\pi) = arg\left[c(B^0 \to \rho^0(770)K^0_S)c^*(B^0 \to (K\pi)^{*+}_0\pi^-)\right]\\
&-\Delta\phi(K^*(892)\pi, (K\pi)^*_0\pi) = arg\left[c(B^0 \to K^{*+}(892)\pi^-)c^*(B^0 \to (K\pi)^{*+}_0\pi^-)\right]
\end{aligned}
\tag{6.23}
$$

- **Two-dimensional likelihood scans,**

$$
\begin{array}{ccc}
-2\beta_{eff}(f_0(980)K^0_S) & \text{vs} & C(f_0(980)K^0_S)\\
-2\beta_{eff}(\rho^0(770)K^0_S) & \text{vs} & C(\rho^0(770)K^0_S)
\end{array}
\tag{6.24}
$$

which are an important goal of this study. This also concerns the fit fractions of components with low significance.

Instead of assuming a parabolic shape of the NLL close to its minimum, the data is refitted under the constraint that the physical parameter under study is fixed (it is also possible to fix several parameters), but allowing all other isobar parameters to be free in the fit. Doing that iteratively, the NLL (in fact $\chi^2 = 2(NLL - NLL_{\text{bestfit}})$) is scanned. An example in $2\beta_{eff}(f_0(980)K^0_S)$ is given in Sec. 6.5. Due to local minima,

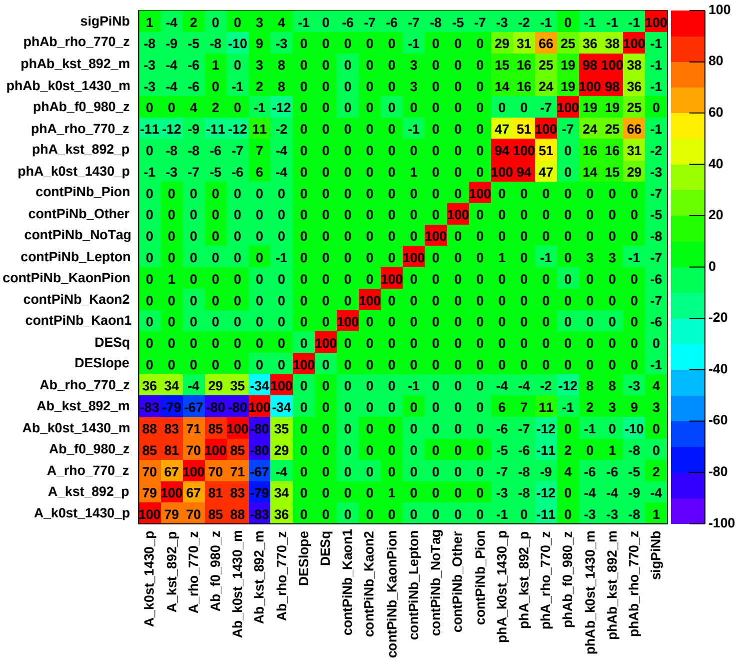

	A_k0st_1430_p	A_kst_892_p	A_rho_770_z	Ab_f0_980_z	Ab_k0st_1430_m	Ab_kst_892_m	Ab_rho_770_z	DESlope	DESq	contPiNb_Kaon1	contPiNb_Kaon2	contPiNb_KaonPion	contPiNb_Lepton	contPiNb_NoTag	contPiNb_Other	contPiNb_Pion	phA_k0st_1430_p	phA_kst_892_p	phA_rho_770_z	phAb_f0_980_z	phAb_k0st_1430_m	phAb_kst_892_m	phAb_rho_770_z	sigPiNb
sigPiNb	1	-4	2	0	0	3	4	-1	0	-6	-7	-6	-7	-8	-5	-7	-3	-2	-1	0	-1	-1	-1	100
phAb_rho_770_z	-8	-9	-5	-8	-10	9	-3	0	0	0	0	0	-1	0	0	0	29	31	66	25	36	38	100	-1
phAb_kst_892_m	-3	-4	-6	1	0	3	8	0	0	0	0	0	3	0	0	0	15	16	25	19	98	100	38	-1
phAb_k0st_1430_m	-3	-4	-6	0	-1	2	8	0	0	0	0	0	3	0	0	0	14	16	24	19	100	98	36	-1
phAb_f0_980_z	0	0	4	2	0	-1	-12	0	0	0	0	0	0	0	0	0	0	0	-7	100	19	19	25	0
phA_rho_770_z	-11	-12	-9	-11	-12	11	-2	0	0	0	0	0	-1	0	0	0	47	51	100	-7	24	25	66	-1
phA_kst_892_p	0	-8	-8	-6	-7	7	-4	0	0	0	0	0	0	0	0	0	94	100	51	0	16	16	31	-2
phA_k0st_1430_p	-1	-3	-7	-5	-6	6	-4	0	0	0	0	0	1	0	0	0	100	94	47	0	14	15	29	-3
contPiNb_Pion	0	0	0	0	0	0	0	0	0	0	0	0	0	0	0	100	0	0	0	0	0	0	0	-7
contPiNb_Other	0	0	0	0	0	0	0	0	0	0	0	0	0	0	100	0	0	0	0	0	0	0	0	-5
contPiNb_NoTag	0	0	0	0	0	0	0	0	0	0	0	0	0	100	0	0	0	0	0	0	0	0	0	-8
contPiNb_Lepton	0	0	0	0	0	0	-1	0	0	0	0	0	100	0	0	0	1	0	-1	0	3	3	-1	-7
contPiNb_KaonPion	0	1	0	0	0	0	0	0	0	0	0	100	0	0	0	0	0	0	0	0	0	0	0	-6
contPiNb_Kaon2	0	0	0	0	0	0	0	0	0	0	100	0	0	0	0	0	0	0	0	0	0	0	0	-7
contPiNb_Kaon1	0	0	0	0	0	0	0	0	0	100	0	0	0	0	0	0	0	0	0	0	0	0	0	-6
DESq	0	0	0	0	0	0	0	0	100	0	0	0	0	0	0	0	0	0	0	0	0	0	0	0
DESlope	0	0	0	0	0	0	0	100	0	0	0	0	0	0	0	0	0	0	0	0	0	0	0	-1
Ab_rho_770_z	36	34	-4	29	35	-34	100	0	0	0	0	0	-1	0	0	0	-4	-4	-2	-12	8	8	-3	4
Ab_kst_892_m	-83	-79	-67	-80	-80	100	-34	0	0	0	0	0	0	0	0	0	6	7	11	-1	2	3	9	3
Ab_k0st_1430_m	88	83	71	85	100	-80	35	0	0	0	0	0	0	0	0	0	-6	-7	-12	0	-1	0	-10	0
Ab_f0_980_z	85	81	70	100	85	-80	29	0	0	0	0	0	0	0	0	0	-5	-6	-11	2	0	1	-8	0
A_rho_770_z	70	67	100	70	71	-67	-4	0	0	0	0	0	0	0	0	0	-7	-8	-9	4	-6	-6	-5	2
A_kst_892_p	79	100	67	81	83	-79	34	0	0	0	0	1	0	0	0	0	-3	-8	-12	0	-4	-4	-9	-4
A_k0st_1430_p	100	79	70	85	88	-83	36	0	0	0	0	0	0	0	0	0	-1	0	-11	0	-3	-3	-8	1

Figure 6.27: *Correlation matrix for the 6-resonance Toy MC fit from Table 6.7.*

in general randomized fits have to be performed on each scan value of the physical parameter under study, which makes this technique very heavy in CPU-computing time, in particular for bi-dimensional scans.

For each exclusive channel (*e.g.* $f_0(980)K_S^0$), the CP-violation (CPV) information is contained in the $(\phi(\sigma), C(\sigma))$ parameters, zero CPV being located at the points $(0°, 0)$ and $(180°, 0)$. A two-dimensional likelihood scan in these two parameters is built using their relations with the fitted isobar amplitudes (see Eqs. 2.44 and 2.45, and the comments in Sec. 6.5). The $(\phi(\sigma), C(\sigma))$ plane can be transformed to the $(S(\sigma), C(\sigma))$ using Eq. 2.46. In doing this transformation part of the information is lost, but a constraint in CPV is easier to set because there is only one CP conserving point, $(0, 0)$. Such 2D scans are made for the $f_0(980)K_S^0$ and $\rho^0(770)K_S^0$ components, and are presented in the next Chapter as one of the physics results of this thesis.

6.7.2 Convolution with systematic uncertainties

Section 7.3 summarizes the estimation of systematic uncertainties. Depending on the relevant parameters, systematic errors are presented in two ways: 1) when considered independent, systematic errors are added in quadrature. 2) As a systematic covariance matrix, which is constructed from shifts in the fit parameters (modulus-phase, or real-imaginary of isobar amplitudes), all independent systematic matrices are just added. This information has to be combined with the statistical likelihood scans.

For the inclusive and exclusive direct CP asymmetries, fit fractions and branching frac-

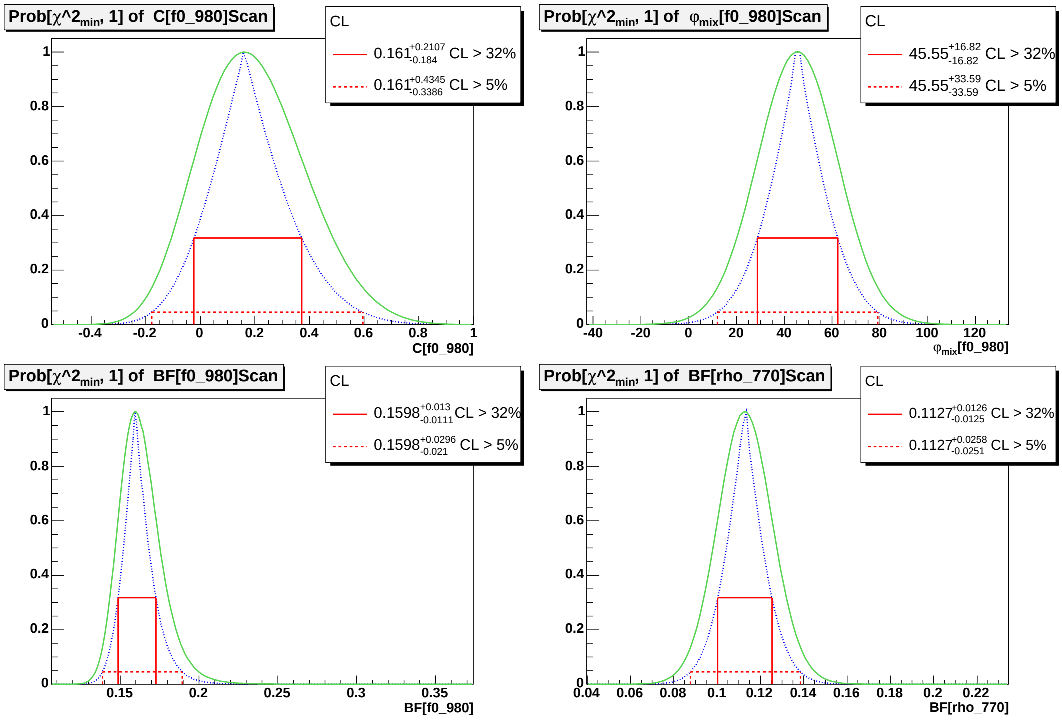

Figure 6.28: *Likelihoods (Solid Green) and Confidence Level (Dashed Blue) of physical parameters extracted from the Toy MC fit in Table 6.7. The curves are constructed with the PL method.* $C(f_0(980)K^0_S)$ *(top left),* $2\beta_{eff}(f_0(980)K^0_S)$ *(top right),* $FF(f_0(980)K^0_S)$ *(bottom left) and* $FF(\rho^0(770)K^0_S)$ *(bottom right). The solid line (dashed) red box is the intervals at* 32% (5%) *of CL.*

tions, the systematic effects are added in quadrature to the asymmetric errors obtained from the statistical likelihood scans. This approach is reasonably safe for these parameters, since local minima solutions are almost degenerated. For phase differences, a more elaborate method is performed, taking into account that values differ significantly among local minima. In this case the statistical likelihood is convoluted with the systematic error, which is assumed to be Gaussian, taking care of the likelihood function periodicity of 360^o.

For the bi-dimensional $\phi(\sigma) - C(\sigma)$ likelihood scans, the simple convolution of the likelihood function with a 2D Gaussian assumes a Gaussian systematic error in $C(\sigma)$. This approach, being only valid near the minimum, fails when approaching the physical boundaries of $C(\sigma)$. In this case a different method has to be performed, which is described below.

When fixing the $c_\sigma = |c_\sigma|\exp(i\delta_\sigma)$ isobar amplitude in the fit, the $\phi(\sigma)$ and $C(\sigma)$ parameters depend only on $\bar{c}_\sigma$. The systematic effects are nearly Gaussian (taking into account the correlations) in the $(\mathcal{R}e(\bar{c}_\sigma), \mathcal{I}m(\bar{c}_\sigma))$ plane, as there is no physical boundary. This plane can be transformed to the $(\phi(\sigma), C(\sigma))$ plane by the relations

$$\begin{aligned} \mathcal{R}e(\bar{c}_\sigma) &= |c_\sigma| \left(\frac{1-C(\sigma)}{1+C(\sigma)}\right)^{1/2} \cos(\delta_\sigma - \phi(\sigma)), \\ \mathcal{I}m(\bar{c}_\sigma) &= |c_\sigma| \left(\frac{1-C(\sigma)}{1+C(\sigma)}\right)^{1/2} \sin(\delta_\sigma - \phi(\sigma)). \end{aligned} \tag{6.25}$$

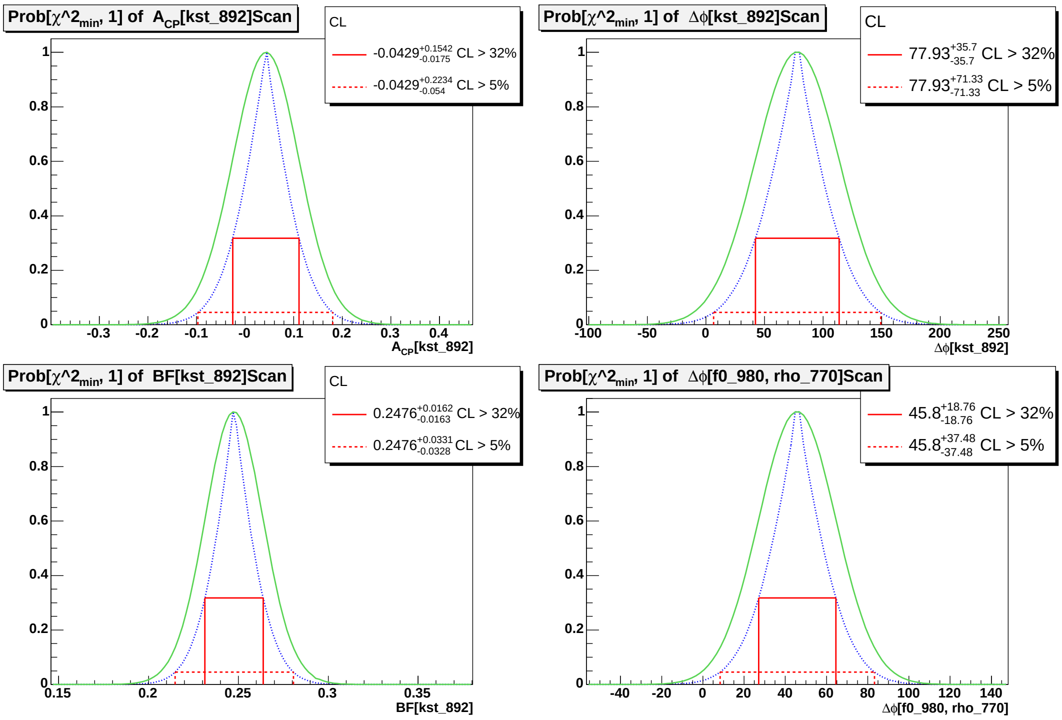

Figure 6.29: *Likelihoods (Solid Green) and Confidence Level (Dashed Blue) of physical parameters extracted from the Toy MC fit in Table 6.7. The curves are constructed with the PL method.* $A_{CP}(K^{*\pm}(892)\pi^{\mp})$ *(top left),* $\Delta\phi(K^{*+}(892)\pi^{-}, K^{*-}(892)\pi^{+})$ *(top right),* $FF(K^{*\pm}(892)\pi^{\mp})$ *(lower left) and* $\Delta\phi(f_0(980), \rho^0(770))$ *(bottom right). The solid line (dashed) red box is the intervals at* 32% *(*5%*) of CL.*

The convoluted likelihood can be then written as,

$$\mathcal{L}_{(\text{stat+syst})}(\phi, C) = \int_{-\pi}^{+\pi}\int_{-1}^{+1} \mathcal{L}_{(\text{stat})}(\phi', C')G(\mathcal{R}e(\bar{c}_\sigma), \mathcal{I}m(\bar{c}_\sigma))|detJ|d\phi' dC', \qquad (6.26)$$

where $G(\mathcal{R}e(\bar{c}_\sigma), \mathcal{I}m(\bar{c}_\sigma))$ is the systematic Gaussian distribution in the $(\mathcal{R}e(\bar{c}_\sigma), \mathcal{I}m(\bar{c}_\sigma))$ plane, and $detJ$ is the Jacobian of the transformation (6.25). This convolution already takes into account the periodicity of the likelihood function in $\phi(\sigma)$, and the fact that $C(\sigma)$ does not extend outside the physical region.

6.8 The Nominal Signal Model

The *nominal model* parameterizes the total signal amplitude as the isobar sum of eight contributions. The signal yield is dominated by the following components:

- $B^0 \to \rho^0(770)K_S$ ($\rho^0(770) \to \pi^+\pi^-$), with an amplitude described with a Gounaris-Sakurai lineshape;

- $B^0 \to f_0(980)K_S$ ($f_0(980) \to \pi^+\pi^-$), with an amplitude described with a Flatté lineshape;
- $B^0 \to K^*(892)^+\pi^-$ ($K^*(892)^+ \to K_S\pi^+$), uses a Relativistic Breit-Wigner for the lineshape;
- $B^0 \to (K\pi)_0^{*+}\pi^-$ ($(K\pi)_0^{*+} \to K_S\pi^+$), corresponding to the $K\pi$ S-wave contribution. It is described with the LASS lineshape, with the dynamical constrains described previously (cf. Sec. 2.4.4). The notation used in the $B^+ \to K^+\pi^-\pi^+$ [23] and $B^0 \to K^+\pi^-\pi^0$ [40] papers is used here as well.

For these four components, there are previous Q2B measurements that have shown uncontroversial signal yields (see Sec. 2.2).

Apart from these dominant four contributions, data favors inclusion of other components:

- A significant signal was spotted with a dedicated quasi-two-body analysis performed on the center of the DP; in consequence a non-resonant term, flat in phase space, is added to the signal model (see Appendix B, Sec. B.2, and Chapter 7, Fig. 7.10).
- Both BABAR and Belle Dalitz analyses of $B^+ \to K^+\pi^-\pi^+$ [24, 23], and the time- and tag-integrated Dalitz analysis of $B^0 \to K_S\pi^+\pi^-$ [42] report a signal excess in the $m_{\pi\pi} \sim 1.2 - 1.5$ GeV range. This signal is taken into account using a two-component model, with a tensor $f_2(1270)$ component, plus the so-called $f_X(1300)$ component. In this analysis, a mass/width likelihood scan for scalar, vector and tensor resonances, favored also such a two-component model (see Appendix B, Sec. B.3).
- Finally, $\chi_c(0)$ is also included (as in [23, 24, 42]).

The present signal model is the same as the one used in the BABAR $B^+ \to K^+\pi^-\pi^+$ [23] analysis, as this mode has a higher signal to background ratio, so is more sensitive to small components. This also accounts for an effort of the collaboration to standarize the BABAR charmless Dalitz analyses.

A large set of additional components has been tested. None was found to be significant when fitting the data with these components, and they are therefore not included in the nominal signal model. Nevertheless, they are considered for the estimation of the systematic uncertainty assigned to the signal model. These additional resonances are:

- $K^{*\pm}(1410)$
- $K^{*\pm}(1680)$
- $K_2^{*\pm}(1430)$
- $\rho(1450)$
- $\rho(1700)$
- χ_{c2}

A twofold process is performed to evaluate a systematical uncertainty. In the first place, data is fitted with each of these components added one-by-one to the nominal model. The fitted value for the isobar fraction and the change in NLL are used to estimate whether this additional component is significant or not (cf. Appendix B); the outcome being positive for the $f_2(1270)$, $f_X(1300)$ and $\chi_c(0)$ resonances, these ones being included in the signal model, and negative for all others, these last ones treated as systematics (see Sec. 7.3.7).

Chapter 7

Results

The selection procedure described in Sec. 5.7 retains a total of 22525 events from the on-peak data sample. The B-meson candidate in each event is mass constrained to ensure that the measurement falls within the Dalitz plot boundary (cf. Sec. 5.2.4). The resulting standard and square Dalitz plots are shown in Fig. 7.1. The density of events is more spread out in the square Dalitz plot (cf. Sec. 2.4.7). The narrow bands correspond to $B^0 \to D^{\mp}\pi^{\pm}$, $B^0 \to J/\Psi K_S^0$ and $B^0 \to \Psi(2S)K_S^0$ B-background events (cf. Sec. 5.8).

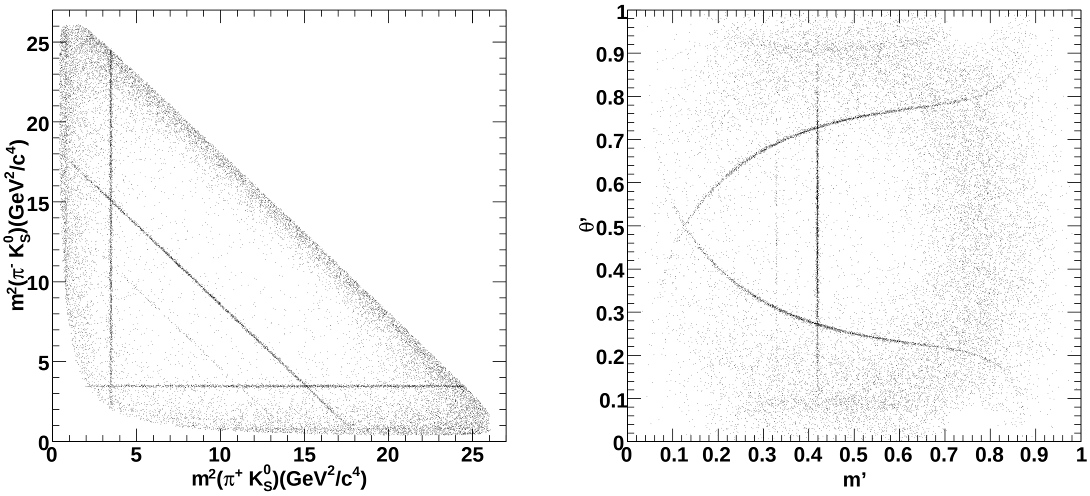

Figure 7.1: *The standard (left) and square (right) Dalitz plots of the selected data sample of 22525 events. The narrow bands correspond to* $B^0 \to D^{\mp}\pi^{\pm}$, $B^0 \to J/\Psi K_S^0$ *and* $B^0 \to \Psi(2S)K_S^0$ *B-background events.*

This final data sample is assumed to consist of signal, continuum background and 10 classes of B-backgrounds. An unbinned maximum likelihood fit is performed, using the likelihood function described in Chapter 6. A total of 12 yields (total signal, 4 classes of B-backgrounds and 7 continuum backgrounds per tagging category), plus 30 relative moduli and phases of isobar amplitudes (cf. Sec. 6.8) result from the fit. All isobar amplitudes are measured relative to $c(B^0 \to f_0(980)K_S^0)$ which is arbitrarily fixed to be real, with module 4. The fact that the results do not depend on this arbitrary convention has been checked. In addition, 34 other parameters (referred as shape parameters) that describe the PDFs used in the likelihood function are left free in the fit. A list of parameters kept fixed in the fit is given in appendix C.

When the fit is repeated starting from input parameter values randomly chosen, convergence towards two solutions (local minima) is observed. They differ by $\Delta NLL = 0.16$ in likelihood units[1]. These global and local minima solutions are referred as solution I and solution II, respectively. Figure 7.2 shows the intensities $|\mathcal{A}(B^0 \to K_S^0\pi^+\pi^-)|^2$ and $|\mathcal{A}(\bar{B}^0 \to K_S^0\pi^+\pi^-)|^2$ in the B^0 and $\bar{B}^0$ square Dalitz plots, respectively, constructed with the fitted isobar parameters from these two solutions. The interference patterns are similar for both solutions, and for both B^0 and $\bar{B}^0$ Dalitz plots.

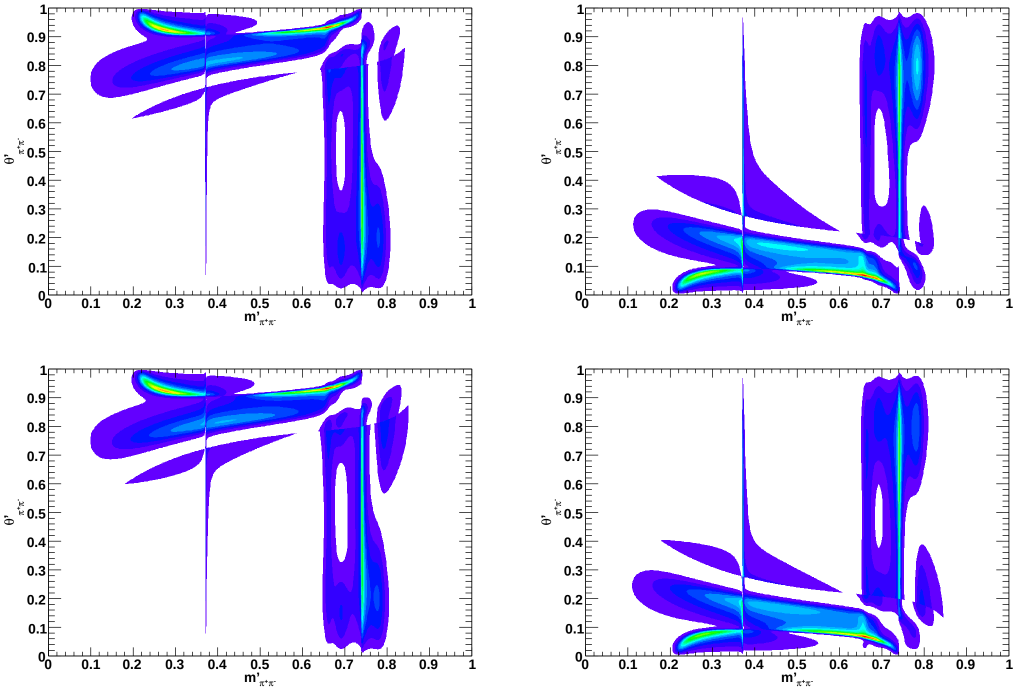

Figure 7.2: *Intensities* $|\mathcal{A}(B^0 \to K_S^0\pi^+\pi^-)|^2$ *and* $|\mathcal{A}(\bar{B}^0 \to K_S^0\pi^+\pi^-)|^2$ *in the* B^0 *(left plot) and* $\bar{B}^0$ *(right plot) square Dalitz plots, respectively, constructed with the fit results on the isobar parameters from solution I (top plots) and solution II (bottom plots). The intensity scale is in arbitrary units.*

The fitted yields and shape parameters are shown in Table 7.1. They are similar in both solutions. In Table 7.2 is shown the list of isobar parameters allowed to vary in the fit. The values of Q2B observables are collected in Table 7.3. As the Q2B observables are functions of isobar parameters, the errors quoted are the propagation using the covariance

---

[1] $\Delta NLL(i) = NLL(i) - NLL(\mathrm{min})$, where $NLL(i)$ is the NLL value for the solution $i = 1, 2$, and $NLL(\mathrm{min})$ is NLL value at the global minimum.

matrices obtained from the minimization routine `Minuit` (cf. Fig. 7.3). Inspection of fit results on the isobar parameters show that most moduli of isobar amplitudes, and thus for A_{CP} and fit fractions, have similar values in both solutions; on the contrary, some isobar phase differences are significantly different. The strongest correlations are among isobar parameters. For both solutions, the `Minuit` correlation matrices for fitted isobar parameters are given in Fig. 7.3. The matrices show similar patterns as on toy studies (cf. Sec. 6.7), with the largest correlations among phases.

Parameter Name	Fit Result Sol-I	Fit Result Sol-II
ΔNLL	0.0	0.16
N($B^0 \to K_S^0\pi^+\pi^-$)	2182 ± 64	2182 ± 64
N($B^0 \to D^+\pi^-$)	3361 ± 60	3362 ± 60
N($B^0 \to J/\Psi K_s^0$)	1804 ± 44	1803 ± 43
N($B^0 \to \eta' K_s^0$)	46 ± 16	44 ± 16
N($B^0 \to \Psi(2S) K_s^0$)	142 ± 13	142 ± 13
N(cont-Lepton)	46 ± 8.9	47 ± 9
N(cont-KaonI)	800 ± 31	800 ± 31
N(cont-KaonII)	2127 ± 49	2127 ± 49
N(cont-KaonPion)	1775 ± 45	1775 ± 45
N(cont-Pion)	2048 ± 48	2048 ± 48
N(cont-Other)	1614 ± 42	1614 ± 42
N(cont-NoTag)	5829 ± 80	5829 ± 80
$f_{core}(\Delta E)$ Signal	0.63 ± 0.14	0.63 ± 0.14
$\mu_{core}(\Delta E)$ Signal	-1.3 ± 0.7 MeV	-1.3 ± 0.6 Mev
$\sigma_{core}(\Delta E)$ Signal	17.1 ± 1.4 MeV	17.1 ± 1.3 Mev
$\mu_{tail}(\Delta E)$ Signal	-7.3 ± 2.9 MeV	-7.4 ± 3.0 Mev
$\sigma_{tail}(\Delta E)$ Signal	31.2 ± 4.6 MeV	31.4 ± 4.6 Mev
Slope(ΔE) Continuum	-8.51 ± 5.77	-8.49 ± 5.77
$\mu(m_{ES})$ Signal	5.2788 ± 0.0001 GeV$/c^2$	5.2788 ± 0.0001 Gev$/c^2$
$\sigma_L(m_{ES})$ Signal	2.24 ± 0.06 MeV$/c^2$	2.24 ± 0.06 Mev$/c^2$
$\sigma_R(m_{ES})$ Signal	2.73 ± 0.07 MeV$/c^2$	2.73 ± 0.07 Mev$/c^2$
Argus Slope(m_{ES}) Continuum	-0.3 ± 0.2	-0.4 ± 0.2
$a_1(NN)$ Continuum	1.9 ± 0.1	1.9 ± 0.1
$a_2(NN)$ Continuum	3.2 ± 0.4	3.2 ± 0.4
$a_3(NN)$ Continuum	-1.1 ± 0.1	-1.1 ± 0.1
$a_5(NN)$ Continuum	-0.47 ± 0.05	-0.48 ± 0.05
$\mu_{common}(\Delta t)$ Continuum	$0.018 \pm 0.007\,ps$	0.018 ± 0.007 ps
$\sigma_{core}(\Delta t)$ Continuum	$1.14 \pm 0.02\,ps$	1.14 ± 0.02 ps
$f_{tail}(\Delta t)$ Continuum	0.16 ± 0.02	0.16 ± 0.02
$\sigma_{tail}(\Delta t)$ Continuum	$2.8 \pm 0.2\,ps$	2.8 ± 0.2 ps
$f_{outlier}(\Delta t)$ Continuum	0.030 ± 0.004	0.030 ± 0.004
$\sigma_{outlier}(\Delta t)$ Continuum	$10.7 \pm 0.9\,ps$	10.7 ± 0.8 ps

Table 7.1: *Nominal fit results for the event yields, shape parameters, and ΔNLL for solutions I and II. The errors shown are statistical only.*

Although errors quoted in Table 7.3 do not include systematic uncertainties, some qualitative statements about the fit results can be stated:

- **Significance of the dominant components**. The dominant components of the signal model, $f_0(980)K_S^0$, $\rho^0(770)K_S^0$, $K^{*\pm}(892)\pi^{\mp}$ and the $K\pi$ S-wave, yield fit fractions significantly different from zero. This is in agreement with previous Q2B and Dalitz plot analyses (cf. Sec. 2.2). Their presence on data is evident in the mass spectra (cf. next section, Sec. 7.1.2). For the non-resonant component the fit finds an isobar fraction that seems very significant considering only the statistical error, but it suffers from large systematic uncertainties (cf. Sec. 7.3.7).

Isobar Amplitude	$\|A\|$ Sol-I	$\phi[deg]$ Sol-I	$\|A\|$ Sol-II	$\phi[deg]$ Sol-II
$A(f_0(980)K_S^0)$	4.0	0.0	4.0	0.0
$\bar{A}(f_0(980)K_S^0)$	3.7 ± 0.4	-73.9 ± 19.6	3.2 ± 0.6	-112.3 ± 20.9
$A(\rho(770)K_S^0)$	0.10 ± 0.02	35.6 ± 14.9	0.09 ± 0.02	66.7 ± 18.3
$\bar{A}(\rho(770)K_S^0)$	0.11 ± 0.02	15.3 ± 20.0	0.10 ± 0.03	-0.1 ± 18.2
$A(NR)$	2.6 ± 0.5	35.3 ± 16.4	1.9 ± 0.7	56.7 ± 23.6
$\bar{A}(NR)$	2.7 ± 0.6	36.1 ± 18.3	3.1 ± 0.6	-45.2 ± 17.8
$A(K^{*+}(892)\pi^-)$	0.154 ± 0.016	-138.7 ± 25.7	0.145 ± 0.017	-107.0 ± 24.1
$\bar{A}(K^{*-}(892)\pi^+)$	0.125 ± 0.015	163.1 ± 23.0	0.119 ± 0.015	76.4 ± 23.0
$A((K\pi)_0^{*+}\pi^-)$	6.9 ± 0.6	-151.7 ± 19.7	6.5 ± 0.6	-122.5 ± 20.3
$\bar{A}((K\pi)_0^{*-}\pi^+)$	7.6 ± 0.6	136.2 ± 19.8	7.3 ± 0.7	52.6 ± 20.3
$A(f_X(1300)K_S^0)$	1.41 ± 0.23	43.2 ± 22.0	1.40 ± 0.28	85.9 ± 24.8
$\bar{A}(f_X(1300)K_S^0)$	1.24 ± 0.27	31.6 ± 23.0	1.02 ± 0.33	-67.9 ± 22.1
$A(f_2(1270)K_S^0)$	0.014 ± 0.002	5.8 ± 19.2	0.012 ± 0.003	23.9 ± 22.7
$\bar{A}(f_2(1270)K_S^0)$	0.011 ± 0.003	-24.0 ± 28.0	0.011 ± 0.003	-83.3 ± 24.3
$A(\chi_{c0}K_S^0)$	0.33 ± 0.15	61.4 ± 44.5	0.28 ± 0.16	51.9 ± 38.4
$\bar{A}(\chi_{c0}K_S^0)$	0.44 ± 0.09	15.1 ± 30.0	0.43 ± 0.08	-58.5 ± 27.9

Table 7.2: *Nominal fit results for the resonant isobar amplitudes for solutions I and II. The errors shown are statistical only.*

- **Statistical significance of small components**. For the subdominant components, $f_X(1300)\ K_S^0$, $f_2(1270)K_S^0$ and $\chi_c(0)K_S^0$, the fit finds small isobar fractions. The significance of all these components is quantified using full likelihood scans, and is presented in Sec. 7.2.4.

- **CP-violation in $B^0 \rightarrow f_0(980)K_S^0$ decays**. Although direct CP-violation for this submode seems not to be significant, the measurement of its β_{eff} phase is significantly different from zero, which implies mixing-induced CP-violation for this submode. However this β_{eff} is compatible with the value from $b \rightarrow c\bar{c}s$ decays.

- **CP-violation in $B^0 \rightarrow \rho^0(770)K_S^0$ decays**. In contrast with the $B^0 \rightarrow f_0(980)K_S^0$ decays, in this submode both direct and mixing-induced CP-violation seem not to be significant.

- **Direct CP-violation in $B^0 \rightarrow K^{*\pm}(892)\pi^{\mp}$ decays**. The central value of the direct CP asymmetry for the submode $K^{*\pm}(892)\pi^{\mp}$ is roughly similar both solutions, pointing to an (statistical only) exclusion of CP conservation at the $\sim 2\sigma$ level.

The quantification of these statements will be better justified in Sec. 7.2, where the correct statistical treatment of local minima solutions is properly taken into account (cf. Sec. 6.7) and the systematic uncertainties are included (cf. Sec. 6.7.2).

7.1 Goodness of Fit and Likelihood Projections

To check the validity of the fits and study the results, 367 toy data samples, corresponding to independent pseudo-experiments with as many events as in the final data sample, and generated using the isobar parameters of solution-I, were fitted with random initial values.

Parameter	Value Sol-I	Value Sol-II
$C(f_0(980)K^0_S)$	0.08 ± 0.19	0.23 ± 0.19
$\beta_{eff}(f_0(980)K^0_S)$	37.0 ± 9.8	56.2 ± 10.4
$FF(f_0(980)K^0_S)$	$13.8^{+1.5}_{-1.4}$	$13.5^{+1.4}_{-1.3}$
$C(\rho^0(770)K^0_S)$	-0.05 ± 0.26	-0.14 ± 0.26
$\beta_{eff}(\rho^0(770)K^0_S)$	10.2 ± 8.9	33.4 ± 10.4
$FF(\rho^0(770)K^0_S)$	$8.6^{+1.4}_{-1.3}$	$8.5^{+1.3}_{-1.2}$
$A_{CP}(K^*(892)\pi)$	-0.21 ± 0.10	$-0.19^{+0.10}_{-0.11}$
$\Delta\phi(K^*(892)\pi)$	58.3 ± 32.7	176.6 ± 28.8
$FF(K^*(892)\pi)$	$11.0^{+1.2}_{-1.0}$	$10.9^{+1.2}_{-1.0}$
$A_{CP}((K\pi)^*_0\pi)$	0.09 ± 0.07	$0.12^{+0.07}_{-0.06}$
$\Delta\phi((K\pi)^*_0\pi)$	72.2 ± 24.6	-175.1 ± 22.6
$FF((K\pi)^*_0\pi)$	45.2 ± 2.3	46.1 ± 2.4
$C(f_2(1270)K^0_S)$	$0.28^{+0.35}_{-0.40}$	0.09 ± 0.46
$\phi(f_2(1270)K^0_S)$	29.8 ± 35.8	107.2 ± 33.3
$FF(f_2(1270)K^0_S)$	$2.3^{+0.8}_{-0.7}$	$2.3^{+0.9}_{-0.7}$
$C(f_X(1300)K^0_S)$	$0.13^{+0.33}_{-0.35}$	$0.30^{+0.34}_{-0.41}$
$\phi(f_X(1300)K^0_S)$	11.5 ± 30.3	153.8 ± 27.5
$FF(f_X(1300)K^0_S)$	$3.6^{+1.0}_{-0.9}$	$3.5^{+1.0}_{-0.8}$
$C(NR)$	0.01 ± 0.25	$-0.45^{+0.28}_{-0.24}$
$\phi(NR)$	0.8 ± 17.5	102.0 ± 26.5
$FF(NR)$	11.5 ± 2.0	12.6 ± 2.0
$C(\chi_c(0)K^0_S)$	$-0.29^{+0.53}_{-0.44}$	$-0.41^{+0.54}_{-0.42}$
$\phi(\chi_c(0)K^0_S)$	46.3 ± 44.7	110.4 ± 46.6
$FF(\chi_c(0)K^0_S)$	$1.04^{+0.41}_{-0.33}$	$0.99^{+0.37}_{-0.30}$
FF_{Tot}	$97.2^{+1.7}_{-1.3}$	$98.3^{+1.5}_{-1.3}$
A^{incl}_{CP}	-0.01 ± 0.05	0.01 ± 0.05
$\Delta\phi(f^0(980)K^0_S, \rho(770)K^0_S)$	-35.6 ± 14.9	-66.7 ± 18.3
$\Delta\phi(\rho(770)K^0_S, K^*(892)\pi)$	174.3 ± 28.0	186.3 ± 29.8
$\Delta\phi(\rho(770)K^0_S, (K\pi)^*_0\pi)$	-172.8 ± 22.6	-170.8 ± 26.8
$\Delta\phi(K^*(892)\pi, (K\pi)^*_0\pi)$	13.0 ± 10.9	15.5 ± 10.2

Table 7.3: *Nominal fit results for the Q2B parameters for solutions I and II. Values are quoted at the 1σ level. As the Q2B parameters are functions of the isobar ones, the errors quoted are the propagation using the covariance matrices obtained from* `Minuit`*. Phases are in degrees and FFs in $\%$.*

Fig. 7.4 shows that the fit on data exhibits an NLL well within the range spanned by the distribution on toy data samples.

It is well known that the test described above, is a necessary but not sufficient condition for ensuring the goodness of unbinned maximum likelihood fits. Thus, the quality of the fitted likelihood function to reproduce the data has to be tested with a more extensive approach. For this, the likelihood function is projected along several directions, and the projection is compared with the distribution obtained on data. This test can be further extended, by exploring the projections in regions where signal or background dominates. Signal- or background-enhanced regions are selected by means of the likelihood ratio variable R

$$R \equiv \frac{\mathcal{L}_{\rm TM}}{\mathcal{L}_{\rm TM} + \mathcal{L}_{\rm SCF} + \mathcal{L}_{\rm Continuum} + \mathcal{L}_{\rm B-background}} \,, \tag{7.1}$$

where the likelihood function of an event $\mathcal{L}$ is split between all components (or groups of components): signal and backgrounds. In the space of observable variables, R approaches

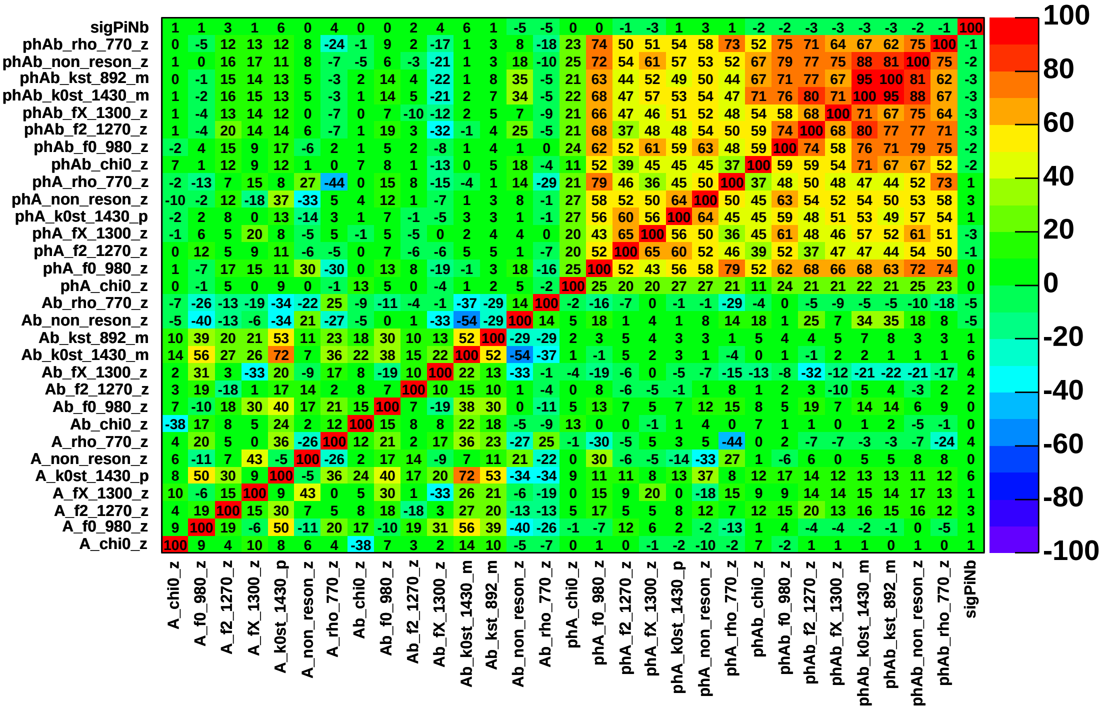

	A_chi0_z	A_f0_980_z	A_f2_1270_z	A_fX_1300_z	A_k0st_1430_p	A_non_reson_z	A_rho_770_z	Ab_chi0_z	Ab_f0_980_z	Ab_f2_1270_z	Ab_fX_1300_z	Ab_k0st_1430_m	Ab_kst_892_m	Ab_non_reson_z	Ab_rho_770_z	phA_chi0_z	phA_f0_980_z	phA_f2_1270_z	phA_fX_1300_z	phA_k0st_1430_p	phA_non_reson_z	phA_rho_770_z	phAb_chi0_z	phAb_f0_980_z	phAb_f2_1270_z	phAb_fX_1300_z	phAb_k0st_1430_m	phAb_kst_892_m	phAb_non_reson_z	phAb_rho_770_z	sigPiNb
sigPiNb	1	1	3	1	6	0	4	0	0	2	4	6	1	-5	-5	0	0	-1	-3	1	3	1	-2	-2	-3	-3	-3	-3	-2	-1	100
phAb_rho_770_z	0	-5	12	13	12	8	-24	-1	9	2	-17	1	3	8	-18	23	74	50	51	54	58	73	52	75	71	64	67	62	75	100	-1
phAb_non_reson_z	1	0	16	17	11	8	-7	-5	6	-3	-21	1	3	18	-10	25	72	54	61	57	53	52	67	79	77	75	88	81	100	75	-2
phAb_kst_892_m	0	-1	15	14	13	5	-3	2	14	4	-22	1	8	35	-5	21	63	44	52	49	50	44	67	71	77	67	95	100	81	62	-3
phAb_k0st_1430_m	1	-2	16	15	13	5	-3	1	14	5	-21	2	7	34	-5	22	68	47	57	53	54	47	71	76	80	71	100	95	88	67	-3
phAb_fX_1300_z	1	-4	13	14	12	0	-7	0	7	-10	-12	2	5	7	-9	21	66	47	46	51	52	48	54	58	68	100	71	67	75	64	-3
phAb_f2_1270_z	1	-4	20	14	14	6	-7	1	19	3	-32	-1	4	25	-5	21	68	37	48	48	54	50	59	74	100	68	80	77	77	71	-3
phAb_f0_980_z	-2	4	15	9	17	-6	2	1	5	2	-8	1	4	1	0	24	62	52	61	59	63	48	59	100	74	58	76	71	79	75	-2
phAb_chi0_z	7	1	12	9	12	1	0	7	8	1	-13	0	5	18	-4	11	52	39	45	45	45	37	100	59	59	54	71	67	67	52	-2
phA_rho_770_z	-2	-13	7	15	8	27	-44	0	15	8	-15	-4	1	14	-29	21	79	46	36	45	50	100	37	48	50	48	47	44	52	73	1
phA_non_reson_z	-10	-2	12	-18	37	-33	5	4	12	1	-7	1	3	8	-1	27	58	52	50	64	100	50	45	63	54	52	54	50	53	58	3
phA_k0st_1430_p	-2	2	8	0	13	-14	3	1	7	-1	-5	3	3	1	-1	27	56	60	56	100	64	45	45	59	48	51	53	49	57	54	1
phA_fX_1300_z	-1	6	5	20	8	-5	5	-1	5	-5	0	2	4	4	0	20	43	65	100	56	50	36	45	61	48	46	57	52	61	51	-3
phA_f2_1270_z	0	12	5	9	11	-6	-5	0	7	-6	-6	5	5	1	-7	20	52	100	65	60	52	46	39	52	37	47	47	44	54	50	-1
phA_f0_980_z	1	-7	17	15	11	30	-30	0	13	8	-19	-1	3	18	-16	25	100	52	43	56	58	79	52	62	68	66	68	63	72	74	0
phA_chi0_z	0	-1	5	0	9	0	-1	13	5	0	-4	1	2	5	-2	100	25	20	20	27	27	21	11	24	21	21	22	21	25	23	0
Ab_rho_770_z	-7	-26	-13	-19	-34	-22	25	-9	-11	-4	-1	-37	-29	14	100	-2	-16	-7	0	-1	-1	-29	-4	0	-5	-9	-5	-5	-10	-18	-5
Ab_non_reson_z	-5	-40	-13	-6	-34	21	-27	-5	0	1	-33	-54	-29	100	14	5	18	1	4	1	8	14	18	1	25	7	34	35	18	8	-5
Ab_kst_892_m	10	39	20	21	53	11	23	18	30	10	13	52	100	-29	-29	2	3	5	4	3	3	1	5	4	4	5	7	8	3	3	1
Ab_k0st_1430_m	14	56	27	26	72	7	36	22	38	15	22	100	52	-54	-37	1	-1	5	2	3	1	-4	0	1	-1	2	2	1	1	1	6
Ab_fX_1300_z	2	31	3	-33	20	-9	17	8	-19	10	100	22	13	-33	-1	-4	-19	-6	0	-5	-7	-15	-13	-8	-32	-12	-21	-22	-21	-17	4
Ab_f2_1270_z	3	19	-18	1	17	14	2	8	7	100	10	15	10	1	-4	0	8	-6	-5	-1	1	8	1	2	3	-10	5	4	-3	2	2
Ab_f0_980_z	7	-10	18	30	40	17	21	15	100	7	-19	38	30	0	-11	5	13	7	5	7	12	15	8	5	19	7	14	14	6	9	0
Ab_chi0_z	-38	17	8	5	24	2	12	100	15	8	8	22	18	-5	-9	13	0	0	-1	1	4	0	7	1	1	0	1	2	-5	-1	0
A_rho_770_z	4	20	5	0	36	-26	100	12	21	2	17	36	23	-27	25	-1	-30	-5	5	3	5	-44	0	2	-7	-7	-3	-3	-7	-24	4
A_non_reson_z	6	-11	7	43	-5	100	-26	2	17	14	-9	7	11	21	-22	0	30	-6	-5	-14	-33	27	1	-6	6	0	5	5	8	8	0
A_k0st_1430_p	8	50	30	9	100	-5	36	24	40	17	20	72	53	-34	-34	9	11	11	8	13	37	8	12	17	14	12	13	13	11	12	6
A_fX_1300_z	10	-6	15	100	9	43	0	5	30	1	-33	26	21	-6	-19	0	15	9	20	0	-18	15	9	9	14	14	15	14	17	13	1
A_f2_1270_z	4	19	100	15	30	7	5	8	18	-18	3	27	20	-13	-13	5	17	5	5	8	12	7	12	15	20	13	16	15	16	12	3
A_f0_980_z	9	100	19	-6	50	-11	20	17	-10	19	31	56	39	-40	-26	-1	-7	12	6	2	-2	-13	1	4	-4	-4	-2	-1	0	-5	1
A_chi0_z	100	9	4	10	8	6	4	-38	7	3	2	14	10	-5	-7	0	1	0	-1	-2	-10	-2	7	-2	1	1	1	0	1	0	1

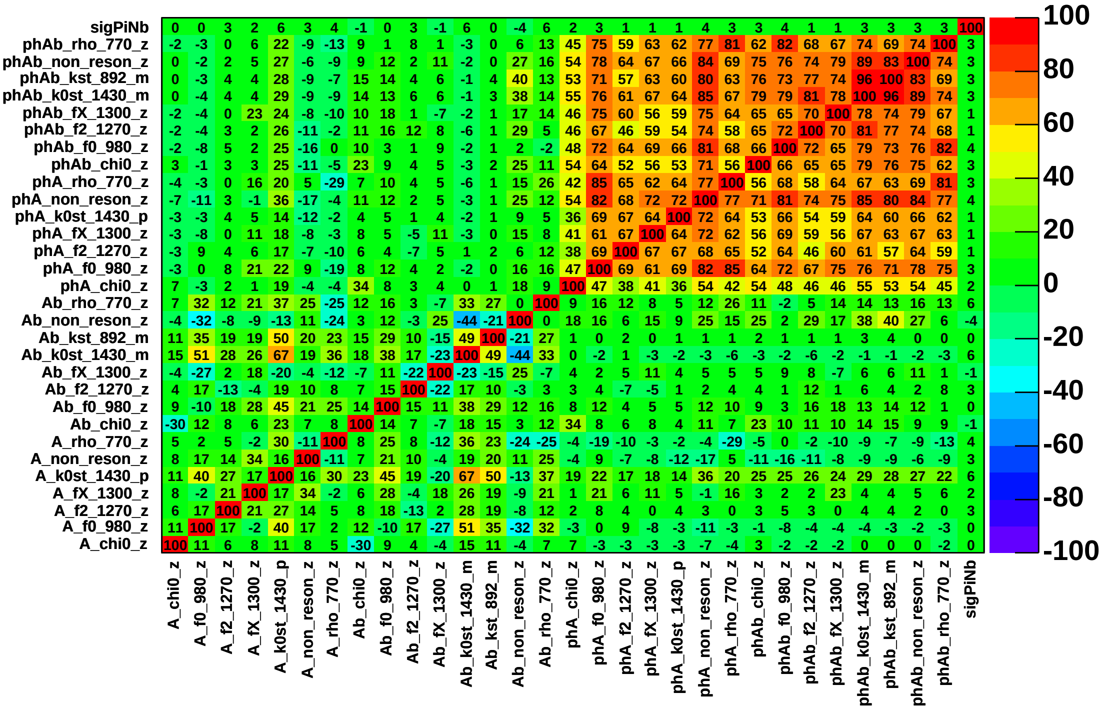

	A_chi0_z	A_f0_980_z	A_f2_1270_z	A_fX_1300_z	A_k0st_1430_p	A_non_reson_z	A_rho_770_z	Ab_chi0_z	Ab_f0_980_z	Ab_f2_1270_z	Ab_fX_1300_z	Ab_k0st_1430_m	Ab_kst_892_m	Ab_non_reson_z	Ab_rho_770_z	phA_chi0_z	phA_f0_980_z	phA_f2_1270_z	phA_fX_1300_z	phA_k0st_1430_p	phA_non_reson_z	phA_rho_770_z	phAb_chi0_z	phAb_f0_980_z	phAb_f2_1270_z	phAb_fX_1300_z	phAb_k0st_1430_m	phAb_kst_892_m	phAb_non_reson_z	phAb_rho_770_z	sigPiNb
sigPiNb	0	0	3	2	6	3	4	-1	0	3	-1	6	0	-4	6	2	3	1	1	1	4	3	3	4	1	1	3	3	3	3	100
phAb_rho_770_z	-2	-3	0	6	22	-9	-13	9	1	8	1	-3	0	6	13	45	75	59	63	62	77	81	62	82	68	67	74	69	74	100	3
phAb_non_reson_z	0	-2	2	5	27	-6	-9	9	12	2	11	-2	0	27	16	54	78	64	67	66	84	69	75	76	74	79	89	83	100	74	3
phAb_kst_892_m	0	-3	4	4	28	-9	-7	15	14	4	6	-1	4	40	13	53	71	57	63	60	80	63	76	73	77	74	96	100	83	69	3
phAb_k0st_1430_m	0	-4	4	4	29	-9	-9	14	13	6	6	-1	3	38	14	55	76	61	67	64	85	67	79	79	81	78	100	96	89	74	3
phAb_fX_1300_z	-2	-4	0	23	24	-8	-10	10	18	1	-7	-2	1	17	14	46	75	60	56	59	75	64	65	65	70	100	78	74	79	67	1
phAb_f2_1270_z	-2	-4	3	2	26	-11	-2	11	16	12	8	-6	1	29	5	46	67	46	59	54	74	58	65	72	100	70	81	77	74	68	1
phAb_f0_980_z	-2	-8	5	2	25	-16	0	10	3	1	9	-2	1	2	-2	48	72	64	69	66	81	68	66	100	72	65	79	73	76	82	4
phAb_chi0_z	3	-1	3	3	25	-11	-5	23	9	4	5	-3	2	25	11	54	64	52	56	53	71	56	100	66	65	65	79	76	75	62	3
phA_rho_770_z	-4	-3	0	16	20	5	-29	7	10	4	5	-6	1	15	26	42	85	65	62	64	77	100	56	68	58	64	67	63	69	81	3
phA_non_reson_z	-7	-11	3	-1	36	-17	-4	11	12	2	5	-3	1	25	12	54	82	68	72	72	100	77	71	81	74	75	85	80	84	77	4
phA_k0st_1430_p	-3	-3	4	5	14	-12	-2	4	5	1	4	-2	1	9	5	36	69	67	64	100	72	64	53	66	54	59	64	60	66	62	1
phA_fX_1300_z	-3	-8	0	11	18	-8	-3	8	5	-5	11	-3	0	15	8	41	61	67	100	64	72	62	56	69	59	56	67	63	67	63	1
phA_f2_1270_z	-3	9	4	6	17	-7	-10	6	4	-7	5	1	2	6	12	38	69	100	67	67	68	65	52	64	46	60	61	57	64	59	1
phA_f0_980_z	-3	0	8	21	22	9	-19	8	12	4	2	-2	0	16	16	47	100	69	61	69	82	85	64	72	67	75	76	71	78	75	3
phA_chi0_z	7	-3	2	1	19	-4	-4	34	8	3	4	0	1	18	9	100	47	38	41	36	54	42	54	48	46	46	55	53	54	45	2
Ab_rho_770_z	7	32	12	21	37	25	-25	12	16	3	-7	33	27	0	100	9	16	12	8	5	12	26	11	-2	5	14	14	13	16	13	6
Ab_non_reson_z	-4	-32	-8	-9	-13	11	-24	3	12	-3	25	-44	-21	100	0	18	16	6	15	9	25	15	25	2	29	17	38	40	27	6	-4
Ab_kst_892_m	11	35	19	19	50	20	23	15	29	10	-15	49	100	-21	27	1	0	2	0	1	1	1	2	1	1	1	3	4	0	0	0
Ab_k0st_1430_m	15	51	28	26	67	19	36	18	38	17	-23	100	49	-44	33	0	-2	1	-3	-2	-3	-6	-3	-2	-6	-2	-1	-1	-2	-3	6
Ab_fX_1300_z	-4	-27	2	18	-20	-4	-12	-7	11	-22	100	-23	-15	25	-7	4	2	5	11	4	5	5	5	9	8	-7	6	6	11	1	-1
Ab_f2_1270_z	4	17	-13	-4	19	10	8	7	15	100	-22	17	10	-3	3	3	4	-7	-5	1	2	4	4	1	12	1	6	4	2	8	3
Ab_f0_980_z	9	-10	18	28	45	21	25	14	100	15	11	38	29	12	16	8	12	4	5	5	12	10	9	3	16	18	13	14	12	1	0
Ab_chi0_z	-30	12	8	6	23	7	8	100	14	7	-7	18	15	3	12	34	8	6	8	4	11	7	23	10	11	10	14	15	9	9	-1
A_rho_770_z	5	2	5	-2	30	-11	100	8	25	8	-12	36	23	-24	-25	-4	-19	-10	-3	-2	-4	-29	-5	0	-2	-10	-9	-7	-9	-13	4
A_non_reson_z	8	17	14	34	16	100	-11	7	21	10	-4	19	20	11	25	-4	9	-7	-8	-12	-17	5	-11	-16	-11	-8	-9	-9	-6	-9	3
A_k0st_1430_p	11	40	27	17	100	16	30	23	45	19	-20	67	50	-13	37	19	22	17	18	14	36	20	25	25	26	24	29	28	27	22	6
A_fX_1300_z	8	-2	21	100	17	34	-2	6	28	-4	18	26	19	-9	21	1	21	6	11	5	-1	16	3	2	2	23	4	4	5	6	2
A_f2_1270_z	6	17	100	21	27	14	5	8	18	-13	2	28	19	-8	12	2	8	4	0	4	3	0	3	5	3	0	4	4	2	0	3
A_f0_980_z	11	100	17	-2	40	17	2	12	-10	17	-27	51	35	-32	32	-3	0	9	-8	-3	-11	-3	-1	-8	-4	-4	-4	-3	-2	-3	0
A_chi0_z	100	11	6	8	11	8	5	-30	9	4	-4	15	11	-4	7	7	-3	-3	-3	-3	-7	-4	3	-2	-2	-2	0	0	0	-2	0

Figure 7.3: *Fit on data correlation matrices between isobar parameters for solutions I (top) and II (bottom) obtained from* `Minuit`.

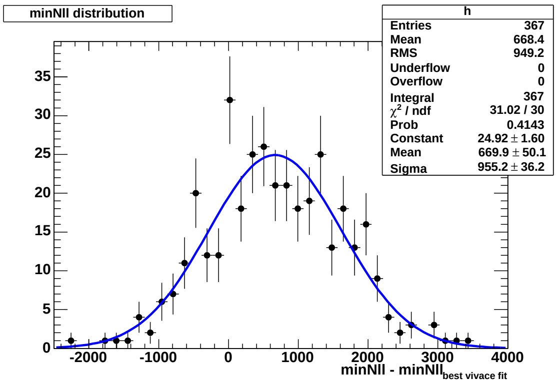

Figure 7.4: *Distribution of the* $NLL - NLL_{data}$ *for 367 toy fits on samples generated with the PDF parameters of solution-I obtained from the fit to data (the zero point corresponds to the NLL fitted on data).*

1 in signal-dominated regions, and zero in background-dominated regions. Cuts on this variable can be used to select subsamples with specific signal-to-background levels. The distribution of R in data, overlaid with the projection along the R variable of the fitted likelihood function, is plotted with linear (logarithmic) vertical and logarithmic (linear) horizontal scales on Fig. 7.5.

7.1.1 Discriminant Variables

The distributions for m_{ES}, ΔE and NN are shown in Fig. 7.6, for different cut values on the likelihood ratio R (in each case, the plotted variable is excluded from the computation of R) corresponding to increasing levels of signal purity. When stated in the caption, a veto is applied on the $D\pi$ and $J/\Psi K^0_S$ B backgrounds, by excluding the bands with $1.75\ \mathrm{GeV}/c^2 < m_{K^0_S\pi^\mp} < 1.9\ \mathrm{GeV}/c^2$ and $3.08\ \mathrm{GeV}/c^2 < m_{\pi^+\pi^-} < 3.12\ \mathrm{GeV}/c^2$, respectively. These figures illustrate the agreement between the PDFs used to model the discriminant variables, and their distributions in the data.

7.1.2 Dalitz Spectra

The dynamical isobar model used to describe the signal distribution along the Dalitz plot can be validated using the same approach. Figs. 7.7–7.10 show the $m_{K^0_S\pi}$ and $m_{\pi^+\pi^-}$ invariant mass spectra.

Similar interference patterns occur on the $m_{K^0_S\pi^+}$ and $m_{K^0_S\pi^-}$ likelihood projections. Thus by folding the SDP with respect to the $\theta'_{\pi^+\pi^-}$ variable at $\theta'_{\pi^+\pi^-} = 0.5$, and defining a symmetrized $m_{K^0_S\pi}$, the symmetrised projections carry essentially the same information, while multiplying the statistics by a factor of 2.

For each meson pair, the full kinematic range is shown (cf. top plots of Fig. 7.7). The $D^\pm$ mass peak is prominent in the symmetrized $m_{K^0_S\pi}$ spectrum, as are the J/Ψ and $\Psi(2S)$ peaks in the $m_{\pi^+\pi^-}$ spectrum. The description of these narrow structures in the Dalitz plot

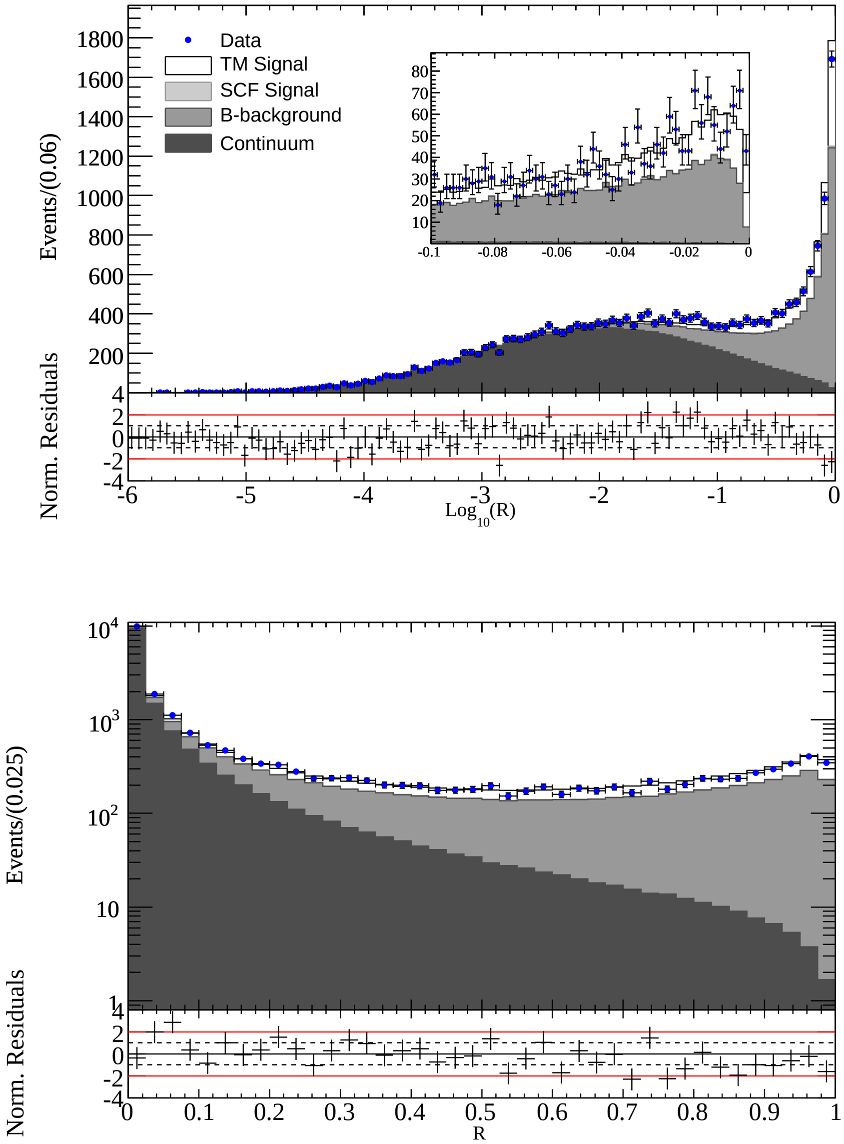

Figure 7.5: *Distribution of the likelihood ration* R *(cf. Eq.(7.1)) for all events (blue points). Superimposed is an MC sample of pseudoexperiments (toys) generated with solution I of the fitted parameters. For the toy distribution is shown the cumulated subdistributions of different signal and background components. Logarithmic and linear scales are used to enhance background (top plot) and the signal (bottom plot and the inset on the top plot). The various components are shaded as follows: Continuum (dark), B backgrounds (grey), SCF (light gray) and TM (white). The SCF is not visible as it is only* 2% *of the signal component.*

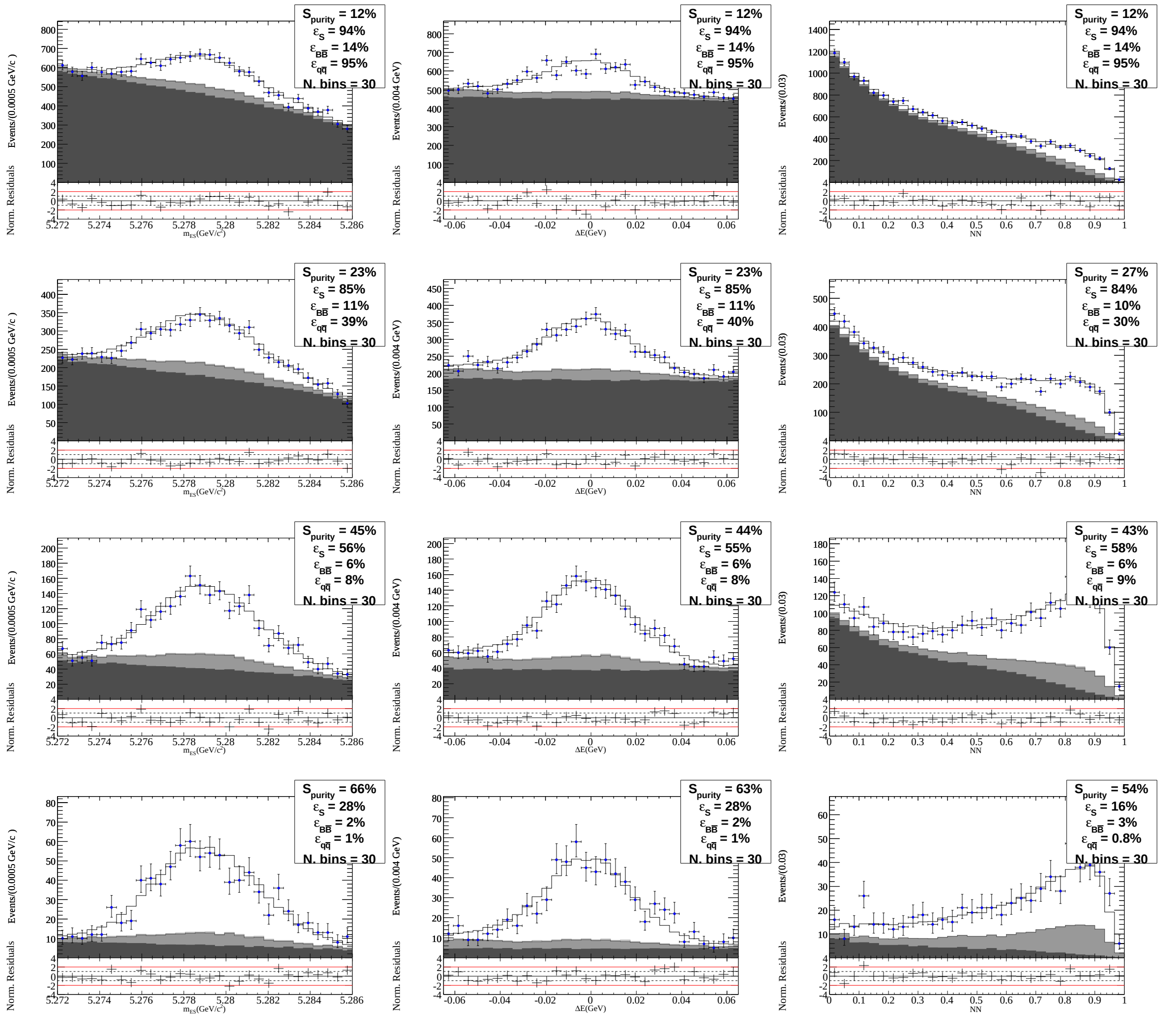

Figure 7.6: *From left to right:* m_{ES}, ΔE *and* NN *distributions. In all plots a veto on the* $D\pi$ *and* $J/\Psi K^0_S$ *components is applied. From top to bottom are shown different signal enhanced samples by removing events with* $R < cut$. *The PDF of the considered variable is not included in the definition of* R. *In the top plots no* R *cut is applied, for plots below, consecutive cuts on* R *are applied in order to have* $N_{\rm sign.}/(N_{\rm sign.}+N_{\rm cont.}) \sim 25\%, 50\%, 75\%$ *respectively. Below each bin are shown the residuals, normalized in error units, the dotted and red lines are the* 1σ *and* 2σ *deviations. In each plot a box showing the signal purity, the signal, B background and continuum efficiencies respectively.*

is illustrated with a zoom on the invariant masses. The $m_{K^0_S\pi}$ invariant mass projection in the region of $D\pi$ is shown in the inset of the top plot of Fig. 7.7. It could be claimed that the likelihood function used to describe this narrow component seems to slightly underestimate the $D\pi$ yield; but on the one hand the statistical significance of this disagreement is not dramatics; and more importantly, even if it was the case, this small imperfection would have essentially no effect on the results presented in Sec. 7.2, as $D\pi$-related fit parameters have negligible correlations with the signal components. Also are shown a zoom on the $m_{\pi^+\pi^-}$ invariant mass in the region of the $J/\Psi K^0_S$ and $\Psi(2S)K^0_S$ bands (insets in bottom plot of Fig. 7.7).

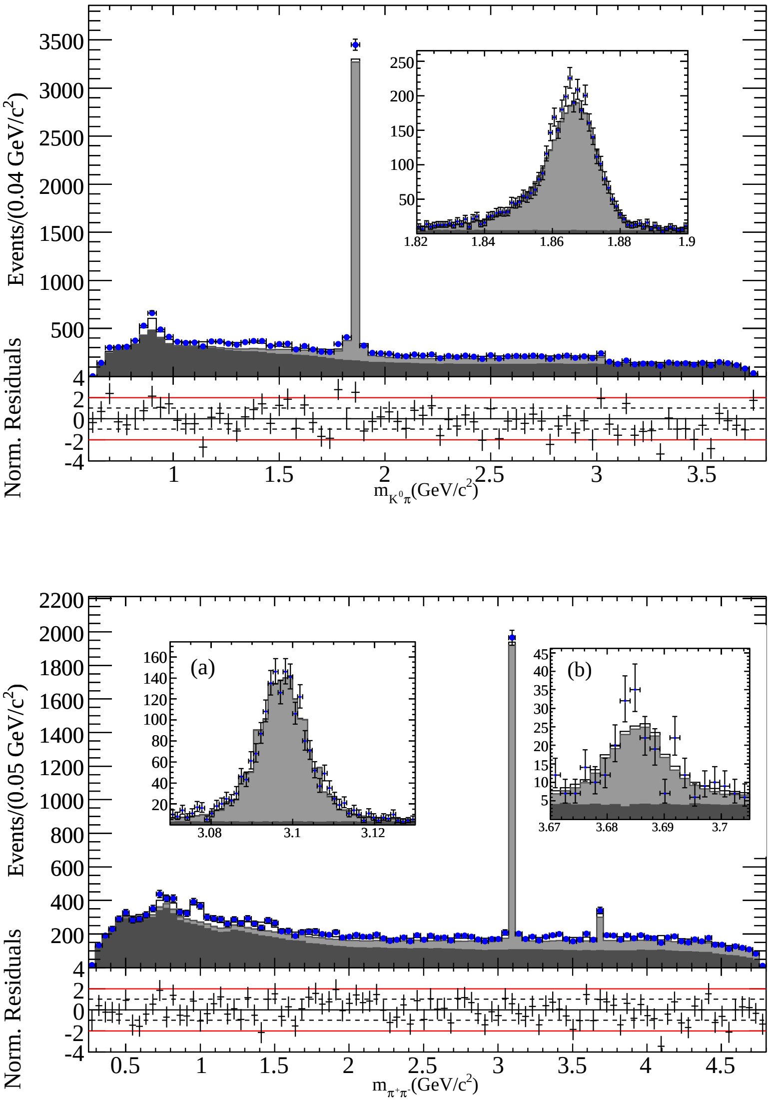

Figure 7.7: *Symmetric* $m_{K^0_S\pi}$ *(top) and* $m_{\pi^+\pi^-}$ *(bottom) distributions for all events. The symmetric* $m_{K^0_S\pi}$ *is defined by folding the SDP with respect to the* $\theta'_{\pi^+\pi^-}$ *variable at* $\theta'_{\pi^+\pi^-} = 0.5$*. Inset in the top plot shows the* $D^\pm$ *mass region in* $1\ \mathrm{MeV}/c^2$ *bins. Insets in the bottom plot show the* J/Ψ *and* $\Psi(2S)$ *mass regions in* $1\ \mathrm{MeV}/c^2$ *and* $2\ \mathrm{MeV}/c^2$ *bins, respectively.*

The $m_{\pi^+\pi^-}$ spectrum is also shown for a zoom in the $m_{\pi^+\pi^-} < 1.8\ \mathrm{GeV}/c^2$ region, separately for negative and positive values of the cosinus of the helicity angle $\cos(\theta_{\pi^+\pi^-})$ (cf. Fig. 7.8). The plots use different cuts on the likelihood ratio R, corresponding to increasing levels of signal purity. The peaks corresponding to the $f_0(980)K_S^0$ and $\rho^0(770)K_S^0$ signal components are evident in the spectrum. A signal excess around $m_{\pi\pi} \sim 1.3~\mathrm{GeV}/c^2$ is also visible. As mentioned before in Sec. 6.8, this signal, also reported by previous $B \to K\pi\pi$ analyses, is described in this isobar model as a coherent sum of $f_2(1270)K_S^0$ and $f_X(1300)K_S^0$ components.

Similarly, Fig. 7.9 shows the $m_{K_S^0\pi}$ projection for a zoom on the $m_{K_S^0\pi} < 1.8~\mathrm{GeV}/c^2$ region, separately for negative and positive values of the cosinus of the helicity angle $\cos(\theta_{K_S^0\pi})$. Peaks corresponding to the $K^{*\pm}(892)\pi^{\mp}$ and $K\pi$ S-wave $(K\pi)_0^{*\pm}\pi^{\mp}$ components are clearly visible. The interference pattern between the scalar and vector K^* is evident from the opposite sign of the forward-backward helicity asymmetries below and above the peak of the $K^*(892)$. This effect is seen both in the symmetrized and in the individual $m_{K_S^0\pi}$ spectra, because the measured phase differences are similar in both cases.

Furthermore, projections on the Δ_{Dalitz} variable are shown. This variable is defined as the smallest of the three invariant masses. The center (edges) of the DP corresponds to high (low) values of this variable. Fig. 7.10 shows zooms on the edges and the center of the Dalitz plot for different cuts on the likelihood ratio. The left hand plots of this figure illustrate the signal density at the center of the DP, which is described in the isobar model by means of a flat non-resonant component over the entire phase space. These plots are in agreement with the sPlot [31] analysis performed in the center of the DP, and presented in Appendix B (cf. Sec. B.2). This analysis showed evidence for the presence of signal and B background events that populate the center of the DP, albeith with a limited discrimination between these two B species. The likelihood projections in the center of the DP agree with this conclusion. A systematic uncertainty on the the non-resonant fit fraction is assigned to take into account he limited signal to B background discrimination in the center of the DP (cf. Sec. 7.3.7).

7.1.3 Time-dependent Asymmetries

The quality of a time-dependent analysis relies crucially on a careful modeling of the Δt distributions. The $B^0 \to K_S\pi^+\pi^-$ sample contains two useful control subsamples for this purpose. The time-dependent CP-violating asymmetries for $B^0 \to D^{\pm}\pi^{\mp}$ and $B^0 \to J/\Psi K_S^0$ decays are well known, and it is straightforward to select events that belong mostly to these B-background species, by means of a simple cut on the Dalitz plot along the bands they populate. Fig. 7.11 shows the distributions of Δt for tagged events in the $D\pi$ and $J/\Psi K_S^0$ bands. The top (middle) plots of the figure show events in which the B^0_{tag} meson is assigned a $\bar{B}^0$ (B^0) tag, and the bottom plot show the (raw) time-dependent CP asymmetry. The left hand plot shows the Δt distribution for events in the $D\pi$ band, and the right hand plot is for events in the $J/\Psi K_S^0$ band. It can be seen that the distributions are well described by the model, and that the time-dependent CP asymmetries follow the expected pattern: a null asymmetry for $D\pi$, and the classical sinusoidal shape for $J/\Psi K_S^0$. In the time-dependent CP asymmetry plot for the $J/\Psi K_S^0$, the horizontal dotted lines correspond to the peak-to-peak amplitude of the sinusoidal distribution using the World Average value of $S_{J/\Psi K_S^0}$ ($0.660 \pm 0.036 \pm 0.012$ [28]), diluted by the factor corresponding to the present analysis (cf. Sec. 5.3). The S parameters for these two components have been let free in the fit. The value obtained for $J/\Psi K_S^0$ is $S_{J/\Psi K_S^0} = (0.690 \pm 0.077)$ (error statistical only), in agreement with

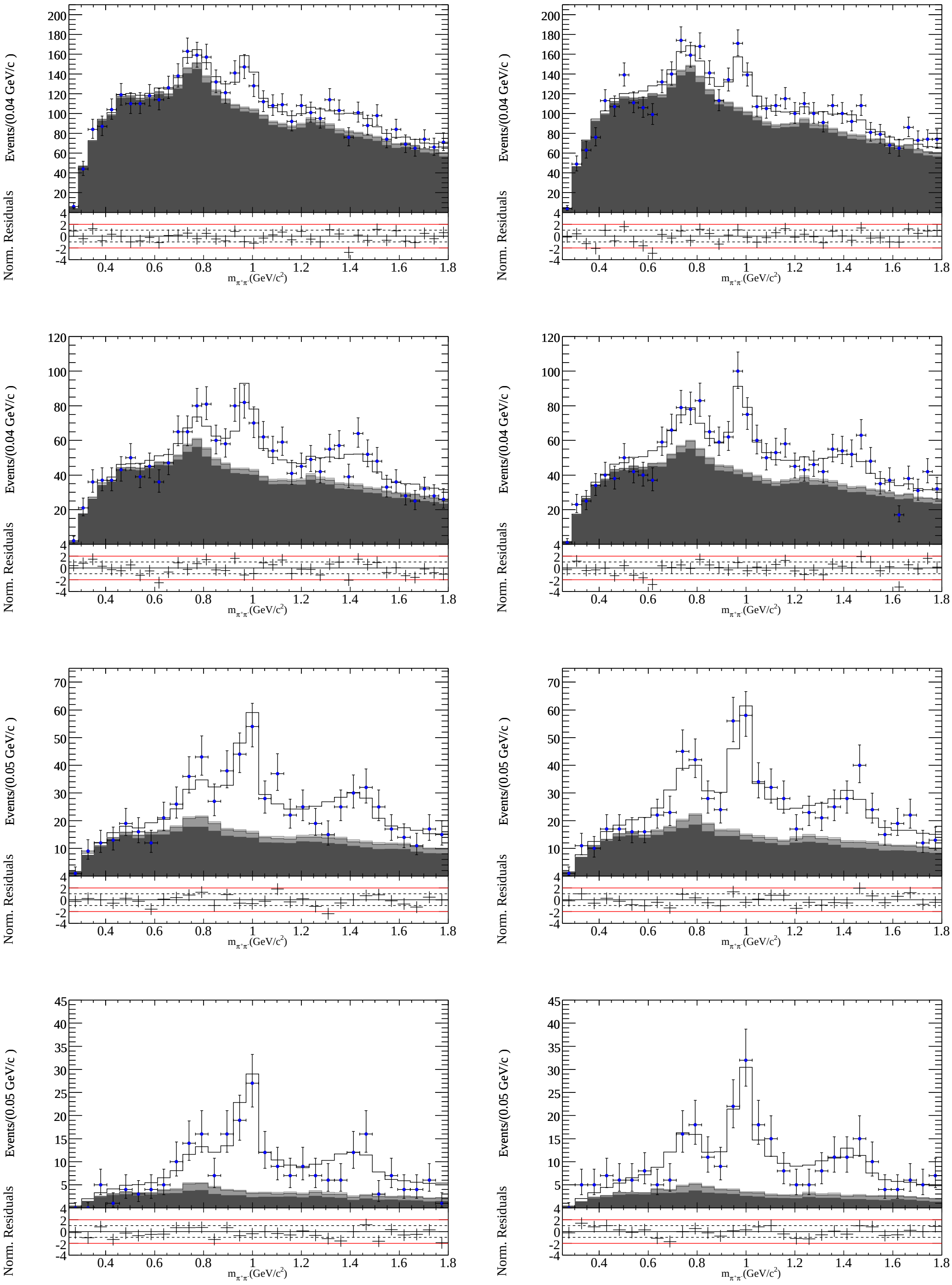

Figure 7.8: *$m_{\pi^+\pi^-}$ distribution, zooming in the $f_0(980)K^0_S$ and $\rho^0(770)K^0_S$ signal region, for positive (left) and negative (right) cosinus of the helicity angle ($\cos(\theta_{\pi^+\pi^-})$). A veto in the $D\pi$ band has been applied. The plots from top to bottom are made with different signal enhancement samples by removing events with $R < cut$. The Δt and DP PDFs have been excluded from the R definition. R cuts are made with the same criteria as in Fig. 7.6.*

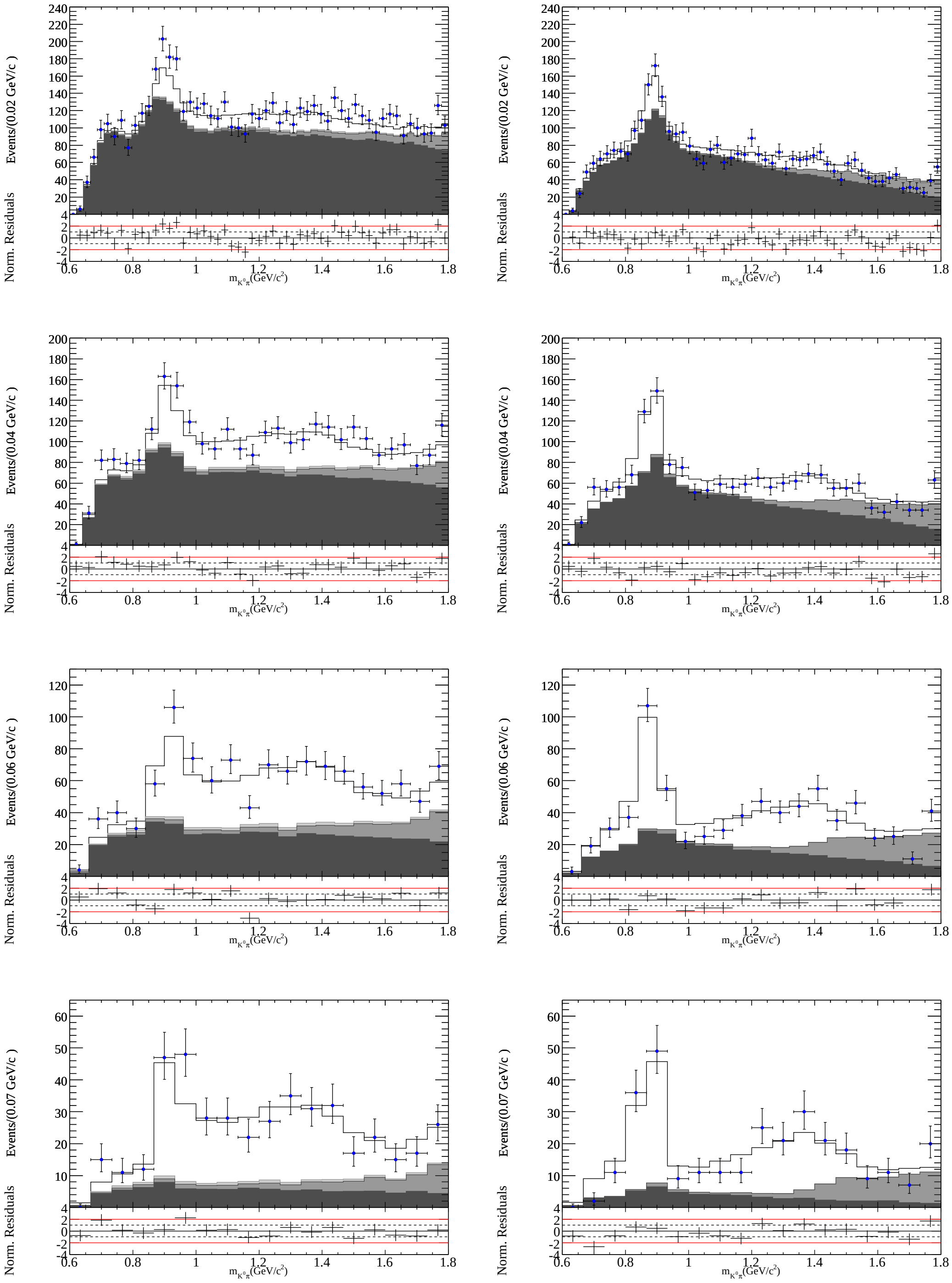

Figure 7.9: *Symmetrized $m_{K^0_S\pi}$ distribution, zooming in the $K^{*\pm}(892)\pi^{\mp}$ and $K\pi$ S-wave $(K\pi)^{*\pm}_0\pi^{\mp}$ signal region for positive (left) and negative (right) cosinus of the helicity angle ($\cos(\theta_{K^0_S\pi})$). A veto in the $J/\Psi K^0_S$ and $\Psi(2S)K^0_S$ bands has been applied. The plots from top to bottom are made with different signal enhancement samples by removing events with $R < cut$. The Δt and DP PDFs have been excluded from the R definition. R cuts are made with the same criteria as in Fig. 7.6.*

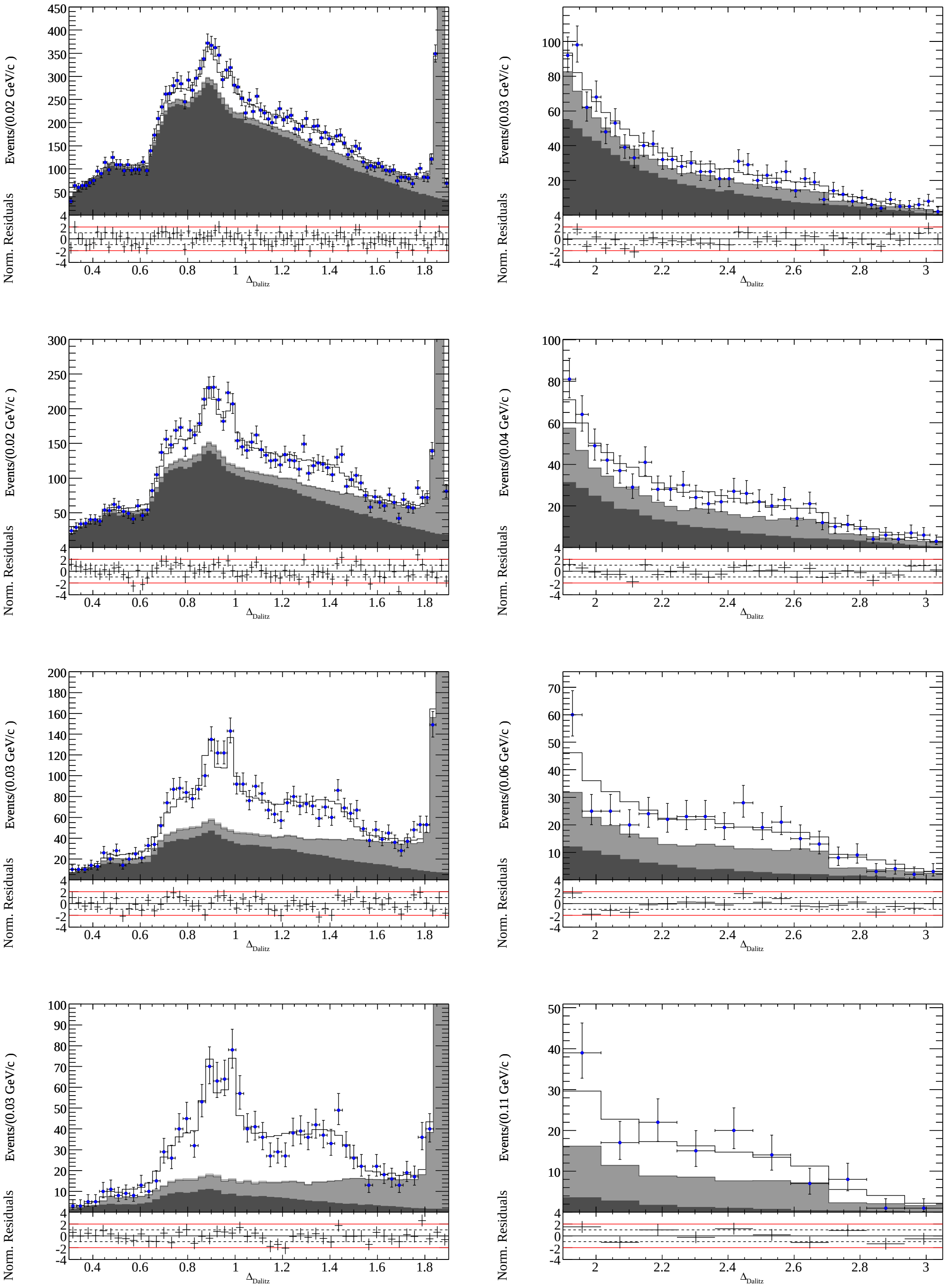

Figure 7.10: Δ_{Dalitz} *distribution. The plot in the left (right) hand side show the distribution for* $\Delta_{\text{Dalitz}} < 1.9\ \text{GeV}/c^2 (> 1.9\ \text{GeV}/c^2)$, *corresponding to the edges (center) of the DP. A veto in the* $J/\Psi K^0_S$ *band has been applied. The plots from top to bottom are made with different signal enhancement samples by removing events with* $R < cut$. *The* Δt *and* DP *PDFs have been excluded from the* R *definition.* R *cuts are made with the same criteria as in Fig. 7.6.*

its World Average value.

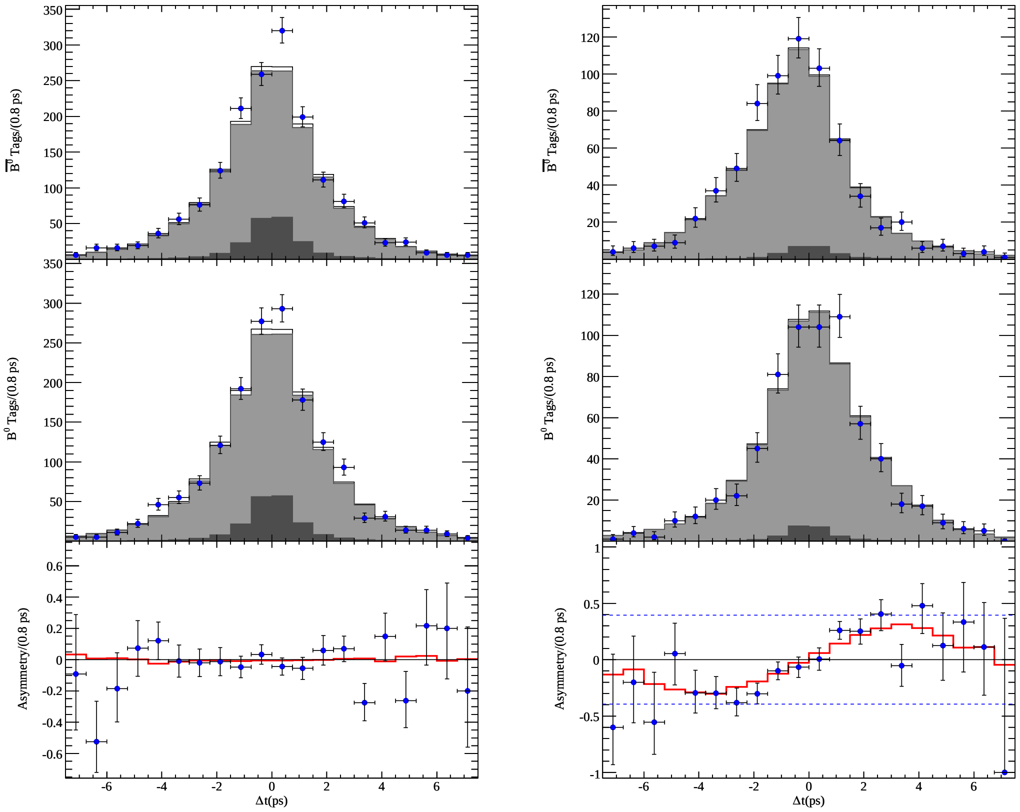

Figure 7.11: Δt *distributions for events in which* $B_{\text{tag}} = \bar{B}^0$, $B_{\text{tag}} = B^0$ *and the derived* Δt*-dependent asymmetry for tagged events in the* $D\pi$ *(left) and* $J/\Psi K_S^0$ *(right) bands. Each plot contains three subplots in which are shown the events tagged for which* $B_{\text{tag}} = \bar{B}^0$ *(top),* $B_{\text{tag}} = B^0$ *(middle) and the derived* Δt*-dependent asymmetry (bottom). The blue dotted lines in the* $J/\Psi K_S^0$ *time-dependent* CP *asymmetry corresponds to the* $\pm|QS(J/\Psi K_S^0)|$ *values, where* Q *is the corresponding dilution factor for the tagging categories taken into account and in the hypothesis of a* 100% *pure* $J/\Psi K_S^0$ *sample.*

Concerning the time-dependent CP-asymmetries of the charmless components of the isobar signal model, the Δt distributions and Δt-dependent asymmetries for the $f_0(980)K_S^0$ and $\rho^0(770)\ K_S^0$ bands, defined as

- $f_0(980)K_S^0 : 0.88\ \text{GeV}/c^2 < m_{\pi^+\pi^-} < 1.1\ \text{GeV}/c^2$,
- $\rho^0(770)K_S^0 : 0.6\ \text{GeV}/c^2 < m_{\pi^+\pi^-} < 0.88\ \text{GeV}/c^2$,

are shown in Figs. 7.12–7.13 for all tagged events and for different cut values on R. For events in the $f_0(980)K_S^0$ band (cf. Fig. 7.12) and no R cut, the time-dependent CP asymmetry can hardly be seen, as it is strongly diluted by background. For increasingly tighter cuts on the R variable, the asymmetry becomes visible. It illustrates the non-vanishing time-dependent CP-violation for the $f_0(980)K_S^0$ component obtained in the fit: $S = -0.96 \pm 0.09$ and $S = -0.90 \pm 0.13$ (statistical uncertainty only) measured for solutions I and II, respectively. The significance of this result properly taking into account the multiple solutions and systematic uncertainties is presented in Sec. 7.2.1. For events in the $\rho^0(770)K_S^0$ band (cf. Fig. 7.13) no significant CP-violation asymmetry is seen.

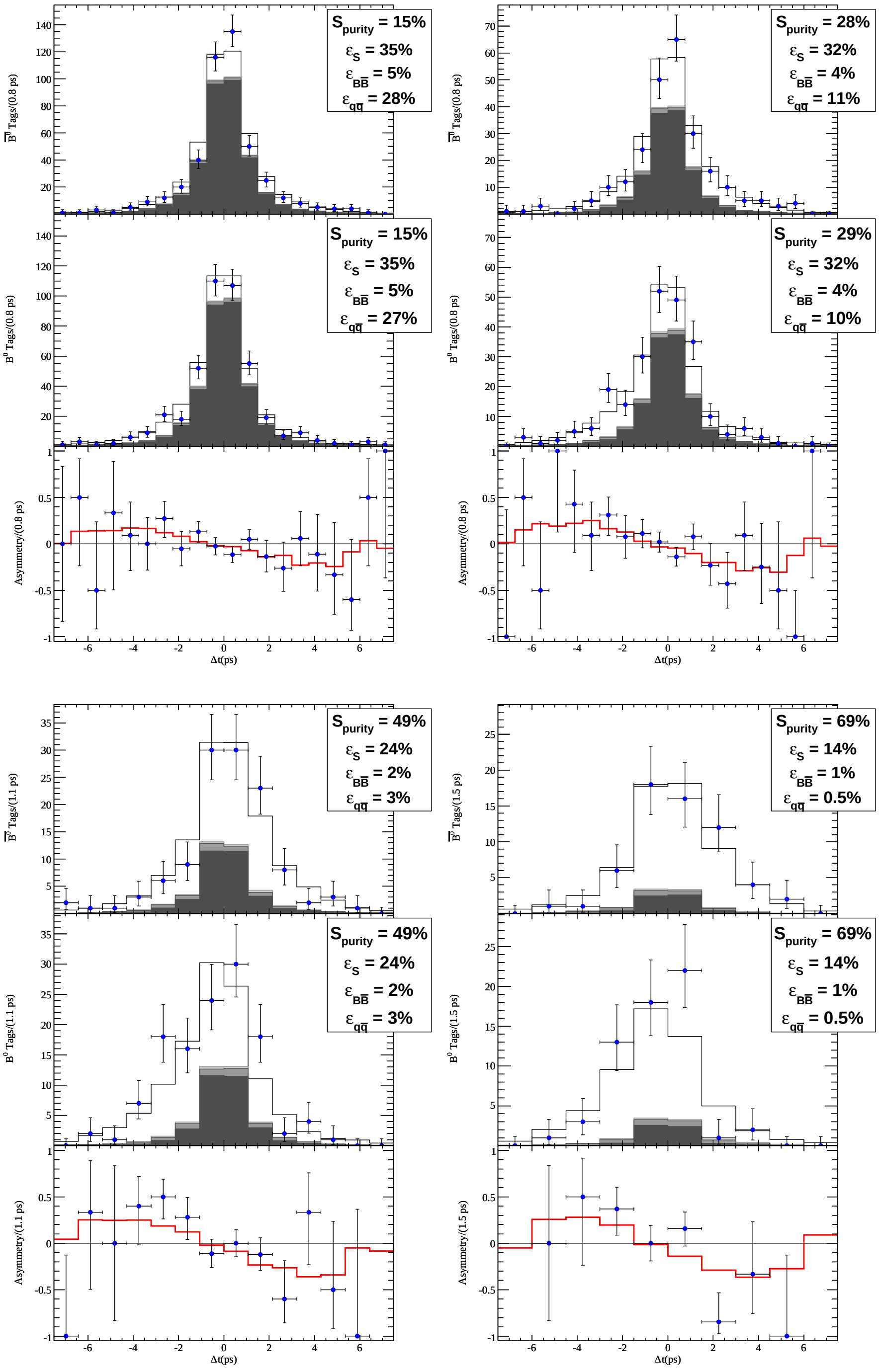

Figure 7.12: *Δt distributions for events in which $B_{\text{tag}} = \bar{B}^0$, $B_{\text{tag}} = B^0$ and the derived Δt-dependent asymmetry for tagged events in the $f_0(980)K_S^0$ band. The $D\pi$ events have been vetoed. Each plot contains three subplots in which are shown the events for which $B_{\text{tag}} = \bar{B}^0$ (top), $B_{\text{tag}} = B^0$ (middle) and the derived Δt-dependent asymmetry (bottom). The plots from top to bottom and left to right are made with different signal enhancement samples by removing events with $R < cut$. The Δt and DP PDFs have been excluded from the R definition. R cuts are made with the same criteria as in Fig. 7.6.*

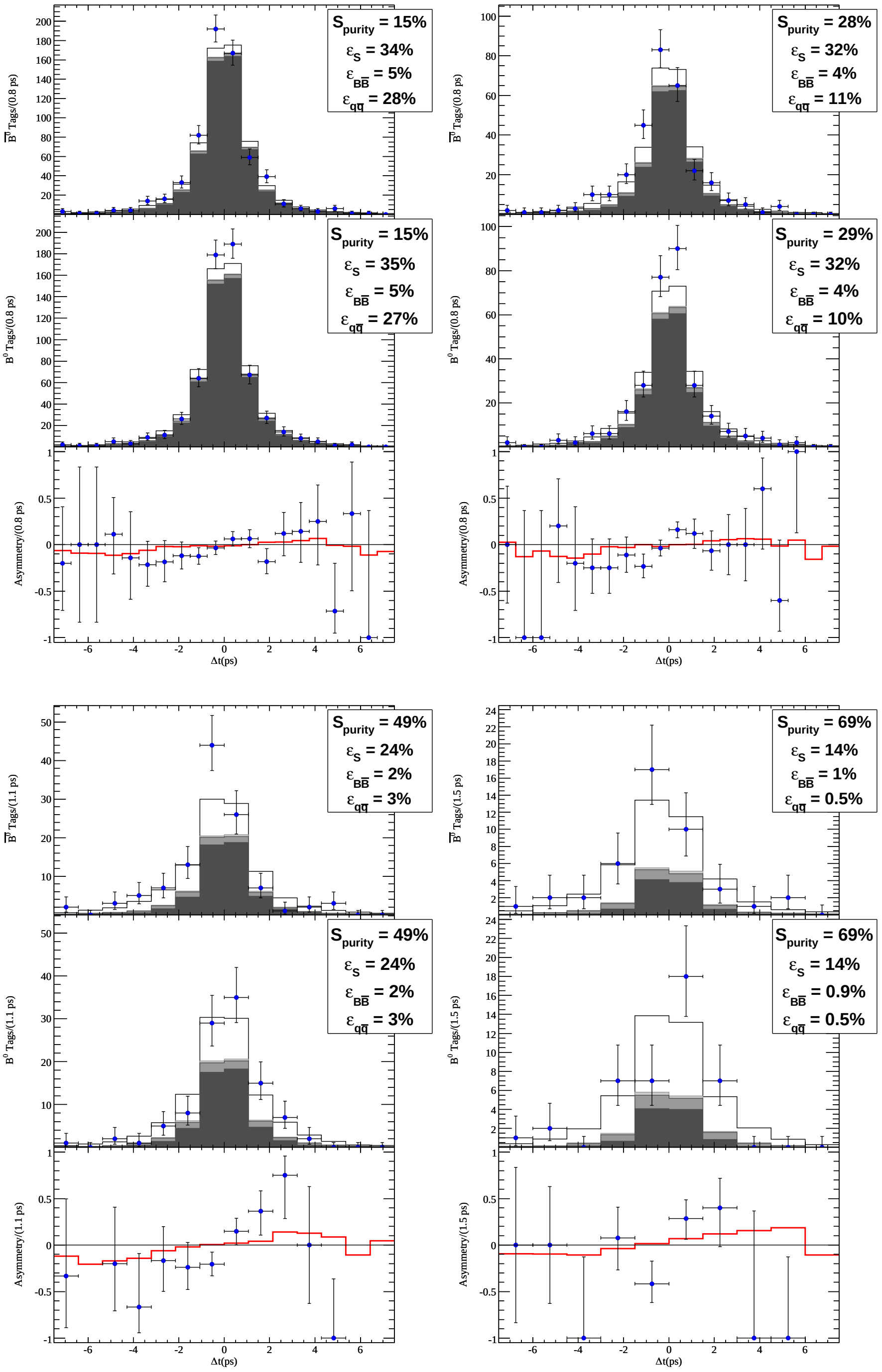

Figure 7.13: *Δt distributions for events in which $B_{\rm tag} = \bar{B}^0$, $B_{\rm tag} = B^0$ and the derived Δt-dependent asymmetry for tagged events in the $\rho^0(770)K^0_S$ band. The $D\pi$ events have been vetoed. Each plot contains three subplots in which are shown the events for which $B_{\rm tag} = \bar{B}^0$ (top), $B_{\rm tag} = B^0$ (middle) and the derived Δt-dependent asymmetry (bottom). The plots from top to bottom and left to right are made with different signal enhancement samples by removing events with $R < cut$. The Δt and DP PDFs have been excluded from the R definition. R cuts are made with the same criteria as in Fig. 7.6.*

7.2 Results on Physical Parameters

Results on the physical parameters using the techniques described in Sec. 6.7.1 are presented here. The convolution with the systematic effects use the framework described in Sec. 6.7.2. The estimation of the systematic uncertainties will be presented in a later section (cf. Sec. 7.3).

7.2.1 Measurement of $\sin 2(\beta_{\text{eff}})$ in penguin dominated modes

The measurement of the time-dependent CP-violation in the penguin dominated modes $f_0(980)K_S^0$ and $\rho^0(770)K_S^0$ is presented as a bi-dimensional likelihood scan in the $(2\beta_{eff}, C)$ plane. These scans are shown in Fig. 7.14. The top plots show the statistical only scans. The bottom plots are confidence level contours, after the bi-dimensional convolution with the covariance matrix of systematic uncertainties (cf. Sec. 6.7.2).

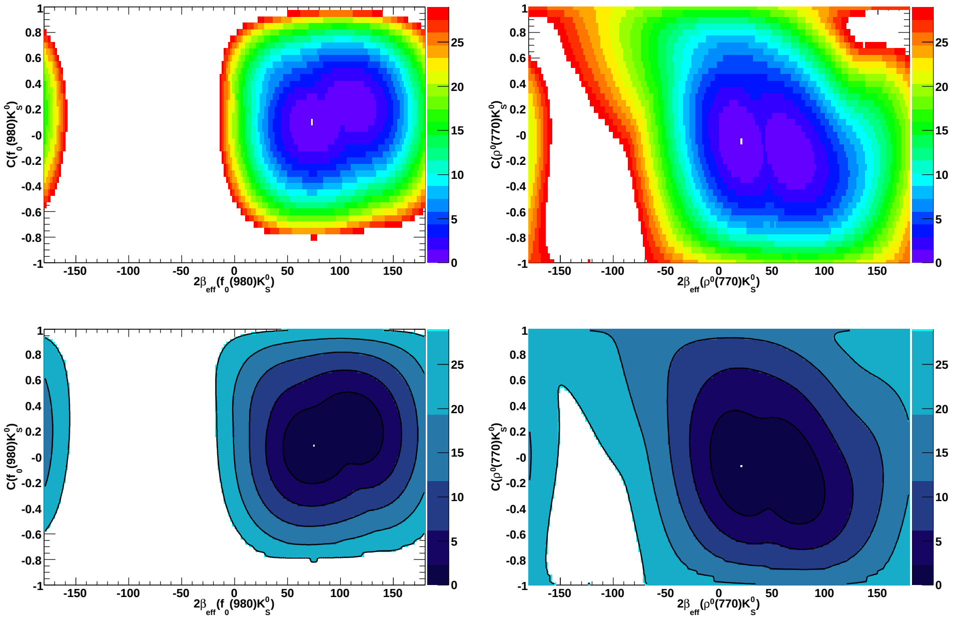

Figure 7.14: $(2\beta_{eff}, C)$ *bi-dimensional likelihood scans for the* $f_0(980)K_S^0$ *(left) and* $\rho^0(770)K_S^0$ *(right) components. The top plots show the statistical-only likelihood scan. The plots at the bottom show the confidence level contours, after convolution with the systematic uncertainties. The shaded areas represent de* 1 *through* 5σ *contours, respectively. The regions in white have* $-2log(L) > 30$.

The plots on the left hand side of the figure show the bi-dimensional scan for the $f_0(980)K_S^0$ resonant state. For this component the CP conserving points, $(0^o, 0)$ and $(180^o, 0)$, are excluded at the 3.8σ and 3.5σ level, respectively. This quantifies the results illustrated on the likelihood projection studies presented in Sec. 7.1.3, where the time-dependent CP-violation for events in the $f_0(980)K_S^0$ band was visible for signal-enhanced samples. As explained in Sec. 2.3, the comparison with the time-dependent CP-violation parameters in $b \to c\bar{c}s$ modes, is a probe for New Physics. There is a twofold ambiguity in the values of time-dependent asymmetries obtained in $b \to c\bar{c}s$ modes, $(42.1^o, 0)$ and $(137.9^o, 0)$ [28], and both are consistent with the present measurement at the 1.2σ and 1.1σ level, respectively. No evidence of physics beyond the SM is found for this component.

The $(2\beta_{eff}, C)$ plane can be transformed to the more familiar (S, C) plane. The corresponding bi-dimensional contours are shown on the left of Fig. 7.15. As the interference information is exploited in Dalitz plot analysis, direct access to the phases is possible. Then, information is lost when passing to the (S, C) plane, but the CP conservation and $b \to c\bar{c}s$ values are each represented by only one point, *i.e.* $(0, 0)$ and $(0.671, 0)$ [28], respectively (market by the red star and triangle in the plot). The physically allowed region is represented within the dotted circle in the figure. Even though part of the information is lost in this plane, the measurement can not cover unphysical regions, which is one of the advantages of Dalitz plot analyses. CP conservation is excluded at the 3.5σ level. The present measurement is consistent with the $b \to c\bar{c}s$ value at the 1.1σ level.

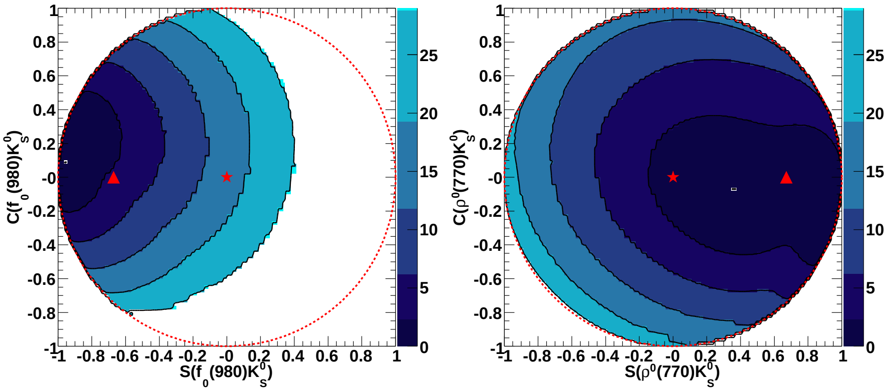

Figure 7.15: (S, C) *confidence level contours for the* $f_0(980)K^0_S$ *(left) and* $\rho^0(770)K^0_S$ *(right) components, constructed out of the* $(2\beta_{eff}, C)$ *bi-dimensional likelihood scans. The shaded areas represent de* 1 *through* 5σ *contours, respectively. The physically allowed region is represented within the dotted red circle, the regions in white have* $-2log(L) > 30$*. The red star and triangle on the plots mark the location of the CP conserving (*$(0, 0)$*) and* $b \to c\bar{c}s$ *(*$(\sin(2\beta_{c\bar{c}s}), 0)$*) values, respectively.*

The bi-dimensional likelihood scan $(2\beta_{eff}, C)$ for the $\rho^0(770)K^0_S$ component is shown on the right hand of Fig. 7.14. Even though the CP conserving point $(180^o, 0)$ is excluded at 3.8σ level, the measurement is consistent with the other $(0^o, 0)$ within 1σ. This is in agreement with the Likelihood projection studies presented in Sec 7.1.3. The measurement is consistent with the $b \to c\bar{c}s$ values within 1σ. The projection in the $2\beta_{eff}(\rho^0(770)K^0_S)$ direction will be used as input in the phenomenological analysis combining the $B \to K^*\pi$ and $B \to \rho K$ systems (cf. Chapter 8). The confidence level contours in the transformed (S, C) plane are shown on the right hand side of Fig. 7.15. This measurement excludes neither CP conservation nor the $b \to c\bar{c}s$ values.

7.2.2 The measurement of the CPS/GPSZ phase difference

The measurement of the $\Delta\phi(K^*\pi)$ CPS/GPSZ phase (cf. Sec. 3.2.2, Eq. 3.11 and Sec. 3.2.6) for the $K^*(892)$ resonant state is presented as a one-dimensional likelihood scan on the left of Fig. 7.16. The blue curve represents the statistical only likelihood scan, and the green curve represents the convolution with the systematic uncertainties. The present measurement does not set a strong constraint in this phase, only the $(-137.0, -5.0)^\circ$ interval is excluded at the 2σ level. This measurement is one of the experimental inputs obtained in this thesis used for the phenomenological analysis of the $B \to K^*\pi$ modes presented in Chapter 8.

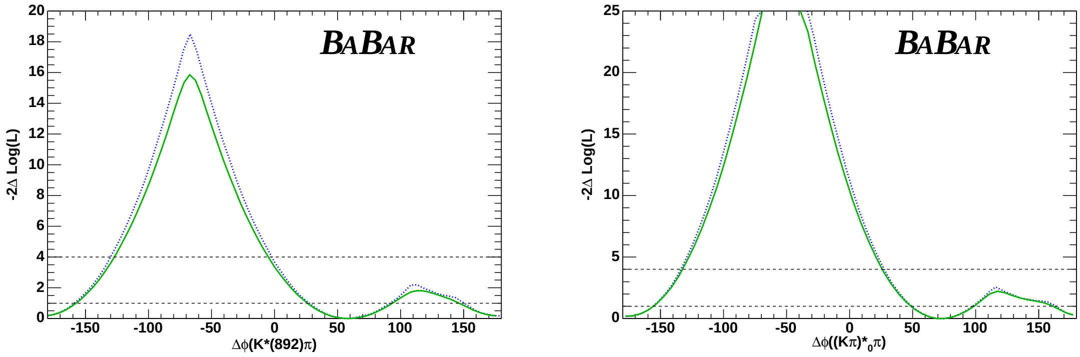

Figure 7.16: *Likelihood scans for the* $\Delta\phi(K^*(892)\pi)$ *(left) and* $\Delta\phi((K\pi)^*_0\pi)$ *(right) phase differences. The plots show the statistical scans (dashed blue), and the convolutions with the systematic uncertainties (solid green). Two horizontal dashed lines at* $-2\Delta log(L) = 1$ *and* $-2\Delta log(L) = 4$ *show the one and two standard deviation intervals, respectively.*

The right hand side plot of Fig. 7.16 shows the measurement of the similar phase difference for the $K\pi$ S-wave, $(K\pi)^*_0$. As for the $K^*(892)$, the measurement sets no strong constraint on this phase, only the interval $(-132.0, 25.0)^o$ is excluded at the 2σ level. The theoretical interpretation of this phase difference is more controversial than the one of the $K^*(892)$ resonant state, and then will not be used for the phenomenological analysis presented in Chapter 8.

7.2.3 Results on direct CP asymmetries

The (statistical-only) likelihood scans for the direct CP asymmetries are shown in Fig. 7.17. These plots display the likelihood curves for each solution (dashed blue) and for the envelope curve (solid blue) constructed with the PL-envelope method (cf. Sec. 6.7.1). The 1σ interval is defined as the range where $-2\Delta log(L) < 1$ (illustrated by a horizontal line). The statistical error is added in quadrature with the systematic uncertainties (cf. Sec. 7.3.1).

Most direct CP-asymmetries are compatible with zero within 1σ. The exception is the one for the $K^*(892)\pi$ mode (cf. second row left plot of Fig. 7.17), where $A_{CP}(K^{*\pm}(892)\pi^{\mp})$

asymmetry excludes the zero value at the 2σ level (taking into account systematic uncertainties). This result has non trivial consequences on the constraint on the strong phase difference between the T^{+-} and P^{+-} QCD amplitudes (cf. Eq. 3.3) of the $B^0 \to K^{*\pm}(892)\pi^{\mp}$ decay amplitude (cf. Chapter 8).

The measurement of the inclusive direct CP asymmetry is shown in the left plot of Fig. 7.18. It is consistent with the CP conservation within 1σ.

7.2.4 Fit fractions and significance of small components

The (statistical-only) likelihood scans for the isobar fractions of the dominant components, $f_0(980)K^0_S$, $\rho^0(770)K^0_S$, $K^*(892)\pi$ and $(K\pi)^*_0$, are shown in Figs. 7.19. These plots display the likelihood curves for each solution (dashed blue) and for the envelop curve (solid blue). They can be constructed using the PL-envelop method, as the significance of these components is well established from previous analyses. The 1σ interval is defined as the range where $-2\Delta log(L) < 1$ (illustrated by a horizontal line). In Sec. 7.3.1 the statistical error is added in quadrature with the systematic uncertainties.

In Fig. 7.20 are shown the likelihood scans of the fit fractions for the "small" components: $\chi_c(0)K^0_S$, $f_X(1300)K^0_S + f_2(1270)K^0_S$, and non-resonant. To evaluate accurately the statistical significance of these components, these scans are obtained with no approximation in the likelihood function. The blue curve represents the statistical-only scan, and the green curve the convolution with the systematic uncertainties. The significance is estimated as `Prob`$(\chi^2(0), 1)$, where $\chi^2(0)$ is the value of the convoluted scan at zero fit fraction.

- The significance obtained for the $\chi_c(0)$ component is 3.8σ (cf. left hand plot of Fig. 7.20). Previous BABAR and Belle $B^+ \to K^+\pi^-\pi^+$ Dalitz plot analyses [23, 24] found significances above 3σ but below 5σ for this component. The previous Belle $B^0 \to K^0_S\pi^+\pi^-$ [42] Dalitz plot analysis found an upper limit that is in agreement with the present result.

- The significance of the non-resonant component is estimated to be 4.6σ, in agreement with the studies performed in the center of the DP (cf. Appendix B), and the likelihood projections (cf. Fig. 7.10). The statistical-only significance is highly suppressed because it suffers of high systematic errors that come from uncertainties on the signal model 7.3.7.

- Finally, the significance for the components $f_X(1300)K^0_S$ and $f_2(1270)K^0_S$ considered separately are 2.9σ and 2.4σ, respectively. As the signal excess at high $m_{\pi^+\pi^-}$ mass is described as a coherent sum of these two components, the significance of the inclusive fit fraction of these two components is calculated, giving the result 4.8σ (cf. right hand plot of Fig. 7.20), which justifies their coherent inclusion.

All the subsmodes are strongly affected by systematic errors, being the signal model uncertainty the dominant one (cf. Sec. 7.3.7).

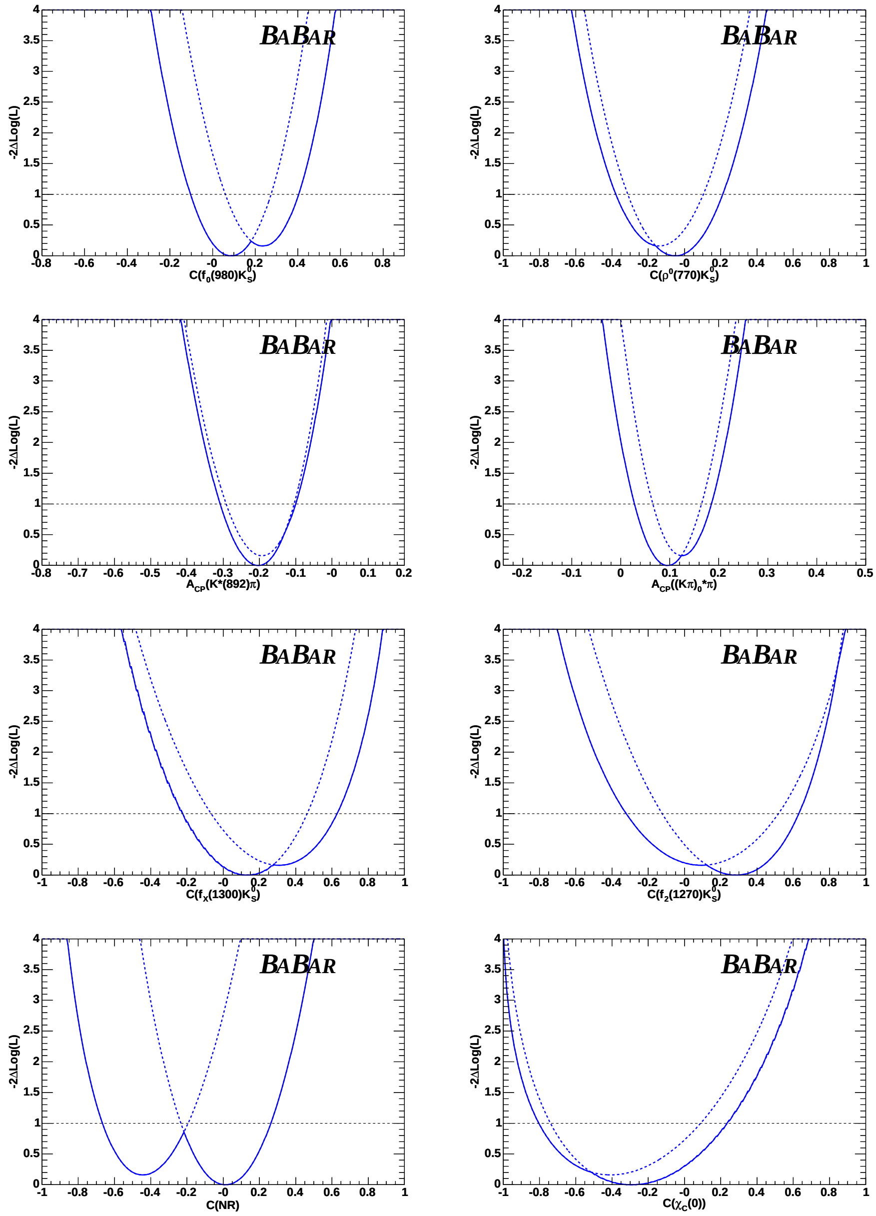

Figure 7.17: *Statistical likelihood scans, constructed with the PL-envelope method, for the* $C(f_0(980)K_S^0)$ *(top left),* $C(\rho^0(770)K_S^0)$ *(top right),* $A_{CP}(K^{*\pm}(892)\pi^{\mp})$ *(middle top left),* $A_{CP}((K\pi)_0^{*\pm}\pi^{\mp})$ *(middle top right),* $C(f_X(130)K_S^0)$ *(middle bottom left),* $C(f_2(1270)K_S^0)$ *(middle bottom right),* $C(NR)$ *(bottom left) and* $C(\chi_C(0))$ *(bottom right) direct* CP*-asymmetries. The likelihood scans curves for each solution (dashed blue) are used to build the envelope curve (solid blue), from which the* 1σ *statistical error are derived. The vertical scale stops at* $-2\Delta log(L) = 4$ *slightly above* 3.84 *which is the* 95% *confidence level. A horizontal dashed line at* $-2\Delta log(L) = 1$ *shows the one standard deviation interval.*

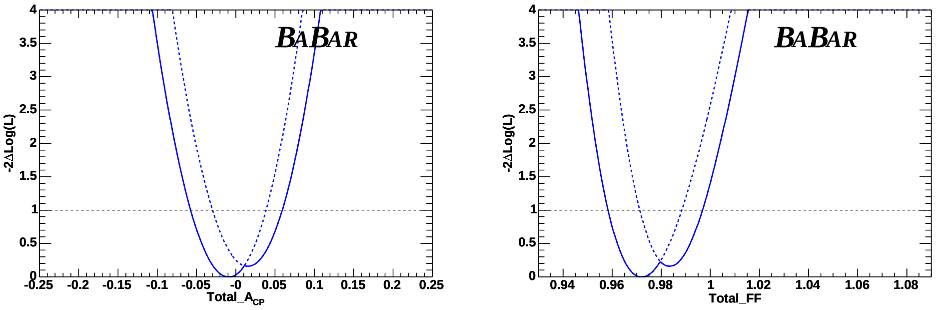

Figure 7.18: *Statistical likelihood scans, constructed with the PL-envelop method, for the inclusive direct CP-asymmetry (left) and fit fraction (right). The plots show the likelihood scan curves for each solution (dashed blue) and the envelope curve (solid blue), which is used to establish the* 1σ *statistical error. The vertical scale stops at* $-2\Delta log(L) = 4$ *slightly above* 3.84 *which is the* 95% *confidence level. A horizontal dashed line at* $-2\Delta log(L) = 1$ *shows the one standard deviation interval.*

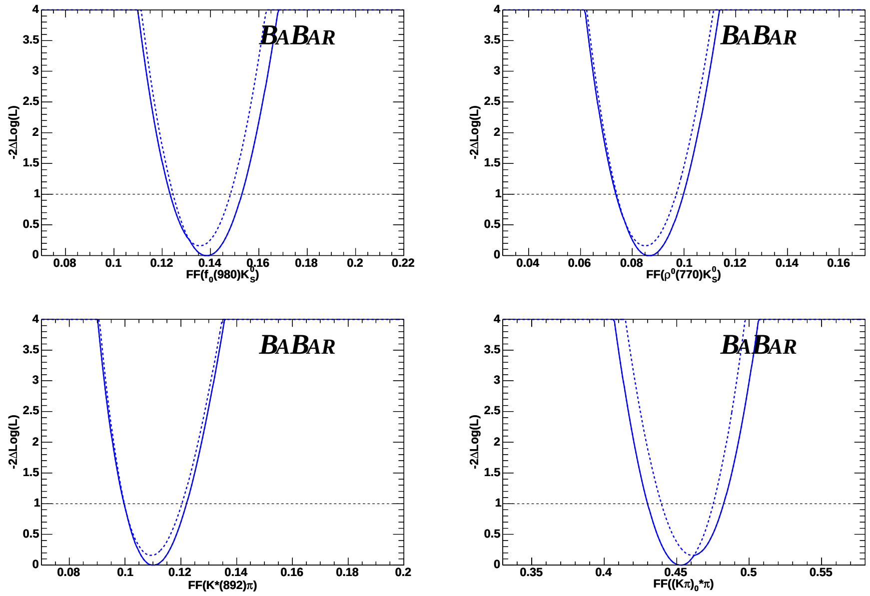

Figure 7.19: *Statistical likelihood scans, constructed with the PL-envelop method, for the* $FF(f_0(980)K^0_S)$ *(top left),* $FF(\rho^0(770)K^0_S)$ *(top right),* $FF(K^{*\pm}(892)\pi^{\mp})$ *(bottom left) and* $FF((K\pi)^{*\pm}_0\pi^{\mp})$ *(bottom right) fit fractions. The plots show the likelihood scan curves for each solution (dashed blue) and the envelope curve (solid blue), which is used to establish the* 1σ *statistical error. The vertical scale stops at* $-2\Delta log(L) = 4$ *slightly above* 3.84 *which is the* 95% *confidence level. A horizontal dashed line at* $-2\Delta log(L) = 1$ *shows the one standard deviation interval.*

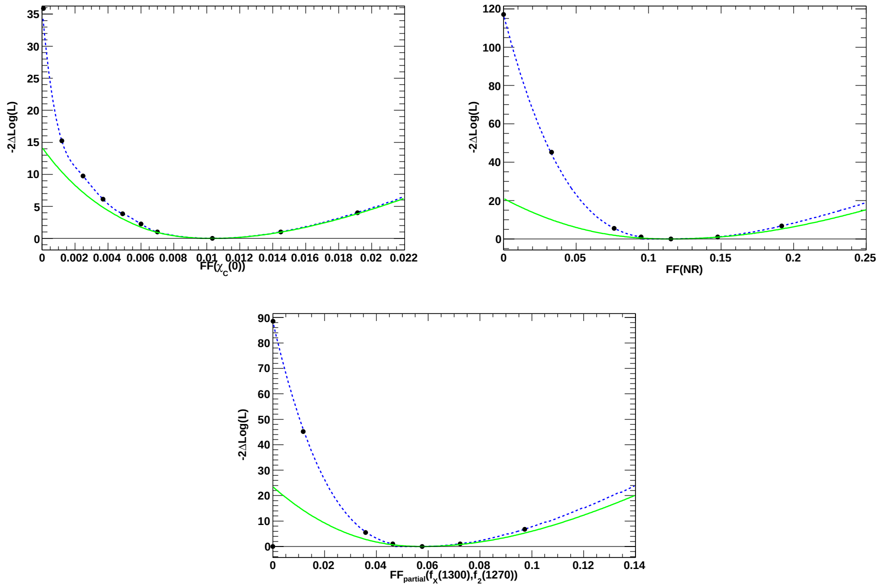

Figure 7.20: *Statistical, and statistical convoluted with systematics likelihood scans, for the* $FF(\chi_{c0}K_S^0)$ *(top left),* $FF(NR)$ *(top right) fit fractions, and the inclusive fit fraction of the* $f_X(1300)K_S^0$ *and* $f_2(1270)K_S^0)$ *components (bottom). The plots show the statistical scans (dashed blue), and the convolutions with the systematics (solid green). The cut at* $FF = 0$ *of the green curve is used to calculate the significance of the component.*

Fig. 7.18 also shows the statistical likelihood scan for the total isobar fraction, which is consistent with 1.0 within 1σ. This indicates that the average interference over the DP is as destructive as constructive.

7.2.5 Results on other phase differences

In this section are presented results on other phase differences which are not the main target of this analysis, but which become accessible with the present data. One of these phase differences, $\Delta\phi(\rho^0(770)K_S^0, K^*(892)\pi)$, is used as input in the phenomenological analysis combining the $B \to K^*\pi$ and $B \to \rho K$ systems. All the measurements are presented as one-dimensional likelihood scans, the blue curves representing the statistical scans, and the green ones the convolution with the systematic uncertainties.

The measurement of the $\Delta\phi(\rho^0(770)K_S^0, K^*(892)\pi)$ phase difference between the $c(\rho^0(770)K_S^0)$ and $c(K^*(892)\pi)$ isobar amplitudes is presented in the top left plot of Fig. 7.21. The constraint set for this phase is not strong, only the $(-112.0, 98.0)^o$ interval is excluded at the 2σ level. In the top right plot of the same figure is shown the measurement of the $\Delta\phi(\rho^0(770)K_S^0, (K\pi)_0^*\pi)$ phase difference between the $c(\rho^0(770)K_S^0)$ and $c((K\pi)_0^*)\pi)$ isobar amplitudes, which is the equivalent of the previous phase for the $K\pi$ S-wave. The interval $(-105.0, 112.0)^o$ is excluded at the 2σ level. No strong constraint is set in these phases because they are extracted from the interference of weakly overlapping components in the

DP.

Other phase differences between components that have strong overlap in the DP can be accessed. The measurement of the phase difference between the $c(K^*(892)\pi)$ and $c((K\pi)^*_0\pi)$ isobar amplitudes is presented in the bottom left plot of the same figure. In this case the value of this parameters are very similar in solutions I and II, an so a strong constraint can be set, as is shown in the figure. Finally, the measurement of the phase difference between the $c(f_0(980)K^0_S)$ and $c(\rho^0(770)K^0_S)$ isobar amplitudes is shown in the bottom right plot of Fig. 7.21. Even though the value differs significantly between solutions I and II, the statistical errors on every solution is of the order of $\sim 18^o$, which translates into a relatively significant constraint on the confidence interval for this phase.

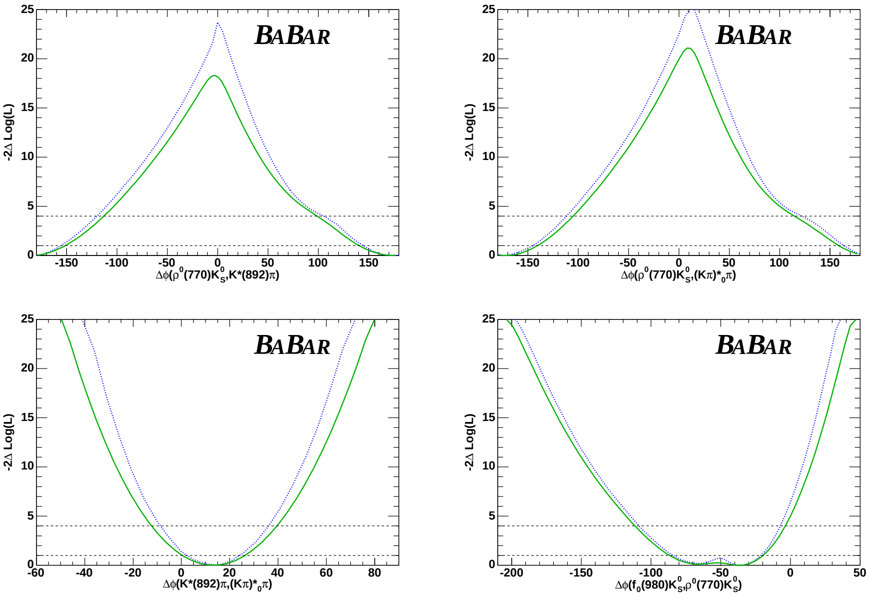

Figure 7.21: *Statistical, and statistical convoluted with systematics likelihood scans, for the* $\Delta\phi(\rho^0(770)K^0_S, K^*(892)\pi)$ *(top left),* $\Delta\phi(\rho^0(770)K^0_S, (K\pi)^*_0\pi)$ *(top right),* $\Delta\phi(K^*(892)\pi, (K\pi)^*_0\pi)$ *(bottom left),* $\Delta\phi(f_0(980)K^0_S, \rho^0(770)K^0_S)$ *(bottom right) phase differences. The plots show the statistical scans (dashed blue), and the convolutions with the systematics (solid green). Two horizontal dashed lines at* $-2\Delta log(L) = 1$ *and* $-2\Delta log(L) = 4$ *shows the one and two standard deviation intervals, respectively.*

The mixing phases for the small components $\phi(f_X(1300)K^0_S)$, $\phi(f_2(1270)K^0_S)$, $\phi(NR)$ and $\phi(\chi_C(0))$, are shown here only for completeness. The statistical likelihood scans for them have been built with the *PL*-envelop method, and have been directly convoluted with the systematic uncertainties. In Fig. 7.22, the envelope of the statistical scans for solutions I and II (dashed blue), and the convolutions with the systematics (solid green) is shown. The plots show that all mixing induced CP-violation are consistent with zero within 1σ as the 0^o and 180^o values are not excluded.

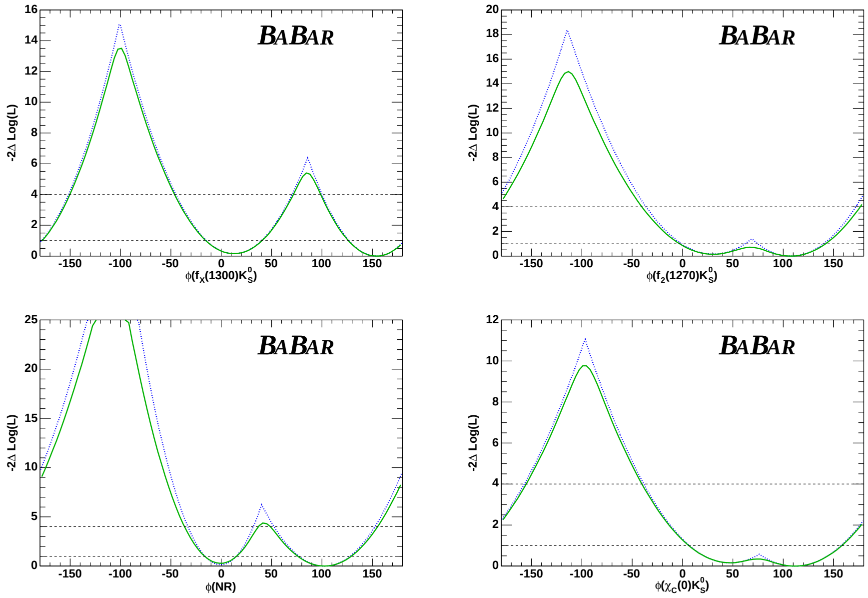

Figure 7.22: *Statistical, and statistical convoluted with systematics likelihood scans (constructed with the PL-envelope method), for the* $\phi(f_X(1300)K^0_S)$ *(top left),* $\phi(f_2(1270)K^0_S)$ *(top right),* $\phi(NR)$ *(bottom left) and* $\phi(\chi_C(0))$ *(bottom right) phase differences. The plots show the envelope of the statistical scans for solutions I and II (dashed blue), and the convolutions with the systematics (solid green). Two horizontal dashed lines at* $-2\Delta log(L) = 1$ *and* $-2\Delta log(L) = 4$ *shows the one and two standard deviation intervals, respectively.*

7.2.6 Summary on results

Tables 7.4 and 7.5 summarize the results on the Q2B parameters for all components in the signal model. Table 7.4 show results on total and partial fit fractions, exclusive and inclusive direct CP-asymmetries for solutions I and II. Each result displays a central value and three errors: statistical, systematic and signal DP model error, respectively. The evaluation of the systematic uncertainties is described in Sec. 7.3. On the same table are displayed the significances of the $\chi_{c0}K^0_S$, non-resonant, $f_X(1300)K^0_S$ and $f_2(1270)K^0_S$ components. The significance for the components $f_X(1300)K^0_S$ and $f_2(1270)K^0_S$ taken together is also given. Table 7.5 reports the 1σ and 2σ intervals for the total and partial isobar fractions, and for the exclusive and inclusive direct CP asymmetries. The fact that for some phases the total intervals have to be expressed as the union of disconnected interval is due to the local minima structure of the likelihood function.

7.2.7 Average signal efficiency and branching fractions

To compute the inclusive and partial branching fractions, the signal model dependent average efficiency $\langle\varepsilon\rangle$ over the DP is needed. This average efficiency is what would be obtained if a MC sample generated with the fit results is subject to reconstruction and selection described

Parameter	**Value Sol-I**	**Value Sol-II**
$C(f_0(980)K^0_S)$	$0.08 \pm 0.19 \pm 0.03 \pm 0.04$	$0.23 \pm 0.19 \pm 0.03 \pm 0.04$
$\beta_{eff}(f_0(980)K^0_S)$	$36.0 \pm 9.8 \pm 2.1 \pm 2.1$	$56.2 \pm 10.4 \pm 2.1 \pm 2.1$
$S(f_0(980)K^0_S)$	$-0.96 \pm 0.09 \pm 0.03 \pm 0.02$	$-0.90 \pm 0.13 \pm 0.03 \pm 0.02$
$\mathrm{Corr}(S(f_0(980)K^0_S), C(f_0(980)K^0_S))$	$+19.7\%$	$+12.5\%$
$FF(f_0(980)K^0_S)$	$13.8^{+1.5}_{-1.4} \pm 0.8 \pm 0.6$	$13.5^{+1.4}_{-1.3} \pm 0.8 \pm 0.6$
$C(\rho^0(770)K^0_S)$	$-0.05 \pm 0.26 \pm 0.10 \pm 0.03$	$-0.14 \pm 0.26 \pm 0.10 \pm 0.03$
$\beta_{eff}(\rho^0(770)K^0_S)$	$10.2 \pm 8.9 \pm 3.0 \pm 1.9$	$33.4 \pm 10.4 \pm 3.0 \pm 1.9$
$S(\rho^0(770)K^0_S)$	$0.35 \pm 0.31 \pm 0.06 \pm 0.03$	$0.91 \pm 0.13 \pm 0.06 \pm 0.03$
$\mathrm{Corr}(S(\rho^0(770)K^0_S), C(\rho^0(770)K^0_S))$	-21.3%	-10.4%
$FF(\rho^0(770)K^0_S)$	$8.6^{+1.4}_{-1.3} \pm 0.5 \pm 0.2$	$8.5^{+1.3}_{-1.2} \pm 0.5 \pm 0.2$
$A_{CP}(K^*(892)\pi)$	$-0.21 \pm 0.10 \pm 0.01 \pm 0.02$	$-0.19^{+0.10}_{-0.11} \pm 0.01 \pm 0.02$
$\Delta\phi(K^*(892)\pi)$	$58.3 \pm 32.7 \pm 4.6 \pm 8.1$	$176.6 \pm 28.8 \pm 4.6 \pm 8.1$
$FF(K^*(892)\pi)$	$11.0^{+1.2}_{-1.0} \pm 0.6 \pm 0.8$	$10.9^{+1.2}_{-1.0} \pm 0.6 \pm 0.8$
$A_{CP}((K\pi)^*_0\pi)$	$0.09 \pm 0.07 \pm 0.02 \pm 0.02$	$0.12^{+0.07}_{-0.06} \pm 0.02 \pm 0.02$
$\Delta\phi((K\pi)^*_0\pi)$	$72.2 \pm 24.6 \pm 4.1 \pm 4.4$	$-175.1 \pm 22.6 \pm 4.1 \pm 4.4$
$FF((K\pi)^*_0\pi)$	$45.2 \pm 2.3 \pm 1.9 \pm 0.9$	$46.1 \pm 2.4 \pm 1.9 \pm 0.9$
$C(NR)$	$0.01 \pm 0.25 \pm 0.06 \pm 0.05$	$-0.45^{+0.28}_{-0.24} \pm 0.06 \pm 0.05$
$\phi(NR)$	$0.8 \pm 17.5 \pm 3.8 \pm 7.5$	$102.0 \pm 26.5 \pm 3.8 \pm 7.5$
$FF(NR)$	$11.5 \pm 2.0 \pm 1.0 \pm 1.7$	$12.6 \pm 2.0 \pm 1.0 \pm 1.7$
NR significance	4.6σ	—
$C(f_2(1270)K^0_S)$	$0.28^{+0.35}_{-0.40} \pm 0.08 \pm 0.07$	$0.09 \pm 0.46 \pm 0.08 \pm 0.07$
$\phi(f_2(1270)K^0_S)$	$29.8 \pm 35.8 \pm 6.2 \pm 10.4$	$107.2 \pm 33.3 \pm 6.2 \pm 10.4$
$FF(f_2(1270)K^0_S)$	$2.3^{+0.8}_{-0.7} \pm 0.2 \pm 0.7$	$2.3^{+0.9}_{-0.7} \pm 0.2 \pm 0.7$
$f_2(1270)K^0_S$ significance	2.4σ	—
$C(f_X(1300)K^0_S)$	$0.13^{+0.33}_{-0.35} \pm 0.04 \pm 0.09$	$0.30^{+0.34}_{-0.41} \pm 0.04 \pm 0.09$
$\phi(f_X(1300)K^0_S)$	$11.5 \pm 30.3 \pm 4.3 \pm 4.5$	$153.8 \pm 27.5 \pm 4.3 \pm 4.5$
$FF(f_X(1300)K^0_S)$	$3.6^{+1.0}_{-0.9} \pm 0.3 \pm 0.9$	$3.5^{+1.0}_{-0.8} \pm 0.3 \pm 0.9$
$f_X(1300)K^0_S$ significance	2.9σ	—
$f_X(1300)K^0_S \cup f_2(1270)K^0_S$ significance	4.8σ	—
$C(\chi_c(0)K^0_S)$	$-0.29^{+0.53}_{-0.44} \pm 0.03 \pm 0.05$	$-0.41^{+0.54}_{-0.42} \pm 0.03 \pm 0.05$
$\phi(\chi_c(0)K^0_S)$	$46.3 \pm 44.7 \pm 4.6 \pm 8.3$	$110.4 \pm 46.6 \pm 4.6 \pm 8.3$
$FF(\chi_c(0)K^0_S)$	$1.04^{+0.41}_{-0.33} \pm 0.04 \pm 0.11$	$0.99^{+0.37}_{-0.30} \pm 0.04 \pm 0.11$
$\chi_c(0)K^0_S$ Stat. significance	3.8σ	—
FF_{Tot}	$97.2^{+1.7}_{-1.3} \pm 2.1 \pm 1.15$	$98.3^{+1.5}_{-1.3} \pm 2.1 \pm 1.15$
A^{incl}_{CP}	$-0.01 \pm 0.008 \pm 0.006$	$0.01 \pm 0.05 \pm 0.008 \pm 0.006$
$\Delta\phi(f^0(980)K^0_S, \rho(770)K^0_S)$	$-35.6 \pm 14.9 \pm 6.1 \pm 4.4$	$-66.7 \pm 18.3 \pm 6.1 \pm 4.4$
$\Delta\phi(K^*(892)\pi, (K\pi)^*_0\pi)$	$13.0 \pm 10.9 \pm 4.6 \pm 4.7$	$15.5 \pm 10.2 \pm 4.6 \pm 4.7$
$\Delta\phi(\rho(770)K^0_S, (K\pi)^*_0\pi)$	$-172.8 \pm 22.6 \pm 10.1 \pm 8.7$	$-170.8 \pm 26.8 \pm 10.1 \pm 8.7$
$\Delta\phi(\rho(770)K^0_S, K^*(892)\pi)$	$174.3 \pm 28.0 \pm 8.7 \pm 12.7$	$-173.7 \pm 29.8 \pm 8.7 \pm 12.7$

Table 7.4: *Summary on fit results for the Q2B parameters (directly quoted in terms of β_{eff} for the $f_0(980)K^0_S$ and $\rho^0(770)K^0_S$ components), the inclusive direct CP asymmetry and total fit fraction for solutions I and II. The results are quoted as a central value and three errors: statistical, systematic and DP signal model uncertainty, respectively. Also shown are the stat+syst linear correlation between C and S for the $f_0(980)K^0_S$ and $\rho^0(770)K^0_S$ components, and the significances of the non-resonant, $f_X(1300)K^0_S$, $f_2(1270)K^0_S$ and $\chi_c(0)K^0_S$ components, and of the $f_X(1300)K^0_S$ and $f_2(1270)K^0_S$ components taken together. Phases are in degrees and FFs in $\%$.*

Parameter	C. Val.	**1σ Coverage**	**2σ Coverage**
$C(f_0(980)K_S^0)$	0.08	$(-0.11, 0.40)$	$(-0.30, 0.59)$
$\beta_{eff}(f_0(980)K_S^0)$	36.0	$(27.1, 66.0)$	$(18.1, 75.8)$
$S(f_0(980)K_S^0)$	-0.95	$(-1.0, -0.73)$	$(-1.0, -0.49)$
$FF(f_0(980)K_S^0)$	13.8	$(11.98, 15.62)$	$(9.91, 17.44)$
$C(\rho^0(770)K_S^0)$	-0.05	$(-0.39, 0.23)$	$(-0.66, 0.49)$
$\beta_{eff}(\rho^0(770)K_S^0)$	10.2	$(0.7, 44.5)$	$(-8.8, 57.0)$
$S(\rho^0(770)K_S^0)$	0.35	$(0.02, 1.0)$	$(-0.35, 1.0)$
$FF(\rho^0(770)K_S^0)$	8.6	$(7.29, 10.09)$	$(5.98, 11.59)$
$A_{CP}(K^*(892)\pi)$	-0.21	$(-0.31, -0.10)$	$(-0.42, 0.00)$
$\Delta\phi(K^*(892)\pi)$	58.3	$(-180.0, -158.1) \cup (27.2, 94.3)$ $\cup(147.4, 180.0)$	$(-180.0, -127.0) \cup (-4.8, 180.0)$
$FF(K^*(892)\pi)$	11.0	$(9.59, 12.56)$	$(8.17, 14.28)$
$A_{CP}((K\pi)_0^*\pi)$	0.09	$(0.02, 0.19)$	$(-0.05, 0.27)$
$\Delta\phi((K\pi)_0^*\pi)$	72.2	$(-180.0, -156.0) \cup (49.8, 97.7)$ $\cup(152.0, 180.0)$	$(-180.0, -131.6) \cup (26.8, 180.0)$
$FF((K\pi)_0^*\pi)$	45.2	$(42.17, 48.85)$	$(34.00, 52.02)$
$C(NR)$	0.01	$(-0.67, 0.28)$	$(-0.87, 0.53)$
$\phi(NR)$	0.8	$(-16.5, 15.1) \cup (75.6, 130.1)$	$(-46.4, 38.1) \cup (49.6, 155.4)$
$FF(NR)$	11.5	$(8.70, 14.2)$	$(5.92, 16.87)$
$C(f_2(1270)K_S^0)$	0.28	$(-0.33, 0.65)$	$(-0.72, 0.94)$
$\phi(f_2(1270)K_S^0)$	29.8	$(-2.1, 141.0)$	$(-40.2, 176.0)$
$FF(f_2(1270)K_S^0)$	2.3	$(1.28, 3.45)$	$(0.33, 4.71)$
$C(f_X(1300)K_S^0)$	0.13	$(-0.24, 0.64)$	$(-0.59, 0.91)$
$\phi(f_X(1300)K_S^0)$	11.5	$(-15.1, 40.4) \cup (136.2, 180.0)$	$(-180.0, -150.2) \cup (-47.6, 71.8)$ $\cup(99.3, 180.0)$
$FF(f_X(1300)K_S^0)$	3.6	$(2.30, 5.03)$	$(1.08, 6.53)$
$C(\chi_c(0)K_S^0)$	-0.29	$(-0.80, 0.24)$	$(-1.0, 0.70)$
$\phi(\chi_c(0)K_S^0)$	46.3	$(8.2, 158.9)$	$(-180.0, -154.8) \cup (-40.2, 180.0)$
$FF(\chi_c(0)K_S^0)$	1.04	$(0.69, 1.46)$	$(0.39, 1.92)$
FF_{Tot}	97.2	$(-0.06, 0.06)$	$(-0.11, 0.11)$
A_{CP}^{incl}	-0.01	$(94.32, 100.67)$	$(91.74, 103.64)$
$\Delta\phi(f^0(980)K_S^0, \rho(770)K_S^0)$	-35.6	$(-86.2, 19.8)$	$(-11.6, -4.1)$
$\Delta\phi(K^*(892)\pi, (K\pi)_0^*\pi)$	13.0	$(0.4, 27.3)$	$(-12.4, 40.0)$
$\Delta\phi(\rho(770)K_S^0, (K\pi)_0^*\pi)$	-172.8	$(-180., -140.2) \cup (159.5, 180.0)$	$(-180.0, -105.2) \cup (114.5, 180.0)$
$\Delta\phi(\rho(770)K_S^0, K^*(892)\pi)$	174.3	$(-180., -151.5) \cup (141.8, 180.0)$	$(-180.0, -112.0) \cup (100.1, 180.0)$

Table 7.5: *Summary on fit results for the Q2B parameters (directly quoted in terms of β_{eff} for the $f_0(980)K_S^0$ and $\rho^0(770)K_S^0$ components), the inclusive direct CP-asymmetry and total fit fraction. On the table are shown the central value (C. Val.), 1σ and 2σ coverage intervals, respectively. The fact that for some phases the total interval have to be expressed as the union of disconnected intervals is due to the local minima structure of the likelihood function. Phases are in degrees and FFs in $\%$.*

in Chapter 5. The efficiency at a given point of the DP is independent on the signal model, so the non-resonant MC sample can be used (with $\sim 6 \times 10^6$ events) to construct the efficiency map (cf. Fig. 7.23). This map is defined as the probability to reconstruct anywhere[2] an event with true SDP coordinates $(m'_{\pi^+\pi^-}, \theta'_{\pi^+\pi^-})$. This efficiency over the DP is then averaged using the truth PDF over the Square DP constructed from the fit results (cf. Fig. 7.2) to obtain the signal model average efficiency. Using the PDF for solution I the efficiency is $(23.14 \pm 0.02)\%$ (the error is statistical only). The signal efficiency has also been calculated using the signal truth PDF obtained from solution II. These two values differ by 0.05%,

---

[2] Note that this ε is different from the from the TM and SCF efficiencies in Fig. 6.7

and this shift is accounted as a systematic uncertainty. In summary, the value of the signal efficiency is (after applying a correction due to K_S^0 reconstruction, Sec. 7.3.2) $(22.73 \pm 0.02 \pm 0.61)\%$. Using this efficiency value, the signal yield, the fit fractions and the number of $B^0\bar{B}^0$ pairs produced during the period 1999-2007, the inclusive and partial branching fractions are calculated. The results are shown on Table 7.6. The errors are the statistical, systematic and DP model uncertainties, respectively.

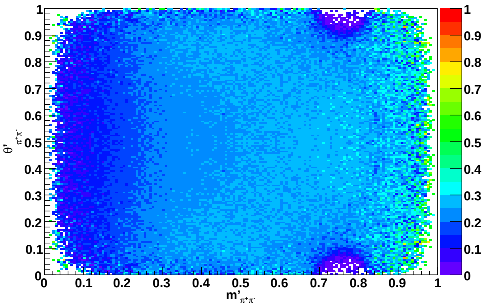

Figure 7.23: *Signal efficiency function over the SDP constructed with the non-resonant MC sample.*

Component	$\mathcal{B}(B^0 \to \text{Mode})(\times 10^6)$
$B^0 \to f_0(980)K^0$	$6.92 \pm 0.77 \pm 0.46 \pm 0.32$
$B^0 \to \rho^0(770)K^0$	$4.31^{+0.70}_{-0.61} \pm 0.29 \pm 0.12$
$B^0 \to K^{*+}(892)\pi^-$	$5.52^{+0.61}_{-0.54} \pm 0.35 \pm 0.41$
$B^0 \to (K\pi)_0^{*+}\pi^-$	$22.67^{+1.65}_{-1.27} \pm 1.20 \pm 0.56$
$B^0 \to f_2(1270)K^0$	$1.15^{+0.42}_{-0.35} \pm 0.11 \pm 0.35$
$B^0 \to f_X(1300)K^0$	$1.82^{+0.55}_{-0.45} \pm 0.16 \pm 0.45$
Non-resonant	$5.77^{+1.61}_{-1.00} \pm 0.53 \pm 0.31$
$B^0 \to \chi_C(0)K^0$	$0.52^{+0.20}_{-0.16} \pm 0.03 \pm 0.06$
$K^0\pi^+\pi^-$ total	$50.15 \pm 1.47 \pm 1.60 \pm 0.73$

Table 7.6: *Summary on branching fractions results (in units of* 10^{-6}*). The first quated error is statistical, the second systematic and the third is the DP model uncertainty. The results are directly quoted in terms of the* K^0 *in the final stat, taking into account for* $\mathcal{B}(K^0 \to K_S^0) = 0.5$.

7.3 Systematics uncertainties

There are several sources of systematic uncertainties in amplitude analyses:

- fit biases coming from reconstruction-related effects, and from the model used to describe the SCF;

- uncertainties on parameters kept fixed in the fit (such as those involved in the Δt resolution model, the fractions of signal events belonging to each tagging category, or the m_{ES} and ΔE distributions);
- statistical uncertainties on the bin contents of the histograms used for the efficiency map, SCF resolution and DP distributions of continuum and B-background. All these effects can be understood as an uncertainty on the shape of the corresponding functions;
- uncertainties on the expected number of background events;
- finally, there are the so-called DP model errors, which arise from uncertainties in the composition of the signal model along the the DP, and its parameterization.

The latter uncertainties are harder to asses as there is no systematical procedure to probe the signal DP model. They are the dominant contributions to the total systematic uncertainties.

7.3.1 Reconstruction and SCF model

Studies on the embedded fits (see Sec. 6.6) have shown that fit biases are small for most of the *Q2B* parameters of interest; the larger observed biases concern the isobar fractions and the total signal yield. These biases are accounted for as systematic uncertainties due to reconstruction and the SCF model. On the isobar fractions, the relative systematic error is 1.2%. On the signal yield a systematic of 0.28σ (~ 14 events out of 2200) is found. The summary of these systematic uncertainties is reported on Table 7.7.

Parameter	**systematic error**	**Parameter**	**systematic error**
$FF(f_0(980)K^0_S)(\%)$	0.5	$FF(\rho^0(770)K^0_S)(\%)$	0.3
$FF(K^*(892)\pi)(\%)$	0.4	$FF((K\pi)^*_0\pi)(\%)$	1.8
$FF(f_2(1270)K^0_S)(\%)$	0.09	$FF(f_X(1300)K^0_S)(\%)$	0.14
$FF(NR)(\%)$	0.5	$FF(\chi_c(0)K^0_S)(\%)$	0.04
Total $FF(\%)$	2.0	Signal yield	14.0

Table 7.7: *Systematic uncertainties on the fit fractions and the signal yield due to reconstruction and the SCF model.*

7.3.2 K_S reconstruction and tracking efficiencies, PID and luminosity

Systematic effects coming from K^0_S reconstruction and tracking efficiencies, PID and luminosity affect the signal efficiency, and so the inclusive and partial branching fractions. The effect on CPV parameters is negligible. Standard BABAR procedures for the estimation of these systematic uncertainties are followed.

- **tracking efficiencies :** a uniform systematic uncertainty over the DP is applied for the reconstruction of charged tracks, taking 0.8% uncertainty per track on the signal efficiency, as suggested by the Tracking Efficiency Task Force [108]. For the present analysis with two charged pions, this gives a total of 1.6% relative systematic uncertainty.

- K_S **reconstruction :** a correction and a systematic uncertainty are applied to the signal efficiency as suggested by the Tracking Efficiency Task Force [109], due to the reconstruction of a K_S^0 with two charged tracks. This correction is a multiplicative factor that takes into account differences between data and MC simulation. The correction applied over the DP average efficiency is of 0.982 ± 0.004, giving an efficiency of 22.73%, with 0.9% of relative systematic uncertainty.

- **PID :** As in the case of tracking efficiency, a uniform systematic over the DP is applied for PID uncertainties, following the same procedure as in [23]. A 1% uncertainty per track and per selector is taken (as suggested by the Tracking Efficiency Task Force). As there are two pions and one pion selector (1% each), the total relative systematic uncertainty is 2.0%.

- **Differences on signal efficiency for sol I and sol II:** For the calculation of the inclusive and partial branching fractions, an average signal efficiency is calculated using the signal truth DP PDF constructed out of the fit results. This efficiency is evaluated using sol I, and the difference with respect to sol II (0.002%) is taken as a systematic uncertainty.

- **Luminosity:** As explained in Sec. 4.1.3, the absolute luminosity at BABAR is estimated from $e^+e^- \to e^+e^-$ and $e^+e^- \to \mu^+\mu^-$ processes, the uncertainty on this estimation is about 1.5% [83]. This uncertainty propagates into the estimation of the counting of $B\bar{B}$ mesons produced at BABAR, which affects the branching fractions (cf. Sec. 2.4.9, Eq. 2.53). This counting has been estimated to have a 1.1% uncertainty [110], using the ratio of hadronic to $\mu^+\mu^-$ production, which gives $N_{B\bar{B}} = (382.86 \pm 4.21) \times 10^6$.

- **Other systematics:** Uncertainties due to vertexing and SVT misalignment are taken from charmonium analyses [111]. These are less than 0.01% for the Q2B parameters and have a negligible effect on the signal efficiency and yield.

Table 7.8 shows the summary on signal efficiency systematics.

7.3.3 Fixed parameters in the likelihood

Systematic errors coming from fixed parameters in the likelihood function are evaluated by varying independently each parameter by $\pm 1\sigma$, where σ refers to the World Average error on the parameter, when available, or a conservative estimate when no measurement is available. The dataset is fitted using both configurations, and the systematic uncertainty is estimated as the shift on the corresponding fit parameters. A list of all fixed parameters, with the values and errors used to evaluate systematics, is given on appendix C. The results of this study are

Effect	**Error**
tracking efficiencies	1.6%
K_S^0 reconstruction	0.9%
PID	2.0%
Difference from solI to solII	0.002%
Total	2.7%

Table 7.8: *Summary of signal efficiency systematics. The systematics errors quoted are relative errors.*

summarized in Tables 7.9, 7.10 and 7.11–7.12 for fit fractions, direct CP asymmetries and phases and signal yield, respectively.

Parameter	$f_0(980)$	$\rho^0(770)$	$K^*(892)$	$(K\pi)_0^*$	$f_2(1270)$	$f_X(1300)$	NR	$\chi_c(0)$	FF_{Tot}
$N_{\text{Neutral Gen.}}$	0.01	0.01	< 0.01	< 0.01	< 0.01	< 0.01	< 0.01	< 0.01	< 0.01
$N_{\text{Charged Gen.}}$	0.01	< 0.01	0.02	< 0.01	< 0.01	< 0.01	< 0.01	< 0.01	0.01
$N_{a_1^+\pi^-}$	< 0.01	< 0.01	< 0.01	< 0.01	< 0.01	< 0.01	< 0.01	< 0.01	< 0.01
$N_{\text{BBkg cat1}}$	< 0.01	< 0.01	< 0.01	< 0.01	< 0.01	< 0.01	< 0.01	< 0.01	< 0.01
$N_{\text{BBkg cat2}}$	0.03	0.03	0.04	< 0.01	< 0.01	< 0.01	< 0.01	< 0.01	0.05
$N_{\text{BBkg cat3}}$	< 0.01	< 0.01	< 0.01	< 0.01	< 0.01	< 0.01	< 0.01	< 0.01	< 0.01
SCF PDF pars.	< 0.01	< 0.01	< 0.01	< 0.01	< 0.01	< 0.01	< 0.01	< 0.01	< 0.01
SCF fraction	0.02	0.02	0.02	< 0.01	< 0.01	< 0.01	< 0.01	< 0.01	0.02
BBkg PDF pars.	0.05	0.13	0.05	< 0.01	< 0.01	< 0.01	< 0.01	< 0.01	0.14
$D^-\pi^+$ Δt resol.	< 0.01	< 0.01	< 0.01	< 0.01	< 0.01	< 0.01	< 0.01	< 0.01	< 0.01
Sig. Δt resol.	0.02	0.01	< 0.01	< 0.01	< 0.01	< 0.01	< 0.01	< 0.01	0.03
Misstag	< 0.01	< 0.01	< 0.01	< 0.01	< 0.01	< 0.01	< 0.01	< 0.01	< 0.01
Δ Misstag	0.01	< 0.01	< 0.01	< 0.01	< 0.01	< 0.01	< 0.01	< 0.01	< 0.01
Tagging effic.	< 0.01	< 0.01	< 0.01	< 0.01	< 0.01	< 0.01	< 0.01	< 0.01	< 0.01
Δm_d(Sig.)	< 0.01	< 0.01	< 0.01	< 0.01	< 0.01	< 0.01	< 0.01	< 0.01	0.02
τ_{B^0}(Sig.)	< 0.01	< 0.01	< 0.01	< 0.01	< 0.01	< 0.01	< 0.01	< 0.01	< 0.01
Δm_d(BBkg)	< 0.01	< 0.01	< 0.01	< 0.01	< 0.01	< 0.01	< 0.01	< 0.01	< 0.01
τ_{B^0}(BBkg)	< 0.01	< 0.01	< 0.01	< 0.01	< 0.01	< 0.01	< 0.01	< 0.01	< 0.01
Subtotal	0.07	0.14	0.07	0.3	0.06	0.17	0.23	0.01	0.15

Table 7.9: *Systematic errors on* **fit fractions** *for* $f_0(980)$, $\rho^0(770)$, $K^*(892)$, $(K\pi)_0^*$, $f_1(1270)$, $f_X(1300)$, NR *and* $\chi_c(0)$ *intermediate states, and in the total isobar fraction due to the uncertainty on the fixed parameters in the likelihood function. The isobar fractions uncertainties are in* $\%$.

7.3.4 Tag-Side Interference Effects

It is usually assumed that the individual final states used for flavor tagging can be reached either from a B^0 or $\bar{B}^0$ meson. This assumption is valid only for the lepton tags. In the case of the non-leptonic tagging decays there is a possibility of mixing from suppressed contributions to the tag-side final state, which gives place to a systematic uncertainty.

One of the examples is the $D^+(\to K^-\pi^+\pi^+)\pi^-$ final state, which is usually associated with $\bar{B}^0$ meson since the charge of the kaon has the same sign as the flavor of a b quark (cf. Sec. 5.3). However, this final state can also be reached from a B^0 meson through

Parameter	$f_0(980)$	$\rho^0(770)$	$K^*(892)$	$(K\pi)^*_0$	$f_2(1270)$	$f_X(1300)$	NR	$\chi_c(0)$	A_{CP}^{inclu}
$N_{\text{Neutral Gen.}}$	< 0.01	< 0.01	< 0.01	< 0.01	< 0.01	< 0.01	< 0.01	< 0.01	< 0.01
$N_{\text{Charged Gen.}}$	< 0.01	< 0.01	< 0.01	< 0.01	< 0.01	< 0.01	< 0.01	< 0.01	< 0.01
$N_{a_1^+\pi^-}$	< 0.01	< 0.01	< 0.01	< 0.01	< 0.01	< 0.01	< 0.01	< 0.01	< 0.01
$N_{\text{BBkg cat1}}$	< 0.01	< 0.01	< 0.01	< 0.01	< 0.01	< 0.01	< 0.01	< 0.01	< 0.01
$N_{\text{BBkg cat2}}$	0.01	< 0.01	< 0.01	< 0.01	< 0.01	< 0.01	< 0.01	< 0.01	< 0.01
$N_{\text{BBkg cat3}}$	< 0.01	< 0.01	< 0.01	< 0.01	< 0.01	< 0.01	< 0.01	< 0.01	< 0.01
SCF PDF pars.	< 0.01	< 0.01	< 0.01	< 0.01	< 0.01	< 0.01	< 0.01	< 0.01	< 0.01
SCF fraction	< 0.01	< 0.01	< 0.01	< 0.01	0.01	< 0.01	< 0.01	< 0.01	< 0.01
BBkg PDF pars.	0.01	0.02	< 0.01	0.02	0.05	0.02	0.04	0.02	< 0.01
$D^-\pi^+$ Δt resol.	< 0.01	< 0.01	< 0.01	< 0.01	< 0.01	< 0.01	< 0.01	< 0.01	< 0.01
Sig. Δt resol.	< 0.01	< 0.01	< 0.01	< 0.01	0.02	< 0.01	< 0.01	< 0.01	< 0.01
Misstag	< 0.01	< 0.01	< 0.01	< 0.01	< 0.01	< 0.01	< 0.01	< 0.01	< 0.01
Δ Misstag	< 0.01	< 0.01	< 0.01	< 0.01	< 0.01	< 0.01	< 0.01	< 0.01	< 0.01
Tagging effic.	< 0.01	< 0.01	< 0.01	< 0.01	< 0.01	< 0.01	< 0.01	< 0.01	< 0.01
Δm_d(Sig.)	< 0.01	< 0.01	< 0.01	< 0.01	< 0.01	< 0.01	< 0.01	< 0.01	< 0.01
τ_{B^0}(Sig.)	< 0.01	< 0.01	< 0.01	< 0.01	< 0.01	< 0.01	< 0.01	< 0.01	< 0.01
Δm_d(BBkg)	< 0.01	< 0.01	< 0.01	< 0.01	< 0.01	< 0.01	< 0.01	< 0.01	< 0.01
τ_{B^0}(BBkg)	< 0.01	< 0.01	< 0.01	< 0.01	< 0.01	< 0.01	< 0.01	< 0.01	< 0.01
Subtotal	0.01	0.02	0.006	0.02	0.05	0.03	0.04	0.02	0.01

Table 7.10: *Systematic errors on* **direct** CP**-asymmetries** *for* $f_0(980)$, $\rho^0(770)$, $K^*(892)$, $(K\pi)^*_0$, $f_1(1270)$, $f_X(1300)$, NR *and* $\chi_c(0)$ *intermediate states, and in the inclusive direct* CP *asymmetry due to the uncertainty on the fixed parameters in the likelihood function.*

Parameter	$2\beta_{eff}(f_0)$	$2\beta_{eff}(\rho^0)$	$\Delta\phi(K^*(892))$	$\Delta\phi((K\pi)^*_0)$	$\phi(f_2)$	$\phi(f_X)$	$\phi(NR)$	$\phi(\chi_c(0))$
$N_{\text{Neutral Gen.}}$	< 0.1	< 0.1	< 0.1	< 0.1	< 0.1	< 0.1	< 0.1	0.2
$N_{\text{Charged Gen.}}$	< 0.1	< 0.1	< 0.1	< 0.1	0.2	< 0.1	< 0.1	0.2
$N_{a_1^+\pi^-}$	< 0.1	< 0.1	< 0.1	< 0.1	< 0.1	< 0.1	< 0.1	< 0.1
$N_{\text{BBkg cat1}}$	< 0.1	< 0.1	< 0.1	< 0.1	< 0.1	< 0.1	< 0.1	0.1
$N_{\text{BBkg cat2}}$	< 0.1	< 0.1	0.3	0.3	1.2	0.1	0.4	0.2
$N_{\text{BBkg cat3}}$	< 0.1	< 0.1	< 0.1	< 0.1	< 0.1	0.1	< 0.1	0.1
SCF PDF pars.	< 0.1	< 0.1	< 0.1	< 0.1	< 0.1	< 0.1	< 0.1	0.2
SCF fraction	0.3	0.2	0.2	< 0.1	1.2	0.2	0.2	0.4
BBkg PDF pars.	0.4	2.6	1.2	1.5	0.8	1.2	1.9	2.2
$D^-\pi^+$ Δt resol.	< 0.1	< 0.1	< 0.1	< 0.1	0.1	< 0.1	< 0.1	0.2
Sig. Δt resol.	0.4	0.3	1.4	1.4	1.3	0.5	0.5	1.3
Misstag	0.1	0.1	< 0.1	0.1	0.3	0.2	0.1	0.4
Δ Misstag	< 0.1	0.2	< 0.1	< 0.1	0.2	0.2	0.1	0.4
Tagging effic.	< 0.1	0.1	< 0.1	< 0.1	0.1	< 0.1	< 0.1	0.3
Δm_d(Sig.)	0.1	0.1	< 0.2	< 0.1	0.5	0.2	0.2	0.2
τ_{B^0}(Sig.)	< 0.1	< 0.1	< 0.1	< 0.1	< 0.1	< 0.1	< 0.1	< 0.1
Δm_d(BBkg)	< 0.1	< 0.1	< 0.1	< 0.1	< 0.1	< 0.1	< 0.1	0.1
τ_{B^0}(BBkg)	< 0.1	< 0.1	< 0.1	< 0.1	< 0.1	< 0.1	< 0.1	< 0.1
Subtotal	0.7	2.6	1.9	2.0	2.4	1.4	2.0	2.7

Table 7.11: *Systematic errors on* **phase differences** $2\beta_{eff}(f_0(980))$, $2\beta_{eff}(\rho^0(770))$*,* $\Delta\phi(K^*(892))$*,* $\Delta\phi((K\pi)^*_0)$, $\phi(f_2(1270))$, $\phi(f_X(1300))$, $\phi(NR)$ *and* $\phi(\chi_c(0))$ *due to the uncertainty on the fixed parameters in the likelihood function. The phases uncertainties are in degrees.*

a $\bar{b} \to c\bar{u}\bar{d}$ decay. Its amplitude is CKM suppressed relative to the dominant $\bar{B}^0$ decay amplitude ($|V_{ub}^* V_{cd}/V_{cb}V_{ud}^*| \approx 0.02$) and has a relative weak phase difference of γ.

This uncertainty is estimated with a standard procedure in time-dependent analyses. 500

Parameter	$\Delta\phi(f_0, \rho^0)$	$\Delta\phi(K^*(892), (K\pi)^*_0)$	$\Delta\phi(\rho^0, (K\pi)^*_0)$	$\Delta\phi(\rho^0, K^*(892))$	**Signal Yield**
$N_{\text{Neutral Gen.}}$	< 0.1	< 0.1	< 0.1	< 0.1	2.0
$N_{\text{Charged Gen.}}$	< 0.1	< 0.1	< 0.1	< 0.1	2.6
$N_{a_1^+\pi^-}$	< 0.1	< 0.1	< 0.1	< 0.1	< 1.0
$N_{\text{BBkg cat1}}$	< 0.1	< 0.1	< 0.1	< 0.1	< 1.0
$N_{\text{BBkg cat2}}$	< 0.1	< 0.1	0.1	< 0.1	5.1
$N_{\text{BBkg cat3}}$	< 0.1	< 0.1	< 0.1	< 0.1	1.1
SCF PDF pars.	< 0.1	< 0.1	< 0.1	< 0.1	< 1.0
SCF fraction	0.2	< 0.1	0.2	0.2	5.7
BBkg PDF pars.	1.6	0.2	1.4	1.5	2.2
$D^-\pi^+$ Δt resol.	< 0.1	< 0.1	< 0.1	< 0.1	< 0.1
Sig. Δt resol.	0.1	< 0.1	0.6	0.7	2.4
Misstag	< 0.1	< 0.1	0.1	0.1	< 1.0
Δ Misstag	< 0.1	< 0.1	< 0.1	< 0.1	< 1.0
Tagging effic.	< 0.1	< 0.1	< 0.1	< 0.1	5.6
Δm_d(Sig.)	< 0.1	< 0.1	0.1	0.1	< 1.0
τ_{B^0}(Sig.)	< 0.1	< 0.1	< 0.1	< 0.1	1.6
Δm_d(BBkg)	< 0.1	< 0.1	< 0.1	< 0.1	< 1.0
τ_{B^0}(BBkg)	< 0.1	< 0.1	< 0.1	< 0.1	< 1.0
Subtotal	1.5	0.2	1.5	1.6	10.7

Table 7.12: *Systematic errors on* **phase differences** $\Delta\phi(f_0, \rho^0)$*,* $\Delta\phi(K^*(892), (K\pi)^*_0)$*,* $\Delta\phi(\rho^0, (K\pi)^*_0))$*,* $\Delta\phi(\rho^0, K^*(892)$ *and in the Signal Yield due to the uncertainty on the fixed parameters in the likelihood function. The phases uncertainties are in degrees.*

MC data samples are generated taking into account the tag-side interference, and then fitted taking/not-taking the effect into account. The systematic effect is estimated as the mean bias on the Q2B parameters, which are shown on Table 7.13.

Par.	**Shift**	**Par.**	**Shift**
$C(f_0(980))$	< 0.01	$C(\rho^0(770))$	0.06
$FF(f_0(980))$	0.04	$FF(\rho^0(770))$	0.02
$2\beta_{eff}(f_0(980))$	1.2	$2\beta_{eff}(\rho^0(980))$	0.3
$A_{CP}(K^*(892))$	< 0.01	$A_{CP}((K\pi)^*_0)$	< 0.01
$FF(K^*(892))$	0.11	$FF((K\pi)^*_0)$	0.13
$\Delta\phi(K^*(892))$	0.6	$\Delta\phi((K\pi)^*_0)$	0.3
$C(f_2(1270))$	0.03	$C(f_X(1300))$	< 0.01
$FF(f_2(1270))$	0.2	$FF(f_X(1300))$	0.01
$\phi(f_2(1270))$	0.8	$\phi(f_X(1300))$	1.9
$C(NR)$	< 0.01	$C(\chi_C(0))$	< 0.01
$FF(NR)$	0.04	$FF(\chi_C(0))$	< 0.01
$\phi(NR)$	1.4	$\phi(\chi_C(0))$	2.1
FF_{Tot}	0.3	A_{CP}^{incl}	< 0.01
$\Delta\phi(f_0, \rho^0)$	3.8	$\Delta\phi(K^*(892), (K\pi)^*_0)$	4.4
$\Delta\phi(\rho^0, (K\pi)^*_0))$	1.8	$\Delta\phi(\rho^0, K^*(892)$	6.2

Table 7.13: *Systematic errors on total fit fraction, inclusive direct* CP *asymmetry and all Q2B parameters due to the Tag-Side Interference effect. The errors on phases are in degrees and those on* FFs *in* $\%$*.*

7.3.5 Continuum PDF

While most of the PDF parameters for the continuum model are free to vary in the nominal fit, the Dalitz plot PDF is uniquely determined as a two-dimensional non-parametric map, built using onpeak sidebands and offpeak data (cf. Sec. 6.3.4). In order to build this continuum DP PDF, the square DP is broken into regions, and smoothed using different smoothing parameters for each region, to take into account the presence of different peaking structures, with different widths (i.e. peaks in the ρ^0, K^* bands due to real ρ^0s and K^*s).

A systematic uncertainty coming from the finite size of the samples used to construct the PDF is estimated. It is evaluated by splitting the continuum $u\bar{u}$, $d\bar{d}$ and $s\bar{s}$, and continuum $c\bar{c}$ MC samples (cf. Sec. 5.1.2) into samples of the same size as are used to build the PDF (on-peak and off-peak). Events on the signal region and sidebands (cf. Sec. 5.7) are used to construct the DP PDFs. A toy MC sample is generated only with the signal (using the nominal signal model and the isobar parameter values of solution I) and continuum-background (with one of the constructed PDFs out of the MC continuum sample) components. The samples are then fitted with all the continuum DP PDFs just constructed. The systematic is evaluated as the RMS of the distributions of the bias on the fit parameters.

Since the empirical shape parameters of the DP continuum PDFs are not determined simultaneously with the signal parameters by the fit, the validity of the sidebands-to-signal region extrapolation has to be tested. This introduces systematic uncertainties. PDFs created with events from different regions of the sideband and signal region of the $(m_{ES}, \Delta E)$ plane, are used to build continuum MC samples. The signal region DP continuum PDF is used to generate high statistic toy MC samples (again, only with the signal and continuum components), which are then fitted using both the signal region and sidebands PDFs. The systematic is evaluated as the RMS of the distributions of the bias on the fit parameters.

A systematic uncertainty is evaluated on the stability of the smoothing procedure. To quantify this effect, a series of PDFs were produced with different smoothing parameters, which are then used to refit the data. The observed shifts in the fit parameters are taken as systematics.

A charge symmetric PDF is used for the continuum DP for all tagging categories, except for the non-tagged events. An additional systematic effect is evaluated by fitting data with the symmetric/non-symmetric DP PDF to evaluate a shift in the Q2B parameters.

The mean biases on the fitted Q2B parameters from these systematic effects are shown on Table 7.14.

7.3.6 B-background PDF

A systematic error is evaluated due to the DP B-background PDFs, which are 2D histograms. The distributions of the peaking B-background components have been modified by shifting their central values by ± the experimental resolution in the reconstructed mass ($\sim 8\ \mathrm{MeV}/c^2$). Their widths have been smeared by the same amount. The systematics are evaluated as the bias in the fit results with respect to the nominal fit configuration.

There is another source of systematic coming from the $J/\Psi K^0_S$ ΔE PDF. The signal and $D\pi$ B-background uses the same parametric ΔE PDF. These fit functions are then able to

Par.	Subtotal	Par.	Subtotal
$C(f_0(980))$	0.01	$C(\rho^0(770))$	< 0.01
$FF(f_0(980))$	0.11	$FF(\rho^0(770))$	0.04
$2\beta_{eff}(f_0(980))$	1.3	$2\beta_{eff}(\rho^0(980))$	1.7
$A_{CP}(K^*(892))$	< 0.01	$A_{CP}((K\pi)_0^*)$	0.01
$FF(K^*(892))$	0.21	$FF((K\pi)_0^*)$	0.07
$\Delta\phi(K^*(892))$	2.7	$\Delta\phi((K\pi)_0^*)$	2.1
$C(f_2(1270))$	< 0.01	$C(f_X(1300))$	0.02
$FF(f_2(1270))$	0.03	$FF(f_X(1300))$	0.12
$\phi(f_2(1270))$	3.0	$\phi(f_X(1300))$	1.9
$C(NR)$	0.02	$C(\chi_C(0))$	0.01
$FF(NR)$	0.22	$FF(\chi_C(0))$	0.01
$\phi(NR)$	1.1	$\phi(\chi_C(0))$	2.3
FF_{Tot}	0.10	A_{CP}^{incl}	< 0.01
$\Delta\phi(f_0, \rho^0)$	1.6	$\Delta\phi(K^*(892), (K\pi)_0^*)$	1.1
$\Delta\phi(\rho^0, (K\pi)_0^*))$	2.9	$\Delta\phi(\rho^0, K^*(892)$	3.9
Signal Yield	20.2		

Table 7.14: *Systematic errors on the Q2B parameters and signal yield due to the uncertainty on the continuum DP PDF. The errors on phases are in degrees and those on FFs in %.*

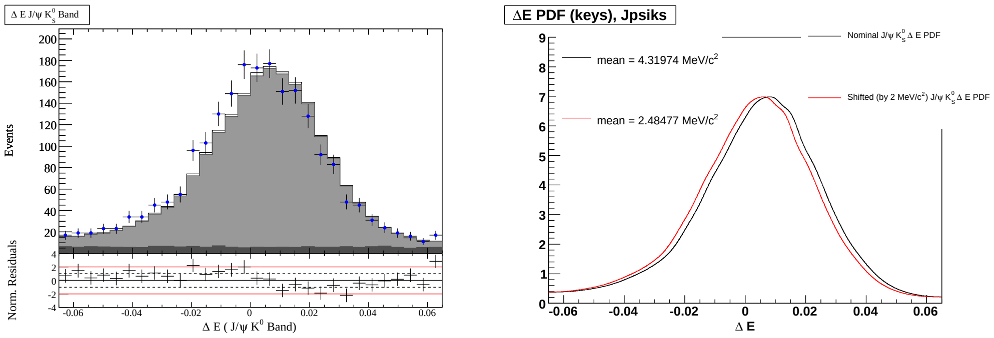

Figure 7.24: *Left: Comparison between data (blue points) and ΔE PDF (histogram) in the $J/\Psi K_S^0$ band, a shift between the two is seen due the bias in the absolute energy scale. Right: the nominal (black) and shifted (red) $J/\Psi K_S^0$ ΔE PDF used for systematic studies.*

adapt their value to the absolute energy scale, *i.e.* the mean value of the ΔE PDF is free to vary in the fit. However, the $J/\Psi K_S^0$ uses a non-parametric PDF for ΔE, constructed from MC. When the fit on data is performed, a shift between the ΔE PDF and data is observed as can be seen in the left hand plot of Fig. 7.24. A systematic is evaluated on this: the ΔE PDF is shifted by the ΔE bias, as shown in the right hand plot of Fig. 7.24, then data is refitted and the bias in the fit results are taken as systematic. The projection plots shown in Sec. 7.1 use the corrected $J/\Psi K_S^0$ ΔE PDF.

The results of all these systematics can be seen in Table 7.15, 7.16 and 7.17-7.18 for fit fractions, direct CP asymmetries and phases and the signal yield, respectively.

Parameter	$f_0(980)$	$\rho^0(770)$	$K^*(892)$	$(K\pi)^*_0$	$f_2(1270)$	$f_X(1300)$	NR	$\chi_c(0)$	FF_{Tot}
Shift $D^+\pi^-$	0.05	0.05	0.01	0.02	0.02	< 0.01	0.05	< 0.01	0.02
Smear $D^+\pi^-$	0.03	0.07	0.01	0.02	< 0.01	< 0.01	0.04	< 0.01	0.04
Shift $J/\Psi K^0_S$	< 0.01	< 0.01	< 0.01	< 0.01	< 0.01	< 0.01	< 0.01	< 0.01	< 0.01
Smear $J/\Psi K^0_S$	< 0.01	< 0.01	< 0.01	0.01	< 0.01	< 0.01	0.02	< 0.01	< 0.01
Shift $\Psi(2S)K^0_S$	0.01	< 0.01	0.03	0.09	< 0.01	0.02	0.05	< 0.01	0.07
Smear $\Psi(2S)K^0_S$	0.01	< 0.01	0.01	0.06	< 0.01	< 0.01	0.05	< 0.01	0.03
Shift $\eta' K^0_S$	< 0.01	0.02	< 0.01	0.01	< 0.01	< 0.01	< 0.01	< 0.01	< 0.01
Smear $\eta' K^0_S$	< 0.02	0.03	< 0.01	0.01	< 0.01	< 0.01	< 0.01	< 0.01	< 0.01
Shift $a_1^+\pi^-$	< 0.01	< 0.01	< 0.01	0.01	< 0.01	< 0.01	0.01	< 0.01	< 0.01
Smear $a_1^+\pi^-$	< 0.01	< 0.01	< 0.01	< 0.01	< 0.01	< 0.01	< 0.01	< 0.01	< 0.01
$PDF_{J/}(\Delta E)$	0.03	0.01	< 0.01	< 0.01	< 0.01	< 0.01	0.07	< 0.01	0.02
Subtotal	0.07	0.09	0.03	0.12	0.02	0.02	0.12	< 0.01	0.08

Table 7.15: *Systematic errors on* **fit fractions** *for* $f_0(980)$, $\rho^0(770)$, $K^*(892)$, $(K\pi)^*_0$, $f_1(1270)$, $f_X(1300)$, NR *and* $\chi_c(0)$ *intermediate states, and in the total isobar fraction due to the uncertainty on the B-background PDFs. The isobar fractions uncertainties are in* $\%$.

Parameter	$f_0(980)$	$\rho^0(770)$	$K^*(892)$	$(K\pi)^*_0$	$f_2(1270)$	$f_X(1300)$	NR	$\chi_c(0)$	A^{incl}_{CP}
Shift $D^+\pi^-$	< 0.01	0.02	< 0.01	< 0.01	0.01	< 0.01	< 0.01	< 0.01	< 0.01
Smear $D^+\pi^-$	< 0.01	0.06	< 0.01	< 0.01	0.05	< 0.01	< 0.01	< 0.01	< 0.01
Shift $J/\Psi K^0_S$	< 0.01	< 0.01	< 0.01	< 0.01	< 0.01	< 0.01	< 0.01	< 0.01	< 0.01
Smear $J/\Psi K^0_S$	< 0.01	< 0.01	< 0.01	< 0.01	< 0.01	< 0.01	< 0.01	< 0.01	< 0.01
Shift $\Psi(2S)K^0_S$	< 0.01	< 0.01	< 0.01	< 0.01	< 0.01	< 0.01	< 0.01	< 0.01	< 0.01
Smear $\Psi(2S)K^0_S$	< 0.01	< 0.01	< 0.01	< 0.01	< 0.01	< 0.01	< 0.01	< 0.01	< 0.01
Smear $\eta' K^0_S$	< 0.01	< 0.01	< 0.01	< 0.01	< 0.01	< 0.01	< 0.01	< 0.01	< 0.01
Shift $\eta' K^0_S$	< 0.01	< 0.01	< 0.01	< 0.01	< 0.01	< 0.01	< 0.01	< 0.01	< 0.01
Shift $a_1^+\pi^-$	< 0.01	< 0.01	< 0.01	< 0.01	< 0.01	< 0.01	< 0.01	< 0.01	< 0.01
Smear $a_1^+\pi^-$	< 0.01	< 0.01	< 0.01	< 0.01	< 0.01	< 0.01	< 0.01	< 0.01	< 0.01
$PDF_{J/}(\Delta E)$	< 0.01	< 0.01	< 0.01	< 0.01	< 0.01	< 0.01	< 0.01	< 0.01	< 0.01
Subtotal	0.01	0.06	< 0.01	< 0.01	0.05	0.01	0.01	0.01	< 0.01

Table 7.16: *Systematic errors on* **direct** CP**-asymmetries** *for* $f_0(980)$, $\rho^0(770)$, $K^*(892)$, $(K\pi)^*_0$, $f_1(1270)$, $f_X(1300)$, NR *and* $\chi_c(0)$ *intermediate states, and in the inclusive* CP*-asymmetry due to the uncertainty on the B-background PDFs.*

7.3.7 Signal Model Systematics

A systematic uncertainty is evaluated on the non-resonant fit fraction. A significant signal was spotted with a dedicated quasi-two-body analysis performed on the center of the DP using the sPlot technique (cf. Appendix B, Sec. B.2). A signal yield of 175 ± 29 events is found, mainly attributed to a non-resonant component contributing to the signal model. This signal yield is highly anticorrelated (-85%) with a non-peaking B background yield. This correlation is due to the low discrimination between these two species. A systematic uncertainty is assigned on the non-resonant fit fraction to address for this effect. In a conservative approach, it is estimated to be 85% of the statistical uncertainty of the signal yield obtained on the DP, which results on 1.6% systematic error on the fit fraction.

Isobar phases are the most interesting results from this Dalitz analysis. For previous amplitude analyses, the dominant source of systematics on these phases came from model-

Parameter	$2\beta_{eff}(f_0)$	$2\beta_{eff}(\rho^0)$	$\Delta\phi(K^*(892))$	$\Delta\phi((K\pi)^*_0)$	$\phi(f_2)$	$\phi(f_X)$	$\phi(NR)$	$\phi(\chi_c(0))$
Shift $D^+\pi^-$	< 0.1	0.7	0.4	0.5	2.4	0.2	0.2	0.3
Smear $D^+\pi^-$	0.5	2.3	1.2	0.9	1.9	1.6	1.3	0.7
Shift $J/\Psi K^0_S$	< 0.1	< 0.1	< 0.1	< 0.1	< 0.1	< 0.1	< 0.1	0.2
Smear $J/\Psi K^0_S$	< 0.1	< 0.1	< 0.1	< 0.1	< 0.1	< 0.1	0.1	0.3
Shift $\Psi(2S)K^0_S$	0.4	0.4	0.7	0.7	< 0.1	0.5	0.7	0.4
Smear $\Psi(2S)K^0_S$	< 0.1	< 0.1	0.2	0.2	0.3	0.2	0.2	0.3
Shift $\eta' K^0_S$	0.2	< 0.1	< 0.1	< 0.1	0.2	0.1	< 0.1	0.1
Smear $\eta' K^0_S$	0.1	< 0.1	< 0.1	< 0.1	0.2	0.1	< 0.1	0.2
Shift $a_1^+\pi^-$	< 0.1	< 0.1	< 0.1	< 0.1	0.1	< 0.1	< 0.1	0.1
Smear $a_1^+\pi^-$	< 0.1	0.1	< 0.1	< 0.1	0.2	< 0.1	< 0.1	0.1
$PDF_{J/}(\Delta E)$	< 0.1	< 0.1	< 0.1	< 0.1	0.2	< 0.1	< 0.1	< 0.1
Subtotal	0.7	2.4	1.4	1.3	3.1	1.7	1.5	1.0

Table 7.17: *Systematic errors on* **phase differences** $2\beta_{eff}(f_0(980))$*,* $2\beta_{eff}(\rho^0(770))$*,* $\Delta\phi(K^*(892))$*,* $\Delta\phi((K\pi)^*_0)$*,* $\phi(f_2(1270))$*,* $\phi(f_X(1300))$*,* $\phi(NR)$ *and* $\phi(\chi_c(0))$ *due to the uncertainty on the B-background PDFs. The phases uncertainties are in degrees.*

Parameter	$\Delta\phi(f_0, \rho^0)$	$\Delta\phi(K^*(892), (K\pi)^*_0)$	$\Delta\phi(\rho^0, (K\pi)^*_0))$	$\Delta\phi(\rho^0, K^*(892)$	**Signal Yield**
Shift $D^+\pi^-$	0.8	0.2	1.1	0.9	1.4
Smear $D^+\pi^-$	3.3	0.3	3.7	3.4	< 1.0
Shift $J/\Psi K^0_S$	< 0.1	< 0.1	< 0.1	< 0.1	< 1.0
Smear $J/\Psi K^0_S$	< 0.1	< 0.1	< 0.1	< 0.1	< 1.0
Shift $\Psi(2S)K^0_S$	0.3	< 0.1	0.3	0.2	2.1
Smear $\Psi(2S)K^0_S$	< 0.1	< 0.1	< 0.2	0.2	1.1
Shift $\eta' K^0_S$	< 0.1	< 0.1	< 0.1	< 0.1	< 1.0
Smear $\eta' K^0_S$	< 0.1	< 0.1	< 0.1	< 0.1	< 1.0
Shift $a_1^+\pi^-$	< 0.1	< 0.1	< 0.1	< 0.1	< 1.0
Smear $a_1^+\pi^-$	< 0.1	< 0.1	0.1	0.2	< 1.0
$J/\ \Delta E$ PDF	< 0.1	< 0.1	< 0.1	< 0.1	1.6
Subtotal	3.4	0.3	3.9	3.6	3.3

Table 7.18: *Systematic errors on* **phase differences** $\Delta\phi(f_0, \rho^0)$*,* $\Delta\phi(K^*(892), (K\pi)^*_0)$*,* $\Delta\phi(\rho^0, (K\pi)^*_0))$*,* $\Delta\phi(\rho^0, K^*(892)$ *and in the Signal Yield due to the uncertainty on the B-background PDFs. The phases uncertainties are in degrees.*

related effects, like shifts in fit parameters when adding/removing components from the nominal signal model. Estimating the uncertainties in this way is very conservative, as it is clear several of these effects are correlated and are often double-counted.

A more detailed study of such effects has been performed. Rather than checking for shifts in fitted values when refitting data with different signal models, the present procedure is based on a study performed on large samples of toy MC events.

Systematic uncertainties from signal model can be separated in two kinds: the ones that come from the fixed parameters on the resonant states lineshapes (*e.g.* the $\rho^0(770)$ mass, width and barrier radius); and the ones coming from the components included in the signal model. The systematic effects from those sources will be described separately.

Lineshape parameters

Using the same approach as in Sec. 7.3.3, systematics from fixed parameters in the lineshape functions are evaluated by changing them incoherently by $\pm 1\sigma$, where σ refers to the World Average error. As mentioned in Sec. 6.3.2, the approximation of neglecting mass resolution effects for the TM events of the χ_{c0} component is not valid. For this reason its width is fixed to $13\ \mathrm{MeV}/c^2$ and data is then refitted. This value is the effective width of a RBW lineshape after convolution with the experimental mass resolution ($5\ \mathrm{MeV}/c^2$ around the χ_{c0} band).

The results are summarized in Tables 7.19–7.22 for isobar fractions, direct CP asymmetries and phases and signal yield, respectively.

Parameter	$f_0(980)$	$\rho^0(770)$	$K^*(892)$	$(K\pi)^*_0$	$f_2(1270)$	$f_X(1300)$	NR	$\chi_c(0)$	FF_{Tot}
$f_0(980)$ mass	0.32	0.20	0.01	0.28	0.03	0.12	0.45	< 0.01	0.19
$f_0(980)$ gP	0.47	0.18	0.03	0.07	0.03	0.19	0.23	< 0.01	0.19
$f_0(980)$ gK	0.06	0.02	< 0.01	0.10	0.02	0.02	0.46	< 0.01	0.31
$\rho^0(770)$ mass	< 0.01	0.01	< 0.01	< 0.01	< 0.01	< 0.01	0.01	< 0.01	< 0.01
$\rho^0(770)$ width	< 0.01	0.01	< 0.01	< 0.01	< 0.01	< 0.01	0.02	< 0.01	< 0.01
$\rho^0(770)$ radius	0.02	0.04	< 0.01	< 0.01	< 0.01	< 0.01	0.02	< 0.01	< 0.01
$K^*(892)$ mass	< 0.01	0.01	< 0.01	< 0.01	< 0.01	< 0.01	0.02	< 0.01	< 0.01
$K^*(892)$ width	< 0.01	< 0.01	0.03	0.03	< 0.01	< 0.01	< 0.01	< 0.01	< 0.01
$K^*(892)$ radius	0.02	0.01	0.06	0.03	< 0.01	0.02	< 0.01	< 0.01	0.02
$(K\pi)^*_0$ mass	0.02	0.02	< 0.01	0.14	0.02	0.03	0.10	< 0.01	0.03
$(K\pi)^*_0$ width	0.02	0.01	0.02	0.07	0.02	< 0.01	0.19	< 0.01	0.17
$f_2(1270)$ mass	< 0.01	0.01	< 0.01	< 0.01	0.01	< 0.01	0.02	< 0.01	< 0.01
$f_2(1270)$ width	< 0.01	0.01	< 0.01	< 0.01	< 0.01	< 0.01	0.01	< 0.01	< 0.01
$f_X(1300)$ mass	0.11	0.14	0.03	0.09	0.10	0.48	0.12	< 0.01	0.23
$f_X(1300)$ width	0.36	0.04	0.03	0.15	0.03	0.11	0.30	< 0.01	0.18
$\chi_C(0)$ mass	< 0.01	0.01	< 0.01	< 0.01	< 0.01	< 0.01	0.02	< 0.01	0.01
$\chi_C(0)$ width	0.03	0.01	0.01	0.03	0.01	0.01	0.12	0.06	0.06
Subtotal	0.69	0.31	0.13	0.39	0.16	0.28	0.86	0.06	0.55

Table 7.19: *Systematic errors on the* **fit fractions** *for* $f_0(980)$, $\rho^0(770)$, $K^*(892)$, $(K\pi)^*_0$, $f_1(1270)$, $f_X(1300)$, NR *and* $\chi_c(0)$ *intermediate states, and in the total isobar fraction due to the uncertainty on lineshapes fixed parameters. The isobar fractions uncertainties are in* $\%$.

Components in the Signal Model

The nominal signal model has been described in Sec. 6.8. Other intermediate modes, with rates too small to be considered, may be present in signal, and ignoring them in the signal DP model introduces a source of systematic error. A list of the supplementary components tested for systematics studies is given below,

- $\rho^0(1450)$,
- $\rho^0(1700)$,
- $f_0(1710)$,
- $\chi_C(2)$,

Parameter	$f_0(980)$	$\rho^0(770)$	$K^*(892)$	$(K\pi)^*_0$	$f_2(1270)$	$f_X(1300)$	NR	$\chi_c(0)$	A^{incl}_{CP}
$f_0(980)$ mass	< 0.01	0.03	< 0.01	< 0.01	0.02	0.01	0.05	< 0.01	< 0.01
$f_0(980)$ gP	< 0.01	0.01	< 0.01	< 0.01	< 0.01	< 0.01	< 0.01	< 0.01	< 0.01
$f_0(980)$ gK	< 0.01	0.01	< 0.01	< 0.01	< 0.01	0.01	0.03	< 0.01	< 0.01
$\rho^0(770)$ mass	< 0.01	< 0.01	< 0.01	< 0.01	< 0.01	< 0.01	< 0.01	< 0.01	< 0.01
$\rho^0(770)$ width	< 0.01	< 0.01	< 0.01	< 0.01	< 0.01	< 0.01	< 0.01	< 0.01	< 0.01
$\rho^0(770)$ radius	< 0.01	< 0.01	< 0.01	< 0.01	< 0.01	< 0.01	< 0.01	< 0.01	< 0.01
$K^*(892)$ mass	< 0.01	< 0.01	< 0.01	< 0.01	< 0.01	< 0.01	< 0.01	< 0.01	< 0.01
$K^*(892)$ width	< 0.01	< 0.01	< 0.01	< 0.01	< 0.01	< 0.01	< 0.01	< 0.01	< 0.01
$K^*(892)$ radius	< 0.01	< 0.01	< 0.01	< 0.01	< 0.01	< 0.01	< 0.01	< 0.01	< 0.01
$(K\pi)^*_0$ mass	< 0.01	< 0.01	< 0.01	< 0.01	< 0.01	0.01	0.02	< 0.01	< 0.01
$(K\pi)^*_0$ width	< 0.01	< 0.01	< 0.01	< 0.01	< 0.01	< 0.01	< 0.01	< 0.01	< 0.01
$f_2(1270)$ mass	< 0.01	< 0.01	< 0.01	< 0.01	< 0.01	< 0.01	< 0.01	< 0.01	< 0.01
$f_2(1270)$ width	< 0.01	< 0.01	< 0.01	< 0.01	< 0.01	< 0.01	< 0.01	< 0.01	< 0.01
$f_X(1300)$ mass	0.01	0.02	< 0.01	< 0.01	0.03	0.02	0.02	< 0.01	< 0.01
$f_X(1300)$ width	< 0.01	< 0.01	< 0.01	< 0.01	< 0.01	< 0.01	0.01	< 0.01	< 0.01
$\chi_C(0)$ mass	< 0.01	< 0.01	< 0.01	< 0.01	< 0.01	< 0.01	< 0.01	< 0.01	< 0.01
$\chi_C(0)$ width	< 0.01	< 0.01	< 0.01	< 0.01	< 0.01	< 0.01	< 0.01	< 0.01	< 0.01
Subtotal	0.02	0.04	< 0.01	< 0.01	0.04	0.03	0.01	0.02	< 0.01

Table 7.20: *Systematic errors on the* **direct** CP**-asymmetries** *for* $f_0(980)$, $\rho^0(770)$, $K^*(892)$, $(K\pi)^*_0$, $f_1(1270)$, $f_X(1300)$, NR *and* $\chi_c(0)$ *intermediate states due to the uncertainty on lineshapes fixed parameters.*

Parameter	$2\beta_{eff}(f_0)$	$2\beta_{eff}(\rho^0)$	$\Delta\phi(K^*(892))$	$\Delta\phi((K\pi)^*_0)$	$\phi(f_2)$	$\phi(f_X)$	$\phi(NR)$	$\phi(\chi_c(0))$
$f_0(980)$ mass	2.0	2.7	0.6	0.7	1.2	0.5	2.1	0.3
$f_0(980)$ gP	0.9	1.5	0.9	0.8	0.6	0.9	0.3	0.6
$f_0(980)$ gK	1.0	0.9	0.3	0.1	0.3	0.7	1.5	< 0.1
$\rho^0(770)$ mass	0.3	0.2	< 0.1	< 0.1	< 0.1	0.1	< 0.1	< 0.1
$\rho^0(770)$ width	0.4	0.2	0.2	0.1	0.1	0.2	< 0.1	< 0.1
$\rho^0(770)$ radius	0.5	0.4	0.2	0.2	0.5	< 0.1	< 0.1	0.2
$K^*(892)$ mass	0.4	0.1	0.2	0.1	< 0.1	0.2	< 0.1	0.1
$K^*(892)$ width	0.2	0.2	0.1	0.1	0.1	0.1	< 0.1	< 0.1
$K^*(892)$ radius	0.4	0.5	0.3	0.1	0.1	0.2	< 0.1	0.1
$(K\pi)^*_0$ mass	0.6	0.5	1.7	1.5	1.1	0.3	< 0.1	1.1
$(K\pi)^*_0$ width	0.4	0.4	0.7	0.7	0.7	0.4	< 0.1	0.2
$f_2(1270)$ mass	0.4	0.2	0.2	0.1	0.1	0.2	0.1	0.1
$f_2(1270)$ width	0.4	0.2	0.1	0.1	0.6	0.2	0.1	0.1
$f_X(1300)$ mass	2.3	2.6	1.1	1.2	1.6	2.0	0.9	0.3
$f_X(1300)$ width	0.3	0.9	1.1	0.8	2.6	0.2	0.3	0.6
$\chi_C(0)$ mass	0.4	0.2	0.2	0.1	0.1	0.2	0.1	0.6
$\chi_C(0)$ width	0.6	0.3	0.3	< 0.1	< 0.1	0.3	< 0.1	0.4
Subtotal	3.8	4.4	2.8	2.4	3.7	2.6	2.9	2.0

Table 7.21: *Systematic errors on the* **phase differences** $2\beta_{eff}(f_0(980))$, $2\beta_{eff}(\rho^0(770))$*,* $\Delta\phi(K^*(892))$*,* $\Delta\phi((K\pi)^*_0)$, $\phi(f_2(1270))$, $\phi(f_X(1300))$, $\phi(NR)$ *and* $\phi(\chi_c(0))$ *due to the uncertainty on lineshapes fixed parameters. The phases uncertainties are in degrees.*

- $K_2^{*\pm}(1430)$,
- $K^*(1410)$,
- $K^*(1680)$.

This list is constructed from PDG [21] by looking at the non-controversial resonances that can decay to $\pi^+\pi^-$ or $\pi^\pm K^0$.

Parameter	$\Delta\phi(f_0, \rho^0)$	$\Delta\phi(K^*(892), (K\pi)^*_0)$	$\Delta\phi(\rho^0, (K\pi)^*_0))$	$\Delta\phi(\rho^0, K^*(892)$	**Signal Yield**
$f_0(980)$ mass	0.8	0.1	5.7	1.4	1.8
$f_0(980)$ gP	1.2	< 0.1	1.9	0.4	4.2
$f_0(980)$ gK	1.5	0.2	3.0	0.7	1.5
$\rho^0(770)$ mass	< 0.1	< 0.1	0.3	0.4	< 1.0
$\rho^0(770)$ width	0.2	< 0.1	0.3	0.3	< 1.0
$\rho^0(770)$ radius	0.2	< 0.1	< 0.1	< 0.1	< 1.0
$K^*(892)$ mass	0.2	0.4	0.3	0.5	< 1.0
$K^*(892)$ width	< 0.1	0.2	0.4	0.6	< 1.0
$K^*(892)$ radius	0.3	0.3	0.9	1.2	< 1.0
$(K\pi)^*_0$ mass	0.1	0.2	1.6	0.7	< 1.0
$(K\pi)^*_0$ width	< 0.1	0.4	0.3	0.1	< 1.0
$f_2(1270)$ mass	< 0.1	< 0.1	0.5	0.5	< 1.0
$f_2(1270)$ width	0.2	< 0.1	0.2	0.2	< 1.0
$f_X(1300)$ mass	0.4	< 0.1	4.6	1.3	1.6
$f_X(1300)$ width	1.3	0.1	0.2	1.0	2.6
$\chi_C(0)$ mass	< 0.1	< 0.1	0.3	0.4	< 1.0
$\chi_C(0)$ width	0.3	< 0.1	0.2	0.3	< 1.0
Subtotal	2.6	0.7	8.5	3.0	5.8

Table 7.22: *Systematic errors on the* **phase differences** $\Delta\phi(f_0, \rho^0)$, $\Delta\phi(K^*(892), (K\pi)^*_0)$, $\Delta\phi(\rho^0, (K\pi)^*_0))$, $\Delta\phi(\rho^0, K^*(892)$ *and in the signal yield due to the uncertainty on line-shapes fixed parameters. The phases uncertainties are in degrees.*

In order to evaluate this systematic, two complementary methods are performed.

- The first method proceeds in two steps: 1) data is fitted, by keeping the isobar parameters of the Nominal Signal Model (NSM) components fixed, while fitting for the ones for the supplementary components. This is implicitly assuming that these supplementary components are small. The fits are made randomizing the initial isobar parameters values, and the best fit values are kept. 2) using the isobar parameters obtained from the first step, one hundred high-statistics toy datasets are generated with the NSM + Supplementary components. These datasets are fitted in two configurations: using the NSM with/without the supplementary components. The systematics are evaluated as the mean shift in fit parameters between both fit configurations. This evaluation of systematics is referred as the **Generating with** method.

- A complementary exercise consists of generating toy datasets (with the same statistics as the data sample), using the results from the NSM fit and fitting them with/without the supplementary components. The purpose here is: if a component is not in data and is included in the signal model, then the fitter will find a non-zero value for its isobar fraction (see appendix B, Sec. B.1), and the correlations with other components can induce biases. One hundred signal-only toys with ~ 1600 signal events are generated. This evaluation of systematics is referred as the **Generating without** method.

Both methods for evaluating systematics are complementary although not completely uncorrelated. A conservative combination is used, by summing independently the estimations from **Generating with** and **Generating without** approaches.

Generating with supplementary components

The results on the fit fractions of the supplementary components after performing step 1 of the **Generating with** method are shown on Table 7.23. Even if the significance of $\rho(1450)$, $\rho(1700)$, $K^{*}(1410)$ and $K^{*}(1680)$ is low, the central values for their fit fractions are considerably large. It is therefore more realistic to use results from from other analyses, when they have better sensitivity to those small components. The numbers for the $\rho(1450)$, $\rho(1700)$ are taken from $B^0 \to (\rho\pi)^0$ analysis [35], in which they found $FF(\rho(1450))/FF(\rho(770)) = 13.0\%$ and $FF(\rho(1700))/FF(\rho(770)) = 7.0\%$ (statistical only error). Similarly, the numbers for $K^{*}(1410)$ and $K^{*}(1680)$ are obtained from the $B^{+} \to K^{+}\pi^{-}\pi^{+}$ analysis [23]. They found $FF((K^{*}(1680))/FF(K^{*}(892)) = 15.6\%$ and $FF((K^{*}(1410))/FF(K^{*}(892)) = 2.7\%$. For the remaining components, the values obtained from the fit to data are used. The values used to perform step 2 of the **Generating with** method are shown in Table 7.23. The resulting shift on the fit parameters are the ones shown on the second column of Table 7.24.

Component	Fit Fraction (From Fit)	Fit Fraction (Used For Toys)	source
$FF(\rho(1450))$	$(13.9 \pm 12.1)\% FF(\rho(770))$	$(13.0 \pm 4.0)\% FF(\rho(770))$	$(\rho\pi)$
$FF(\rho(1700))$	$(14.2 \pm 11.6)\% FF(\rho(770))$	$(7.0 \pm 4.0)\% FF(\rho(770))$	$(\rho\pi)$
$FF(f_0(1710))$	$(3.0 \pm 11.2)\% FF(f_0(980))$	$(3.0 \pm 11.2)\% FF(f_0(980))$	(Fit to Data)
$FF(\chi_C(2))$	$(1.5 \pm 0.7)\% FF(\chi_C(0))$	$(1.5 \pm 0.7)\% FF(\chi_C(0))$	(Fit to Data)
$FF(K_2^{*}(1430))$	$(4.1 \pm 1.5)\% FF((K\pi)_0^{*})$	$(4.1 \pm 1.5)\% FF((K\pi)_0^{*})$	(Fit to Data)
$FF(K^{*}(1410))$	$(36.0 \pm 16.4)\% FF(K^{*}(892))$	$(2.7)\% FF(K^{*}(892))$	$(K^{+}\pi^{-}\pi^{+})$
$FF(K^{*}(1680))$	$(76.5 \pm 22.2)\% FF(K^{*}(892))$	$(15.6)\% FF(K^{*}(892))$	$(K^{+}\pi^{-}\pi^{+})$

Table 7.23: *Values of fit fractions obtained from fit to data (second column) and the ones used for toy generation (third column) of the supplementary components.*

Generating without supplementary components

No significant bias on the fit parameters using this method are observed; the RMS of the distributions are taken as the systematic errors. The results from these method are shown on third column of Table 7.24.

7.3.8 Total Systematics

The systematic effects have been presented mostly as shifts on the Q2B parameters. For the isobar parameters p_i (the module or the phase of a given isobar amplitude) a systematic covariance matrix V^{syst} is also evaluated for each systematic effect (cf. Sec. 6.7.2). The matrix element $V_{i,j}^{\text{syst}}$ is constructed from the isobar parameter shifts δp_i as,

$$V_{i,j}^{\text{syst}} = \delta p_i \delta p_j. \tag{7.2}$$

The total systematic matrix is the simple sum of partial systematic matrices. Table 7.25 shows the total systematic errors on the signal yields and the Q2B parameters. Table 7.26 shows the total systematic error on the isobar parameters, the systematic correlation matrix is reported in Fig. 7.25.

Par.	**Gen. with**	**Gen. without**	**Subtotal**
$C(f_0(980))$	0.04	0.02	0.04
$FF(f_0(980))$	0.50	0.27	0.6
$2\beta_{eff}(f_0(980))$	1.3	3.9	4.1
$C(\rho^0(770))$	0.02	0.02	0.03
$FF(\rho^0(770))$	0.20	0.11	0.23
$2\beta_{eff}(\rho^0(980))$	2.2	2.9	3.7
$A_{CP}(K^*(892))$	0.02	0.01	0.02
$FF(K^*(892))$	0.70	0.45	0.8
$\Delta\phi(K^*(892))$	3.9	7.1	8.1
$A_{CP}((K\pi)^*_0)$	0.02	0.01	0.02
$FF((K\pi)^*_0)$	0.30	0.80	0.90
$\Delta\phi((K\pi)^*_0)$	2.0	4.0	4.4
$C(f_2(1270))$	0.04	0.06	0.07
$FF(f_2(1270))$	0.40	0.57	0.69
$\phi(f_2(1270))$	6.9	7.7	10.4
$C(f_X(1300))$	0.05	0.07	0.09
$FF(f_X(1300))$	0.50	0.71	0.87
$\phi(f_X(1300))$	3.0	3.4	4.5
$C(NR)$	0.02	0.03	0.04
$FF(NR)$	0.20	0.57	0.60
$\phi(NR)$	7.1	1.5	7.5
$C(\chi_C(0))$	0.03	0.04	0.05
$FF(\chi_C(0))$	0.05	0.07	0.09
$\phi(\chi_C(0))$	5.6	6.1	8.2
FF_{Tot}	0.99	0.58	1.15
A_{CP}^{incl}	0.004	0.004	0.006
$\Delta\phi(f_0, \rho^0)$	3.7	2.4	4.4
$\Delta\phi(K^*(892), (K\pi)^*_0)$	2.4	4.0	4.7
$\Delta\phi(\rho^0, (K\pi)^*_0))$	7.3	4.7	8.7
$\Delta\phi(\rho^0, K^*(892)$	9.8	8.0	12.7
Signal Yield	31.7	—	31.7

Table 7.24: *Systematic errors on total fit fraction, inclusive direct CP-asymmetry, all the Q2B parameters and in the Signal Yield due to the signal model uncertainty. Errors on phases are in degrees and FFs in $\%$.*

Parameter	**Total**	**Parameter**	**Total**
$C(f_0(980))$	0.05	$C(\rho^0(770))$	0.10
$FF(f_0(980))$	1.03	$FF(\rho^0(770))$	0.52
$2\beta_{eff}(f_0(980))$	5.9	$2\beta_{eff}(\rho^0(980))$	7.0
$A_{CP}(K^*(892))$	0.02	$A_{CP}((K\pi)^*_0)$	0.03
$FF(K^*(892))$	1.00	$FF((K\pi)^*_0)$	2.08
$\Delta\phi(K^*(892))$	9.3	$\Delta\phi((K\pi)^*_0)$	6.0
$C(f_2(1270))$	0.11	$C(f_X(1300))$	0.10
$FF(f_2(1270))$	0.74	$FF(f_X(1300))$	0.94
$\phi(f_2(1270))$	12.1	$\phi(f_X(1300))$	6.2
$C(NR)$	0.08	$C(\chi_C(0))$	0.06
$FF(NR)$	2.0	$FF(\chi_C(0))$	0.11
$\phi(NR)$	8.4	$\phi(\chi_C(0))$	9.5
FF_{Tot}	2.40	A_{CP}^{inclu}	0.01
$\Delta\phi(f_0, \rho^0)$	7.5	$\Delta\phi(K^*(892), (K\pi)^*_0)$	6.6
$\Delta\phi(\rho^0, (K\pi)^*_0))$	13.3	$\Delta\phi(\rho^0, K^*(892)$	15.4
Signal Yield	42.1		

Table 7.25: *Total Systematic errors on the Q2B parameters and signal yield. Errors on phases are in degrees and FFs in $\%$.*

Isobar Amplitude	$\lvert c \rvert$	$\phi[deg]$	$\lvert \bar{c} \rvert$	$\bar{\phi}[deg]$
$f_0(980)K^0_S$	`Fix`	`Fix`	0.18	5.8
$\rho(770)K^0_S$	0.01	8.0	0.01	11.5
$K^{*+}(892)\pi^-$	0.02	18.6	0.02	19.7
$(K\pi)^{*+}_0\pi^-$	0.6	15.7	0.7	14.8
`non-resonant`	0.4	16.7	0.5	10.9
$f_X(1300)K^0_S$	0.3	17.4	0.2	15.8
$f_2(1270)K^0_S$	0.004	10.7	0.007	9.1
$\chi_{c0}K^0_S$	0.034	20.2	0.048	19.1

Table 7.26: *Total systematic error on isobar parameters.*

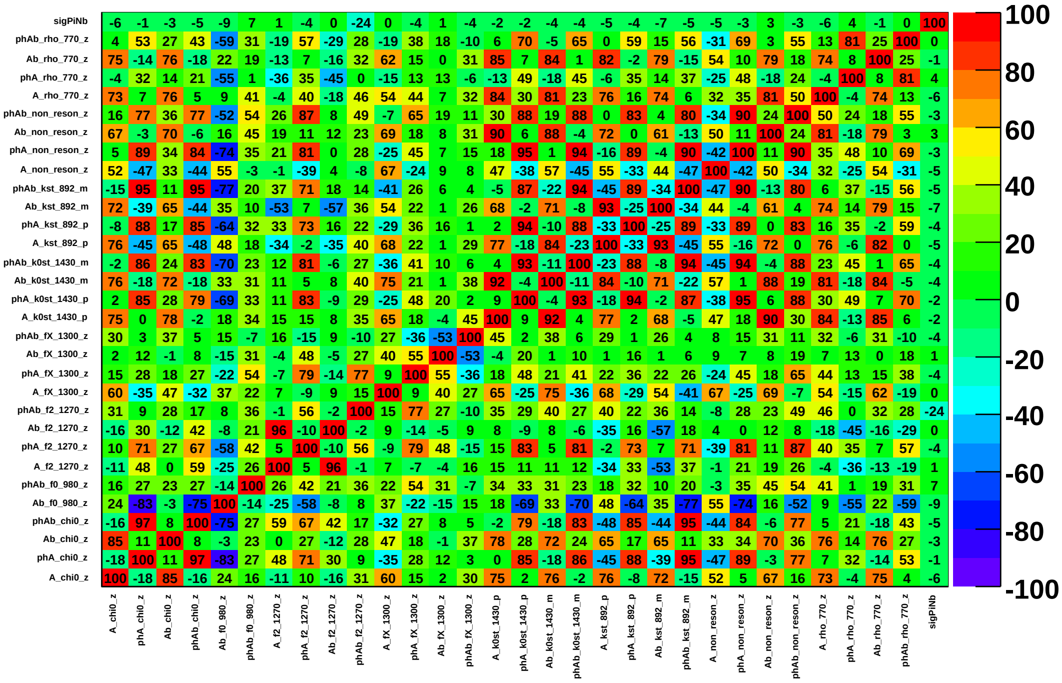

	A_chi0_z	phA_chi0_z	Ab_chi0_z	phAb_chi0_z	Ab_f0_980_z	phAb_f0_980_z	A_f2_1270_z	phA_f2_1270_z	Ab_f2_1270_z	phAb_f2_1270_z	A_fX_1300_z	phA_fX_1300_z	Ab_fX_1300_z	phAb_fX_1300_z	A_k0st_1430_p	phA_k0st_1430_p	Ab_k0st_1430_m	phAb_k0st_1430_m	A_kst_892_p	phA_kst_892_p	Ab_kst_892_m	phAb_kst_892_m	A_non_reson_z	phA_non_reson_z	Ab_non_reson_z	phAb_non_reson_z	A_rho_770_z	phA_rho_770_z	Ab_rho_770_z	phAb_rho_770_z	sigPiNb
sigPiNb	-6	-1	-3	-5	-9	7	1	-4	0	-24	0	-4	1	-4	-2	-2	-4	-4	-5	-4	-7	-5	-5	-3	3	-3	-6	4	-1	0	100
phAb_rho_770_z	4	53	27	43	-59	31	-19	57	-29	28	-19	38	18	-10	6	70	-5	65	0	59	15	56	-31	69	3	55	13	81	25	100	0
Ab_rho_770_z	75	-14	76	-18	22	19	-13	7	-16	32	62	15	0	31	85	7	84	1	82	-2	79	-15	54	10	79	18	74	8	100	25	-1
phA_rho_770_z	-4	32	14	21	-55	1	-36	35	-45	0	-15	13	13	-6	-13	49	-18	45	-6	35	14	37	-25	48	-18	24	-4	100	8	81	4
A_rho_770_z	73	7	76	5	9	41	-4	40	-18	46	54	44	7	32	84	30	81	23	76	16	74	6	32	35	81	50	100	-4	74	13	-6
phAb_non_reson_z	16	77	36	77	-52	54	26	87	8	49	-7	65	19	11	30	88	19	88	0	83	4	80	-34	90	24	100	50	24	18	55	-3
Ab_non_reson_z	67	-3	70	-6	16	45	19	11	12	23	69	18	8	31	90	6	88	-4	72	0	61	-13	50	11	100	24	81	-18	79	3	3
phA_non_reson_z	5	89	34	84	-74	35	21	81	0	28	-25	45	7	15	18	95	1	94	-16	89	-4	90	-42	100	11	90	35	48	10	69	-3
A_non_reson_z	52	-47	33	-44	55	-3	-1	-39	4	-8	67	-24	9	8	47	-38	57	-45	55	-33	44	-47	100	-42	50	-34	32	-25	54	-31	-5
phAb_kst_892_m	-15	95	11	95	-77	20	37	71	18	14	-41	26	6	4	-5	87	-22	94	-45	89	-34	100	-47	90	-13	80	6	37	-15	56	-5
Ab_kst_892_m	72	-39	65	-44	35	10	-53	7	-57	36	54	22	1	26	68	-2	71	-8	93	-25	100	-34	44	-4	61	4	74	14	79	15	-7
phA_kst_892_p	-8	88	17	85	-64	32	33	73	16	22	-29	36	16	1	2	94	-10	88	-33	100	-25	89	-33	89	0	83	16	35	-2	59	-4
A_kst_892_p	76	-45	65	-48	48	18	-34	-2	-35	40	68	22	1	29	77	-18	84	-23	100	-33	93	-45	55	-16	72	0	76	-6	82	0	-5
phAb_k0st_1430_m	-2	86	24	83	-70	23	12	81	-6	27	-36	41	10	6	4	93	-11	100	-23	88	-8	94	-45	94	-4	88	23	45	1	65	-4
Ab_k0st_1430_m	76	-18	72	-18	33	31	11	5	8	40	75	21	1	38	92	-4	100	-11	84	-10	71	-22	57	1	88	19	81	-18	84	-5	-4
phA_k0st_1430_p	2	85	28	79	-69	33	11	83	-9	29	-25	48	20	2	9	100	-4	93	-18	94	-2	87	-38	95	6	88	30	49	7	70	-2
A_k0st_1430_p	75	0	78	-2	18	34	15	15	8	35	65	18	-4	45	100	9	92	4	77	2	68	-5	47	18	90	30	84	-13	85	6	-2
phAb_fX_1300_z	30	3	37	5	15	-7	16	-15	9	-10	27	-36	-53	100	45	2	38	6	29	1	26	4	8	15	31	11	32	-6	31	-10	-4
Ab_fX_1300_z	2	12	-1	8	-15	31	-4	48	-5	27	40	55	100	-53	-4	20	1	10	1	16	1	6	9	7	8	19	7	13	0	18	1
phA_fX_1300_z	15	28	18	27	-22	54	-7	79	-14	77	9	100	55	-36	18	48	21	41	22	36	22	26	-24	45	18	65	44	13	15	38	-4
A_fX_1300_z	60	-35	47	-32	37	22	7	-9	9	15	100	9	40	27	65	-25	75	-36	68	-29	54	-41	67	-25	69	-7	54	-15	62	-19	0
phAb_f2_1270_z	31	9	28	17	8	36	-1	56	-2	100	15	77	27	-10	35	29	40	27	40	22	36	14	-8	28	23	49	46	0	32	28	-24
Ab_f2_1270_z	-16	30	-12	42	-8	21	96	-10	100	-2	9	-14	-5	9	8	-9	8	-6	-35	16	-57	18	4	0	12	8	-18	-45	-16	-29	0
phA_f2_1270_z	10	71	27	67	-58	42	5	100	-10	56	-9	79	48	-15	15	83	5	81	-2	73	7	71	-39	81	11	87	40	35	7	57	-4
A_f2_1270_z	-11	48	0	59	-25	26	100	5	96	-1	7	-7	-4	16	15	11	11	12	-34	33	-53	37	-1	21	19	26	-4	-36	-13	-19	1
phAb_f0_980_z	16	27	23	27	-14	100	26	42	21	36	22	54	31	-7	34	33	31	23	18	32	10	20	-3	35	45	54	41	1	19	31	7
Ab_f0_980_z	24	-83	-3	-75	100	-14	-25	-58	-8	8	37	-22	-15	15	18	-69	33	-70	48	-64	35	-77	55	-74	16	-52	9	-55	22	-59	-9
phAb_chi0_z	-16	97	8	100	-75	27	59	67	42	17	-32	27	8	5	-2	79	-18	83	-48	85	-44	95	-44	84	-6	77	5	21	-18	43	-5
Ab_chi0_z	85	11	100	8	-3	23	0	27	-12	28	47	18	-1	37	78	28	72	24	65	17	65	11	33	34	70	36	76	14	76	27	-3
phA_chi0_z	-18	100	11	97	-83	27	48	71	30	9	-35	28	12	3	0	85	-18	86	-45	88	-39	95	-47	89	-3	77	7	32	-14	53	-1
A_chi0_z	100	-18	85	-16	24	16	-11	10	-16	31	60	15	2	30	75	2	76	-2	76	-8	72	-15	52	5	67	16	73	-4	75	4	-6

Figure 7.25: *Total systematic correlation matrix on the isobar parameters.*

7.4 Conclusion

Using an amplitude analysis technique of B^0 decays to $K^0_S\pi^+\pi^-$, inclusive and exclusive branching frations and direct CP-asymmetries have been measured; phase differences of resonant states contributing to the Dalitz plot have been measured. Two solutions, with equivalent goodness-of-fit figures of merit, were found. The analysis has been intensively tested in order to ensure its robustness. The total errors on the phase differences are dominated by statistical uncertainties. The dominant systematics are uncertainties on the isobar model used to describe the signal intensity in the Dalitz plot. The main targets of this analysis are the measurements of ΔS on the penguin dominated decays $B^0 \to f_0(980)K_S^0$ and $B^0 \to \rho^0(770)K_S^0$, and the measurement of phase differences for the $\rho^0(770)K_S^0$ and $K^{*\pm}(892)\pi^{\mp}$ resonant states. The constraints on phases for non-overlapping resonances are statistically limited. The measurements on the $\rho^0(770)K_S^0$ and $K^{*\pm}(892)\pi^{\mp}$ components can be used to set non-trivial constraints in the $(\bar{\rho}, \bar{\eta})$ plane following the methods proposed in Refs. [74, 75, 77, 112], as explained in Chapter 3.

Part IV

Results Interpretation

Chapter 8

Interpretation of experimental results of the $B \to K^{*}\pi$ and $B \to \rho K$ Modes

This chapter presents the numerical results for the theoretical methods described in chapter 3. First, a short description of the *R*fit approach is given, which is the statistical framework used to quote constraints on the different parameters (cf. Sec. 8.1). In the next step the $B \to K^{*}\pi$ system is considered (cf. Sec. 8.3). Constraints on the yet unmeasured observables and on ratios of QCD amplitudes are set using the global CKM fit as an external input to fix the CKM parameters. The CPS/GPSZ method is tested, using the current available data, as an independent constraint on the $(\bar{\rho}, \bar{\eta})$ plane. In a second step the $B \to \rho K$ system is considered (cf. Sec. 8.4). In spite of the lack of experimental observables the possible constraints on ratios of QCD amplitudes are studied. In a third step, the combined $K^{*}\pi/\rho K$ system is considered (cf. Sec. 8.5). Improved constraints on the unavailable observables and on ratios of QCD amplitudes related to both $B \to K^{*}\pi$ and $B \to \rho K$ systems are set. The possible improvements on the CKM constraints given a scenario of controlled theoretical hypothesis are also studied. Finally, an extrapolation exercise is made to test the potential for CKM physics of $K^{*}\pi + \rho K$ observables, considering the expected statistics at LHCb and SuperB in 2015.

8.1 The *R*fit approach

The numerical results of the phenomenological analysis presented in this chapter uses the frequentist method known as *R*fit, which takes into account at the same time the experimental measurements as well as the theoretical uncertainties. The different elements of the *R*fit method (metrology, hypothesis testing) are described in detail in references [113] and [114]; the elements needed for the following discussion are briefly described below.

The principal tool of the *R*fit method is the likelihood function $\mathcal{L}$, which is constructed as the product of two contributions:

$$\mathcal{L} = \mathcal{L}_{\mathrm{exp}}(x_{\mathrm{exp}} - x_{\mathrm{theo}}) \cdot \mathcal{L}_{\mathrm{theo}}(y_{\mathrm{QCD}}) \; . \tag{8.1}$$

The first term measures the agreement between the experimental measurements x_{exp} and their theoretical functions $x_{\rm theo}$ in the SM framework; the second term expresses the available information on the theoretical parameters $y_{\rm QCD}$.

The treatment of the experimental likelihood $\mathcal{L}_{\rm exp}$ is standard, and is given by the product:

$$\mathcal{L}_{\rm exp}(x_{\rm exp} - x_{\rm theo}) = \prod_{i=1}^{N_{\rm exp}} \mathcal{L}_{exp}(i) \ , \tag{8.2}$$

where the $N_{\rm exp}$ individual components of the likelihood are the different available measurements; in the simplest case, these measurements are independent Gaussians,

$$\mathcal{L}_{\rm exp}(i) = \frac{1}{\sqrt{2\pi}\sigma_{\rm exp}(i)} \exp\left[-\frac{1}{2}\left(\frac{x_{\rm exp}(i) - x_{\rm theo}(i)}{\sigma_{\rm exp}}\right)\right] \ . \tag{8.3}$$

The theoretical component $\mathcal{L}_{\rm theo}$ of the likelihood function is given by the product:

$$\mathcal{L}_{\rm theo}(y_{\rm QCD}) = \prod_{k=1}^{N_{\rm QCD}} \mathcal{L}_{\rm theo}(k) \ , \tag{8.4}$$

where the individual components $\mathcal{L}_{\rm theo}(k)$ take into account the imperfect knowledge of the theoretical parameters $y_{\rm QCD}$, for which no statistical uncertainty can be easily defined. Those parameters are usually hadronic parameters, obtained from theoretical calculations based on approximations or hypothesis difficult to validate.

The *R*fit method consists in assigning an interval to every theoretical parameter $y_{\rm QCD}$, defined in such a way that their likelihood function $\mathcal{L}_{\rm theo}$ has a uniform value (equal to 1) if the parameter is within this interval, and has a null value outside. By construction, this allowed interval is arbitrary; it does not come from an experimental uncertainty, nor from the statistical limitation in a numerical calculation, but from the intuition of the theoretician. The *R*fit approach allows to establish a coherent treatment of uncertainties of this kind: once the theoretician provides the allowed intervals for the theoretical parameters, the allowed regions of the parameters that are pretended to be extracted, will be those in which the different observables are consistent with the values of these parameters, and with the theoretical parameters contained in their intervals.

8.2 Experimental Measurements

All measurements used in this analysis correspond to results available at the time of the ICHEP08 conference. World average values are used, which are obtained from the "Heavy Flavor Averaging Group" (HFAG) [28]. The Branching Fractions, direct CP-asymmetries and phases differences used for the phenomenological analysis are summarized in Table 8.1. The definitions of these observables in terms of the decay amplitudes are given in Secs. 3.2.2, 3.3.3 and 3.4.2.

For the phases, several values are quoted when multiples solutions are found, as in the analysis of the $B^0 \to K^0_S\pi^+\pi^-$ channel, presented in part III of this thesis. The $\Delta\chi^2$ of the local minima solutions with respect to the global one is quoted.

Parameter	*B*A*B*AR	Belle	CLEO	WA
$\mathcal{B}(K^{*+}\pi^-)$	$12.6^{+2.7}_{-1.6} \pm 0.9$ [40]	$8.4 \pm 1.1^{+1.0}_{-0.9}$ [42]	$16^{+6}_{-5} \pm 2$ [115]	10.3 ± 1.1
$\mathcal{B}(K^{*0}\pi^0)$	$3.6 \pm 0.7 \pm 0.4$ [40]	$0.4^{+1.9}_{-1.7} \pm 0.1$ [42]	$0.0^{+1.3+0.5}_{-0.0-0.0}$ [115]	2.4 ± 0.7
$\mathcal{B}(K^{*0}\pi^+)$	$10.8 \pm 0.6^{+1.1}_{-1.3}$ [23]	$9.7 \pm 0.6^{+0.8}_{-0.9}$ [24]	$7.6^{+3.5}_{-3.0} \pm 1.6$ [115]	10.0 ± 0.8
$\mathcal{B}(K^{*+}\pi^0)$	$6.9 \pm 2.0 \pm 1.3$ [116]	–	$7.1^{+11.4}_{-7.1} \pm 1.0$ [115]	6.9 ± 2.3
$\mathcal{A}_{CP}(K^{*+}\pi^-)$	$-0.30 \pm 0.11 \pm 0.03$ [118]	–	$0.26^{+0.33+0.10}_{-0.34-0.08}$ [119]	-0.25 ± 0.11
$\mathcal{A}_{CP}(K^{*0}\pi^0)$	$-0.15 \pm 0.12 \pm 0.02$ [118]	–	–	-0.15 ± 0.12
$\mathcal{A}_{CP}(K^{*0}\pi^+)$	$0.032 \pm 0.052^{+0.16}_{-0.13}$ [23]	$-0.032 \pm 0.059^{+0.044}_{-0.033}$ [117]	–	$-0.020^{+0.067}_{-0.062}$
$\mathcal{A}_{CP}(K^{*+}\pi^0)$	$0.04 \pm 0.29 \pm 0.05$ [116]	–	–	0.04 ± 0.29
$\Delta\phi(K^*\pi)$	$58.3 \pm 32.7 \pm 9.3$ (global min.)	–	–	58.3 ± 34.0
	$176.6 \pm 28.8 \pm 9.3$ ($\Delta\chi^2 = 0.16$)	–	–	176.6 ± 30.3
$\phi(K^{*0}\pi^0/K^{*+}\pi^-)$	$-21.2 \pm 20.6 \pm 8.0$ [118]	–	–	-21.2 ± 22.1
$\bar{\phi}(\bar{K}^{*0}\pi^0/K^{*-}\pi^+)$	$-5.2 \pm 20.6 \pm 17.8$ [118]	–	–	-5.2 ± 27.2
$\mathcal{B}(K^+\rho^-)$	$8.0^{+0.8}_{-1.3} \pm 0.6$ [40]	$15.1^{+3.4+2.4}_{-3.3-2.6}$ [121]	$16^{+8}_{-6} \pm 3$ [115]	$8.6^{+0.9}_{-1.1}$
$\mathcal{B}(K^0\rho^0)$	$4.9 \pm 0.8 \pm 0.9$ [45]	$6.1 \pm 1.0^{+1.1}_{-1.2}$ [42]	< 39 [122]	$5.4^{+0.9}_{-1.0}$
$\mathcal{B}(K^0\rho^+)$	$8.0^{+1.4}_{-1.3} \pm 0.6$ [120]	–	< 48 [125]	$8.0^{+1.5}_{-1.4}$
$\mathcal{B}(K^+\rho^0)$	$3.56 \pm 0.45^{+0.57}_{-0.46}$ [23]	$3.89 \pm 0.47^{+0.43}_{-0.41}$ [24]	$8.4^{+4.0}_{-3.4} \pm 1.8$ [115]	$3.81^{+0.48}_{-0.46}$
$\mathcal{A}_{CP}(K^+\rho^-)$	$0.14 \pm 0.06 \pm 0.01$ [118]	$0.22^{+0.22+0.06}_{-0.23-0.02}$ [121]	–	0.15 ± 0.06
$\mathcal{A}_{CP}(K^0\rho^0)$	$-0.02 \pm 0.27 \pm 0.10$ [123]	$0.03^{+0.24}_{0.23} \pm 0.16$ [124]	–	0.01 ± 0.20
$\mathcal{A}_{CP}(K^0\rho^+)$	$-0.12 \pm 0.17 \pm 0.02$ [120]	–	–	-0.12 ± 0.17
$\mathcal{A}_{CP}(K^+\rho^0)$	$0.44 \pm 0.10^{+0.06}_{-0.14}$ [116]	$0.405 \pm 0.101^{+0.036}_{-0.077}$ [117]	–	$0.419^{+0.081}_{-0.104}$
$2\beta_{\text{eff}}(K^0\rho^0)$	$20.4 \pm 19.6 \pm 7.1$ (global min.)	–	–	20.4 ± 20.8
	$33.4 \pm 20.8 \pm 7.1$ ($\Delta\chi^2 = 0.16$)	–	–	33.4 ± 22.0
$\phi(K^0\rho^0/K^{*+}\pi^-)$	$-174.3 \pm 28.0 \pm 15.4$ (global min.)	–	–	-174.3 ± 32.0
	$173.7 \pm 29.8 \pm 15.4$ ($\Delta\chi^2 = 0.16$)	–	–	173.7 ± 33.5
$\phi(K^+\rho^-/K^{*+}\pi^-)$	$-21.2 \pm 21.6 \pm 17.8$ [118]	–	–	-21.2 ± 28.0
$\bar{\phi}(K^-\rho^+/K^{*-}\pi^+)$	$-42.4 \pm 20.6 \pm 8.0$ [118]	–	–	-42.4 ± 22.1
$\phi(K^+\rho^0/K^{*0}\pi^+)$	$29.0 \pm 16.6 \pm 10.0$ [23]	–	–	29.0 ± 19.4
$\bar{\phi}(K^-\rho^0/\bar{K}^{*0}\pi^-)$	$-26.1 \pm 15.5 \pm 6.8$ [23]	–	–	-26.1 ± 16.9

Table 8.1: *Experimental results on Branching Fractions (in units of* 10^{-6}*), direct* CP*-asymmetries and phase differences (in degrees) used for the phenomenological analysis described in Chapter 3. The notation* K^* *refers to the* $K^*(892)$ *resonant state. Phases without reference were obtained in the experimental analysis described in Part III of this thesis.*

All Branching fractions and direct CP-asymmetries are modeled as asymmetric Gaussian measurements. When the experimental measurement presents multiple solutions the asymmetric errors take into account the presence of local minima. This approach is relatively safe when the values of these observables does not vary significantly from one solution to the other (cf. table 7.3). In the case of phases, when multiple solutions are present the measurement is described by the complete experimental likelihood (see for instance the case of $\Delta\phi(K^*\pi)$ in the left hand side plot of Fig. 7.16).

8.3 Isospin analysis of the $B \to K^*\pi$ modes

The theoretical framework for the phenomenological analysis of the $B \to K^*\pi$ system was described in Sec. 3.2. Here the corresponding numerical results are presented. As explained in Sec. 3.5, two scenarios are considered for the phenomenological analysis. In scenario 1, the CKM parameters are fixed using external inputs (from the global CKM fit), constraints in the ratio of the hadronic parameters as well as on the unmeasured observables are set. The discussion starts (Sec. 8.3.1) by studying the constraints that can be set on the unmeasured phase differences $\phi^{(0+,+0)}$ and $\bar{\phi}^{(0+,+0)}$ (cf. Eq. 3.13). Then, the constraints on the ratio of hadronic amplitudes are explored (Sec. 8.3.2). The consistency of the hadronic hypothesis described in Sec. 3.2.7 with the current data is discussed. Finally, scenario 2 is considered, where the hadronic hypothesis described in Sec. 3.2.7 is applied. The CPS/GPSZ method, as a tool to extract $(\bar{\rho}, \bar{\eta})$, is studied.

8.3.1 Constraints on unmeasured experimental measurements

The constraints on the magnitude of the $|\phi^{(0+,+0)}|$ and $|\bar{\phi}^{(0+,+0)}|$ phase differences are shown in Fig. 8.1. The present method has no sensitivity to the sign of these phases, as the only inputs for the $B^+ \to K^{*0}\pi^+$ and $B^+ \to K^{*+}\pi^0$ decay modes are CP-asymmetries and Branching fractions. The 1σ coverage for these observables are given by:

$$|\phi^{(0+,+0)}| \in (0, +85^o)\,, \tag{8.5}$$

$$|\bar{\phi}^{(0+,+0)}| \in (+68^o, +107^o)\,, \tag{8.6}$$

at 32% CL, with the solutions centered at $|\phi^{(0+,+0)}| = +58.0^o$ and $|\bar{\phi}^{(0+,+0)}| = +95.0^o$, respectively.

8.3.2 Constraints on the ratio of QCD amplitudes

The results on the ratio of hadronic amplitudes are presented separately for each of the two solutions of the phases coming from the $B^0 \to K^0_S\pi^+\pi^-$ analysis (*i.e.* $\Delta\phi(K^*\pi)$) and for the corresponding envelope, *i.e.* the constraint obtained when using the complete likelihood of the measured $\Delta\phi(K^*\pi)$ observable (cf. see left hand plot of Fig. 7.16). All the results are presented as bi-dimensional confidence level (C.L.) contours in the $\mathrm{arg.}$ *v.s.* $log_{10}(\mathrm{mod.})$ plane of the given QCD ratio.

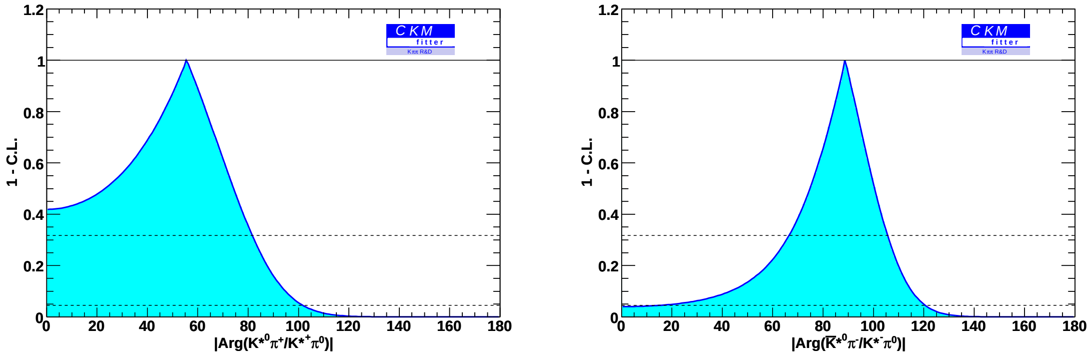

Figure 8.1: *Constraint on the* $|\phi^{(0+,+0)}|$ *(left) and* $|\bar{\phi}^{(0+,+0)}|$ *(right) unmeasured phases from the* $B^+ \to K^0_S\pi^+\pi^0$ *analysis (cf. Eq.(3.13)). There is no sensitivity to the sign of the corresponding phases. The dotted lines at* 0.32 *and* 0.05 *set the confidence interval at* 1σ *and* 2σ*, respectively.*

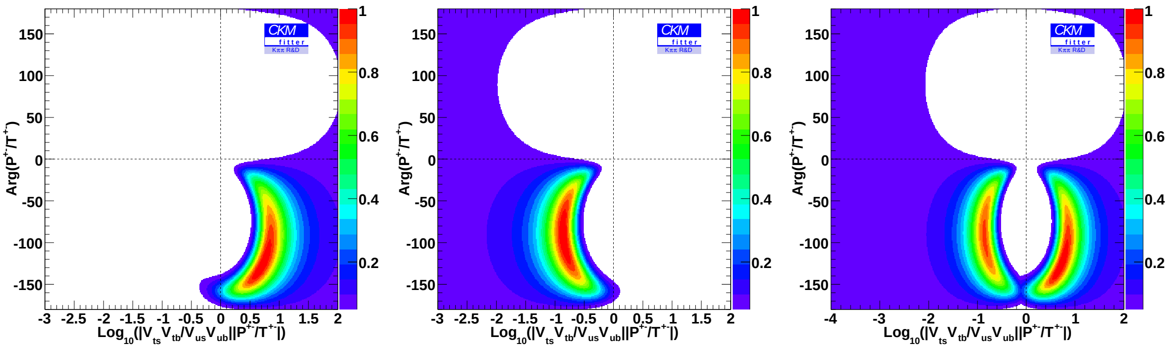

Figure 8.2: *Constraint on the argument-magnitude plane for the QCD ratio* P^{+-}/T^{+-}*. As the tree amplitude is CKM suppressed with respect to the penguin amplitude, the magnitude of this ratio is "normalized" by the corresponding ratio of CKM matrix elements,* $|V_{ts}V^*_{tb}/V_{us}V^*_{ub}|$*. A logarithmic scale is used on the horizontal axis. The left hand side and middle plots show the results using the global and local minima of the* $\Delta\phi(K^*\pi)$ *phase (cf. Table 8.1), respectively. The right hand side plot shows the corresponding envelope of the two solutions. White regions are excluded with a less than* 5% *C.L.*

Fig. 8.2 shows the results for the P^{+-}/T^{+-} ratio. As the tree amplitude is CKM suppressed with respect to the penguin amplitude, the magnitude of this ratio is "normalized" by the corresponding ratio of CKM matrix elements, $|V_{ts}V^*_{tb}/V_{us}V^*_{ub}|$. The left hand and middle plots show the results using the global and local minima of the $\Delta\phi(K^*\pi)$ phase (cf. table 8.1), respectively. The one on the right hand side shows the envelope of the first two. White regions are excluded with a less than 5% C.L. For both constraints, positive values of the strong phase difference between P^{+-} and T^{+-} are excluded at $\sim 95\%$ CL. This is due to the 2σ significance of the $\mathcal{A}_{CP}(K^{*+}\pi^-)$ direct CP asymmetry. The result using the global minimum (cf. left hand side plot of Fig. 8.2) constraint the magnitude of this ratio to be at high values. In contrast, the constraint using the local minimum (cf. middle plot of Fig. 8.2) excludes them. The latters constraint is more in agreement with the SM prediction, where this ratio is predicted to be around one [126].

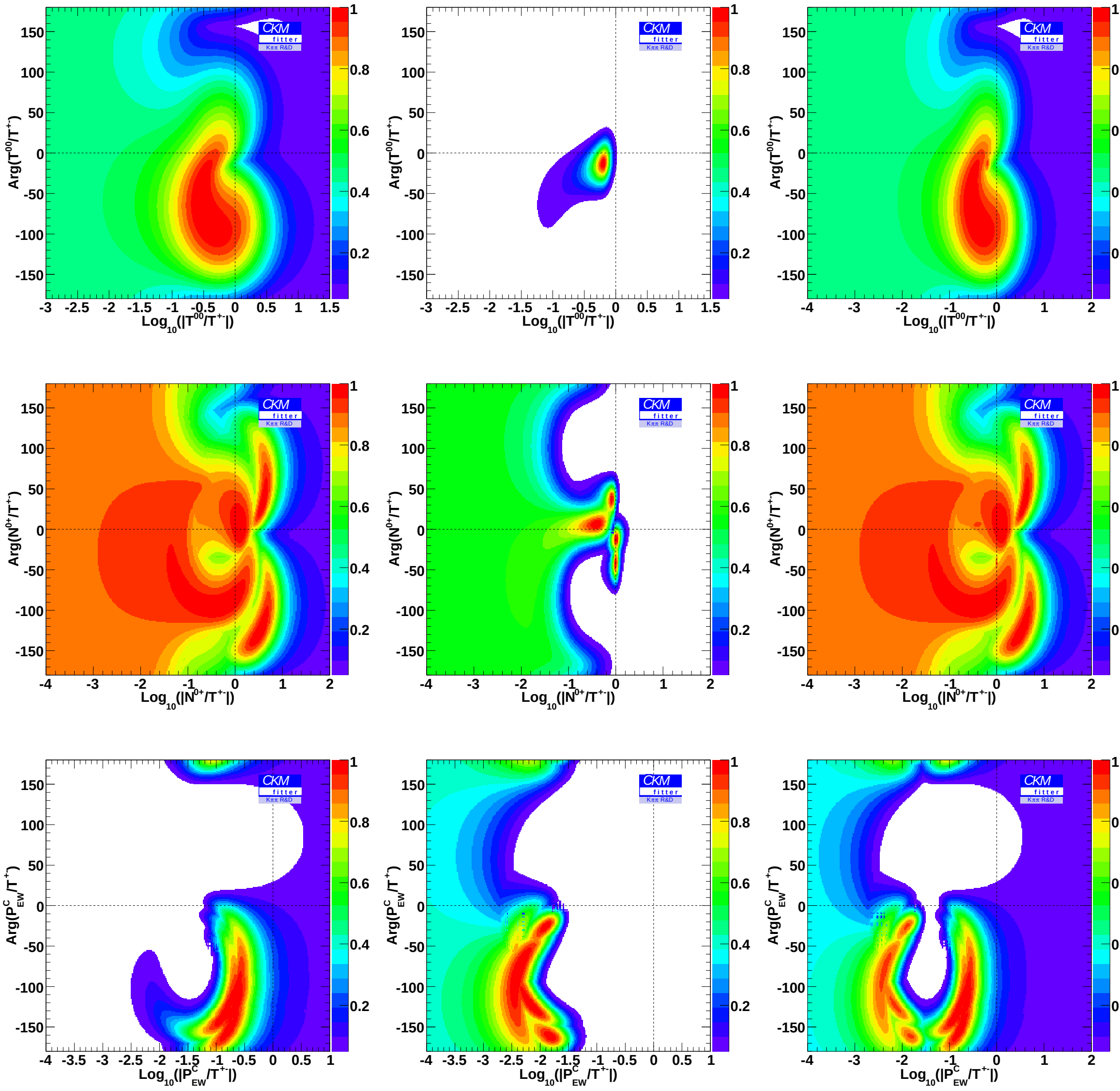

Figure 8.3: *Constraints on the argument-magnitude plane for the* T_C^{00}/T^{+-} *(top),* N^{0+}/T^{+-} *(middle) and* P_C^{EW}/T^{+-} *(bottom) QCD ratios. A logarithmic scale is used on the horizontal axis. The left hand side and middle plots show the results using the global and local minima of the* $\Delta\phi(K^*\pi)$ *phase (cf. Table 8.1), respectively. The right hand side plot shows the corresponding envelope of the two solutions. White regions are excluded with a less than* 5% *C.L.*

Fig. 8.3 shows the same constraints for the T_C^{00}/T^{+-}, N^{0+}/T^{+-} and P_C^{EW}/T^{+-} ratios of QCD amplitudes. It is interesting to note that the constraints on the magnitude of all these ratios have the same qualitative behavior than the one for the P^{+-}/T^{+-} normalized ratio: constraints using the global minimal solution of the $\Delta\phi(K^*\pi)$ phase (cf. left hand side plots of Fig. 8.3) tend to allow high values of the magnitude of the QCD ratios; in contrast the constraints using the local minimum exclude high values of the magnitude of these parameters. The results using the local minimum are more in agreement with the SM, where color suppressed (T_C^{00}, P_C^{EW}) and OZI suppressed (N^{+0}) amplitudes are predicted to be smaller than T^{+-}, the color allowed tree amplitude [126].

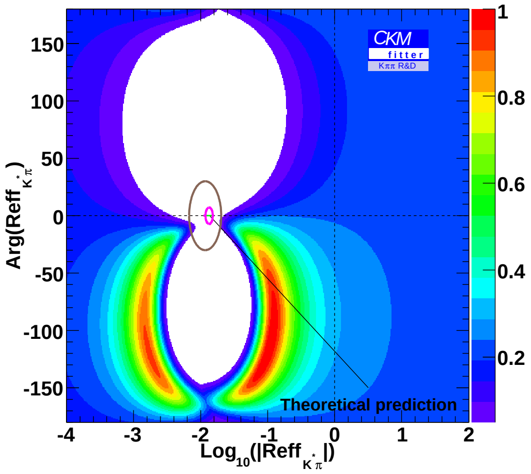

Figure 8.4: *Constraint on the argument-magnitude plane for the* $R_{\rm eff}(K^*\pi) = P^{EW}/T_{3/2}$ *QCD ratio, where* $T_{3/2} = T^{+-} + T_C^{00}$ *(cf. Eq.(3.59)). A logarithmic scale is used on the horizontal axis. White regions are excluded with a less than* 5% *C.L. The magenta and brown ellipses represents the allowed regions using the theoretical errors for the "aggressive" and "conservative" scenarios (cf. Sec. 3.2.7).*

More interesting is the result on the $R_{\rm eff}(K^*\pi) = P^{EW}/T_{3/2}$ ratio (cf. Eq.(3.59)), which is shown in Fig. 8.4. The same pattern as before is followed for this QCD ratio: the constraint obtained with the global minimum solution excludes low values, while the one using the local minimum excludes high values. Fig. 8.4 shows the constraint obtained by using the complete experimental likelihood for the phases. Superimposed on the figure is the region allowed by the theoretical hypothesis described in Sec. 3.2.7 (magenta ellipse) taking the theoretical errors from the GPSZ [75] authors. The data are marginally consistent with this hypothesis (the inconsistency is beyond $\sim 2\sigma$). In contrast, the $P^{EW} = 0$ hypothesis is more consistent with data. The plot also shows the allowed region using the conservative theoretical error described in Sec. 3.2.7 (brown ellipse), it seems that the GPSZ error has to be increased by a factor of 5 to start being consistent with the current data. This result has to be taken with care, as the inconsistency is not very significant. More statistics are needed to confirm these findings.

In summary, the multiple solutions from the measurement of the $\Delta\phi(K^*\pi)$ phase set different constraints on the ratios of QCD amplitudes. The local minimum solution sets more standard constraints on these parameters as they exclude high values for SM suppressed amplitudes. The result on the $P^{EW}/T_{3/2}$ suggest that the data are marginally consistent with the theoretical hypothesis described in Sec. 3.2.7, the theoretical error suggested in [75] has to be increased by a factor of 5 in order to reach agreement with the current data.

8.3.3 Constraints on the $(\bar{\rho}, \bar{\eta})$ plane

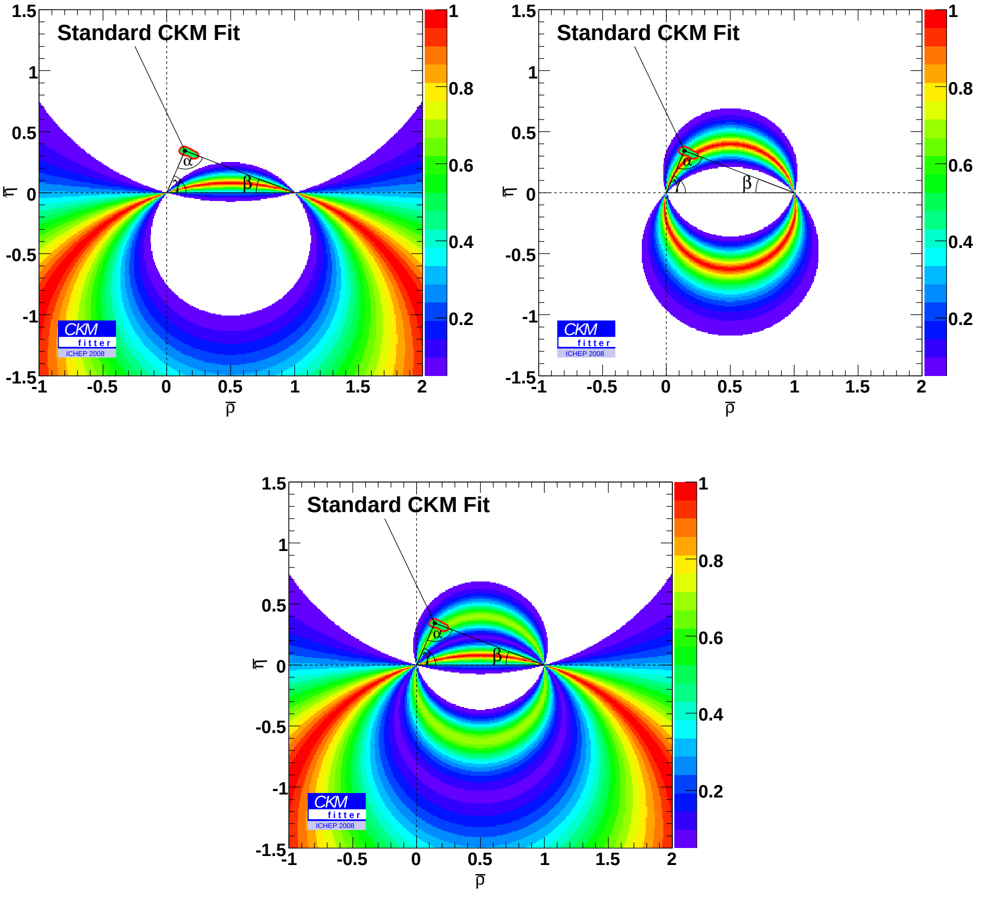

Figure 8.5: *Constraints on the $(\bar{\rho}, \bar{\eta})$ obtained applying the CPS/GPSZ method (cf. Sec. 3.2.6), using the $P^{EW} = 0$ hypothesis. No theoretical uncertainties are taken into account. The top left and right hand side plots show the constraints using the global and local minima for the $\Delta\phi(K^*\pi)$ observable. In the bottom plot is shown the corresponding envelope. The global CKM fit with the latest measurements presented in ICHEP08 is superimposed for comparison. White regions are excluded with a less than 5% C.L.*

The constraints on the $(\bar{\rho}, \bar{\eta})$ plane with the CPS/GPSZ (cf. Sec. 3.2.6) observables, and using the hypothesis of $P^{EW} = 0$ ($R_{\rm eff} = 0$ and no theoretical error, cf. Eq.(3.59)) are shown in Fig. 8.5. The global CKM fit with the latest measurements presented at ICHEP08 is superimposed for comparison. The hypothesis of $P^{EW} = 0$ is used in order to stress the fact that under this hypothesis the constraint established is on the α UT angle and not on γ. The top left and right hand side plots show the constraints using the global and local minimum of the $\Delta\phi(K^*\pi)$ phase, respectively. Two solutions in α are obtained for every solution of the $\Delta\phi(K^*\pi)$ phase. As expected, the global minimum excludes the standard CKM fit as it prefers high values of the P^{EW} QCD amplitude. The bottom plot shows the envelope of the constraints using the multiple solutions of $\Delta\phi(K^*\pi)$ phase, where the four solutions for the α angle are superimposed.

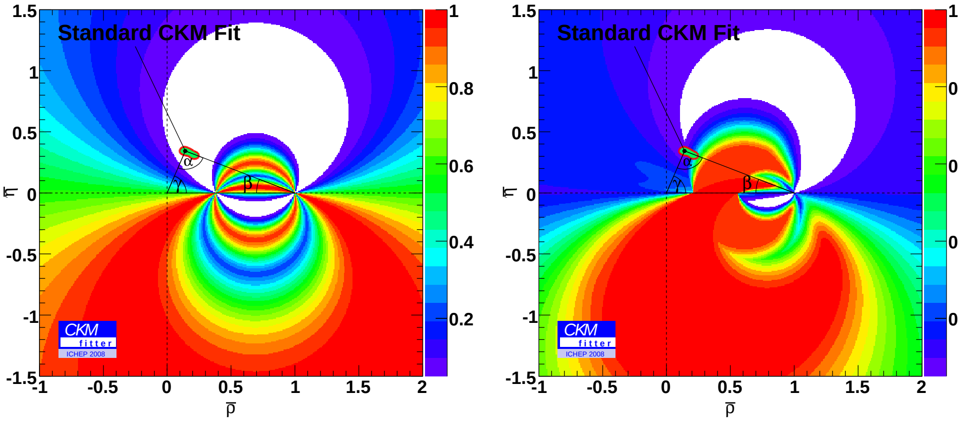

Figure 8.6: *Constraints on the* $(\bar\rho, \bar\eta)$ *obtained applying the CPS/GPSZ method (cf. Sec. 3.2.6), using the hypothesis of* $R_{\rm eff} = 1.35\%$*. In the left is shown the constraint without theoretical uncertainties. In the right is shown the constraint assuming a conservative theoretical uncertainty of* 30% *on the* $R_{\rm eff}$ *parameter. The constraints are already the envelope of the multiple solutions for the* $\Delta\phi(K^*\pi)$ *observable. The global CKM fit with the latest measurements presented in ICHEP08 is superimposed for comparison. White regions are excluded with a less than* 5% *C.L.*

Fig. 8.6 shows the constraint in the $(\bar\rho, \bar\eta)$ plane using the hadronic hypothesis described in Sec. 3.2.7. The left hand side plot shows the envelope of the multiple solutions for the $\Delta\phi(K^*\pi)$ phase for $R_{\rm eff} = 1.35\%$ with no theoretical error. The hypothesis of non-zero P^{EW} has the effect of shifting the constraint from α to $\phi_{3/2}$ (cf. Eq.(3.48)), *i.e.* the constraints are not any more circles passing through the origin, but circles passing through a shifted point in the horizontal axis. The marginal consistency with the global CKM fit is due to the theoretical hypothesis used. As shown in the previous section, the data are marginally consistent with this assumption about electroweak penguins. The effect of changing the value of the theoretical parameter $R_{\rm eff}$ from 0 to 1.35% has a significant effect on the $(\bar\rho, \bar\eta)$ constraints. It seems that small changes in the theoretical hypothesis can lead to significant changes on the CKM constraints, meaning that the CPS/GPSZ method is totally dominated by the theoretical uncertainties. This is more easily seen on the right hand plot of Fig. 8.6, which shows the $(\bar{\rho}, \bar{\eta})$ constraint assuming conservative theoretical errors (30% uncertainty on the r_{VP} parameter, see Sec. 3.2.7). The theoretical error strongly dilutes the constraint, the results can be made as consistent as desired with the global CKM fit by choosing a sufficiently high theoretical error.

The conclusion that the CPS/GPSZ method is totally dominated by the theoretical uncertainties can be understood as follows: the hadronic hypothesis relates a tree amplitude to a penguin amplitude. As the penguin amplitude is CKM enhanced by a factor of ~ 50, a small theoretical error on $R_{\rm eff}$ can be highly amplified.

8.4 Isospin analysis of the $B \to K\rho$ system

Due to the reduced number of experimental observables for the $B \to K\rho$ system no constraints on the $(\bar{\rho}, \bar{\eta})$ can be set. Still experimental bounds on some ratios of QCD amplitudes can be constructed. This is the case of p^{+-}/t^{+-} ratio, which is shown in the left hand side plot of Fig. 8.7. As for $B \to K^*\pi$, this ratio is scaled by the appropiate CKM factors. Negative values of the phase of this ratio are excluded at $> 95\%$ C.L., because of the $\sim 2.5\sigma$ significance of the $B^0 \to K^+\rho^-$ direct CP asymmetry.

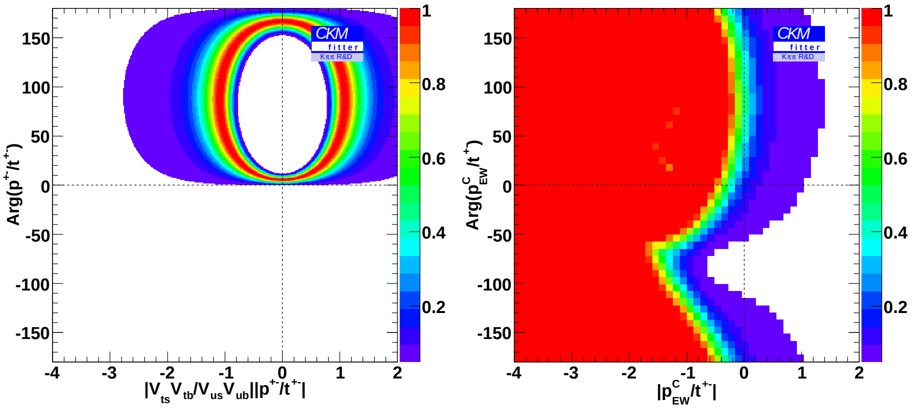

Figure 8.7: *Constraint on the argument-magnitude plane for the* p^{+-}/t^{+-} *and* p_C^{EW}/t^{+-} *QCD ratios. As the tree amplitude is CKM suppressed with respect to the penguin amplitude, the magnitude of this ratio is "normalized" by the corresponding ratio of CKM matrix elements,* $|V_{ts}V_{tb}^*/V_{us}V_{ub}^*|$*. A logarithmic scale is used on the horizontal axis. White regions are excluded with a less than* 5% *C.L.*

Another example is the case of the p_C^{EW}/t^{+-} QCD ratio, shown on the right hand side plot of Fig. 8.7. High values of the magnitude of this ratio are excluded by the data. For the remaining of QCD ratios no significant constraints can be set.

8.5 Isospin analysis of the combined $B \to K^*\pi$ and $B \to \rho K$ modes

The combined analysis $K^*\pi/\rho K$ aims to use all the available experimental information with a minimum set of theoretical hypothesis. As explained in Sec. 3.4, the advantage of combining the $B \to K^*\pi$ and $B \to \rho K$ systems is based on availability of several experimental observables (phase differences) extracted from the interferences of $K^*\pi$ and ρK resonances contributing to the same Dalitz plot, with the inclusion of only one additional parameter, a phase difference relating both $B \to K^*\pi$ and $B \to \rho K$ systems. The combinations of these two systems promises to improve the constraints on the QCD and CKM parameters given the redundant and independent experimental measurements. Nevertheless, at least one theoretical hypothesis has to be made in order to brake RpI and set a constraint on CKM parameters.

This last section follows the same approaches as for the $B \to K^*\pi$ system. In a first stage, constraints on the unavailable experimental observables as well as on the ratio of QCD amplitudes are set. The current hypothesis being tested are the ones from the CPS/GPSZ methods, which have been proven in the previous section to be totally dominated by theoretical uncertainties. A different approach will be followed here, by studying improvements on the precision on the experimental observable $\phi_{3/2}$ as the both systems are combined. As this observable can be translated into a constraint on $(\bar{\rho}, \bar{\eta})$ when a theoretical hypothesis on the QCD amplitudes is assumed (*e.g.* $P^{EW} = 0$ implies $\phi_{3/2} = \alpha$), these improvements on the sensitivity on $\phi_{3/2}$ will improve the constraint on the $(\bar{\rho}, \bar{\eta})$ plane.

8.5.1 Constraints on unavailable experimental measurements

Here the predictions on the unavailable observables related to both $B \to K^*\pi$ and $B \to \rho K$ systems are presented. These are all the phase differences coming from the $B^+ \to K^0_S\pi^+\pi^0$ Dalitz plot: $\phi^{(0+,+0)}$ and $\bar{\phi}^{(0+,+0)}$, which are only related to the $B \to K^*\pi$ system and previously discussed in Sec. 8.3.1; $\phi(K^{*+}\pi^0, K^0\rho^+)$ and $\bar{\phi}(K^{*-}\pi^0\bar{K}^0\rho^-)$ (cf. see Sec. 3.4.2), which are measured from the interference of $K^*\pi$ and ρK resonances. The constraints on these phase differences are shown in Fig. 8.8.

It is clearly seen that adding the extra information from the combined $B \to K^*\pi$ and $B \to \rho K$ systems raises the degeneracy in the constraint on the $\phi^{(0+,+0)}$ and $\bar{\phi}^{(0+,+0)}$ phases, compared with the constraints obtained with the $B \to K^*\pi$ system alone (cf. Fig. 8.1). For the $\phi^{(0+,+0)}$ phase the positive solution is lightly preferred by data. In contrast, the positive solution for the $\bar{\phi}^{(0+,+0)}$ is now excluded at the level of $\sim 2\sigma$. The corresponding coverage for these two phases at 38% C.L. are the following,

$$\phi^{(0+,+0)} \in (-79^o, +80^o)\,, \tag{8.7}$$
$$\bar{\phi}^{(0+,+0)} \in (-102^o, -60^o)\,, \tag{8.8}$$

with the central values, $+52^o$ and -84^o, respectively.

The constraints on the $\phi(K^{*+}\pi^0, K^0\rho^+)$ and $\bar{\phi}(K^{*-}\pi^0\bar{K}^0\rho^-)$ phases also show two mi-

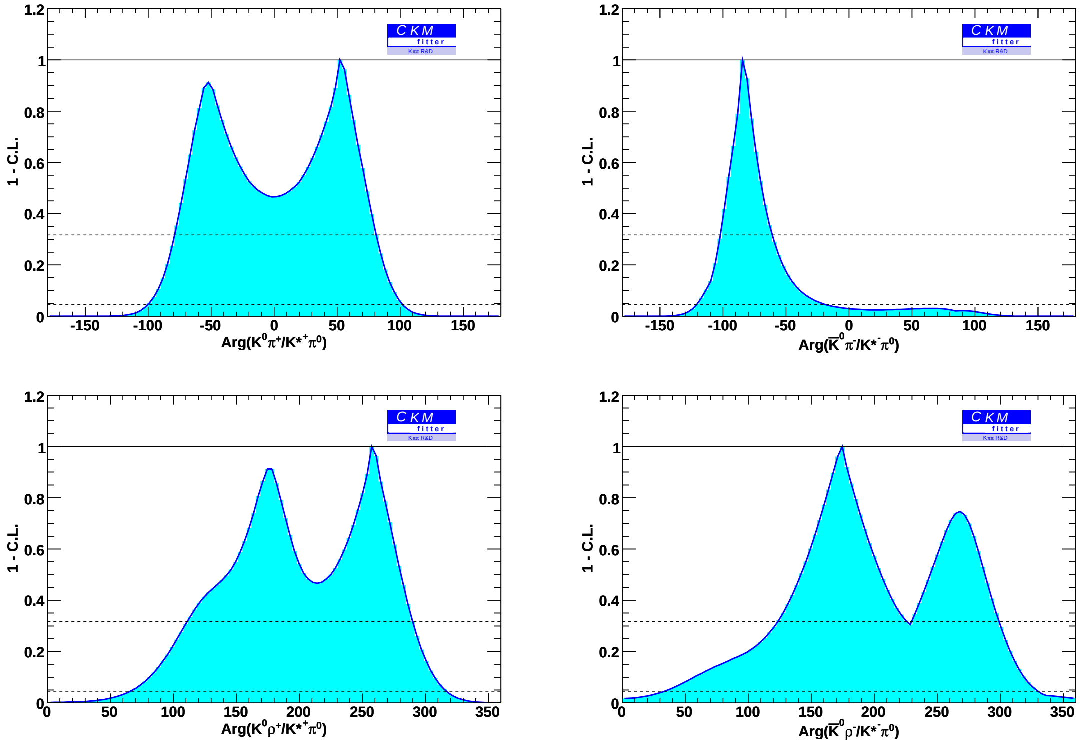

Figure 8.8: *Constraint on the* $\phi^{(0+,+0)}$ *(top left),* $\bar{\phi}^{(0+,+0)}$ *(top right),* $\phi(K^{*+}\pi^0, K^0\rho^+)$ *(bottom left) and* $\bar{\phi}(K^{*-}\pi^0\bar{K}^0\rho^-)$ *(bottom right) unmeasured phases from the* $B^+ \to K^0_S\pi^+\pi^0$ *analysis (cf. Eq.(3.13) and Sec. 3.4.2). The dotted lines at* 0.32 *and* 0.05 *set the confidence interval at* 1σ *and* 2σ*, respectively.*

nima. The corresponding coverage for these two phases at 38% C.L. are the following,

$$\phi(K^{*+}\pi^0, K^0\rho^+) \in (+111^o, +290^o)\,, \tag{8.9}$$

$$\bar{\phi}(K^{*-}\pi^0, \bar{K}^0\rho^-) \in (+124^o, +299^o)\,, \tag{8.10}$$

with the central values, $+259^o$ and $+175^o$, respectively.

For all the phases, there is almost no exclusion at 5% C.L., except for the $\bar{\phi}^{(0+,+0)}$, which excludes positive values at the $\sim 2\sigma$ level.

8.5.2 Constraints on the ratio of QCD amplitudes

The constraints on the ratio of QCD amplitudes for the $B \to K^*\pi$ system, P^{+-}/T^{+-}, T_C^{00}/T^{+-}, N^{0+}/T^{+-}, P_C^{EW}/T^{+-} and $R_{\rm eff}(K^*\pi)$, are shown in the left hand side plots of Figs. 8.9 and 8.10. The constraints on the P^{+-}/T^{+-} and T_C^{00}/T^{+-} QCD ratios do not improve significantly because they are mostly determined by the observables related to the $B^0 \to K^{*\pm}\pi^\mp$ and $B^0 \to K^{*0}\pi^0$ neutral decays. This is also the case for the $R_{\rm eff}(K^*\pi)$ parameter. In contrast, for the N^{0+}/T^{+-} and P_C^{EW}/T^{+-} QCD ratios some degeneracies are raised. The same pattern as with the $B \to K^*\pi$ system alone is followed, the global minimum solution for the phases obtained from the $B^0 \to K_S^0\pi^+\pi^-$ preferring high values while the local minimum excludes them.

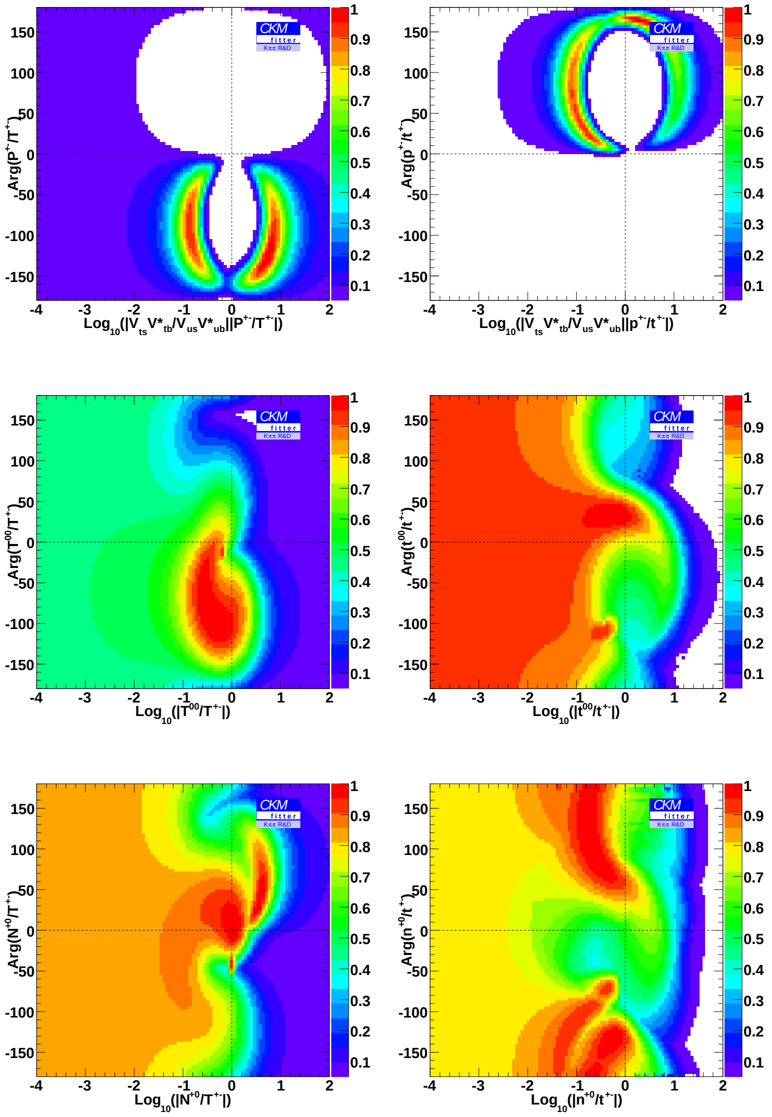

Figure 8.9: *Constraint on the argument-magnitude plane for the* P^{+-}/T^{+-} *(top left),* T_C^{00}/T^{+-} *(middle left) and* N^{0+}/T^{+-} *(bottom left) QCD ratios of the* $B \to K^*\pi$ *system, and* p^{+-}/t^{+-} *(top right),* t_C^{00}/t^{+-} *(middle right) and* n^{0+}/t^{+-} *(bottom right) QCD ratios of the* $B \to \rho K$ *system. A logarithmic scale is used on the horizontal axis. White regions are excluded with a less than* 5% *C.L.*

The additional information contained in the cross phases related with the interference of $K^*\pi$ and ρK resonances can be used to set constraints on the ratio of QCD amplitudes for the $B \to \rho K$ system, p^{+-}/t^{+-}, t_C^{00}/t^{+-}, n^{0+}/t^{+-}, p_C^{EW}/t^{+-} and $R_{\text{eff}}(\rho K)$, which are shown in the right hand side plots of Figs. 8.9 and 8.10. Degeneracies on the p^{+-}/t^{+-} are raised, and negative values of its phase are still are excluded at 95% C.L. due to the significance of the direct CP asymmetry $A_{CP}(B^0 \to K^+\rho^-)$. Soft constraints are set on the t_C^{00}/t^{+-}, n^{0+}/t^{+-} QCD ratios. The constraint on the p_C^{EW}/t^{+-} parameter improves, an upper limit of $|p_C^{EW}/t^{+-}| < 1.0$ can be set at the level of 95% C.L. No significant constraint is set for the $R_{\text{eff}}(\rho K)$ QCD ratio. The same pattern as with the $B \to K^*\pi$ system is followed, the global minimum solution for the phases obtained from the $B^0 \to K_S^0\pi^+\pi^-$ prefer hight values while the local minimum excludes them.

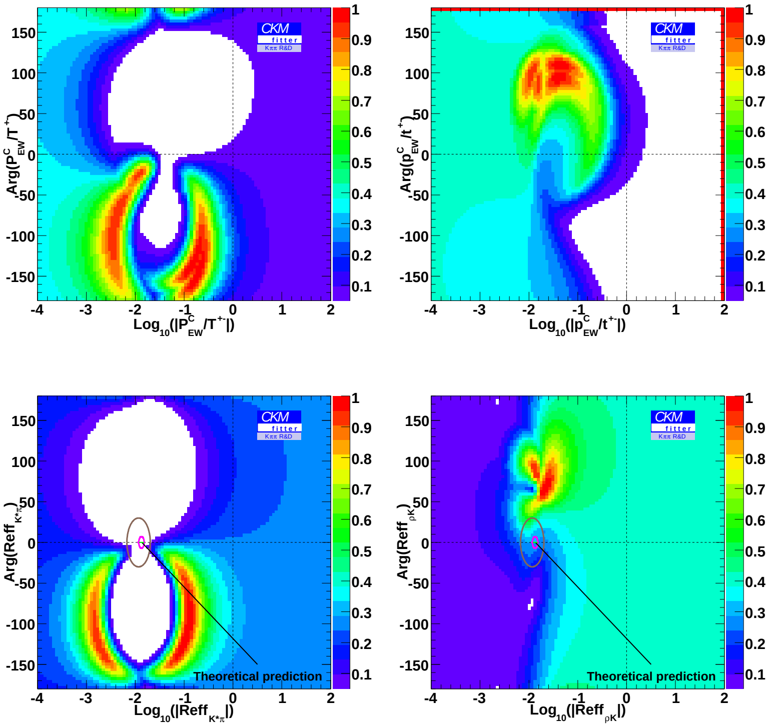

Figure 8.10: *Constraint on the argument-magnitude plane for the P_C^{EW}/T^{+-} (top left) and $R_{\text{eff}}(K^*\pi)$ (bottom left) QCD ratios of the $B \to K^*\pi$ system, and p_C^{EW}/t^{+-} (top right) and $R_{\text{eff}}(\rho K)$ (bottom right) QCD ratios of the $B \to \rho K$ system. A logarithmic scale is used on the horizontal axis. White regions are excluded with a less than 5% C.L.*

In summary, the additional information carried by the observables relating the $B \to K^*\pi$ and $B \to \rho K$ systems helps to improve most of the QCD ratios. Some QCD ratios related to $B \to K^*\pi$ improve because degeneracies are raised. Constraints are set for all the QCD parameters related to $B \to \rho K$ system, including the ones unconstrained by the observables from $B \to \rho K$ alone.

8.5.3 Constraints on the $\phi_{3/2}$ observable

The main theoretical hypothesis used so far has been tested with the $B \to K^*\pi$ system analysis. It was shown that the constraints on the CKM parameters were totally dominated by the theoretical uncertainties, making the CPS/GPSZ method unusable for all practical purposes. This section studies the $\phi_{3/2}(K^*\pi)$ and $\phi_{3/2}(\rho K)$ observables (cf. Eq.(3.48)) when combining the $B \to K^*\pi$ and $B \to \rho K$ systems. Their explicit definition in terms of measurable quantities is given below,

$$\phi_{3/2}(K^*\pi) = arg\left(\frac{q}{p}\frac{A(\bar{B}^0 \to K^{*-}\pi^+) + \sqrt{2}A(\bar{B}^0 \to \bar{K}^{*0}\pi^0)}{A(B^0 \to K^{*+}\pi^-) + \sqrt{2}A(B^0 \to K^{*0}\pi^0)}\right) , \tag{8.11}$$

$$\phi_{3/2}(\rho K) = arg\left(\frac{q}{p}\frac{A(\bar{B}^0 \to K^-\rho^+) + \sqrt{2}A(\bar{B}^0 \to \bar{K}^0\rho^0)}{A(B^0 \to K^+\rho^-) + \sqrt{2}A(B^0 \to K^0\rho^0)}\right) . \tag{8.12}$$

Both are independent functions of the observables, and can provide constraints on the $(\bar{\rho}, \bar{\eta})$ with additional theoretical input, *e.g.* $P^{EW} = 0 \to \phi_{3/2} = 0$.

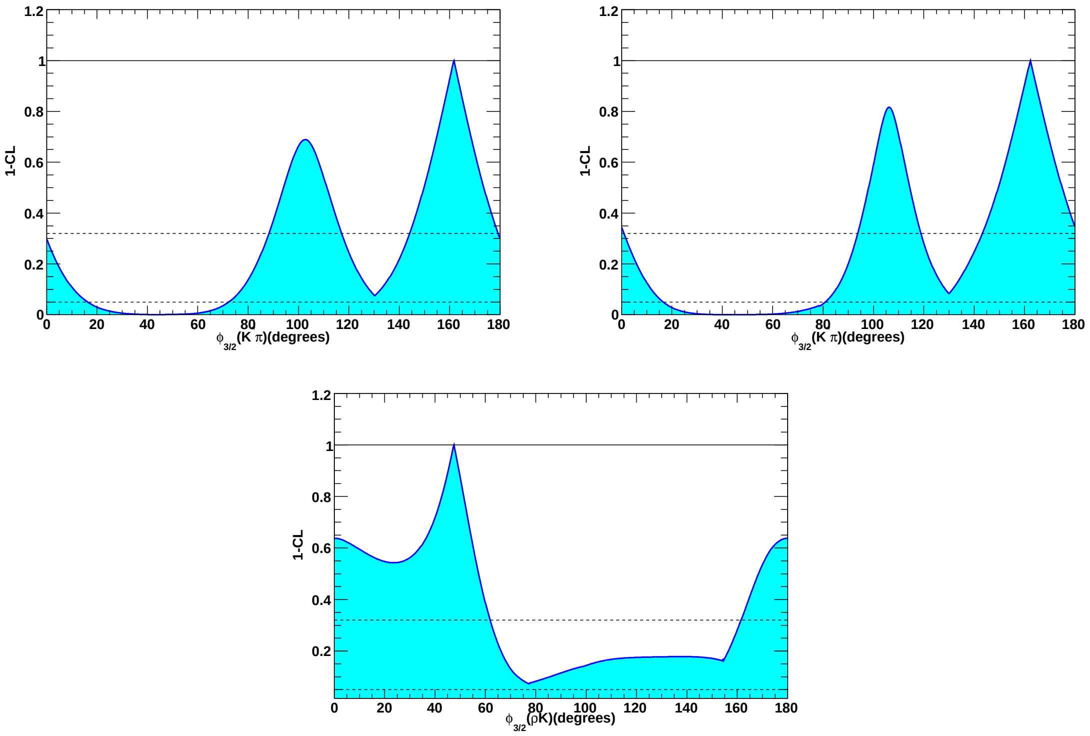

Figure 8.11: *Constraints on the $\phi_{3/2}(K^*\pi)$ and $\phi_{3/2}(\rho K)$ observables. At the top the constraint on $\phi_{3/2}(K^*\pi)$ using the observables from the $B \to K^*\pi$ system alone (left) and using the combined $K^*\pi/\rho K$ system (right) are shown. At the bottom the constraint on $\phi_{3/2}(\rho K)$ using the observables from the combined $K^*\pi/\rho K$ system is shown. The dotted lines at* 0.32 *and* 0.05 *set the confidence interval at* 1σ *and* 2σ*, respectively.*

The constraint on $\phi_{3/2}(K^*\pi)$ when using only observables from the $B \to K^*\pi$ system is shown in the left hand side plot of Fig. 8.11. Two maxima can be seen, which corresponds to the multiple solutions on the phases from the $B^0 \to K^0_S\pi^+\pi^-$ analysis. The width around each maximum is $\sim 18^o$, the presence of multiple solutions reduces significantly the constraint. The constraint on $\phi_{3/2}(K^*\pi)$ when all the available observables of the combined $K^*\pi/\rho K$ system is shown on the right hand side plot of Fig. 8.11. Again two maxima are seen, shifted by $\sim 5^o$ with respect to the previous case. More interesting is that the width around each maxima reduces to 15^o. The gain of $\sim 3^o$ in precision in the extraction of the $\phi_{3/2}(K^*\pi)$ observable is obtained when including the observables for the combined $K^*\pi/\rho K$ system. Given a theoretical hypothesis, this translates in an improvement on the possible constraint that can be set on the $(\bar{\rho}, \bar{\eta})$ plane. The measurement of the yet unavailable phases will further improve the constraint.

No constraint on the $\phi_{3/2}(\rho K)$ observable can be set when considering the $B \to \rho K$ alone due to the lack of experimental information. This is not the case when considering the combined $K^*\pi/\rho K$ system. A constraint can be set on this observable, as is shown in the bottom plot of Fig. 8.11. The $\phi_{3/2}(\rho K)$ observable can be fixed with information from the interference of different $K^*\pi$ and ρK resonances. With the current experimental inputs and errors only a weak constraint is set.

Once a theoretical hypothesis has been fixed, the information contained in both $\phi_{3/2}(K^*\pi)$ and $\phi_{3/2}(\rho K)$ observables can be combined to set an stronger constraint on the CKM parameters. The combination is not so trivial as these obsevables are experimentally correlated, and the details of their constraint on the $(\bar{\rho}, \bar{\eta})$ plane depend on the theoretical hypothesis used.

8.5.4 Extrapolation to 2015

This section studies an extrapolation for integrated luminosities expected for the Belle-upgrade, SuperB, and/or LHCb projects, in order to estimate the future performances of the analysis presented in this section. A total of $75ab^{-1}$ of data are expected for 2015 obtained only by the SuperB project. The central values of the experimental observables used for this exercise are shown in Table. 8.2.

The inputs for this exercise are all the 27 possible experimental observables from the combined $K^*\pi/\rho K$ system. The central values of branching ratios and direct CP asymmetries are taken from [127], where QCD factorization is assumed to calculate them. The values of the phases are chosen such that the constraint in the $(\bar{\rho}, \bar{\eta})$ is completely consistent with the standard CKM fit. All the measurements are assumed to be dominated by systematic uncertainties. 2% and 3% errors in braching fractions of charged and neutral modes, respectively, are used. In the same way, 2% and 3% are used for the errors on the CP asymmetries for charged and neutral modes, respectively. Finally, 5^o and 8^o error are used for the phases obtained from charged and neutral modes, respectively. The experimental errors assumed are roughly equivalent to the current systematic errors.

Using the inputs described in table 8.2, $\phi_{3/2}$ is obtained with an error of 5^o. The constraint on the $(\bar{\rho}, \bar{\eta})$ plane is shown in Fig. 8.12. $R_{\text{eff}} = 1.35\%$ is assumed, and no theoretical uncertainties are taken into account. Under the hypothesis of very small theoretical uncertainties, the constraints set on the CKM parameters are competitive with that of the global

Parameter	value	Parameter	value
$\mathcal{B}(K^{*+}\pi^-)$	9.13 ± 0.27	$\mathcal{B}(K^+\rho^-)$	13.42 ± 0.40
$\mathcal{B}(K^{*0}\pi^0)$	3.89 ± 0.12	$\mathcal{B}(K^0\rho^0)$	7.53 ± 0.23
$\mathcal{B}(K^{*0}\pi^+)$	8.90 ± 0.27	$\mathcal{B}(K^0\rho^+)$	10.27 ± 0.31
$\mathcal{B}(K^{*+}\pi^0)$	5.25 ± 0.16	$\mathcal{B}(K^+\rho^0)$	4.81 ± 0.15
$\mathcal{A}_{CP}(K^{*+}\pi^-)$	0.476 ± 0.024	$\mathcal{A}_{CP}(K^+\rho^-)$	-0.314 ± 0.016
$\mathcal{A}_{CP}(K^{*0}\pi^0)$	-0.047 ± 0.021	$\mathcal{A}_{CP}(K^0\rho^0)$	0.033 ± 0.016
$\mathcal{A}_{CP}(K^{*0}\pi^+)$	-0.002 ± 0.024	$\mathcal{A}_{CP}(K^0\rho^+)$	-0.005 ± 0.016
$\mathcal{A}_{CP}(K^{*+}\pi^0)$	0.412 ± 0.021	$\mathcal{A}_{CP}(K^+\rho^0)$	-0.463 ± 0.023
$\Delta\phi(K^*\pi)$	30.5 ± 8.0	$2\beta_{\text{eff}}(K^0\rho^0)$	19.0 ± 8.0
$\phi(K^{*0}\pi^0/K^{*+}\pi^-)$	-59.1 ± 8.0		
$\bar{\phi}(\bar{K}^{*0}\pi^0/K^{*-}\pi^+)$	4.8 ± 8.0		
$\phi(K^{*0}\pi^+/K^{*+}\pi^0)$	65.0 ± 5.0		
$\bar{\phi}(\bar{K}^{*0}\pi^+/K^{*-}\pi^0)$	35.1 ± 5.0		
$\phi(K^0\rho^0/K^{*+}\pi^-)$	-52.7 ± 8.0		
$\phi(K^+\rho^-/K^{*+}\pi^-)$	31.9 ± 8.0	$\bar{\phi}(K^-\rho^+/K^{*-}\pi^+)$	47.8 ± 8.0
$\phi(K^+\rho^0/K^{*0}\pi^+)$	-17.0 ± 5.0	$\bar{\phi}(K^-\rho^0/\bar{K}^{*0}\pi^-)$	16.4 ± 5.0
$\phi(K^0\rho^+/K^{*+}\pi^0)$	26.6 ± 5.0	$\bar{\phi}(\bar{K}^0\rho^-/K^{*-}\pi^0)$	-12.0 ± 5.0

Table 8.2: *Experimental errors expected for 2015, and central values used for the prospective studies of constraints in the* $(\bar{\rho}, \bar{\eta})$ *plane. Branching fractions are units of* 10^{-6} *and phases are in degrees.*

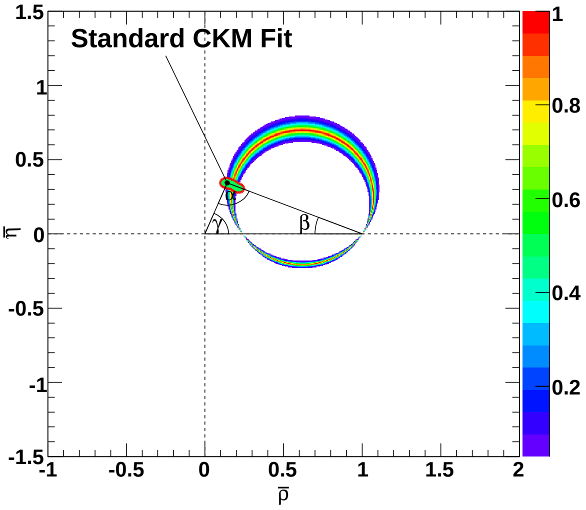

Figure 8.12: *Extrapolation exercise on the possible constraints obtained on the* $(\bar{\rho}, \bar{\eta})$ *plane for and integrated luminosity of* $75ab^{-1}$*, which is expected for 2015 with the SuperB project. As theoretical input it is assumed* $R_{\text{eff}} = 1.35\%$*, no theoretical uncertainties are taken into account. The global CKM fit with the latest measurements presented in ICHEP08 is superimposed for comparison. White regions are excluded with a less than* 5% *C.L.*

CKM fit. The potential of this method for CKM physics will depend on the evolutions of the usable theoretical frameworks and the relevant theoretical uncertainties.

8.6 Summary

Using the global CKM fit results as an external inputs to fix the CKM parameters, constraints have been set on unavailable experimental observables and on the ratios of QCD amplitudes in the $K^*\pi$ and the ρK systems. When considering $B \to K^*\pi$ alone, the constraints on the QCD ratios related to that system are weak, mainly because there are multiple solutions for the phases extracted from the $B^0 \to K^0_S\pi^+\pi^-$ analysis presented in this thesis. Considering $B \to \rho K$ alone, experimental bounds are set for a couple of QCD ratios only. When considering the combined $K^*\pi/\rho K$ system, constraints on all QCD ratios improve due to the additional experimental information contained in the phase differences related with interferences of $K^*\pi$ and ρK resonances.

The CPS/GPSZ (cf. Sec. 3.2.6) method has been revisited and tested. The validity of this external hypothesis is tested, both in terms of the structure of the isospin relations, and by using the available experimental measurements. It is shown that for the $B \to K^*\pi$ system, the measurements do not favor the scenario of negligible P^{EW}; besides, the current measurements on $K^*\pi$ have a weak consistency with the proposed theoretical estimators of P^{EW}. As a result, the constraints on CKM parameters are dominated by theoretical uncertainties.

Finally, a method that exploits the entire set of measurements on the $K^*\pi$ and ρK systems is developed. The potential of this combined analysis $K^*\pi/K\rho$ is estimated with the help a prospective analysis, based on an extrapolation of the current experimental uncertainties. The results allow to illustrate the physics potential of these analyses in the context of the LHCb experiment, the SuperB and Belle-upgrade projects, in scenarios with controlled theoretical uncertainties.

Chapter 9

Conclusion

The results obtained in this thesis can be summarized into two parts:

- A complete data analysis work for the charmless decay $B^0 \rightarrow K^0_S \pi^+ \pi^-$ has been performed with a time-dependent amplitude analysis. Measurements of inclusive and exclusive branching fractions and direct CP asymmetries are performed. Moreover, phase differences between resonant states are extracted, mainly for the $f_0(980)K^0_S$, $\rho^0(770)K^0_S$ and $K^{*\pm}(892)\pi^{\mp}$ resonant components.

- A phenomenological analysis using the available experimental information on the $B \rightarrow K^* \pi$ and $B \rightarrow \rho K$ systems is performed, with the methods described in Chapter 3.

9.1 Time-dependent amplitude analysis of the charmless decay mode $B^0 \rightarrow K^0_S \pi^+ \pi^-$

The results of a time-dependent amplitude analysis of $B^0 \rightarrow K^0_S \pi^+ \pi^-$ decays, obtained from a data sample of 383×10^6 $B\bar{B}$ decays, are presented. Event rates for signal, continuum and B-backgrounds are measured. Furthermore, 15 pairs of relative phases and magnitudes for the different resonances are measured, taking advantage of the interference between them in the Dalitz plot. From the measured isobar amplitudes the following Q2B parameters are derived: exclusive branching fractions, direct CP asymmetries and phase differences of the resonant decay modes. The main results are summarized below:

- Two solutions are found by the fit, with equivalent goodness-of-fit. The values of the fit fractions and the direct CP asymmetries are similar in both solutions; on the contrary, some isobar phase differences are significantly different. This result comes from a double ambiguity to resolve the interference pattern in the Dalitz plot. The results on the physical parameters are obtained by studying the complete likelihood function around its two maxima, applying no approximation in the construction of the confidence intervals on the measured parameters.

- The measurement of the $(\beta_{\rm eff}, C)$ parameters in the $f_0(980)K^0_S$ channel is in good agreement with the values from golden modes. The measurement excludes CP conservation with 3.5σ significance including systematic uncertainties. The total error is dominated by statistical effects, and the dominant contribution to systematic uncertainties comes from the isobar model.
- For the $\rho^0(770)K^0_S$ channel, the $\beta_{\rm eff}$ parameter is measured for the first time. The $(\beta_{\rm eff}, C)$ measurement is also in agreement with the golden modes. It is compatible with CP conservation within 1σ. As for $f_0(980)K^0_S$, the total error is dominated by statistical effects, and the dominant contribution to systematic uncertainties comes from the isobar model.
- For the $K^{*+}(892)\pi^-$ channel, the measurement of the direct CP violation asymmetry is $A_{\rm CP} = -0.20 \pm 0.10 \pm 0.02 \pm 0.01$; the null value is excluded at 2σ. The relative phase $\Delta\phi(K^{*-}(892)\pi^+, K^{*+}(892)\pi^-)$ between the decay amplitude and its CP conjugated amplitude is measured for the first time. The small overlap of the $K^{*+}(892)\pi^-$ with other resonances limits the sensitivity to measure $\Delta\phi(K^{*-}(892)\pi^+, K^{*+}(892)\pi^-)$, which only allows to exclude the interval $[-132^\circ : +25^\circ]$ (at 95% CL). Although the measurement of $\Delta\phi(K^{*-}(892)\pi^+, K^{*+}(892)\pi^-)$ is dominated by the statistics, the separation between the maxima of the likelihood function dilutes even more the constraint obtained.
- The presence of a significant contribution to the $\pi^+\pi^-$ spectrum, in the region around $m_{\pi^+\pi^-} \sim 1.5~{\rm GeV}/c^2$, is established with a 4.8σ significance. This signal is described as the coherent sum of two contributions, the $f_2(1270)$ tensor and a unlisted resonance $f_X(1300)$, which has been identified for the first time in $B^+ \to K^+\pi^-\pi^+$ decays [23, 24]. As in previous Dalitz analyses, the best fit is obtained using a scalar for the $f_X(1300)$.

All the measurements presented are consistent with previous analyses, and are more precise than results from Q2B analyses. From the measured decay amplitudes and the signal yield, the inclusive direct CP asymmetry and branching fraction are derived. The inclusive direct CP asymmetry is consistent with zero and the inclusive branching fraction is consistent with previous results.

A preliminary version of this work has been presented, on behalf the *BABAR* collaboration, at the Lepton-Photon conference in 2007 (`arXiv:0708.2097`). The final version is currently in internal review by the collaboration, and is planned to be submitted for publication in *Physical Review D*.

9.2 Phenomenological Interpretation of the $B \to K^*\pi$ and $B \to K\rho$ modes

At first, this thesis aimed at producing an extension of the CPS/GPSZ method (cf. Sec. 3.2.6), which claims to allow access to the angle γ of the CKM UT under the hypothesis of negligible electroweak penguins (P^{EW}). The plan was to maximize the use of available experimental information. However, this reasoning has also helped to revisit certain conditions invoked by the CPS/GPSZ methods. A correct method is developed which shows that the constrained UT angle under the $P^{EW} = 0$ assumption is the angle α of the CKM UT (not γ). The validity of this external hypothesis is tested, both in terms of the structure of isospin relations, and by using the available experimental measurements. It is shown that for the $B \to K^*\pi$ system, the measurements do not favor the scenario of negligible P^{EW}; besides, the current measurements on $K^*\pi$ have a weak compatibility with the available theoretical estimators of P^{EW}. As a result, the constraints on CKM parameters are dominated by theoretical uncertainties.

Finally, a method that exploits the entire set of measurements on the $K^*\pi$ and ρK systems is developed. The potential of this combined analysis $K^*\pi/K\rho$ is estimated with the help a prospective analysis, based on an extrapolation of the current experimental uncertainties. The results allow to illustrate the physics potential of these analyses in the context of the LHCb experiment, the SuperB and Belle-upgrade projects.

A preliminary version of this phenomenological work is presented in this thesis. The final version is likely contain some extensions of the method, in a context more expanded that only isospin symmetry. The final goal is to summit this work to publication in *Journal of High Energy Physics*.

Part V

Appendix

Appendix A

Probability density distributions of fit variables

This appendix provides additional details on the parameterizations used for the discriminant variables entering in the likelihood function. The PDFs for the signal (TM and SCF), continuum and B background species are described.

A.1 Signal and Continuum background

A.1.1 The kinematic variables, m_{ES} and ΔE

Signal

- $\mathbf{m_{ES}}$**:** The distribution of TM events is parameterized with a bifurcated Crystal Ball function $bCB(m; m_0, \sigma_L, \sigma_R, \alpha, n))$,

  $$bCB(m) = \frac{1}{N} \cdot \begin{cases} \exp\left(-(m-m_0)^2/(2\sigma_R^2)\right) & , \quad m > m_0 \\ \exp\left(-(m-m_0)^2/(2\sigma_L^2)\right) & , \quad m_0 - \alpha\sigma_L < m \leq m_0 \\ \frac{(n/\alpha)^n \exp\left(-\alpha^2/2\right)}{((m_0-m)/\sigma_L + n/\alpha - \alpha)^n} & , \quad m \leq m_0 - \alpha\sigma_L \end{cases} \tag{A.1}$$

  which is a combination of bifurcated Gaussian function with a power law tail. N is a normalization parameter. The values for $\alpha = 1.9$, $n = 10.0$ are used, and the m_0, σ_L and σ_R parameters are determined by the fit.

  The SCF events are parameterized with a smooth histogram known as Keys PDFs [128] (cf. top right plot of Fig. A.1).

  The top plots of Fig. A.1 show the parameterization used for TM (left) and SCF (right) superimposed to the non-resonant MC sample.

- $\mathbf{\Delta E}$**:** The distribution of TM events is parameterized with a double Gaussian, with all five parameters determined by the fit to data.

  SCF events are parameterized with a single Gaussian PDF $G(m; m_0, s_0)$, where the mean and width parameters are determined from MC samples and fixed to $m_0 = (1.7 \pm 1.4) \times 10^{-2}\ \mathrm{GeV}/c^2$, and $s_0 = (1.0 \pm 0.1) \times 10^{-1}\ \mathrm{GeV}/c^2$.

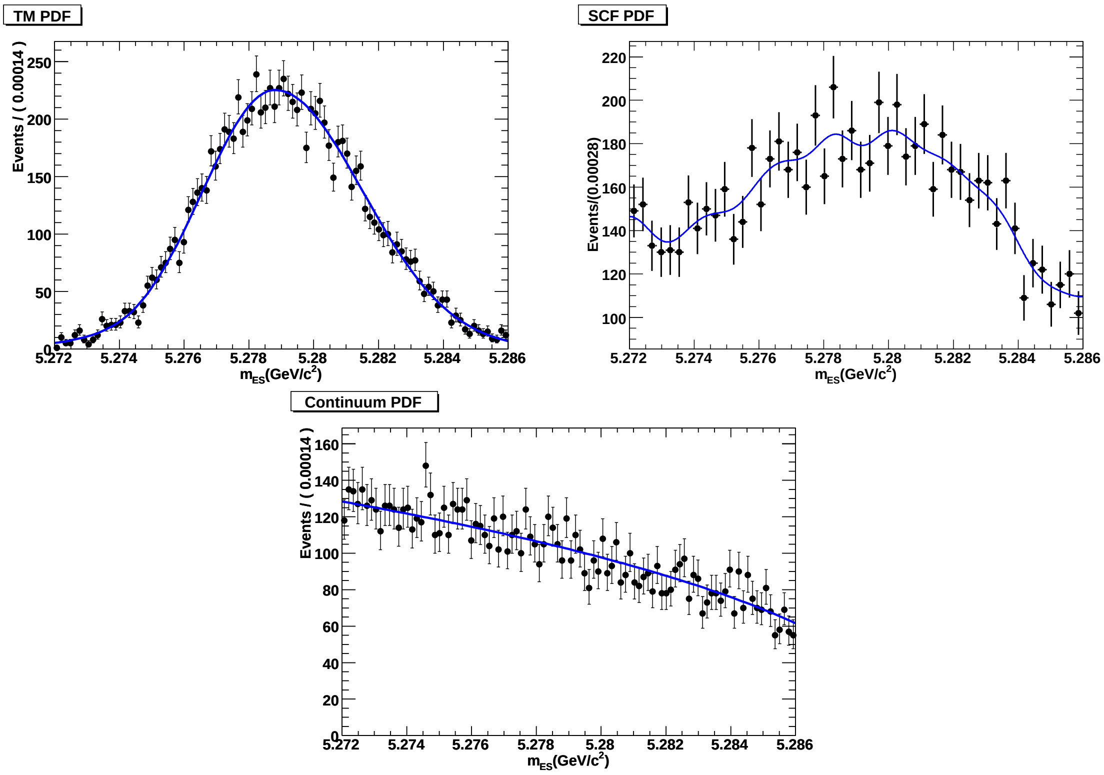

Figure A.1: *Distribution of m_{ES} for TM (top left) and SCF (top right) non-resonant MC and Off Peak data (bottom). Superimposed are the PDFs used for the maximum likelihood fit.*

The top plots of Fig. A.2 shows the parameterization used for TM (left) and SCF (right) superimposed to the non-resonant MC sample.

Continuum background

- $\mathbf{m_{ES}}$**:** The continuum PDF is parameterized with a two parameter function known as $\mathrm{Argus}(m; m_0, \xi)$ [103], where m_0 is a threshold parameter known as endpoint,

$$\mathrm{Argus}(m) = \frac{1}{N} \cdot \begin{cases} 0 & , \quad m > m_0 \\ m\left(1 - \left(\frac{m}{m_0}\right)^2\right)^{1/2} \exp \xi \left(1 - \left(\frac{m}{m_0}\right)^2\right) & , \quad m \leq m_0 \end{cases} \tag{A.2}$$

  N is again a normalization parameter. Since the shape parameter ξ has been found to be compatible within statistical error among all tagging categories (including `NoTag`), a single average $< \xi >$ is used, determined by the fit to data, simultaneously with the signal parameters. The kinematic endpoint m_0 is fixed to $5.2897\ \mathrm{GeV}/c^2$. The bottom plot of Fig. A.1 shows a fit to the off-peak sample.

- $\mathbf{\Delta E}$**:** The continuum PDF is parameterized with a second order polynomial. Again, the same parameters are used for all tagging categories. The two polynomial parameters are obtained by the fit. The bottom plot of Fig. A.2 shows a fit to the off-peak sample.

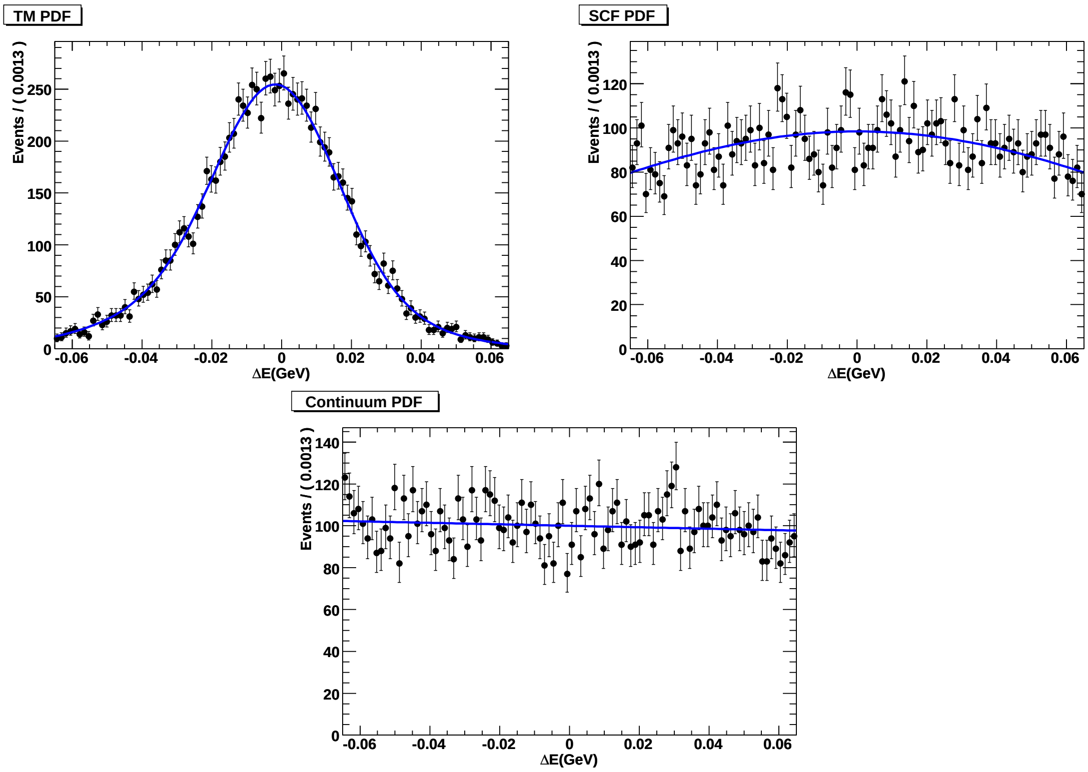

Figure A.2: *Distribution of ΔE for TM (top left) and SCF (top right) non-resonant MC and Off Peak data (bottom). Superimposed are the PDFs used for the maximum likelihood fit.*

A.2 The Neural Network

In view of the correlation between the NN and the DP coordinates for continuum background (see Sec. 6.2), the NN PDF for continuum does not factorize any more in the likelihood function. This effect is taken into account by introducing a Dalitz plot-dependence of the NN variable for continuum.

Signal

Keys PDFs are used, distinguishing for tagging categories, for the empirical MC shape of TM and SCF events. Figs. A.3 and A.4 show the nonparametric Keys PDFs used for the TM (left plots) and the SCF (right plots) for the seven tagging categories.

Continuum background

To account for the NN continuum correlation with the DP, a function that varies with Δ_{Dalitz} (cf. Fig. 6.6) is used,

$$P_{q\bar{q}}(NN; \Delta_{\mathrm{Dalitz}}, A, B_0, B_1, B_2) = (1 - NN)^A \left(B_2 NN^2 + B_1 NN + B_0 \right) . \tag{A.3}$$

The A and B coefficients are linear functions of Δ_{Dalitz},

$$\begin{array}{rcl} A & = & a_1 + a_4 \Delta_{\mathrm{Dalitz}}, \\ B_0 & = & c_0 + c_1 \Delta_{\mathrm{Dalitz}}, \\ B_1 & = & a_3 + c_2 \Delta_{\mathrm{Dalitz}}, \\ B_2 & = & a_2 + c_3 \Delta_{\mathrm{Dalitz}}, \end{array} \tag{A.4}$$

where the a_i and c_i coefficients are obtained by the fit. Fig. A.5 shows the fit results of the polynomial (Eq. A.3) for off-peak events, in different domains on Δ_{Dalitz}.

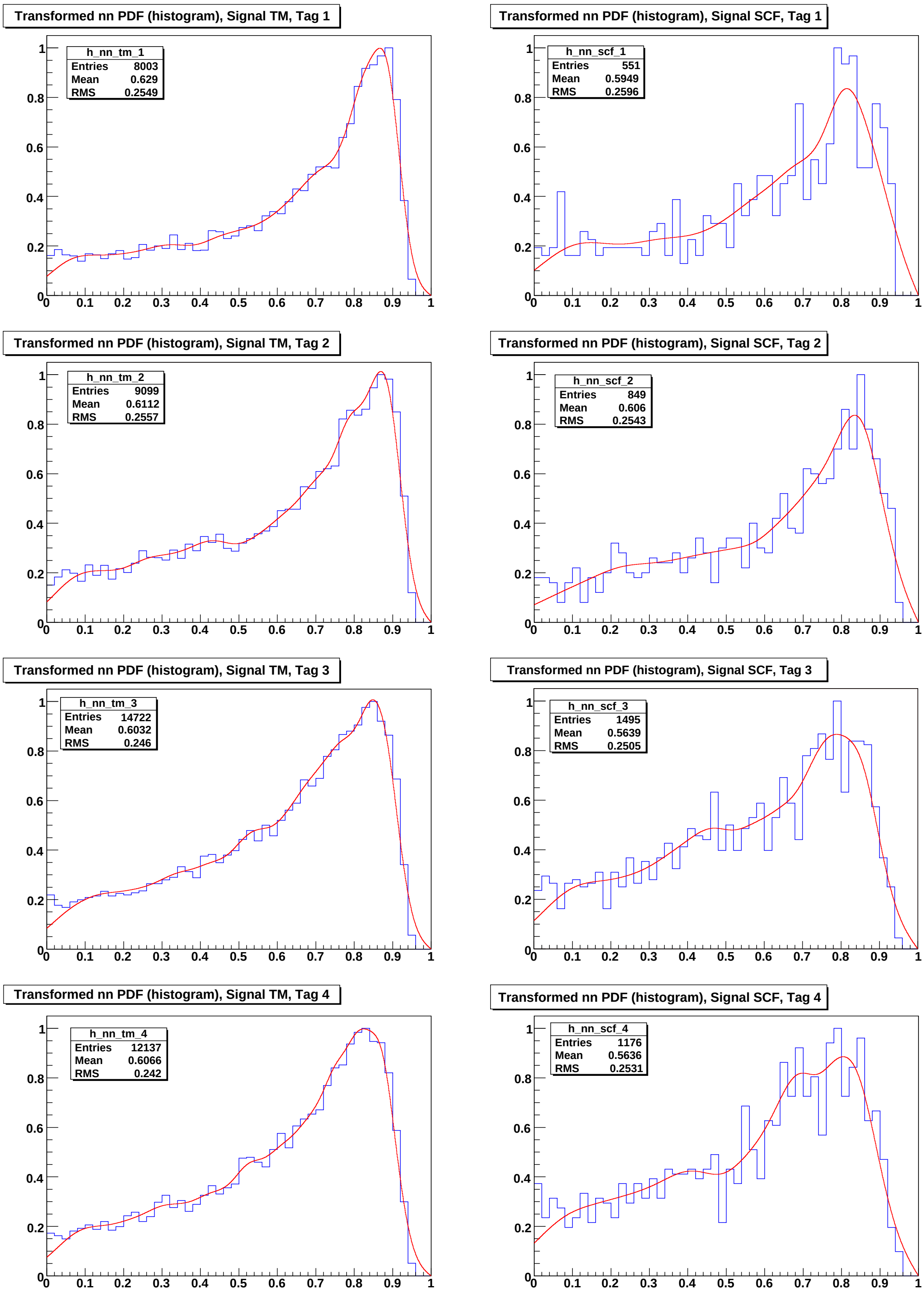

Figure A.3: *NN signal PDFs for the TM (left) and SCF components (right) in the* `Lepton` *(top),* `Kaon1` *(middle top),* `Kaon2` *(middle bottom) and* `KaonPion` *(bottom) tagging categories. The histograms are non-resonant MC and the curve is the Keys PDF.*

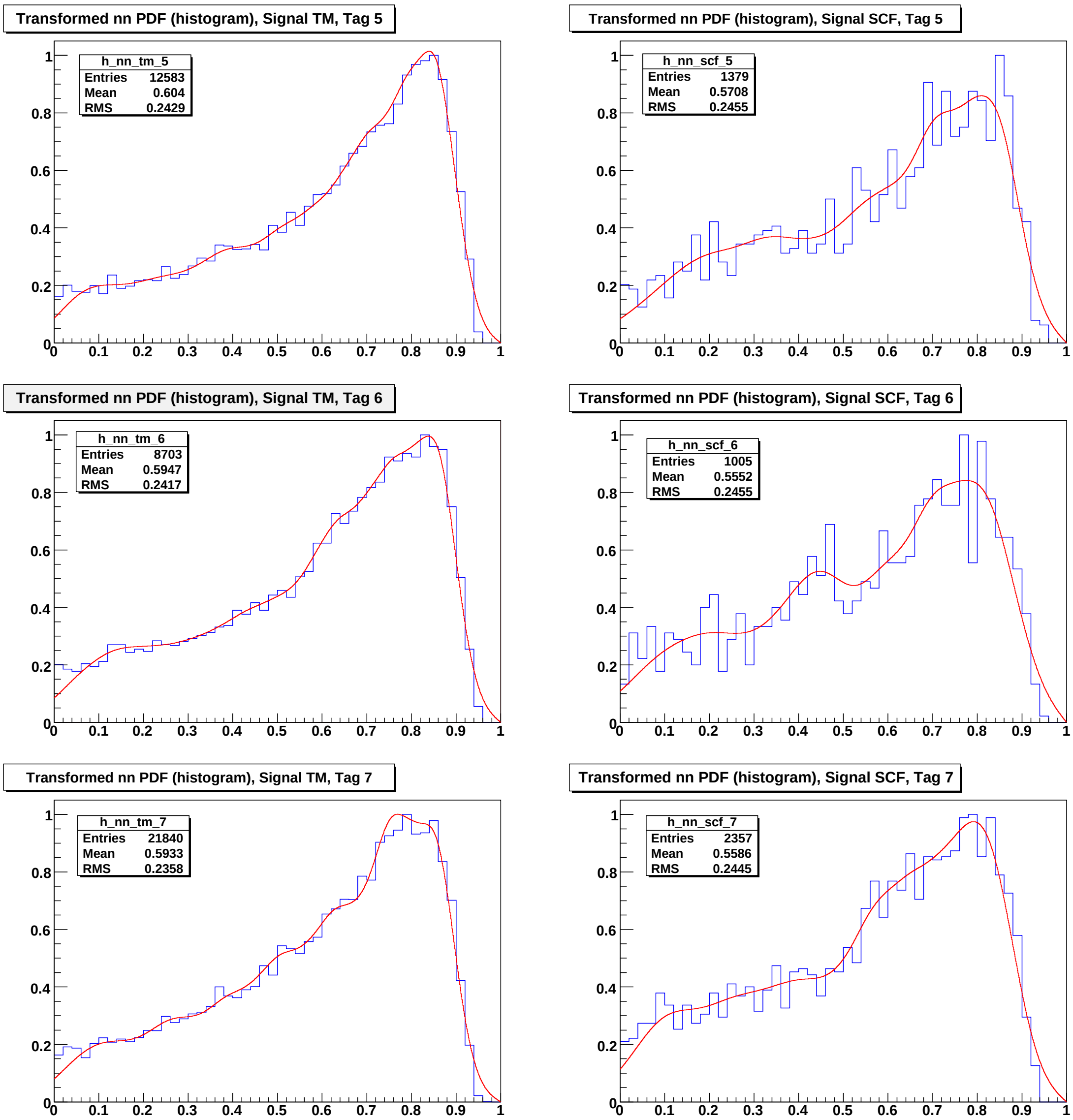

Figure A.4: *NN signal PDFs for the TM (left) and SCF components (right) in the* `Pion` *(top),* `Other` *(middle) and* `NoTag` *(bottom) tagging categories. The histograms are non-resonant MC and the curve is the Keys PDF.*

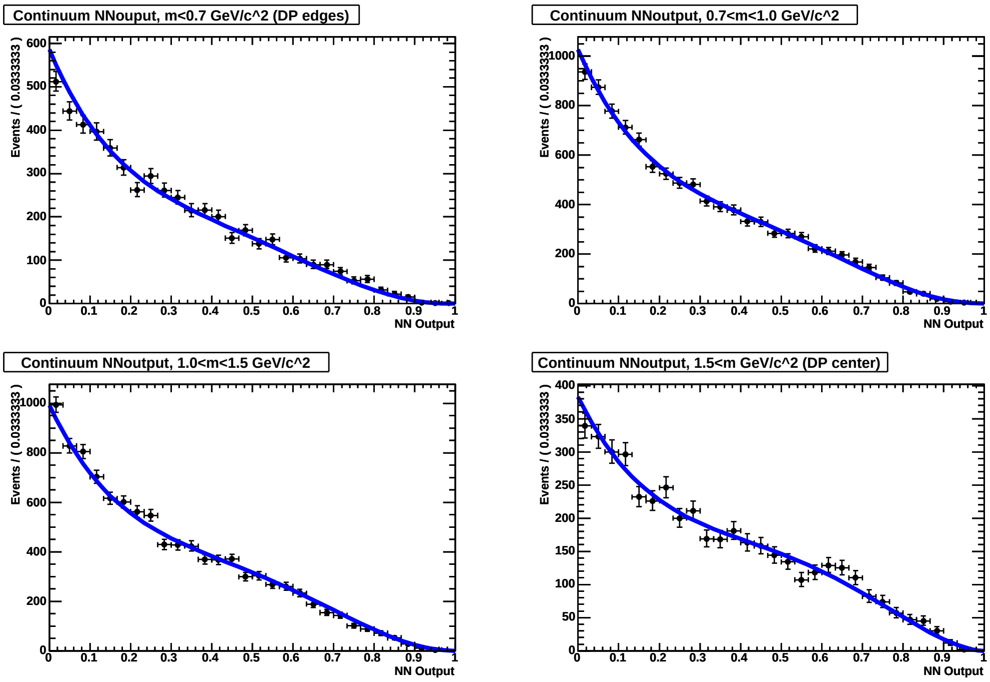

Figure A.5: *Fit of* NN *to the off-resonance data. The fit result is projected in four different domains on* Δ_{Dalitz}*, spanning from the DP edges (top, left) to the DP center (bottom, right).*

A.3 PDFs for B Backgrounds

This section illustrates the PDFs used to describe the different B background components detailed in Section 5.8.

A.3.1 $B^0 \to D^-(\to K^0_S\pi^-)\pi^+$

As the $B^0 \to D^-(\to K^0_S\pi^-)\pi^+$ B-background component has the same final state as the signal, it shares its m_{ES} and ΔE PDFs. A Keys PDF is used for the NN; and a non-parametric PDF is used is used for the DP. Fig. A.6 illustrates the shape of these four PDFs, using exclusive MC samples of $B^0 \to D^-(\to K^0_S\pi^-)\pi^+$ events.

A.3.2 $B^0 \to J/\Psi(\to \ell^+\ell^+)K^0_S$

As the m_{ES} construction does not depend on the masses of particles in the final state, the m_{ES} distribution for the $B^0 \to J/\Psi(\to \ell^+\ell^+)K^0_S$ component is expected to be very similar as that of signal, so this PDF is shared with the signal. The ΔE PDF uses a non-parametric Keys obtained from exclusive MC; its central value in MC was shifted according to the fitted value of ΔE for the signal. A Keys PDF is used for the NN; and a non-parametric PDF is used is used for the DP. Fig. A.7 illustrates the shape of these four PDFs, using exclusive MC samples of $B^0 \to J/\Psi(\to \ell^+\ell^+)K^0_S$ events.

A.3.3 Other B backgrounds

For the remaining B background classes, a Keys PDF is used to describe their m_{ES}, ΔE and NN PDFs. As discussed on Sec. 6.3.3, for the DP a non-parametric PDF is used for all B background components (cf. top plots on Fig. A.6–A.15).

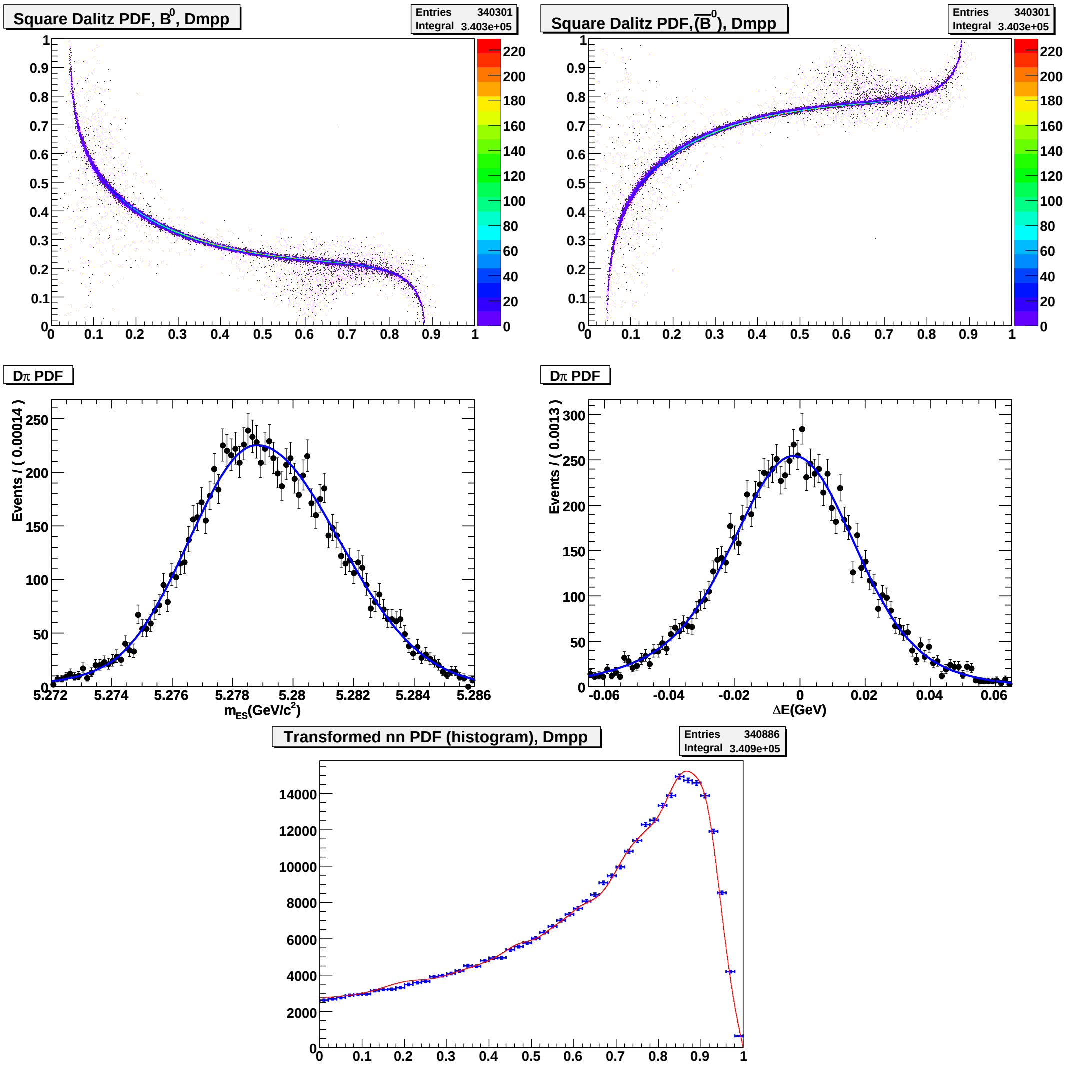

Figure A.6: *PDFs used for the $B^0 \to D^-(\to K^0_S\pi^-)\pi^+$ B-background component. Square DP (the top left and right plots are B^0 and $\bar{B}^0$ tags, respectively), m_{ES} (middle left) and ΔE (middle right), and NN (bottom) PDFs.*

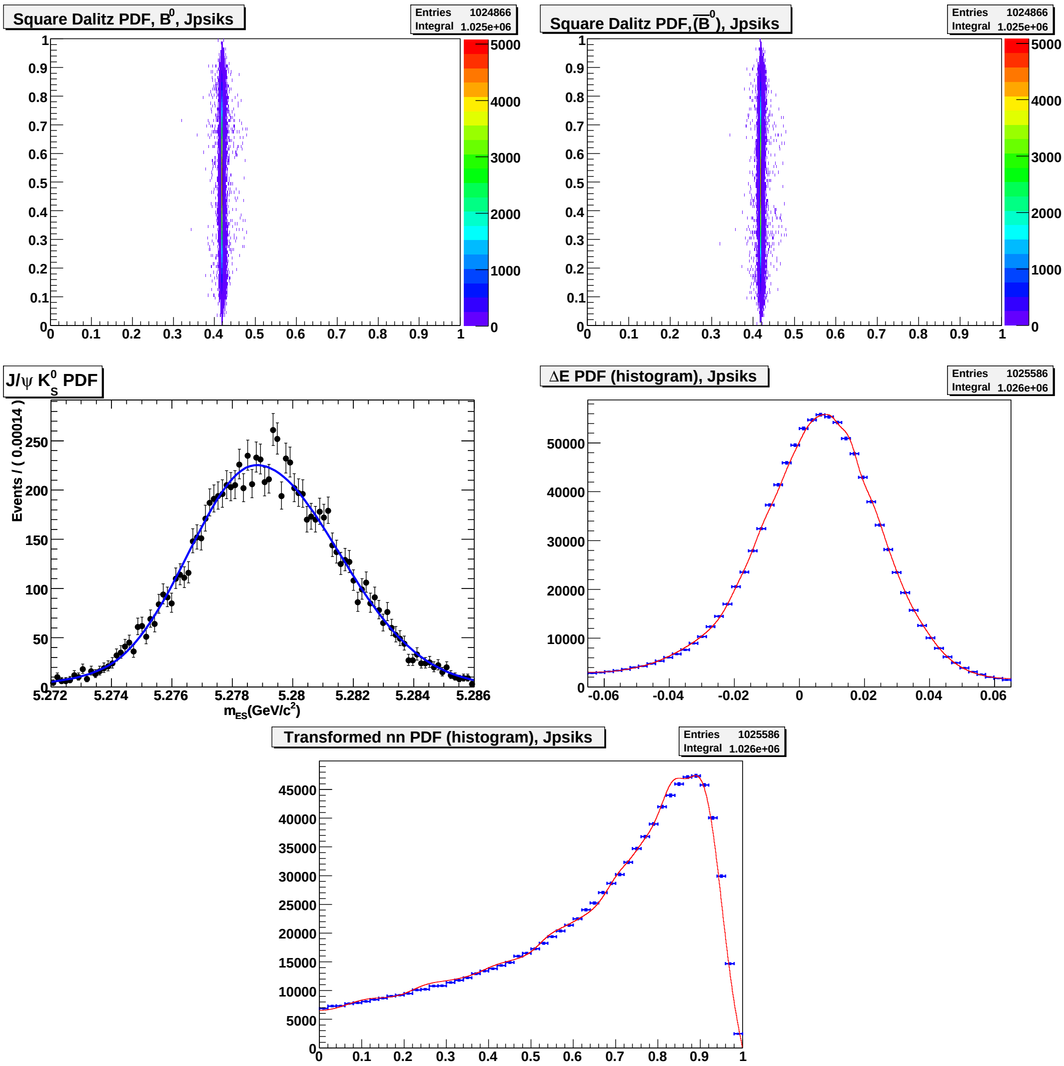

Figure A.7: *PDFs used for the* $B^0 \to J/\Psi K^0_S$ *B-background component. Square DP (the top left and right plots are* B^0 *and* $\bar{B}^0$ *tags, respectively),* m_{ES} *(middle left) and* ΔE *(middle right), and* NN *(bottom) PDFs.*

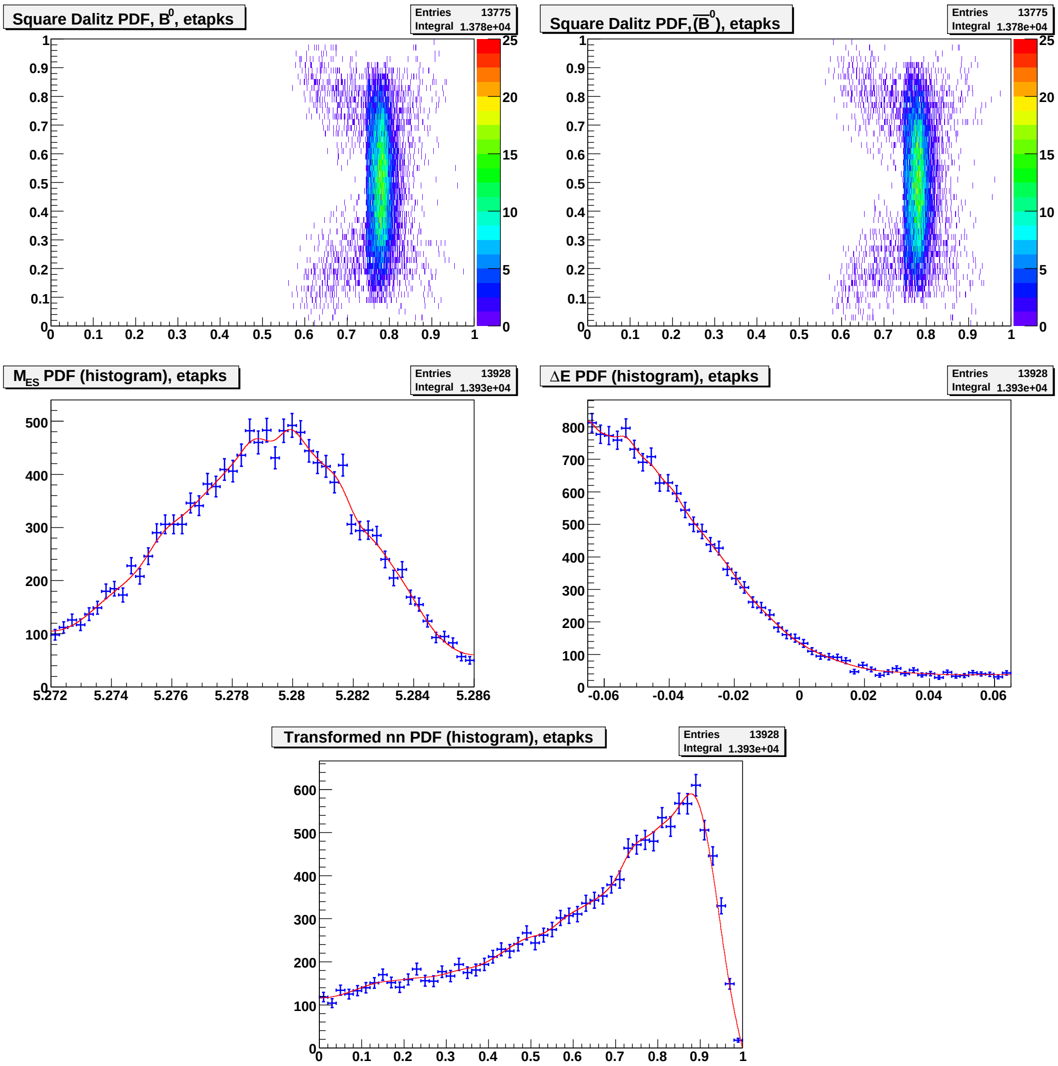

Figure A.8: *PDFs used for the $B^0 \to \eta' K^0_S$ B-background component. Square DP (the top left and right plots are B^0 and $\bar{B}^0$ tags, respectively), m_{ES} (middle left) and ΔE (middle right), and NN (bottom) PDFs.*

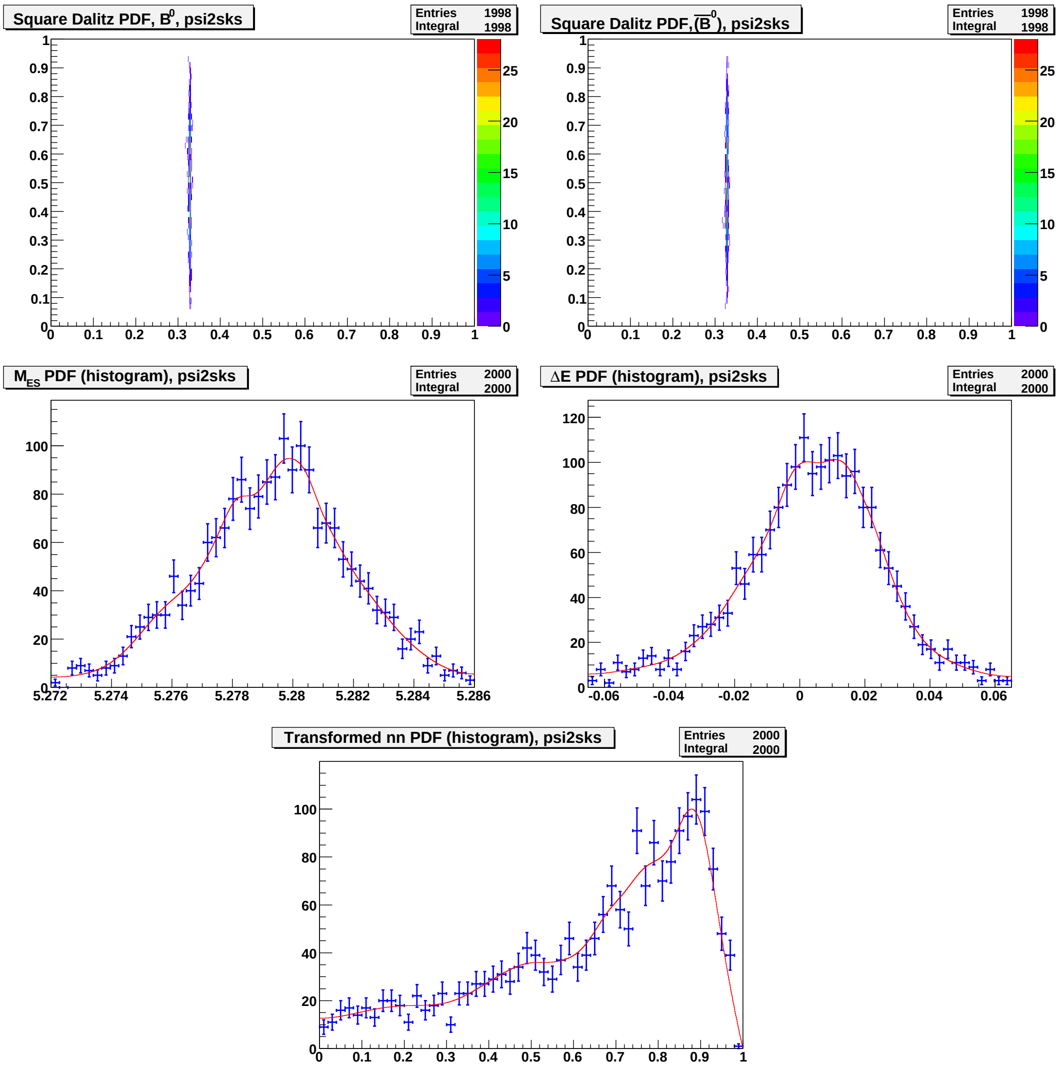

Figure A.9: *PDFs used for the $\Psi(2S)K^0_S$ B-background component. Square DP (the top left and right plots are B^0 and $\bar{B}^0$ tags, respectively), m_{ES} (middle left) and ΔE (middle right), and NN (bottom) PDFs.*

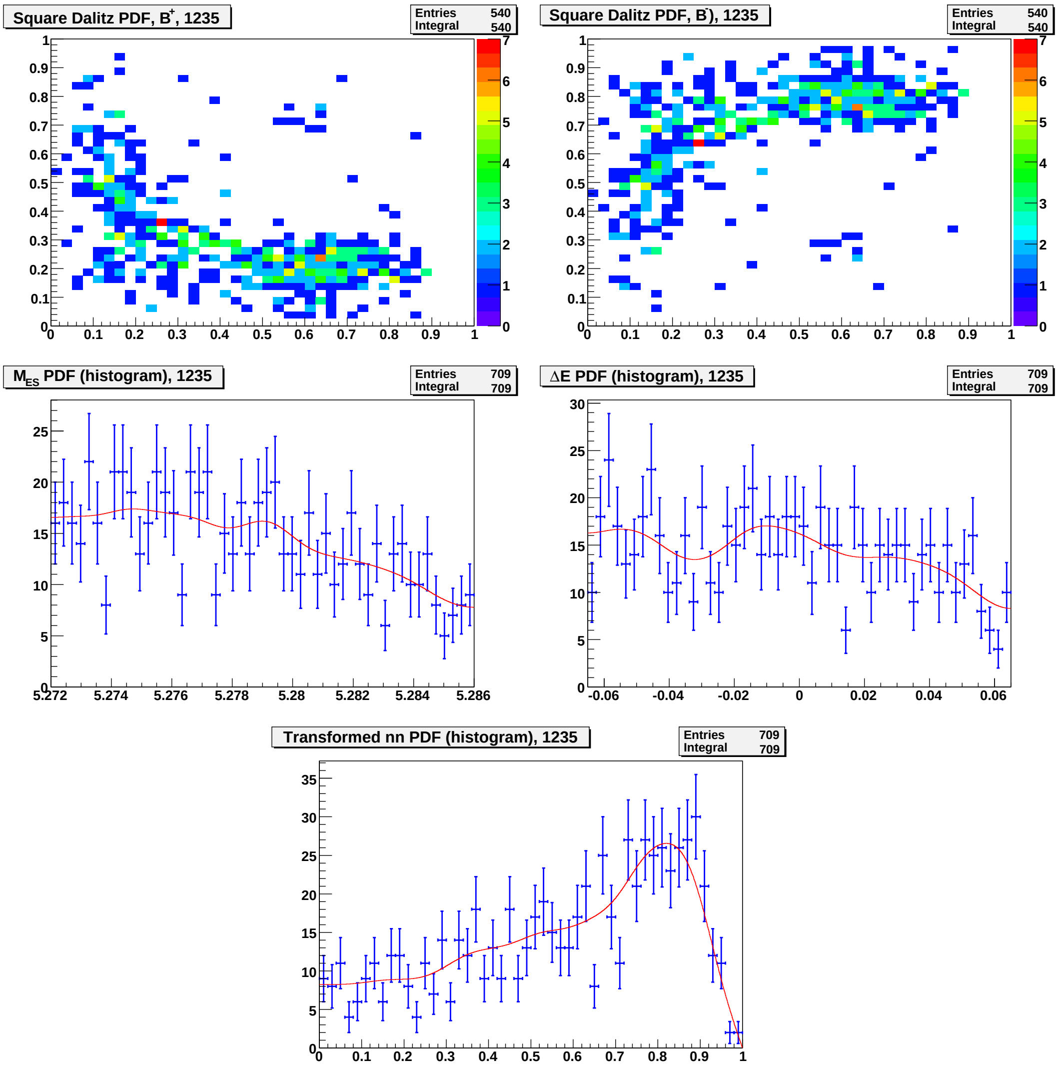

Figure A.10: *PDFs used for the charged generic* B*-background component. Square DP (the top left and right plots are* B^0 *and* $\bar{B}^0$ *tags, respectively),* m_{ES} *(middle left) and* ΔE *(middle right), and* NN *(bottom) PDFs.*

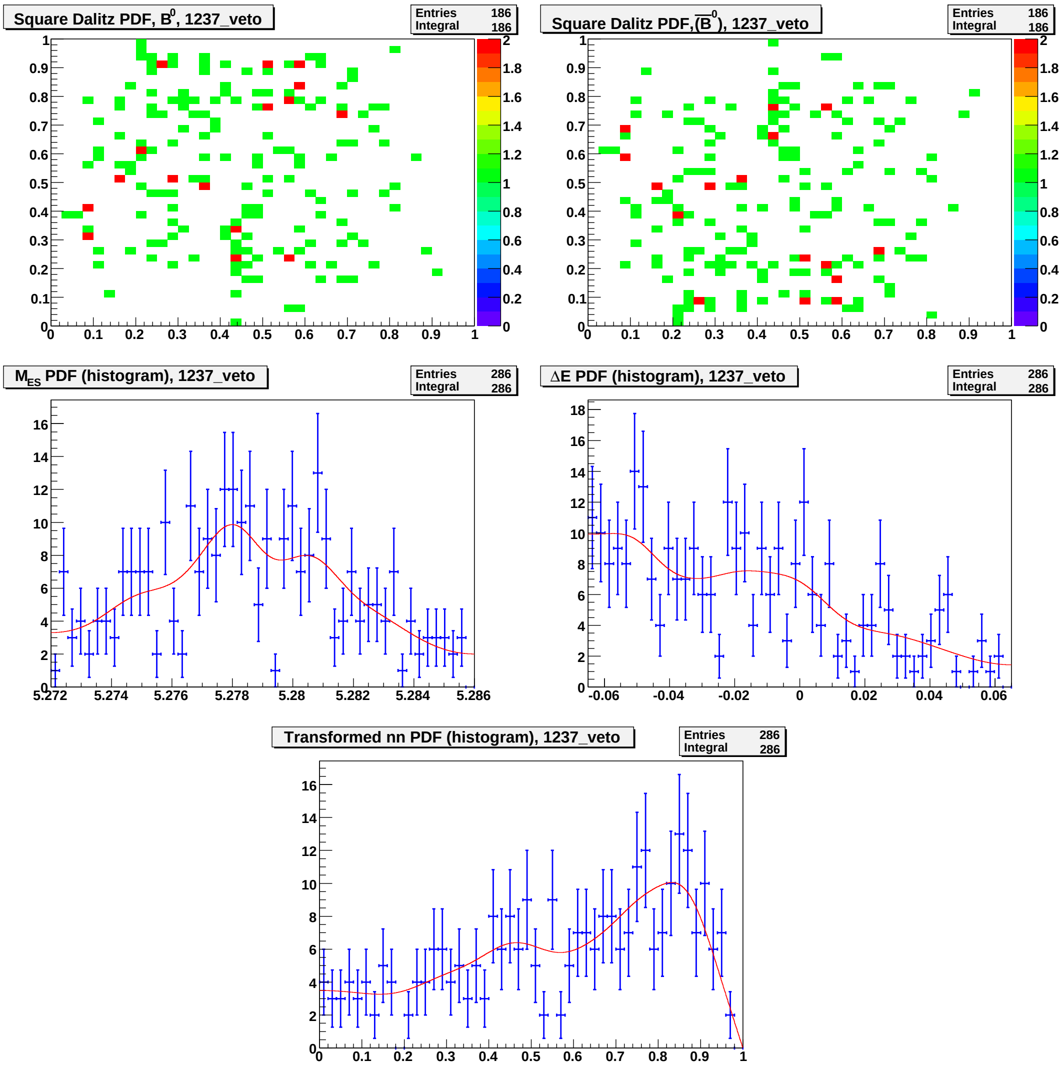

Figure A.11: *PDFs used for the neutral generic B-background component. Square DP (the top left and right plots are B^0 and $\bar{B}^0$ tags, respectively), m_{ES} (middle left) and ΔE (middle right), and NN (bottom) PDFs.*

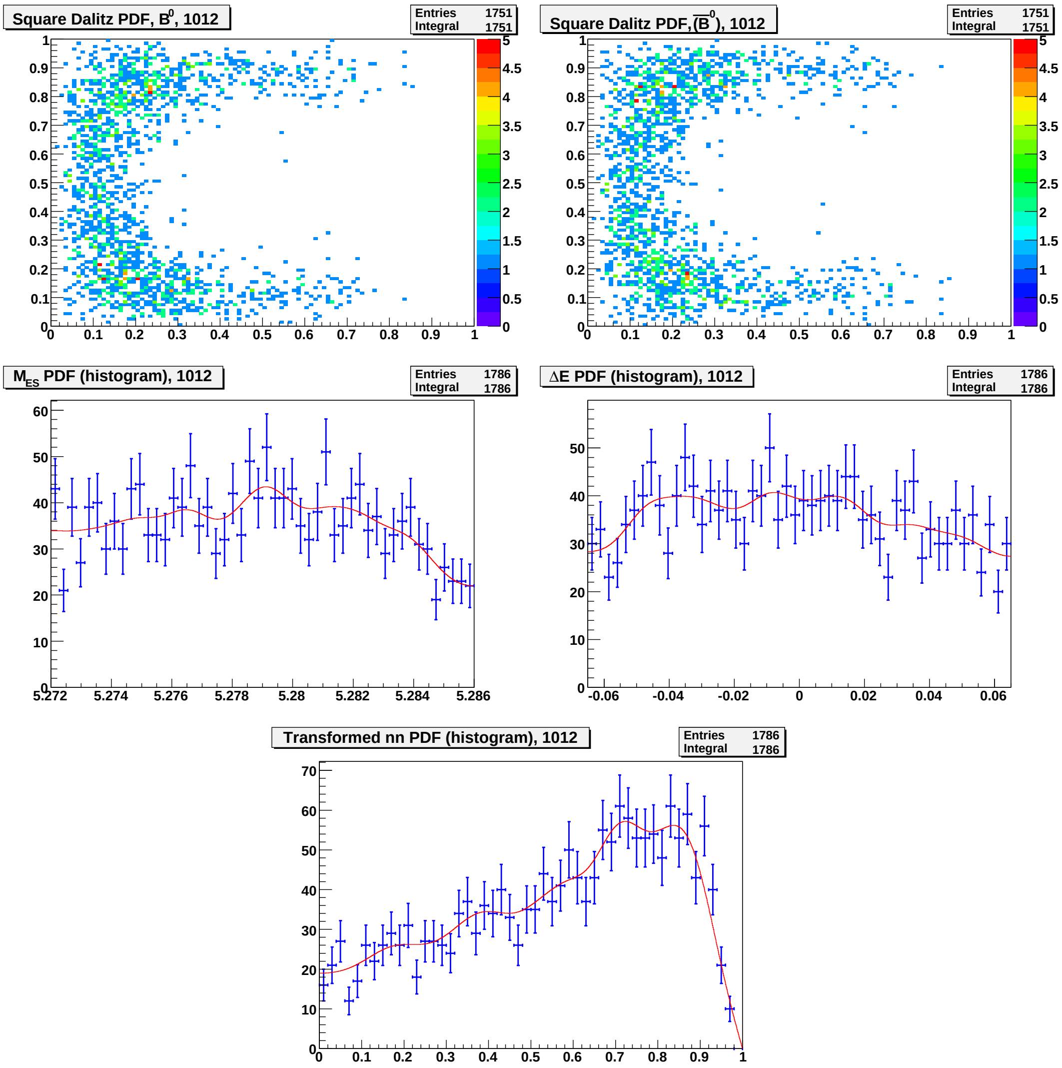

Figure A.12: *PDFs used for the $a_1^+\pi^-$ B-background component. Square DP (the top left and right plots are B^0 and $\bar{B}^0$ tags, respectively), m_{ES} (middle left) and ΔE (middle right), and NN (bottom) PDFs.*

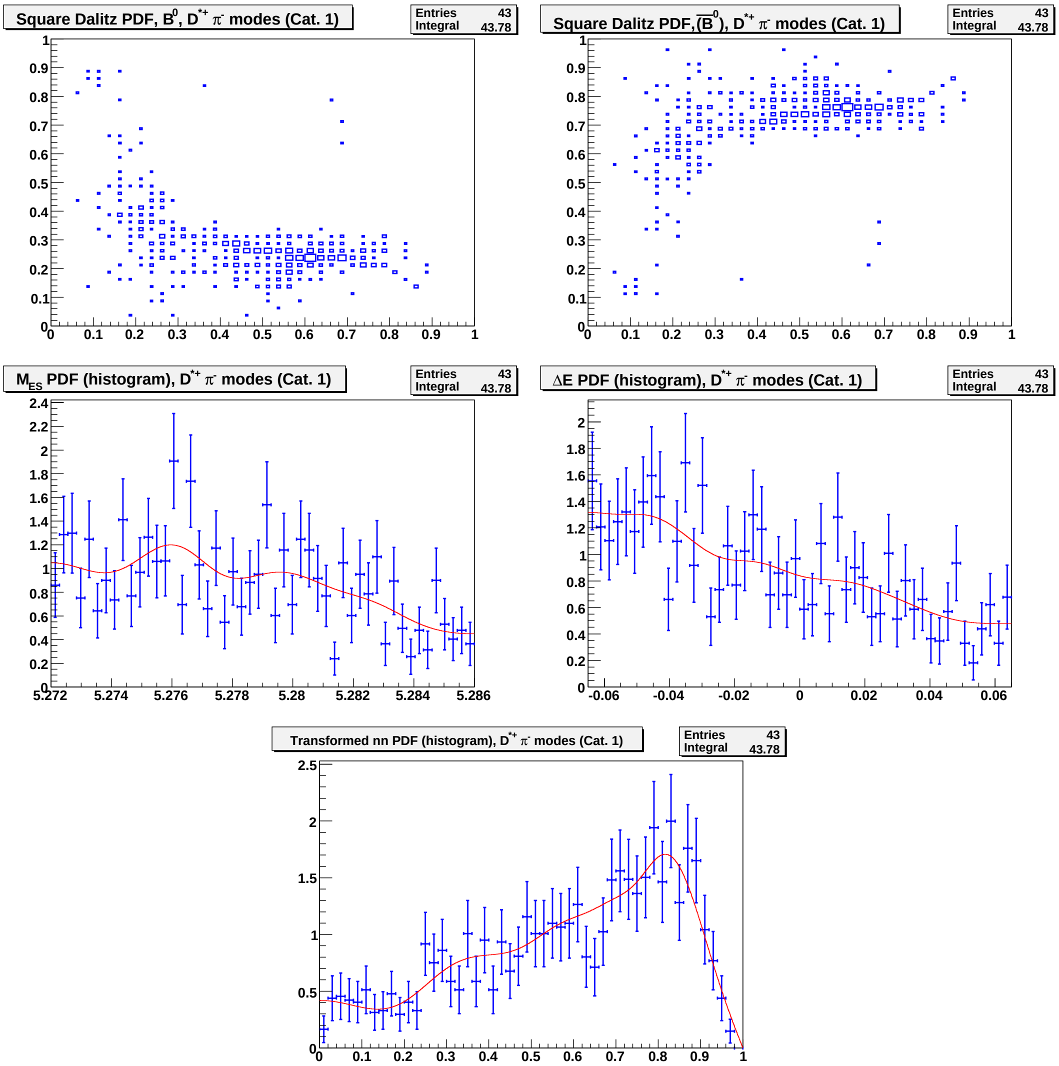

Figure A.13: *PDFs used for the mixed B-background modes referred as “category 1“ in Table 5.7. Square DP (the top left and right plots are B^0 and $\bar{B}^0$ tags, respectively), m_{ES} (middle left) and ΔE (middle right), and NN (bottom) PDFs.*

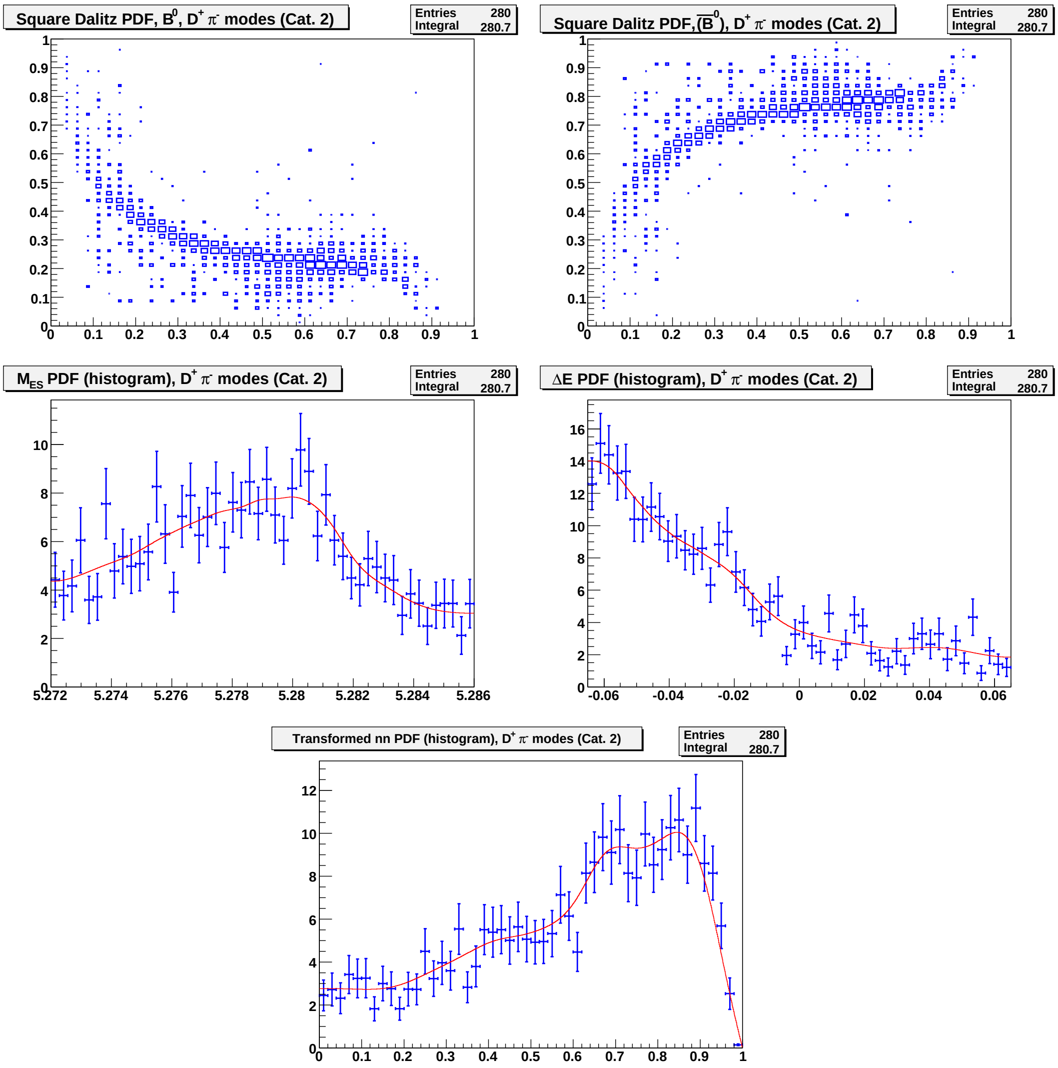

Figure A.14: *PDFs used for the mixed B-background modes referred as "category 2" in Table 5.7. Square DP (the top left and right plots are B^0 and $\bar{B}^0$ tags, respectively), m_{ES} (middle left) and ΔE (middle right), and NN (bottom) PDFs.*

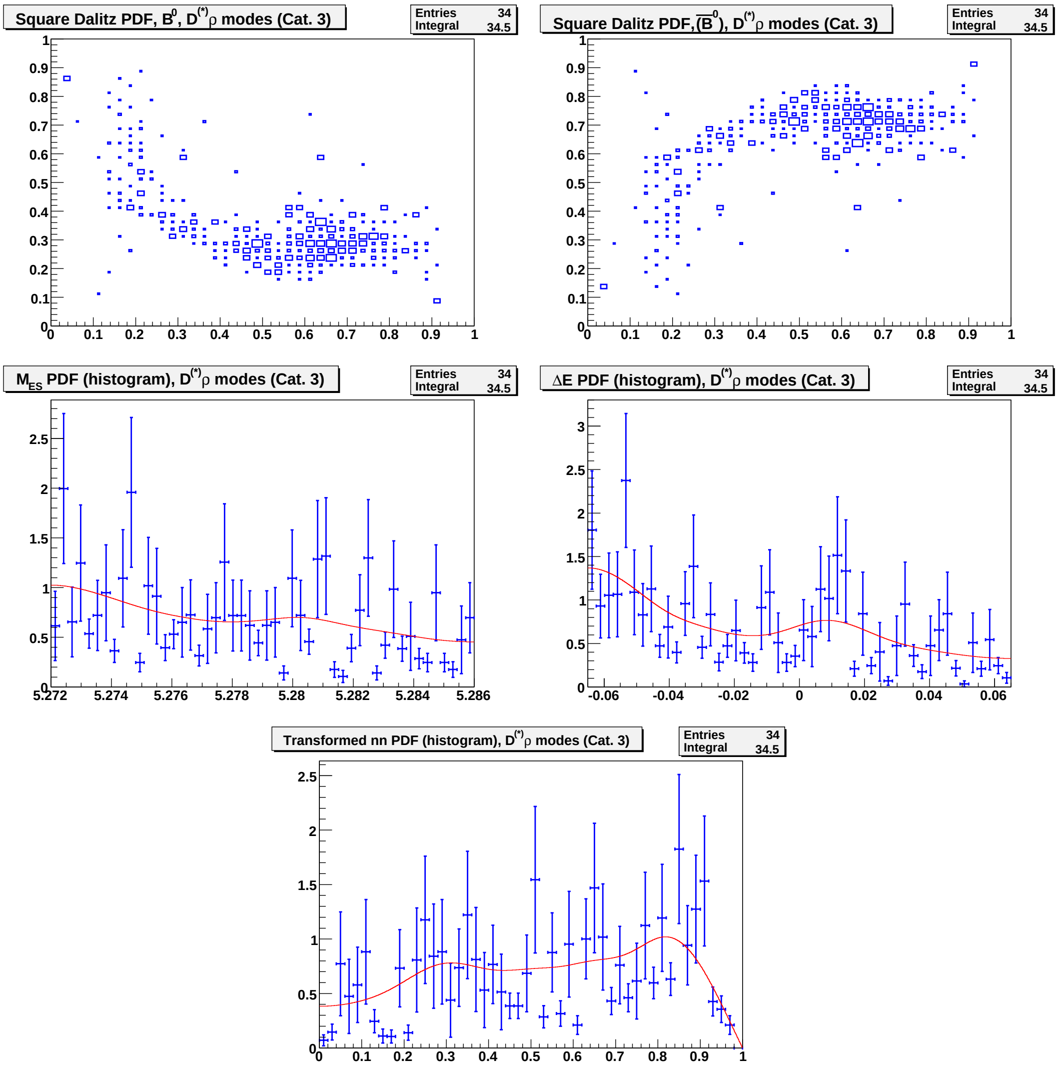

Figure A.15: *PDFs used for the mixed B-background modes referred as “category 3“ in Table 5.7. Square DP (the top left and right plots are B^0 and $\bar{B}^0$ tags, respectively), m_{ES} (middle left) and ΔE (middle right), and NN (bottom) PDFs.*

Appendix B

Probing the Signal DP Model

It is expected that the same intermediate resonant states that contribute to the $B^+ \to K^+\pi^-\pi^+$ channel, will also be present in the $B^0 \to K^0_S\pi^+\pi^-$ model. As the charged mode is cleaner experimentally (higher signal rates and lower backgrounds), its isobar model can be used as a probe for smaller resonant contributions.

For the $B^0 \to K^0_S\pi^+\pi^-$ channel, Q2B analyses have established uncontroversial signal yields for the $f_0(980)K^0_S$, $\rho^0(770)K^0_S$, $K^{*\pm}(892)\pi^\mp$ and $(K\pi)^{*\pm}_0\pi^\mp$. components (cf. Sec. 2.2). The $f_0(980)K^+$, $\rho^0(770)K^+$, $K^{*0}(892)\pi^+$ and $(K\pi)^{*0}_0\pi^+$ are also present in the $B^+ \to K^+\pi^-\pi^+$ signal. In addition to these, the isobar model of the charged mode includes a non-resonant, and a $\chi_c(0)K^0_S$ component. Furthermore, the signal around $m_{\pi\pi} \sim 1.5\ \mathrm{GeV}/c^2$ is described by using a $f_2(1270)K^0_S$, and a scalar denoted as $f_X(1300)K^0_S$.

Internal coherence in the treatment of $B \to K\pi\pi$ modes calls for the present analysis to use the same signal DP model as the $B^+ \to K^+\pi^-\pi^+$ BABAR analysis [23]. This appendix describes some consistency tests performed on the $B^0 \to K^0_S\pi^+\pi^-$ data sample to validate this approach.

B.1 Addition of other components to the minimal model

In principle, the isobar model should include all possible intermediate states that may contribute to the signal, but with finite available statistics only the most prominent components are actually considered, and the less significant ones are treated as systematic effects on the signal isobar model. A “minimal” signal model is then defined as composed of: $f_0(980)K^0_S$, $\rho^0(770)K^0_S$, $K^{*\pm}(892)\pi^\mp$ and $(K\pi)^{*\pm}_0\pi^\mp$.

In the *blind analysis* approach used in BABAR, the relevance of considering other intermediate states is studied, by means of "blind fits" to data. In these blind fits, only the changes in likelihood value ΔNLL, when fitting with/without one extra component, and the corresponding fitted isobar fraction FF for this extra component, are actually inspected. This ΔNLL is defined as

$$\Delta NLL = NLL_{\text{Minimal}} - NLL_{\text{Extra Comp.}} \tag{B.1}$$

where NLL_{Minimal} is the NLL value at minimum with the Minimal Model, and $NLL_{\text{Extra Comp.}}$

is the NLL at minimum when an extra component is added. This definition is such that ΔNLL is positive when the addition of an extra component improves the fit.

The criteria used to interpret these numbers are defined from toy studies, where toy datasets are generated using the minimal model, then fitted with/without a given extra component, to evaluate the expected values for ΔNLL and FF when a fake component is added to the signal model. The configuration for generating these toy datasets is as follows,

- **Signal Model ("minimal"):** $f_0(980)K_S^0$ ($FF = 16\%$), $\rho^0(770)K_S^0$ ($FF = 10\%$), $K^*(892)\pi$ ($FF = 27\%$) and $K^*(1430)\pi$ ($FF = 48\%$).
- **Yields:** 1700 signal, 19400 Continuum, 3200 $D\pi$, 1700 $J/\psi K_S^0$, 130 $\psi(2S)K_S^0$ and 1300 Generic.

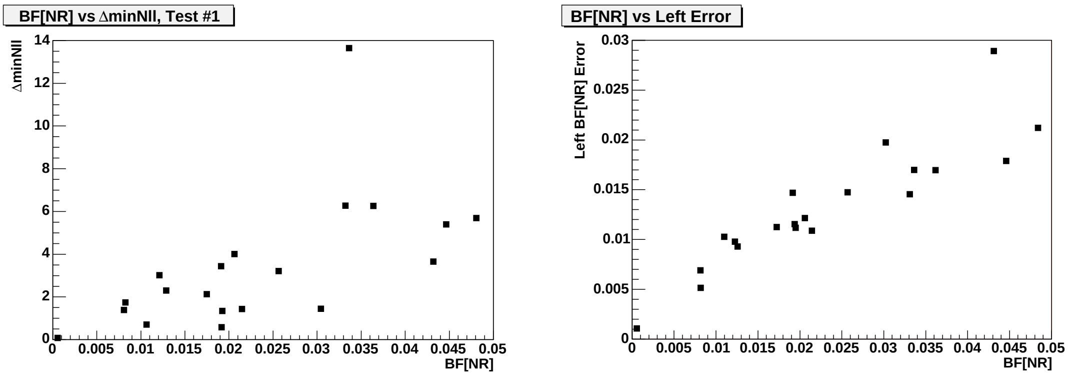

Figure B.1: *Results of including a fake component in the signal model. Datasets have been generated with the minimal model (see text), and fitted including a fake non-resonant (NR) component. On the left: NLL vs FF of the fake NR component. On the right : σ_{FF} vs FF value.*

Left plot in Fig. B.1 shows the results obtained when fitting with an extended model where a uniform non-resonant (NR) component is added to the minimal signal model. In the plot are shown the values of the ΔNLL *vs.* the fitted FF for the "fake" extra component. Similar patterns arise when adding other components. As seen in the figure, this fake component induces changes up to $\Delta NLL \sim 7-8$ likelihood units, and the fitted FF can reach values up to $\sim 5\%$. It is worth stressing that, by definition, the values of FF are biased since they are bound to be positive. Now, one observes that the significances of the fitted "fake" FF do not appreciably exceed the $\sim 1\sigma$ level (cf. right plot in Fig. B.1). The decision on declaring a component not to be significant, is based on whether its addition to the signal model in the blind fit to data follows the pattern illustrated in Fig. B.1. If it is not the case, the component is considered to have a potentially significant contribution to the signal rate, and should be considered for inclusion in the signal model.

Different components have been tested on blind fits to data. Table B.1 shows the components tested and the results. Clearly, the largest improvement in NLL comes from adding a non-resonant component to the fit. For the $m_{\pi\pi}$ mass spectrum, adding $f_2(1270)K_S^0$,

Component	$\Delta(NLL)$	FF
$f_2(1270)K^0_S$	+19.5	$\sim 3.8\%$
$f_0(1370)K^0_S$	+31.1	$\sim 4.2\%$
$\rho^0(1450)K^0_S$	+35.2	$\sim 13.1\%$
$f_0(1500)K^0_S$	+11.0	$\sim 1.6\%$
$\rho^0(1700)K^0_S$	+7.6	$\sim 2.9\%$
$K^{*\pm}_2(1430)\pi^{\mp}$	+13.7	$\sim 7.1\%$
$K^{*\pm}_0(1680)\pi^{\mp}$	+25.1	$\sim 7.7\%$
$K^{*\pm}_0(1410)\pi^{\mp}$	+18.3	$\sim 3.4\%$
$NonResonant$	+117.0	$\sim 23.6\%$

Table B.1: *List of intermediate states tested.*

$f_0(1370)K^0_S$ or $\rho^0(1450)K^0_S$ components improve the fit quality by significant amounts. For the $m_{K^0_S\pi^\pm}$ spectrum, adding the components $K^{*\pm}_2(1430)\pi^\mp$, $K^{*\pm}(1680)\pi^\mp$ and $K^{*\pm}(1410)\pi^\mp$ also improve the fit quality.

In each case, additional tests are to be performed to complement these elements of interpretation.

B.2 Probing for a non-resonant component

The sPlot technique [31] in the center of the DP has been performed, in order to test for a non-resonant (NR) component. A fit to the events in the center of the DP is performed, using only m_{ES} and ΔE variables with the following configuration,

- The DP center is defined as $m_{\pi^\pm K^0_S} > 2.0\ \mathrm{GeV}/c^2$ and $m_{\pi^+\pi^-} > 2.0\ \mathrm{GeV}/c^2$ (see left hand plot of Fig. B.2).
- The $J/\psi K^0_S$ and $\psi(2S)K^0_S$ have been cut by vetoing the $3.07 < m_{\pi^+\pi^-} < 3.12\ \mathrm{GeV}/c^2$ and $3.67 < m_{\pi^+\pi^-} < 3.705\ \mathrm{GeV}/c^2$ bands.
- The fit assumes the sample is composed of three species: signal (mostly NR if this component were present), continuum and B background.
- No cut on the NN is made nor is the NN used in the fit, due to its correlation with the DP for the continuum: when approaching the DP center, the continuum NN shape becomes more and more twisted towards higher values, i.e. the discrimination with respect to signal decreases.
- The signal PDF is the same as in the nominal fit, with its parameters fixed. The same holds for the continuum PDF, with the Argus parameter floated. For the B background a 2D Keys histogram is used, built from generic MC (see right hand plot of Fig. B.2).
- With just these two variables, using the nominal, tight m_{ES} and ΔE window (cf. Sec. 5.7), the discrimination among species would be too low, and the fit would obtain

excessive correlations between signal and background yields. The window is thus enlarged to $5.25 < m_{ES} < 5.288\ \mathrm{GeV}/c^2$ and $|\Delta E| < 100\ \mathrm{MeV}$; nevertheless, a high anticorrelation of -85% between signal and B background remains.

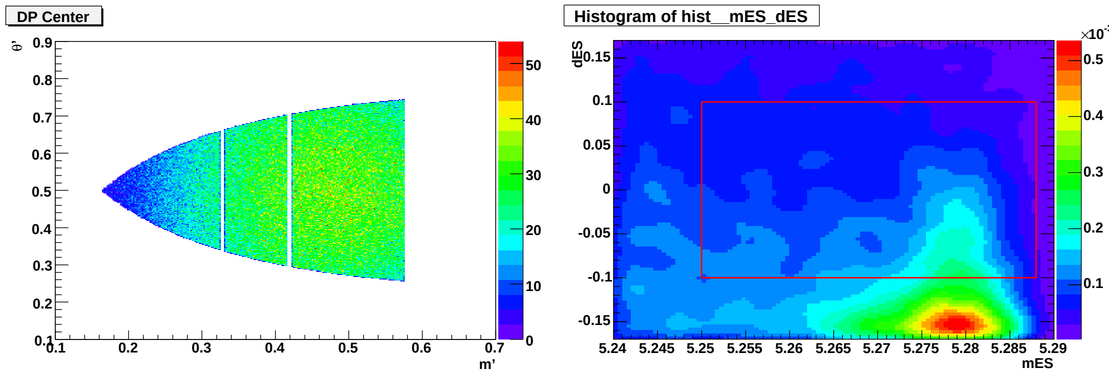

Figure B.2: *On the left: definition of the DP center used for the sPlot study. On the right:* m_{ES} *and* ΔE *B-background PDF used for the fit to yields. The PDF is a 2D Keys histogram constructed from generic MC. The red rectangle represents the* m_{ES} *and* ΔE *fit region.*

The results on the fit to yields are shown in Fig. B.3 and on Table B.2. The sPlots for the NN variable are shown in Fig. B.4. Superimposed to the signal and continuum sPlots are the NN distributions for non-resonant MC and off-peak, respectively, which are normalized to the expected number of events in the center of the DP.

Inspection of Figs. B.3 suggests the presence of a significant rate of B events in the DP center; the sPlots in Fig. B.4 suggest to interpret these events as signal events. With both statements taken together, there is evidence for signal in the center of the DP. Such signal can only originate from a non-resonant component. This component is then added to the signal DP model, the parameterization being the same as in [23].

Yield	Fitted value
Signal	175 ± 29
Continuum	6036 ± 185
B Generic	354 ± 175
Signal - B generic correlation	-85%

Table B.2: *Results for the fit to yields, performed in DP center using only* m_{ES} *and* ΔE.

B.3 Probing the signal around $\mathbf{m}_{\pi\pi} \sim \mathbf{1.5}\ \mathrm{GeV}/\mathbf{c}^{\mathbf{2}}$

Previous analyses [23, 24, 42] have observed prominent signal rates in the $m_{\pi\pi}$ mass spectrum located around $\sim 1.5\ \mathrm{GeV}/c^2$. In the charged mode, this signal is described with

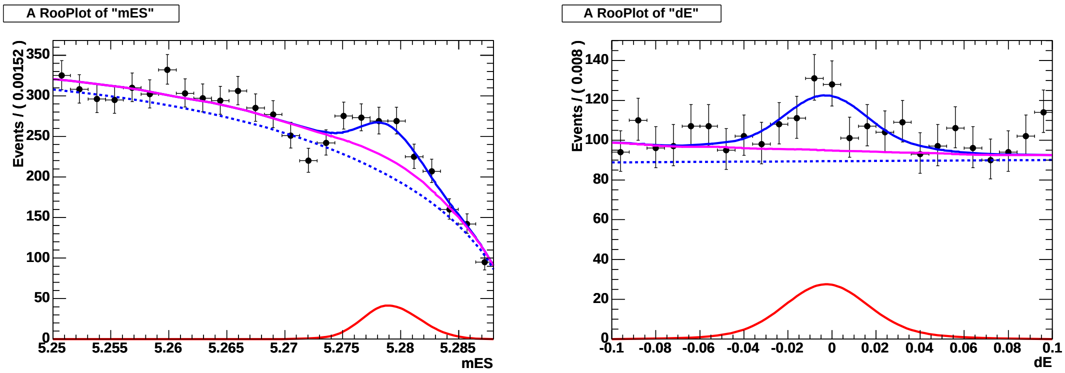

Figure B.3: m_{ES} *(left) and* ΔE *(right) projections for fit to yields in the DP center. Black dots are data. The dashed blue, magenta and red curves are the continuum, continuum+B-background and signal PDFs, respectively. For the* ΔE *projection an additional cut in* m_{ES} *have been applied to enhance the Signal/Background ratio.*

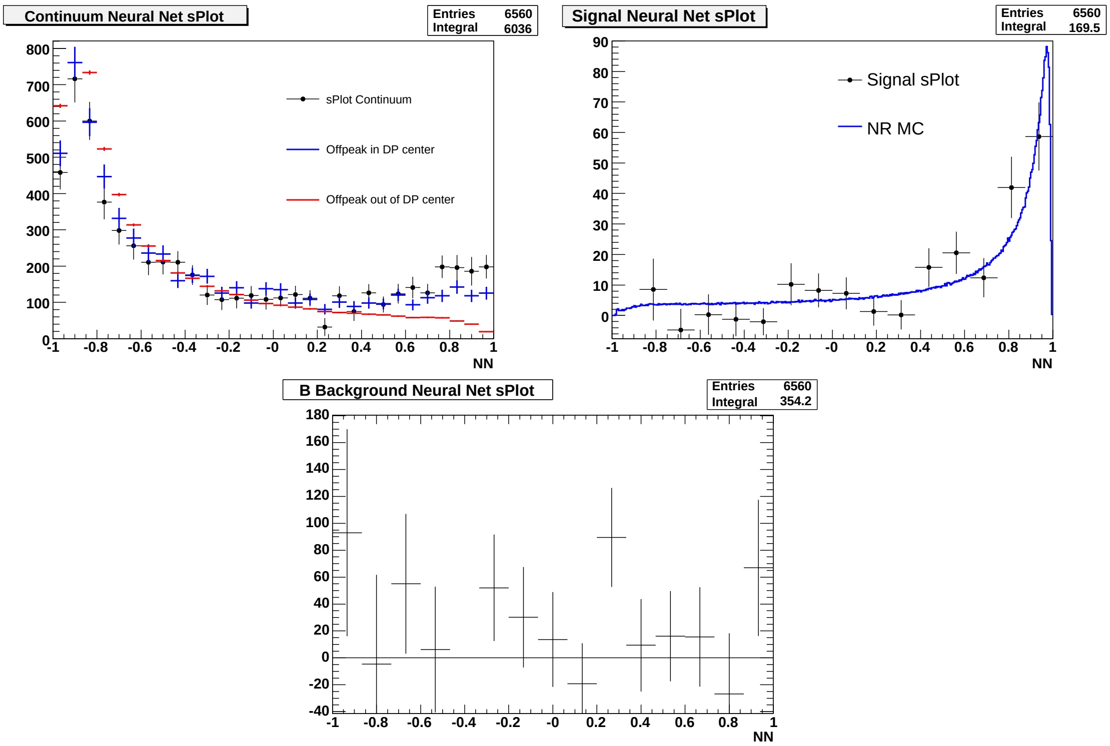

Figure B.4: NN *sPlot in the DP center for continuum (upper left), Signal (upper right) and B-background (lower). The blue/red points in the continuum sPlot are the offpeak in/out the DP center. For the Signal the blue line is non-resonant MC.*

two resonant components: the $f_2(1270)$ tensor, and a scalar denoted as $f_X(1300)$. This $f_X(1300)$ is modeled with a Relativistic Breit-Wigner lineshape, with fitted mass and width of $(1449\pm13)\ \mathrm{MeV}/c^2$ and $(129\pm25)\ \mathrm{MeV}/c^2$, respectively. Data prefers a scalar $f_X(1300)$ over vector and tensor. In the present analysis, this signal excess could be the source for the large significance for the high-mass resonances tested in the blind fits.

To address this issue of signal excess in the $\pi^+\pi^-$ mass spectrum above the $f_0(890)$, blind fits to the onpeak data in a number of different configurations are performed. The now minimal configuration includes now the non-resonant amplitude. Table B.3 shows the changes in likelihood and isobar fractions for fits including additional (or replacement) resonances.

	$\Delta(NLL)$	$BFf_X(1300)$	$BFf_2(1270)$	$BF\rho^0(1450))$
Minimal+$f_X(1300)$(scalar)	0	$\sim 6.0\%$		
Minimal+$f_X(1300)$(vector)	-20	$\sim 7.6\%$		
Minimal+$f_X(1300)$(tensor)	-5	$\sim 4.6\%$		
Minimal+$f_X(1300)$(scalar)+$f_2(1270)$	+17	$\sim 3.2\%$	$\sim 2.3\%$	
Minimal+$f_X(1300)$(vector)+$f_2(1270)$	+10	$\sim 8.1\%$	$\sim 1.6\%$	
Minimal+$f_X(1300)$+$\rho^0(1450))$ + $f_2(1270)$	+23	$\sim 6.5\%$	$\sim 1.6\%$	$\sim 2.1\%$
$\rho^0(1450)$ + $f_2(1270)$ (no $f_X(1300)$)	-5		$\sim 0.7\%$	$\sim 8.3\%$
$f_0(1500)$ instead of $f_X(1300)$	-3	$\sim 3.1\%$		
$f_0(1500)$ + $f_2(1270)$	+11	$\sim 5.0\%$	$\sim 1.8\%$	
$f_0(1500)$ + $f_2(1270)$+$\rho^0(1450)$	+16	$\sim 3.1\%$	$\sim 1.4\%$	$\sim 8.4\%$

Table B.3: *List of intermediate states being tested.*

A few conclusions can be drawn from these results:

- the data slightly prefers the $f_X(1300)$ (as in the charged $B^+ \to K^+\pi^-\pi^+$ analyses) to the $f_0(1500)$ (as in the three-kaon $B^+ \to K^+K^-K^+$ and $B^0 \to K_SK^+K^-$ analyses).
- there is a further improvement in the fit with the inclusion of an $f_2(1270)$,
- the improvement with the inclusion of a $\rho^0(1450)$ is less significant,
- even including $\rho^0(1450)$ and $f_2(1700)$ and excluding $f_X(1300)$, there is still significant improvement by adding the $f_X(1300)$ alone,
- for the $f_X(1300)$, data slightly prefers the scalar over the vector or the tensor.

In addition to these studies in likelihood changes, two-dimensional scans on the mass and width of the $f_X(1300)$ component have been performed. For these scans, the signal model contains both $f_2(1270)$, and the $f_X(1300)$ (scalar) components. Fig. B.5 shows the one-dimensional scan for the mass and the width. The best mass and width values are found to be $\sim 1450\ \mathrm{MeV}/c^2$ and $\sim 80\ \mathrm{MeV}/c^2$, respectively, which are consistent with the Belle $B^0 \to K^0_S\pi^+\pi^-$ result [42] within 2.2σ level, statistical-only.

B.4 Probing the $m_{K_S\pi}$ spectrum above $\sim 1.5\ \mathrm{GeV}/c^2$

For the $m_{K^0_S\pi^\pm}$ spectrum, adding the components $K_2^{*\pm}(1430)\pi^\mp$, $K^{*\pm}(1680)\pi^\mp$ and $K^{*\pm}(1410)\pi^\mp$ also improve the fit quality significantly. The issue here is that the significance of these additions could be due to imperfections on the parameterization of the $K\pi$ S-wave,

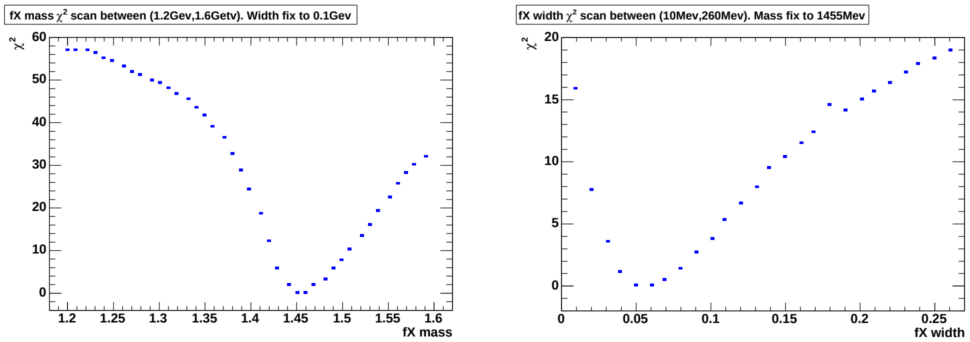

Figure B.5: *One-dimensional likelihood scans on the* $f_X(1300)$ *mass (left) and width (right), where the signal model is composed of the minimal model, the* $f_2(1270)$*, and the* $f_X(1300)$ *(scalar) component.*

and/or to correlations with the $m_{\pi\pi}$ spectrum and the non-resonant component. Since the isobar model for the charged mode did not include any additional $m_{K^0_S\pi^\pm}$ resonance, the same approach is followed in this analysis. A further, a posteriori, justification is provided by the good agreement of the isobar model with data, in the projections of the $m_{K^0_S\pi^\pm}$ spectra (see Sec. 7.1.2).

B.5 Summary

As the tests performed on data suggest, a non-resonant component is added to the signal model to describe signal events in the center of the DP. Also, the $f_2(1270)$ and the scalar $f_X(1300)$, are used to describe the signal excess seen on the high $m_{\pi\pi}$ mas spectrum. In addition, the $\chi_c(0)K^0_S$ is also included, as in the *BABAR* $B^+ \to K^+\pi^-\pi^+$ analysis [23]. When including these last components to the signal model, a likelihood change of ~ 45 NLL units is found. The nominal signal model includes these resonances. As a last check, additional components are added to the nominal signal model one-by-one; the results are shown on Table B.4. None of these components appears to be significant, with maybe the expection of the $\rho^0(1450)$. As described in Sec.7.3, this last one is an important contribution in the evaluation of signal model systematics.

Component	$\Delta(NLL)$	$BF(\%)$
$f_0(1710)K^0_S$	+2.5	1.0 ± 0.7
$\rho^0(1450)K^0_S$	+14.0	7.2 ± 1.7
$\rho^0(1700)K^0_S$	+1.6	0.5 ± 0.4
$K^*(1680)$	+6.7	2.6 ± 1.0
$\chi_c(2)$	-0.3	0.02 ± 0.02

Table B.4: *List of additional intermediate states tested with the nominal signal model.*

Appendix C

List of Fixed Parameters in the Nominal Fit

The list of fixed parameters in the nominal fit can be seen in the Tables C.1, C.2 and C.3 (the lineshape parameters have been already described in the Chapter 2, and given on Tables 2.3 and 2.4).

Parameter	**Value**
Neutral Generic Yield	114 ± 6
Charged Generic Yield	282 ± 10
$a_1^+\pi^-$ Yield	7.3 ± 0.7
BBkg Category 1 Yield	43.8 ± 2.5
BBkg Category 2 Yield	281 ± 20
BBkg Category 2 Yield	34.5 ± 4.6
$D^+\pi^-$ A_{CP} Parameter	0.0 ± 0.04
$J/\psi K_S^0$ C Parameter	0.0 ± 0.03
$J/\psi K_S^0$ S Parameter	0.668 ± 0.026
$\eta' K_S^0$ C Parameter	-0.09 ± 0.06
$\eta' K_S^0$ S Parameter	0.61 ± 0.07
Neutral Generic C Parameter	0.0 ± 0.6
Neutral Generic S Parameter	0.0 ± 0.6
Neutral Generic A_{CP} Parameter	0.0 ± 0.6
Neutral Generic ΔC Parameter	0.0 ± 0.6
Neutral Generic ΔS Parameter	0.0 ± 0.6
$\psi(2S)K_S^0$ C Parameter	0.14 ± 0.09
$\psi(2S)K_S^0$ S Parameter	0.95 ± 0.13
$a_1^+\pi^-$ C Parameter	-0.1 ± 0.17
$a_1^+\pi^-$ S Parameter	0.37 ± 0.22
$a_1^+\pi^-$ A_{CP} Parameter	-0.07 ± 0.07
$a_1^+\pi^-$ ΔC Parameter	0.26 ± 0.17
$a_1^+\pi^-$ ΔS Parameter	-0.14 ± 0.22
BBkg Category 1 A_{CP} Parameter	0.0 ± 0.1
BBkg Category 2 A_{CP} Parameter	0.0 ± 0.04
BBkg Category 3 A_{CP} Parameter	0.0 ± 0.12
Charged Generic Charge Asymmetry	0.0 ± 0.6

Table C.1: *List of fixed parameters in the fit. The errors are World Average error on parameter, when available, or a conservative estimate when measurement is available.*

Parameter	**Value**
SCF fraction cat. Lepton	$(2.4 \pm 1.1)\%$
SCF fraction cat. Kaon1	$(4.0 \pm 1.0)\%$
SCF fraction cat. Kaon2	$(4.0 \pm 1.0)\%$
SCF fraction cat. Pion	$(4.6 \pm 1.2)\%$
SCF fraction cat. Kaon1Pion	$(3.7 \pm 1.1)\%$
SCF fraction cat. Other	$(4.7 \pm 1.5)\%$
SCF fraction cat. NoTag	$(4.6 \pm 0.9)\%$
signal B^0 life time τ	1.537 ± 0.008
signal B^0 oscillation frequency Δm	0.502 ± 0.004
Neutral BBkg B^0 life time τ	1.537 ± 0.008
Neutral BBkg B^0 oscillation frequency Δm	0.502 ± 0.004
CombRgmean1 (ΔE SCF parameter)	0.0002 ± 0.0140
CombRgwidth1 (ΔE SCF parameter)	0.10 ± 0.02
tagging efficiency cat. Lepton	$(8.7 \pm 0.1)\%$
tagging efficiency cat. Kaon1	$(11.0 \pm 0.1)\%$
tagging efficiency cat. Kaon2	$(17.2 \pm 0.1)\%$
tagging efficiency cat. Pion	$(14.3 \pm 0.1)\%$
tagging efficiency cat. KaonPion	$(13.8 \pm 0.1)\%$
tagging efficiency cat. Other	$(9.6 \pm 0.1)\%$
$\omega[Lepton]$	0.028 ± 0.004
$\omega[Kaon1]$	0.056 ± 0.005
$\omega[Kaon2]$	0.150 ± 0.005
$\omega[Pion]$	0.326 ± 0.006
$\omega[KaonPion]$	0.231 ± 0.006
$\omega[Other]$	0.418 ± 0.008
$\Delta\omega[Lepton]$	-0.0002 ± 0.008
$\Delta\omega[Kaon1]$	-0.008 ± 0.009
$\Delta\omega[Kaon2]$	-0.002 ± 0.008
$\Delta\omega[Pion]$	0.06 ± 0.01
$\Delta\omega[KaonPion]$	-0.029 ± 0.01
$\Delta\omega[Other]$	0.054 ± 0.012

Table C.2: *List of fixed parameters in the fit. The errors are World Average error on parameter, when available, or a conservative estimate when measurement is available.*

Parameter	**Value**
f_{core} signal Δt resolution	0.895 ± 0.001
s^b_{core} cat. $Lepton$ signal Δt resolution	-0.07 ± 0.05
s^b_{core} cat. $Kaon1$ signal Δt resolution	-0.14 ± 0.04
s^b_{core} cat. $Kaon2$ signal Δt resolution	-0.21 ± 0.04
s^b_{core} cat. $Pion$ signal Δt resolution	-0.21 ± 0.04
s^b_{core} cat. $KaonPion$ signal Δt resolution	-0.18 ± 0.04
s^b_{core} cat. $Other$ signal Δt resolution	-0.17 ± 0.04
s^b_{core} cat. $NoTag$ signal Δt resolution	-0.21 ± 0.03
s^σ_{core} signal Δt resolution	1.104 ± 0.004
s^b_{tail} signal Δt resolution	-1.264 ± 0.005
s^σ_{tail} signal Δt resolution	3.0 ± 0.1
s^b_{out} signal Δt resolution	$0.$
s^σ_{out} signal Δt resolution	0.005 ± 0.008
f_{core} BBkg Δt resolution	0.730 ± 0.017
s^b_{core} cat. $Lepton$ BBkg Δt resolution	0.15 ± 0.07
s^b_{core} cat. $Kaon1$ BBkg Δt resolution	0.11 ± 0.07
s^b_{core} cat. $Kaon2$ BBkg Δt resolution	-0.11 ± 0.05
s^b_{core} cat. $Pion$ BBkg Δt resolution	-0.18 ± 0.05
s^b_{core} cat. $KaonPion$ BBkg Δt resolution	-0.15 ± 0.05
s^b_{core} cat. $Other$ BBkg Δt resolution	-0.13 ± 0.06
s^b_{core} cat. $NoTag$ BBkg Δt resolution	-0.11 ± 0.04
s^σ_{core} BBkg Δt resolution	1.08 ± 0.04
s^b_{tail} BBkg Δt resolution	-0.6 ± 0.1
s^σ_{tail} BBkg Δt resolution	3.0
s^b_{out} BBkg Δt resolution	0.0
s^σ_{out} BBkg Δt resolution	8.0

Table C.3: *List of fixed parameters in the fit. The errors are World Average error on parameter, when available, or a conservative estimate when measurement is available.*

Bibliography

[1] J. Christenson, J. Cronin, V. Fitch, et R. Turlay, *Evidence for the 2π decay of the $K_2^0 meson$*, Phys. Rev. Lett. **13** , p.138-140 (1964).

[2] A.D. Sakharov, JETP Lett. **5**, 24 (1967).

[3] M. Kobayashi and T. Maskawa, Prog. Theor. Phys. **49**, 652 (1973).

[4] N. Cabibbo, Phys. Rev. Lett. **10** 531 (1963).

[5] D. Casadei, *Searches for Cosmic Antimatter*, arXiv:astro-ph/04055417 (2006).

[6] The ALEPH, DELPHI, L3, OPAL, SLD Collaborations, the LEP Electroweak Working Group, the SLD Electroweak and Heavy Flavor Groups, Phys. Rept. **427** (2006) 257.

[7] Y. Fukuda *et al.*, [Super-Kamiokande], Phys, Rev. Lett. **81** (1998) 1562. [arXiv:hep-ex/9807003].

[8] P. Higgs, *Broken symmetries and the masses of gauge bosons*, Phys. Rev. Lett. **13** (1964), n 16, p. 508-509.

[9] R. Barate *et al.*, *LEP Working Group for Higgs boson searches, Phys. Lett.* **B565**, 61 (2003).

[10] B. Pontecorvo, Sov. Phys. JETP **6** (1957), p. 429; Z. Maki, M. Nakagawa and S. Sakata, Prog. Theor. Phys. **28** (1962), p. 870.

[11] C. Jarlskog, Phys. Rev. Lett. **55**, 1039 (1985).

[12] L.L. Chau, W.Y. Keung, Phys. Rev. Lett. **53**, 1039 (1984).

[13] L. Wolfenstein, Phys. Rev. Lett. **51**, 1945 (1983).

[14] J. Charles *et al.* [CKMfitter Group], *CP violation and the CKM matrix: Assessing the impact of the asymmetric B factories*, Eur. Phys. J. C **41** (2005).

[15] A big part of general plots and results are available on the CKMfitter web page: http ://ckmfitter.in2p3.fr

[16] K. Lande et al., Phys. Rev., **103**:1901-1904, 1956.

[17] H. Albrecht *et al.*, Phys. Lett., **B192**:245, 1987.

[18] A. Abulencia *et al.*, Phys.Rev. Lett., **97**:062003, 2006.

[19] B. Aubert *et al.*, Phys. Rev. Lett., **98**:211802, 2007;

[20] G. C. Branco, L. Lavoura and J. P. Silva, *CP Violation*, International Series of Monographs on Physics (1999).

[21] Particle Data Group (S. Eidelman *et al.*), *Phys. Lett.* **B592**, 1 (2004), and 2007. Partial update for the 2008 edition available on http://pdg.lbl.gov/

[22] A. Einstein, B. Podolsky, and N. Rosen, *Can quantum-mechanical description of physical reality be considered complete?, Phys. Rev.* **47** 777 (1935).

[23] B. Aubert *et al.* [*BABAR*Collaboration], Phys. Rev. **D78**:012004, 2008. [arXiv:hep-ex/0803.4451]

[24] A. Garmash *et al.* [Belle Collaboration], Phys. Rev. Lett. , **96**:251803, 2006.

[25] P.F. Harrison and H.R. Quinn (Eds.), *The BABAR physics book*, SLAC-R-504, (1998).

[26] B. Aubert *et al.* [*BABAR*Collaboration], *Observation of CP violation in the* B^0 *meson system*, Phys. Rev. Lett. **87**, 091801 (2001). [arXiv:hep-ex/0107013].

[27] K. Abe *et al.* [Belle Collaboration], *Observation of large CP violation in the neutral B meson system*, Phys. Rev. Lett. **87**, 091802 (2001). [arXiv:hep-ex/0107061].

[28] The Heavy Flavor Averaging Group (HFAG), Winter 2007 averages, http://www.slac.stanford.edu/xorg/hfag/

[29] B. Aubert *et al.* [*BABAR*Collaboration], *Observation of direct CP violation in* $B^0 \to K^+\pi^-$ *decays*, Phys. Rev. Lett. **93** 131801 (2004). [arXiv:hep-ex/0407057].

[30] Y. Chao *et al.* [Belle Collaboration], *Evidence for direct CP violation in* $B^0 \to K^+\pi^-$ *decays*, Phys. Rev. Lett. **93**, 191802 (2004). [arXiv:hep-ex/0408100].

[31] M. Pivk and F. R. Le Diberder. *sPlot: A statistical tool to unfold data distributions., Nucl. Inst. Meth.* **A555**,356–369,(2005).

[32] A. Abulencia *et al.*, [CDF Collaboration], *Phys. Rev. Lett.*, **97**, 242003 (2006).

[33] B. Aubert *et al.*, [*BABAR* Collaboration], *Measurement of Branching Fractions and Bounds on the Charge Asymmetries of the Three-Body charged* B *Decays., Phys. Rev. Lett.* **91**:051801 (2003).

[34] B. Aubert *et al.*, [*BABAR* Collaboration], *An Amplitude Analysis for the decay* $B^\pm \to \pi^\pm\pi^\mp\pi^\pm$*., Phys. Rev.* D**72**:052002 (2007).

[35] B. Aubert *et al.*, [BABAR Collaboration], *Measurement of CP-violation asymmetries in $B^0 \to (\rho\pi)^0$ using a time-dependent Dalitz plot analysis.*, *Phys. Rev.* D**76**:012004 (2007).

[36] A. Kusaka *et al.*, [Belle Collaboration], *Measurement of CP Asymmetry in a Time-Dependent Dalitz Analysis of $B^0 \to (\rho\pi)^0$ and a Constraint on the Quark Mixing Matrix Angle ϕ_2. Phys. Rev. Lett.* **98**, 221602 (2007), hep-ex/0701015.

[37] B. Aubert *et al.*, [BABAR Collaboration], *Dalitz plot analysis of the decay $B^\pm \to K^\pm K^\mp K^\pm$.*, *Phys. Rev.* D**74**:032003 (2006).

[38] B. Aubert *et al.*, [BABAR Collaboration], *Measurement of CP-Violating Asymmetries in the decay $B^0 \to K^+K^-K^0$.*, *Phys. Rev. Lett.* **99**:161802 (2007).

[39] A. Garsmash *et al.*, [Belle Collaboration], *Phys. Rev.* D**75**:012006 (2007).

[40] B. Aubert *et al.*, [BABAR Collaboration], *Dalitz Plot Analysis of the Decay $B^0(\bar{B}^0) \to K^+\pi^-\pi^0$.*, *Phys. Rev.* D**78**:052005 (2008). [arXiv:hep-ex/0711.4417].

[41] B. Aubert *et al.*, [BABAR Collaboration], *Measurement of the neutral B decay Branching Fractions to $B^0 \to K^0\pi^+\pi^-$ final states and the charge asymmetry of $B^0 \to K^{*+}(892)\pi^-$.*, *Phys. Rev.* D**73**:031101 (2006).

[42] A. Garsmash *et al.*, [Belle Collaboration], *Dalitz analysis of the three-body charmless $B^0 \to K^0\pi^+\pi^-$ decay.*, *Phys. Rev.* D**75**:012006 (2007).

[43] B. Aubert *et al.*, [BABAR Collaboration], *Measurements of the Branching Fraction and CP-Violation Asymmetries in $B^0 \to f_0(980)K^0_S$.*, *Phys. Rev. Lett.* **94**:041802 (2005).

[44] K. Abe *et al.*, [Belle Collaboration], *Measurements of time-dependent CP violation in $B^0 \to \omega K^0_S$, $f_0(980)K^0_S$, $K^0_S\pi^0$ and $K^+K^-K^0_S$ decays.*, Unpublished. [arXiv:hep-ex/0609006] (2006).

[45] B. Aubert *et al.*, [BABAR Collaboration], *Measurement of the CP Asymmetry and Branching Fration of $B^0 \to \rho^0 K^0_S$ Decays.*, *Phys. Rev. Lett.* **98**:051803 (2007).

[46] H. Y. Cheng, C. K. Chua and K. C. Yang, *Charmless hadronic B decays involving scalar mesons: Implications on the nature of light scalar mesons.*, *Phys. Rev.* D**73**:014017 (2006).

[47] C. W. Chiang *et al.*, *Charmless $B \to VP$ decays using flavor symmetry.*, *Phys. Rev.* D**69**:0344001 (2004).

[48] H. Y. Cheng, C. K. Chua and A. Soni, *Effects of final-state-interactions on mixing-induced CP violation in penguin-dominated B decays.*, *Phys. Rev.* D**72**:014006 (2005).

[49] P. Sanchez, Thesis of the University of Birmingham, *Time-Dependent Dalitz-Plot Analysis of the Charmless Decay $B^0 \to K^0_S\pi^+\pi^-$ ar BABAR.*, (October 2007).

[50] G. N. Fleming, *Recoupling Effects in the Isobar Model. I. General Formalism for Three-Pion Scattering.*, *Phys. Rev.*, 134(2B):B551-B560 (1964).

[51] D. J. Herndon, P. Söding and R. J. Cashmore, *Generalized isobar model formalism.*, *Phys. Rev.* D**11** (11):3165-3182 (1975).

[52] E.P. Wigner, *Phys. Rev.* **70** (1946) 15.

[53] E.P. Wigner and L. Eisenbud, *Phys. Rev.* **72** (1947) 29.

[54] S. U. Chung *et al.*, *Partial wave analysis in the K-matrix formalism.*, *Ann. Physik.*, 4:404 (1995).

[55] W. M. Yao *et al.*, [PDG Collaboration] Journal of Physics G**33**, 1 (2006).

[56] J. D. Jackson, *Remarks on the phenomenological analysis of resonances.*, *Nuov. Cim.*, 34:1644-1666 (1964).

[57] G. J. Gounaris and J. J. Sakurai, *Phys. Rev. Lett.* **21**, 244 (1968).

[58] S. M. Flaté, *Phys. Lett.*, B**63**:224 (1976).

[59] M. Ablikim *et al.*, [BES Collaboration], *Phys. Lett.* B**607**:243-253 (2005).

[60] W. M. Dunwoodie, Private communication.

[61] D. V. Bugg, *Phys. Lett.* D**572**:1-7 (2003).

[62] P. Estabrooks, *Phys. Rev.* D**19** (1979) 2678 .

[63] D. Aston *et al.*, *Nucl. Phys.* **B296** (1988) 493.

[64] J. Blatt and V. E. Weisskopf, *Theoretical Nuclear Physics.*, J. Willey (New York) 1952.

[65] F. von Hippel and C.Quigg, *Phys. Rev.*, D**5**, 624 (1972).

[66] D. London and R. D. Peccei, *Phys. Lett.*, B**223**, 257 (1989); M. Gronau, *Phys. Rev. Lett.* **63**, 1451 (1989); B. Grinstein, *Phys. Lett.* B**229**, 280 (1989).

[67] Y. Nir and H.R. Quinn, *Phys. Rev. Lett.* **67**, 541 (1991).

[68] M. Gronau and D. London, *Isospin Analysis of CP Asymmetries In B Decays*, *Phys. Rev. Lett.* **65**, 3381 (1990).

[69] J. Malcles, Theèse de l'Universite Paris VI - Pierre et Marie Curie, *Étude des désintegrations $B^{\pm} \to K^{\pm}\pi^0$ et $B^{\pm} \to \pi^{\pm}\pi^0$* avec le détecteur BABAR et contraints des modes $B \to \pi\pi$, $K\pi$ et KK sur la matrice CKM. (avril 2006).

[70] D. London, N. Sinha and R. Sinha, *Phys. Rev.* D**60**:074202 (1999).

[71] F. J. Botella and M. Nebot, *Phys. Rev.* D**71**:094008 (2005).

[72] R. Camacho, J. Charles, J. Ocariz and A. Pérez, in preparation.

[73] M. Pivk and F. R. Le Diberder, *Eur. Phys. J.* C**39** (2005) 397-409.

[74] M. Cuichini, M. Pierini and L. Silvestrini, *Phys. Rev.* D**74**:051301 (R) (2006).

[75] M. Gronau, D. Pirjol, A. Soni and J. Zupan, *Phys. Rev.* D**75**:014002 (2006).

[76] A. E. Snyder and H. R. Quinn, *Phys. Rev.*, D**48**, 2139 (1993).

[77] N. G. Deshpande, N. Sinha and R.Sinha, *Phys. Rev. Lett.*, **90**:061802 (2003). [arXiv:hep-ph/0207257].

[78] A. J. Buras and L. Silvestrini, *Nucl. Phys.* B **569**, 3 (2000).

[79] C. W. Bauer, I. Z. Rothstein and I.W. Stewart, arXiv:her-ph/0510241.

[80] G. Buchalla, A. J. Buras and M. E. Lautenbacher, *Rev. Mod. Phys.* **68** (1996) 1124 [arXiv:hep-ph/9512380].

[81] M.Beneke, G. Buchalla, M. Neubert, C.T. Sachrajda, *QCD factorization in* $B \to K\pi, \pi\pi$ *and extraction of Wolfenstein parameters,* Nucl.Phys. B606 p245-321 (2001). [arXiv:hep-ph/0608243].

[82] *PEPII: An asymmetric B factory, Conceptual Design Report*, SLAC-R-418, LBL-5379 (1993).

[83] B. Aubert *et al.*, [BABAR Collaboration], *The BABAR Detector*, *Nucl. Inst. Meth.* **A479**,1,(2002).

[84] P. Oddone, in *Proceedings of the UCLA Workshop: Linear Collider* $B\overline{B}$ *Factory Conceptual Design,* edited by D. Stork, World Scientific (1987), p.243.

[85] B. Aubert *et al.*, [BABAR Collaboration], *Observation of the bottomonium ground state in the decay* $\Upsilon(3S) \to \gamma\eta_b$, arXiv:0807.1086 [`hep-ex`] (2008).

[86] R. Dermisek and J. F. Gunion, *Phys. Rev. Lett.* **95**, 041801 (2005).

[87] B. Aubert *et al.*, [BABAR Collaboration], *Search for Invisible Decays of a Light Scalar in Radiative Transitions* $\Upsilon(3S) \to \gamma A^0$, arXiv:0808.0017 [`hep-ex`] (2008).

[88] C. Bozzi *et al.*, *The Babar silicon vertex tracker, Nucl. Inst. Meth.* **A 435** (1999) 24-33; C. Bozzi *et al.*, *The design and construction of the Babar silicon vertex tracker*, *Nucl. Inst. Meth.* **A 447** (2000) 15-25.

[89] A. Boucham *et al.*, *Nucl. Inst. Meth.* **A 409** (1998) 46; M. H. Kelsey *et al.*, [BABAR Collaboration], *Nucl. Inst. Meth.* **A 535** (2004) 206.

[90] P. Billoir, *Nucl. Inst. and Meth.* **A 225** (1984) 225; D. N. Brown, E. A. Charles, D. A. Riberts, *The BABAR track fitting algorithm*, *Proceedings of ICHEP 2000*, Padova, Italy, 2000.

[91] I. Adam *et al.*, [BABAR -DIRC Collaboration], *Nucl. Inst. Meth.* **A 538** (2005) 281.

[92] B. Lewandowski *et al.*„ *Nucl. Inst. Meth.* **A 494** (2002) 303.

[93] F. Anulli *et al.*, *Nucl. Phys.* **B** - Proceedings Supplements. Vol 61, Issue 3, (1998), 244-249.

[94] D. J. Lange, *The* `EvtGen` *particle decay simulation package.*, *Nucl. Inst. Meth.*, **A 462** (2001) 152-155.

[95] T. Lange, *Hight-energy physics events generation with PYTHIA 5.7 and JETSET 7.4.*, *Comp. Phys. Comm.*, **82** (1994) 74.

[96] S. Agostinelli *et al*, `GENAT4`*: A simulation toolkit.*, *Nucl. Inst. Meth.*, **A 506** (2003) 250-303.

[97] B. Hartfiel, *PID using DIRC Global Likelihoods*, BABAR Analysis Document #649 (2005). Unpublished.

[98] W. Hulsbergen, *A Kalman Filter for BABAR Decay Chain Fitting*, Internal Documentation, http://www.slac.stanford.edu/BFROOT/www/Physics/Tools/Vertex/treefitter/. Unpublished.

[99] D. Lange *et al.*, *A B Flavor tagging algorithm for CP violation measurements with the BABAR experiment.*, BABAR Analysis Document #1025 (2005). Unpublished.

[100] H. Albrecht *et al.*, [ARGUS Collaboration], *Z. Phys.* C**62**, 371 (1994).

[101] P. Gay, B. Michel, J. Proriol, and O. Deschamps, "*Tagging Higgs Bosons in Hadronic LEP-2 Events with Neural Networks.*", In Pisa 1995, New computing techniques in physics research, 725 (1995)

[102] N. Danielson *et. al*, *Background fighting in Charmless Two-body analyses*, BABAR Analysis Document #346 (2001). Unpublished.

[103] ARGUS Collaboration, H. Albrecht *et. al.*, *Z. Phys.*, **C48**:543, 1990.

[104] The RootFit Toolkit for Data Modeling:
`http://roofit.sourceforge.net/`

[105] G. Cavoto *et. al*, *Measurement of CP-violating Asymmetries in $B^0 \to \pi^+\pi^-$ and $B^0 \to K^+\pi^-$ Decays*, BABAR Analysis Document #989 (2005). Unpublished.

[106] P. Burchat *et. al*, *Supporting document of the summer 2004 $\sin 2\beta$ analysis*, BABAR Analysis Document #929 (2004). Unpublished.

[107] B. Aubert *et al.*, [BABAR Collaboration], *Study of time-dependent asymmetries and flavor oscillations in neutral B decays at the $\Upsilon(4S)$.*, *Phys. Rev.* D**66**:052003 (2002).

[108] E. Varnes *et al.*, *Measurement of the* `GoodTrackLose` *efficiency using SVT tracks.*, BABAR Analysis Document #157 (2001). Unpublished.

[109] A. telnov, A. Gritsan *$K_S^0 \to \pi^+\pi^-$ Reconstruction Efficiency in BABAR: Release-10 data vs. SP4 Monte Carlo.*, BABAR Analysis Document #677 (2003). Unpublished.

[110] C. Hearty, *Measurement of the Number of $\Upsilon(4S)$ Mesons Produced in Run-1 (B Counting),* Analysis Document #134 (2001). Unpublished.

[111] B. Aubert *et al.*, *Phys. Rev.* **D66**:032003 (2002).

[112] H. J. Lipkin, Y. Nir, H. Quinn and A. Soni, *Penguin trapping with isospin analysis and CP asymmetries in B decays.*, *Phys. Rev.* D**44**, 1454-1460 (1991).

[113] A. Höcker, H. Lacker, S. Laplace and F. Le Diberder, *Eur. Phys. J.*, C**21**, 255 (2001).

[114] J. Charles, A. Höcker, H. Lacker, S. Laplace, F.R. Le Diberder, J. Malclès, J. Ocariz, M. Pivk, L. Roos [CKMfitter Group], *Eur. Phys. J.* **C** 41, 1-131 (2005).

[115] C. P. Jessop *et al.*, *Study of charmless hadronic B meson decays to pseudoscalar vector final states.*, *Phys. Rev. Lett.* **85**, 2881-2885 (2000).

[116] B. Aubert *et al.*, [BABAR Collaboration], *Evidence for the Decay $B^\pm \to K^{*\pm}\pi^0$*, *Phys. Rev.* **D71**:111101 (2005).

[117] I. Adachi *et al.*, [Belle Collaboration], Belle BELLE-CONF-0827 (2008).

[118] B. Aubert *et al.*, [BABAR Collaboration], *Amplitude Analysis of the Decay $B^0 \to K^+\pi^-\pi^0$*, [arXiv:hep-ex/0807.4567] (2008).

[119] Bob I. Eisenstein *et al.*, [CLEO Collaboration], *Phys. Rev.* **D68**:017101 (2003).

[120] B. Aubert *et al.*, [BABAR Collaboration], *Branching fraction measurements of charged B decays to $K^{*+}K^+K^-$, $K^{*+}\pi^+K^-$, $K^{*+}K^+\pi^-$ and $K^{*+}\pi^+\pi^-$ final states.*, *Phys. Rev.* **D74**:051104 (2006).

[121] P. Chang *et al.*, [Belle Collaboration], *Observation of the decays $B^0 \to K^+\pi^-\pi^0$ and $B^0 \to \rho^-K^+$.*, *Phys.Lett.* **B599**:148-158 (2004).

[122] E. Eckhart *et al.*, [CLEO Collaboration], *Phys. Rev. Lett.* 89:251801 (2002).

[123] B. Aubert *et al.*, [BABAR Collaboration], *Time-dependent Dalitz Plot Analysis of $B^0 \to K_S^0\pi^+\pi^-$.*, [arXiv:hep-ex/0708.2097] (2007).

[124] `CKM 2008` preliminary.

[125] D. M. Asner *et al.*, [CLEO Collaboration], *Phys. Rev.* **D53**:1039-1050 (1996).

[126] Q. Chang, X. Li and Y. Yang, *Revisiting $B \to K\pi$, $K^*\pi$ and ρK decays: CP violations and implication for New Physics*, arXiv:hep-ph/0807.4295.

[127] Q. Chang, X. Li and Y. Yang, *Revisiting $B \to K\pi$, $K^*\pi$ and ρK decays: CP violations and implication for New Physics*, arXiv:hep-ph/0807.4295.

[128] K. S. Crammer, *Kernel Estimation of Parameterization of Discriminant Variabel Distributions*, ALEPH 99-144 (1999) (see also http://www-wisconsin.cern.ch/ crammer/keys.html).

[129] E. Noether, *Invariance variations problem*, Nachr. v. d.Ges D. Wiss. zu Göttingen , p235-257 (1918).

[130] W. Pauli, *Exclusion Principle, Lorentz Group and Reflexion of Space-Time and Charge,* New York, Mc Graw-Hill (1955).

[131] G. Lüders, *Proof of the TCP theorem*, Ann. Phys. **2** , p.1 (1957).

[132] T. Lee at C. Yang, Phys. Rev. **104** , p.254, (1956).

[133] C. Wu, E. Ambler, R. Hayward, D. Hoppes et R. Hudson, *Experimental test of parity conservation in beta decays*, Phys. Rev. **105** , p.1413-1414 (1957).

[134] R.L. Garwin *et al.*, Phys. Rev. **105**, 1415-1417 (1957); J.I. Friedman and V.L. Telegdi, Phys. Rev. **106**, 1290-1293 (1957).

[135] V. Fanti *et al.* [NA48 Collaboration], *A new measurement of direct CP violation in two pion decays of the neutral kaon*, Phys. Lett. B **465** 335 (1999). [arXiv:hep-ex/9909022].

[136] The KLOE collaboration *et al.* JHEP12(2006)011.

[137] C.A. Baker *et al.*, Phys. Rev. Lett. **97**:131801, 2006.

[138] S. Gjesdal *et al.*, Phys. Lett. **52B**, 113 (1974); S. Bennett *et al.*, Phys. Rev. Lett. **19**, 993 (1967); D. Drftan *et al.*, Phys. Rev. Lett. **19**, 987 (1987).

[139] M. Gronau and D. Wyler, *Phys. Lett.* **265B**, 172 (1991).

[140] M. Gronau and D. London, *Phys. Lett.* **253B**, 483 (1991).

[141] D. Atwood, I.Dunietz and A. Soni, *Phys. Rev. Lett.* **78**, 3257-3260 (1997).

[142] A. Giri, Y. Grossman, A. Soffer and J. Zupan, eConf **C0304052** (2003); *Phys. Rev.* D**68**: 054018 (2003).

[143] M. Gronau and D. London, *Phys. Lett.* D**55**, 2845 (1997).

[144] Y. Nir and D. Silverman, *Nucl. Phys.* D**B345**, 301 (1990).

[145] A.J. Buras and R. Fleischer, *Eur. Phys. J.* **C11**, 93 (1999).

[146] M. Neubert and J.L. Rosner, *Phys. Lett.* B**441**, 403 (1998); *Phys. Rev. Lett.* **81**, 5076 (1998).

[147] M. Gronau, D. Pirjol and T. M. Yan, *Phys. Rev.* D**60**, 034021 (1999); Erratum-ibid. D**69**, 119901 (2004).

[148] G. Buchalla, A.J. Buras and M.E. Lautenbacher, *Rev. Mod. Phys.* **68**, 1125 (1996).

[149] J. Charles, Thèse de l'Université Paris-Sud, April 1999, LPT-Orsay 99-31;
available at http://www.tel.ccsd.cnrs.fr (ID 00002502).

[150] M. Ciuchinni, G. D'Agostini, E. Fraco, V. Lubicz, G. Martineli, F. Parodi, R. Roudeau and A. Stocchi, *J. High Energy Physics.*, **0107**, 013 (2001).

[151] B. Aubert *et al.*, [BABAR Collaboration], *Phys. Rev. Lett.* **95**:121802 (2005).

Abstract

A time-dependent amplitude analysis of $B^0 \rightarrow K^0_S\pi^+\pi^-$ decays is performed to extract the CP violation parameters of $f_0(980)K^0_S$ and $\rho^0(770)K^0_S$, and direct CP asymmetries of $K^*(892)^{\pm}\pi^{\mp}$. The results are obtained from a data sample of $(383 \pm 3) \times 10^6$ $B\bar{B}$ decays, collected with the *BABAR* detector at the PEP-II asymmetric-energy B factory at SLAC. Two solutions are found, with equivalent goodness-of-fit merits. Including systematic and Dalitz plot model uncertainties, the combined confidence interval for values of β_{eff} in B^0 decays to $f_0(980)K^0_S$ is $18^\circ < \beta_{\text{eff}} < 76^\circ$ (at 95% C.L.); CP conservation in B^0 decays to $f_0(980)K^0_S$ is excluded at 3.5σ, including systematics. For B^0 decays to $\rho^0(770)K^0_S$, the combined confidence interval is $-9^\circ < \beta_{\text{eff}} < 57^\circ$ (at 95% C.L.). In decays to $K^*(892)^{\pm}\pi^{\mp}$ the measured direct CP asymmetry parameter is $A_{\text{CP}} = -0.20 \pm 0.10 \pm 0.01 \pm 0.02$. The measured phase difference between the decay amplitudes of $B^0 \rightarrow K^*(892)^+\pi^-$ and $\bar{B}^0 \rightarrow K^*(892)^-\pi^+$ excludes the $[-132^\circ : +25^\circ]$ interval (at 95% C.L.). Branching fractions and CP asymmetries are measured for all significant intermediate resonant modes.

The measurements on $\rho^0(770)K^0_S$ and $K^{*\pm}(892)\pi^{\mp}$ are used as inputs to a phenomenological analysis of $B \rightarrow K^*\pi$ and $B \rightarrow \rho K$ decays based solely on $SU(2)$ isospin symmetry. Adding external information on the CKM matrix, constraints on the hadronic parameter space are set. For $B \rightarrow K^*\pi$, the preferred intervals for color-allowed electroweak penguins are marginally compatible with theoretical expectations. The constraints on CKM parameters are dominated by theoretical uncertainties. A prospective study, based on the expected increase in precision from measurements at LHCb, and at future programs such as Super-B or Belle-upgrade, illustrates the physics potential of this approach.

Keywords:

BABAR
CP violaion
CKM matrix

Résumé

Une analyse en amplitudes dépendantes du temps des désintégrations $B^0 \to K^0_S\pi^+\pi^-$ est effectuée afin de mesurer les paramètres de violation de CP des modes $f_0(980)K^0_S$ et $\rho^0(770)K^0_S$, ainsi que l'asymétrie directe de CP pour $K^*(892)^{\pm}\pi^{\mp}$. Les résultats sont obtenus à partid d'un échantillon de $(383 \pm 3) \times 10^6$ paires $B\bar{B}$, enregistrées par le détecteur *BABAR* auprès du collisionneur asymétrique PEPII au SLAC. Deux solutions sont trouvées, avec des figures de mérite équivalentes sur la qualité de l'ajustement. En incluant les incertitudes systématiques et provenant du modèle de Dalitz utilisé, l'intervalle de confiance combiné sur β_{eff} dans le mode $f_0(980)K^0_S$ est $18^\circ < \beta_{\text{eff}} < 76^\circ$ (à 95% C.L.) ; la conservation de CP dans ce mode est exclue à 3.5 écarts standard. Pour le mode $\rho^0(770)K^0_S$, l'intervalle de confiance combiné est est $-9^\circ < \beta_{\text{eff}} < 57^\circ$ (à 95% C.L.). Pour le mode $K^*(892)^{\pm}\pi^{\mp}$, le paramètre d'asymétrie directe de CP est $A_{\text{CP}} = -0.20 \pm 0.10 \pm 0.01 \pm 0.02$. La mesure de la phase relative entre les amplitudes de désintégration $B^0 \to K^*(892)^+\pi^-$ et $\bar{B}^0 \to K^*(892)^-\pi^+$ exclut l'intervalle $[-132^\circ : +25^\circ]$ (à 95% C.L.). Les rapports d'embranchement et les asymétries directes de CP sont mesurées pour tous les modes résonants intermédiaires significatifs.

Les mesures obtenues dans les modes $\rho^0(770)K^0_S$ et $K^{*\pm}(892)\pi^{\mp}$ sont utilisées comme paramètres d'entrée dans une analyse phénoménologique des désintégrations $B \to K^*\pi$ et $B \to \rho K$, basée uniquement sur la symétrie d'isospin $SU(2)$. L'ajout d'informations extérieures sur la matrice CKM permet de poser des contraintes sur l'espace des paramètres hadroniques. Pour $B \to K^*\pi$, les intervalles obtenus sur les pingouins électrofaibles ne sont que marginalement en accord avec les attentes théoriques. Les contraintes sur la matrice CKM sont dominées par des incertitudes d'origine théorique. Une étude de prospective, utilisant les améliorations attendues sur les mesures de ces modes à LHCb, ou dans les programmes futurs tels que Super-B ou Belle-upgrade, permet d'illustrer le potentiel de physique de cette approche.

Mots clés:

BABAR
violation de CP
matrice CKM